

Transactions of the ASME®

Technical Editor
ARTHUR J. WENNERSTROM
Senior Associate Technical Editor
G. K. SEROVY
Associate Technical Editors
Advanced Energy Systems
S. I. FREEDMAN
Environmental Control
H. E. HESKETH
Fuels and Combustion Technologies
R. E. BARRETT
Gas Turbine
S. KUO
Internal Combustion Engine
K. J. SPRINGER
Nuclear Engineering
S. M. CHO
Power
R. W. PORTER

**BOARD ON
COMMUNICATIONS**
Chairman and Vice-President
K. N. REID, JR.

Members-at-Large
J. T. COKONIS
M. FRANKE
M. KUTZ
F. LANDIS
J. R. LLOYD
T. C. MIN
R. E. NICKELL
R. E. REDER
R. ROCKE
F. W. SCHMIDT
W. O. WINER

President, **R. ROSENBERG**
Executive Director,
D. L. BELDEN
Treasurer, **ROBERT A. BENNETT**

PUBLISHING STAFF
Mng. Dir., Mktg., **JOS. SANSONE**
Managing Editor,
CORNELIA MONAHAN
Sr. Production Editor,
VALERIE WINTERS
Editorial Prod. Asst.,
MARISOL ANDINO

Transactions of the ASME, Journal of
Turbomachinery (ISSN 0889-504X) is published
quarterly (Jan., Apr., July, Oct.) for \$95 per year by
The American Society of Mechanical Engineers, 345
East 47th Street, New York, NY 10017. Second-class
postage paid at New York, NY and additional
mailing offices. POSTMASTER: Send address
change to The Journal of Turbomachinery, c/o The
AMERICAN SOCIETY OF MECHANICAL
ENGINEERS, 22 Law Drive, Box 2300, Fairfield, NJ
07007-2300.

CHANGES OF ADDRESS must be received at Society
headquarters seven weeks before they are to be
effective. Please send old label and new address.

PRICES: To members, \$27.00, annually; to
nonmembers, \$95.00.

Add \$12.00 for postage to countries outside the
United States and Canada.

STATEMENT from By-Laws. The Society shall not be
responsible for statements or opinions advanced in
papers or ... printed in its publications (B 7.1, para. 3).

COPYRIGHT © 1988 by the American Society of
Mechanical Engineers. Reprints from this publication
may be made on condition that full credit be given the
TRANSACTIONS OF THE ASME—JOURNAL OF
TURBOMACHINERY, and the author, and
date of publication be stated.

INDEXED by Applied Mechanics Reviews and
Engineering Information, Inc.

Journal of Turbomachinery

Published Quarterly by The American Society of Mechanical Engineers

VOLUME 110 • NUMBER 1 • JANUARY 1988

TECHNICAL PAPERS

- 1 **Growth of Secondary Losses and Vorticity in an Axial Turbine Cascade (87-GT-114)**
D. G. Gregory-Smith, C. P. Graves, and J. A. Walsh
- 9 **The Base Pressure and Loss of a Family of Four Turbine Blades (87-GT-202)**
L. Xu and J. D. Denton
- 18 **Tip Leakage Flow in a Linear Turbine Cascade (87-GT-222)**
J. Moore and J. S. Tilton
- 27 **Modeling the Unsteady Flow in a Turbine Rotor Passage (87-GT-197)**
D. J. Doorly
- 38 **A Trace Gas Technique to Study Mixing in a Turbine Stage (87-GT-118)**
H. D. Joslyn and R. P. Dring
- 44 **The Influence of Rotation on the Heat Transfer Characteristics of Circular, Triangular, and Square-Sectioned Coolant Passages of Gas Turbine Rotor Blades (87-GT-121)**
S. P. Harasgama and W. D. Morris
- 51 **Time-Averaged Heat-Flux Distributions and Comparison With Prediction for the Teledyne 702 HP Turbine Stage (87-GT-120)**
M. G. Dunn and R. E. Chupp
- 57 **Film Cooling and Heat Transfer in Nozzles (87-GT-117)**
J. Stoll and J. Straub
- 66 **Stagnation Film Cooling and Heat Transfer, Including Its Effect Within the Hole Pattern (86-WA/HT-48)**
W. J. Mick and R. E. Mayle
- 73 **Turbulence Measurements in Turbine Blade Passages and Implications for Heat Transfer (87-GT-195)**
W. J. Priddy and F. J. Bayley
- 80 **Measurements of the Turbulent Transport of Heat and Momentum in Convexly Curved Boundary Layers: Effects of Curvature, Recovery and Free-Stream Turbulence (87-GT-199)**
J. Kim and T. W. Simon
- 88 **A Study of the Effects of Thermal Barrier Coating Surface Roughness on the Boundary Layer Characteristics of Gas Turbine Aerofoils (87-GT-223)**
R. M. Watt, J. L. Allen, N. C. Baines, J. P. Simons, and M. George
- 94 **A Review of Staggered Array Pin Fin Heat Transfer for Turbine Cooling Applications (87-GT-201)**
J. Armstrong and D. Winstanley
- 104 **Aerodynamic Design of a Power Turbine for an Aircraft Derivative Marine Gas Turbine (87-GT-9)**
Ji Guiming, Tan Zengxiang, and Zhang Mingchang
- 110 **Performance Characteristics of Two- and Three-Dimensional Impellers in Centrifugal Compressors (86-GT-154)**
H. Harada
- 115 **Analysis of Measurements in Vaned Diffusers of Centrifugal Compressors (87-GT-170)**
W. Stein and M. Rautenberg
- 122 **Swirling Impeller Flow (87-GT-19)**
H. Krain
- 129 **Blade Excitation by Broad-Band Pressure Fluctuations in a Centrifugal Compressor (87-GT-17)**
U. Haupt, M. Rautenberg, and A. N. Abdel-Hamid
- 138 **The Measurement of Boundary Layers on a Compressor Blade in Cascade: Part 2—Suction Surface Boundary Layers (87-GT-249)**
S. Deutsch and W. C. Zierke
- 146 **The Measurement of Boundary Layers on a Compressor Blade in Cascade: Part 3—Pressure Surface Boundary Layers and the Near Wake (87-GT-250)**
S. Deutsch and W. C. Zierke

TECHNICAL BRIEFS

- 153 **A Note on Spanwise Mixing**
P. W. James

ANNOUNCEMENTS

- 17 **Change of address form for subscribers**
Inside back cover Reference citation format
Outside back cover Information for authors

D. G. Gregory-Smith

School of Engineering and Applied Science,
University of Durham,
Durham, DH1 3LE, United Kingdom

C. P. Graves

Gilbert Gilkes & Gordon Ltd.,
Kendal, Cumbria, LA9 7BZ, United Kingdom

J. A. Walsh

Logica Space and Defence Systems Ltd.,
London, W1A 4SE, United Kingdom

Growth of Secondary Losses and Vorticity in an Axial Turbine Cascade

The growth of losses, secondary kinetic energy, and streamwise vorticity have been studied in a high turning rotor cascade. Negative vorticity associated with the passage vortex agreed well with predictions of classical secondary flow theory in the early part of the blade passage. However, toward the exit, the distortion of the flow by the secondary velocities rendered the predictions inaccurate. Areas of positive vorticity were associated with the feeding of loss into the bulk flow and have been related to separation lines observed by surface flow visualization.

Introduction

The term "secondary flows" is usually used to describe the transverse velocities that are generated when a shear flow is turned. In a turbine, secondary flows are generated from the endwall boundary layers on the casing or hub of the machine, and because the turning is great, the secondary flows may be large. The practical significance is the change in deflection through a blade row and the generation of secondary losses, which may amount to half the total losses through the machine.

In terms of classical secondary flow theory, e.g., Squire and Winter (1951), Hawthorne (1951, 1967), Came and Marsh (1974), and Horlock and Lakshminarayana (1973), the turning of the vorticity vector through a blade row gives a component of vorticity in the streamwise direction, thus generating transverse velocities. In the secondary flow approximation (Hawthorne, 1967), the vortex filaments are convected by a primary flow, which is undisturbed by the secondary velocities. Thus the Bernoulli surfaces (surfaces of constant total pressure) remain parallel to the endwall throughout the blade row, and are not distorted by the secondary flow. Downstream of the blade row there are three contributions to the streamwise vorticity. Firstly, there is the distributed secondary vorticity, which generates secondary velocities in the blade passage. Then there are two shed vorticities that appear in the blade wake, the trailing filament vorticity that arises from the stretching of the vortex lines as they pass around the blades, and the trailing shed vorticity that arises from the spanwise variation in circulation around the blades.

This cascade volume view (i.e., looking at only the inlet and outlet flows of the blade row) does not consider the complex details of the flow within the blade passage. These details have to be understood if an understanding of the loss generating

Table 1 Cascade design data

Flow inlet angle	42.75 deg
Blade exit angle	-67.5 deg
Blade chord	216 mm
Axial chord	175 mm
Span	457 mm
Pitch	191 mm
Aspect ratio	2.1
Reynolds number (blade chord and exit velocity)	5×10^5

Table 2 Inlet boundary layer data

Boundary layer type	Natural	Thick	Thin
Displacement thickness	12.1 mm	27.9 mm	9.7 mm
Momentum thickness	9.9 mm	19.7 mm	7.6 mm
Estimated 99 percent thickness	102 mm	150 mm	82 mm
Total pressure loss coefficient	0.084	0.175	0.054

mechanisms is to be gained. In recent years a lot of effort has been made to look at the details of endwall flows in axial turbines. These have been comprehensively reviewed by Sieverding (1985). Most of the work has been carried out using pressure probes to gain quantitative data for flow angles and total pressure losses, and using flow visualization to give qualitative information on separation lines and the formation of vortices. However little appears in the published literature on the quantitative development of streamwise vorticity that can be linked with the ideas of classical secondary flow theory. The reason for this may be the difficulty in differentiating experimental data and the fairly high resolution of data points required to get acceptable accuracy.

A program at Durham University is studying the details of secondary flows in a high turning turbine rotor blade. Some results for the flow development have been reported by Gregory-Smith and Graves (1983). This paper presents data on the development of streamwise vorticity through the blade passage and aims to relate this to the generation of loss caused by the secondary flows.

Apparatus

The turbine rotor blades were set in a linear cascade and operated at incompressible flow velocities. The cascade is

Contributed by the Gas Turbine Division of THE AMERICAN SOCIETY OF MECHANICAL ENGINEERS and presented at the 32nd International Gas Turbine Conference and Exhibit, Anaheim, California, May 31-June 4, 1987. Manuscript received at ASME Headquarters February 10, 1987. Paper No. 87-GT-114.

described in detail by Graves (1985), and Table 1 gives the main geometric parameters.

The cascade was traversed using a five-hole cobra-type probe at ten axial positions as shown in Fig. 1. In addition flow visualization was carried out on the endwall and blade surfaces using a fluorescent powder dye and light oil mixture. The above measurements were made with a "natural" inlet boundary layer. Traverses at the upstream and downstream positions were also carried out for a "thickened" and "thinned" inlet boundary layer. The features of the inlet boundary layers are summarized in Table 2.

The loss coefficient is defined with respect to the *inlet* dynamic pressure.

The measurements were recorded using a data acquisition system controlled by a microcomputer and the recorded data were transferred to a mainframe computer for analysis and plotting. The angles, velocity vectors, and pressures were obtained directly from the calibration of the five-hole probe. However the derivation of vorticity is not straightforward and is described below.

Derivation of Streamwise Vorticity

The vorticity vector Ω is defined as the curl of the velocity vector \mathbf{q}

$$\Omega = \nabla \times \mathbf{q}$$

A Cartesian coordinate system is set up as x , y , z in the axial, tangential (or pitchwise), and radial (or spanwise) directions, with velocity components u , v , and w , respectively. Thus the components of vorticity are

$$\begin{aligned}\Omega_x &= \frac{\partial w}{\partial y} - \frac{\partial v}{\partial z} \\ \Omega_y &= \frac{\partial u}{\partial z} - \frac{\partial w}{\partial x} \\ \Omega_z &= \frac{\partial v}{\partial x} - \frac{\partial u}{\partial y}\end{aligned}\quad (1)$$

In secondary flow theory, the streamwise vorticity is taken as the component of vorticity in the primary flow direction rather than the component in the local flow direction. Thus the streamwise vorticity may be taken as

$$\Omega_s = \Omega_x \cos \alpha_p + \Omega_y \sin \alpha_p \quad (2)$$

where α_p is the primary flow angle. It may be noted that the radial component Ω_z has no effect, since in a linear cascade the primary flow has no radial component by definition.

Estimation of the gradients $\partial/\partial z$ and $\partial/\partial y$ in the radial and tangential directions can be made from the data on a given transverse plane, because the spacing of data points is fairly close on each traverse plane. The axial gradient $\partial/\partial x$ is more difficult since the axial spacing is too large to allow reasonable direct estimation. An alternative is to use the incompressible Helmholtz equation

$$\mathbf{q} \times \Omega = \frac{1}{\rho} \nabla p_0 \quad \text{where } p_0 = \text{total pressure}$$

Taking the radial, or z , component

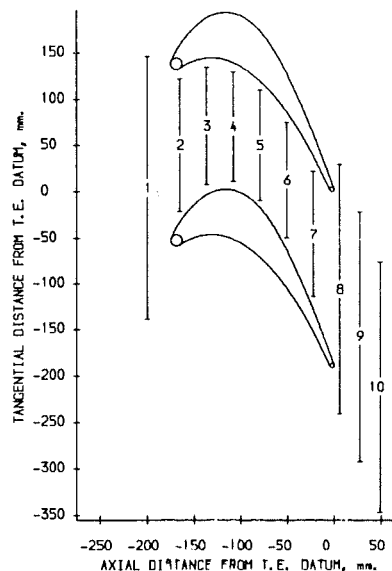


Fig. 1 Cascade design data

$$u\Omega_y - v\Omega_x = \frac{1}{\rho} \frac{\partial p_0}{\partial z}$$

Thus

$$\Omega_y = \frac{1}{u} \left[\frac{1}{\rho} \frac{\partial p_0}{\partial z} - v\Omega_x \right]$$

with Ω_x given from equation (1).

So the axial and tangential components of vorticity, required for the streamwise vorticity given by equation (2), may be found from the gradients of velocity and stagnation pressure on a given traverse plane. In this cascade, the flow at midspan was very little affected by the secondary flows on the endwalls. Thus the primary flow angle α_p in equation (2) was taken as the angle at midspan for the given tangential position. For traverse planes within the blade, the value of α_p varied considerably across the pitch, but downstream of the trailing edge α_p was fairly constant.

The differentiation of experimental data is notoriously difficult, since experimental scatter can cause unrealistic values of gradient. The approach used was to fit a least-square bicubic spline surface to the data points, and to take the gradient of the surface in the required direction at each data point coordinate. The tightness of fit of a spline is controlled by the number of interior knots, and the position and number of knots can only really be determined by inspection. With the large amounts of data, it was impractical to inspect each set, but some typical sets were inspected and the results applied generally. It was found that if the fit was made too close, the spline "wriggled" through the data. However too loose a fit would miss real characteristics of the data. The procedure finally adopted was to start with relatively few knots and compare the sum of the residuals with the variance of the data. The number of knots was progressively increased until the sum was sufficiently small. The criterion chosen was that the average residual had to be less than 5 percent of the variance. As the results show, this approach gave a reasonable picture of

Nomenclature

p_0 = total pressure
 \mathbf{q} = velocity vector
 u = velocity component in x direction

v = velocity component in z direction
 x = axial coordinate
 y = tangential or pitchwise coordinate

z = radial or spanwise coordinate
 α = flow angle in x - y plane
 ρ = density
 Ω = vorticity

the growth of streamwise vorticity through the cascade, although there are a few places where unlikely values appear.

The values of vorticity obtained were made dimensionless by using the upstream velocity and the blade chord. The choice of chord was somewhat arbitrary; other length scales such as pitch, span, or inlet boundary layer thickness could have been chosen.

Results

Surface Flow Visualization. Figures 2 and 3 show pictures of the flows on the endwall and suction surfaces. The surfaces were covered with thin plastic adhesive film before painting

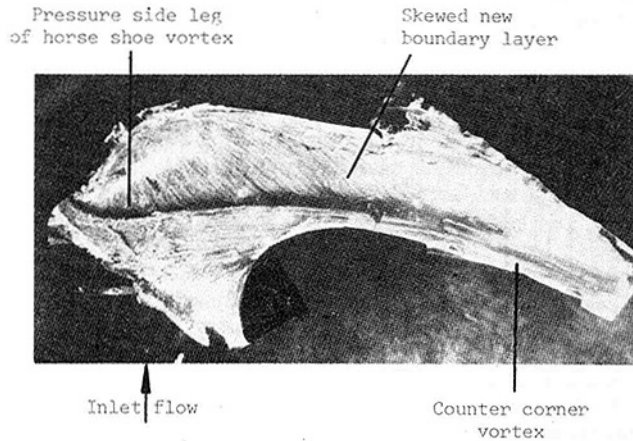


Fig. 2 Endwall flow

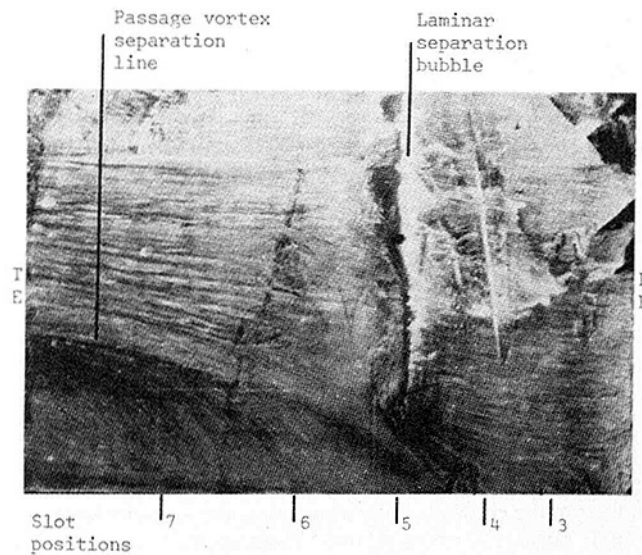


Fig. 3 Suction surface flow

with the dye and oil mixture, and the film removed for photography. The pictures were taken using ultraviolet light, which improved the contrast due to the fluorescence of the pigment. Figure 2 shows the complicated flow pattern on the endwall, with the blade profile appearing somewhat unclear due to the ragged edges of the plastic film. Most clearly shown is the cross-passage separation line between the blades due to the pressure side leg of the horseshoe vortex and the passage vortex. There are strong cross-passage flows on the downstream side of this separation that feed low-momentum fluid into the passage vortex. After meeting the suction surface the separation line follows the blade surface, but is displaced from it by a small distance. This is due to the presence of a countervortex in the suction surface and endwall corner. The picture is similar to that reported by other workers, e.g., Langston et al. (1977) and Marchal and Sieverding (1977), although the visualization did not extend sufficiently far upstream to detect the saddle point near the leading edge.

In Fig. 3, which is a developed view of the suction surface, a laminar separation bubble is clearly seen extending some 75 percent of the spanwise distance from midspan to the endwall. The separation line due to the suction surface leg of the horseshoe vortex may be seen moving up the suction surface and disappearing into the separation bubble. This is different from that observed by other workers who used a boundary layer trip to avoid the separation bubble, e.g., Marchal and Sieverding (1977). The separation line due to the passage vortex is seen to move up the suction surface as the vortex grows in size, and there is evidence of strong spanwise flows away from the endwall. Also indicated on Fig. 3 are the slot traverse positions in the second half of the blade passage; these will be referred to in the next section.

Area Plots. In Fig. 4 onward a selection of results are presented as area plots at a number of the traverse planes within the passage. The contours of vorticity and total pressure loss and the secondary velocity vectors are placed alongside each other for easy comparison. The vertical axis is the spanwise distance from the endwall. The horizontal axis is the pitchwise distance measured from a trailing edge datum and positive going from suction to pressure surface. Thus the suction surface appears on the left and the pressure surface on the right.

In Fig. 4, at slot 3 (22 percent of axial chord from the leading edge), the passage vortex has started to form, as shown by the negative vorticity near the endwall and by the velocity vectors. There is a small amount of positive vorticity near the suction surface corner, which may arise from the suction side leg of the horseshoe vortex as it reaches the suction surface. The total pressure contours are beginning to roll up under the action of the passage vortex. By slot 5, Fig. 5, the passage vortex has intensified, with high values of negative

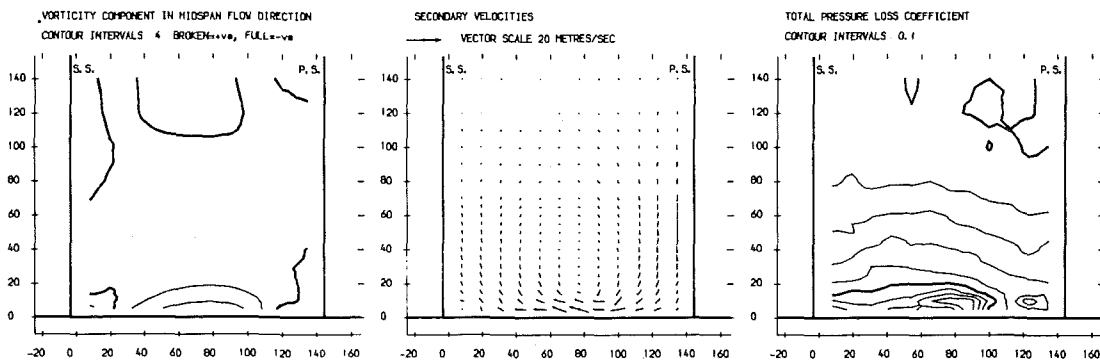


Fig. 4 Slot 3 natural inlet boundary layer

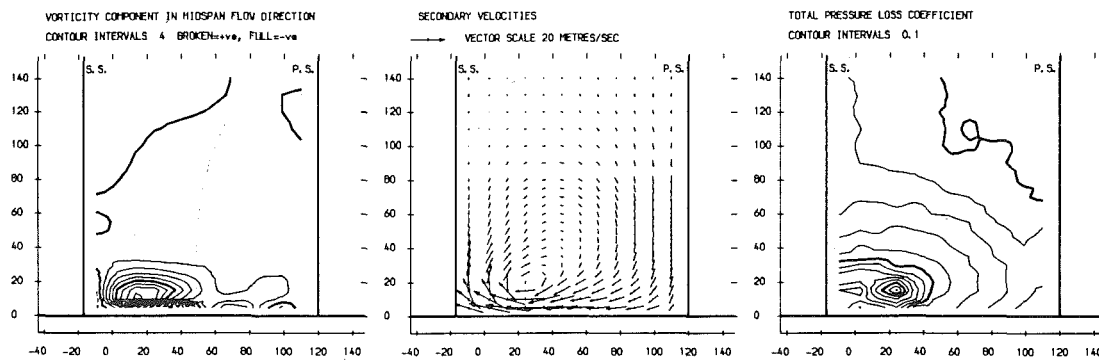


Fig. 5 Slot 5 natural inlet boundary layer

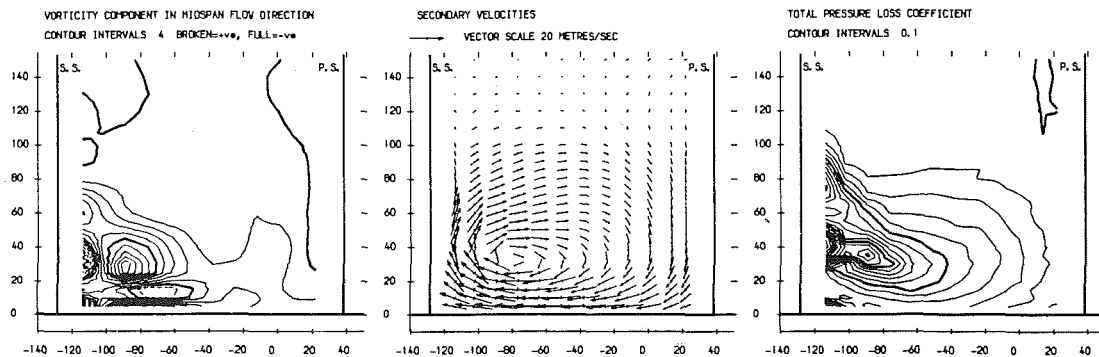


Fig. 6 Slot 7 natural inlet boundary layer

vorticity, and the vortex center has moved closer to the suction surface. There is a small area of positive vorticity in the suction surface corner, as the countervortex starts to grow. It extends some 20 mm up the suction surface to the position where the flow visualization in Fig. 3 would indicate the presence of the passage vortex separation line. However this description must be tentative because another thin area of positive vorticity is seen close to the end wall from about 10 mm to 50 mm tangential position. This may be due to the separation line on the end wall which Fig. 2 shows to be about 25 mm from the suction surface, i.e., at a tangential coordinate of 10 mm. A separation line will lead to an area of positive vorticity, but the tangential extent of this area on the endwall seems too great. It may be that the positive vorticity arises, at least in part, from poor surface fitting at the edge of the map of data points. The rolling up of the total pressure contours is quite severe with the clear formation of a loss core. There is a small region of higher loss near the suction surface at about 15 mm from the end wall. This is probably due to loss from the blade surface being fed into the bulk flow by the passage vortex separation line.

At slot 7, Fig. 6, near the trailing edge, the passage vortex dominates the scene with a large peak of negative vorticity. The secondary velocities are quite large, up to about 25 m/s compared with the exit midspan velocity of 35 m/s. Within the region of the passage vortex is enclosed a region of small positive vorticity. This is most likely due to the problems of surface fitting where there are adjacent very high values of negative vorticity. The positive vorticity in the corner vortex is quite clear, but it is now separated from a larger positive region centered at about 35 mm from the endwall. There is also a high loss peak close to the suction surface at about 40 mm from the endwall. The flow visualization in Fig. 3 shows the passage vortex separation line to be about 70 mm from the endwall at slot 7. So the region of high loss and positive vorticity is about halfway up the suction surface to the separation line. At 60 mm from the endwall, there is a peak in negative

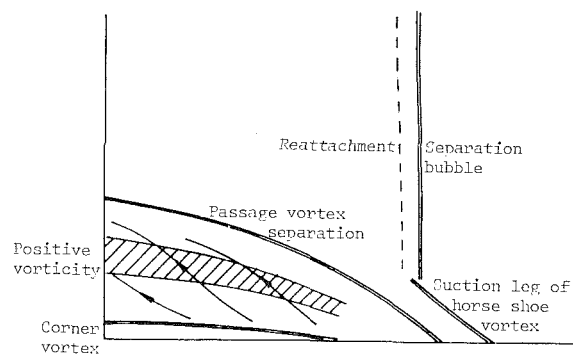


Fig. 7 Suction surface flow features

vorticity, which corresponds to the clear region on the flow visualization picture below the separation line. This line corresponds to the smaller loss peak on the suction surface at 75 mm from the endwall, while above this, the vorticity becomes weakly positive at about 90 mm. These same features are also seen at slot 6 (not shown here) with the high positive vorticity and loss peak close to the suction surface at 25 mm from the end wall, the negative peak of vorticity at 40 mm, and the separation line and smaller loss peak at 45 mm.

While it can easily be understood that a separation line must involve two areas of vorticity with opposite sign, the large positive patch of vorticity and associated loss peak, seen about halfway up the suction surface to the vortex separation line, does not correspond to any separation line on the surface flow visualization, either here or reported elsewhere. Nor is the positive vorticity clear from visual inspection of the secondary flow vectors. The clear area just below the separation line may be explained by the high negative vorticity producing a scouring action close to the blade surface. Below the clear area, the surface flow lines form an S shape, as shown in the sketch of Fig. 7. Although this is not very clear from the photograph of Fig. 3, it is shown by other photographs, and has also been

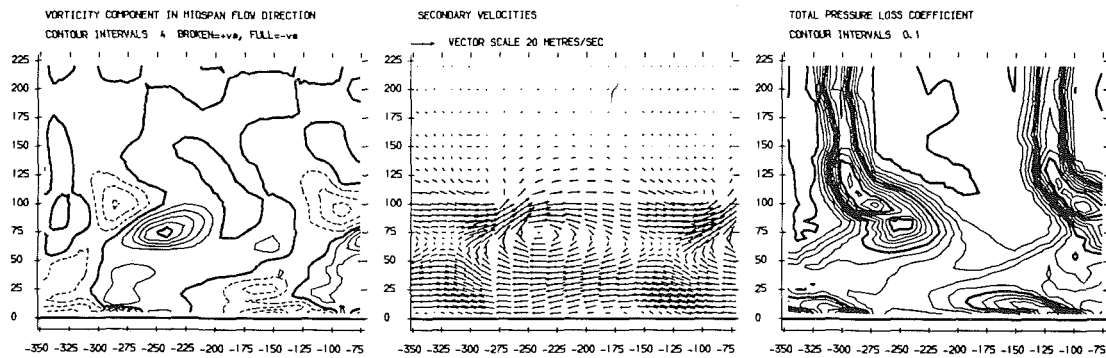


Fig. 8 Slot 10 natural inlet boundary layer

observed by other authors (e.g., Langston et al., 1977). It appears that the curving back away from the spanwise direction caused by positive vorticity is also accompanied by an accumulation of loss brought up from the blade surface. This would explain the shape of the downstream loss core picture, with relatively low loss below the core (see Fig. 8).

Figure 8 (slot 10) also shows the shed vorticity, which is positive, in the blade wakes. In classical theory terms this corresponds to the trailing filament and trailing shed vorticity. By slot 10 the wake is distorted by the under and overturning crossflows as seen in the vector plots. The results at slot 8 (not shown) just downstream of the trailing edge show the shed vorticity contained in a near-vertical wake. The shed vorticity has separated into two distinct areas. The lower one near the wall is linked with the corner vortex seen at slot 7, Fig. 6, but it contains more positive vorticity than in the corner vortex alone. The upper area seen at about 100 mm from the endwall contains the positive patch of vorticity discussed above, although convected away from the endwall by the passage vortex. The peak value of negative vorticity in the passage vortex is lower than at slot 7, due to viscous dissipation as the flow proceeds downstream. Near midspan the streamwise vorticity is close to zero, as expected, giving some confidence in the method of obtaining vorticity by surface fitting. The loss at midspan shows the two-dimensional blade wakes, with a fair level of repeatability, which was achieved by increasing the number of data points there. The blade wake runs into the loss core, with a double loss peak. Near the endwall, the loss associated with corner vortex may be seen to be located in the same region as the positive vorticity, i.e., near the endwall at about -200 mm to -100 mm tangential position.

It may be noticed that in the figures showing the vorticity the only evidence of the suction side leg of the horseshoe vortex (which gives positive vorticity) is at slot 3 close to the suction surface and endwall corner. The flow visualization in Fig. 3 shows the separation line joining the laminar separation bubble and then disappearing. Moore (1983) has shown that fluid from the suction side leg of the horseshoe vortex is convected around the outside of the passage vortex away from the suction surface. However his cascade was of lower aspect ratio so that the passage vortices from the two endwalls interacted strongly, and also the blades had a boundary layer trip. It may be that the difference in the two cascades has a large effect on the flow, but in this work no evidence is seen of the vorticity due to the suction side leg of the horseshoe vortex being convected away from the suction surface.

Pitch-Averaged Results. The data were averaged across the pitch, taking a mass mean where appropriate, e.g., for loss and crossflow velocities. Presented here is a selection of the results for yaw angle, total pressure loss coefficient and the kinetic energy of the secondary velocities (made dimensionless

with respect to inlet mainstream velocity), and the streamwise vorticity.

Results for slots 3, 5, 7, and 10 are shown in Fig. 9. At slot 3 there is small overturning of 10 deg with a corresponding generation of weak negative vorticity, the mean mainstream turning being from the nominal inlet angle of 42.75 deg to about 19 deg. The loss is similar to that shown at slot 1, just upstream of the cascade, with a small generation of secondary kinetic energy. At slot 5, the profiles of overturning and vorticity are similar to those at slot 3, but of a greater magnitude. The positive vorticity point near the endwall should probably be ignored as it is caused by the patch seen in Fig. 5 and discussed earlier. However, the secondary kinetic energy is now quite large near the wall and the loss profile shows the effect of the rolling up of the Bernoulli surfaces to form the loss core. Up to slot 5, the streamwise vorticity and yaw angle appear similar to what would be expected from secondary flow theory. However beyond slot 5, e.g., at slot 7, the distortion of the Bernoulli surfaces greatly affects the streamwise vorticity generation, which gives an uneven profile caused by the patches of positive vorticity seen in Fig. 6. The peak intensity is less, as is the magnitude of overturning, with some underturning becoming apparent. The peak secondary kinetic energy is also reduced, and the loss peak is farther away from the wall. At the downstream slot 10, the shed vorticity in the blade wakes causes two regions of pitch-averaged positive vorticity, separated by a region of negative vorticity. The yaw angle shows a sharp underturning at slot 10, and the overturning near the endwall is reduced by the effects of the corner countervortex. The secondary kinetic energy shows two peaks, corresponding to the positions of maximum overturning and underturning. The loss core peak has been convected away from the endwall, reduced in magnitude, and broadened compared with slot 7. A second peak is seen near the endwall due to the loss from the corner vortex, and at midspan the profile loss is apparent.

Effect of Inlet Boundary Layer Thickness. The flows at the downstream traverse plane, slot 10, with the thick and thin inlet boundary layer are shown in Figs. 10 and 11. These may be compared with Fig. 8 for the natural inlet boundary layer. The positions of the main features of the flow are very similar with the loss core, endwall loss region, and apparent vortex center being at nearly the same coordinate values. The main difference seems to be that as the inlet boundary layer is thickened, the features become broader and less intense. This is particularly true for the vorticity. Figure 10 shows that both the positive and negative vorticity peak values are much lower than in Fig. 11. This may be understood in terms of the inlet normal vorticity to the cascade; the thinner boundary layer will have higher vorticity values that are more concentrated near the endwall. However secondary flow theory would not predict the convection of the vorticity away from the endwall

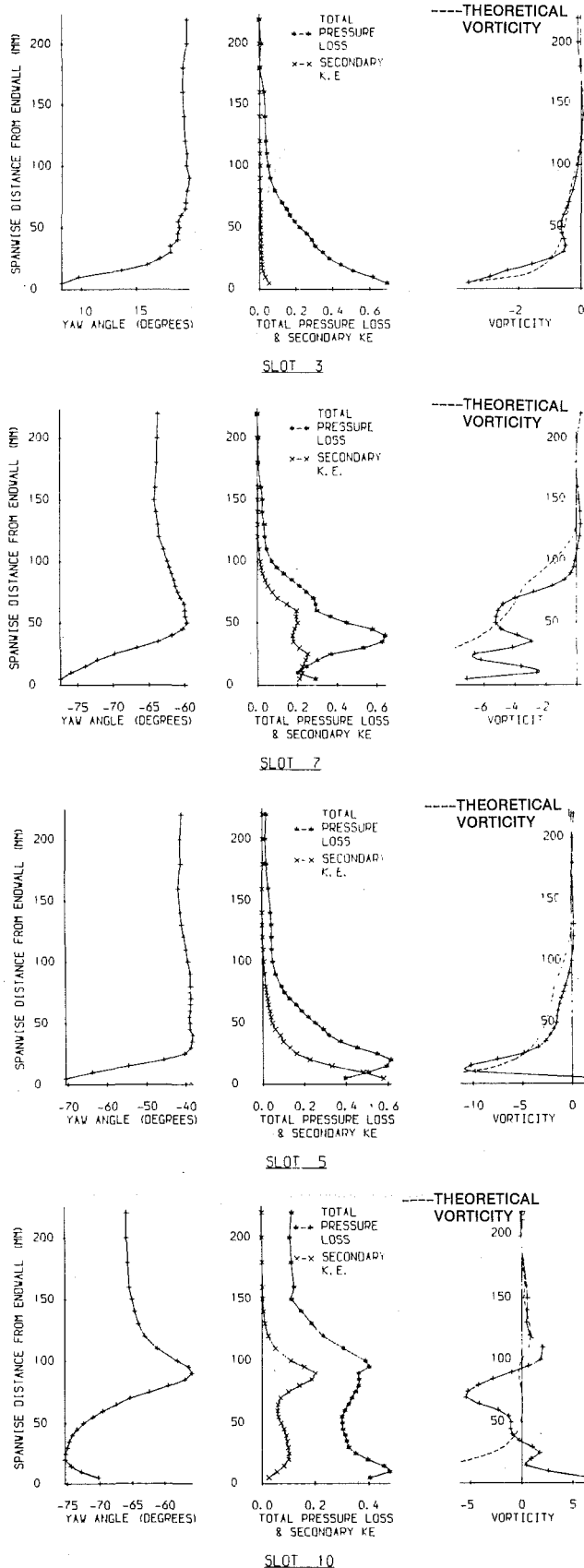


Fig. 9 Pitch-averaged results

so that the passage vortex is similarly placed irrespective of boundary layer thickness. It should be noted that even for the thin boundary layer, the ratio of thickness to blade pitch is

Table 3

Boundary layer type	Natural	Thick	Thin
Slot 10 mixed-out loss coefficient	0.294	0.413	0.298
Mixed-out profile loss	0.103	0.106	0.116
Gross secondary loss	0.191	0.307	0.182
Inlet loss	0.084	0.175	0.054
Net secondary loss	0.107	0.132	0.128

quite large (0.43) compared to most other workers (see Sieverding, 1985).

Area-Averaged Results. The growth of loss, secondary kinetic energy, and streamwise vorticity are shown in Fig. 12. The quantity concerned was mass meaned over the traverse plane for each slot, the positions of which are indicated underneath the loss curve. Upstream and downstream, the averaging was done over one pitch width, whereas the data were taken over about 1.5 pitch. The error bands shown were obtained by varying the tangential position of the pitch distance for the averaging. Some caution should be exercised for slots 8 and 9, because the data points were not sufficiently close within the blade wakes to give good definition. This explains the large error band on the loss for slot 8 and why the loss falls from slot 8 to 10. The dotted line shows a more reasonable trend, the point at slot 8 being estimated from slot 7 plus an allowance for the additional profile loss. Although the loss is suspect at slots 8 and 9, the vorticity and secondary kinetic energy seem reasonable.

The vorticity and secondary kinetic energy grow steadily through the cascade (apart from the vorticity at slot 4, which seems high). After the trailing edge the vorticity drops suddenly due to the addition of the shed vorticity in the blade wakes. The secondary kinetic energy starts to decay slowly after the trailing edge. It may be noted that this is in contrast to Moore and Adhye's (1985) results, where both the level of kinetic energy and its rate of decay were much higher. The difference may be due to the lower aspect ratio of their cascade, with interaction of the two passage vortices, such that the whole flow is dominated by secondary effect. The loss also grows steadily although it appears to increase more rapidly toward the trailing edge as loss from the blade suction surface is fed into the bulk flow. It should be noted that the traverse did not go close enough to the blades or endwall to pick up the thin boundary layers, so these results represent what is happening to the bulk flow, rather than giving the true total loss at each plane.

At the downstream plane, slot 10, the mixed-out loss values were calculated, from which the total net secondary loss may be estimated. These are shown in Table 3 along with the results for the thick and thin inlet boundary layers.

The use of mixed-out loss rather than the actual loss at the traverse plane should remove the dependence of the loss on the downstream traverse plane position, at least to some extent. There will be an increase due to shearing on the endwall, but this is likely to be small compared with the loss growth through the cascade. Table 3 shows no clear trend of net secondary loss with inlet boundary layer thickness, and this has been found by other workers, e.g., Atkins (1985).

Theoretical Comparison

The classical secondary flow theory was applied to the cascade. At exit, it was not expected to give good comparisons with experiments because of the distortion of the Bernoulli surfaces, clearly seen in the experiments. However a comparison may be made within the blade passage, at least on a pitch-averaged basis for secondary vorticity. The theoretical

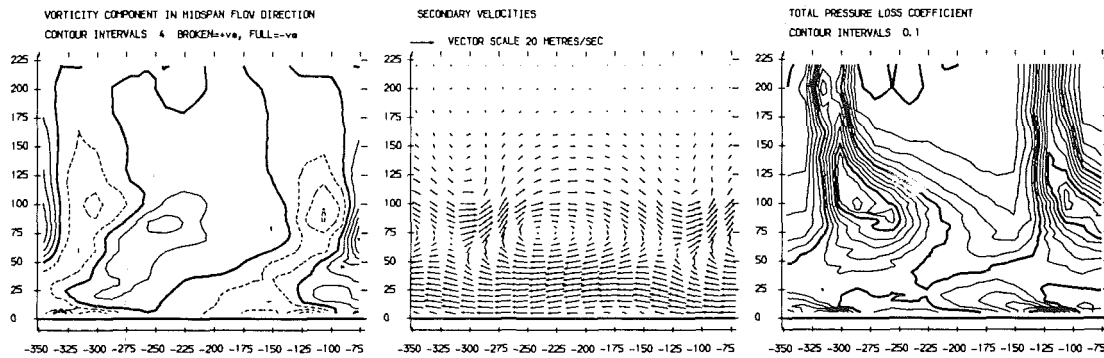


Fig. 10 Slot 10 thick inlet boundary layer

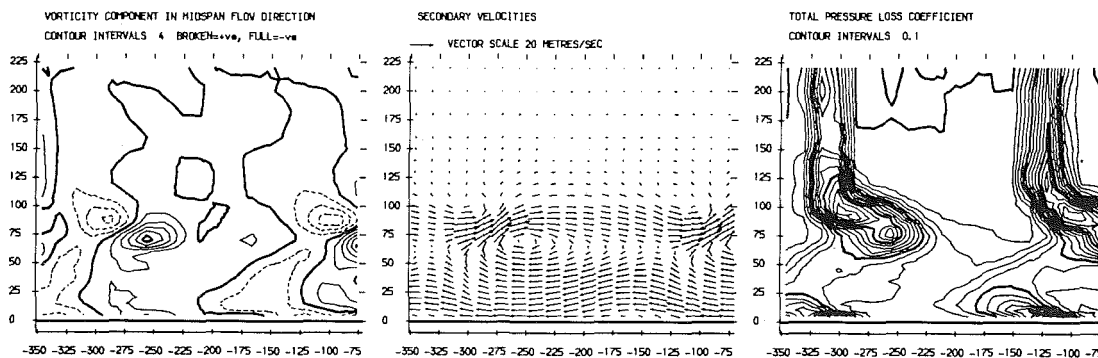


Fig. 11 Slot 10 thin inlet boundary layer

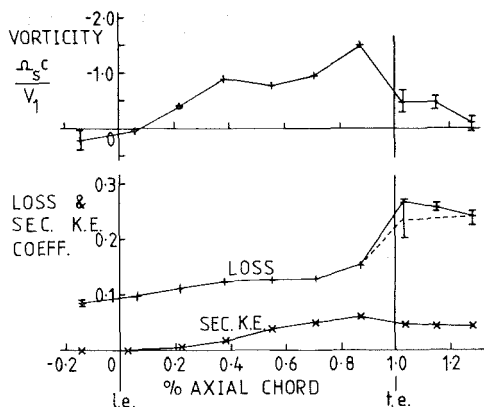


Fig. 12 Area-averaged loss, secondary kinetic energy, and vorticity

prediction was made by using the Came and Marsh (1974) formula taking the turning angle from the pitch-averaged yaw angle at the slot traverse position concerned. Figure 9 also shows the theoretical results for slots 3, 5, 7, and 10. For slot 10, the theoretical prediction includes the blade shed vorticity components. The theoretical prediction derived the inlet normal vorticity from a power law inlet boundary layer profile of thickness 102 mm and exponent 0.149. Since a power law profile gives a discontinuity in slope at the boundary layer edge, some smoothing was done between 80 mm and 120 mm.

At slot 3, the agreement is very good, but by slot 5, the vorticity is predicted too high beyond 25 mm. At slot 7, the vorticity is predicted much too high near the end wall, while at slot 10, the prediction seems to bear little relation to the experiment. There seems to be a progressive deterioration beyond slot 5, which accords with the observation of the rolling up of the total pressure contours from slot 5 onward. The action of the secondary flows produces this distortion, and also produces a convection of itself away from the endwall.

There is no mechanism for this in the theory. Thus at slot 7 the agreement away from the endwall is probably rather fortuitous; the overprediction of vorticity due to not taking the Bernoulli surface twisting into account has been balanced by the outward convection of vorticity by the secondary flows. At slot 10, this outward convection is clear with the negative peak at around 70 mm from the wall. In addition the effects of viscosity are evident close to the wall, with the positive vorticity arising from a combination of the corner vortex and shed vorticity.

The above observations suggest that some modification to the theoretical method might be made to account for the Bernoulli surface distortion and the outward convection of vorticity. Glynn (1982) produced a method for tracing the Bernoulli surfaces through the cascade giving a loss core due to the rolling up of the surfaces. Work currently in progress at Durham University is investigating this approach further with the aim of producing a simple and fast estimation for secondary flows without the need for a fully three-dimensional calculation method.

Conclusions

- 1 The development of secondary flows and losses through a cascade of high turning rotor blades has been studied. Of particular interest is the presentation of the development of streamwise vorticity. To obtain this was not straightforward, but required the differentiation of experimental data using surface fits. Apart from one or two places, the results seem to be reasonable.

- 2 The development of the flow has been related to surface flow visualization, particularly with respect to the separation lines caused by the passage vortex and the two legs of the horseshoe vortex.

- 3 The development of the negative streamwise vorticity related to the passage vortex has been illustrated. Areas of positive vorticity are seen to be associated with separation lines and the feeding of loss into the mainstream. The main

positive area in the latter part of the passage lies about halfway between the endwall and the separation line on the suction surface caused by the passage vortex. This is associated with a significant feeding of loss into the bulk flow from the lower part of the suction surface.

4 The suction side leg of the horseshoe vortex is only seen in the early part of the passage. It appears either to be dissipated or absorbed into a separation bubble on the suction surface toward midspan. The pressure side leg merges with the passage vortex, which has the same sense of vorticity.

5 The streamwise vorticity predicted by secondary flow theory agrees well with observation in the first half of the passage. However in the second half, the progressive distortion of the Bernoulli surfaces and the outward convection of the passage vortex cause a deterioration in the validity of the theoretical prediction. The theory predicts that downstream of the blades, the magnitude of streamwise vorticity will drop due to the addition of the trailing shed and trailing filament vorticity in the blade wakes. A drop is observed, but the distribution of vorticity downstream is very different from that predicted. In addition viscous effects are seen to modify the vorticity, particularly close to the endwall.

6 Development of the theoretical method is suggested to include the effects of convection and Bernoulli surface distortion.

7 The effect of inlet boundary layer thickness is seen to affect the intensity of the secondary flow features, but with little change to their location.

Acknowledgments

This work has been carried out with the support of the Procurement Executive of the Ministry of Defence. The authors also gratefully acknowledge additional support from Rolls-Royce plc and permission to publish this paper. The authors

also thank M. Howard for his contribution to the derivation of streamwise vorticity.

References

- Atkins, M. J., 1985, "End Wall Profiling in Axial Flow Turbines," Ph.D. Thesis, Cambridge University, United Kingdom.
- Came, P. M., and Marsh, H., 1974, "Secondary Flow in Cascades: Two Simple Derivations for the Components of Vorticity," *Journal Mechanical Engineering Sciences*, Vol. 16, pp. 391-401.
- Glynn, D. R., 1982, "Calculation of Secondary Flow in Cascades Including Effects of Bernoulli Surface Distortion," *International Journal of Heat and Fluid Flow*, Vol. 3, pp. 73-80.
- Graves, C. P., 1985, "Secondary Flows and Losses in Gas Turbines," Ph.D. Thesis, Durham University, United Kingdom.
- Gregory-Smith, D. G., and Graves, C. P., 1983, "Secondary Flows and Losses in a Turbine Cascade," in: *Viscous Effects in Turbomachines*, AGARD CP 351.
- Hawthorne, W. R., 1951, "Secondary Circulation in Fluid Flow," *Proceedings Royal Society, Series A*, Vol. 206, pp. 374-387.
- Hawthorne, W. R., 1967, "The Applicability of Secondary Flow Analysis to the Solution of Internal Flow Problems," in: *Fluid Mechanics of Internal Flow*, G. Sovran, ed., Elsevier, New York, pp. 238-269.
- Horlock, J. H., and Lakshminarayana, B., 1973, "Secondary Flows: Theory, Experiments and Applications in Turbomachinery Aerodynamics," *Annual Review of Fluid Mechanics*, Vol. 5, pp. 247-280.
- Langston, L. S., Nice, M. L., and Hooper, R. M., 1977, "Three-Dimensional Flows Within a Turbine Cascade Passage," *ASME Journal of Engineering for Power*, Vol. 99, pp. 21-28.
- Marchal, P., and Sieverding, C. H., 1977, "Secondary Flows Within Turbomachinery Blading," in: *Secondary Flows in Turbomachines*, AGARD CP 214.
- Moore, J., 1983, "Flow Trajectories, Mixing and Entropy Fluxes in a Turbine Cascade," in: *Viscous Effects in Turbomachines*, AGARD CP 351.
- Moore, J., and Adhye, R. Y., 1985, "Secondary Flows and Losses Downstream of a Turbine Cascade," *ASME Journal of Engineering for Gas Turbines and Power*, Vol. 107, pp. 961-969.
- Sieverding, C. H., 1985, "Recent Progress in the Understanding of Basic Aspects of Secondary Flows in Turbine Blade Passages," *ASME Journal of Engineering for Power*, Vol. 107, pp. 248-257.
- Squire, H. B., and Winter, K. G., 1951, "The Secondary Flow in a Cascade of Airfoils in a Non-uniform Stream," *Journal of Aeronautical Sciences*, Vol. 18, pp. 271-277.

The Base Pressure and Loss of a Family of Four Turbine Blades

L. Xu

J. D. Denton

Whittle Laboratory,
University of Cambridge,
Cambridge CB3 0DY, United Kingdom

Measurements of the effect of trailing edge geometry on the base pressure and loss of a family of four turbine cascades are presented. The measurements were made in the transonic range of Mach number from 0.8 to 1.2. It is found that, for blades with typical trailing edge thickness, the trailing edge loss is the major source of profile loss at these speeds and that the base pressure plays a dominant role in determining the loss. For blades with thick trailing edges an accurate prediction of base pressure is crucial to loss prediction. However, it is found that current methods of base pressure prediction are unable to give reliable predictions.

1 Introduction

The high loss associated with the thick trailing edges of cooled transonic turbine blades has been recognized for many years. The loss arises from a combination of the low base pressure and the large trailing edge blockage (e.g., [1]). However, the exact mechanism that causes the reduction in base pressure and increase in loss at transonic speeds is still poorly understood. This is partly because of the extremely complex flow that occurs close to the trailing edge and partly due to the fact that the small scale of practical trailing edges makes detailed measurements very difficult. Although many theoretical methods for base pressure prediction have been developed over some 30 years it seems that none of them can yet be applied with confidence to transonic turbine blades.

Deich et al. [2] systematically investigated the effects of trailing edge thickness and shape on loss over a range of Mach numbers. However, they do not present detailed experimental data and so their results are of little help in understanding the loss mechanism. However, they were able to correlate trailing edge loss as a linear function of trailing edge thickness. Prust and Helon [3] performed cascade tests at subsonic speeds on blades with different trailing edge shapes and thicknesses; they concluded that the loss is proportional to the drag coefficient, which is a function of the base pressure. As a result it is now widely accepted that a knowledge of the base pressure is essential to estimate both the loss coefficient and also the coolant flow when trailing edge ejection is applied.

Conventional base flow theories, which largely originate from the work of Chapman and Korst [4-6], regard the separated shear layer immediately behind the trailing edge as a single parameter equilibrium flow and the effect of the upstream boundary layer is also included through only a single parameter, namely its momentum thickness. These assumptions greatly simplify the theory and may be reasonable for external base flows such as those around supersonic wings and rockets. However, the boundary layer on a turbine blade is far too complex to be described by a single parameter, especially

on the suction surface of a transonic blade where a shock wave-boundary layer interaction will inevitably occur. Sieverding's very detailed measurements of base pressure [7] clearly show that the base pressure increases when this interaction occurs close to the trailing edge. Conventional base pressure theories cannot predict this effect. The presence of vortices in the separated shear layer has also been demonstrated by Camus [17] and this suggests that the cause of the low base pressure may be the high entrainment rate of fluid from the base region into the shear layer, which is induced by the vortex motion. The whole process is extremely complex and more rigorous and detailed measurements are needed. Despite this unsteadiness the flow is usually described in conventional time-mean terminology. From this viewpoint the distribution of shear stress in the shear layer plays a key role in the generation of the low base pressure. The higher the shear stress the greater the entrainment rate and the lower the base pressure. This mechanism helps to explain the difference between laminar and turbulent boundary layers and also the dependence of the base pressure on the Reynolds number.

Since shape factor H is an indicator of the structure of the boundary layer and in particular its shear stress distribution, its value just upstream of the trailing edge might be expected to have an important influence on the base pressure. This is confirmed by the results of Paige [8] who found that changing the Reynolds number of a transonic turbine blade from 7×10^5 to 3×10^5 at a constant Mach number had very little effect on the momentum thickness but the boundary layer shape factor and the base pressure both changed significantly. The boundary layer upstream of the trailing edge was less full at the lower Re and the base pressure was higher. Similar comparisons can be found in the results presented in [7] where the base pressure changed by about 15 percent according to whether or not a shock wave-boundary layer interaction occurred. The corresponding change in H was also about 15 percent; although there was also a change in θ , it was far too small to explain the change in base pressure.

The importance of the base pressure is illustrated by the fact that although Paige's blade was designed to reduce the strength of the shock wave-boundary layer interaction, and succeeded in doing this, because of its lower base pressure its

Contributed by the Gas Turbine Division of THE AMERICAN SOCIETY OF MECHANICAL ENGINEERS and presented at the 32nd International Gas Turbine Conference and Exhibit, Anaheim, California, May 31-June 4, 1987. Manuscript received at ASME Headquarters February 19, 1987. Paper No. 87-GT-202.

Table 1 Blade geometric parameters

Parameter	Blade RD	Blade DK	Blade DN	Blade DC
Span h , mm	101.6	101.6	101.6	101.6
Pitch p , mm	35.15	35.15	35.15	35.15
Throat width/chord ratio	0.3214	0.3214	0.3214	0.3214
Stagger angle, deg	29.6	29.6	29.6	29.6
Inlet flow angle, deg	56.7	56.7	56.7	56.7
Number of blades	6	6	6	6
Trailing edge wedge angle	9 deg	9 deg	9 deg	6 deg
Chord c , mm	41.7	39.6	44.0	41.7
p/c	0.842	0.888	0.799	0.842
h/c	2.44	2.57	2.31	2.44
Throat width o , mm	13.4	12.7	14.1	13.4
$\arccos(o/p)$, deg	67.6	68.8	66.4	67.6

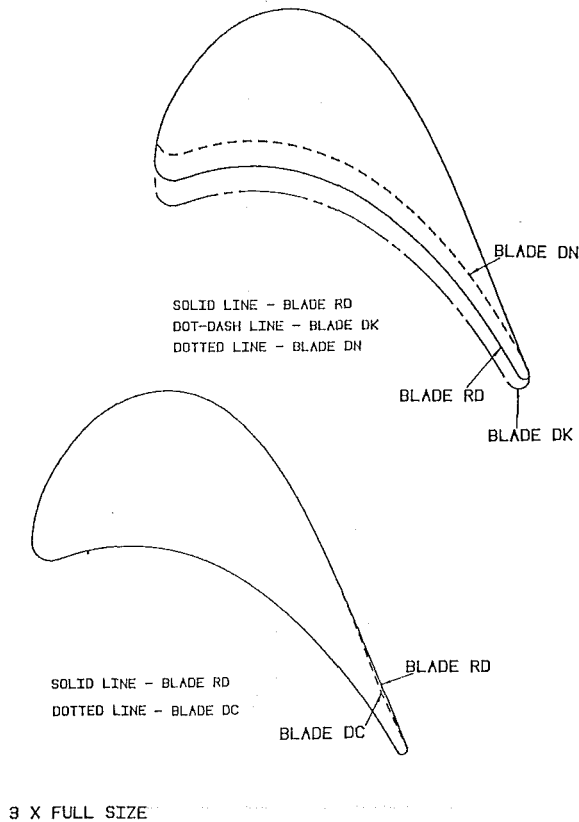


Fig. 1 Profiles of four cascades

overall loss was no less than that of the blade it was designed to replace.

This paper presents experimental results for four different cascades and a comparison of the results with numerical predictions. The effect of the trailing edge thickness on the loss is first examined. This is followed by an investigation of the effects of different suction surface curvatures downstream

of the throat. The effect of trailing edge ejection on the base pressure and loss are also briefly investigated.

2 Apparatus and Instrumentation

The datum blade profile, RD, is a typical midheight section from a highly loaded transonic aircraft gas turbine. The blade has been extensively tested at the Whittle laboratory and elsewhere and therefore its detailed performance is well documented [9]. The blade has 123 deg of turning and a design exit Mach number of 1.15.

Two other blades, DK and DN, were derived from RD by moving the pressure surface tangentially and changing the pitch so that the trailing edge thickness was changed while the flow passage within the blade remained unchanged. This leads to a slight difference in the leading edge radius of the blades but the flow up to the throat should be very similar for all three. Downstream of the throat the suction surface flows will differ because the different trailing edge thicknesses generate different amounts of expansion and different shock strengths. Since the opening to pitch ratios also differ the exit flow angles will not be the same. These compromises are inevitable when investigating the effects of different trailing edge thickness on the flow. A fourth blade, DC, was derived from RD by changing the suction surface downstream of the throat to make it slightly concave. This provides a different Mach number distribution and boundary layer development on the suction surface downstream of the throat and the effect of these on the base pressure can be compared with the datum. The four blade profiles are shown in Fig. 1 and their main geometric parameters are listed in Table 1. The coordinates of the datum blade RD can be found in [16].

The blades were tested in the transonic cascade tunnel at the Whittle Laboratory; a description of the tunnel can be found in [10]. The Reynolds number based on blade chord and downstream flow conditions was held constant at $8.0 (\pm 0.2) \times 10^5$. The isentropic exit Mach number was varied from 0.8 to 1.2. The two central blades of the six-blade cascade were instrumented with static pressure tappings on the pressure and suction surfaces, respectively, and a tapping at the center of the trailing edge circle of both blades was used to

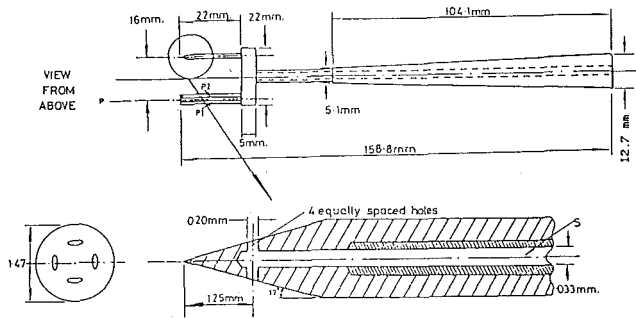
Nomenclature

a = speed of sound
 C = blade axial chord
 E = kinetic energy loss coefficient
 H = boundary layer shape factor
 M = Mach number
 p = static pressure
 P_c = stagnation pressure coefficient

Re = Reynolds number
 t = trailing edge thickness
 U = Velocity
 β = flow angle
 δ^* = boundary layer displacement thickness
 θ = boundary layer momentum thickness

Subscripts

1 = upstream of cascade
 2 = far downstream of cascade
 b = base
 e = edge of boundary layer
 o = stagnation conditions
 s = static conditions
 te = trailing edge
 x = traverse position



DETAILS OF NUMBER 2 PROBE NEPTUNE TYPE

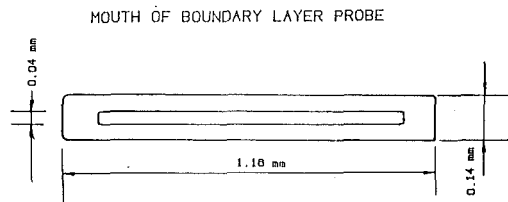


Fig. 2 Details of the pressure probes

measure the base pressure. The traverses were made with the combined stagnation-static-yaw probe shown in Fig. 2 and the error in the local Mach number is estimated to be less than 0.01, except in the transonic regime where it is less than 0.02. The standard traverse condition was 40 percent axial chord behind the trailing edge and the traverses covered two blade pitches. However, only the second half of the data, covering the wake of the fourth blade, was used to evaluate the loss and flow angle.

At the design condition of $M_2 = 1.15$ further traverses were made at different distances behind the trailing edge and a boundary layer traverse was performed close to the trailing edge on the suction surface.

3 Cascade Test Results

3.1 Surface Mach Number Distribution. The isentropic Mach number distributions on the blade surfaces are plotted in Fig. 3. The farthest downstream point in all cases is obtained from the base pressure measurement. It can be seen that the pressure surface is almost identical for all four blades but on the suction surfaces differences occur due to the different leading edge radii and to the different trailing edge shock-expansion systems. Two characteristics common to all four cascades are worth noting: (1) The blades are highly loaded over the whole chord with only a small amount of diffusion on the suction surface downstream of the throat; (2) all blades showed signs of separation downstream of the start of the diffusion on the suction surface at exit Mach numbers over unity. Some (e.g., DK) also show signs of reattachment just upstream of the trailing edge while some (e.g., DN) have separation up to the trailing edge without reattachment. This boundary layer behavior will be shown to have a significant effect on the base pressure.

3.2 Boundary Layer Upstream of the Trailing Edge. The boundary layers at about 98 percent chord on the suction surface were measured using a flattened pitot tube (Fig. 2) at an exit Mach number of 1.15. The integral parameters are listed in Table 2. The high shape factors indicate that the layers are "separational" in all cases but the momentum thickness on blades DN and DK is about 50 percent greater than on the

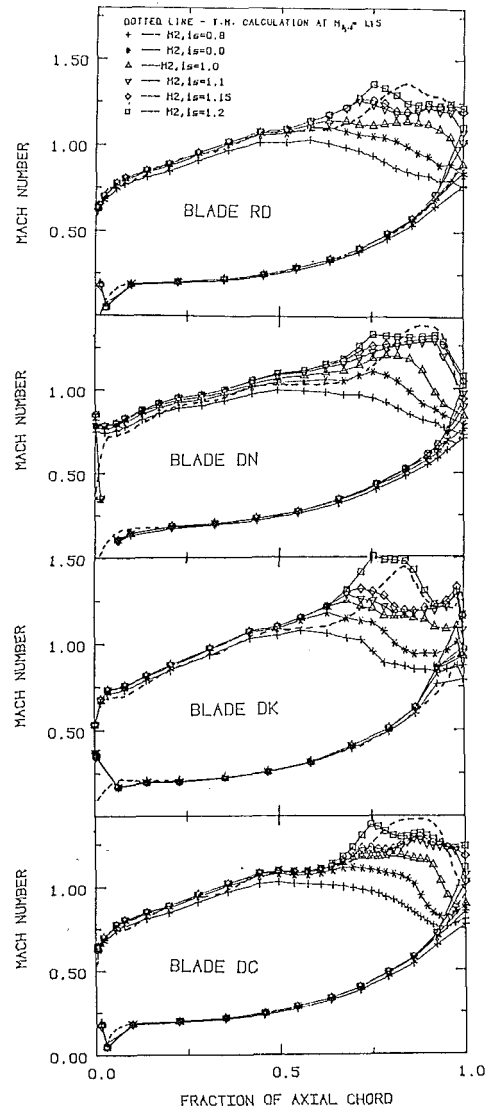


Fig. 3 Isentropic surface Mach numbers

Table 2 Boundary layer integral parameters

Blade	d^*	θ	H
Blade RD	0.133	0.046	2.924
Blade DC	0.143	0.048	2.952
Blade DK	0.178	0.76	2.340
Blade DN	0.169	0.070	2.433

datum blade RD. These differences in momentum thickness are thought to be due to different mechanisms in the two cases. For DK the shock wave-boundary layer interaction is considerably stronger than on the other blades while in the case of DN it is believed that the suction surface boundary layer undergoes early transition because of the overacceleration around the thinner leading edge.

3.3 Base Pressure Measurements. The variation of base pressure with back pressure is presented in Fig. 4. Except for RD and DC at $M_2 > 1.15$, all the base pressures are higher than the back pressure. Generally a thinner trailing edge tends to have a higher base pressure both because the boundary layer is thicker relative to the trailing edge and because the suction surface Mach number immediately upstream of the trailing edge tends to be lower.

The high level of the base pressures on these blades is be-

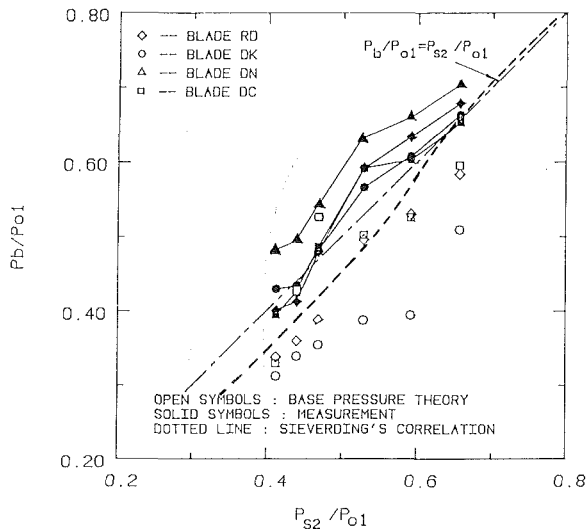


Fig. 4 Comparison of the base pressure prediction with Sieverding's correlation

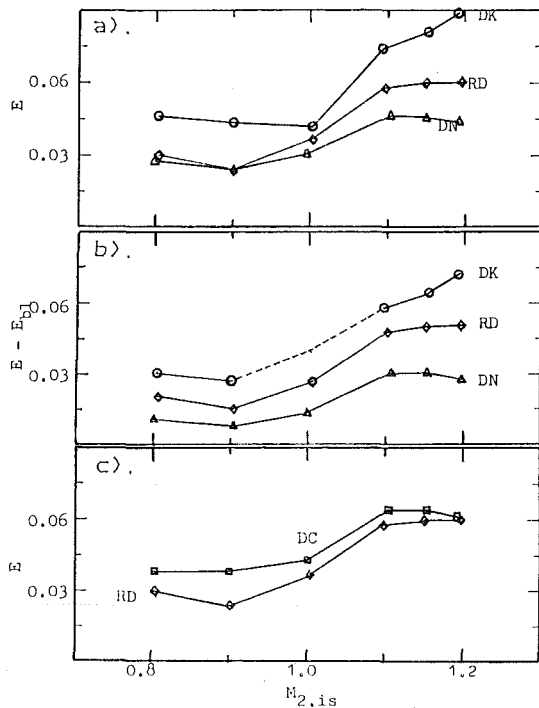


Fig. 5 Comparison of losses

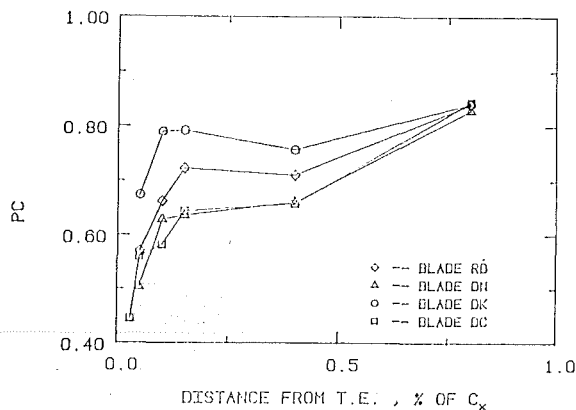


Fig. 6 Variation of loss behind blade

lied to be a direct result of the boundary layers being either separated or close to separation upstream of the trailing edge. This in turn is thought to be induced by the high wedge angle. As a result the base pressure is invariably more or less equal to the pressure behind the suction surface shock wave-boundary layer interaction.

3.4 Comparison of Losses. The kinetic energy loss coefficients of blades RD, DK, and DN are compared in Fig. 5(a). As is usual for such blades, the loss coefficient increases with Mach number and there is a particularly steep rise at exit Mach numbers around unity. This rise coincides with the decrease of base pressure shown in Fig. 4. At high speeds the change of loss with trailing edge thickness is closely linear. At lower speeds the losses of blades RD and DN are similar despite the fact that the boundary layer loss of DN is about 50 percent greater than that of RD. If we assume that the boundary layer loss is only a weak function of exit Mach number then subtracting this component from the overall loss. Figure 5(b) shows clearly that the trailing edge loss is directly proportional to the thickness even at subsonic speeds. These results also show how the trailing edge loss is the major component of the overall loss. For RD, for example, the boundary layer loss is only about 30 percent of the total loss.

3.5 Comparison of Blades RD and DC. A comparison of RD and DC, which have the same trailing edge thickness, shows the effect of the different extent of the suction surface separation on the loss. The concave curvature of the suction surface of DC close to the trailing edge is more prone to separation than is RD and a separation occurs even at subsonic speeds. However, the flow reattaches just upstream of the trailing edge where the blade surface angle is less than that of RD. As a result the base pressure of DC is considerably lower than those of RD at subsonic speeds, while at supersonic speeds where both blades have similar levels of separation, the base pressures are similar. This is reflected in the loss curves shown in Fig. 5(c).

3.6 Loss Development Downstream of the Trailing Edge. Because loss generation is an interactive process between different mechanisms it is impossible to break down the loss into different components. The conservation equations applied downstream of the blade show that the value of mixed-out loss is completely determined once the flow leaves the trailing edge; however, it is revealing to try to find where in the wake loss (i.e., entropy) is generated most rapidly. Wake traverses were made at distances of 5, 10, 15, 40, and 80 percent axial chord behind the trailing edge. Very close to the trailing edge the probe accuracy is reduced by the very rapid variation in flow properties. Far downstream the periodicity degenerates due to reflections of shock and expansion waves from the free jet. As a result measurements at these positions are not as accurate as those at the usual traverse position. The results are presented in the form of relative stagnation pressure drop, $PC = (P_{01} - P_{0x}) / (P_{01} - P_{02})$ where P_{0x} is the mass-averaged stagnation pressure at the measuring plane. At the cascade inlet $PC = 0$ while at the far downstream mixed-out plane $PC = 1$.

Figure 6 shows that there is a very steep increase of PC close to the trailing edge, indicating that about 20 percent of the loss occurs in the immediate vicinity of the trailing edge where little of the shock loss has yet occurred. It is thought that this loss is due to intense viscous mixing. At 80 percent axial chord downstream about 80 percent of the total loss has occurred indicating that there is still significant shock and mixing loss taking place well downstream of the blade. It is an interesting question whether any of this loss can be recovered in a downstream blade row.

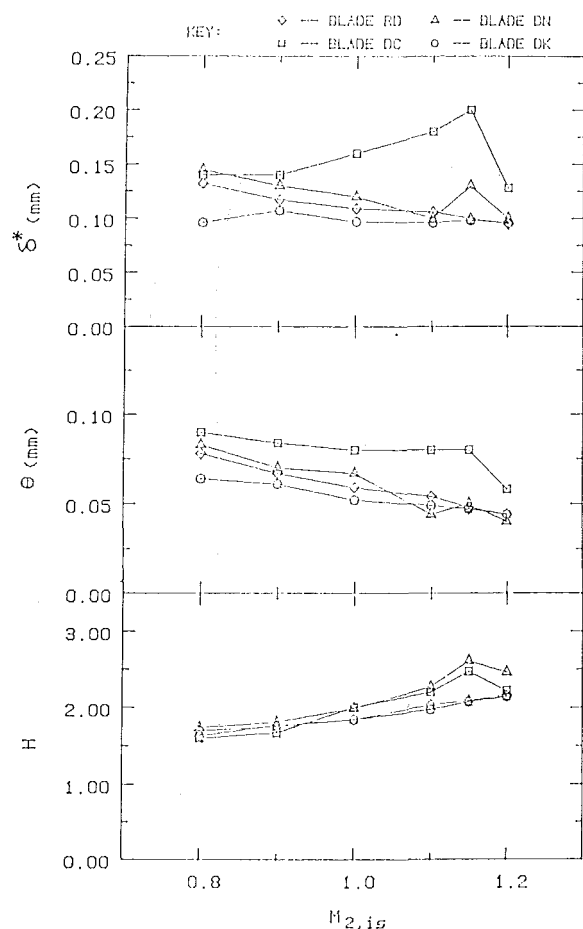


Fig. 7 Predicted boundary layer parameters

4 Comparison With Numerical Predictions

4.1 Calculation Procedure. A combination of methods was used to predict the flow field. The inviscid flow was calculated using a time marching Euler solver [11], which should include the shock loss. The boundary layer development was calculated using the integral boundary layer program developed by Herbert and Calvert [12]. Once the mainstream flow and the boundary layer parameters were known a base pressure prediction based on Carriere's method [6] was used at supersonic speeds while Nash's method [5] was used at subsonic speeds. Finally the mass and momentum conservation equations are applied between the trailing edge plane and far downstream to calculate the mixed-out loss. The details of the methods can be found in [5, 6, 11, 12] and their application is described in [13]. In reality the inviscid flow, the boundary layers, and the base flow interact with one another and the calculation should be iterative. However, in view of the shock smearing in the Euler solver and the limitations of the boundary layer method in dealing with shock wave-boundary layer interaction, this interaction is not thought to be worthwhile at present. Hence, the calculations were carried out successively, without iteration. An advantage of this approach is that the calculated values can be replaced by measured ones when available and so the error in that part of the calculation can be assessed.

4.2 Inviscid Flow Field. The predicted blade surface Mach number distributions are compared with the measured ones at $M_2 = 1.15$ in Fig. 3. The comparison at other speeds is similar. No special modeling of the trailing edge flow was used. The agreement is fairly good on the pressure surface and

on the suction surface up to the location of the shock wave. The calculation always predicts this to lie farther downstream than the measurements and the predicted peak Mach number is always higher. The magnitude of the discrepancy increases with the strength of the shock wave and hence with trailing edge thickness. As a result the calculation will overestimate the shock loss. Also the errors in the Mach number distribution over the rear of the suction surface will induce errors in both the boundary layer and the base pressure predictions.

4.3 Boundary Layer Predictions. The calculated integral parameters of the boundary layer on the suction surface just upstream of the trailing edge are plotted against Mach number in Fig. 7. Although the shape factors are high and the predictions indicate that the boundary layer is close to separation, no separation is actually predicted. This is possibly a consequence of the errors in the inviscid calculations that predicted the diffusion starting too close to the trailing edge and overestimated the acceleration prior to it. The predicted displacement thicknesses are similar for all four blades and the differences between them are due to differences in the predicted diffusion over the rear suction surface. The predicted value of momentum thickness is close to the measured value for blades RD and DC at $M_2 = 1.15$. The calculations show that, provided the boundary layers remain attached, the variation of momentum thickness with exit Mach number should be small.

4.4 Base Pressure. The upper part of Fig. 8 shows the base pressure predictions for the three blades. In the case of blade DN the ratio of boundary layer thickness to trailing edge thickness is outside the range of the base pressure theory and no prediction could be obtained. All the predicted base pressures are significantly lower than the measurements. This is thought to be because Carriere's prediction method assumes fully developed boundary layers with shape factor about 1.5, while the actual boundary layers are much closer to separation with shape factors about 2.5. As a result the shear stress in the boundary layer is much less than is assumed in the model and the base pressure is correspondingly higher. The same explanation applies to Sieverding's [7] experiments, which also showed high base pressures on a model trailing edge.

Also plotted in Fig. 8 is the base pressure predicted by the inviscid time marching calculation. In this calculation a cusp is fitted to the trailing edge to model the actual base triangle. The average pressure on the sides of this cusp can be taken as a predicted base pressure. This pressure is to some extent related to the shape of the cusp but is not strongly dependent on it. Schlieren photographs of the base region usually show the separated zone behind the trailing edge to be of the order 1.5-2 trailing edge thicknesses in length and so the length of the cusp was set to a similar value.

As can be seen this inviscid calculation gives a much better prediction of base pressure than does the base pressure theory. The reason why an inviscid computation can give reasonable predictions of base pressure, which is generally considered to be a viscous phenomenon, is an interesting question. In brief it is considered that the base pressure is largely predetermined by the global conservation equations, in exactly the same way as the pressure on the rear face of an orifice plate is completely predictable despite the fact that the mechanism of dissipation behind it is entirely viscous. If the inviscid calculation predicts the momentum flux just upstream of the trailing edge accurately for a specified downstream pressure then the base pressure is fixed by applying conservation of momentum between the two planes. For a cascade of unstaggered flat plates (or for a single plate in a wind tunnel) the flow just upstream of the trailing edge will be uniform and at sonic conditions and so the base pressure is uniquely fixed. For a turbine cascade the momentum flux is itself influenced by the base pressure

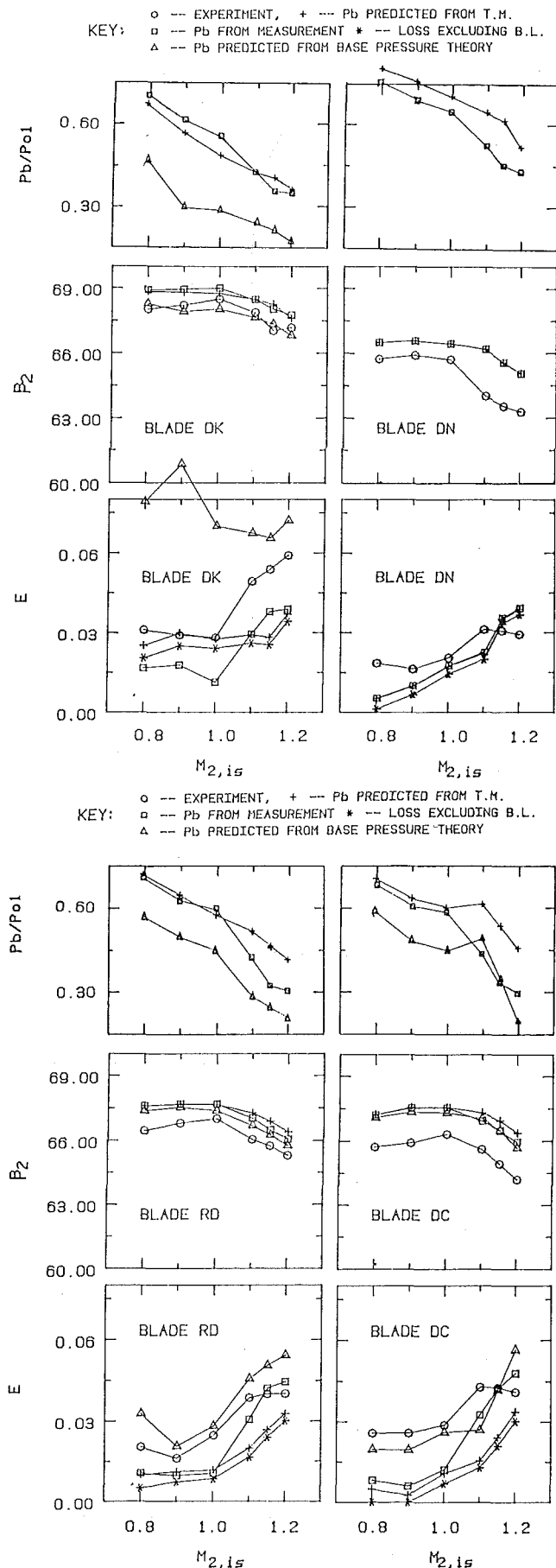


Fig. 8 Comparison of the predicted cascade performance with experiment

and the implication from the success of the inviscid prediction is that this influence is not great. The measured base pressures are compared with the base pressure theory and with Sieverding's correlation in Fig. 4. It can be seen that the measured pressures are considerably higher than either prediction.

4.5 Loss and Deviation Prediction. The measured and predicted losses are compared in the lower part of Fig. 8. Three different predictions are shown, namely: one with the base pressure taken from experiment, one with the base pressure taken from the base pressure theory, and one with the base pressure taken from the inviscid calculation. In addition, to illustrate the magnitude of the boundary layer loss, predictions using the inviscid prediction of base pressure but without any boundary layer loss are included.

It can be seen that the predicted exit angles are consistently about 1-1.5 deg higher than those measured (i.e., the experiments show underturning). Those calculated using the base pressure theory are in slightly better agreement than the other predictions.

The loss predictions show even larger discrepancies. The results for blade DN at subsonic speeds show that the boundary layer loss is greatly underestimated. This can only partly be explained by the fact that the predicted velocities on the rear suction surface are lower than those measured. The loss calculated using predicted base pressures generally shows a more rapid increase at transonic speeds than that measured. This is thought to be partly due to the inclusion of numerical loss from the time marching calculation in the predictions. The main causes of the discrepancies are thought to be the underestimation of the boundary layer loss and the underestimation of the base pressure by the base pressure theory. For blades RD and DC these two errors partly cancel and the predictions using base pressure theory are closer to the measurements.

It is clear from the results that predictions of loss for transonic blades of this type is far from an exact science.

5 Effect of Ejection on Base Pressure and Loss

The work of Motallebi and Norbury [14] and of Sieverding [15] shows that a small amount of flow ejection into the base region can produce a significant increase in base pressure. However, the effect on loss has not been explored and it is not clear whether the loss reduction expected from the increase in base pressure is sufficient to compensate for the additional loss suffered by the ejected flow in the internal passages used to supply it to the base region. To investigate this, high-pressure air from the blade pressure surface was introduced into the base region by three small passages. Details of these are shown in Fig. 9. Their opening into the trailing edge was 1.5 mm \times 2.5 mm and their length was about 4 mm. The passages were spaced 16 mm apart and covered half the blade span. Within this half span the ejection rate was about 1 percent of the mainstream flow rate.

5.1 Ejection Geometry. Two slightly different geometries were tried as illustrated in Fig. 9. In one the pressure surface and the trailing edge were connected by holes, which will be referred to as "ducts." In the other the connection was via "slots," which effectively thinned the trailing edge locally. Wake traverses were performed at 40 percent axial chord behind the trailing edge at three spanwise positions. At positions 1 and 3 the probe was located midway between the ejection slots while at position 2 it was directly behind a slot. Only the third blade in the cascade was modified for ejection and traverses were continued over two blade pitches so that the modified blade wake could be compared with that of a normal blade. The loss plotted in Fig. 10 is that obtained from the wake of blade 3.

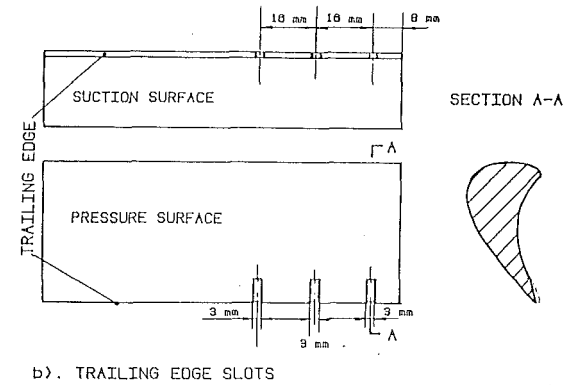
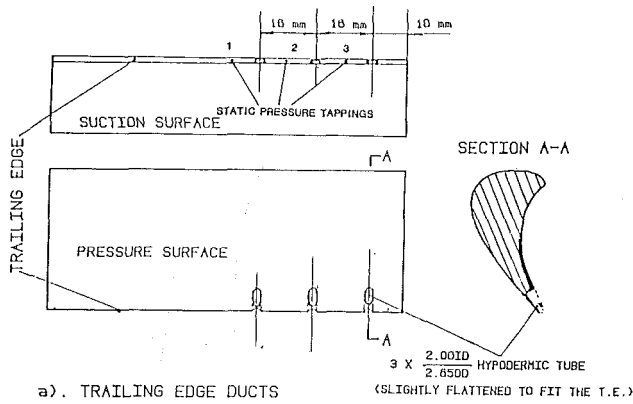


Fig. 9 Sketch of trailing edge ejection devices, ejection from pressure surface: blade DK

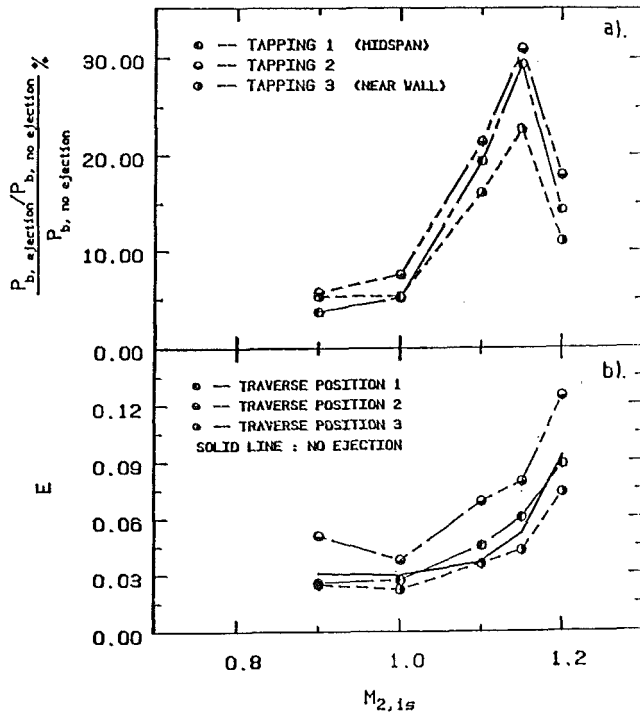


Fig. 10 Effect of trailing edge ejection on base pressure and loss

5.2 Base Pressure. The change in base pressure due to ejection from the ducts is shown in Fig. 10. The three tappings give slightly different results because number one is at midspan and is only partly influenced by the ejection while tapping number three is in a region influenced by secondary flow. The change in base pressure is always positive and increases in magnitude as the flow becomes transonic.

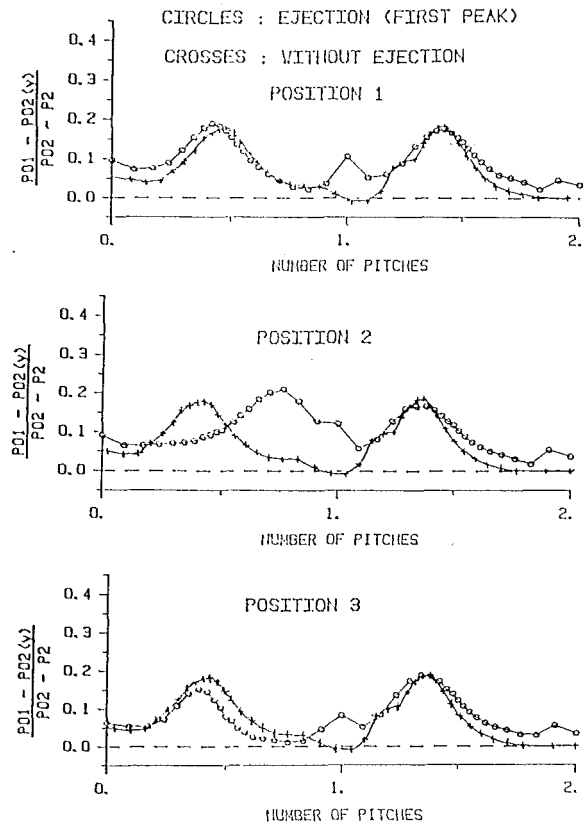


Fig. 11(a) Comparison of the stagnation pressure profiles in the wakes with and without trailing edge ejection; $M_{2is} = 1.15$

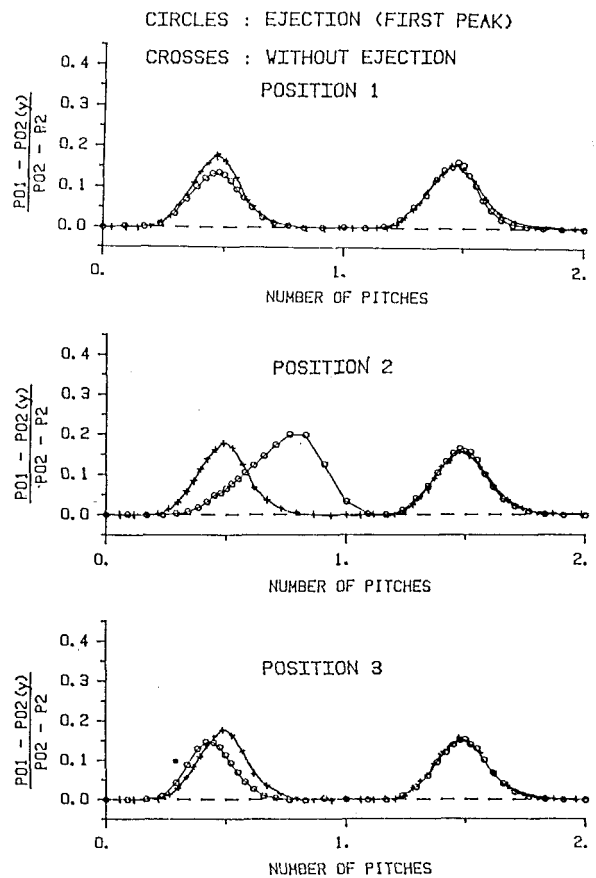


Fig. 11(b) Comparison of the stagnation pressure profiles in the wakes with and without trailing edge ejection; $M_{2is} = 0.9$

CONTOUR HEIGHT 0.005 P_0/P_{01}
 MAXIMUM VALUE 1.000 P_0/P_{01}
 MINIMUM VALUE 0.950 P_0/P_{01}

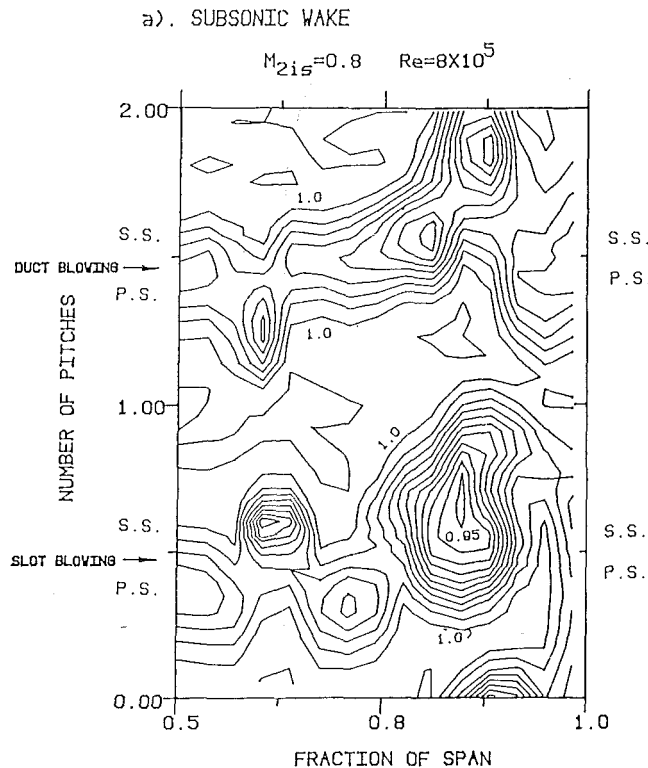


Fig. 12(a) Stagnation pressure contours of blade DK, measured at 40 percent of axial chord downstream of the trailing edge

CONTOUR HEIGHT 0.005 P_0/P_{01}
 MAXIMUM VALUE 1.000 P_0/P_{01}
 MINIMUM VALUE 0.920 P_0/P_{01}

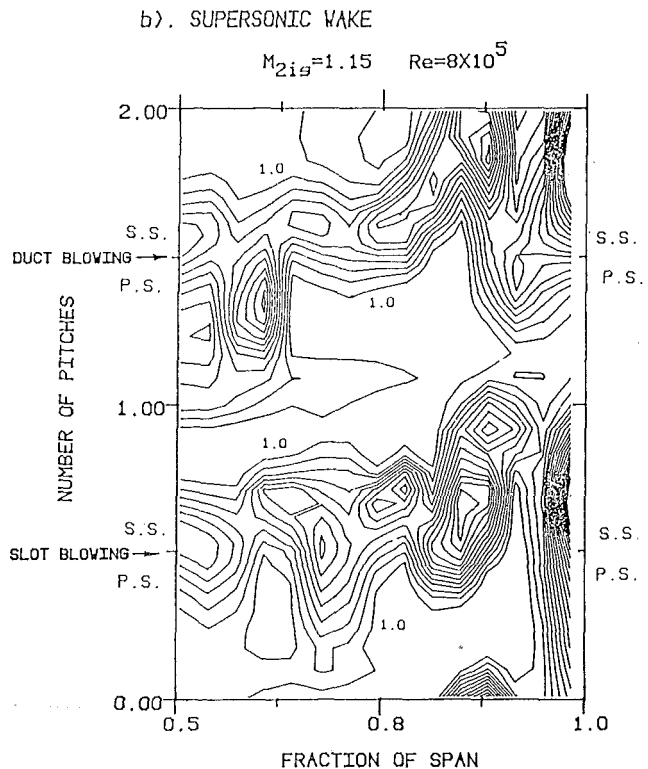


Fig. 12(b) Pitot pressure contours of blade DK, measured at 40 percent of axial chord downstream of the trailing edge

5.3 Effect of Ejection on Loss. The measured losses are shown in Fig. 10 for ejection from the ducts. The loss at position 3 is significantly reduced by the ejection but that at position 2 is considerably increased. The loss at position 1 is also increased by loss originating from the point of ejection. In fact Fig. 11 shows that, at subsonic speeds, the loss at position 1 is significantly reduced compared to that of the adjacent blade. The displacement of the wake at traverse point 2 indicates a considerable overturning of the wake behind the slot. In order to investigate this three dimensionality further a pitot rake was used to obtain stagnation pressure contours behind both types of modified trailing edge. The results are shown in Fig. 12. It is clear that high loss cores are generated behind both the ducts and the slots and that no region of two-dimensional flow exists. The flow is extremely complex with significant differences being produced by the small geometric differences between the slots and the ducts. All that can be concluded is that considerable extra loss is generated in the flow passing through the slots or ducts and it is not obvious that the reduction in base pressure is sufficient to compensate for this.

6 Conclusions

The major conclusions to be drawn from this work are:

1 At transonic speeds trailing edge loss is the major component of profile loss, even for blades with moderate trailing edge thickness. Typically about 70 percent of the loss generation occurs downstream of the trailing edge.

2 The blades tested have a comparatively high base pressure at transonic speeds. This is thought to be due to a combination of the high wedge angle with a thick boundary layer upstream of the trailing edge.

3 The trailing edge loss is directly proportional to trailing edge thickness with the constant of proportionality being greater at transonic and supersonic speeds.

4 Conventional base pressure theories are unable satisfactorily to predict the base pressure of transonic turbine blades because they do not make allowance for the detailed state of the boundary layer upstream of the trailing edge. The shear stress in this boundary layer as reflected in its shape factor is believed to be an important parameter.

5 The loss prediction method used in this investigation requires an accurate prediction of the suction surface pressure distribution upstream of the trailing edge in order to predict the boundary layer loss. As a result of this and of the inaccurate base pressure prediction the accuracy of loss prediction is poor.

6 Inviscid calculations using time-marching solutions of the Euler equations can give a surprisingly good prediction of the base pressure. This is worth further investigation to see whether it applies to other blades and whether it can be used as a basis of a general prediction method.

7 Introduction of trailing edge ejection through simple passive devices can give significant increases in base pressure. However, the additional loss suffered by the ejected fluid may not compensate for the reduction of trailing edge loss and further investigation is necessary to quantify this.

Acknowledgments

The cascade tests were supported by the Royal Aircraft Establishment, Farnborough. The authors wish to thank Dr. J. J. Camus of the Whittle Lab for many helpful discussions of the test results.

References

- 1 MacMartin, I. P., and Norbury, J. E., "The Aerodynamics of a Turbine Cascade With Supersonic Discharge and Trailing Edge Blowing," ASME Paper No. 74-GT-120, 1974.

- 2 Deich, M. E., Filipov, G. A., and Lazarev, L. Ya., *Atlas of Axial Turbine Blade Characteristics*, CEGB Trans 4563, 1965.
- 3 Prust, H. W. Jr., and Helon, R. M., "Effect of Trailing Edge Geometry and Thickness on the Performance of Certain Turbine Stator Blading," NASA TN D-6637, 1972.
- 4 Korst, H. H., *A Theory for Base Pressure in Transonic and Supersonic Flow*, 1956.
- 5 Nash, J. F., "An Analysis of 2-D Turbulent Base Flow Including the Effect of the Approaching Boundary Layer," ARC R&M No. 3344, 1962.
- 6 Carrierre, P., "Analyse Theorique du Decollement et du Recollement Turbulent au Bord de Fuite d'un Aubage aux Vitesses supersoniques," *Flow Research on Blading*, Lang S. Dzung, ed., 1970.
- 7 Sieverding, C. Stanislas, M., and Snoech, J., "The Base Pressure Problem in Transonic Cascade," ASME Paper No. 79-GT-120, 1979.
- 8 Paige, R. W., "A Computational Method for the Aerodynamic Design of Transonic Turbine Blades," PhD Thesis, University of Cambridge, Cambridge, United Kingdom, 1983.
- 9 Camus, J.-J., "Transonic Cascade Tunnel Commissioning Tests," 2.RD Profile CUEDA/A-Turbo 103, 1980.
- 10 Gostelow, J. P., and Watson, D. J., "A Closed Circuit Variable Density Air Supply for Turbomachinery Research," ASME Paper 76-GT-62, 1976.
- 11 Denton, J. D. and Xu, L., "A New Approach to the Calculation of Transonic Flow Through Two Dimensional Turbomachine Blade Row," ASME Paper No. 85-GT-5, 1985.
- 12 Herbert, M. V., and Calvert, W. J., "Description of an Integral Method for Boundary Layer Calculation in Use at NGTE With Special Reference to Compressor Blades," NGTE Memorandum M82019, 1982.
- 13 Xu, L., "The Base Pressure and Trailing Edge Loss of Transonic Turbine Blades," PhD Thesis, University of Cambridge, Cambridge, United Kingdom, 1986.
- 14 Motallebi, F., and Norbury, J. F., "The Effect of Base Bleed on Vortex Shedding and Base Pressure in Compressible Flow," *Journal of Fluid Mechanics*, Vol. 110, Sept. 1981.
- 15 Sieverding, C., "The Influence of Trailing Edge Ejection on the Base Pressure in Transonic Turbine Cascade," ASME Paper No. 83-GT-50, 1983.
- 16 Haller, B. R., "The Effects of Film Cooling on the Aerodynamic Performance of Transonic Turbine Blades," PhD Thesis, University of Cambridge, Cambridge, United Kingdom, 1980.
- 17 Bryanston-Cross, P. J., and Camus, J.-J., "Auto and Cross Correlation Measurements in a Turbine Cascade Using a Digital Correlator," ASME Paper No. 82-GT-132.

Tip Leakage Flow in a Linear Turbine Cascade

J. Moore
J. S. Tilton

Department of Mechanical Engineering,
Virginia Polytechnic Institute and
State University,
Blacksburg, VA 24061

An experimental and analytical study of flow in the tip clearance gap of a linear turbine rotor blade cascade has been performed. Measurements of wall static pressures and flow velocities are used to verify a flow model involving a vena contracta, near the tip gap entrance, followed by flow mixing to fill the gap. A frequently referenced potential flow theory for flow into a tip gap is found to be in error and the correct theory is shown to model the unloading along the pressure surface of the blade and the endwall static pressure distribution up to the vena contracta accurately. A combined potential flow and mixing model accounts for the pressure rise in the tip gap due to mixing. Turbine tip heat transfer is also discussed and a correlation of local heat transfer rates for essentially incompressible flow over unshrouded turbine rotor blades is presented.

Introduction

Efficiency losses and high heat transfer to blade tips are two major problems caused by tip leakage flows in gas turbines; thus tip leakage contributes important limitations to overall performance and durability. The strategy employed to reduce the leakage losses is to reduce the flows by reducing the discharge coefficients of the tip gaps (Booth et al., 1982; Wadia and Booth, 1982) or by reducing the clearances themselves (Hennecke, 1985). Both reduction of the discharge coefficients and reduction of heat transfer to the blade tips (Metzger and Bunker, 1985) require detailed understanding of the flows in the tip leakage gaps. It is therefore surprising that there is so little emphasis on these details in the literature.

Rains' Flow Models. Rains (1954) considered flow through the tip gap of a compressor blade. He noted that the pressure gradient across the blade is much larger than that along the blade. Thus, the tip gap flow can be considered as normal to the camber line of the blade. He presented an idealized flow model based on incompressible potential flow theory and also suggested a "more plausible" flow model with separation, reattachment, and flow mixing. These two models are shown in Fig. 1.

For the potential flow model Bernoulli's equation was applied between the conditions far upstream and downstream of the tip gap to give

$$U_t = \left[\frac{2}{\rho} (p_{t1} - p_2) \right]^{1/2} \quad (1)$$

Referring to Fig. 1(a), the pressure all along the free streamline under the blade was taken as equal to p_2 . The contraction ratio, σ , giving the ratio of the downstream jet width to the tip gap height, was determined to be $\pi/(\pi+2)$ or 0.611. With the exception of tip pressure measurements made on the pressure and suction sides of the tip gap on the endwalls, no

Contributed by the Gas Turbine Division of THE AMERICAN SOCIETY OF MECHANICAL ENGINEERS and presented at the 32nd International Gas Turbine Conference and Exhibit, Anaheim, California, May 31-June 4, 1987. Manuscript received at ASME Headquarters February 19, 1987. Paper No. 87-GT-222.

experimental confirmation of his potential flow theory was provided.

Rains' "more plausible" model contains mixing after the vena contracta, shown in Fig. 1(b).

Booth et al. (1982) stated that at normal tip clearances, 1-2 percent of the blade height, viscous effects are fairly small, being reduced to those creating separations and reattachments, but they did not mention mixing. They sought to reduce the tip gap discharge coefficient by adjusting the blade tip shape.

Wadia and Booth (1982) then modeled the tip gap leakage flow with a two-dimensional viscous analysis. For a flat tip, their experimental data, from pressure taps located under the tip gap, but not including any on the blade tip, were compared with their theory. Both the data and the theory showed the pressure falling at the tip gap entrance and then remaining

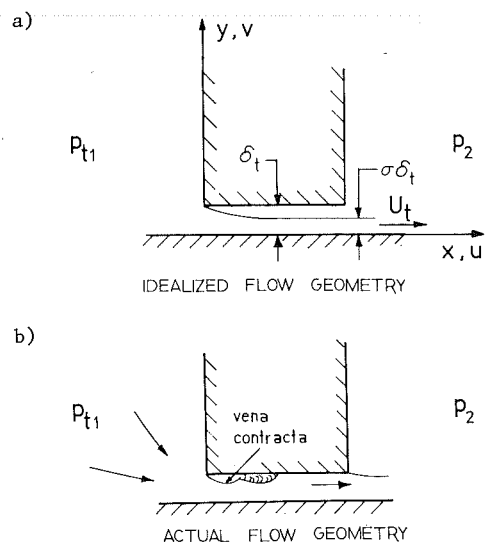


Fig. 1 Comparison of tip clearance flow geometries (after Rains, 1954)

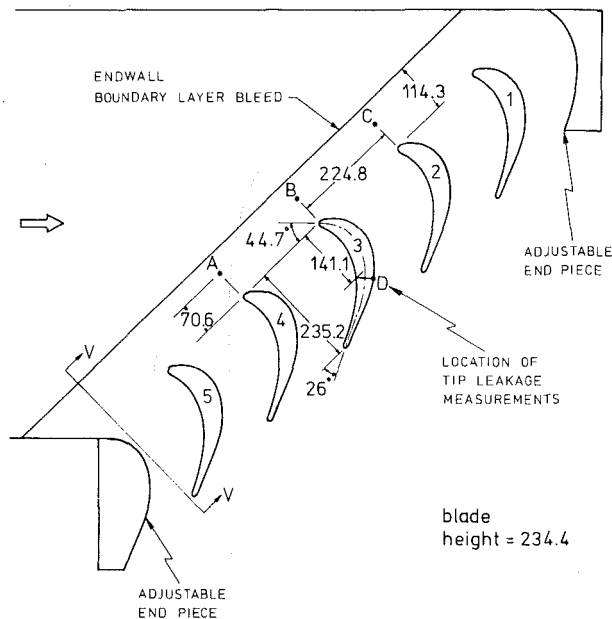


Fig. 2 Cascade geometry; linear dimensions in mm

relatively constant up to the gap exit, similar to what Rains' potential flow model would predict and, rather surprisingly, showing no evidence of a vena contracta.

Tip Gap Exit Measurements of Graham. Graham (1985) measured velocity profiles near the tip gap exit, close to the suction surface, of a turbine blade in a linear water-flow cascade. He presented results for three tip gap heights: 3.9, 2.8, and 1.8 percent of blade height; the corresponding ratios of local blade thickness to tip gap height were 2.5, 3.5, and 5.2, respectively.

With the largest tip gap, Graham noted an area of relatively low velocity (approximately 1/2 the potential flow velocity) near the blade tip, which he explained as due to "the wake of the large entry bubble observed just inside the edge between the pressure surface and the tip surface." As the clearance gap was reduced from 3.9 to 2.8 percent he found the bubble-wake region to be significantly reduced with little change in the velocity or size of the "main potential flow region." At 1.8 percent clearance, the flow was approaching a fully developed profile with similar velocity distributions near both surfaces and a reduced velocity in the middle of the flow.

Graham did not attempt to explain his results in terms of Rains' flow models but they are, in fact, qualitatively consistent; the differences between the cases are simply explained by the different distance-to-height ratios, x/δ_t , (see Fig. 1(a)), of

the measurements. For example, with the largest tip clearance, the potential flow has a quite uniform velocity and it extends to approximately 60 percent of the tip gap from the endwall; this profile represents the flow distribution at the vena contracta, i.e., at x/δ_t of about 2.0. At large distance-to-height ratios, the flow becomes attached on both walls and the velocity distribution approaches a fully developed profile.

Present Contribution. In this paper we will describe some measurements and observations of tip leakage flow development in a linear turbine cascade. A physical interpretation of the results is then developed based on potential flow theory, potential flow theory with mixing, and boundary layer theory. The literature on flow and heat transfer near the entrance of round and rectangular channels is used to complement the present measurements and theoretical models. As a result, a picture of flow in the tip clearance gap and heat transfer to the tips of turbine rotor blades is obtained that should be useful in the design of unshrouded turbine rotors.

Experimental Apparatus

Cascade Test Section. The cascade consisted of five blades and a pair of adjustable end pieces, creating six passages. The cascade geometry is shown in Fig. 2 and a cross-sectional view $V-V$ is shown in Fig. 3. The blades were designed to be almost identical to ones built earlier by Moore and Ransmayr (1984), and are geometrically similar to blades used by Langston et al. (1977). This blade profile was chosen for the tip clearance study because of the previous work done on it at VPI&SU, and in order to complement the wealth of information now available on it, for example, see Moore et al. (1987) and Graziani et al. (1980).

One major difference from the previous VPI&SU turbine cascade was the presence of a tip gap, which necessitated that the blades be supported from one end only, the other end being the blade's bottom surface. Also, different locations for additional static pressure tapings were utilized. Other than this, the blades were constructed following the method described in Moore and Ransmayr (1984). The blade sizes were not altered; the blade overall dimensions are:

Axial chord	=	235.2 mm
Blade height	=	234.4 mm
Pitch	=	224.8 mm

The airfoil section is that of a reaction turbine rotor with mean camber line angles of $\beta_1 = 43.99$ deg and $\beta_2 = 25.98$ deg. The air inlet angle is 44.7 deg, close to zero incidence. The Zweifel loading parameter is 1.124.

Trip wires of 0.51 mm diameter were epoxied to the blade surfaces in an attempt to start uniform turbulent profile

Nomenclature

A, B, C, D = measurement locations, Fig. 2
 C_D = discharge coefficient, equation (12)
 C_{ps} = static pressure coefficient = $(p - p_{s0}) / \frac{1}{2} \rho U_0^2$
 C_{pt1} = total pressure coefficient upstream of tip gap = $(p_{t1} - p_{s0}) / \frac{1}{2} \rho U_0^2$
 p = static pressure
 p_{s0} = endwall static pressure upstream of blade 3
 p_{t1} = total pressure upstream of tip gap

p_2 = static pressure downstream of tip gap
 \dot{Q} = volume flow rate through tip gap per unit length
 $Re_{\delta t}$ = tip gap Reynolds number = $\rho \bar{u} \delta_t / \mu$
 u, v = velocity components, Fig. 1(a)
 \bar{u} = area-averaged velocity
 U_{max} = maximum velocity in tip gap
 U_0 = free-stream velocity upstream of cascade
 U_t = velocity reached in tip

gap with potential flow analysis, Fig. 1(a)
 x, y = Cartesian coordinates, Fig. 1(a)
 X/c = axial distance from blade leading edge/axial chord
 δ_t = tip gap height
 δ^* = displacement thickness
 ΔZ = blade height
 ρ = density
 σ = contraction ratio or coefficient

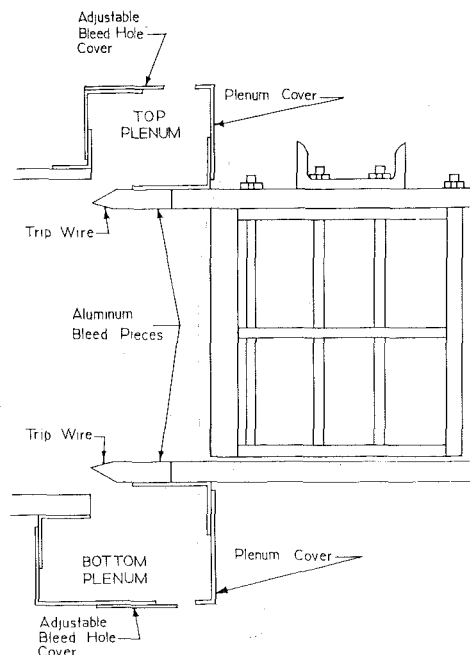


Fig. 3 View V-V of cascade test section (see Fig. 2)

boundary layers in the spanwise direction. They were located approximately 3 mm downstream of the joints of the leading edge Plexiglas tubes and the Plexiglas sides. The areas of contact between the Plexiglas sides and the bottom aluminum formers were bonded together with silicon rubber to prevent any air leaks into the tip gap region. All surface irregularities were removed and joints and countersunk screw holes were filled with plasticene to create a smooth surface.

The five blades were bolted through the top endwall to a piece of aluminum channel, as shown in Fig. 3. This channel was secured to the two wooden end pieces, which had no tip gap and were themselves bolted to the top and bottom endwalls.

Tip Gap. The tip clearance gap was 2.1 percent of the blade span, 5.0 mm. Across the blade row, the tip gap varied from 2.0 to 2.3 percent. However, for the middle three blades, the variation was only between 2.0 and 2.1 percent.

Using Graham's (1985) tentative plot of various tip leakage flow regimes, a tip clearance of at least 1.2 percent in an engine operating at standard speed is expected to produce a tip leakage vortex in the blade passage. The 2.1 percent tip clearance at zero endwall speed of the present study also produced this flow behavior.

Endwall Boundary Layer Bleeds. Two boundary layer bleeds, one on either endwall upstream of the blade row, were located approximately one half of an axial chord upstream of the blade leading edges, as shown in Fig. 2. They reduced the size of the endwall boundary layers as they entered the blade cascade. The purpose of this was to reduce secondary flows so that the three-dimensional flow development would be dominated by the tip gap leakage flow. The tests with the earlier VPI&SU turbine cascade used a thick inlet boundary layer, $\delta_{99}/\Delta Z = 0.16$. Here an attempt was made to reduce the inlet boundary layer thickness below that of the tip clearance gap, $\delta_i/\Delta Z = 0.021$.

The two bleed pieces were constructed of 19-mm-thick aluminum, 76 mm wide. The leading edges were chamfered to produce the shape shown in Fig. 3. The chamfer was selected to reduce the possibility of flow separation occurring over the leading edge of the bleed pieces. The height of the bleeds, from the leading edge of the chamfer to the endwall, was 25.4 mm.

A 0.51-mm-dia trip wire was epoxied on the tunnel side of the chamfer on each of the two aluminum bleed pieces, approximately 9.5 mm downstream of the leading edges, as shown in Fig. 3. The trip wire assisted the establishment of a uniform turbulent endwall boundary layer entering the blade row.

The plenum chambers for the endwall bleeds were built from 3 mm aluminum. They were made to be as identical as possible, to produce uniform effects on the flow. The air flow left the plenum through a series of bleed holes. These holes, symmetrically located around the blade positions to produce similar flow, were sized to have the same pressure drop as flow through the blade cascade. Outside of, and bolted to, the plenum were sliding bleed hole covers which could be adjusted to change the area of the bleed holes, as can be seen in Fig. 3. These bleed hole covers were used with the two wooden bleeds to provide and maintain cascade flow repeatability.

Measurement Locations Upstream. The three-dimensional viscous flow calculations of Moore and Moore (1985) showed a static pressure contour extending approximately straight upstream from the leading edges of the blades, with a value corresponding to the upstream static pressure. This contour appeared to intersect the blade close to the location of the camber line at the leading edge. Similar behavior is observed in the two-dimensional inviscid flow calculations of Langston et al. (1977) and Graziani et al. (1980). Hence, measurements of the upstream static pressure and the upstream endwall boundary layers were made along such contour lines.

The velocity profiles of the endwall boundary layers were measured using a pitot probe at locations *A*, *B*, and *C*, 30 percent of an axial chord upstream of the leading edges of blades 4, 3, and 2, respectively, as shown in Fig. 2. Corresponding upstream static pressures were measured at the endwall, axially upstream of points *A*, *B*, and *C*, 1/3 of an axial chord upstream of the leading edges. These velocity and pressure measurements were made on both the top and the bottom walls.

Blade Static Pressures. Blade loading was measured on blade 3, the middle blade, using static pressure tappings at 45 percent span from the top endwall. The axial locations of the planes used to locate the static pressure tappings are shown in Fig. 4. These planes closely correspond to the measurement planes used by Moore and Ransmayr (1984) and by Langston et al. (1977).

Flow repeatability was established using static pressure tappings on the blade leading edges and by adjusting the cascade end pieces. All five round leading edges were instrumented with three static pressure tappings; Fig. 4 shows the angular locations.

Tip Leakage Flow. The tip leakage flow considered in detail in this paper is that entering the tip gap on the pressure side of blade 3 at plane 6*a*, at 60 percent of an axial chord, and exiting on the suction side at plane 7*aa*, at 72 percent of an axial chord. This assumed flow path is perpendicular to the camber line of the blade, as suggested by Rains (1954) and also as indicated by endwall flow visualization in the present study.

The pressure distribution through the tip gap, on plane 6*a*-7*aa*, was measured using wall static pressure tappings on the bottom of blade 3 and on the endwall beneath blade 3, at the points shown in Fig. 4. For the bottom endwall, these points were supplemented with data from beneath blade 2 and from plane 6*a*-6*a* beneath blade 3.

Blade unloading on the pressure surface at plane 6*a* was measured on blade 2 with static pressure tappings at 0.5, 1.0, 1.5, 2.0, 2.5, and 5.9 tip gap heights from the bottom end of the blade.

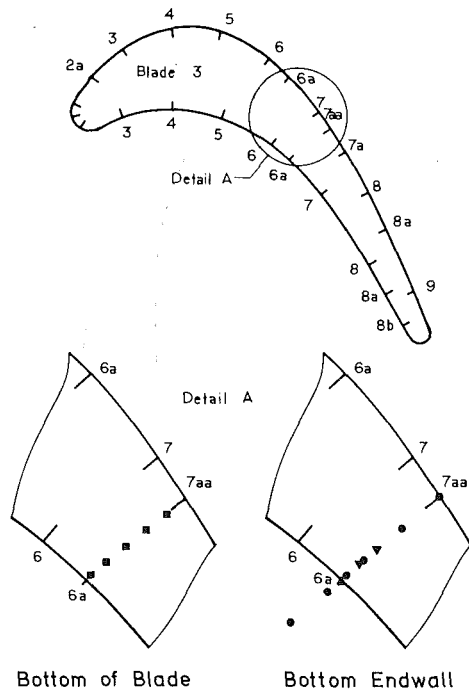


Fig. 4 Locations of static pressure tappings

Tip Gap Exit. The tip gap exit velocity profile was measured at location D in Fig. 2. The tip of the pitot probe was located 6 mm upstream of the tip gap exit at plane 7aa, so as not to interfere with the corresponding reference static pressure tapping on the endwall.

Measuring Equipment. Two pitot probes, both constructed for this study, were used for measurement of velocity profiles. Both probes had flattened tips to provide more accurate total pressure readings. The thickness of the probe tips was 0.53 mm. A one-dimensional traversing gear arrangement was used with the pitot probes. A dial gage, readable to ± 0.01 mm, was used to locate the probes. Pressure readings were converted into electrical signals by a Statham pressure transducer.

Results and Discussion

Flow Conditions. The inlet free stream velocity was $U_0 = 20.1$ m/s. The air density and viscosity were 1.11 kg/m³ and 0.000188 kg/ms, respectively, at the standard test conditions of 94.9 kPa and 298 K. The Reynolds number based on the blade axial chord and an exit velocity of 32.3 m/s was 4.5×10^5 .

Upstream Endwall Boundary Layers. The integral parameters of the turbulent endwall boundary layers, at $X/c = -0.30$, were as follows:

Boundary layer thickness δ_{99}	=	2.18 mm (± 0.13)
Displacement thickness δ^*	=	0.28 mm (± 0.02)
Momentum thickness θ	=	0.19 mm (± 0.01)
Shape factor H_{12}	=	1.47

These values show the average and maximum deviation from the average for measurement locations A, B, and C on both the top and bottom walls. The boundary layers had the same uniform thickness on both walls, and this thickness of 2.2 mm was less than half of the tip clearance height of 5.0 mm.

Blade Loading. The static pressure distribution around the blade at 45 percent span is presented in Fig. 5. The results are compared with values from Moore and Ransmayr (1984),

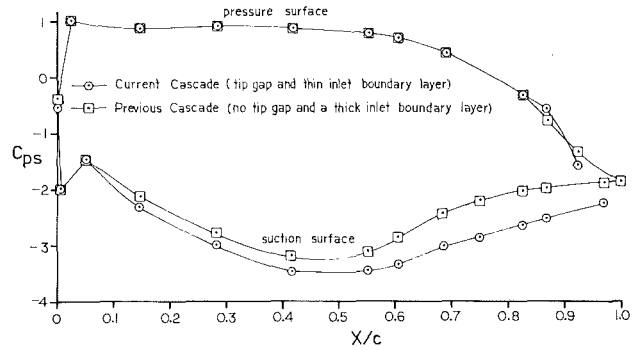


Fig. 5 Static pressure distribution around blade 3 at 45 percent span

who used the same blade shape and size but had no tip gap in a slightly different wind tunnel configuration. The agreement is good, especially on the pressure surface. However, there are quite large differences along the suction surface.

One reason for this is that the ratio of the inlet boundary layer displacement thickness to the passage height for the present tests is much smaller ($\delta^*/\Delta Z = 0.0012$) than that of Moore and Ransmayr ($\delta^*/\Delta Z = 0.023$). The effectively larger mass flow rate in the present tests increased the loading on the blade. This effect of lowered suction surface pressures, caused by a thinner inlet boundary layer, was also observed by Graziani et al. (1980).

Secondly, the thinner inlet boundary layer, combined with the presence of a tip gap, alters the three dimensionality of the flow. The present cascade had a smaller passage vortex in the upper half of the passage, little evidence of a horseshoe vortex in the bottom half, and a tip leakage vortex. Thus, the three-dimensional flow in the present tests is quite different from that of the earlier tests; and variations in the wall static pressure, especially on the suction surface, are also correspondingly different.

Flow Visualization. Flow visualization tests were performed to study the flow pattern on the tip gap endwall and on the suction surface of blade 3. The visualization was achieved by painting a mixture of diesel oil and titanium dioxide onto an aluminum sheet taped to the bottom wall and onto a Mylar sheet taped to the suction surface.

Endwall Surface Flow Visualization. A schematic of the endwall surface flow visualization around and under blade 3 is given in Fig. 6.

At the endwall, the turbulent inlet boundary layer appears to split close to point L, along the thick dashed lines L1 and L2. This flow approaching the blade leading edge, instead of rolling into a horseshoe vortex, as is common in a blade row with no tip gap, flows either under the tip clearance to the suction side of the blade, or across the passage as a secondary flow toward the suction side of the next blade. Upstream of L1, this flow stays attached under the blade until it separates along S1, when it encounters the flow in the passage on the suction side of the blade. Here, S1 lies under the blade outline; it continues downstream, moving out into the flow passage as the tip leakage flow penetrates into the flow path.

The tip leakage flow separates along line S1 and secondary flow moving from the pressure side of the passage to the suction side of the passage separates along line S2 as they meet. Flow in the region between S1 and S2 appears to be quite three dimensional and is difficult to interpret.

Downstream of L1, running the remaining length of the blade, lie a separation line and a reattachment line, S3 and R1, respectively. As will be discussed below, this seems to be a laminar boundary layer separation followed by a turbulent boundary layer reattachment. This laminar boundary layer could be created in the blade passage after the inlet turbulent

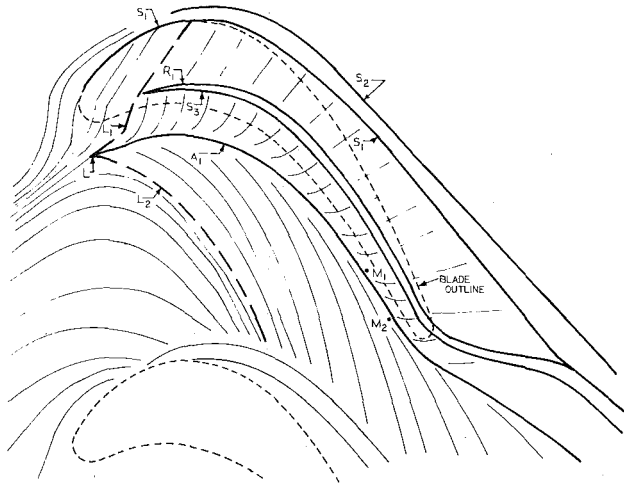


Fig. 6 Schematic of endwall flow visualization showing details of flow under blade 3

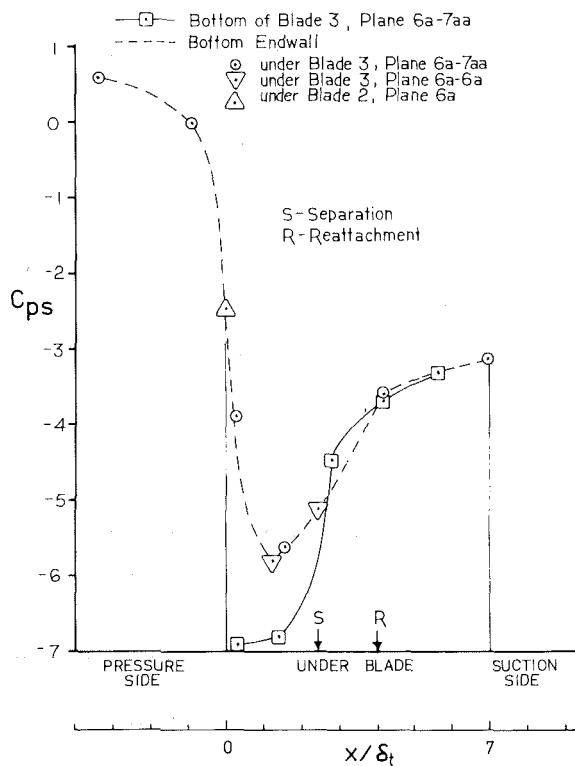


Fig. 7 Tip gap static pressure distributions, plane 6a-7aa

boundary layer is convected away, and might be caused by inviscid free-stream flow then flowing down toward the endwall. This inviscid flow seems to attach as a laminar flow along $A1$ and then accelerate away from this line in a divergent flow pattern. This was confirmed by static pressure measurements along two planes of the blade passage which show pressure maxima at the marked points $M1$ and $M2$ (Tilton, 1986). Belik (1977) and Senoo (1958) are apparently the only ones to have validated this laminar endwall boundary layer hypothesis in a turbine cascade (Sieverding, 1985). Our results, indicating laminar separation of the endwall boundary layer beneath the blades, constitutes a third observation of this behavior.

The tip leakage vortex dissipates downstream, as is suggested by $S1$ and $R1$ merging. The flow continues to separate along $S3$ and $S2$ as the two passage flows mix together.

Suction Surface Flow Visualization. Evidence of a tip

leakage vortex was seen along the bottom of the suction surface. The extent of the influence of the vortex up the suction surface away from the tip gap increased until about halfway along the suction surface and thereafter it remained constant at about 12 percent of blade height. Near the trailing edge, the leakage vortex seemed to be mixing and causing more rapid divergence of the limiting streamlines.

Tip Gap Static Pressures. Figure 7 shows wall static pressure distributions for the tip gap along plane 6a-7aa, which is approximately the path of flow entering the tip clearance at plane 6a. The static pressures along the bottom endwall, represented by the dotted line, show the flow accelerating rapidly as the tip gap is approached. At the entrance of the tip gap, the static pressure coefficient C_{ps} has fallen from 0.61 to -2.44 . The flow continues to accelerate along the endwall until approximately 18 percent through the gap ($x/\delta_t \approx 1.3$) where C_{ps} is -5.8 . Along the blade bottom, near the entrance to the tip clearance, the static pressure coefficient reaches a minimum value for this plane, $C_{ps, \min} = -6.9$. Now, in the same region through the tip gap, 18-20 percent, both the endwall and blade bottom pressures start to rise rapidly, reaching about the same pressure at the tip gap exit, $C_{ps} = -3.1$.

Several observations can be made. The velocity on the blade bottom is expected to be quite high with such a low pressure. Assuming Bernoulli's equation applies, the velocity can be estimated from

$$\frac{U_{\max}}{U_0} = (C_{pt, 1} - C_{ps, \min})^{1/2} \quad (2)$$

With $C_{pt, 1, \text{ideal}} = 1.0$ and $C_{ps, \min} = -6.9$, $U_{\max}/U_0 = 2.81$ and $U_{\max} = 56.5$ m/s.

Also, mixing seems to occur in the final 80 percent of the tip gap, as evidenced by the pressure rise on both the endwall and the bottom of the blade. This suggests the presence of a vena contracta at the minimum pressure along the endwall. This vena contracta has been hypothesized by Rains (1954) and has been partially observed by Graham (1985).

From the flow visualization, separation was seen to occur on the endwall at approximately 35 percent along plane 6a-7aa, with reattachment at approximately 56 percent, marked by S and R , respectively, in Fig. 7. At the separation point C_{ps} is read as -5.1 . Bernoulli's equation can be used again to find the velocity ratio for potential flow along the endwall, thus

$$\left(\frac{U}{U_{\max}}\right)_{\text{endwall}} = \left(\frac{C_{pt, 1} - C_{ps}}{C_{pt, 1} - C_{ps, \min}}\right)_{\text{endwall}}^{1/2} \quad (3)$$

using $C_{pt, 1, \text{ideal}} = 1.0$, from the vena contracta, $C_{ps, \min} = -5.8$, to this separation point, the flow slows to $(U/U_{\max})_{\text{endwall}} = 0.95$.

Turbulent boundary layer separation usually occurs in the range of $U/U_{\max} = 0.5-0.7$, whereas laminar separation occurs when $U/U_{\max} \approx 0.95$. Thus, this value suggests laminar separation and supports the conclusion of Belik (1977) and Senoo (1958) that the endwall boundary layer can be laminar. The present results suggest that the endwall boundary layer downstream of lines $L1$ and $L2$ in Fig. 6 is initially laminar.

Tip Gap Exit Velocity Distribution. The tip gap exit velocity profile for plane 6a-7aa is plotted in Fig. 8. The endwall boundary layer has a thickness of about 2 mm and its shape corresponds quite closely to a $1/7$ th power law; thus it appears to be a turbulent boundary layer. It is concluded that, after the laminar boundary layer separation on the endwall at approximately 35 percent of the way into the tip gap ($x/\delta_t = 2.5$), the reattachment that follows at approximately 56 percent ($x/\delta_t = 3.9$) is probably turbulent.

Tip Gap Reynolds Number. The mean exit velocity at

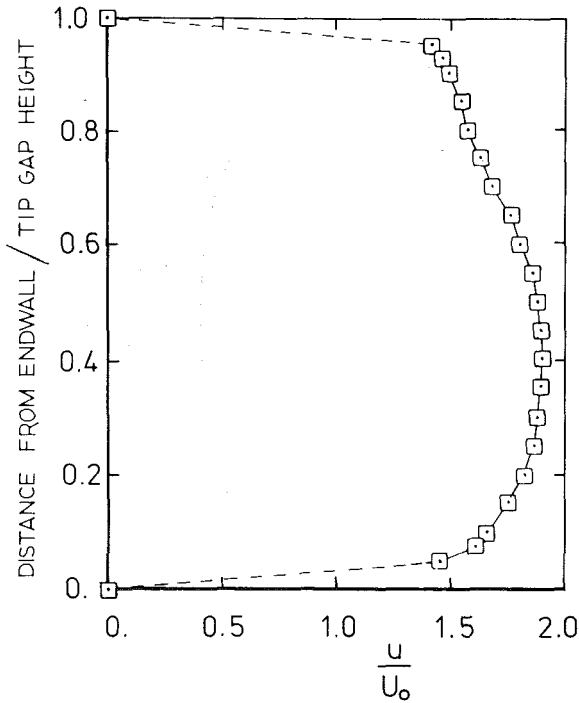


Fig. 8 Tip gap exit velocity distribution at plane 7aa

plane 7aa is found from Fig. 8 to be about $1.71 U_0$ or 34.3 m/s. The tip gap height was 5 mm. Thus the Reynolds number for tip gap flow at plane 6a-7aa in the present tests was $Re_{\delta_t} = \rho \bar{u} \delta_t / \mu = 1.0 \times 10^4$.

Flow Analysis

Potential Flow. Potential flow theory has been used before to describe flow into a tip gap. Rains, in 1954, developed a model, based on flow at rest entering a slot, Fig. 1(a), where, based on symmetry, the centerline of the slot was the bottom endwall. His solution yielded the following equation for obtaining the velocity at any position in the flow field:

$$z = x + iy = \frac{\delta_t \sigma}{\pi} \left[\ln \left(\frac{U_t + \zeta}{U_t - \zeta} \right) - \frac{2U_t}{\zeta} + \frac{i\pi}{2} \right] \quad (4)$$

where σ , the contraction ratio, is $\pi/(\pi+2)$, ζ is the complex velocity, $u - iv$, and U_t is the tip clearance velocity normal to the blade. Using Bernoulli's equation between the upstream and downstream pressures, P_{t1} and P_2 , respectively, then

$$U_t = \left[\frac{2}{\rho} (p_{t1} - p_2) \right]^{1/2} \quad (1)$$

This solution has two limiting cases. One is for flow along the endwall and the other is for flow on the pressure surface of the blade as the tip gap is approached. Rayleigh in 1876 (following Kirchhoff, in 1869) also solved this potential flow problem, however, just for these two limiting cases. The two theories, Rayleigh's and Rains', were compared and were found to be in disagreement. The discrepancy was found to be in Rains' theory. The corrected general solution was found to be

$$z = x + iy = \frac{2\delta_t \sigma}{\pi} \left[\ln \left(\frac{U_t + \zeta}{U_t - \zeta} \right) - \frac{U_t}{\zeta} \right] \quad (5)$$

This solution, derived from an analysis by Milne-Thomson (1968), matches the two limiting cases of Rayleigh's theory.

Comparison With Static Pressure Data. The static pressure data for flow through the tip gap along plane 6a-7aa are compared with Rayleigh's theory, for the endwall in Fig.

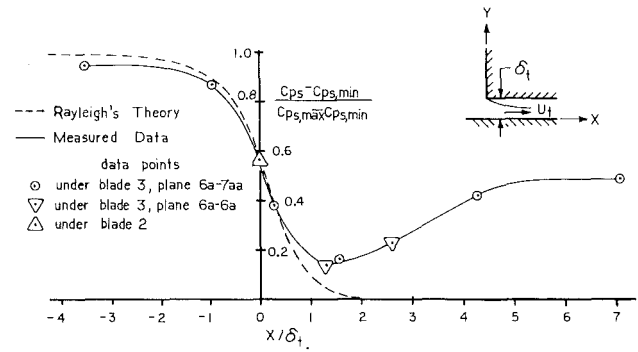


Fig. 9 Static pressures on the endwall compared with potential flow theory

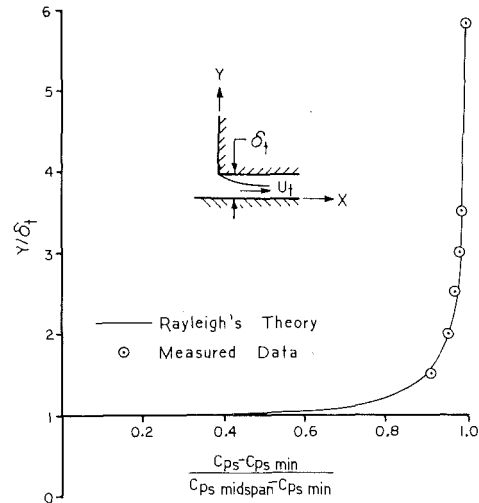


Fig. 10 Static pressures on the blade pressure surface compared with potential flow theory

9, and for the pressure surface of the blade in Fig. 10. The static pressure coefficients were normalized in the following way:

$$(C_{ps} - C_{ps, \min}) / (C_{ps, \max} - C_{ps, \min})$$

For all the data, a value of $C_{ps, \min} = -6.85$ was used. This was the average value of the lowest pressures obtained on the bottom of the blade, rather than on the endwall; see Fig. 7. As noted in Fig. 1(a), the free streamline, as predicted by potential flow theory, would have approximately the same pressure as the bottom of the blade. This is due to the dead flow region between the free streamline and the blade bottom surface where pressure differences are small. Then, with curved streamlines, there will exist a higher pressure at the bottom endwall than at the free streamline, which our data confirm. Thus, Rayleigh's theory, since it is based on a general solution of the flow region, would suggest using this minimum value, and not the minimum pressure along the endwall.

However, the value of $C_{ps, \max}$ used for normalizing each limiting case differed. For the bottom endwall, $C_{pt, 1, \text{ideal}} = 1.0$ was used as the maximum possible value. For the pressure surface of the blade, $C_{ps, \text{midspan}} = 0.71$ was used as $C_{ps, \max}$, obtained from data shown in Fig. 5.

Along the endwall, good agreement is found at the tip gap entrance, for Rayleigh the normalized value is 0.58, and for our data the value is 0.56. Variations soon occur further into the gap as mixing begins, which Rayleigh's theory does not predict. Upstream of the gap the normalized data do not approach 1.0 because the actual C_{ps} is approximately 0.6, rather than the ideal value of 1.0.

The static pressure distribution on the pressure surface of the blade shows excellent agreement at all points with

Rayleigh's theory. For this case, the blade is seen to unload on the pressure surface over about two tip gap heights from the end of the blade.

Comparison With the Contraction Coefficient. Another comparison can be made with the potential flow theory and our investigation. Rayleigh shows the theoretical contraction coefficient is 0.611. A two-dimensional contraction coefficient σ can be calculated from the data as follows:

- (i) Volume flow rate per unit length $= \dot{Q} = \sigma \cdot U_{\max} \cdot \delta_t$
- (ii) $U_{\max}/U_0 = (C_{pt,1} - C_{ps, \min})^{1/2}$
combining (i) and (ii)
- (iii) $\dot{Q} = \sigma U_0 \delta_t (C_{pt,1} - C_{ps, \min})^{1/2}$
- (iv) Measured volume rate $\dot{Q} = \int u dy = \bar{u} \delta_t$,

where \bar{u} ($= 34.3$ m/s) is the area average exit velocity at plane 7aa; see Fig. 8. Combining (iii) and (iv)

$$\sigma = \frac{\bar{u}}{U_0 (C_{pt,1} - C_{ps, \min})^{1/2}} \quad (6)$$

$$= \frac{34.3}{(20.1)(1.0 - (-6.9))^{1/2}}$$

$$\therefore \sigma = 0.607$$

This lends further support to the idea that the tip leakage flow exhibits a vena contracta near the entrance of the tip gap. The agreement between the theoretical contraction coefficient and that deduced from the measurements is excellent. It also suggests that tip gap flow coefficients may be better analyzed using the minimum static pressure under the blade, rather than an overall static pressure drop from the pressure side to the suction side, which is how it is usually done now.

Potential Flow With Mixing. A simple two-dimensional potential flow with mixing model for flow through the tip gap, see Fig. 11, was developed for comparison with our data. For this model, values of $C_{pt,1}$ and $C_{ps, \text{exit}}$ were assumed fixed at values of 1.0 and -3.1 , respectively. This was equivalent to fixing the upstream and exit pressures. $C_{pt,1} = 1.0$ is the ideal value and $C_{ps, \text{exit}} = -3.1$ was obtained from Fig. 7. Now, as in the Results section, using the Bernoulli equation for the flow into the tip gap up the vena contracta

$$C_{pt,1} - C_{ps, \min} = U_{\max}^2 / U_0^2 \quad (7)$$

Assuming mixing occurs between the vena contracta and the tip gap exit, the momentum equation yields

$$\frac{P_{\text{exit}} - P_{\min}}{\rho U_{\max}^2} = \sigma - \sigma^2 = 0.611 - (0.611)^2 \quad (8)$$

$$= 0.2377$$

and

$$C_{ps, \text{exit}} - C_{ps, \min} = 0.475 U_{\max}^2 / U_0^2 \quad (9)$$

Combining equations (7) and (9)

$$C_{ps, \min} = \frac{1}{0.525} [C_{ps, \text{exit}} - 0.475 C_{pt,1}] \quad (10)$$

$$= \frac{1}{0.525} [-3.1 - 0.475(1.0)]$$

$$\therefore C_{ps, \min} = -6.81$$

This is the pressure the model will asymptotically approach within the distance of approximately two tip gaps under the blade, as seen in Fig. 9. It agrees well with the measured minimum static pressure coefficient of -6.9 , see Fig. 7.

On the endwall at the tip gap entrance, the model predicts

$$C_{ps} = C_{ps, \min} + 0.58(C_{pt,1} - C_{ps, \min}) \quad (11)$$

$$= -6.81 + 0.58[1.0 - (-6.81)]$$

$$C_{ps} = -2.28$$

--- Potential Flow with Mixing Analysis
 --- Potential Flow Analysis
 —□— Bottom of Blade 3, Plane 6a-7aa
 - - - - Bottom Endwall
 ○ under Blade 3, Plane 6a-7aa
 ▽ under Blade 3, Plane 6a-6a
 △ under Blade 2, Plane 6a

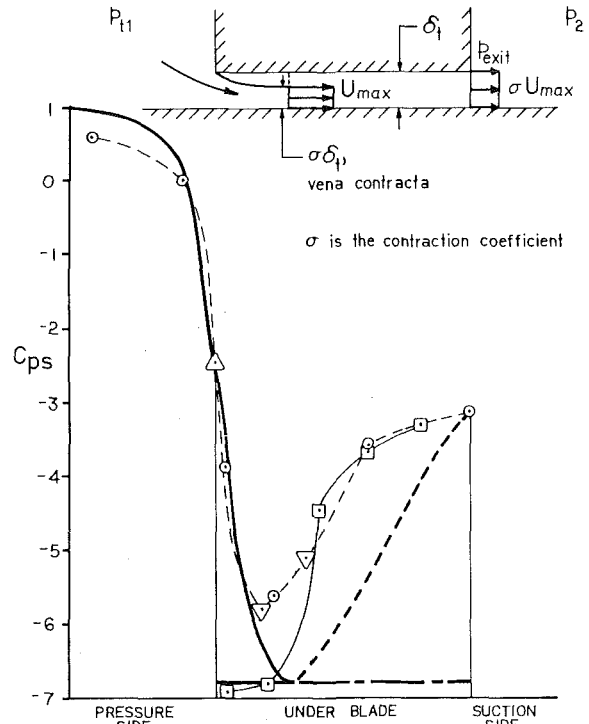


Fig. 11 Tip gap static pressure distributions compared with flow models

Again, this compares well with the measured value of -2.44 from Fig. 7.

The endwall static pressure distribution for this model is compared to the measured data in Fig. 11. The pressure drop into the gap is predicted well, as the vena contracta is approached. If no mixing occurred after the vena contracta, the pressure would remain at the minimum pressure, as shown by the intermittent line. With mixing, the rate of theoretical pressure rise can only be estimated by the present analysis, shown by the dotted line; however the magnitude of the pressure rise is well modeled.

One difference between this model, which includes mixing, and flow in the actual turbine cascade, is that the flow area in tip gap region increases perpendicular to the camber line across the blade width. Thus, in reality, the flow area is not constant and the flow geometry is not exactly two-dimensional. Secondly, this model does not account for the observed laminar boundary layer separation or the turbulent boundary layer reattachment on the endwall in the tip gap, both of which were noted in Fig. 7. However, for a simple analysis, this two-dimensional potential flow model is surprisingly accurate and it does aid in understanding the physics of tip gap flow.

Overall Discharge Coefficient of Tip Gap. An overall discharge coefficient for the tip gap can be evaluated using the measured exit flow rate and the overall pressure difference, $P_{11} - P_{\text{exit}}$. Thus

$$C_D = \frac{\bar{u}}{U_0 (C_{pt,1} - C_{ps, \text{exit}})^{1/2}} \quad (12)$$

with $\bar{u} = 34.3$ m/s, $U_0 = 20.1$ m/s, $C_{pt,1} = 1.0$, and $C_{ps, \text{exit}} = -3.1$, $C_D = 0.843$.

The effect of mixing in the tip gap, with its corresponding pressure rise, is seen to be an increase in the discharge coefficient from 0.61 to 0.84.

This value of 0.843 at a Reynolds number of 1.0×10^4 compares well with the experimental value of 0.851 obtained by Wadia and Booth (1982) with a flat tip at a Reynolds number of 0.65×10^4 on their water table discharge rig.

The present potential flow with mixing analysis shown schematically in Fig. 11 gives an overall discharge coefficient

$$C_D = \sigma[1 - 2(\sigma - \sigma^2)]^{-1/2} \quad (13)$$

and from potential flow theory $\sigma = \pi/(\pi + 2) = 0.611$; thus

$$C_D = 0.8436.$$

This agrees well with the present value and with that of Wadia and Booth, lending further support to the idea that incompressible flows in flat tip gaps with sharp entrances exhibit a vena contracta with a contraction coefficient of about 0.61.

Performance of Tip Gap as a Short Tube. In hydraulic engineering, a short cylindrical tube 2.5 to 3 diameters in length with sharp upstream corners, used for flow measurement, is called a standard short tube (Brater, 1959). The flow in such tubes was measured by Weisbach (1855, 1896) and ever since his data have been quoted. Weisbach found a vena contracta, due to the sharp corner, followed by flow mixing to fill the tube. With a large upstream flow area compared with the area of the tube, and with tube lengths of about three diameters, the discharge coefficient was 0.82 (± 0.02).

The hydraulic diameter of a tip gap is equal to two tip gap heights. Thus flow in a standard short tube of three diameters in length is equivalent to flow in a blade width of six tip gap heights. For plane 6a-7aa in the present tests the blade width was seven tip gap heights and the tip gap Reynolds number was in the range of Weisbach's tests, so it is perhaps not surprising that the discharge coefficient agrees so well with Weisbach's value.

Vennard (1961) has performed further analysis of Weisbach's data. Vennard noted that the overall head loss in the short tube was 0.50 exit velocity heads. He then used a mixing analysis, based on a contraction coefficient of 0.617 (from Weisbach's orifice measurements), to evaluate the contribution due to mixing losses in the deceleration zone downstream of the vena contracta. The rest of the losses he attributed to a loss in the acceleration zone up to the vena contracta. These he estimated to be about 4 percent of the velocity head at the vena contracta, $U_{\max}^2/2g$.

Heat Transfer

Heat Transfer to Rotor Blade Tips. Mayle and Metzger (1982) considered the mean heat transfer to the flat ungrooved tip of an unshrouded turbine blade. They used an experimental model in which the endwall could be rotated past a stationary test surface. There was no measurable effect of the moving wall on the mean heat transfer for the range of parameters

Re_{δ_t}	$0.8 \times 10^4 - 3.1 \times 10^4$
L/δ_t	6-41
Re_L	$0.5 \times 10^5 - 6.2 \times 10^5$
$\omega R/\bar{u}$	0.1-1.0

where L is the flow length over the blade tip and ωR is the velocity of the moving wall relative to the blade tip. They concluded that the blade tip heat transfer coefficients can be determined from experiments without a moving wall, or as Metzger later said (1985) "for clearances normally employed, the relative motion of the shroud has a negligible effect on the blade tip heat transfer."

Metzger and Bunker (1985) then measured local surface heat transfer rates to a model turbine blade tip in a test ap-

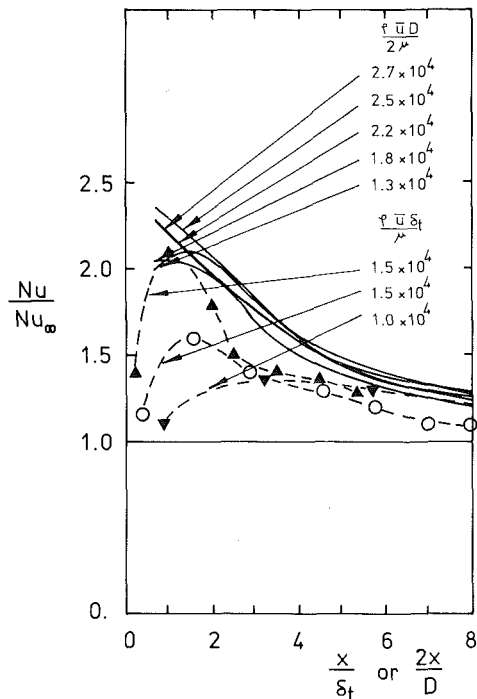


Fig. 12 Correlation of local heat transfer to a model turbine blade tip with heat transfer near the entrance of a circular tube. Ratio of local Nusselt number to that with fully developed flow. — Metzger and Bunker (1985)—model turbine; — Boelter et al. (1948)—circular tube with right-angle-edge entrance. δ_t = tip gap height; D = tube diameter.

paratus with no relative motion of the endwall. They tested both ungrooved and grooved tip geometries. Their results for the flat ungrooved geometries are presented as measured data points joined by dotted lines in Fig. 12. The local Nusselt numbers are normalized with the fully developed channel values expected by Metzger; they are presented as a function of distance, in tip gap heights, downstream of the tip gap entrance.

Figure 12 also shows curves representing measured distributions of local heat transfer near the entrance of a circular tube with a right-angle-edge entrance; these distributions are from measurements made by Boelter et al. for NACA (1948). It should be noted that the comparison with NACA data given by Metzger and Bunker is for the bare sharp-edged entrance shown by Kays and Crawford (1980), not for the right-angle-edge entrance, which is more appropriate and shows different development in the first two diameters along the tube, i.e., in the region of most interest in turbine tip cooling. Also worth noting is that Metzger and Bunker chamfered their upstream blade face to give a 70 deg edge instead of a right-angle-edge.

The Nusselt number ratio Nu/Nu_{∞} in Fig. 12 is presented as a function of tip gap Reynolds number, $\rho\bar{u}\delta_t/\mu$, and the equivalent tube Reynolds number $\rho\bar{u}D/2\mu$. The NACA data are for the Reynolds number range 1.3×10^4 to 2.7×10^4 and the data are quite consistent for $x/\delta_t > 2$. For Reynolds numbers greater than 2.0×10^4 , the data show the Nusselt number ratio rising monotonically toward a value of 2.5 at the tube entrance although data were obtained only at one-third and one diameter along the tube. Below a Reynolds number of 2.0×10^4 , the NACA data show a tendency toward reduced Nusselt numbers at $x/\delta_t < 2$. This trend is supported by the data of Metzger and Bunker although there appears to be some inconsistency at a Reynolds number of 1.5×10^4 . Metzger and Bunker found quite low heat transfer ($Nu/Nu_{\infty} < 1.5$) at a Reynolds number of 1.0×10^4 , but really there are few data points in this case.

With the grooved tip geometries, the heat transfer distribu-

tions measured by Metzger and Bunker over the blade tip upstream of the groove were similar to the distributions with no tip groove. However, the heat transfer distributions over the blade tip downstream of the tip groove showed a peak much closer to the upstream edge. The flow downstream of the groove therefore seems to exhibit an effectively higher Reynolds number, possibly due to turbulence created by the groove.

Figure 12 provides a useful correlation for turbine tip heat transfer. The physics underlying the factor of 2.0–2.5 enhancement over the first two tip lengths is clearly associated with the leading edge separation and the recirculation next to the vena contracta. It may be, for example, that the head loss of 4 percent of the kinetic energy at the vena contracta, which Vennard suggests for the acceleration zone (1961), results in turbulence kinetic energy which could contribute to the enhancement. Thus the flow physics described in this paper may help explain the available data on turbine tip heat transfer. But it should be remembered that all the flows discussed in this paper were essentially incompressible.

Conclusions

An experimental investigation has been performed to study the details of flow in the tip clearance gap of a linear turbine blade cascade. The cascade was designed and built to be geometrically similar to the earlier VPI&SU cascade; however, the new cascade also had a tip gap and two endwall boundary layer bleeds upstream of the blade row. The cascade flow had an exit Reynolds number based on axial chord of 4.5×10^5 and the tip gap was 2.1 percent of blade height.

Static pressure measurements were made on the blades and on the endwall with particular attention given to the tip gap at about 60 percent of axial chord. A minimum static pressure coefficient of -6.9 (based on inlet free-stream velocity head) was obtained along the bottom of the blade, near the tip gap inlet. A vena contracta was evident, also in the tip gap entrance region, and a contraction coefficient of 0.61 was calculated from measured data. Mixing occurred after the vena contracta with the static pressure across the tip gap exit being fairly uniform.

Potential flow theory accurately models the unloading along the pressure surface of the blade and the endwall static pressure distribution of the tip gap, up to the vena contracta. It also predicts a contraction coefficient of 0.61 . A combined potential flow and mixing model accounts for the pressure rise in the tip gap due to mixing. It predicts a minimum static pressure coefficient under the blade of -6.8 , which agrees well with measured data.

The discharge coefficient for the tip gap at about 60 percent of axial chord, based on the overall pressure difference, was calculated from measured data to be 0.84 . This agrees well with the potential flow and mixing model which gives 0.8436 .

For incompressible flow, the flow development in flat tip gaps with sharp upstream corners is similar to that in a "standard short tube," which has been well known to hydraulic engineers since Weisbach's experiments in 1855.

A correlation of local heat transfer rates for low Mach number flow over unshrouded turbine rotor blades has been presented. The enhanced heat transfer near the tip gap entrance is clearly associated with the leading edge separation and recirculation next to the vena contracta.

In practice, unshrouded turbine rotor blades in gas turbines operate with transonic flow. Flow in the tip clearance gaps is then probably choked at least over part of the blade chord.

The published literature appears to contain little information on tip leakage flow and heat transfer in this compressible flow regime.

Acknowledgments

The authors wish to thank Rolls-Royce plc, Aero Division, for supporting this work under a cooperative agreement with Virginia Polytechnic Institute and State University. They are also grateful for the helpful discussions with C. Graham of Rolls-Royce and F. Simon of NASA Lewis Research Center.

References

- Belik, L., 1977, "Three Dimensional and Relaminarization Effects in Turbine Blade Cascades—An Experimental Study," *Proceedings of 1977 Joint JSME/ASME Gas Turbine Congress*, pp. 301–310.
- Boelter, L. M. K., Young, G., and Iversen, H. W., 1948, "An Investigation of Aircraft Heaters XXVII—Distribution of Heat Transfer Rate in the Entrance Section of a Circular Tube," NACA TN 1451, July 1948.
- Booth, T. C., Dodge, P. R., and Hepworth, H. K., 1982, "Rotor-Tip Leakage: Part I—Basic Methodology," *ASME Journal of Engineering for Power*, Vol. 104, pp. 154–161.
- Brater, E. F., 1959, "Hydraulics," in: *Civil Engineering Handbook*, L. C. Urquhart, ed., 4th ed., McGraw-Hill, New York.
- Graham, J. A. H., 1985, "Investigation of a Tip Clearance Cascade in a Water Analogy Rig," ASME Paper No. 85-IGT-65.
- Graziani, R. A., Blair, M. F., Taylor, J. R., and Mayle, R. E., 1980, "An Experimental Study of Endwall and Airfoil Surface Heat Transfer in a Large Scale Turbine Blade Cascade," *ASME Journal of Engineering for Power*, Vol. 102, pp. 257–267.
- Hennecke, D. K., 1985, "Active and Passive Tip Clearance Control," *Tip Clearance Effects in Axial Turbomachines*, von Karman Institute for Fluid Dynamic, Lecture Series 1985-05.
- Kays, W. M., and Crawford, M. C., 1980, *Convective Heat and Mass Transfer*, 2nd ed., McGraw-Hill, New York.
- Kirchhoff, G., 1869, "Zur Theorie freier Flussigkeits-strahlen," *J. fur Mathematik*, Crelle, Vol. LXX, No. 4, Berlin.
- Langston, L. S., Nice, M. L., and Hooper, R. W., 1977, "Three-Dimensional Flow Within a Turbine Cascade Passage," *ASME Journal of Engineering for Power*, Vol. 99, pp. 21–28.
- Mayle, R. E., and Metzger, D. E., 1982, "Heat Transfer at the Tip of an Unshrouded Turbine Blade," *The Seventh International Heat Transfer Conference*, Munich, Vol. 3, pp. 87–92.
- Metzger, D. E., and Bunker, R. S., 1985, "Cavity Heat Transfer on a Transverse Grooved Wall in a Narrow Flow Channel," ASME Paper No. 85-HT-57.
- Milne-Thomson, L. M., 1968, *Theoretical Hydrodynamics*, MacMillan, 5th ed., pp. 332–334.
- Moore, J., and Moore, J. G., 1985, "Performance Evaluation of Linear Turbine Cascades Using Three-Dimensional Viscous Flow Calculations," *ASME Journal of Engineering for Gas Turbines and Power*, Vol. 107, No. 4, pp. 969–975.
- Moore, J., and Ransmayr, A., 1984, "Flow in a Turbine Cascade: Part I—Losses and Leading-Edge Effects," *ASME Journal of Engineering for Gas Turbines and Power*, Vol. 106, No. 2, pp. 400–408.
- Moore, J., Shaffer, D. M., and Moore, J. G., 1987, "Reynolds Stresses and Dissipation Mechanisms Downstream of a Turbine Cascade," *ASME JOURNAL OF TURBOMACHINERY*, Vol. 109, pp. 258–267.
- Rains, D. A., 1954, "Tip Clearance Flows in Axial Flow Compressors and Pumps," California Institute of Technology, Hydrodynamics and Mechanical Engineering Laboratories, Report No. 5, June 1954.
- Rayleigh, J. W. S., 1876, "Notes on Hydrodynamics," *Scientific Papers*, Vol. 1; Dover Publications, 1964, pp. 297–304.
- Senoo, Y., 1958, "The Boundary Layer on the End Wall of a Turbine Nozzle Cascade," *Transactions of the ASME*, Vol. 80, pp. 1711–1720.
- Sieverding, C. H., 1985, "Recent Progress in the Understanding of Basic Aspects of Secondary Flows in Turbine Blade Passages," *ASME Journal of Engineering for Gas Turbines and Power*, Vol. 107, pp. 248–257.
- Tilton, J. S., 1986, "Tip Leakage Flow in a Linear Turbine Cascade," M. S., Thesis, Virginia Polytechnic Institute and State University, Blacksburg, VA.
- Vennard, J. K., 1961, "One-Dimensional Flow," *Handbook of Fluid Dynamics*, V. L. Streeter, 1st ed., McGraw-Hill, New York.
- Wadia, A. R., and Booth, T. C., 1982, "Rotor-Tip Leakage: Part II—Design Optimization Through Viscous Analysis and Experiment," *ASME Journal of Engineering for Power*, Vol. 104, pp. 162–168.
- Weisbach, J., 1896, *Lehrbuch der Ingenieur- und Maschinen-Mechanik*, 5th ed., Friedrich Vieweg und Sohn, Braunschweig.

Modeling the Unsteady Flow in a Turbine Rotor Passage

D. J. Doorly

University College,
London, United Kingdom

The effects of the wakes shed by an upstream blade row in forcing the transition of an otherwise laminar rotor blade boundary layer are well recognized. Previous experiments have demonstrated that the forced transition of the laminar boundary layer may greatly influence the surface heat flux. The effect of the wakes on the surface heat flux when the undisturbed boundary layer is already turbulent have been studied using an experimental simulation technique. The results have been analyzed with a view to establishing how well the effects of the wakes can be described by a model which treats only their turbulence content. The effects of wake passing at a reduced Reynolds number are also reported.

Introduction

The unsteady flow that occurs in the passages of an axial flow turbomachine is currently the focus of much attention, within the context of aerodynamic, heat transfer, and blade flutter studies. Recent experiments have demonstrated that flow unsteadiness can affect the aerodynamic and, for turbines, the heat transfer performance of the blades. There is thus a clear need to develop theoretical models of this flow. By identifying the mechanisms through which the unsteadiness affects the blade performance, the experiments can play a vital role in the process of model development.

In an axial flow turbomachine, the unsteadiness of the flow arises largely through the relative motion of the alternately stationary and rotating annular blade rows, which comprise each compressor and turbine stage. The principal components of the unsteadiness have been described by Doorly (1983), Doorly and Oldfield (1985a, b) and Doorly et al. (1985) and are summarized as follows.

(1) Wake Passing. The exit flow from a given blade row is nonuniform in the circumferential direction, primarily due to the presence of wakes, which are shed at the trailing edge of each blade. These wakes subject the blades of the downstream row to a periodically varying inlet velocity, and turbulence flow field, since the relative rotation of the rows causes the downstream blades to "chop" through the wakes.

(2) Shock Wave Passing (for transonic stages only). Shock waves generated by a transonic blade row impinge on the blades of the downstream row. Each downstream blade consequently chops periodically through shock waves, in addition to wakes.

(3) Potential Flow Interactions. Periodic variations in the potential flowfield around each blade are caused by the relative motion between it and the blades of the rows im-

mediately upstream and downstream, respectively. This form of unsteadiness decays rapidly with increased row spacing.

(4) Additional High-Energy Turbulence. In contrast to the preceding effects, random, high-energy turbulence may also occur. For example, in the high-pressure turbine stage, flame unsteadiness in the combustion chamber may generate high levels of turbulence, which persists through the first and second turbine blade rows.

For the high-pressure turbine rotor operating just transonically, the shock waves are comparatively weak. Furthermore, the midheight axial gap between rows may be sufficiently large so as to reduce potential flow interactions. Wake-passing and turbulence effects may thus be considered to dominate the unsteadiness, at least as a first approximation.

Unsteady Flow Studies. There have been a number of studies of the aerodynamic effects of wake passing on turbomachinery blade performance, using low-speed rotating compressors (Walker and Oliver, 1972; Walker, 1974; Evans, 1982) and turbines (Dring, 1982; Hodson, 1984). These experiments have shown that the wakes shed by the blades of one row induce an unsteady transition of the boundary layer on the blades comprising the downstream blade row. Furthermore, the increased profile loss of a blade tested in a machine over that experienced in a low disturbance cascade flow has been attributed (Samoilvich and Yablokov, 1974; Hodson, 1984) to the forced transition process. The combined effects of the wakes and secondary flow vortex generated by the blades of one row on the blades of the downstream row have recently been investigated (Binder, 1985).

Less attention has been directed toward an assessment of the effects of flow unsteadiness on the heat transfer rate to turbine blades, although much could be inferred from the boundary layer behavior reported in the aerodynamic studies. An early investigation (Bayley and Priddy, 1981), however, indicated that high free-stream turbulence greatly enhanced the mean heat transfer level. Measurements to a fully rotating turbine stage (Dunn, 1985; Dunn et al., 1986) have shown that significant heat transfer effects may arise not merely from the

Contributed by the Gas Turbine Division of THE AMERICAN SOCIETY OF MECHANICAL ENGINEERS and presented at the 32nd International Gas Turbine Conference and Exhibit, Anaheim, California, May 31-June 4, 1987. Manuscript received at ASME Headquarters February 19, 1987. Paper No. 87-GT-197.

flow unsteadiness produced on the downstream blades by those upstream, but also vice versa through potential flow interaction. It is unlikely, therefore, that the significance of potential flow interaction can be entirely discarded.

The above studies indicated that the response of the transition behavior of the blade boundary layer to the imposed unsteadiness plays a fundamental role in determining the scale of the heat transfer and aerodynamic effects. A major effect of the wakes is to increase the turbulence level; of relevance therefore are the results of more detailed studies of the factors affecting boundary layer transition in the presence of free-stream turbulence. This has been addressed by Wittig and Rued (1986) and Blair (1983). The consequences of the transition process in terms of profile loss are dealt with by Kiock and Hoheisel (1986) and in terms of surface heat flux by Gaugler (1985).

Modeling the Unsteady Transition Process: Experimental Techniques. Boundary layer transition, especially in response to highly unsteady flow, is a complex process. The boundary layer may be regarded as a nonlinear system primarily responding to (and in some circumstances interacting with) disturbances in the outer free stream. The basic character or state of the boundary layer may be described principally by the operating Reynolds number, the geometry, and for compressible flows, the Mach number. Other variables such as wall heating or cooling may also contribute to the basic state description of the boundary layer. The stability of the boundary layer, and the disturbance modes to which it is most susceptible, depend on the basic state described by the abovementioned variables. To develop a theoretical model of the transition process, the relative importance and effects of the various disturbances present in the particular free-stream environment on the boundary layer response need to be studied.

In turbomachinery flow research, recent developments in instrumentation and data acquisition techniques are now beginning to make possible the measurement of the flow quantities and heat transfer in fully rotating, three-dimensional test rigs (Epstein et al., 1985; Dunn et al., 1986). There are still many difficulties in the provision of both adequate instrumentation and flow visualization, within the limitations imposed by the rig complexity. More significantly however, such test rigs suffer from an inherent disadvantage in that it is difficult to vary conveniently the disturbance parameters, and furthermore, generally impossible to impose separately the various components of unsteadiness.

A technique has been developed at Oxford, however, as described by Doorly (1983), Doorly and Oldfield (1985a, b), and Doorly et al. (1985), which achieves an effective simulation of several of the major phenomena at the expense of a nonexact representation of the full three-dimensional flow. This simulation allows the relative significance of some of the major possible sources of unsteadiness to be assessed, both individually and in combination. In this technique, wake and

shock passing are simulated on a fixed blade mounted in a two-dimensional cascade. A short duration wind tunnel, combined with a rotating wake generator positioned upstream of the cascade, provides an unsteady flow at the cascade inlet, which simulates that experienced by a rotor blade in an engine. The device is not expected to be a substitute for fully rotating instrumented test rigs. It is intended to serve as a tool for studying some features of the unsteadiness in greater detail than may presently be possible with a rotating rig, thus complementing results from the fully rotating stage. Where differences arise due to the effects not represented by the simulation, the scale of the differences may help assess the importance of the neglected effects, and thereby further contribute to theoretical modeling.

The design and construction of the wake generator is reported fully by Doorly (1983). The basic geometry of the device and the nature of the transient wind tunnel to which it is attached have already been extensively reported (Doorly and Oldfield, 1985a, b; Doorly et al., 1985; Jones et al., 1979) and will not be repeated here. The periodic chopping of the turbine blade through the vane wakes is simulated by moving a row of cylindrical bars across the flow, upstream of the entrance to a fixed cascade of rotor blades. At sufficiently high Mach numbers, shock waves are also generated by the bars, so that shock wave passing may also be simulated. The wind tunnel provides, as base, a wide Reynolds and Mach number operating range at varying gas-to-wall temperature ratios for the fixed rotor cascade. Altering the size, spacing, and Mach number of the wake-generator bars, together with the addition of turbulence grids, allows a broad range of unsteadiness parameters to be attained.

Purpose of Present Paper. The results that have been reported to date have concentrated largely on the simulation of essentially "simple" unsteady flows; i.e., isolated wake and shock disturbances. The present paper considers, firstly, the results of the simulation of more complex unsteady flows in greater detail than reported earlier, and secondly, investigates the dependence of the unsteady effects on the operating Reynolds number. The objectives of the work are likewise twofold. Firstly, the validity of a simple model of the effects of wake passing (suggested by the earlier studies of "simpler" unsteadiness) is investigated in more complex flows and under a wider range of influences. The comparison serves to indicate deficiencies in the modeling. Secondly, the additional experimental data may both provide clues as to the reasons for the deficiencies, and guide the development of a more complete model.

As before, the investigation is restricted to the first 50 percent surface distance on the suction surface. Beyond this point, the boundary layer is almost invariably turbulent, as the strong acceleration is generally absent and there are additional strong disturbances due to passage shocks. The pressure surface boundary layer structure is complex even under steady flow conditions and will be considered in the future.

Nomenclature

E = exponentiation (base 10)	s = surface distance measured from leading edge	$\gamma(x)$ = intermittency factor
F = Fourier transform operator	t = time	ν = kinematic viscosity
FFT = Fast Fourier transform	Tu = turbulence intensity	Subscripts, superscripts, and special symbols
F^{-1} = Inverse Fourier transform	U = free-stream velocity	' = complex conjugate
K = Acceleration parameter	x/s = fractional surface distance from leading edge	* = cross-correlation operator
NGV = nozzle guide vane	x = distance	$\bar{}$ = time mean value
\dot{q} = heat flux		∞ = free-stream conditions
$\dot{q}_N(t, x)$ = normalized unsteady heat flux		

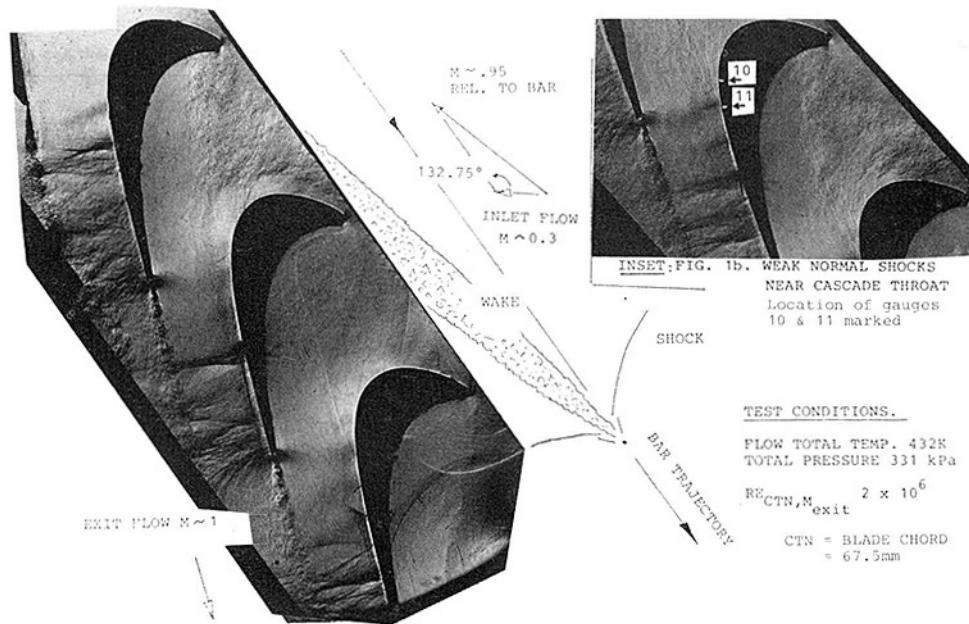


Fig. 1 Schlieren photograph of shock wave and wake from 1.7-mm-dia bar entering turbine rotor cascade

Experimental Arrangement

The geometry of the wake generator, the cascade and blade profile, and the transient wind tunnel operation are comprehensively described in the references already noted. In addition, the rotor profile used for this work has been the subject of a detailed boundary layer and aerodynamic study under steady flow conditions, using a very large-scale model in the Oxford blowdown tunnel (King, 1986). Film cooling studies (again with steady flow) have been performed by Horton et al. (1985) and aerodynamic and loss measurements were reported by Nicholson (1981). The Schlieren photograph of Fig. 1 shows the cascade at design operating conditions, together with the shock wave and wake from a cylindrical bar moving across the flow. The measured Mach number distribution (using the data of Nicholson, 1981), together with the gage positions and operating conditions, are shown in Figs. 1 and 2. The heat flux measuring technique uses machinable glass ceramic model blades (as described by Jones et al., 1979), high-frequency analog circuitry (Oldfield et al., 1982) and a high-speed (up to 2 MHz) multichannel data acquisition system (Doorly et al., 1985).

The experiments performed to fix the size of cylindrical bar to model the NGV wake were described by Doorly (1983). Two sizes were used for this work; the small (diameter 0.91 mm) bars were selected as representative of the wake from a modern efficient uncooled NGV, the large (diameter 1.71 mm) bars were expected to model a worst case cooled NGV. With eight bars fitted to the wake generator, the midspan bar spacing was equal to 2.05 times the rotor cascade pitch, closely modeling the actual NGV/rotor pitch ratio. (The effects of isolated wakes and shocks were studied previously with only two bars fitted.)

The processing procedure that was applied to the signals to correct for surface temperature rise is described by Doorly (1983). The mean heat flux levels presented here have, however, been obtained by averaging 3000 high-speed samples, corresponding to a 15 ms interval. This is in contrast to the data reported by Doorly et al. (1985), where the averaging was performed using only about 50 slow-speed (computer sampled) values. The differences in the results are only noticeable for the highly unsteady signals, where the present

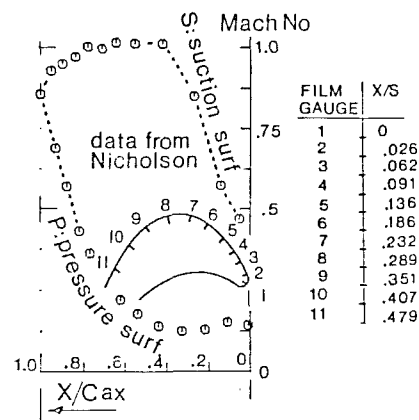


Fig. 2 Blade Mach number distribution (from the data of Nicholson, 1981), and location of thin film heat flux gauges

processing is considered more accurate (although the form of the results is nevertheless unchanged).

Effect of Free-Stream Turbulence on Boundary Layer Transition

(1) Mean and Unsteady Heat Flux. Heat flux measurements were first performed under conditions of varying levels of free-stream turbulence. Although turbulence represents a form of unsteadiness, the overall passage flow, which largely determines the basic boundary layer state, generally remains unchanged, and steady for turbine cascades.

The particular rotor profile investigated (Fig. 2) is characterized by a high acceleration on the early part of the suction surface. This exerts a strongly stabilizing effect on the boundary layer.

An acceleration parameter, defined by

$$K = \frac{v_{\infty}}{U_{\infty}^2} \frac{dU_{\infty}}{dx} \quad (1)$$

is often used to quantify the acceleration. The best estimate of K for the rotor profile considered may be obtained using the

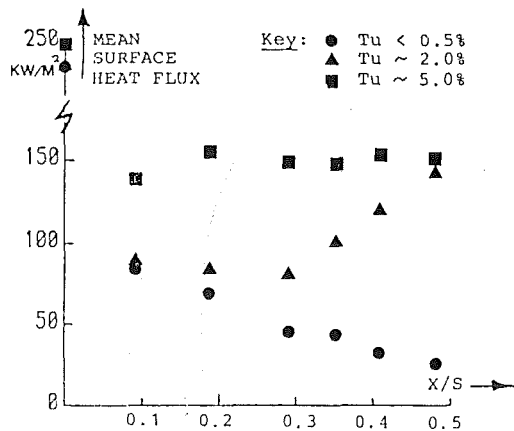


Fig. 3 Effect of free-stream turbulence on mean heat flux

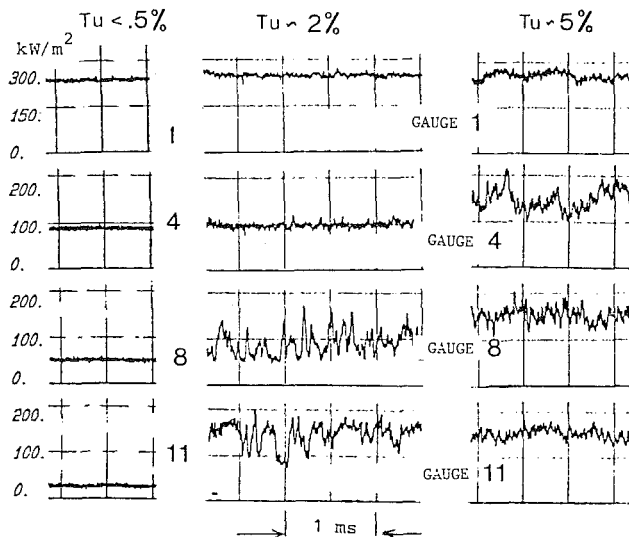


Fig. 4 Unsteady surface heat flux signals for free-stream Tu levels of < 0.5, 2, and 5 percent

very detailed pressure measurements of King (1986). These show that the acceleration of the flow around the blade leading edge circle is followed by a sharp deceleration at an x/s of about 0.018, due to a blend point irregularity. This is followed by a strong acceleration which continues to an x/s of 0.2, with K at least $1.5E-6$ or slightly greater throughout. Farther downstream of $x/s=0.2$, the acceleration parameter drops to K of $0(0.4E-6)$ at an x/s of 0.3, and reaches zero by an x/s of about 0.4. In addition to the strong acceleration, the convex curvature is also expected to exert a stabilizing effect, and reduce the turbulent heat flux (Gillis and Johnston, 1979).

The mean heat fluxes under conditions of 0.5, 2, and 5 percent Tu are shown in Fig. 3. Portions of the unsteady heat flux signals at each condition, at various points on the surface, are shown in Fig. 4. (The turbulence was not measured in this work, but previously obtained measurements of the turbulence intensity from the 5 percent Tu grid, and of the turbulence intensities in the absence of a grid, were used. The 2 percent Tu level was estimated using the work of Naudascher et al., 1970.)

With low free-stream turbulence, the strong acceleration ensures that the boundary layer remains laminar throughout, as characterized by a diminishing heat flux, and the absence of oscillations on the high-frequency signals. Conversely, at a high (5 percent) level of free-stream turbulence, a much more rapid transition occurs, and a fully turbulent boundary layer exists by an x/s of 0.2. This is characterized by a high mean heat flux, together with random high-frequency oscillations on the unsteady signal.

At the intermediate (2 percent) turbulence level, a transitional boundary layer extends from an x/s of 0.1 to 0.5. The unsteady heat flux signals begin to show characteristic, random increases above the laminar level at gage 4. These disturbances are amplified, and the mean heat flux rises, until eventually a fully turbulent state is reached. The transition is nearly complete in this case, by gage 11 ($x/s=0.479$).

The gradual transition that occurs at the intermediate level of turbulence is similar to the natural transition of the flat plate boundary layer. At the high turbulence intensities, in contrast, the transition is completed very early. It may be linked to separation and turbulent reattachment in the vicinity of the blend point irregularity, as suggested by some of the unsteady heat flux signals given by Doorly (1983).

In both cases, the transition behavior is in contrast to that observed by Priddy et al. (1982) on the suction surface of the rotor profile they investigated. In their experiments, the start of transition was found to be delayed to an x/s of order 0.5. At this point, the acceleration ceases and a sharp transition was linked to a separation and reattachment. In their case, however, the operating Reynolds number was much lower. The Reynolds number is of great significance for the transition process, even under highly unsteady flow, as will be discussed later. A careful study of the process of natural transition (which is initiated in this case, by the intermediate level of turbulence), is of considerable importance in studying the transition process forced by the wakes. This was clearly demonstrated by Pfeil et al. (1982) in studies of wake passing on the flat plate boundary layer. Furthermore, study of the unsteady heat flux signals for this case aids the interpretation of the signals in more complex flows.

(2) Natural Transition: Unsteady Surface Heat Flux. Free-stream disturbances induce randomly distributed, localized breakdowns of the laminar boundary layer structure forming turbulent spots. These spots are convected downstream with the flow, and through a combination of stream and spanwise growth, together with the formation of new spots, eventually merge forming a fully turbulent boundary layer. The nature of this transition process, involving random spot formation, spreading, and merging, is closely reflected in the unsteady heat transfer traces. It is important to note that the heat flux gages used for this work measured 10 mm in the spanwise direction, and 0.5 mm in the streamwise direction. The heat flux measured by a gage at any instant thus depends on the instantaneous spatial distribution of turbulent spots over the gage area. Since all the spots progress at a uniform rate, the spatial distribution of spots over succeeding downstream gages should be similar (the differences being caused by spot growth and new spots formed in the interval).

The unsteady heat flux signals may be scaled and nondimensionalized, by first subtracting the mean laminar level, and then dividing by the difference between mean turbulent and laminar levels; i.e., a normalized unsteady surface heat flux at a distance x from the leading edge may be defined by

$$\dot{q}_N(t, x) = \frac{\dot{q}(t, x) - \dot{q}_{LAM}(x)}{\dot{q}(x)_{TURB} - \dot{q}_{LAM}(x)} \quad (2)$$

The time mean value of $\dot{q}_N(t, x)$ is equal to the intermittency factor $\gamma(x)$. This describes the mean fraction of time when the boundary layer at x may be considered to be fully turbulent, i.e., $\gamma(x)$ varies between 0 (laminar) and 1 (fully turbulent).

The way in which the transition process affects the heat flux can be clearly identified, by plotting $\dot{q}_N(t, x)$ as a relief plot, Fig. 5. The slight enhancement of laminar heat flux by free-stream turbulence at the leading edge is clearly evident (although the film was not positioned quite at the stagnation point). The subsequent irregular formation and rearward convection of the distribution of turbulent spots is also clearly shown. The transition is well under way by gage 6, and the

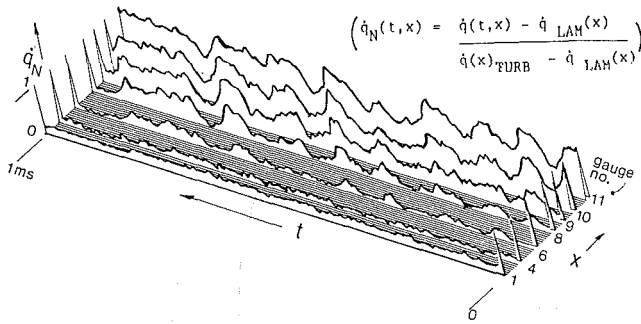


Fig. 5 Relief plot of normalized heat flux \hat{q}_N for 2 percent Tu

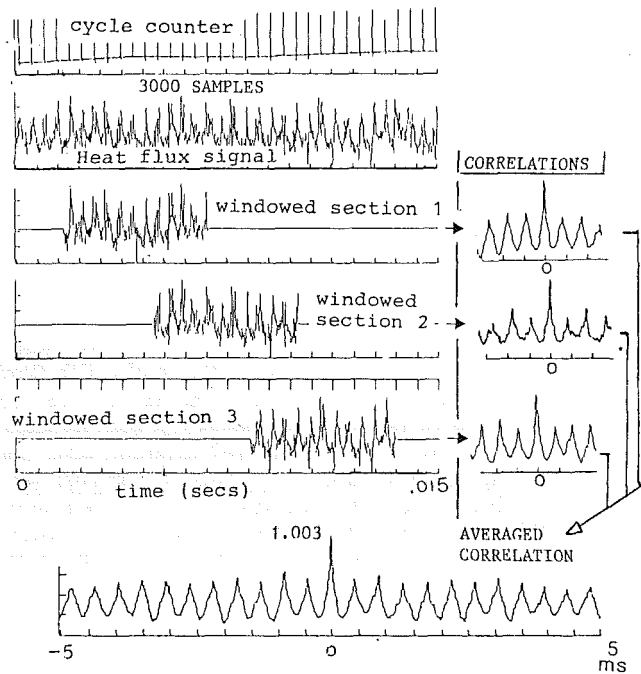


Fig. 6 FFT correlation of the unsteady heat flux signals

signals from the succeeding gages are obviously correlated in shape, though displaced by an increasing time delay. As discussed in the following section, the time delay was established using FFT cross-correlation techniques and found to be close to the mean propagation rate of a turbulent spot in a laminar flat plate boundary layer.

(3) **Application of Cross-Correlation Techniques.** If $q_1(t)$ is the fluctuating heat transfer measured at gage 1 and $q_2(t)$ that measured at gage 2, the cross correlation of gages 1 and 2 is

$$\hat{q}_1 * \hat{q}_2 = \int_{-\infty}^{\infty} \hat{q}_1(t) \hat{q}_2(t + \tau) dt \quad (3)$$

The correlation is scaled by dividing by the product of the rms value of each trace, i.e.,

$$\hat{q}_{12}(\tau) = \frac{\hat{q}_1 * \hat{q}_2}{\sqrt{(\hat{q}_1)^2} \cdot \sqrt{(\hat{q}_2)^2}} \quad (4)$$

Calculation of equation (2) may be accelerated by using the relation

$$\begin{aligned} \hat{q}_1 * \hat{q}_2 &= F^{-1}(F[\hat{q}_1 * \hat{q}_2]) \\ &= F^{-1}[F'(\hat{q}_1) \cdot F(\hat{q}_2)] \end{aligned} \quad (5) \quad (6)$$

where F is the Fourier transform operator, F^{-1} the inverse Fourier transform, and $(\cdot)'$ denotes the complex conjugate. In

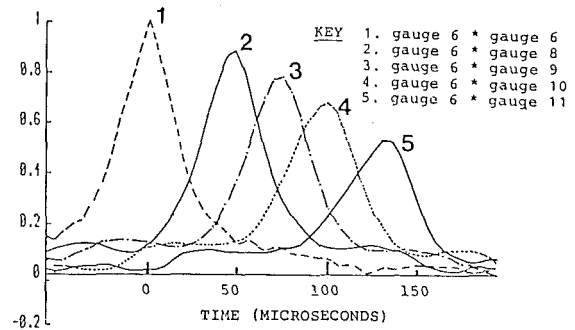


Fig. 7 Cross correlations of the unsteady heat flux signals for natural transition

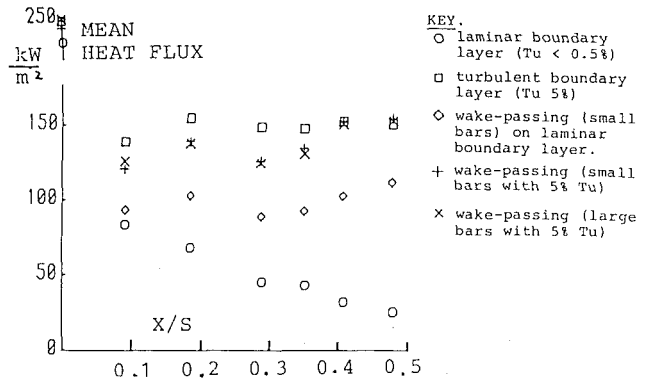


Fig. 8 Effect of wake passing on mean heat flux to laminar and turbulent boundary layer

practice, the FFT algorithm is used to evaluate equation (6). As this corresponds to cyclic correlation, to avoid end effects when dealing with periodic fluctuations, half of one trace is set to zero, and the extreme ends of the correlelogram discarded. (To ensure proper scaling of the correlation, the rms value of the two signals should only be computed over the corresponding window widths.)

The process is illustrated schematically in Fig. 6 for the correlation of one gage with itself, i.e., the autocorrelation. For 3000 high-speed samples, the trace is first partitioned into three overlapping sections of 2048 points, which are then windowed. Three estimates of the cross correlation of the signals from the selected gages are made, and the results averaged. (Clearly higher accuracy could be achieved by also averaging over several repeat tests.) The small error (<0.8 percent) in the magnitude of the computed autocorrelation is due to windowing effects.

The cross correlations of the unsteady heat transfer signals from gage 6 and downstream gages 8, 9, 10, and 11 are shown in Fig. 7. The peak of each cross correlation corresponds to the mean time for the turbulent spots (which are responsible for the heat transfer effects) to travel from gage 6 to the specified gage. The peaks of the cross correlation diminish, due to the growth of the spots and the generation of additional ones downstream of gage 6. By comparing the transit times obtained from the cross correlations with the mean time of flight of a phenomenon traveling at the free-stream velocity over the same distance, the mean propagation rate of the spots was found to be 0.65. This compares closely with the mean value for a turbulent spot in the flat plate boundary layer obtained by Wygnanski et al. (1976).

Effects of Combined Unsteadiness and Free-Stream Turbulence

(1) **Experimental Results.** The mean surface heat flux for combined wake passing, using small and large bars, and 5 per-

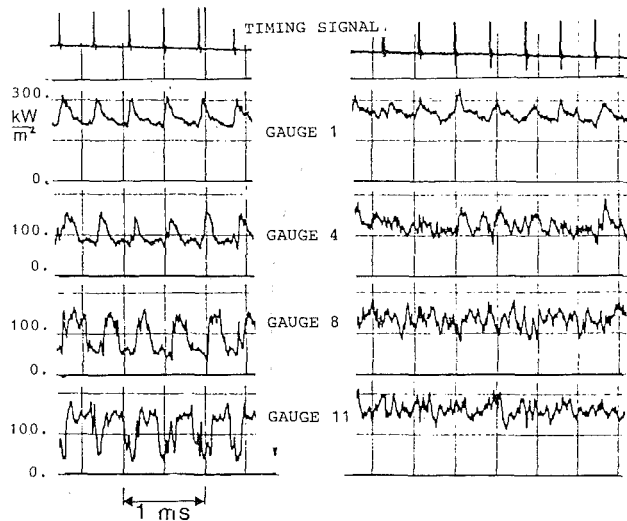


Fig. 9 Unsteady surface heat flux signals with wake passing for low free-stream Tu , and 5 percent Tu

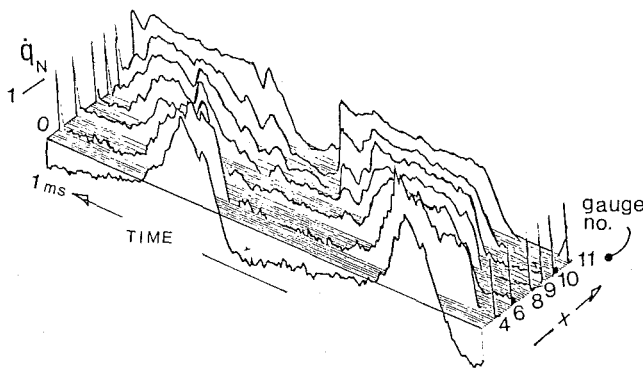


Fig. 10 Relief plot of normalized heat flux \dot{q}_N for wake passing with low free-stream Tu ; this clearly shows the formation of a turbulent patch by each successive wake

cent Tu at design conditions, is shown in Fig. 8. Included in the figure are mean levels for wake passing alone (with the small bars fitted), 5 percent Tu acting alone, and for undisturbed flow. Figure 9 shows corresponding portions of the unaveraged unsteady heat flux signals for wake passing, and wake passing with superposed turbulence, respectively. In both cases, the wake generator was run at the design speed and with the small bars fitted, representing the design NGV/rotor pitch ratio. The wake from a given bar consequently impinges simultaneously with the shock wave from the succeeding bar on the suction surface (Doorly and Oldfield, 1985b, Fig. 14). As the shock waves are weak, the wake-passing effects dominate, and so the flow is hereafter simply referred to as wake-passing flow.

Considering the case of wakes acting alone, each wake induces a response resembling a square wave jump from the laminar to the turbulent heat flux level and back. As in the case of natural transition with 2 percent turbulence (Fig. 8), the mean heat flux lies at a level between that of a laminar and a fully turbulent boundary layer, respectively, depending on the intermittency ratio. The nature of the forced transition process initiated by the wakes is clearly different, as shown by a surface plot of the normalized heat flux, $\dot{q}_N(t, x)$ (Fig. 10). At each gage (apart from the leading edge gage), a comparison of Figs. 5 and 10 indicates that successive wakes generate turbulent patches. (The laminar heat flux in the vicinity of the leading edge gage is very susceptible to the location of the

stagnation point. As a result of the large incidence changes induced by the wakes, it is not possible to define a meaningful normalized heat flux for the leading edge gage. This accounts for the negative $\dot{q}_N(t, x)$ values for the first gage, and is also the reason that the trace is not scaled.)

As distinct from the random turbulent spots associated with a gradual, natural transition (Fig. 5), each wake generates a turbulent patch that extends across the entire blade span during each cycle, giving a characteristic square wave shape. The very fine boundary layer structure is still most probably three dimensional. The patches are convected downstream (Fig. 10) and in addition, the duration of turbulent boundary layer flow during each cycle increases with distance from the leading edge x . This is due to a difference between the propagation rates of the leading and trailing edges of the turbulent patches.

Since the regions of high heat flux correspond to the location of the turbulent patches, a contour plot of the surface in Fig. 10 yields an $X-T$ diagram, which shows the leading and trailing edge trajectories of the turbulent patches induced by the wakes. The trajectory of the leading and trailing edges of the wake in the free stream may be calculated using the "striped air" calculation procedure described by Doorly (1983). In this approach, the velocity deficit of the wake is considered to be infinitesimally small, so that the results of a steady flow computation may be used to chart the progress of the wakes through the blade passage. For highly accelerating flows (as occurs in the turbine rotor), the procedure gives a somewhat surprisingly good approximation to the true wake trajectory, as was found by comparing the results with flow visualization studies. The trajectories of the wake in the free stream, and those of the turbulent patches in the boundary layer, may be superimposed on the $X-T$ diagram, revealing the relationship between the time history of the external free-stream disturbances (the wakes), and the unsteady transition. The procedure has been described for isolated wake disturbances by Doorly and Oldfield (1985b) and Doorly et al. (1985).

The results of applying this procedure indicated that the change from laminar to turbulent flow at a given location commenced somewhat after the arrival of the wake at the given point. The relaxation back to the laminar state was found to occur a considerable time after the wake had passed. The latter effect was attributed to the slow rate of propagation of turbulence within the boundary layer, compared to the rate at which the free stream sweeps the wake away.

(2) Development of a Simple Model. The experimental studies of the effects of turbulence, and *isolated* wake passing acting alone, indicated that the high turbulence content of the wakes is largely responsible for the forced transition process, which in turn determines the surface heat flux. This suggests a simple model of the wake-passing process (appropriate for such high Reynolds number turbine flows). In this model, the velocity deficit in the wake is ignored, so that the wake is idealized as a band of constant, high-intensity turbulence, and the striped air method is used to calculate the trajectory of the wake by the free-stream passage flow. It is assumed that the leading edge of the wake immediately induces a full transition of the underlying boundary layer at a given location x . At each location x , allowance is made (as discussed earlier) for the delay before relaminarization occurs after the trailing edge of the wake has passed over x .

(3) Comparison of Measured Heat Flux and Model Prediction. This model was first applied to the simple case of wake passing (with the small bar wakes) on a laminar boundary layer (corresponding to $Tu < 0.5$ percent). A comparison between the unsteady surface heat flux predicted by this method, and the measured, ensemble-averaged heat flux is shown in

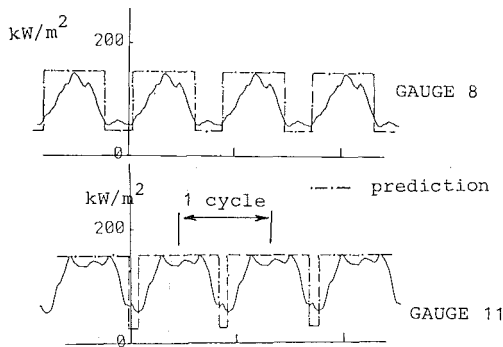


Fig. 11 Comparison between measured ensemble averaged heat flux for wake passing on laminar boundary layer, and predictions of simple model

Fig. 11, for two gage positions on the suction surface. There are two areas of disagreement between the heat flux predicted by the simple model and that actually measured. Firstly, in each cycle, the measured heat flux rise associated with the jump from a laminar to a turbulent state occurs noticeably after that predicted by the model. Secondly, the measured turbulent heat flux produced by each wake is lower than that predicted by the model.

Applying the model to superposed wake passing and 5 percent turbulence, it predicts that the results should be almost identical with those for turbulence alone, since the turbulence by itself is sufficient to induce an early transition in this case. A relatively weak, periodic increase in heat flux, due to the additional turbulence content of the wake, might however be expected, as the turbulent heat flux was found to increase with increased Tu level in flat plate studies (Blair and Werle, 1979). From Fig. 8, the effects of wake passing with superimposed 5 percent turbulence are certainly not greatly different from the results with 5 percent turbulence alone, and are virtually identical by an x/s of 0.5. Far from indicating an increase in the heat flux due to the additional presence of the wakes, however, the measurements in fact point to a decrease due to the wakes on the early portion of the blade (particularly between $x/s=0.1$ and 0.3). Over the region $x/s=0.1$ to 0.3, the lower turbulent heat flux level, compared with that anticipated on the basis of the simple model, roughly accords with the similar discrepancy noted above in Fig. 11 for wake passing alone. Thereafter, the mean heat flux level associated with combined wakes and turbulence is somewhat higher than the mean, instantaneous level caused by wakes alone.

Analysis of Unsteady Heat Flux Signals for Wake Passing on Turbulent Boundary Layer

Before discussing the deficiencies in the simple model, the results of a detailed study of the unsteady heat flux measurements for wake passing on a turbulent boundary layer will be reported. In view of the high Reynolds number and turbulence levels of typical modern high-pressure turbine rotors, this is expected to be the most usual condition. The analysis of the unsteady signals reveals more information concerning the phenomena that occur in wake passing on a turbulent boundary layer, and provides clues as to the reasons for the deficiencies in the simple model.

(1) **Autocorrelation Analysis of Signals.** The methods described previously were used to obtain the autocorrelation of the unsteady heat flux signals from a number of gages between the leading edge (gage 1) and an x/s of approximately 0.5 (gage 11) (Fig. 12). Apart from the leading edge gage, the unprocessed signals for combined wake passing and free-stream turbulence do not appear to the eye to be markedly

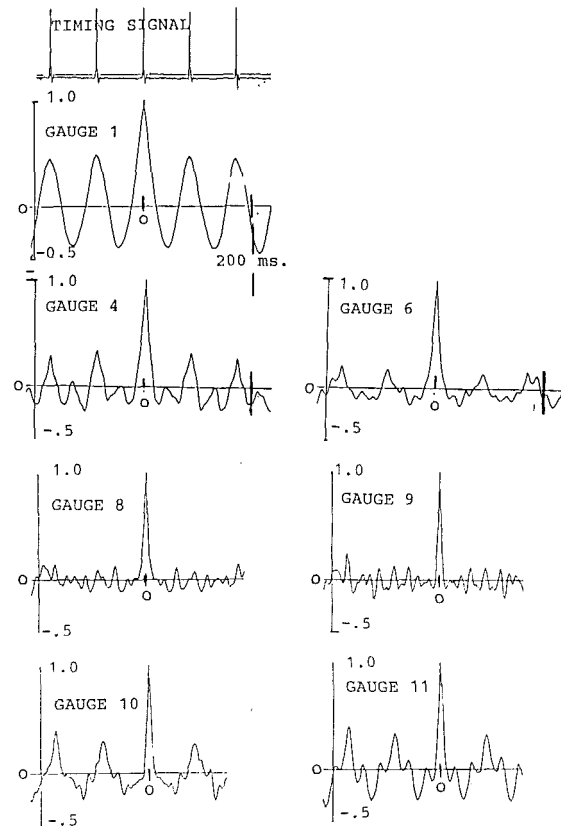


Fig. 12 Autocorrelation of the unsteady heat flux signals for combined wake passing and 5 percent Tu

periodic. The autocorrelation, however, provides a very sensitive indication of whether the passing wakes have any significant regular cyclic effect on the heat flux.

Starting at the leading edge, the strongly periodic character of the autocorrelation indicates an appreciable regular cyclic variation in the heat flux. The heat flux signals are clearly periodic, and although random, turbulent disturbances make the cycles appear irregular, there is clearly a regular underlying variation. This is attributed to the incidence change in the vicinity of the stagnation point. Between gages 4 and 6, the magnitude of the periodicity rapidly diminishes, and is effectively lost in the autocorrelation of signals from gages 8 and 9. The conclusion is that in this region, there is no significant variation in the heat flux during each cycle; thus the periodic addition of packets of increased turbulence by each passing wake does not cyclically increase the heat flux as might be expected. It is inferred that the boundary layer is already saturated by free-stream turbulence so the additional contribution of the wakes has no effect. Appreciable periodicity reappears farther downstream on the signals from gages 10 and 11. If the wake turbulence causes this, then it is difficult to see how the previous argument concerning boundary layer turbulence saturation continues to hold.

The dilemma can be resolved by comparing the ensemble-averaged heat flux signals for combined wake passing and free-stream Tu , with the signals for wake passing alone (Fig. 13). This plot shows the time in each cycle where the wakes impinge, so any regular enhancement directly caused by the wakes should be obvious. Considering firstly the results for the leading edge gage, there is a clear enhancement of the heat flux occurring between successive wakes due to the background turbulence. Some enhancement of the heat flux coincident with the arrival of the wakes is also evident in the heat flux signals from gages 4 and 6. There is, however, no significant enhancement associated with the wakes at the loca-

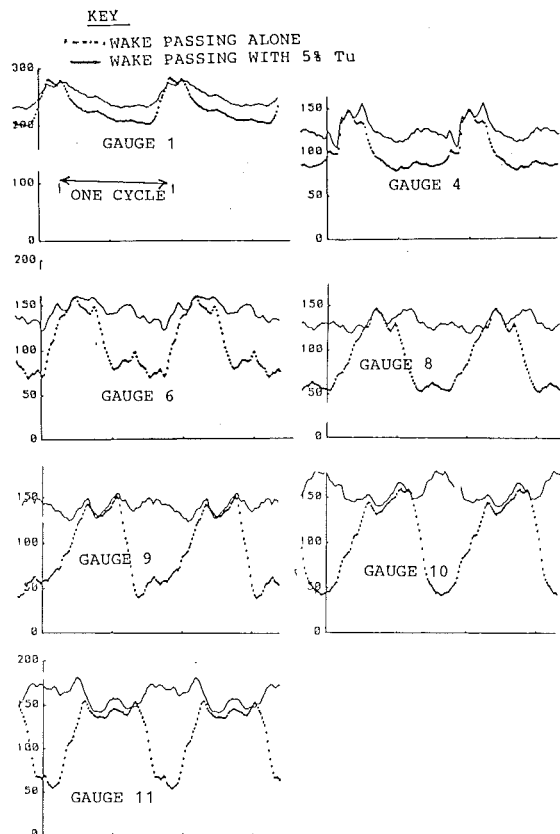


Fig. 13 Comparison between ensemble-averaged heat flux for wake passing alone, and wake passing with 5 percent Tu

tions of gages 8 and 9, although the averaging reveals a cyclic regularity in the traces.

The results from gages 10 and 11, however, do show a marked cyclic variation in the heat flux. Instead of an increased transient heat flux coincident with the wakes, however, the increase occurs *between* the wakes. The increase cannot therefore be attributed to the turbulence content of the wakes, so the boundary layer still appears to be "turbulence saturated." A plausible explanation for the cyclic increase in heat flux is that the gages are located close to the passage throat. The location of the passage throat for this profile appears to be very sensitive to incidence, as was discovered by King (1986), using a very large-scale model in the Oxford blowdown tunnel.

The geometric throat lies between the trailing edge of the pressure surface of the upper cascade blade, and a region on the suction surface of the lower blade, which is inclined at a small angle to local flow direction. Slight changes in the incidence angle were found to have a significant effect on the throat location. The Schlieren photograph (Fig. 1) shows two weak normal shocks in this region at a particular instant in the wake-passing cycle. These shocks appear to be present at certain times in a cycle and absent at other times. The flow at this Mach number is very sensitive to exit pressure and it was not possible to establish a pattern for a complete cycle, using a limited number of single photographs taken in separate tests. It seems certain, however, that the cyclic effects on the heat flux in the region of the throat are associated with a periodic variation in the external passage flow, rather than due to the direct effect of wake turbulence on the boundary layer in the region.

(2) Cross-Correlation Analysis. The unsteady heat transfer signals in the absence of wake passing, from a gage located at a point where the boundary layer is fully turbulent,

were found to be strongly correlated with the corresponding signals from a gage a very short distance downstream, and to become progressively less correlated with the signals from gages farther downstream. Measuring the increasing time delay of the peak of the cross correlations, as described for transitional flow, indicates that the signals are convected with a velocity of about $0.7 U_\infty$ (Doorly, 1983). It is therefore concluded that the observed high-frequency oscillations in the unsteady heat flux signals are due to relatively large-scale eddies which persist over a large number of boundary layer thicknesses. The cross correlations of the unsteady heat flux signals from a turbulent boundary layer provide more information than in the case of transitional flow. In the latter case, the correlation records only the trajectory of the gross change from laminar to turbulent flow associated with a turbulent patch, as this dominates the signal. For a turbulent boundary layer, the absence of these state changes means that the signals reveal more about the actual boundary layer structure.

The space-time correlation of the unsteady heat flux at a given point x and a point a variable distance downstream is given by

$$\hat{q}(x, t, r) = \frac{\hat{q}(x, t) * (x+r, t)}{\sqrt{(\hat{q}(x))^2} \sqrt{(\hat{q}(x+r))^2}} \quad (7)$$

In shorthand notation, $\hat{q}_{6,8}$ denotes the cross correlation of the signals from gages 6 and 8, i.e., $\hat{q}_6 * \hat{q}_8$. A mean eddy life may be defined for the boundary layer features responsible for the unsteady heat flux oscillations, in terms of distance r over which the peak of the space-time cross correlation falls below a threshold value (Bradshaw, 1971). Setting the threshold value equal to $1/3$ implies that the eddies are considered to be fully dispersed at a distance downstream when the peak of the correlation falls below this level. This is taken as the distance traveled during the mean life of an eddy and the corresponding time is the mean eddy lifetime. The mean eddy life provides a crude estimate of the time constant of the boundary layer flow, since the total duration of a phenomenon is typically of order three times its time constant. The time constant of the turbulent boundary layer (approximately $1/3$ of the mean eddy lifetime) may be crudely related to the ratio of total turbulent kinetic energy divided by the production rate of turbulent kinetic energy.

The cross correlation was used to determine whether the addition of wake passing radically altered the turbulent boundary layer structure insofar as this could be deduced from a study of propagation rates and eddy life. A selection of the cross correlations of the signals from successive gages were compared under conditions of free-stream turbulence alone, wake passing alone, and combined wake passing and free-stream turbulence (Fig. 14). The correlations of the unsteady heat flux signals for wake passing alone are highly periodic, and the amplitude diminishes very slowly with distance downstream. In a similar fashion to that of a transitional boundary layer (Fig. 7), the cross correlation of these signals primarily records the gross convection of turbulent patches. As each wake cyclically induces a patch of similar extent, the correlations are highly periodic.

The first group of plots, Fig. 14(a), shows the cross correlation of the unsteady heat flux signals from gage 6 with the downstream gages 8, 9, and 10. For the turbulent boundary layer signals, whether or not subjected to wake passing, the peak of the cross correlation taking gage 6 as origin falls below the threshold value between gages 9 and 10. An estimate of the mean eddy lifetime is thus shown on the third correlation, together with the boundary layer time constant ($1/3$ of this). It is interesting to compare this time scale with that over which the passage flow varies (indicated by the period of the correlations with wake passing alone).

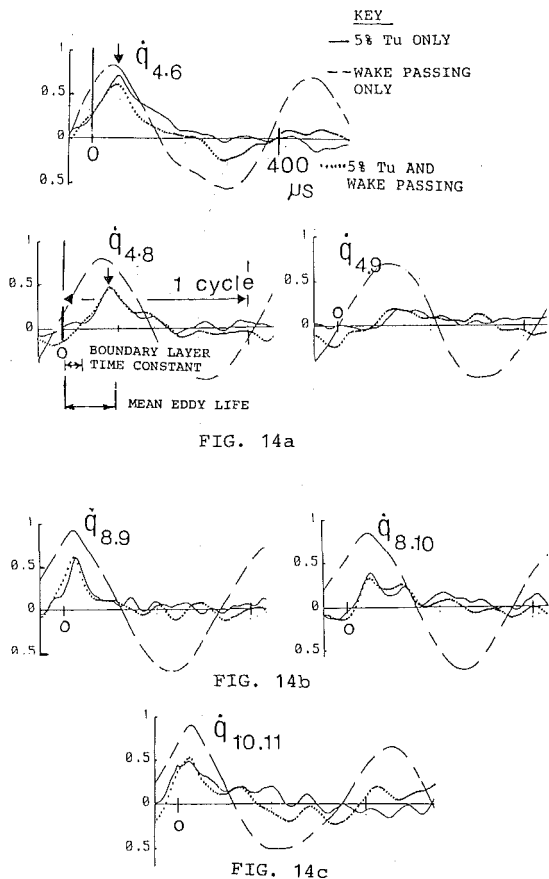


Fig. 14 Cross correlations of the unsteady heat flux signals

The second group (14b) shows the correlations with gage 9 as origin. This gage is located in the area where it is inferred that the boundary layer is "saturated" with turbulence; the peaks of the corresponding correlations seem to diminish more rapidly than upstream, possibly suggesting higher rates of turbulent production.

Finally the cross correlation of the signals from the gages located in the region of the throat (gages 10 and 11) are shown, Fig. 14(c). The similarity of the correlations for turbulence alone and combined wake passing and free-stream turbulence tends to suggest that the turbulent boundary layer structure is not significantly altered by the wake passing.

Importance of the Wake Deficit

The obvious feature of the wake that is neglected by the simple model is the velocity deficit. As well as subjecting the blade boundary layer to a highly turbulent band of fluid, the wake simultaneously induces an appreciable variation in the local incidence angle at inlet. Estimation of the periodic incidence change (Doorly, 1983) indicated maximum amplitudes approximately 10 to 15 percent for the bar diameter used. The studies of the heat flux effects of isolated wakes (on which the model was based) did not appear to indicate an effect due to the incidence change, apart from in the immediate vicinity of the leading edge. At all other points, the transient heat flux levels were identical to those of a turbulent boundary layer (produced by an artificial trip, or high free-stream turbulence).

In altering the simulation from that of isolated wake passing to actual engine representative wake passing, the frequency increases by a factor of four. Instead of the convection of isolated wakes (completely separated, by regions of calm flow, from succeeding wakes) through the blade passage, at full fre-

quency simulation, there are generally two wakes in each passage at any given time. Mathematically, the boundary conditions have been altered so that the external, passage flow cannot relax between cycles.

In studies of the effect of flow oscillation on the flat plate boundary layer, it has been found that the unsteadiness becomes significant when the reduced frequency parameter

$$w = \frac{2\pi fL}{U_\infty}, \text{ where } L = \text{external flow length scale}$$

(here blade chord) becomes significantly greater than one. In the case of wake passing at the design condition, based on a representative Mach number of 0.8, w is approximately 3, so that the flow is truly unsteady. In addition, the rapid succession of wakes may significantly alter the mean aerodynamics of the flow about the blade, particularly through changing the effective incidence. Unfortunately, blade surface pressure measurements were not made under conditions of full frequency wake passing, nor have the effects of incidence changes on the heat flux under steady, turbulent flow conditions been investigated for this profile. It would be interesting to study this in the future.

The results of these investigations, however, strongly suggest that the wake deficit must be accounted for in modeling the unsteady flow. Although clearly significant, the turbulence content of the wake does not entirely dominate the unsteady process. The striped air calculation, which ignores the wake velocity deficit, needs to be replaced by a computation that allows a finite wake strength. This can be accomplished using a numerical solution of the unsteady Euler equations where a periodic wake deficit is specified at the inlet to the cascade. Various finite difference schemes have been used for this (e.g., Ipsas et al., 1980; Hodson, 1983; and others). In order to handle effects associated with the sensitivity of the throat location, however, a Navier-Stokes, or some form of viscous/inviscid coupling, is required to treat the separation of the flow from the rotor trailing edge effectively. A full Navier-Stokes modeling of the flow through a complete rotor stage has been performed by Rai (1985). At present, however, the computing requirements are extremely large. If the potential interactions are neglected, a Navier-Stokes solver applied only to the rotor and using prescribed unsteady inlet conditions would be far simpler and may be of considerable use.

Reynolds Number Dependence of Unsteady Effects

The operating Reynolds number (based on blade chord and cascade exit conditions) was halved from $2.0E6$ to $1.0E6$, and the effect of wake passing the suction surface heat flux measured. The purpose was to investigate the Reynolds number dependence of the unsteady transition induced by the wakes in an otherwise laminar boundary layer and to explore further the usefulness of models of transition based on the results for high Re flow. The flow Reynolds number has a very strong effect on the stability of the blade boundary layer, and in addition, halving Re doubles the acceleration parameter K . For accelerating flow, the value of K has been shown to affect the location of transition profoundly.

The effect of Tu levels between 1 and 10 percent on the transition behavior, and surface heat flux of the flat plate boundary layer in accelerating flow, has been investigated by Wittig and Rued (1986). Results were given for constant K values up to approximately $2.0E-6$, and for K a function of distance, with K_{max} up to $6.0E-6$. These experiments indicated that for constant K , equal to $2.3E-6$, transition was entirely suppressed for 2.3 percent Tu , and was delayed for $Tu=4$ percent for Reynolds numbers of up to $3.5E5$. [This agrees with evidence that suggests that for K above $3.0E-6$, relaminarization of a turbulent boundary layer may occur (Kays and Crawford,

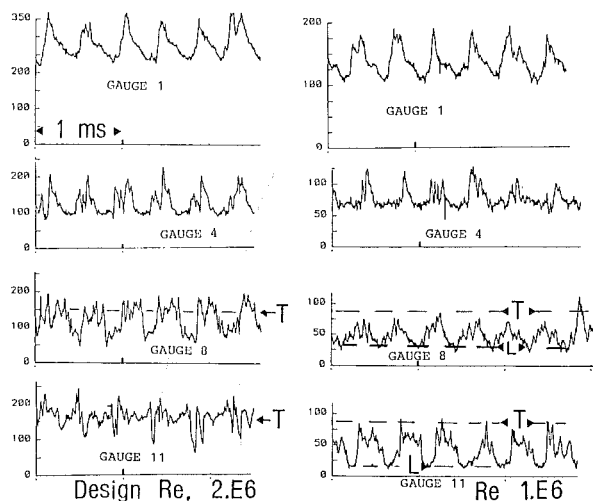


Fig. 15 Dependence of unsteady heat flux on Reynolds number Re ; level "T" corresponds to mean heat flux for fully turbulent boundary layer, level "L" to laminar boundary layer

1980).] At very high accelerations, transition was suppressed for Tu up to 4 percent; higher levels of Tu were found however, to produce a transitional type of boundary layer under such conditions.

The unsteady heat flux signals for wake passing (using the large diameter bars) at design and reduced Re are compared in Fig. 15. The results were obtained for an exit Mach number of over 2, as a downstream throat had not been fitted to the tunnel for these tests. The suction surface Mach number distribution should be almost identical to that at the design exit Mach number of 0.96, up to gage 10, and only slightly higher at gage 11. The sensitivity of the flow near the throat to incidence changes, which caused the effects reported earlier, is entirely removed at high exit Mach numbers. The levels marked "T" and "L" correspond respectively to the results for fully turbulent (caused by $Tu=5$ percent) and a laminar boundary layer ($Tu<0.5$ percent), shown earlier. For the low Re case, the level "T" is obtained by scaling that for the high Re case by 2, since \dot{q} is proportional to Re . At design Re , each passing wake causes the formation of a turbulent patch, which is clearly evident on the traces from gages 4 onward. The patches have almost completely merged by gage 11, partly due to the boundary layer lag caused by the slow propagation of the patch trailing edge. At the reduced Reynolds number, in contrast, the turbulent patches are less clearly defined at gage 4. Furthermore by gage 8, at the lower Reynolds number, even the high Tu contained in the wakes is insufficient to sustain fully turbulent patches. [The turbulence content of the wakes generated by the cylindrical bars was not measured but was estimated using the results of Uberoi and Freymuth (1969), and the velocity triangle for the simulation Fig. 1.] The peak level of Tu contained in the wakes at the cascade inlet (of order 100 bars diameter downstream along the wake path) was estimated to be of order 10–20 percent. Despite this, at low Re , it is not until the acceleration diminishes by gage 11, and the local Reynolds number Re_x is larger, that the clear pattern of wake-induced turbulent patches emerges. As a consequence of the absence of the patches over the early part of the blade, the spreading effect caused by the propagation within the boundary layer is greatly reduced. Consequently, the patches have still not merged by gage 11, in contrast to the results at high Re .

Conclusions

The analysis of the unsteady heat flux signals has provided

new information on the unsteady suction surface boundary layer in the presence of combined wake passing and free-stream turbulence. The analysis was guided by investigating the validity of a simple model under more complex flow conditions, and at a Reynolds number very much lower than those for which it was developed. This model was derived from earlier experimental studies of isolated wakes and weak shocks, which suggested that the wakes affected the heat flux primarily by inducing an early transition. The model assumed that the high turbulence content of the wakes resulted in the immediate formation of a turbulent patch in an otherwise laminar boundary layer, during each cycle. It predicted that the mean heat flux could be calculated by applying an intermittency factor (dependent on surface position), to the heat flux levels corresponding to steady fully turbulent, and laminar boundary layers, respectively. The intermittency function was largely derived from a simple flow computation, which treated the wake merely as a band of turbulence, neglecting the velocity deficit.

It was shown that at high Reynolds numbers, the model does agree qualitatively with the results, in that the effect of wake passing on an already turbulent boundary layer is fairly small. The fact that there is some effect, noticeably a *reduction* in heat flux (on the early part of the suction surface), indicates a deficiency in such simple modeling. The results of auto and cross-correlation analysis suggested that the additional turbulence imposed by the wakes had little effect on the heat flux associated with a turbulent boundary layer. It was concluded that the wake velocity deficit is instead responsible for the effect. Suggestions for improving the unsteady passage flow model by incorporating the wake velocity deficit were given.

Studies of the effects of wake passing at half the design Reynolds number further showed that even the high turbulence content of the wakes is not sufficient to induce an early, intermittently turbulent boundary layer. It was indicated that this was linked to the higher acceleration parameter that results when the Reynolds number is decreased. Some allowance for a Reynolds number and acceleration parameter dependence must therefore be incorporated in a model of the unsteady transition process.

Acknowledgments

Dr. M. L. G. Oldfield made many helpful suggestions while the experiments were performed at Oxford. The support of the S.E.R.C. through the award of a Postdoctoral Research Fellowship is gratefully acknowledged, as are the financial contributions made by the S.E.R.C. and Rolls-Royce.

References

- Ashworth, D. A., LaGraff, J. E., Schultz, D. L., and Grindrod, K. J., 1985, "Unsteady Aerodynamic and Heat Transfer Processes in a Transonic Turbine Stage," *ASME Journal of Engineering for Gas Turbines and Power*, Vol. 107, pp. 1022–1030.
- Bayley, F. J., and Priddy, W. J., 1981, "Effects of Free-Stream Turbulence Intensity and Frequency on Heat Transfer to Turbine Blading," *ASME Journal of Engineering for Power*, Vol. 103, pp. 60–64.
- Binder, A., 1985, "Turbulence Production Due to Secondary Vortex Cutting in a Turbine Rotor," *ASME Journal of Engineering for Gas Turbines and Power*, Vol. 107, pp. 1039–1046.
- Blair, M. F., 1983, "Influence of Free-Stream Turbulence on Turbulent Boundary Layer Heat Transfer and Mean Profile Development. Parts 1 and 2," *ASME Journal of Heat Transfer*, Vol. 105, pp. 33–47.
- Blair, M. F., and Werle, M. L., 1979, "An Experimental and Analytical Study of Boundary Layers in Highly Turbulent Freestreams," U.T.R.C. Report No. R78-914388-5, July.
- Bradshaw, P., 1971, *Introduction to Turbulence and Its Measurement*, Pergamon Press, pp. 55–63.
- Doorly, D. J., 1983, D. Phil Thesis, Oxford University; also available as

O.U.E.L. report 1515/84; partly reproduced by D. L. Schultz in V.K.I. L.S. 86/06.

Doorly, D. J., and Oldfield, M. L. G., 1985a "Simulation of Wake-Passing in a Stationary Turbine Rotor Cascade," *AIAA Journal of Propulsion and Power*, Vol. 1, No. 4, pp. 316-318.

Doorly, D. J., and Oldfield, M. L. G., 1985b, "Simulation of the Effects of Shock-Wave Passing on a Turbine Rotor Blade," *ASME Journal of Engineering for Gas Turbines and Power*, Vol. 107, pp. 998-1006.

Doorly, D. J., Oldfield, M. L. G., and Scrivener, C. T. J., 1985, "Wake-Passing in a Turbine Rotor Cascade," AGARD CP-390 Paper No. 7, Bergen, Norway.

Dring, R. P., Joslyn, H. D., Hardin, L. W., and Wagner, J. H., 1982, "Turbine Rotor-Stator Interaction," *ASME Journal of Engineering for Power*, Vol. 104, pp. 729-743.

Dunn, M. G., 1985, "Turbine Heat Flux Measurements: Influence of Slot Injection on Vane Trailing Edge Heat Transfer and Influence of Rotor on Vane Heat Transfer," *ASME Journal of Engineering for Gas Turbines and Power*, Vol. 107, No. 1, pp. 76-83.

Dunn, M. G., George, W. K., Rae, W. J., Woodward, S. H., Moller, J. C., and Seymour, P. J., 1986, "Heat-Flux Measurements for the Rotor of a Full-Stage Turbine: Part II—Description of Analysis Technique and Typical Time-Resolved Measurements," *ASME JOURNAL OF TURBOMACHINERY*, Vol. 108, pp. 98-107.

Epstein, A. H., Guenette, G. R., Norton, R. J. G., and Cao Yuzhang, 1985, "High Frequency Response Heat Flux Gauges for Metal Blading," AGARD-CPP-390, Bergen, Norway.

Evans, R. L., 1982, "Boundary Layer Transition and Separation on a Compressor Rotor Airfoil," *ASME Journal of Engineering for Power*, Vol. 104, pp. 251-253.

Gaugler, R. E., 1985, "A Review and Analysis of Boundary Layer Transition Data for Turbine Application," ASME Paper No. 85-GT-83.

Gillis, J. C., and Johnston, J. P., 1979, "Experiments on the Turbulent Boundary Layer Over Convex Walls and Its Recovery to Flat Wall Conditions," in: *Turbulent Shear Flows*, Vol. 2, Bradbury, Durst, and Launder, eds., Springer.

Hodson, H. P., 1984, "Boundary Layer and Loss Measurements on the Rotor of an Axial-Flow Turbine," *ASME Journal of Engineering for Gas Turbines and Power*, Vol. 106, pp. 391-400.

Hodson, H. P., 1983, Ph.D. Thesis, Cambridge University.

Hoheisel, H., Kiock, R., Lichtfuss, H. J., and Fottner, L., 1987, "Influence of Free-Stream Turbulence and Blade Pressure Gradient on Boundary Layer

and Loss Behavior of Turbine Cascades," *ASME JOURNAL OF TURBOMACHINERY*, Vol. 109, pp. 210-219.

Horton, F. G., Schultz, D. L., and Forest, A. E., 1985, "Heat Transfer Measurements With Film Cooling on a Turbine Blade Profile in Cascade," ASME Paper No. 85-GT-117.

Ispas, I., Grollius, H., and Gallus, H. E., 1980, "Über den Einfluss von Nachlaufdüellen auf die instationäre Druckverteilung an den nachfolgenden Schaufelreihen in Axialverdichtern und Axialturbinen," V.D.I.-Berichte No. 361, 1980.

Jones, T. V., Schultz, D. L., Oldfield, M. L. G., and Daniels, L. C., 1979, "A New Transient Facility for the Measurement of Heat Transfer Rates," AGARD CP 229, *High Temperature Problems in Gas Turbine Engines*.

Kays, W. M., and Crawford, M. E., 1980, *Convective Heat and Mass Transfer*, McGraw-Hill, pp. 161-232.

King, P. I., 1986, D. Phil Thesis, Oxford University.

Naudascher, E., Asce, M., and Farrell, C., 1970, "Unified Analysis of Grid Turbulence," *J. Eng. Mech. Div. Proc. Am. Soc. Civ. Eng.*, Vol. 96, No. EM2.

Nicholson, J. H., 1981, D. Phil Thesis, Oxford University.

Pfeil, H., Herbst, R., and Schroeder, T., 1983, "Investigation of the Laminar-Turbulent Transition of Boundary Layers Disturbed by Wakes," *ASME Journal of Engineering for Power*, Vol. 105, pp. 130-137.

Priddy, W. J., and Bayley, F. J., 1982, "Heat Transfer to Turbine Blading," International Conference on Heat and Mass Transfer, Dubrovnik.

Rai, M. M., 1985, "Navier Stokes Simulation of Rotor-Stator Interaction Using Patched and Overlaid Grids," AIAA Paper No. 85-1519-CP.

Rued, K., and Wittig, S., 1986, "Laminar and Transitional Boundary Layer Structures in Accelerating Flow With Heat Transfer," *ASME JOURNAL OF TURBOMACHINERY*, Vol. 108, pp. 116-123.

Samoilovich, G. S., and Yablokov, L. D., 1971, "Profile Losses With Unsteady Flow Through Turbomachine Cascades," *Teploenergetika*, Vol. 18, No. 4, pp. 73-75.

Uberoi, M. S., and Freymuth, P., 1969, "Spectra of Turbulence in Wakes Behind Circular Cylinders," *Phys. of Fluids*, Vol. 12, No. 7.

Walker, G. J., 1974, "The Unsteady Nature of Boundary Layer Transition on an Axial Flow Compressor Blade," ASME Paper No. 74-GT-135.

Walker, G. J., and Oliver, A. R., 1972, "The Effect of Interaction Between Wakes From Blade Rows in an Axial Flow Compressor on the Noise Generated by Blade Interaction," ASME Paper No. 72-GT-15.

Wynanski, I., Sokolov, M., and Friedman, D., 1976, "On a Turbulent Spot in a Laminar Boundary Layer," *Journal of Fluid Mechanics*, Vol. 78, pp. 785-787.

A Trace Gas Technique to Study Mixing in a Turbine Stage

H. D. Joslyn

R. P. Dring

United Technologies Research Center,
East Hartford, CT 06108

An experimental technique to study mixing in a turbine stage is demonstrated. An axisymmetric, radial temperature profile at the inlet to the first stator of a large-scale, low-speed, single-stage, axial flow turbine model is simulated with a radial trace gas concentration distribution. Mixing or redistribution of the inlet profile by three-dimensional aerodynamic mechanisms (other than temperature-driven mechanisms) is determined from trace gas concentration measurements made in both the stationary and rotating frames of reference at various locations through the turbine. The trace gas concentration contours generated are consistent with flow pitch angle measurements made downstream of the first stator and with surface flow visualization on the rotor airfoil and the hub endwall. It is demonstrated that this trace gas technique is well suited to quantify many aspects of the redistribution and diffusion of an inlet temperature profile as it is convected through a turbine stage.

Introduction

Economic, environmental, and energy conservation measures have been the driving forces behind industry-wide efforts aimed at increasing gas turbine performance by increasing turbine inlet gas temperatures. These same forces have also dictated the need to improve engine durability and hence, reduce operating costs. Improved performance and durability while operating at increased turbine inlet temperatures requires that a suitable circumferentially averaged, radial temperature profile be generated at the combustor exit (turbine inlet) and adequate cooling be provided to the turbine hot section components. The maximum allowable inlet profile temperature is set by the turbine hot section component structural and durability characteristics and by the effectiveness of hot section component cooling techniques [1].

Complex three-dimensional aerodynamic flow fields near the turbine hub and tip endwalls [2, 3] make them difficult to cool. This dictates the need to tailor the inlet temperature profile to provide gas temperatures at the hub and tip endwall regions that are lower than the maximum inlet gas temperature. Material fatigue and high stress levels due to centrifugal forces in the rotating blade rows also dictate the need for temperatures at the hub that are lower than the maximum inlet temperature. In practice, the turbine inlet radial temperature profile can be well controlled with the introduction of compressor discharge air through discrete dilution jets [1].

If design systems only had to predict the decrease in temperature due to work extraction in a turbine stage and if "strip theory" assumptions were valid, then the prediction of hot section component heat loads and the requirements for cooling would be relatively straightforward since the gas path

heat load predictions [4] are based on the local convective heat transfer coefficient, the maximum allowable material (metal) temperature, and the local gas path adiabatic recovery temperature. Much work has been done to determine local heat transfer coefficients (e.g., [3, 5]) and material limits. However, although the turbine inlet radial temperature profile can be carefully tailored, the gas path adiabatic temperature cannot be accurately predicted due to the action of complex three-dimensional aerodynamic mechanisms [6] that can redistribute (mix) the inlet temperature profile as the flow passes through the turbine.

The objective of this experimental program is to demonstrate the suitability of using this trace gas technique to determine the redistribution of a simulated inlet temperature profile by three-dimensional aerodynamic mechanisms. It is recognized that the temperature drop due to work extraction and the effect of any temperature-driven secondary flows [6] are not modeled by this approach; however, this program is aimed specifically at examining inlet temperature profile distortion due to pressure and rotationally driven flow mechanisms such as endwall secondary flow vortices [7], rotor tip leakage flow [8], and the relative eddy [9].

Experimental Program

The experimental program was conducted in the United Technologies Research Center's Large-Scale Rotating Rig (LSRR). The LSRR is a large-scale, low-speed, experimental aerodynamic test facility designed to simulate the flow field in axial flow turbomachines. For the present program, a single-stage turbine model typical of the first stage of a high-pressure turbine was installed in the facility. The turbine model is shown in Fig. 1 and the relevant model aerodynamic and geometric design parameters are presented in Table 1. The experiment was conducted at the nominal design flow coefficient ($C_x/U_m = 0.78$). Several other detailed experimental studies

Contributed by the Gas Turbine Division of THE AMERICAN SOCIETY OF MECHANICAL ENGINEERS and presented at the 32nd International Gas Turbine Conference and Exhibit, Anaheim, California, May 31-June 4, 1987. Manuscript received at ASME Headquarters February 10, 1987. Paper No. 87-GT-118.

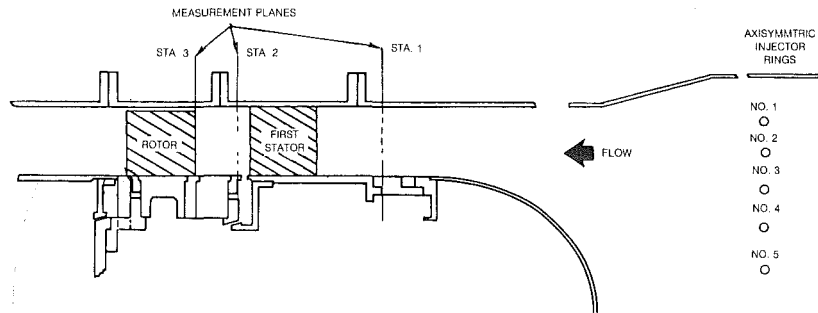


Fig. 1 Model geometry—axisymmetric inlet temperature profile simulation

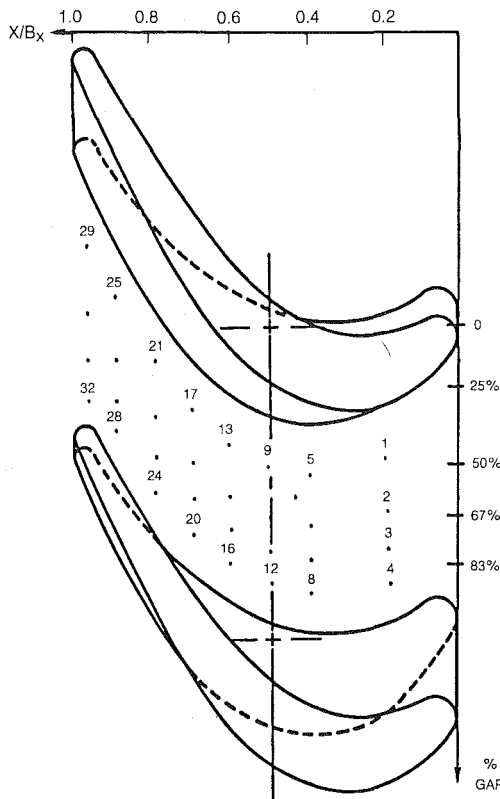


Fig. 2 Rotor hub endwall CO₂ sampling taps

of turbine aerodynamics and heat transfer have been previously conducted in this turbine model [10–12].

A mass transfer analogy, i.e., the use of a trace gas, was chosen to study turbine inlet temperature profile redistribution since, for the present application, a mass transfer process could be set up with greater accuracy in the boundary conditions (a well-defined, axisymmetric, radial inlet trace gas concentration profile with “adiabatic” surfaces throughout the model) than the corresponding heat transfer process. The application of the mass transfer analogy to obtain temperature field redistributions has been well documented [13, 14]. The main assumption in this analogy is that the turbulent Prandtl number (governing heat transfer) and the turbulent Schmidt number (governing mass transfer) vary in such a manner that their ratio is close to unity at all locations through the flow field.

In the present study an axisymmetric, radial temperature profile at the turbine inlet (Station 1, Fig. 1) was simulated with a radial trace gas concentration profile of carbon dioxide (CO₂). Although other gases, e.g., ethylene, with a molecular

Table 1 Aerodynamic and geometric parameters for LSRR

	GUIDE VANE	ROTOR
THROUGHFLOW VELOCITY, C_x	19 m/s (75 ft/s)	
INLET TOTAL PRESSURE	= AMBIENT, 1 atm	
INLET TOTAL TEMPERATURE	= AMBIENT, (530°R)	
FLOW COEFFICIENT, C_x/U_m	= 0.78	
AXIAL CHORD, b_x	0.151 m (5.93 in.)	0.161 m (6.34 in.)
NUMBER OF AIRFOILS	22	28
ASPECT RATIO S/b_x	1.01	0.946
INTERAIRFOIL GAP	0.65 (bx)	
TIP CLEARANCE		0.01 (bx)
MIDSPAN INLET METAL ANGLE	90 deg	42 deg
MIDSPAN EXIT METAL ANGLE	21 deg	26 deg
EXIT VELOCITY, ABSOLUTE FRAME	64 m/s (210 ft/s)	34 m/s (112 ft/s)
EXIT Re No./in.	1.09×10^5	1.04×10^5

weight closer to air have been used to study aerodynamic mixing [15], CO₂ was chosen for this study for reasons of safety. At the design flow coefficient, approximately 45 cubic feet per minute of trace gas would be required to achieve the desired degree of resolution of the trace gas concentration.

An axisymmetric inlet CO₂ profile was generated with an array of five concentric injector rings located in a plane 76 in. upstream of the first stator (Fig. 1). These rings were located far enough upstream ($x/b_x = 12.8$ axial chords) of the first stator so that the total pressure nonuniformity introduced by the ring wakes was completely mixed out at the first stator inlet traverse plane (Station 1). A flow area contraction of 3 to 1 between the injector ring location and Station 1 also contributed to this absence of ring wakes. The rings were fabricated from stainless steel tubes 0.5 in. in diameter. Each ring contained 144 holes of 0.015 in. diameter uniformly distributed around its circumference. The tube diameter and hole size were selected to provide a uniform (axisymmetric) distribution of CO₂ around the inlet annulus. CO₂ was injected into the inlet flow from each of these rings. By controlling the flow of CO₂ to each ring independently, the radial distribution of CO₂ at Station 1 could be tailored to simulate any number of axisymmetric turbine inlet temperature profiles.

CO₂ concentrations in the turbine model were determined from gas samples drawn through conventional surface static pressure taps located on the rotor airfoil and hub endwall, and through pneumatic traverse probes in the flow field. Specifically, on the rotor airfoil surface, 22 static pressure taps located around its perimeter at each of seven spanwise locations (2, 12.5, 25, 50, 75, 87.5, and 98 percent span) were used to obtain gas samples. These are the same taps used previously to obtain rotor airfoil surface pressure distributions in an experimental study of stator–rotor interaction and negative incidence separation [10, 11].

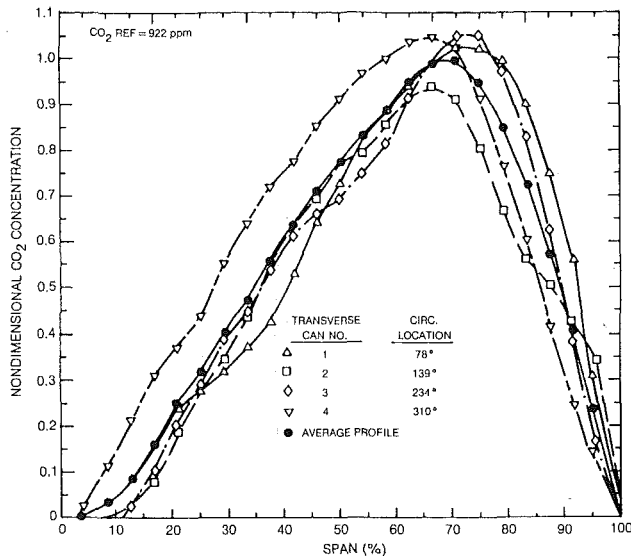


Fig. 3 Spanwise CO₂ profiles at stator inlet (Station 1)

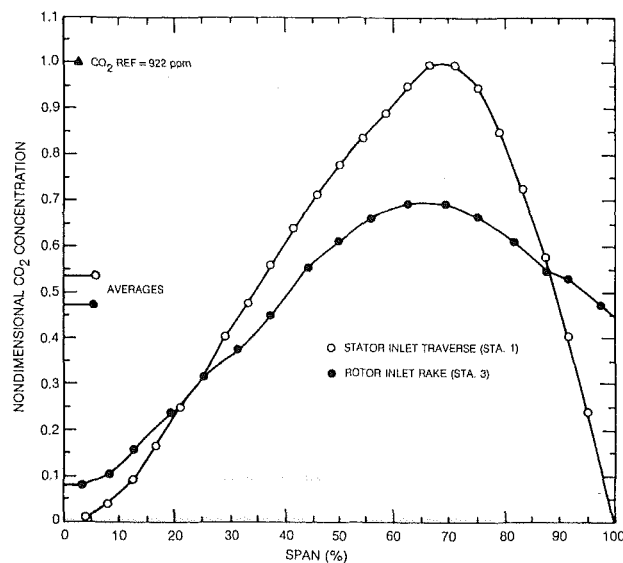


Fig. 4 Distortion of axisymmetric CO₂ profile through the stator row

On the rotor hub endwall, an array of 32 static pressure taps (Fig. 2) was installed for trace gas sampling. Four absolute frame traverse probes were located one axial chord upstream of the first stator leading edge (Fig. 1, Station 1) and at circumferential positions of 78, 139, 234, and 310 deg from the top of the inlet annulus. Concentration measurements from these probes were used to determine the CO₂ flow rate required for each injector ring to obtain the desired inlet CO₂ profile at Station 1 and also to determine the degree of non-axisymmetry in the inlet profile.

A multi-element, absolute frame, radially traversed probe that had sensors distributed circumferentially over one first stator pitch was installed downstream of the first stator trailing edge (Station 2, $x/b_x = 0.126$). CO₂ contours obtained from this probe rake were compared with previously measured flow pitch angle contours at the first stator exit [16]. A multi-element rotating frame rake probe with sensors distributed radially from 3 to 95 percent span was installed on the hub and in line with the rotor leading edge (Station 3, Fig. 1). Radial CO₂ distributions obtained from this probe rake were com-

pared to the averaged inlet (Station 1) CO₂ profile to determine the degree of spanwise mixing of the inlet profile through the first stator passage.

Gas samples from both the rotating frame rake probe and the rotor airfoil and hub endwall taps were selectively drawn through the rotating frame instrumentation package, which consisted of two computer-controlled Scanivalves (Model No. 48J9), a single Scanivalve fluid switch (Model NO. WS6-12-SPL), and a Dublin high-speed rotary pneumatic union (Model No. 1590). The scanivalve transducer was removed for these tests and the scanivalve was used as a 48 prt fluid switch. The stationary (absolute) frame output of the rotary union was fed into a Beckman Non-Dispersive Infrared (NDIR) analyzer (Model 865), which was used to measure the gas sample CO₂ concentration. A separate scanivalve and gas sample acquisition system was connected to the absolute frame traverse probes (Station 1) and the traverse rake (Station 2). The output of this system was also fed into the NDIR analyzer. At the beginning of each data acquisition cycle, the system was calibrated from 0 to 2500 parts per million (ppm) and the ambient CO₂ level of the inlet flow upstream of the injector rings was measured. The inlet ambient CO₂ level was also measured at the end of each data acquisition cycle. In the data reduction, the average of the two ambient CO₂ measurements was subtracted from all the other CO₂ measurements.

To achieve reasonably good resolution in the experiment, the maximum CO₂ concentration in the profile at Station 1 was set at approximately 1000 ppm above ambient. The accuracy of the NDIR was 5 ppm and the ambient CO₂ level was typically 375 ppm. Therefore, the ambient or zero reference CO₂ level was known to within 1 or 0.5 percent of the difference between the maximum and the ambient concentration.

Experimental Results

Inlet CO₂ Profile Generator. The initial phase of the experimental program focused on the CO₂ profile generator checkout and the establishment of a suitable axisymmetric inlet CO₂ profile at Station 1. Since the CO₂ flow rate through each of the five injector rings could be controlled independently, any number of inlet profiles could be generated. For this study of spanwise mixing, the inlet CO₂ profile was chosen to increase monotonically from the hub to about 75 percent span and to decrease from there to the tip. To generate a monotonically increasing CO₂ inlet profile, the CO₂ flow rate through the smallest diameter ring (No. 5 of Fig. 1) was set at the lowest flow rate of any of the five rings. The flow rate was progressively increased through each of the larger diameter rings.

The resulting spanwise profiles of nondimensional CO₂ concentration measured at each of the four circumferential inlet traverse locations (Station 1) at one axial chord upstream of the first stator are shown as the open symbols in Fig. 3. The circumferentially averaged CO₂ inlet profile is denoted by the solid symbols. All the measurements are nondimensionalized relative to the maximum averaged CO₂ concentration, which was typically 1000 ppm above ambient. Although there is some degree of nonaxisymmetry, the intended monotonic behavior is achieved from 0 to 75 percent span. This averaged CO₂ profile is representative of a turbine inlet temperature profile that has its maximum level skewed toward the tip.

Spanwise Mixing in the First Stator. The amount of spanwise mixing occurring in the first stator passage was assessed by comparing the averaged CO₂ profile obtained at the first stator inlet (Station 1, Fig. 3) with the profile obtained from the rotating frame probe rake located downstream of the first stator on the rotor hub and in line with the rotor leading edge plane (Station 3). This comparison between the first stator inlet and exit CO₂ profiles is shown in Fig. 4. All the data

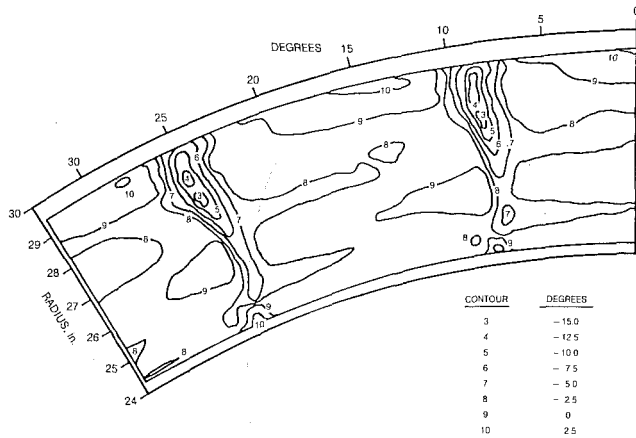


Fig. 5(a) Pitch angle contours at stator exit (Station 2)

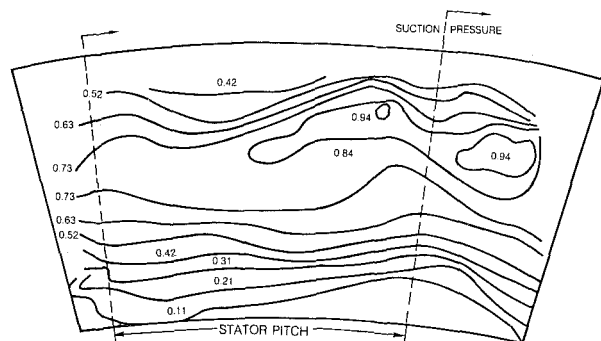


Fig. 5(b) CO₂ concentration contours at stator exit (Station 2)

presented are nondimensionalized by the maximum CO₂ level (922 ppm) above ambient of the stator inlet profile. This maximum level corresponds to a nondimensional concentration of unity in Fig. 4. Using the measured CO₂ concentrations and the radial distribution of axial velocity from a streamline curvature calculation, a continuity check was made between Station 1 and Station 3 by calculating the total mass flow of CO₂ at both locations. The mass averages, 0.545 and 0.461, respectively, of the two profiles agree to within 15 percent. Considering the degree of nonaxisymmetry in the inlet profile (Fig. 3), this is reasonably good agreement.

It should be noted that some of this difference may also be due to calculating the CO₂ mass flow at the stator exit (Station 3) by using the radial distribution of axial velocity predicted by the streamline curvature calculation which may not accurately represent the actual axial velocity distribution. At the stator inlet (Station 1), the axial velocity is nearly constant and well represented by the streamline curvature calculation. It is also worth noting that the mass flow of the injected CO₂ represents only 0.05 percent of the total mass flow through the turbine model. Therefore, the injected CO₂ does not have a measurable effect on the aerodynamics of the turbine.

As seen in Fig. 4, the overall effect of the stator aerodynamic flow field on the axisymmetric radial inlet CO₂ profile is to reduce the maximum concentration level at 75 percent span and to increase the concentration levels near both the hub and tip endwalls. This redistribution of the inlet profile is due to the stator hub and tip endwall secondary flow vortices [15, Fig. 2]. These results are consistent with radial-circumferential traverse measurements of the flow pitch angle and also with the traverse rake CO₂ measurements made at the stator exit (Station 2).

Contour plots generated from the flow pitch angle measurements and traverse rake measurements of CO₂ con-

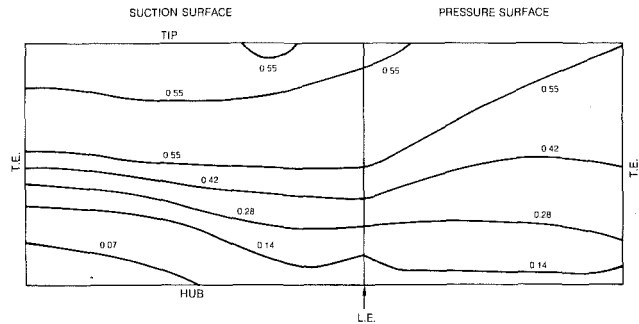


Fig. 6(a) Rotor surface CO₂ concentration contours

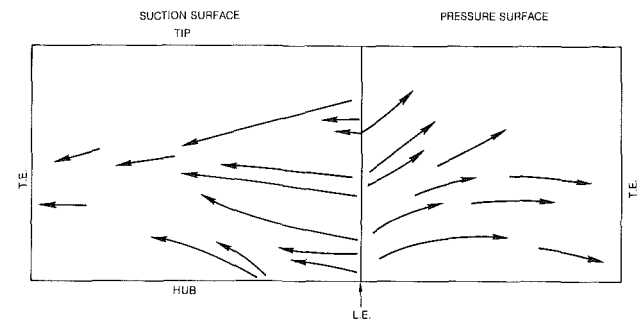


Fig. 6(b) Rotor surface flow visualization

centration are shown in Figs. 5(a) and 5(b). The pitch angle contours shown in Fig. 5(a) were generated from data [16] acquired using a three element hot film probe traversed at the same axial locations as the CO₂ traverse rake (Station 2). The CO₂ concentrations shown in the contours of Fig. 5(b) are nondimensionalized by the maximum averaged CO₂ concentration of the inlet profile (Station 1). This is the same CO₂ concentration level used to nondimensionalize the results presented in Figs. 3 and 4.

Near the tip region, the pitch angle contours indicate the existence of strong radial inflows (negative pitch angles) in the stator wakes. The effect of this radial inflow on the axisymmetric CO₂ inlet profile can be seen in the CO₂ concentration contours (Fig. 5b) which display a dip toward the hub at locations approximately one stator gap apart in the tip region. This effect is much less pronounced in the hub region where the pitch angles are in general much smaller.

Near both the hub and tip, the CO₂ contours are displaced away from the endwalls near the suction side of the wake and toward the endwalls on the pressure side of the wake. These displacements are due to the endwall passage vortices and are most noticeable in the hub region where the endwall secondary flow is stronger. In the tip region, the radial displacements are predominantly due to the radial inflow in the stator wakes. Note that although there are local regions of radially redistributed flow, the inlet CO₂ profile has basically retained its axisymmetric character at the first stator exit as indicated by the overall axisymmetric nature of the contours in Fig. 5(b).

Spanwise Mixing in the Rotor. CO₂ concentration contours determined from gas sample measurements taken through static pressure taps at the seven spanwise rows on the rotor pressure and suction surfaces are compared with rotor surface flow visualization results in Figs. 6(a) and 6(b). The surface flow trajectories indicated by the arrows in Fig. 6(b) were reconstructed from flow visualization surface traces obtained using an ammonia/Ozalid paper surface indicator technique [17]. The radial displacement of the rotor pressure surface concentration contours (Fig. 6a) indicates the existence of

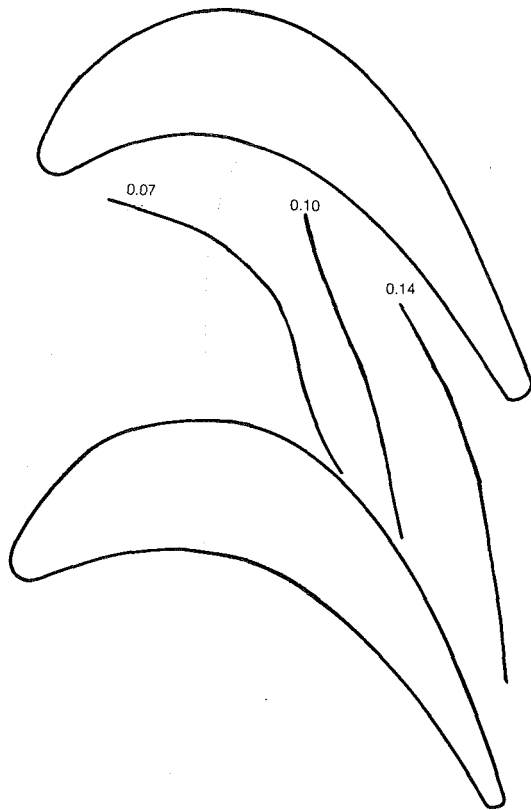


Fig. 7(a) Rotor hub endwall CO₂ concentration contours

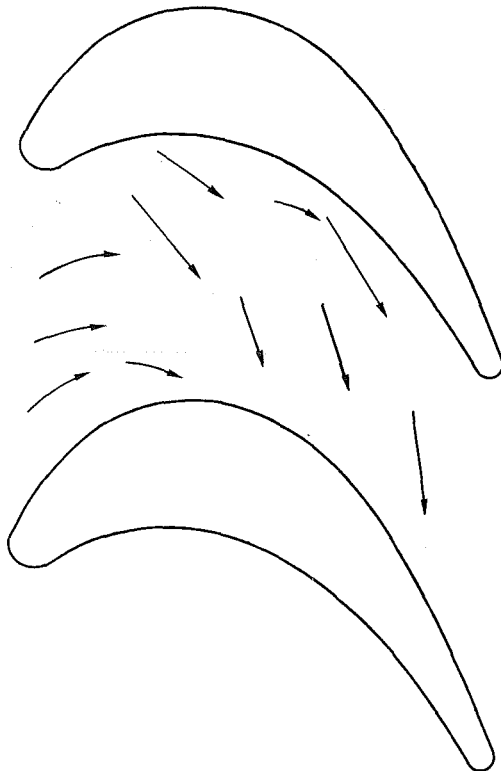


Fig. 7(b) Rotor hub endwall flow visualization

strong radial outflows on the outer half span. This is confirmed by the surface flow visualization results. An inviscid aerodynamic mechanism, the relative eddy, has been identified as the source of this radial outflow on the rotor pressure surface [18]. This mechanism occurs only in rotating tur-

bomachinery airfoil passages and not in stators or in stationary cascades. Over the inner half span, the pressure surface CO₂ contours exhibit very little radial displacement of the flow except near the hub. This is also confirmed by the surface flow visualization.

On the rotor suction surface, the CO₂ contours indicate there is no significant radial displacement of the surface flow near the leading edge or in the region near midspan. Near the hub, as the trailing edge is approached, the contours indicate significant radial displacements of the surface flow. This is confirmed by the suction surface flow visualization. The outward radial displacement of the CO₂ contours near the hub region is due to the hub passage secondary flow vortex, which sweeps low CO₂ concentration fluid off the hub endwall and carries it up onto the rotor suction surface. This endwall flow also accounts for the large region of low CO₂ concentration (0.07) on the aft portion of the rotor near the hub. Over the inner half span of the suction surface, both the CO₂ contours and the surface flow visualization indicate the flow is similar in many respects to the flow over a stationary cascade of airfoils such as that studied by Langston [19] and those by Moore and Ransmayr [20].

This is not the case for the outer half span. Here, the CO₂ contours and the surface flow visualization are different. The surface flow visualization shows strong radial inflow due to the tip endwall secondary flow system. In the tip region this includes the rotor tip leakage flow, the scrapping vortex (if it exists), and the tip endwall secondary flow passage vortex. Overall, the surface flow visualization over the outer half span resembles the surface flow visualization over the inner half span. The CO₂ concentration contours, however, display very little radial displacement over the region between 75 to 100 percent span and they are also at fairly constant levels in this region. This is due to the relatively weak CO₂ gradients in the rotor inlet CO₂ profile near the tip and also due to the rotor tip leakage flow which carries high CO₂ concentration fluid through the tip gap from the rotor pressure surface.

Surface flow visualization on the rotor tip and radial-circumferential traverse measurements downstream of the rotor trailing edge indicate that after the leakage flow crosses the tip and is discharged into the passage on the suction surface side, it rolls up to form a leakage vortex that remains in close proximity to the rotor suction surface [16, Fig. 2, 11, Fig. 9]. It is the tip leakage flow vortex and the relatively weak gradients in the rotor inlet CO₂ profile near the tip (Fig. 4) that account for the nearly constant, high CO₂ concentrations on the rotor suction surface over the outer half span.

A comparison of the CO₂ contours and surface flow visualization on the rotor hub endwall is presented in Figs. 7(a) and 7(b). The CO₂ concentration contours on the hub endwall extend across the passage from the pressure to the suction surface and increase in level as the rotor trailing edge plane is approached. CO₂ concentrations measured on the rotor hub endwall (Fig. 7a) are generally much lower than those measured on the blade surface (Fig. 6a). This indicates that very little of the trace gas in the high CO₂ concentration region of the inlet profile reaches the hub endwall. A correlation of the CO₂ concentration levels in the hub contours with the levels in the inlet profile (Fig. 4) indicates that the fluid reaching the endwall near the rotor trailing edge entered the blade row at approximately 13 percent span. The increase in CO₂ concentration as the trailing edge of the rotor is approached is due to the scrubbing action of the rotor hub endwall vortex, which removes fluid from the pressure surface and sweeps it across the endwall toward the suction surface. If it were not for this aerodynamic mechanism, the CO₂ concentration on the rotor hub endwall would be uniform and at the same level measured at the hub by the rotating inlet rake (Station 3). The flow visualization (Fig. 7b) shows the same

pressure to suction surface flow as indicated by the CO₂ contours.

Summary

Based on the CO₂ concentration measurements and the surface flow visualization, it is apparent that significant spanwise mixing of the axisymmetric inlet profile occurs in both the stator and rotor passages as the inlet flow proceeds through the turbine stage. This mixing is due to three-dimensional aerodynamic mechanisms (passage endwall secondary flow vortices, rotor tip leakage flow, the relative eddy, and radial flow in the airfoil wakes).

The CO₂ trace gas technique yields surface concentration contours that are consistent with and also supplement and quantify the surface flow visualization technique, especially in regions of very complex flow such as at the rotor tip. This technique represents an accurate, straightforward method for tracking fluid flow and for determining spanwise mixing in a turbine stage.

A more comprehensive study of spanwise mixing in an axial flow turbine is currently in progress [21]. In this program, detailed radial-circumferential measurements of total and static pressure and flow velocity will be made upstream and downstream of each airfoil row in the UTRC one and one-half stage axial turbine model.

Acknowledgments

This work was funded by the Pratt and Whitney Engineering Division of UTC.

References

- 1 Oates, G. C., ed., "The Aerothermodynamics of Aircraft Gas Turbine Engines," AFAPL-TR-78-52, July 1978.
- 2 Langston, L. S., Nice, M. S., and Hooper, R. M., "Three-Dimensional Flow Within a Turbine Cascade Passage," *ASME Journal of Engineering for Power*, Vol. 99, 1977, p. 21.
- 3 Graziani, R. A., Blair, M. F., Taylor, J. R., and Mayle, R. E., "An Experimental Study of Endwall and Airfoil Surface Heat Transfer in a Large Scale

Turbine Blade Cascade," *ASME Journal of Engineering for Power*, Vol. 102, 1980, p. 257.

4 Horlock, J. H., *Axial Flow Turbines*, Robert E. Krieger Publishing Company, Huntington, NY, 1973.

5 Metzger, D. E., ed., "Fundamental Heat Transfer Research for Gas Turbine Engines," NASA Conference Publication 2178, Oct. 1980.

6 Butler, T. L., Sharma, O. P., Joslyn, H. D., and Dring, R. P., "Redistribution of an Inlet Temperature Distortion in an Axial Flow Turbine Stage," AIAA Paper No. AIAA-86-1468, June 1986.

7 Hawthorne, W. R., "Secondary Vorticity in Stratified Compressible Fluids in Rotating Systems," CUED/A-Turbo/TR 63, University of Cambridge, England, 1974.

8 Booth, T. C., Dodge, P. R., and Hepworth, H. K., "Rotor-Tip Leakage: Part I—Basic Methodology," *ASME Journal of Engineering for Power*, Vol. 104, 1982, pp. 154-161.

9 Dring, R. P., and Joslyn, H. D., "The Relative Eddy in Axial Turbine Rotor Passages," ASME Paper No. 83-GT-22, 1983.

10 Dring, R. P., Joslyn, H. D., Hardin, L. W., and Wagner, J. W., "Turbine Rotor-Stator Interaction," *ASME Journal of Engineering for Power*, Vol. 104, 1982, pp. 729-742.

11 Joslyn, H. D., and Dring, R. P., "Turbine Rotor Negative Incidence Stall," ASME Paper No. 83-GT-23, 1983.

12 Dring, R. P., and Joslyn, H. D., "Measurements of Turbine Rotor Blade Flows," *ASME Journal of Engineering for Power*, Vol. 103, 1981, pp. 400-405.

13 Eckert, E. R. G., and Goldstein, R. J., *Measurement Methods in Heat Transfer*, 2nd ed., Hemisphere, Washington, DC, 1976.

14 Pederson, D. R., Eckert, E. R. G., and Goldstein, R. J., "Film Cooling With Large Density Differences Between the Mainstream and the Secondary Fluid Measured by the Heat-Mass Transfer Analogy," *ASME Journal of Heat Transfer*, Vol. 99, 1977, pp. 620-627.

15 Denton, J. D., and Usui, S., "Use of a Tracer Gas Technique to Study Mixing in a Low Speed Turbine," ASME Paper No. 81-GT-86, 1981.

16 Sharma, O. P., Butler, T. L., Joslyn, H. D., and Dring, R. P., "Three Dimensional Unsteady Flow in an Axial Flow Turbine," *AIAA Jour. of Propulsion and Power*, Jan. 1985.

17 Joslyn, H. D., and Dring, R. P., "Surface Indicator and Smoke Flow Visualization Techniques in Rotating Machinery," presented at Symposium on Transport Phenomena in Rotating Machinery, Honolulu, HI, Apr. 1985; published in *Heat Transfer and Fluid Flow in Rotating Machinery*, Hemisphere, Washington, DC, Aug. 1986.

18 Dring, R. P., and Joslyn, H. D., "The Relative Eddy in Axial Turbine Rotor Passages," ASME Paper No. 83-GT-22, 1983.

19 Langston, L. S., Nice, M. S., and Hooper, R. M., "Three-Dimensional Flow Within a Turbine Cascade Passage," *ASME Journal of Engineering for Power*, Vol. 99, 1977, pp. 21-28.

20 Moore, J., and Ransmayr, A., "Flow in a Turbine Cascade: Part I—Losses and Leading-Edge Effects," *ASME Journal of Engineering for Gas Turbines and Power*, Vol. 106, 1984, pp. 400-408.

21 Joslyn, H. D., and Dring, R. P., "An Experimental Study of Turbine Inlet Temperature Profile Attenuation," AFOSR Contract No. F49620-86-C-0020, currently in progress.

The Influence of Rotation on the Heat Transfer Characteristics of Circular, Triangular, and Square-Sectioned Coolant Passages of Gas Turbine Rotor Blades

S. P. Harasgama

Propulsion Dept.,
Royal Aircraft Establishment,
Pyestock, Hampshire, United Kingdom

W. D. Morris

Head of Mechanical Engineering Dept.,
University College of Swansea,
Swansea, United Kingdom

This paper reports on the influence of Coriolis-induced secondary flow and centripetal buoyancy on the heat transfer within typical turbine rotor blade cooling passages. The experimental results indicate that for through-flow Reynolds numbers up to 30,000 increasing rotational speed tends to increase the mean levels of heat transfer relative to the stationary case when the flow is radially outward. This trend is reversed when the flow is radially inward. Increasing centripetal buoyancy for radially outward flow tends to decrease the mean level of heat transfer and in some cases these levels fall below the equivalent stationary values. When the flow is radially inward, increasing centripetal buoyancy generally results in an increase in mean heat transfer, and in this case increasing buoyancy tends to increase the leading (suction) side heat transfer while reducing it on the trailing (pressure) side. Original correlations proposed by Morris et al. for leading side heat transfer in a circular duct are shown to hold for triangular and square ducts when the hydraulic diameter concept is used.

Introduction

Since increasing turbine entry temperature is a prerequisite for increasing the thermodynamic efficiency of gas turbines, the use of cooling air in the stator and rotor blades of present-day aircraft gas turbines is widespread and essential. The coolant reduces the metal temperatures to below the material melting temperature and thereby increases the durability of the blade. Future engines will tend to have significantly higher gas temperatures, thereby promoting the requirement for more efficient blade cooling configurations. The coolant passages are of complex shape and tend to have transverse ribs and pin-fins to enhance the heat transfer process. In current turbines the coolant side heat transfer approaches and in some cases exceeds that on the hot gas side, as typified by Fig. 1. Only recently has there been an effort to study the internal heat transfer processes and the effects of rotation on internal heat transfer are only now being addressed.

Morris et al. (Morris, 1981; Morris and Ayhan, 1979, 1982; Morris and Harasgama, 1985) have reported some experiments on the effects of rotation on turbine blade coolant passages of an idealized nature while Clifford (1985) has

reported an experiment on a multipass cooling configuration with transverse ribbing. Recently Johnson et al. (1986) have conducted tests on a rotating U-bend configuration and Isakov and Trushin (1985) reported results for radial inflow and outflow in a circular duct with varying rotational speeds.

The turbine designer currently resorts to the use of heat transfer correlations formed in the main from data gathered on stationary tests and applies these to the calculation of heat transfer coefficients in rotating passages. In doing so he ignores three fundamental effects present in the rotating passage, namely Coriolis and centripetal acceleration and, in the case of an accelerating/decelerating rotor, the rate of change of angular velocity. Experimental and theoretical work on the effects of rotation have been undertaken by Barua (1955), Benton and Boyer (1966), Mori and Nakayama (1968), Ito and Nanbu (1971), Skiaderis and Spalding (1977), Metzger and Stan (1977), Lokai and Limanski (1975), and Zysina-Molozken et al. (1977). In general the investigators concentrated on the effects due to Coriolis acceleration, which showed that for radially outward flow, Coriolis acceleration has a beneficial effect on heat transfer. However, significant scatter existed in the various results, which prompted Morris (1981) to argue that these discrepancies could be attributed to centripetal buoyancy as illustrated in Figs. 2(a) and 2(b). This indicates that for radially outward flow centripetal buoyancy reduces heat transfer, while the converse is true for radially in-

Contributed by the Gas Turbine Division of THE AMERICAN SOCIETY OF MECHANICAL ENGINEERS and presented at the 32nd International Gas Turbine Conference and Exhibit, Anaheim, California, May 31-June 4, 1987. Manuscript received at ASME Headquarters February 10, 1987. Paper No. 87-GT-121.

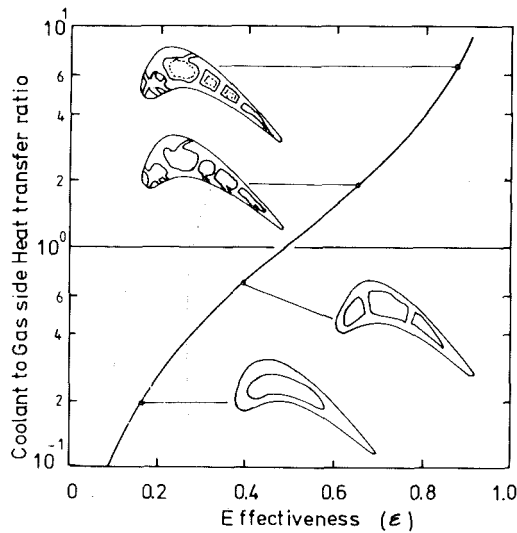


Fig. 1 Influence of cooled blades on effectiveness

ward flow. All the data were gathered for leading (suction) side only and no conclusions were made as to the trailing (pressure) side characteristics.

Original work by Morris and Ayhan (1979; 1982) on circular ducts with inward and outward flow led to correlations for leading side heat transfer as follows:

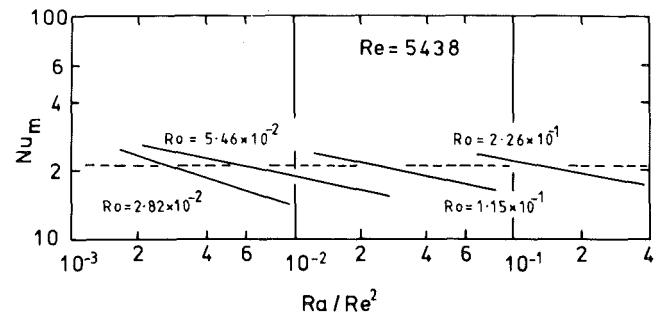
For radially outward flow

$$Nu = 0.022 \left[\frac{Ra}{Re^2} \right]^{-0.186} Re^{0.8} Ro^{0.33} \quad (1)$$

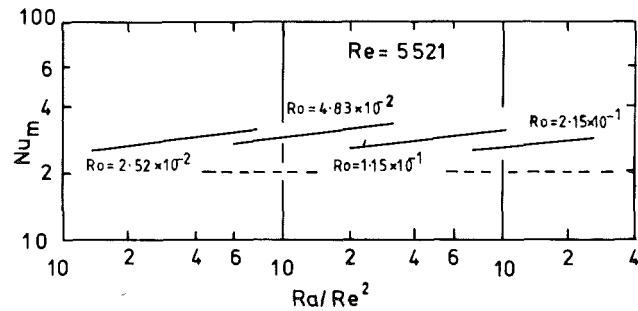
and for radially inward flow

$$Nu = 0.036 \left[\frac{Ra}{Re^2} \right]^{0.112} Re^{0.8} Ro^{-0.083} \quad (2)$$

These correlations were posed for test sections fitted with a calming section so that the flow was hydrodynamically fully developed before the onset of heating. Clifford et al. (1984) reported results for a triangular duct with radial outflow and a sharp-edged entry ($AR = 12:1$); Figs. 3 and 4 summarize their findings. Increasing the Rayleigh number (increasing buoyancy) tends to reduce the mean Nusselt number (Fig. 3) for Reynolds numbers up to 25,000. At a Reynolds number of 45,000 the buoyancy effect is not present, but with rotation the Nusselt numbers are lower than the corresponding stationary values. Increasing the rotational Reynolds number produces an increase in Nusselt number up to Reynolds numbers of 25,000; thereafter the trend was reversed for $Re = 45,000$. Morris and Harasgama (1985) investigated the ef-



(a) Radial outflow



(b) Radial inflow

----- zero speed value

Fig. 2 Influence of rotation on mean heat transfer in a circular tube (Morris and Ayhan, 1979, 1982)

fects of rotation on a square-sectioned duct with radially outward and inward flow having a sharp-edged entry ($AR = 12:1$). The results shown on Figs. 5 and 6 indicate that the data on the leading side correlated well with equations (1) and (2), but that trailing side heat transfer was higher than predicted by equation (1) for outward flow and lower than that predicted by equation (2) for inward flow. This effect is attributed to the reversal in the direction of Coriolis-induced secondary flows.

The results reported to date and the foregoing discussion indicate that both centripetal buoyancy and Coriolis-induced secondary flows have a marked effect on the heat transfer within turbine rotor blade cooling passages. An increase in buoyancy tends to decrease the heat transfer with radially outward flow while the converse is true for radial inflow. This

Nomenclature

AR = ratio of inlet delivery duct area to coolant passage area
 C_p = constant-pressure specific heat of coolant
 d = hydraulic diameter of duct
 h = heat transfer coefficient
 H = midspan eccentricity
 J = rotational Reynolds number
 k = thermal conductivity of coolant
 L = length of duct
 Nu = Nusselt number
 Pr = Prandtl number

Ra = rotational Rayleigh number
 Re = through-flow Reynolds number
 Ro = inverse Rossby number
 T_c = coolant temperature
 T_g = hot gas temperature
 T_m = metal temperature
 ΔT_w = wall-to-coolant temperature difference
 V = mean coolant velocity in duct
 β = coefficient of volume expansion of coolant

ϵ = effectiveness = $(T_g - T_m)/(T_g - T_c)$
 μ = absolute viscosity of coolant
 ν = kinematic viscosity of coolant
 ρ = density of coolant
 Φ = functional relationship
 Ω = angular velocity

Subscripts

∞ = evaluated for fully developed flow
 m = mean value for the duct

arises because increases in buoyancy retard the flow close to the duct walls with radial outflow, but accelerate the flow near the walls for radial inflow. Increasing rotational speed (Coriolis acceleration) with outward flow tends, in general, to increase the Nusselt number due to enhanced mixing. With radial inflow, increases in angular velocity cause a reduction in leading side heat transfer; this effect is present in all the geometries studied but no simple physical explanation can be proposed for the effect as yet. Note that Johnson et al. (1986) have recently reported that increasing angular speed can, in certain cases, lead to a reduction in Nusselt number with radial inflow.

The work reported in this paper forms an ongoing program of research in conjunction with other University-based heat transfer research groups to carry out experimental and numerical studies on the effects of rotation on the heat transfer characteristics of turbine rotor blade cooling passages. This paper reports on a new experimental facility and results therefrom on a circular tube with sharp-edged entry ($AR=49:1$) and radially outward flow. Results are also presented for a triangular duct and a square duct with radial inflow and sharp-edged entry ($AR=12:1$).

Experimental Facilities and Program

At present two facilities exist for the determination of heat transfer in rotating passages. The first rig, shown in Fig. 7, is designated the MK 1 rig and has been extensively detailed by Morris et al. (Morris, 1981; Morris and Ayhan, 1979, 1982; Morris and Harasgama, 1985). The second test rig, recently completed, and designated the MK 2 rig, is functionally similar to the MK 1 rig but enables speeds of 5000 rpm to be

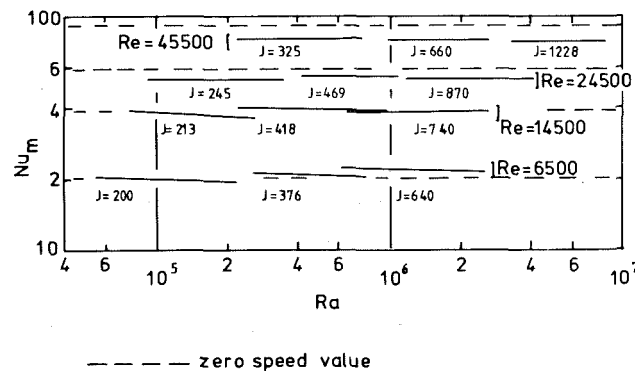


Fig. 3 Influence of buoyancy on Nusselt number for radial outflow, triangular duct (Clifford et al., 1984)

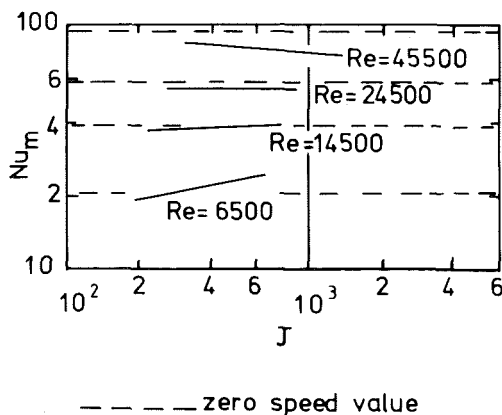


Fig. 4 Variation of Nusselt number with rotational Reynolds number triangular duct, and radial outflow (Clifford et al., 1984)

attained, thereby increasing the range of rotational Reynolds numbers and Rayleigh numbers that can be simulated. The MK 2 rig (Fig. 8) consists of a shaft, hollow at one end, on which is mounted the hollow cylindrical rotor arm. A counterbalance is located on the opposite side of the rotor arm. The test module (Fig. 9) is mounted inside the arm and can be indexed around within the arm to study girthwise variations in heat transfer. A 25 kW d-c electric motor with variable speed control is used to drive the entire system. Air, measured using an accurate "Rotameter" flowmeter, is supplied to the test section via the rotating seal airbox mounted on the hollow end of the shaft. A pair of slip rings takes power to the heater coil on the test section; the power supplied is monitored on a "Cambridge" wattmeter. A 26-channel silver/silver graphite

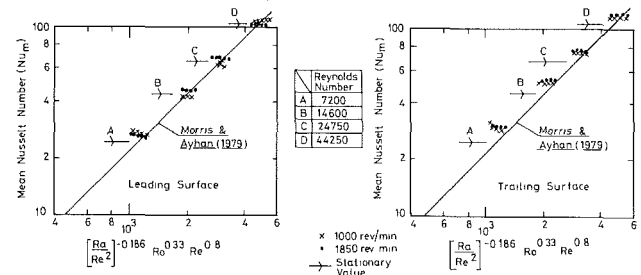


Fig. 5 Correlation of square duct outward flow data with equation (1) (Morris and Harasgama, 1985)

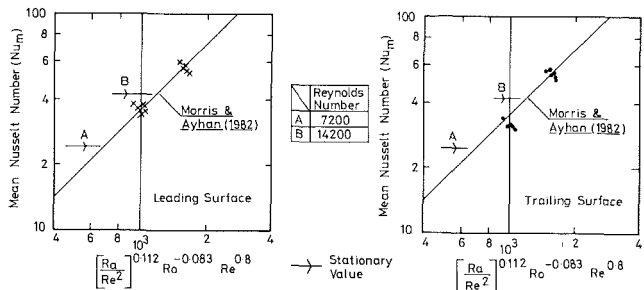
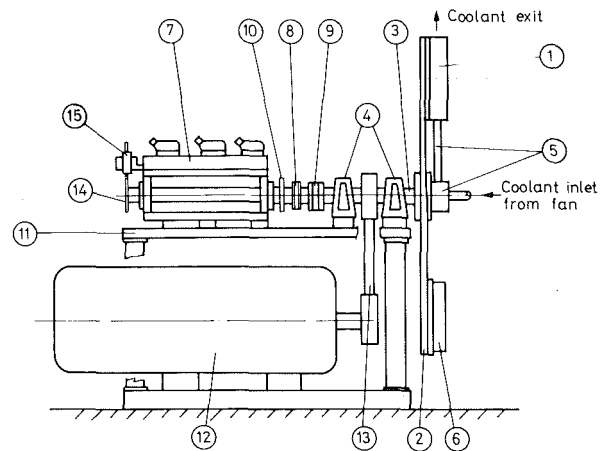


Fig. 6 Correlation of square duct inward flow data with equation (2) (Morris and Harasgama, 1985)



- 1. Test Section
- 2. Rotating Arm
- 3. Shaft
- 4. Bearings
- 5. Plenum / Seal
- 6. Balance Weight
- 7. Instrument Slipping
- 8. Coupling
- 9. Power Slipping
- 10. Thermocouple Terminals
- 11. Frame
- 12. Motor
- 13. Pulley
- 14. Shaft Encoder
- 15. Magnetic Pickup

Fig. 7 The MK-1 rotor rig

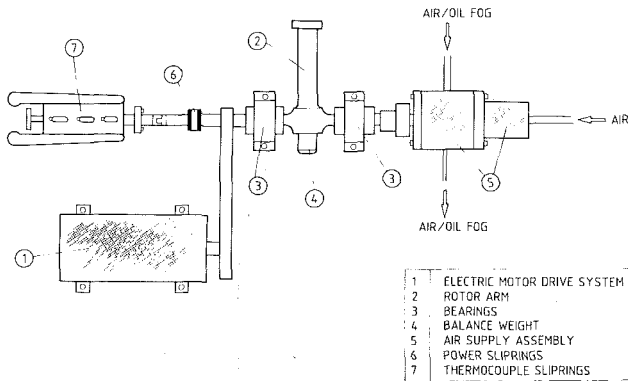


Fig. 8 The MK-2 rotor rig

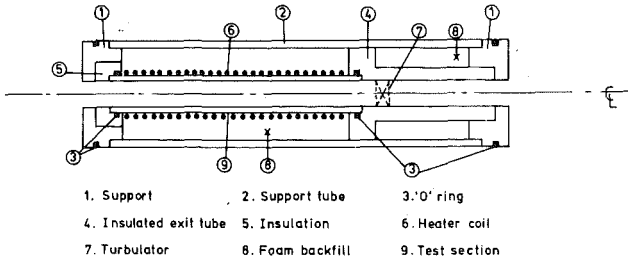


Fig. 9 Test module for MK-2 rig

slip ring unit is used to transmit data from chromel/alumel thermocouples to the DEC LSI 11/03 computer data logger. Typically 15 thermocouples are embedded on the centerline of the duct on the leading side while 8 thermocouples are placed on the trailing side. Further details of the test modules are given in Fig. 9 and Clifford et al. (1984) and Morris and Harasgama (1985). A single thermocouple records the inlet air temperature. Exit air temperature is recorded by first mixing out any temperature gradients in the flow (using a turbulator) and the resulting temperature is recorded using two thermocouples. The data analysis technique is the same as that used by Morris et al. The present results were all analyzed using the same heat balance technique and were found to agree to within 10 percent. All data and results could be plotted out on-line using a Calcomp-81 (A3) flat bed plotter which formed part of the data acquisition, analysis, and display system (Harasgama, 1984).

The experimental program is detailed in Table 1. Tests were conducted on a triangular-sectioned duct with radial inflow and sharp-edged entry. Similar tests were performed on a square-sectioned duct with radial inflow; both sets of tests were conducted on the MK 1 rig. The MK 2 rig was used to test a circular duct with sharp-edged entry and radially outward flow.

Morris (1981) has indicated that by using dimensional analysis the influence of rotation on heat transfer may be represented as

$$Nu = \Phi(Re, Pr, Ra, J, L/d, H/d) \quad (3)$$

where $Nu = hd/K$; $Re = Vd/\nu$; $Pr = \mu Cp/K$; $Ra = \Omega^2 H \beta d^3 (\Delta T_w) Pr/\nu^2$; $J = \Omega d^2/\nu$. (Note: in some cases the inverse Rossby number, defined as $Ro = \Omega d/V$, is used instead of J .)

For the present experiments the fluid used for the coolant was air and the duct length and midspan eccentricity were held constant; therefore

$$Nu_m = \Phi(Re, Ra, J) \quad (4)$$

In view of equation (4), all the relevant variables were cast in terms of Reynolds number, rotational Reynolds number (J), and rotational Rayleigh number (Ra) for presentation purposes.

Table 1 Test configurations and variables

Configuration and Test Facility	d (mm)	L (mm)	H (mm)	Ω (rev/min)	Re	J	Ra	Ro
Triangular Duct, 10 mm Base, 30° Apex angle, Inward Flow, AR = 12:1, Tested on MK 1 Rig. Leading side data only.	7.67	150	250	0 to 1850	7,000 15,000 25,000	0 to 670	0 to 3.5×10^6	0 to 0.103
Square duct, 7.5 mm x 7.5 mm Inward Flow, AR = 12:1, Tested on MK 1 Rig. Leading and Trailing side data.	7.5	150	250	0 to 1000	7,000 15,000 21,000	0 to 360	0 to 1.5×10^6	0 to 0.042
Circular duct, Diameter = 5.0 mm, Outward Flow, AR = 49:1, Tested on MK 2 Rig. Leading and Trailing Side data.	5.00	100	350	0 to 2000	7,000 15,000 25,000	0 to 350	0 to 2.1×10^6	0 to 0.049

Results and Discussion

Experiments for all configurations were first conducted statically to determine the Nusselt numbers for a range of Reynolds numbers. In all cases the zero speed Nusselt numbers were within 10~15 percent of the Dittus-Boelter (1930) correlation as defined by

$$Nu = 0.023 Re^{0.8} Pr^{0.4} \quad (5)$$

With rotation the data tended to fall into two categories, irrespective of the geometric configuration, namely radial inflow and radial outflow.

Radially Inward Flow. Considering the triangular duct first, Fig. 10 shows the variation of mean Nusselt number on the leading side with rotational Reynolds number (J) for three different through-flow Reynolds numbers. Since the rotational Reynolds number quantifies the effect of Coriolis acceleration, it is interesting to note the downward trend in Nusselt number for all values of through-flow Reynolds numbers. This corroborates data reported earlier by Morris and Ayhan (1982) for circular-sectioned ducts. Although increasing the rotational Reynolds number brings about a decrease in Nusselt number, the overall influence of rotation at the lower through-flow Reynolds numbers is beneficial to heat transfer. However, at the highest value of Reynolds number ($Re \sim 25,000$) the Nusselt numbers are lower than the corresponding stationary values, especially for the higher rotational speed.

The influence of centripetal buoyancy, characterized by the rotational Rayleigh number, is shown on Fig. 11 for the leading side on the triangular duct. For the lowest Reynolds number (≈ 7000) and rotational Reynolds number ($J = 370$), increasing buoyancy tends to increase the mean level of heat transfer. This effect has previously been reported by Morris and Ayhan (1982) for circular ducts. At the intermediate Reynolds number of 15,000, buoyancy does not appear to have a marked effect, while for the highest value of Reynolds number (25,000) increasing buoyancy causes a reduction in heat transfer and can cause it to fall below the zero speed equivalent. For higher values of rotational Reynolds number ($J = 670$), increasing buoyancy only has an effect at the lowest Reynolds number (≈ 7000) where it causes an increase in heat transfer. At the highest levels of rotational Reynolds number and through-flow Reynolds number the overall influence of rotation is to cause the mean level of heat transfer to fall below that of the equivalent stationary case.

Results for the square duct are given in Fig. 12. This indicates the variation of mean Nusselt number with increasing Rayleigh number for both leading and trailing sides. As the

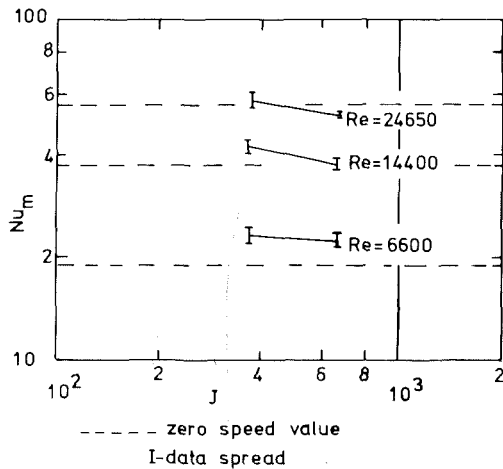


Fig. 10 Variation of mean Nusselt number with rotational Reynolds number, triangular duct, inward flow

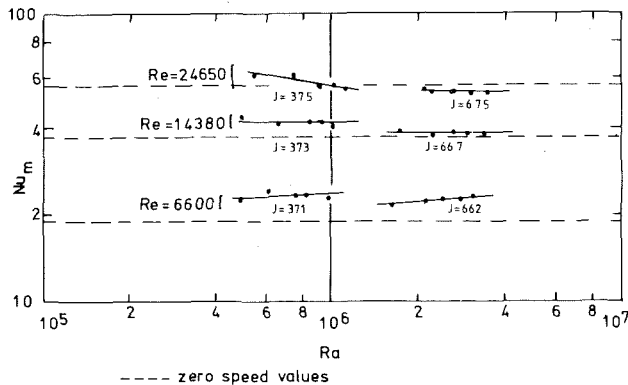


Fig. 11 Variation of mean Nusselt number with rotational Rayleigh number triangular duct, inward flow

Rayleigh number is increased at a nominal Reynolds number of 7000, the tendency is for the leading side heat transfer to increase. This effect is also evident for the triangular duct (Fig. 11). What is interesting is that at the same time the trailing side heat transfer decreases. It appears that this is the first report of such a phenomenon. A possible explanation is that as buoyancy increases the leading side heat transfer, Coriolis-induced secondary flow entrains this "hotter" fluid and deposits it on the trailing edge bringing about an attendant reduction in heat transfer. The effect is also just noticeable at a Reynolds number of 15,000, but for $Re=20,000$ through-flow forced convection overshadows the buoyancy effect. In all cases the overall influence of rotation is to increase the mean levels of heat transfer to above the zero speed equivalents.

Radially Outward Flow. Preliminary results for the circular sectioned duct as tested on the MK 2 rig are shown on Fig. 13. Here, the increase in rotational Reynolds number increases the mean Nusselt for both through-flow Reynolds numbers of 7000 and 25,000. The trailing side heat transfer is higher than the leading side values because the Coriolis-generated secondary flows operate in an opposite sense to those found with radial inflow. Although as yet there are insufficient data on this configuration to categorize the effects of buoyancy, Fig. 13 indicates that rotation reduces the mean levels of heat transfer to below the corresponding stationary values, a feature previously attributed to rotational buoyancy.

Correlation of Data

The correlations of data for the square duct with radial inflow and outflow and sharp-edged entry have already been

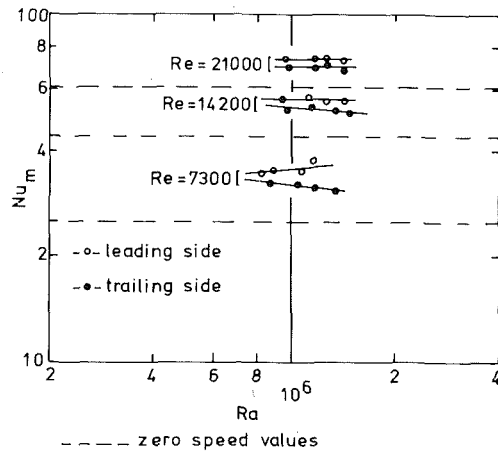


Fig. 12 Variation of mean Nusselt number with Rayleigh number, square duct, inward flow

presented by Morris and Harasgama (1985) and are reproduced in Figs. 5 and 6. Since the original proposals by Morris and Ayhan (1979, 1982) were for a circular duct, leading side, and hydrodynamically fully developed flow at inlet, the square duct results correlate surprisingly well with equation (2). The trailing side heat transfer values for radial inflow are lower by about 12 percent due to the effects of the entrainment of hot fluid to the trailing side as described above.

The results for the triangular duct with radial outflow, previously reported by Clifford et al. (1984), have now been correlated on the basis of equation (1) and are presented in Fig. 14. The correlation with equation (1) is excellent and the sharp-edged entry condition is overshadowed by the effects of rotation.

Finally, Figs. 15 and 16 show the case of the circular duct, radial outflow, and sharp-edged entry. Figure 15, portraying data for the leading side, indicates that this correlates with equation (1). Since Morris and Ayhan (1979) proposed this equation for a circular duct with fully developed flow at entry, it appears from the present data that inlet effects are relatively minor in comparison with the influence of rotation. Figure 16 shows again that with radial outflow equation (1) underpredicts the trailing side heat transfer by around 10 percent due to the enhancement brought about by Coriolis-induced secondary flows.

Conclusions and Recommendations

The present program of research into the effects of rotation on heat transfer within simple turbine blade cooling passages has concentrated on the fundamental aspects of Coriolis acceleration and centripetal buoyancy, characterized by the rotational Reynolds number and rotational Rayleigh number, respectively. Within these restrictions the following conclusions may be made:

- 1 For radially inward flow the mean Nusselt numbers with rotation generally tend to be higher than the corresponding zero speed cases. Increasing centripetal buoyancy generally tends to increase the heat transfer further on the leading side while reducing it on the trailing side. In the author's opinion this is the first report on the latter phenomenon, which is attributed to a coupling between Coriolis-induced secondary flows and centripetal buoyancy. Increase in rotational Reynolds number has a detrimental effect on heat transfer on the leading side, which corroborates earlier work by Morris and Ayhan (1982).

- 2 With radially outward flow rotation causes a reduction in the mean Nusselt number on the leading side with respect to the zero speed equivalents. Increasing buoyancy causes a reduction in heat transfer, which may then be some 10-20 per-

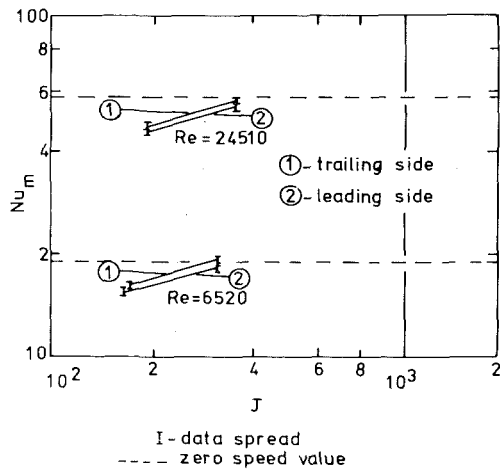


Fig. 13 Variation of mean heat transfer with rotational Reynolds number, circular duct, outflow

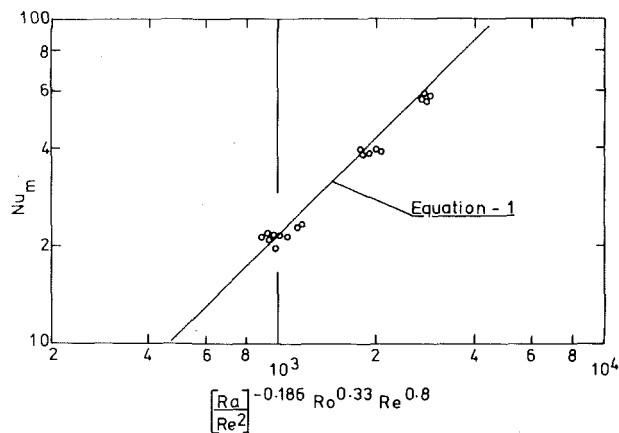


Fig. 14 Correlation of triangular duct, outward flow, leading side data

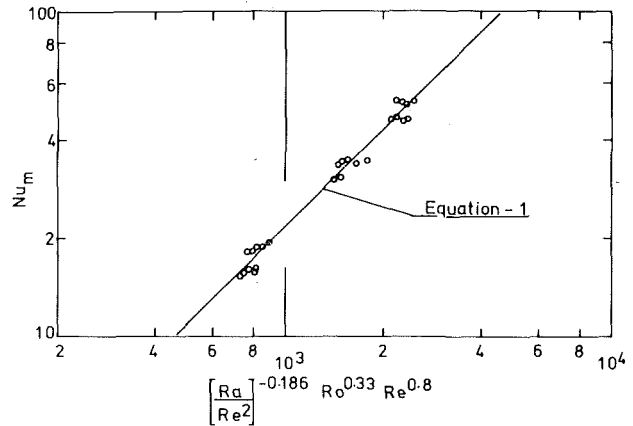


Fig. 15 Correlation of circular duct, outward flow, leading side data

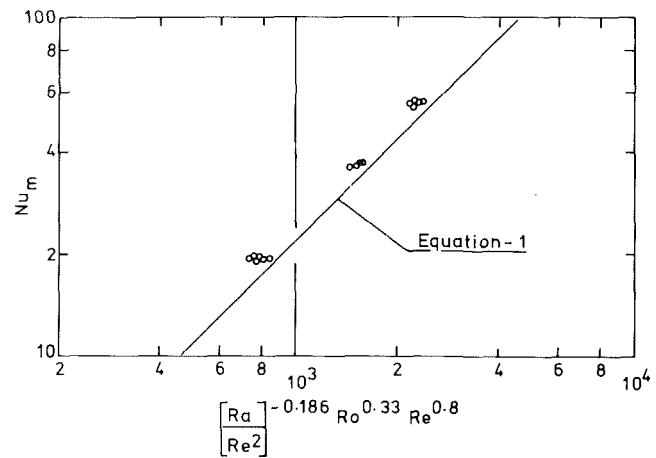


Fig. 16 Correlation of circular duct, outward flow, trailing side data

cent below the zero speed equivalents. Trailing side heat transfer is usually higher than that on the leading side due to the secondary flows. Increases in rotational speed cause an increase in the mean Nusselt number, again due to a strengthening of the secondary flows.

3 Original correlations by Morris (1981) and Morris and Ayhan (1979, 1982), equations (1) and (2), are shown to be valid for the configurations tested to date. This is true only when applied to the leading sides of the ducts tested. When the flow is radially outward, trailing side heat transfer is under-predicted by some 15 percent by equation (1), while for radial inflow equation (2) overpredicts trailing side heat transfer by around 10 percent. In view of the good agreement of equations (1) and (2) in correlating data for the tested configurations, it is recommended that these correlations be used at the preliminary stages in the design of turbine rotor blade cooling passages for the evaluation of leading side heat transfer coefficients.

Acknowledgments

Thanks are due to Mr. A. Hird who built the MK 2 rig and serviced both test rigs and also for his help in acquiring the data for the circular duct. The financial support of the Ministry of Defence and the Science and Engineering Council is gratefully acknowledged.

References

- Barua, S. N., 1955, "Secondary Flow in a Rotating Straight Pipe," *Proc. Roy. Soc., A*, Vol. 227, p. 133.
- Benton, J. S., and Boyer, D., 1966, "Flow Through a Rapidly Rotating Conduit of Arbitrary Cross-Section," *J. Fluid Mech.*, Vol. 26, Part 1, p. 69.
- Clifford, R. J., 1985, "Rotating Heat Transfer Investigations on a Multi-pass Cooling Geometry," presented at Conference on Heat Transfer and Cooling in Gas Turbines, Bergen, Norway, May 6-10, 1985; AGARD-CP-390.
- Clifford, R. J., Morris, W. D., and Haragama, S. P., 1984, "An Experimental Study of Local and Mean Heat Transfer in a Triangular-Sectioned Duct Rotating in the Orthogonal Mode," *ASME Journal of Engineering for Gas Turbines and Power*, Vol. 106, pp. 661-667.
- Dittus, F. W., and Boelter, L. M. K., 1930, *Univ. Calif. Publs., Engng.*, Vol. 2, p. 443.
- Haragama, S. P., 1984, "The Engineering Research Laboratories Data Acquisition Systems," Dept. of Engineering Design and Manufacturing, University of Hull, Hull, United Kingdom.
- Iskakov, K. M., and Trushin, V. A., 1985, "The Effect of Rotation on Heat Transfer in the Radial Cooling Channels of Turbine Blades," *Teplotenergetika*, Vol. 32, pp. 52-55; translated in *Thermal Engineering*, Vol. 32.
- Ito, H., and Nanbu, K., 1971, "Flow in Rotating Straight Pipes of Circular Cross-Section," *ASME Journal of Basic Engineering*, Vol. 93, p. 383.
- Lokai, V. I., and Limanski, A. S., 1975, "Influence of Rotation on Heat and Mass Transfer in Radial Cooling Channels of Turbine Blades," *Izvestiya VUZ, Aviatsionnaya Tekhnika*, Vol. 18, p. 69.
- Mori, Y., and Nakayama, W., 1968, "Convective Heat Transfer in Rotating Radial Circular Pipes (1st Report - Laminar Region)," *Int. Journal Heat and Mass Transfer*, Vol. 11, p. 1027.
- Mori, Y., and Nakayama, W., 1968, "Convective Heat Transfer in Rotating Radial Circular Pipes (1st Report - Laminar Region)," *Int. Journal Heat and Mass Transfer*, Vol. 11, p. 1027.
- Morris, W. D., 1981, *Heat Transfer and Fluid Flow in Rotating Coolant Channels*, Research Studies Press-Wiley.
- Morris, W. D., and Ayhan, T., 1979, "Observations on the Influence of Rotation on Heat Transfer in the Coolant Channels of Gas Turbine Rotor Blades," *Proc. I. Mech. E.*, Vol. 193, p. 303.

Morris, W. D., and Ayhan, T., 1982, "An Experimental Study of Turbulent Heat Transfer in a Tube Which Rotates About an Orthogonal Axis," *Proc. XIV ICHMT Symposium on Heat and Mass Transfer in Rotating Machinery*, Dubrovnik, Yugoslavia, August 30-September 3.

Morris, W. D., and Haragama, S. P., 1985, "Local and Mean Heat Transfer on the Leading and Trailing Surfaces of a Square Sectioned Duct Rotating in the Orthogonal Mode," presented at Conference on Heat Transfer and Cooling in Gas Turbines, Bergen, Norway, May 6-10, 1985; AGARD-CP-390.

Skiadareisis, D., and Spalding, D. B., 1977, "Heat Transfer in a Pipe Rotating About a Perpendicular Axis," ASME Paper No. 77-WA/HT-39.

Wagner, J. H., Kim, J. C., and Johnson, B. V., 1986, "Rotating Heat Transfer Experiments With Turbine Airfoil Internal Passages," ASME Paper No. 86-GT-133.

Zysina-Molozken, L. M., Dergach, A. A., and Kogan, G. A., 1977, "Experimental Investigation of Heat Transfer in a Radially Rotating Pipe," *HGEE High Temp.*, Vol. 14, p. 988.

Time-Averaged Heat-Flux Distributions and Comparison With Prediction for the Teledyne 702 HP Turbine Stage

M. G. Dunn

Calspan Corporation,
Buffalo, NY 14225

R. E. Chupp

Teledyne CAE,
Toledo, OH 43612

Time-averaged heat-flux distributions are reported for the vane and blade of the Teledyne CAE 702 HP full-stage rotating turbine. A shock tube is used as a short-duration source of heated air to which the turbine is subjected and thin-film gages are used to obtain the heat-flux measurements. The thin-film gages were concentrated on the midspan region from the leading edge to near the trailing edge. The blade contained two contoured inserts with gages spaced very close together so that the leading edge distribution could be resolved. The NGV and blade results are compared with predictions obtained using a flat-plate technique, an eddy-diffusing model (STAN 5), and a $k-\epsilon$ model. The results of the comparison between data and prediction suggest that: (a) first, the vane data are bounded by the turbulent flat plate and the fully turbulent STAN 5 prediction. For the vane, the $k-\epsilon$ prediction is in relatively good agreement with the STAN 5 prediction and (b) secondly, the blade data are acceptably predicted by the $k-\epsilon$ prediction on both the pressure and the suction surfaces. The STAN 5 fully turbulent calculation for the blade falls above the data (essentially in agreement with the turbulent flat-plate calculation) and the STAN 5 fully laminar falls substantially below the data. With the exception of the pressure loadings and the geometry, the code inputs used for these predictions were identical to those previously used to predict the Garrett TFE 731-2 HP turbine and the Garrett LART HP turbine.

Introduction

The results described in this paper represent the initial step in an investigation designed to determine the interaction between the vane and the blade and to test the utility of predictive codes against the data that are obtained. The overall program is structured so that time-averaged, time-resolved, and phase-averaged data have been obtained. However, this paper will be confined to a discussion of the time-averaged results and their comparison with predictions. The turbine stage has been constructed so that the spacing between the vane and rotor can be set at any desired value. The data reported here were all obtained for a spacing of approximately 19 percent of vane axial chord. Measurements are currently ongoing for a spacing on the order of 50 percent.

The turbine stage tested is that of the Teledyne J402-CA-702 turbojet engine. The turbine stage of this engine is a highly loaded, moderately high reaction, state-of-the-art design. The corrected speed is 19,510 rpm, corrected weight flow is 3.92 lb/sec and the overall total-to-total pressure ratio is 3.62.

There are 23 vanes that are convectively cooled with a pressure-side trailing edge discharge. There are 35 blades that are uncooled and are highly tapered, highly cambered, and have elliptical leading edges. This turbine was ideal for the research reported here because it is a state-of-the-art turbine stage.

The experimental technique utilizes the short-duration shock-tunnel approach for which a shock tube is used to generate a short-duration source of heated and pressurized air which is eventually directed into the turbine stage. Fast-response, thin-film thermometers are used to measure the surface temperature histories at prescribed positions on the vane or blade. Heat-flux values are then calculated from these temperature histories in a manner previously described [1, 2]. With this experimental technique, one can simultaneously duplicate the turbine design point flow function, the corrected speed, the stage pressure ratio (static and total), the stage total temperature ratio, and the wall-to-total-temperature ratio. The design point duplication was verified for this measurement program by measuring: (a) the rotor speed, (b) the total pressure in the flow stream entering the nozzle guide vane, (c) the total pressure in the flow stream exiting the rotor, (d) the surface pressure upstream of the NGV and downstream of the rotor, and (e) the total temperature in the flow stream ahead

Contributed by the Gas Turbine Division of THE AMERICAN SOCIETY OF MECHANICAL ENGINEERS and presented at the 32nd International Gas Turbine Conference and Exhibit, Anaheim, California, May 31-June 4, 1987. Manuscript received at ASME Headquarters February 10, 1987. Paper No. 87-GT-120.

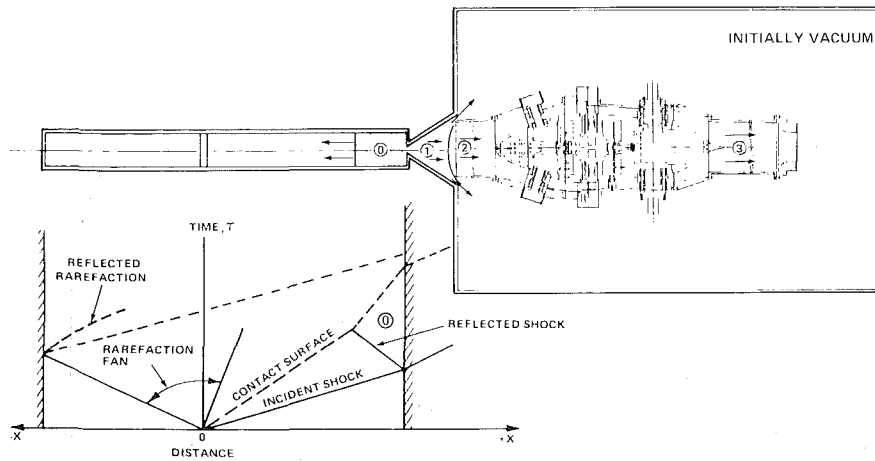


Fig. 1 Schematic of experimental apparatus and wave diagram

of the NGV and downstream of the rotor. The operating point was established using a trial and error procedure, which involved changing the flow control nozzle to be described later.

The balance of the paper provides a brief summary of the experimental apparatus, the experimental condition, a discussion of the experimental results, and a comparison of these results with predictive techniques.

Experimental Apparatus

The experimental apparatus, sketched in Fig. 1, consists of a 0.20-m (8-in.) i.d. helium-driven shock tube with a 12.2-m (40-ft) long driver tube and a 15.2-m (50-ft) long driven tube, as a short-duration source of heated air, supplying the test section device located near the exit of the primary shock-tunnel nozzle. The receiver tank is initially evacuated to a pressure of approximately 1 torr in order to minimize the initial resistance of the turbine wheel and to improve the flow establishment characteristics of the model. The test section device housing the turbine stage consists of a forward transition section with a circular opening facing the supersonic primary nozzle flow. This transition section is followed by a 360 deg annular passage containing the NGV row, the rotor, and an exit passage. A contoured nozzle is located at the end of the exit passage and is used to establish the pressure and temperature ratio across the turbine stage. Several iterations on this nozzle area were required before the desired stage pressure and temperature ratios were achieved. The forward bullet nose houses a 100-channel slip ring unit and the aft bullet nose houses an air-driven motor that is used to accelerate the turbine from rest to the desired speed just prior to initiation of the experiment and prior to the arrival of the test-gas flow.

The heat-flux gage instrumentation used in this program consisted of button-type gages on the vane and a combination of button-type and contoured-insert type on the blade as described in [3]. The heat-flux instrumentation was concentrated on the meanline, but a few selected measurements were obtained at other blade locations, as will be illustrated. Figure

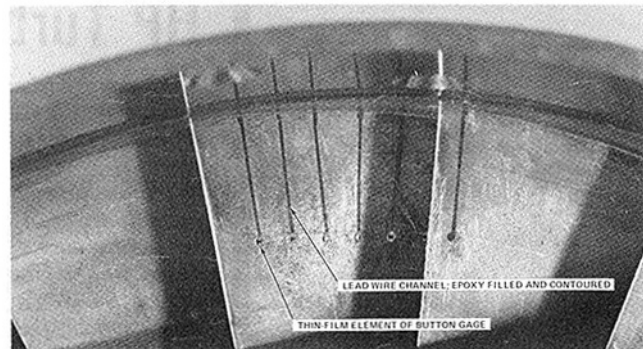


Fig. 2 Photograph of vane suction surface instrumentation

2 is a photograph of the vane suction surface heat-flux instrumentation. The vanes were hollow and discrete hole injection was to be used at a later date. Therefore, in order to perform heat-flux measurements on the vanes, it was necessary to install the heat-flux gage within the vane wall and to route the lead wires in channels burned into the vane surface. These channels were then filled with epoxy and polished smooth with the surface as illustrated on Fig. 2. The orientation of the thin film heat-flux elements (0.004 in. wide by 0.020 in. long) was with the length normal to the axial direction. On both the suction and pressure surfaces, the button gages were placed on the order of 0.150 in. to 0.200 in. apart. A leading edge insert was not used on the vane.

Figures 3 and 4 are photographs of the button-type gage instrumentation on the blade suction and pressure surfaces, respectively. For each of these surfaces, the gage nearest the leading edge coincides with a particular location on one of the leading edge inserts to be described below. At about midchord and at about 90 percent chord, additional gages were placed at about 40 and 60 percent span, thus providing two locations on each blade surface for which data were obtained at 50 ± 10 percent span.

Nomenclature

<p>Flow function = $\dot{W}\sqrt{\theta}/\delta$</p> <p>$H_0$ = total enthalpy</p> <p>$H_w(T)$ = wall enthalpy</p> <p>N_{corr} = corrected rotor speed = $N_{phy}/\sqrt{\theta}$</p> <p>N_{phy} = physical rotor speed</p> <p>$\dot{q}(T)$ = heat flux corrected for</p>	<p>A = NGV inlet area</p> <p>$\dot{q}(T_w)$ = cold-wall heat flux</p> <p>S = distance measured along surface</p> <p>S_T = distance measured along surface from leading edge to trailing edge</p> <p>St = Stanton number</p>	<p>variable thermal properties of the Pyrex substrate</p> <p>T_w = initial wall temperature</p> <p>T = local temperature of thin-film gage evaluated as a function of time</p> <p>T_0 = total temperature</p> <p>\dot{W} = weight flow through turbine</p> <p>$\delta = P_{t,in}/14,696$</p> <p>$\theta = T_0/518R$</p>
---	---	---

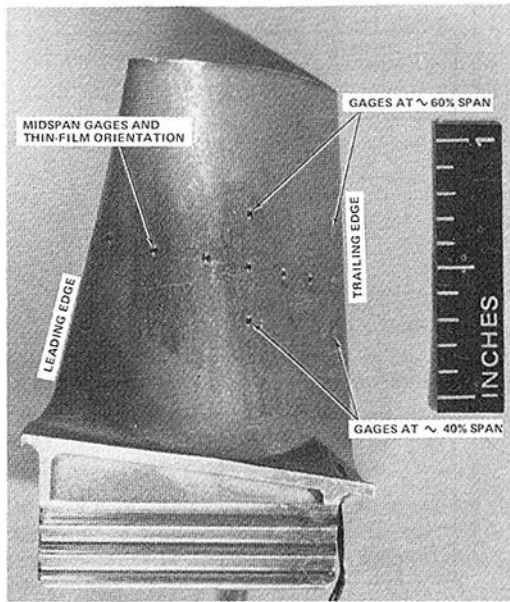


Fig. 3 Photograph of blade suction surface button gages

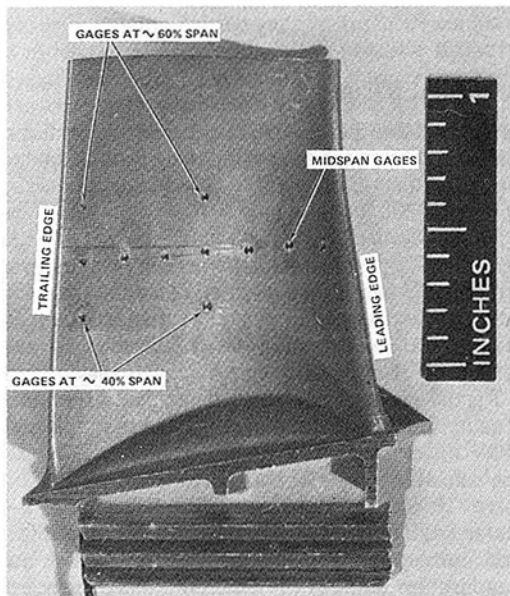


Fig. 4 Photograph of blade pressure surface button gages

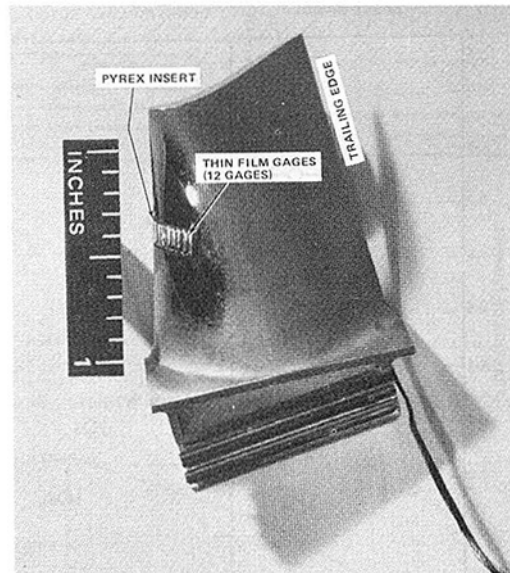


Fig. 5 Photograph of blade suction surface leading edge insert

Table 1 Test conditions and parameters

Reflected-shock Pressure	7.43×10^3 kPa	1078 psia
Reflected-shock Temperature	561 °K	1010 °R
NGV Inlet Total Temperature	561 °K	1010 °R
NGV Inlet Total Pressure	6.67×10^2 kPa	96.75 psia
NGV Inlet Static Pressure	6.60×10^2 kPa	95.73 psia
Area on which Stanton Number is based	2.42×10^{-2} m ²	0.26 ft ²
Approximate Weight Flow Rate	8.61 kg/s	18.95 #/s
Physical Rotor Speed	27,000 rpm	
Wall Temperature	294 °K	530 °R
Rotor Exit Total Pressure	2.15×10^2 kPa	31.24 psia
Rotor Exit Static Pressure	1.60×10^2 kPa	23.19 psia
Assumed Free Stream Turbulence, NGV		5%
Assumed Free Stream Turbulence, Blade		5%

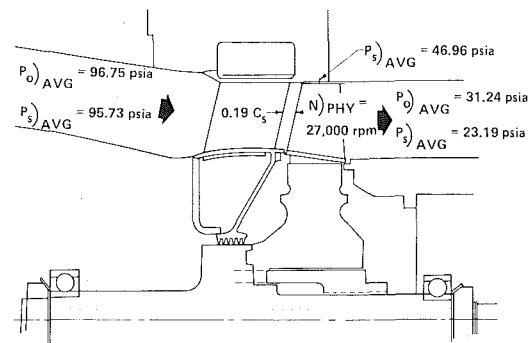


Fig. 6 Sketch of stage configuration and time-averaged pressures

Figure 5 is a photograph of one of the two blade leading edge inserts. The gage distribution on the inserts was selected so that one insert provided a dense pack on one surface (a spacing on the order of 1.0 mm or 0.040 in.) and a wider spacing on the other surface. The second insert will have the dense-pack side on the opposite surface of the first insert. Each of these inserts was contoured to the blade leading edge profile prior to painting the thin-film gages. As can be seen from the photograph, the blade surface in the immediate vicinity of the insert is also polished by this process. The particular insert shown in Fig. 5 contains one gage at the geometric stagnation point, eight gages on the suction surface, and three on the pressure surface.

Experimental Conditions

Table 1 gives the experimental conditions and measured parameters for the results presented here. The results presented in this table represent the average of the values ob-

tained for many separate experimental runs. Figure 6 is a sketch of the stage configuration illustrating several of the measured parameters of interest.

The total pressure and total temperature profile across the flow channel (hub to tip) were measured upstream of the NGV entrance and just downstream of the rotor exit. These profiles were obtained at a single circumferential location in the channel. These measurements were taken in order to determine the approximate operating condition. They were not taken with the intent to determine turbine efficiency. The upstream probes were aligned with the turbine axis while the exit probes were located 15 deg off axis at the predicted average flow exit angle.

The rotor exit flow angle changes from hub to tip, but no attempt was made to align the probes with the flow angle across the channel. The probe used to obtain these temperature

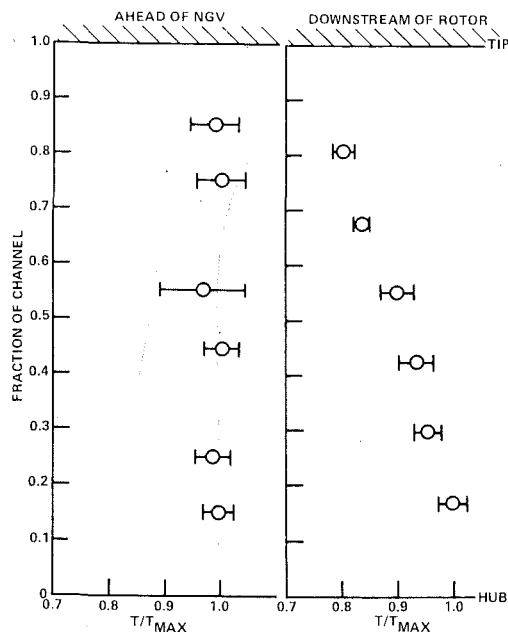


Fig. 7 Total temperature measurement upstream and downstream of stage

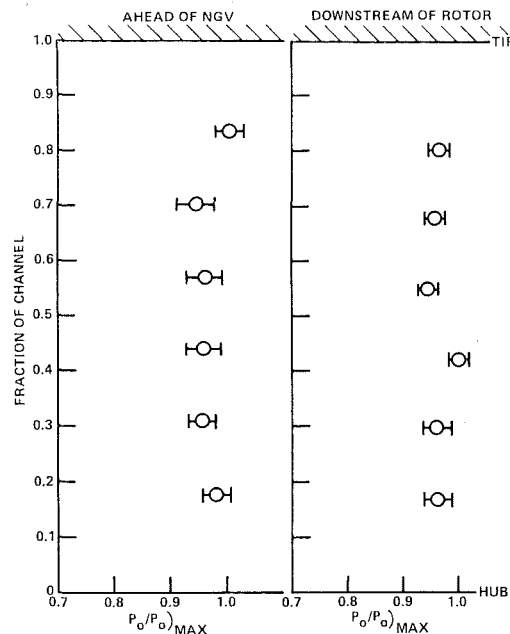


Fig. 8 Total pressure measurements upstream and downstream of stage

values consists of a 0.001-in.-dia chromel-alumel butt-welded thermocouple housed in a 0.050-in.-dia sheath as described in [3]. The pressure measurements were obtained using a 0.060-in.-dia hypodermic tubing approximately 1 in. long and beveled at the inlet leading to piezoelectric pressure transducer. The bevel angle was designed to provide flow angle insensitivity up to ± 10 deg. Both near the tip and near the hub the allowable 10 deg of flow variation was exceeded. The pressure rake was calibrated when completely assembled by subjecting each probe to several different, but known, pressures. Figures 7 and 8 are plots of the total temperature measurements across the flow channel upstream of the NGV and downstream of the rotor. The temperatures have been normalized by the maximum temperature recorded at the particular rake location.

Figure 7 illustrates the total temperature distribution across the entrance and exit flow channel from hub to tip. Six measurements were obtained across the channel which measured approximately 1.5-in. The circle represents the average value and the bars the standard deviation. Ahead of the NGV inlet the total temperature profile is relatively flat and nearly equal to 1.0. Downstream of the rotor, the temperature was highest near the hub and continually decreased as the tip was approached. This exit temperature profile reflects work extraction, the influence of boundary layer and tip vortex interactions, and/or possible flow separation on the suction side near the hub.

Figure 8 is a corresponding plot of the total pressure profile across the flow channel obtained upstream of the NGV entrance and downstream of the rotor. Once again, the circle represents the average value and the bar the standard deviation. The upstream rake was aligned with the model axis. The resulting pressure profile is relatively uniform with the maximum values occurring at the outermost probe locations. The downstream rake was again set for an exit swirl angle of 15 deg, which is consistent with the anticipated value near midspan. The downstream profile was also relatively uniform with the maximum value occurring near midspan. The average value of total pressure ahead of the NGV divided by the average value of total pressure downstream of the rotor was used to set the operating point. As noted above, this pressure ratio could be changed by altering the exit nozzle area.

Experimental Results

The Stanton number used here is based on conditions at the NGV inlet and was evaluated using the relationship

$$St_{inlet} = \frac{\dot{q}(T)}{(\dot{W}/A)(H_0 - H_w(T))} \quad (1)$$

In equation (1), H_0 is the real gas enthalpy determined from [4], $\dot{q}(T)$ is the heat flux evaluated for each gage accounting for the variable thermal properties of the substrate, $H_w(T)$ is the real-gas wall enthalpy evaluated for each gage at the wall temperature corresponding to $\dot{q}(T)$, \dot{W} is the turbine weight flow, T is the gage temperature evaluated as a function of time at the sampling frequency, and A is the cross-sectional area at the NGV inlet. The Stanton number defined in equation (1) can be shown to be equivalent to the cold-wall Stanton number. Thus, the cold-wall heat flux $\dot{q}(T_w)$ can be calculated from the results presented herein by multiplying the Stanton number by $(\dot{W}/A)(H_0 - H_w(T_w))$. The mean and the standard deviation of the Stanton number have been computed for each heat-flux gage using the expression

$$St_{mean} = \frac{1}{N} \sum_{i=1}^n (St)_i \quad (2)$$

$$St_{standard\ deviation} = \left[\frac{1}{N} \sum_{i=1}^n (St_i - St_{mean})^2 \right]^{0.5} \quad (3)$$

On all the data plots presented here, the symbol will represent the mean value of the Stanton number given by equation (2) and the bar will represent \pm one standard deviation as given by equation (3). If the bar does not appear along with the symbol, then the standard deviation falls within the symbol unless otherwise noted.

NGV Measurements and Predictions

Figures 9 and 10 present the measured Stanton number distributions for the vane and blade, respectively. The turbine aspect ratio is about one and the vane leading edge radius of curvature is on the order of 0.14 in. The rotor diameter is on

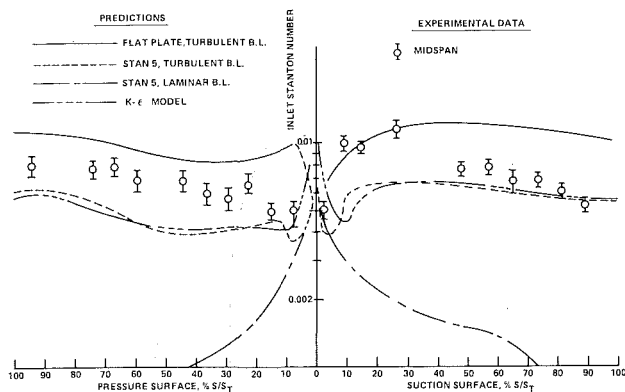


Fig. 9 Stanton number distribution for Teledyne 702 NGV midspan

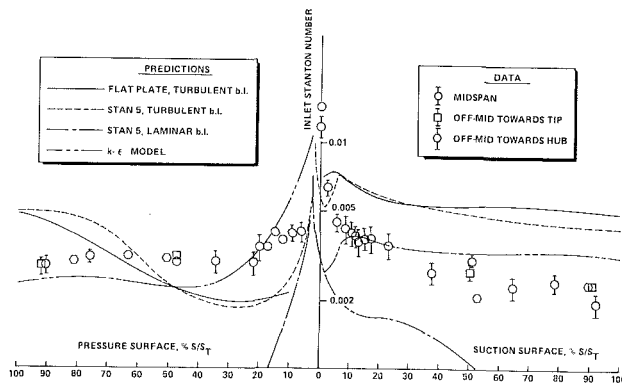


Fig. 10 Stanton number distribution for Teledyne 702 blade

the order of 9.6 in., the blade leading edge can be approximated by a minor ellipse with a minor diameter of 0.08 in., and the tip clearance at 27,000 rpm was approximately 0.015 in.

The vane did not have a leading edge insert so the measurement nearest the geometric stagnation point was at about 2.5 percent wetted distance on the suction side. The value at the first measuring station on the suction surface was about the same as measured at 8 percent on the pressure surface. By 9 percent wetted distance, the suction surface Stanton number has increased by a factor of two. The region between 2.5 and 9 percent wetted distance corresponds to a decreasing surface pressure region in Fig. 11. Between 9 percent and the peak Stanton number at 27 percent, the local pressure continued to decrease finally reaching a minimum at 80 percent wetted distance. The pressure side pressure distribution is relatively flat between 8 and 40 percent, then decreases rapidly to reach the trailing edge value. The pressure surface Stanton number peaks at about 65 percent wetted distance and remains near that value for the balance of the surface.

The stage Stanton number predictions described here were performed using the pressure loading given in Fig. 11. These results were calculated using a series of aerodynamic computer codes. First, the velocity triangles were determined using the Flagg code [5] where throat areas, efficiencies, and overall total-to-total pressure ratio are specified based on turbine design and measured performance data. Pressure loading was calculated for the airfoils near the stagnation point using the PANEL code [6] and away from the stagnation point using the three-dimensional Denton code [7]. The data were faired in by hand between the two solutions. The Denton code employed in these calculations is a new version where flow rate can be input and a reasonable match with the velocity triangles from the Flagg code was achieved.

The calculated pressure loading data for both the vane and blade are shown in Fig. 11. The upper portion of this figure is the vane surface pressure normalized by the absolute total pressure at the vane inlet as a function of wetted distance. The lower portion of Fig. 11 is the blade surface pressure normalized by the blade relative total pressure as a function of wetted distance. Experimentally determined surface pressure measurements are not available for comparison with these predictions. However, miniature Kulite wafer pressure gages are currently being installed in the blades and data will be available in the near future.

The vane heat-flux calculations utilized the absolute total pressure, the known geometry, and the pressure distributions given in Fig. 11. The blade heat-flux calculations utilized the relative total pressure, the known geometry, and the pressure distribution given in Fig. 11. The specific techniques used were the standard flat plate, a modified version of STAN

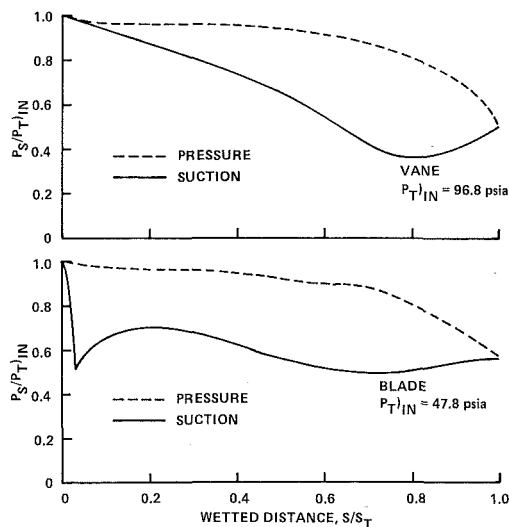


Fig. 11 Surface pressure distribution for vane and blade relative to inlet total pressure

5 [8], and version of the kinetic-energy-dissipation ($k-\epsilon$) model [9] of the turbulence. The version of STAN 5 used in these calculations is a modification of that due to Gaugler [9]. One of these modifications allowed the initial conditions to be given by the solution for a compressible laminar boundary layer on the stagnation line of a cylinder. The STAN 5 calculation does not account for the influence of free-stream turbulence. It is desirable that in the model the location of transition be dependent on the free-stream turbulence level. In principle, the two-equation model of turbulence can accommodate these effects. Free-stream turbulence is incorporated in the two-equation model as a boundary condition at the boundary layer edge and a low Reynolds number model simulates transition which is sensitive to the free-stream turbulence level. The particular $k-\epsilon$ model used to obtain the predictions described here is discussed in [8]. Results obtained using these predictive techniques for two other (Garrett TFE 731-2 and Garrett LART) turbines were previously [8] reported. The only changes made to the code input parameters to obtain the predictions reported here were the pressure loadings and the Teledyne turbine geometry. The assumed turbulence intensity for the $k-\epsilon$ calculation at the inlet to the vane and also to the blade row was 5 percent.

The NGV predictions are presented in Fig. 9 and are compared with the experimental data. The turbulent boundary layer flat-plate prediction generally overpredicts the data with the exception of the initial portion of the suction surface. The STAN 5 and the $k-\epsilon$ results are consistent with each other on both the pressure and suction surfaces. For the early portion

of the suction surface (up to 30 percent wetted distance) these predictions are significantly below the data. However, beyond 30 percent, the agreement is reasonably good, being within 10 to 15 percent of the data. The laminar boundary-layer prediction is reasonably close to the data up to about 3 percent wetted distance, but then falls off very rapidly and is far below the data. It appears that there may have been a short period of laminar flow on the suction surface, but transition occurred prior to 9 percent of wetted distance. The rapid increase in heat transfer on the suction surface is transition related and not due to local separation because the vane leading edge is relatively blunt and the inlet Mach number is sufficiently low that separation is unlikely.

On the pressure surface of the vane, the general shape of the STAN 5 and $k-\epsilon$ predictions is consistent with the data, but the values are about 35 percent low. On the other hand, the turbulent flat-plate prediction is on the order of 25 percent higher than the data. The laminar boundary-layer prediction quickly falls far below the data suggesting that the pressure surface boundary layer was turbulent.

Figure 10 presents the Stanton number distributions for the blade and a comparison with turbulent flat plate, STAN 5, and $k-\epsilon$ predictions. The pressure distributions used to perform these calculations are given in Fig. 11. Note that on the suction surface the calculated pressure decreases very rapidly up to about 3 percent wetted distance, then rises reaching a maximum of 0.71 at 20 percent wetted distance followed by a minimum of 0.50 at 70 percent wetted distance. Beyond 70 percent, the ratio increases to nearly the pressure surface value at the trailing edge. On the pressure surface, the pressure decreases slowly to 70 percent wetted distance then decreases rapidly reaching a minimum at the trailing edge.

The blade pressure data in Fig. 11 are plotted relative to the calculated stagnation point from the PANEL code. The stagnation point was 0.12 cm (0.049 in.) around on the pressure side from the geometric stagnation point. This positive incidence on the blade leading edge satisfies the assumed flow conditions but led to an apparent flow separation at 3 percent wetted distance on the suction side.

The calculated heat transfer data for the blade, as shown in Fig. 10, reach a peak at about 3 percent from the geometric stagnation point on the pressure side because the calculated stagnation point is located there. It is not known where the maximum measured heat transfer occurs because the first two heat flux gages on the pressure side insert were lost. This was not a concern for the vane because the calculated stagnation point was close to the geometric stagnation point. The STAN 5 calculation was performed for the blade assuming a fully turbulent boundary layer and a fully laminar boundary layer. On the suction surface, the turbulent STAN 5 significantly overpredicts the data beyond 5 percent wetted distance and the laminar prediction is well below the data beyond 2 percent wetted distance. At about 6 percent on the suction surface, the STAN 5 calculation wanted to separate. However, the experimental data show no indication of a separated region. This would indicate that the calculated pressure loading data are incorrect in this region and the blade incidence is not as positive as calculated. Planned blade surface pressure measurements should resolve this discrepancy. The turbulent flat-plate technique gives results that are essentially in agreement with the STAN 5 prediction. The $k-\epsilon$ prediction is a reasonable approximation to the data, being generally within 20 percent. On the pressure surface both the turbulent STAN 5 and the $k-\epsilon$ prediction are near the data with the $k-\epsilon$ being a closer prediction in both shape and magnitude than the STAN 5 turbulent. Once again, the turbulent flat-plate prediction is in essential agreement with the fully turbulent STAN 5. The STAN 5 laminar boundary layer prediction fell far below the data on the pressure surface.

Also presented on Fig. 10 are the blade data obtained at 40 and 60 percent of span. These measurements were obtained only at wetted distances of 50 and 90 percent. The pressure surface off-midspan data were generally in agreement with the midspan suggesting that the heat flux was relatively uniform over that surface between 40 and 60 percent span. However, the data point on the suction surface at about 50 percent wetted distance indicates that there may have been some local separation on the suction surface near the hub as suggested earlier during the discussion of the rotor exit total temperature profile.

The general characteristics of the agreement described here for the Teledyne turbine are consistent with those reported in [8] for the Garrett TFE-731 HP turbine vane and blade and the Garrett LART rotor blade [8, 10]. The LART vane comparison was not good, which was very different from the agreement found both here and for the TFE-731 vane.

Conclusions

Detailed measurements of local heat flux on the Teledyne 702 HP vane and blade have been obtained at known flow conditions. A comparison has been presented between the experimental results and STAN 5 and $k-\epsilon$ predictions. It is demonstrated that the same STAN 5 and $k-\epsilon$ formulation used to predict the Garrett TFE 731-2 HP and the LART heat-flux distributions performed reasonably well for the Teledyne turbine stage.

Acknowledgments

The authors would like to thank Prof. Bill Rae, Prof. Dale Taulbee, David Rigby, and Le Tran of CUBRC for generating the STAN 5 and $k-\epsilon$ predictions. We would also like to thank Lev Ginzburgsky, Bob Gray, Susan Hyde, and Chris Twardochleb of Teledyne CAE for generating the vane and blade pressure distributions and for helping with setting the experimental conditions. The research described in this paper was supported by Teledyne CAE Independent Research and Development funds.

References

- 1 Dunn, M. G., "Heat-Flux Measurements for the Rotor of a Full-Stage Turbine: Part I—Time-Averaged Results," *ASME JOURNAL OF TURBOMACHINERY*, Vol. 108, 1986, pp. 90-97.
- 2 Dunn, M. G., George, W. K., Rae, W. J., Woodward, S. H., Moller, J. C., and Seymour, P. S., "Heat-Flux Measurements for the Rotor of a Full-Stage Turbine: Part II—Description of Analysis Technique and Typical Time-Resolved Measurements," *ASME JOURNAL OF TURBOMACHINERY*, Vol. 108, 1986, pp. 98-107.
- 3 Dunn, M. G., Lukis, G., Uros, M., Hiemenz, R. J., Orszulik, R. L., and Kay, N. J., "Instrumentation for Gas Turbine Research in Short-Duration Facilities," *Aerospace Congress and Exposition (SAE)*, Long Beach, CA, Oct. 15-18, 1984, Paper No. 841504.
- 4 *Handbook of Supersonic Aerodynamics*, NAVORD Report 1488, Vol. 5, 1953.
- 5 Flagg, E. E., "Analytical Procedure and Computer Program for Determining the Off-Design Performance of Axial Flow Turbines," NASA CR-710, 1966.
- 6 McFarland, E. R., "Solution of Plane Cascade Flow Using Improved Surface Singularity Methods," *ASME Journal of Engineering for Power*, Vol. 104, 1982, pp. 668-674.
- 7 Denton, J. D., and Singh, U. K., "Time Marching Methods for Turbomachinery Flow Calculations. Part I—Basic Principles and 20 Applications and 11 Three Dimensional Flows," *Application of Numerical Methods to Flow Calculations in Turbomachinery*, VKI Lecture Series 1979-7, 1979.
- 8 Rae, W. J., Taulbee, D. B., Civinskis, K. B., and Dunn, M. G., "Turbine-Stage Heat Transfer: Comparison of Short-Duration Measurements With State-of-the-Art Predictions," *AIAA Paper No. 86-1465*, 1986.
- 9 Gaugler, R. E., "Some Modifications to, and Operating Experience With, the Two-Dimensional Finite-Difference, Boundary-Layer Code, STAN 5," *ASME Paper No. 81-GT-89*, 1981.
- 10 Dunn, M. G., Martin, H. L., and Stanek, M. J., "Heat Flux and Pressure Measurements and Comparison With Prediction for a Low Aspect Ratio Turbine Stage," *ASME JOURNAL OF TURBOMACHINERY*, Vol. 108, 1986, pp. 108-115.

Film Cooling and Heat Transfer in Nozzles

J. Stoll

J. Straub

Lehrstuhl A für Thermodynamik,
Technische Universität München,
Munich, Federal Republic of Germany

In this paper experimental and theoretical investigations on heat transfer and cooling film stability in a convergent-divergent nozzle are presented. Compressed air is injected into hot air in the inlet region of the nozzle and the influence of the strong favorable pressure gradient in the nozzle on turbulent heat transfer and mixing is examined. The experiments cover measurements of wall pressures, wall temperature, and wall heat flux. Calculations with parabolic finite difference boundary layer code have been performed using a well-known $k-\epsilon$ -turbulence model with an extension paying regard to acceleration. As a result the calculated wall heat flux is compared with the measured heat flux.

Introduction

Some authors have already worked on heat transfer in nozzles (e.g., Back et al., 1964, 1970, 1972; Boldmar et al., 1967, 1972; Winkler and Grigull, 1977; Bauer et al., 1977, 1978) and an increasing number of investigations has been undertaken on heat transfer in accelerated compressible flow (e.g., Kays et al., 1970; Blair, 1982; Wang et al., 1985; Rued and Wittig, 1985).

Much fundamental research has been done considering the injection geometry and the stability of cooling films. Many publications have dealt with the comparison of adiabatic and isothermic wall experiments trying to generalize the results using scaling laws (Jones and Forth, 1986) and trying to generalize the results using dimensionless variables based on recovery temperatures (Ligrani and Camci, 1985) and giving density ratio and variable property corrections in the case of compressible flow.

Only a few authors have examined the influence of mainstream pressure gradients on heat transfer to film-cooled surfaces (Hay et al., 1985). Heat transfer to a film-cooled nozzle wall is as much influenced by the strong favorable pressure gradient as by large density ratio. Furthermore the recovery temperature of both the hot gas and the coolant are submitted to substantial changes in the streamwise direction. Therefore a presentation of our test results in nondimensional form would not allow for generalization.

In order to generalize results, it is important to test and improve existing computer codes in comparison with experimental data. The work on comparison of finite difference codes for prediction of heat transfer to film-cooled surfaces (Crawford, 1986) is still continuing. In the present investigation we compare calculations with a low Reynolds number $k-\epsilon$ model (Lam and Bremhorst, 1981) modified for accelerated flows to our experiments.

Experiments

Experimental Setup. The experimental investigations have been performed in the wind tunnel of our institute. Compressed air is used both as hot medium and as coolant. The hot air is compressed in a two-stage radial compressor to a maximum stagnation pressure of 0.28 MPa and a maximum stagnation temperature of 485 K. The hot air passes a mixer, a straightener, and a transition pipe, where the cross section is changed from a round to a rectangular one of nearly the same area before it enters the test section with 2.8 kg/s maximum mass flow rate.

The cooling air is compressed in a smaller two-stage compressor with intermediate heat exchanger. It enters the test section with a stagnation temperature of approximately 305 K and a maximum mass flow rate of 0.25 kg/s. The whole apparatus is driven in steady state.

Test Section. The test section is an asymmetric rectangular water-cooled CD nozzle (Fig. 1), which is designed for a normal shock at its exit in the maximum loading case of the compressor allowing a maximum outlet Mach number of 2.25. The geometry of the rectangular test section in the x, y plane is shown in Fig. 1. The depth normal to Fig. 1 is 99 mm (Fig. 3) avoiding serious three-dimensional effects. The rectangular 30 deg-15 deg semiangle convergent-divergent nozzle is constructed with a plane and a contoured wall. Thus it is possible to examine the influence of the favorable pressure gradient in the absence of effects of wall curvature.

The nozzle was built up with 35 separately water-cooled segments (Fig. 3) of copper on each of the two side walls to allow very accurate measurements of the heat flux from the air to the nozzle walls. By adjusting the cooling water flow rate for each segment it is possible to establish a defined thermal boundary condition. The segments are well insulated from each other by air and a thin stainless steel tube at the nozzle surface. The gas side nozzle walls have been chrome plated in order to avoid oxidation and to reduce thermal radiation. The average surface roughness has been determined as $7.3 \pm 1.3 \mu\text{m}$.

The mass flux ratio in the case of the film cooling experiments is defined by varying the hot air mass flow and the

Contributed by the Gas Turbine Division of THE AMERICAN SOCIETY OF MECHANICAL ENGINEERS and presented at the 32nd International Gas Turbine Conference and Exhibit, Anaheim, California, May 31-June 4, 1987. Manuscript received at ASME Headquarters February 10, 1987. Paper No. 87-GT-117.

cooling air mass flow for different slot heights for the cooling film. The inlet region of the nozzle with inlet geometry is shown in Fig. 2.

Measurement Techniques. The experimental investigation covers measurements of wall temperature, wall heat flux, wall pressures, stagnation pressure and temperature and measurements of the mass flow rates. Wall temperature and wall heat flux were measured with the heat flux meters as shown in Fig. 2 using two thermocouples installed in the copper segments. Under steady-state conditions the wall heat flux and the wall temperature are calculated from the one-dimensional heat conduction equation. Two-dimensional finite element calculations for the copper segments have proved the high accuracy of this simple method. The thermocouples are connected to a scanner and a digital voltmeter.

The wall pressures are taken from the small steel tubes between the copper segments and transferred to a Scanivalve pressure scanning system. Total pressures and total temperatures are taken from combined probes.

The mass flow rate of the hot air is calculated from one-dimensional gas dynamics relations in the absence of a cooling film. The mass flow rate of the cold air is measured with a standard orifice. The inlet velocities are calculated from the inlet geometry (Figs. 2 and 3). An HP 1000 Minicomputer was used to acquire the data from the pressure scanning system and the digital voltmeter during the test run, allowing immediate evaluation of the mass flow rates and the distribution of pressure, wall temperature, and wall heat flux. By using the computer for continuously evaluating the wall temperature and the wall heat flux during scanning, it was possible to establish isothermal wall conditions by manually adjusting the cooling water control in an acceptable time.

Calculations

Mean Flow Equations. The mean flow equations have

been derived from the conservation equations using Favre mass-averaged decomposition, thus keeping the correlation terms arising from density fluctuations to a minimum and maintaining almost the same forms as the equations written for incompressible flows (Favre, 1965, 1975; Vandrome and Minh, 1984). Additional density fluctuation correlations remain unmodeled in this presentation; they are omitted right from the very beginning. The equations are given in general coordinates for stationary conditions. The mathematical notations for operators and operations in general coordinates is defined in (Klingbeil, 1966).

Continuity equation

$$\text{div}(\bar{\rho}\bar{\mathbf{w}}) = 0 \quad (1)$$

Momentum equations

$$\text{Div}(\bar{\rho}\bar{\mathbf{w}}\bar{\mathbf{w}}) = -\text{grad}\bar{p} + \text{Div}\bar{\boldsymbol{\tau}} + \text{Div}(-\bar{\rho}\bar{\mathbf{w}}''\bar{\mathbf{w}}'') \quad (2)$$

Total enthalpy equation

$$\text{div}(\bar{\rho}\bar{\mathbf{w}}\bar{H}) = \text{div}(\lambda\text{grad}\bar{T}) + \text{div}(\bar{\boldsymbol{\tau}}\cdot\bar{\mathbf{w}}) + \text{div}(-\bar{\rho}\bar{\mathbf{w}}''\bar{H}'') \quad (3)$$

$$\bar{H} = \bar{h} + \frac{\bar{\mathbf{w}}\cdot\bar{\mathbf{w}}}{2} + \frac{\bar{\mathbf{w}}''\cdot\bar{\mathbf{w}}''}{2} = \bar{h} + \frac{\bar{\mathbf{w}}\cdot\bar{\mathbf{w}}}{2} + k \quad (4)$$

$$H'' = h'' + \bar{\mathbf{w}}\cdot\mathbf{w}'' + \frac{\mathbf{w}''\cdot\mathbf{w}''}{2} - \frac{\bar{\mathbf{w}}''\cdot\bar{\mathbf{w}}''}{2} \quad (5)$$

Assuming an ideal gas, the connection between the variables is given by the ideal gas law

$$\bar{p} = \bar{\rho}\bar{R}\bar{T} \quad (6)$$

and the equation of state for the enthalpy

$$d\bar{h} = c_p d\bar{T} \quad (7)$$

Turbulent Transport. Neglecting turbulent diffusive

Nomenclature

c_p	= specific heat at constant pressure
C_μ, C_1, C_2, C_3	= turbulence model constants
f_μ, f_1, f_2, f_3	= turbulence model wall functions
f	= wall function = $\min(R_t/3.72 R_k, 1.)$
H	= total enthalpy
h	= specific enthalpy
\mathbf{I}	= unity tensor
k	= turbulent kinetic energy
K	= acceleration
	parameter = $-(\mu/\rho^2 u_\infty^2)(\partial p/\partial x)$
l	= turbulent mixing length
\dot{m}	= mass flow
p	= pressure
Pr_t	= turbulent Prandtl number = $\mu_t c_p / \lambda_t$
R	= gas constant
Re_k	= turbulence Reynolds number = $k^2 \rho / \epsilon \mu$
Re_t	= turbulence Reynolds number = $\sqrt{k} y \rho / \mu$
Re_l	= turbulence Reynolds number = $\sqrt{k} l \rho / \mu$
s	= slot height
T	= temperature
u	= mean velocity in streamwise direction
u_τ	= friction velocity = $(\mu_w / \rho_w)(\partial u / \partial y)$
u'', v'', w''	= fluctuating velocities in x, y, z directions
\mathbf{w}	= velocity vector in general coordinates
x, y, z	= quasi-orthogonal streamwise coordinates
x	= streamwise direction; distance from slot
y	= cross-stream coordinate; distance from wall

z	= coordinate parallel to the wall
x_t	= distance from turbulence grid
Δy	= stream tube width
Δx^+	= dimensionless streamwise step = $\Delta x u_\tau (\rho_w / \mu_w)$
y^+	= dimensionless wall distance = $y u_\tau (\rho_w / \mu_w)$
δ	= boundary layer thickness
ϵ	= turbulent dissipation rate = $(1/\bar{\rho}) \boldsymbol{\tau}'' : \text{Grad } \mathbf{w}''$
λ	= thermal conductivity
μ	= dynamic viscosity
ν	= kinematic viscosity = μ/ρ
ρ	= density
σ_ϵ	= turbulent diffusion Prandtl number for turbulent dissipation rate
τ	= shear stress
$\boldsymbol{\tau}$	= stress tensor
	= $\mu \{ \text{Grad } \mathbf{w} + (\text{Grad } \mathbf{w})^T - (2/3) \text{div}(\mathbf{w})\mathbf{I} \}$

Subscripts and Superscripts

$\bar{\quad}$	= denotes time-averaged value
\sim	= denotes mass-averaged mean value
$''$	= denotes fluctuating part of variable
0	= denotes stagnation condition
c	= coolant
w	= wall
∞	= free stream
r	= recovery condition
t	= turbulent

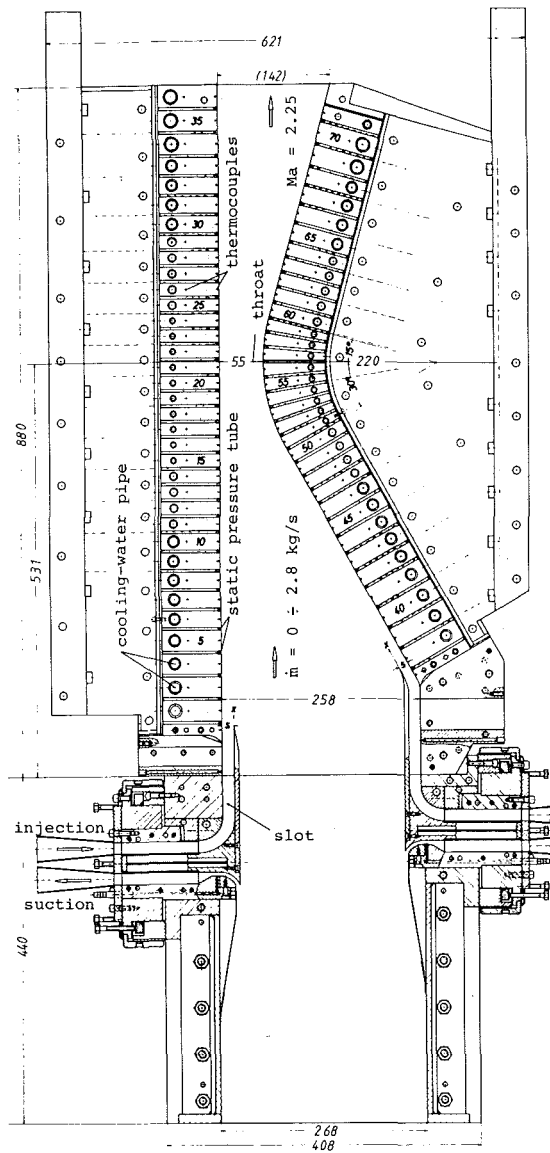


Fig. 1 Test section

transport in the streamwise direction, the reduced boundary layer equations contain only two important terms: $-\rho \overline{u''v''}$ and $-\rho \overline{v''H''}$. The turbulent stress $-\rho \overline{u''v''}$ in the momentum equation and the turbulent total enthalpy flux $-\rho \overline{v''H''}$ in the total enthalpy equation are modeled using the eddy viscosity concept

$$-\rho \overline{u''v''} = \mu_t \frac{\partial u}{\partial y} \quad (8)$$

and after rearranging

$$-\rho \overline{v''H''} = -\rho \overline{v''h''} - \overline{u''\rho''v''} - \rho \overline{v''k''} \quad (9)$$

The eddy diffusivity concept for the turbulent heat flux is

$$-\rho \overline{v''h''} = \lambda_t \frac{\partial \overline{T}}{\partial y} = \frac{\lambda_t}{c_p} \frac{\partial \overline{h}}{\partial y} \quad (10)$$

and for the flux of turbulent kinetic energy it is

$$-\rho \overline{v''k''} = \mu_t \frac{\partial k}{\partial y} \quad (11)$$

The equation for the total enthalpy flux may now be written

$$-\rho \overline{v''H''} = \frac{\lambda_t}{c_p} \frac{\partial \overline{H}}{\partial y} + \left(\mu_t - \frac{\mu_t}{Pr_t} \right) \left\{ \frac{\partial (\overline{u^2}/2)}{\partial y} + \frac{\partial k}{\partial y} \right\} \quad (12)$$

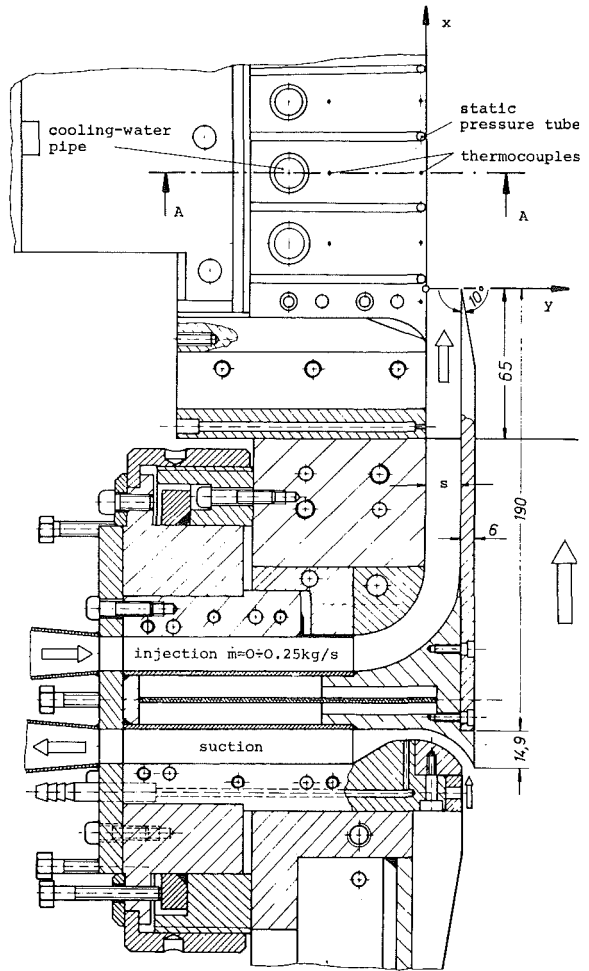


Fig. 2 Inlet geometry

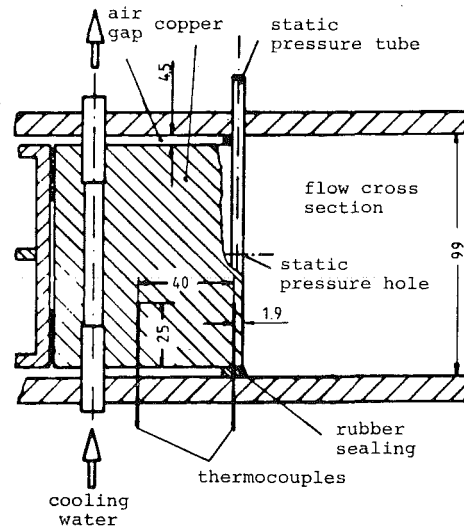


Fig. 3 Sectional view; copper segment

where Pr_t is a turbulent Prandtl number relating the turbulent conductivity λ_t to the turbulent viscosity μ_t . The turbulent viscosity μ_t is assumed to be proportional to a turbulence velocity scale and a turbulence length scale. Following the proposal of Jones and Launder (1972) the turbulence viscosity may be obtained from

$$\mu_t = C_\mu f_\mu \bar{\rho} \frac{k^2}{\epsilon} \quad (13)$$

where ϵ is the turbulent dissipation rate; C_μ is a constant and f_μ is a function introduced to account for viscous effects in the near wall region.

The k - ϵ Model. The transport equations for k and ϵ originally derived from the momentum equations are given in modeled form (Jones and Launder, 1972; Lam and Bremhorst, 1981). Although the ϵ equation can be derived with the assumption $\nu_t = \mu_t/\rho = \text{const}$, it has been widely used for variable property flows (Hein et al. 1980; Vandromme and Minh, 1984; Rodi and Scheurer, 1985).

Turbulent energy equation

$$\text{div}(\bar{\rho}\bar{w}k) = \text{div}((\mu + \mu_t) \text{grad } k) + P_k - \bar{\rho}\epsilon \quad (14)$$

$$P_k = -\overline{\bar{\rho}\tilde{w}''\tilde{w}''} : \text{Grad } \bar{w} \quad (15)$$

$$\bar{\rho}\epsilon = \overline{\tau''} : \text{Grad } \bar{w}'' \quad (16)$$

Turbulent dissipation rate equation

$$\begin{aligned} \text{div}(\bar{\rho}\bar{w}\epsilon) = \text{div}\left(\left(\mu + \frac{\mu_t}{\sigma_\epsilon}\right) \text{grad } \epsilon\right) \\ + C_1 f_1 \frac{\epsilon}{k} P_k - C_2 f_2 \bar{\rho} \frac{\epsilon^2}{k} + P_\epsilon \end{aligned} \quad (17)$$

$$P_\epsilon = -2\overline{\tau''} : \{\text{Grad } \bar{w} \cdot \text{Grad } \bar{w}'' + \text{Grad } \bar{w}'' \cdot \text{Grad } \bar{w}\} \quad (18)$$

$$-2\overline{\tau''} : \{\tilde{w}'' \cdot \text{Grad}(\text{Grad } \bar{w})\} \quad (19)$$

The generation terms P_k and P_ϵ are written in their original form first to give attention to effects of acceleration. For the production of turbulent energy in a boundary layer the use of streamline quasi-orthogonal coordinates leads to

$$P_k = -\overline{\bar{\rho}\tilde{u}''\tilde{v}''} \frac{\partial \bar{u}}{\partial y} - \overline{\bar{\rho}\tilde{u}''\tilde{u}''} \frac{\partial \bar{u}}{\partial x} - \overline{\bar{\rho}\tilde{v}''\tilde{v}''} \bar{u}\Gamma_{21}^2 \quad (20)$$

where Γ_{21}^2 is one of the Christoffel symbols arising from tensor analysis and might be interpreted as a measure of stream tube growth; $\Gamma_{21}^2 \approx (1/\Delta y)(\partial \Delta y/\partial x)$ (Γ_{11}^1 is neglected; $\Gamma_{11}^1 \approx 0$).

Elimination of Γ_{21}^2 using the equation of continuity yields

$$P_k = -\overline{\bar{\rho}\tilde{u}''\tilde{v}''} \frac{\partial \bar{u}}{\partial y} - (\overline{\bar{\rho}\tilde{u}''\tilde{u}''} - \overline{\bar{\rho}\tilde{v}''\tilde{v}''}) \frac{\partial \bar{u}}{\partial x} + \overline{\tilde{v}''\tilde{v}''} \bar{u} \frac{\partial \bar{\rho}}{\partial x} \quad (21)$$

which is consistent with Hanjalic and Launder (1980), Rodi and Scheurer (1983), and Back et al. (1964) except for the variable density term being important in the supersonic region. The first term of P_k is the most important one in a boundary layer and is obtained without additional modeling assumptions

$$-\overline{\bar{\rho}\tilde{u}''\tilde{v}''} \frac{\partial \bar{u}}{\partial y} = \mu_t \left(\frac{\partial \bar{u}}{\partial y}\right)^2 \quad (22)$$

Concerning the remaining terms of P_k , it is better to retain the view of P_k being an exchange term between the energy of turbulent motion and mean flow appearing with reverse sign in the equation of mechanical energy of the mean flow. In the case of a boundary layer ($\tilde{u}''\tilde{u}'' > \tilde{v}''\tilde{v}''$) in an accelerated flow ($\partial \bar{u}/\partial x > 0$, $\partial \bar{\rho}/\partial x < 0$) the remaining terms of P_k are always negative, transferring turbulent kinetic energy to mechanical energy of the mean flow.

The acceleration terms are an order of magnitude smaller than the production P_k but the small imbalance $P_k - \bar{\rho}\epsilon$ is influenced effectively. However, it would be hasty to rush to the conclusion that there is a decay of turbulent viscosity in an accelerated flow leaving the turbulent dissipation rate unconsidered. There is a quite similar behavior of the term P_ϵ in the

dissipation rate equation and the ideal for modeling is already given by Hanjalic and Launder (1972). If the increase of the standard production of ϵ in the low Reynolds number region (Kebede et al., 1985) is assumed to be already considered when introducing the f_1 function, and

$$-2\overline{\tau''} : \{\tilde{w}'' \cdot \text{Grad}(\text{Grad } \bar{w})\} \quad (23)$$

is neglected, as in the standard model (Lam and Bremhorst, 1981), P_ϵ reduces to the transfer term

$$P_\epsilon = -2\overline{\tau''} : \left[\begin{array}{cccc} 2 \frac{\partial u''}{\partial x} \frac{\partial \bar{u}}{\partial x} & \frac{\partial v''}{\partial x} \text{div } \bar{w} & \frac{\partial w''}{\partial x} \frac{\partial \bar{u}}{\partial x} \\ \frac{\partial u''}{\partial y} \text{div } \bar{w} & 2 \frac{\partial v''}{\partial y} \bar{u}\Gamma_{21}^2 & \frac{\partial w''}{\partial y} \bar{u}\Gamma_{21}^2 \\ \frac{\partial u''}{\partial z} \frac{\partial \bar{u}}{\partial x} & \frac{\partial v''}{\partial z} \bar{u}\Gamma_{21}^2 & 0 \end{array} \right] \quad (24)$$

with

$$\text{div } \bar{w} = \frac{\partial \bar{u}}{\partial x} + \bar{u}\Gamma_{21}^2 \quad (25)$$

Since the transfer term contains components of

$$\overline{\bar{\rho}\epsilon = \tau''} : \text{Grad } \bar{w}'' = \tau'' : \left[\begin{array}{ccc} \frac{\partial u''}{\partial x} & \frac{\partial v''}{\partial x} & \frac{\partial w''}{\partial x} \\ \frac{\partial u''}{\partial y} & \frac{\partial v''}{\partial y} & \frac{\partial w''}{\partial y} \\ \frac{\partial u''}{\partial z} & \frac{\partial v''}{\partial z} & \frac{\partial w''}{\partial z} \end{array} \right] \quad (26)$$

it seems reasonable to model the transfer term proportional to the dissipation rate and the acceleration of the flow. In the present calculations, we used the compressible analogy to the relation (Hanjalic and Launder, 1980; Rodi and Scheurer, 1983)

$$P_\epsilon = -C_3 f_3 \frac{\epsilon}{k} \left\{ \bar{\rho}(\tilde{u}''\tilde{u}'' - \tilde{v}''\tilde{v}'') \frac{\partial \bar{u}}{\partial x} - \overline{\tilde{v}''\tilde{v}''} \bar{u} \frac{\partial \bar{\rho}}{\partial x} \right\} \quad (27)$$

although the dependence on $\tilde{u}''\tilde{u}''$, $\tilde{v}''\tilde{v}''$, and $\bar{u}(\partial \bar{\rho}/\partial x)$ might be a subject for further discussion.

The constants and wall functions in the turbulence model equations (13), (14), (17), (21), and (27) are taken from Lam and Bremhorst (1981)

$$C_\mu = 0.09 \quad f_\mu = (1 - e^{-0.0165 \text{Re}_k})^2 \left(1 + \frac{20.5}{\text{Re}_t}\right) \quad (28)$$

$$\sigma_\epsilon = 1.3 \quad (29)$$

$$C_1 = 1.44 \quad f_1 = 1 + \left(\frac{0.05}{f_\mu}\right)^3 \quad (30)$$

$$C_2 = 1.92 \quad f_2 = 1 - e^{-\text{Re}_t^2} \quad (31)$$

$$\text{Re}_t = \frac{k^2 \rho}{\epsilon \mu} \quad \text{Re}_k = \frac{\sqrt{ky} \rho}{\mu} \quad (32)$$

Very little is known about the turbulence quantities $\tilde{u}''\tilde{u}''$ and $\tilde{v}''\tilde{v}''$ in accelerated flows appearing in the transfer terms in the turbulent transport equations. In accordance with measurements in zero pressure gradient flow, a turbulence structure coefficient for $\tilde{u}''\tilde{u}''$ was used with a fixed value

$$\frac{\tilde{u}''\tilde{u}''}{k} = 1 \quad (33)$$

and $\tilde{v}''\tilde{v}''$ was calculated from a standard relation (e.g., Ljuboja and Rodi, 1981; Gibson, 1978) with the additional assumption $P_k \approx \bar{\rho}\epsilon$

$$\frac{\widetilde{v''v''}}{k} = 0.52 \left(\frac{1 - 0.25f}{1 + 0.667f} \right) \quad (34)$$

For the additional constant in the dissipation rate equation we used

$$C_3 = 4.44 \quad f_3 = 1 \quad (35)$$

as originally given by Hanjalic and Launder (1980).

For the turbulent Prandtl number the equation

$$\text{Pr}_t = 0.67 \frac{1 + 0.675f}{1 + 0.5f} (1 + 0.167f) \quad (36)$$

is used as developed by Ljuboja and Rodi (1981) from an analysis of the $\widetilde{v''T''}$ equation. In a boundary layer

$$f = \frac{\text{Re}_t}{3.72\text{Re}_k} = \frac{k^{3/2}}{3.72\epsilon y} \approx \frac{(-u''v'')^{3/2}}{0.41\epsilon y} = \frac{L}{0.41y} = 1 \quad (37)$$

yields $\text{Pr}_t = 0.86$ as used in most calculations. In the outer region $f \rightarrow 0$ leads to $\text{Pr}_t = 0.67$, which is consistent with some measurements (Townsend, 1976). The equation for Pr_t was used without modifications in the present calculations although other measurements (Fiedler, 1974; Chambers et al., 1985) indicate that the turbulent Prandtl number in a turbulent mixing layer should be even lower, e.g., $\text{Pr}_t \approx 0.5$, calling for a change of constants in the Pr_t formula.

Initial and Boundary Conditions

Boundary Conditions. The wall pressures obtained from the experiments were used as a boundary condition for the calculations performed with the parabolic finite difference code. In the absence of curvature effects a cross-stream zero pressure gradient was assumed in the present calculations. The assumption of negligible curvature is also valid in the case of film cooling for velocity ratios less than 3 (Abramovich, 1963). The measured wall temperatures were used as the thermal boundary condition, and the calculated wall heat flux is compared with the measured heat flux.

Velocity and kinetic energy were set to zero at the wall, and the dissipation rate of turbulent kinetic energy at the wall was calculated from the reduced turbulent kinetic energy equation

$$\epsilon_w = \frac{\mu}{\rho} \left(\frac{\partial^2 k}{\partial y^2} \right)_w \quad (38)$$

All variables were submitted to a vanishing cross-stream gradient as a free-stream boundary condition. In the absence of cross-stream diffusive transport the mean flow equations reproduce the isentropic relation, and the turbulence transport equations automatically reduce to the decay equations

$$u_\infty \frac{\partial k}{\partial x} = -\epsilon \quad (39)$$

$$u_\infty \frac{\partial \epsilon}{\partial x} = -C_2 \frac{\epsilon^2}{k} \quad (40)$$

Initial Conditions. As initial velocity profiles, the profile for a zero pressure gradient boundary layer developed on the surface from the suction to the coolant entry (Fig. 2) was used for the hot gas, and a velocity profile for fully developed channel flow was used for the cooling film. The mass flux of the coolant and the free-stream velocity were obtained from the experiment. Since the slot was not removed in the absence of coolant injection, we assumed a slightly smaller initial boundary layer thickness. In the near-wall regions the velocity profiles were determined by the law of the viscous sublayer.

The temperature profiles were obtained from the generalized Crocco relation

$$T = T_w + (T_r - T_w) \frac{u}{u_\infty} - r \frac{u^2}{2c_p} \quad (41)$$

$$r = 0.88 \quad (42)$$

In the fully turbulent region the turbulent kinetic energy of the hot gas boundary layer is obtained from

$$k = \frac{\tau}{\sqrt{c_{\mu\rho}}} \quad (43)$$

with an additional wall damping correction.

The turbulent mixing length is defined by the ramp function $l = \min(0.41y, \mu\delta)$, with λ as defined by Crawford and Kays (1976). The turbulent dissipation rate is calculated from (Norris, 1975)

$$\epsilon = C_\mu^{1/4} \frac{k^{3/2}}{l} \left(1 + \frac{1.9}{\text{Re}_t} \right) \quad (44)$$

A smooth distribution of all variables between fully turbulent region and free stream was obtained using the Wake function

$$W\left(\frac{y}{\delta}\right) = 2 \left(3 \left(\frac{y}{\delta}\right)^2 - 2 \left(\frac{y}{\delta}\right)^3 \right) \quad (45)$$

The free-stream value of the turbulent kinetic energy was obtained from $k_\infty = 3/2 Tu_\infty^2 u_\infty^2$ with $Tu_\infty = 1.5$ percent from the experiments of Bauer et al. (1980) in the same test section. The free-stream dissipation rate of turbulent energy was calculated from the decay of grid turbulence

$$\epsilon_\infty = \frac{u_\infty k_\infty}{c_2 - 1} \frac{1}{x_t} \quad x_t = 0.5 \text{ m} \quad (46)$$

The turbulent kinetic energy at the entry of the cooling film was fixed at 5 percent.

Solution Procedure

The mean flow equations for momentum and total enthalpy and the transport equations for turbulent energy and turbulent dissipation rate were solved on a streamline grid with a new computer code developed by the authors. The finite difference equations were obtained by integrating the differential equations over the grid defined control volume according to the Gaussian integration rule

$$\iiint_V \text{div vector} dV = \iint_S \text{vector} \cdot \mathbf{n} dS \quad (47)$$

where V = control volume; S = surface of control volume; \mathbf{n} = unity vector normal to the surface. Thus conservation of convective and diffusive transport is guaranteed automatically. The usual ω transformation (Patankar and Spalding, 1970; Crawford and Kays, 1976) is omitted for simplicity and more attention to the slowly varying region of the viscous sublayer.

The finite difference equations are solved fully implicit in the streamwise direction without iteration and interpolation for the boundary conditions.

In order to obtain grid-independent solutions a nonequidistant grid with 100 nodes was established in the cross-stream direction with a constant spreading rate of 1.1 at the starting location. The first grid node away from the wall was at a distance of $y^+ = 0.1$ approximately constant during the whole calculation. A constant forward step $\Delta x = 10^{-3}$ m was chosen in the present calculations, giving a nondimensional step size of $300 < \Delta x^+ < 1000$. The results remained unchanged for smaller step size. The calculation time per forward step was 0.025 s on a CDC Cyber 875 and the total computing time was 20 s per run.

The independence of the results from the calculation procedure has been examined in comparison with a modified ver-

sion of the GENMIX computer code (Patankar and Spalding, 1970).

Results

Heat transfer and film cooling have been studied for four different mainstream conditions. Mass flow, stagnation pressure, stagnation temperature, average entry velocity, and isothermal wall temperature for the heat transfer experiments are given in Table 1.

The measured pressures along the flat side of the nozzle are shown in Fig. 4. The acceleration parameter K is of the order 10^{-6} and a typical value at the throat is 0.3×10^{-6} . The wall heat flux measurements are plotted in Fig. 5 in comparison with the results calculated with the finite difference code.

In the case of film cooling, heat transfer results are shown for two mainstream conditions in Figs. 7, 9, 11, and 13 for different coolant mass flow rates. The wall heat flux is plotted again in comparison with the finite difference calculations and the measured wall temperatures used as thermal boundary condition of the calculations are given in Figs. 6, 8, and 10, and 12.

Injection mass flow, mass flow ratio, mass flux ratio, momentum flux ratio, injection velocity ratio, average injection velocity, injection temperature, and temperature ratio at the entry of the injected cold air are given in Tables 2-5.

Conclusions

Experiments and calculations on heat transfer and film cooling stability in a convergent-divergent nozzle are presented.

Heat Transfer. The maximum wall heat flux is determined slightly upstream from the throat as indicated in earlier measurements. In contrast to many simple correlation methods finite difference calculations predict the location of the maximum very well, but most standard turbulence models (e.g., Crawford and Kays, 1976; Norris, 1975; Norris and Reynolds, 1975; Jones and Launder, 1972; Lam and Bremhorst, 1981; Chien, 1982) underpredict the wall heat flux by approximately 10 percent. The underprediction of heat transfer has also been observed by Crawford (1986) comparing calculations with WR (Wilcox and Rubesin, 1980), JL (Jones and Launder, 1972) and CH (Chien, 1982) and two-equation turbulence models with the favorable pressure gradient experiments of (Julien et al., 1969; Theilbar et al., 1969). Kays et al. (1970) have used a zero-equation model very similar to the STAN5 zero-equation model (Crawford and Kays, 1976), but with a higher Karman constant (0.44) in comparison to their measurements of the heat transfer to a highly accelerated turbulent boundary layer. This modification also improves the agreement between calculation and our measurements.

In the present investigation, we used a standard model (Lam and Bremhorst, 1981), but we retained the acceleration terms appearing in the turbulence transport equations and we used $C_3 = 4.44$ as originally given by Hanjalic and Launder (1980). If the turbulence structure is assumed to be similar to the structure of a fully turbulent zero pressure gradient boundary layer, the wall heat flux is predicted very well.

Film Cooling. In the case of film cooling there is no influence of the throat on the cooling film stability. It should be pointed out that an injection mass flow ratio of only $\dot{m}_c/\dot{m} = 2.1$ percent (Table 3) yielded a significant decrease in heat transfer as well in the subsonic as in the supersonic region. An approximate comparison of mass flow ratios for axisymmetric nozzles may be obtained with simple geometry relations.

Table 1 Mainstream conditions

Symbol	O	Δ	\square	\diamond	
\dot{m}	1.971	2.221	2.457	2.695	kg/s
P_o	190329	217227	242624	268616	Pa
T_o	447.4	458.6	467.8	476.3	K
u	55.34	56.02	59.02	59.60	m/s
T_w	309.5	309.5	318.0	323.0	K

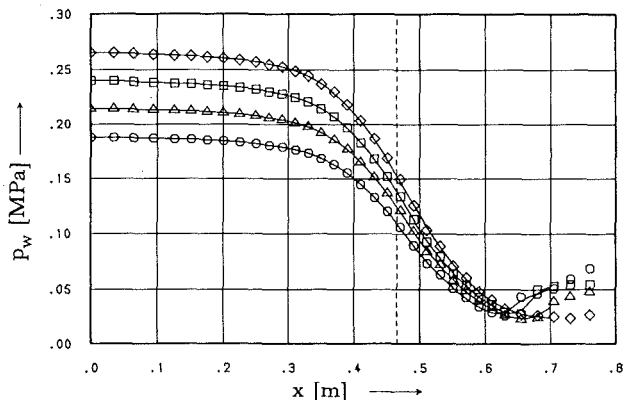


Fig. 4 Wall pressure $p_w(x)$ along plane nozzle wall

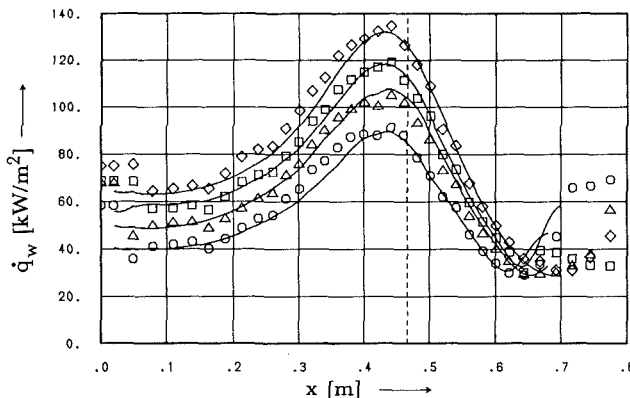


Fig. 5 Wall heat flux $q_w(x)$; \diamond , \square , Δ , \circ measurements; — finite difference calculation

The calculated results are fairly good but not yet fully satisfactory for all injection rates. In contrast to the standard models predicting the wall heat flux again too small, the model with the additional acceleration terms overpredicts the heat transfer in the throat region for high injection rates.

Turbulence Model. The calculations are very sensitive to the choice of the additional constant and C_3 should be finally fixed from comparison of predictions with experiments for many different accelerated flow cases. Assumed the turbulence structure is described well with equations (33) and (34), the overprediction of heat transfer for high injection rates indicates that the constant $C_3 = 4.44$ as originally given by Hanjalic and Launder (1980) might be too big.

Since acceleration acts in a different way on $\overline{u''u''}$ and $\overline{v''v''}$ it might also be necessary to examine the structure of accelerated boundary layers and mixing layers experimentally and to use a complete Reynolds stress model. Additionally it will be necessary to develop a $\overline{v''T''}$ equation for accelerated flows and to prove the concept of a turbulent Prandtl number. Finally it is important to improve the standard models in comparison with experiments in zero pressure gradient, large density ratio boundary layers.

Table 2 Injection conditions for mainstream mass flow; $\dot{O}m = 1.971$ kg/s, slot height $s = 5 \times 10^{-3}$ m

Symbol (figs.6,7)	X	Y	Z	
\dot{m}_c	0.084	0.059	0.045	kg/s
\dot{m}_c/\dot{m}	4.3	3.0	2.3	%
$\frac{(\rho u)_c}{\rho u}$	2.12	1.49	1.13	
$\frac{(\rho uu)_c}{\rho uu}$	2.88	1.45	0.84	
u_c/u	1.36	0.97	0.75	
u_c	75.3	53.8	41.3	m/s
T_c	293.3	296.6	298.1	kg/s
T_c/T	0.66	0.67	0.67	

Table 3 Injection conditions for mainstream mass flow; $\Delta\dot{m} = 2.221$ kg/s, slot height $s = 5 \times 10^{-3}$ m

Symbol (figs.8,9)	X	Y	Z	
\dot{m}_c	0.081	0.055	0.046	kg/s
\dot{m}_c/\dot{m}	3.7	2.5	2.1	%
$\frac{(\rho u)_c}{\rho u}$	1.79	1.22	1.01	
$\frac{(\rho uu)_c}{\rho uu}$	2.04	0.97	0.67	
u_c/u	1.14	0.79	0.66	
u_c	64.4	44.4	37.2	m/s
T_c	300.4	302.6	303.8	K
T_c/T	0.66	0.66	0.66	

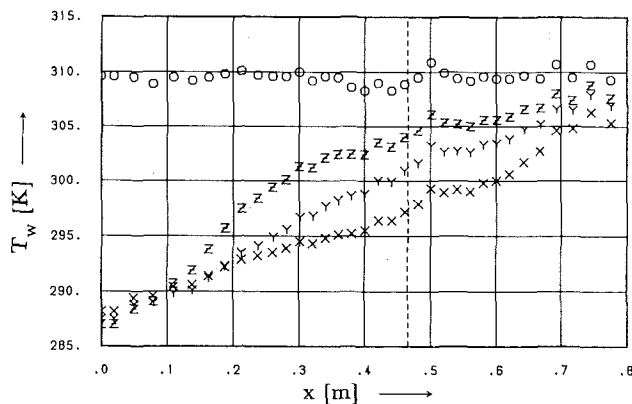


Fig. 6 Wall temperature $T_w(x)$ along plane nozzle wall

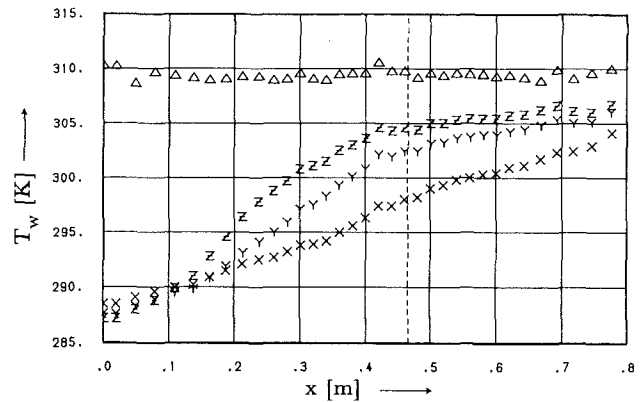


Fig. 8 Wall temperature $T_w(x)$ along plane nozzle wall

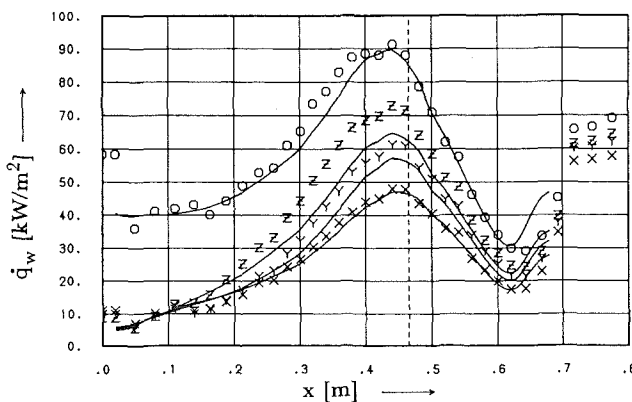


Fig. 7 Wall heat flux $\dot{q}_w(x)$; O,X,Y,Z measurements; _____ finite difference calculation

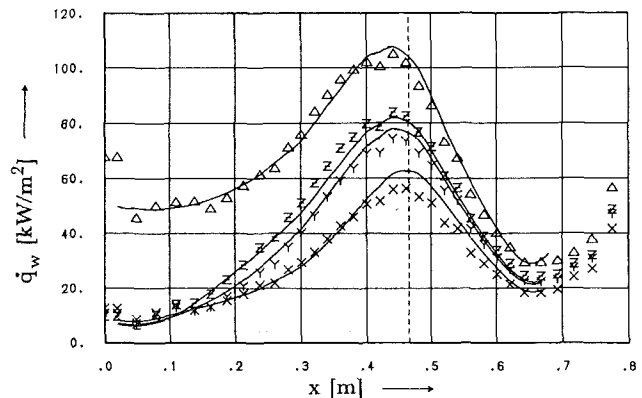


Fig. 9 Wall heat flux $\dot{q}_w(x)$; Δ, X, Y, Z measurements; _____ finite difference calculation

References

Abramovich, G. N., 1963, *The Theory of Turbulent Jets*, The M.I.T. Press, Massachusetts Institute of Technology, Cambridge, MA.

Back, L. H., Massier, P. F., and Gier, H. L., 1964, "Convective Heat Transfer in a Convergent-Divergent Nozzle," *Int. Journal Heat Mass Transfer*, Vol. 7, pp. 549-568.

Back, L. H., Cuffel, R. F., and Massier, P. F., 1970, "Laminarization of a Turbulent Boundary Layer in Nozzle Flow—Boundary Layer and Heat Transfer Measurements With Wall Cooling," *ASME Journal of Heat Transfer*, Vol. 92, pp. 333-344.

Back, L. H., and Cuffel, R. F., 1972, "Turbulent-Boundary-Layer Measurements Along a Supersonic Nozzle With and Without Wall Cooling," *ASME Journal of Heat Transfer*, Vol. 94, pp. 242-243.

Bauer, K., Winkler, W., and Grigull, U., 1978, "Heat Transfer in Compressible Turbulent Boundary Layer," *Proceedings International Heat Transfer Conference*, Toronto, Vol. 5, pp. 191-196.

Bauer, K., Straub, J., and Grigull, U., 1980, "Influence of Free-Stream Turbulence Intensity on Heat Transfer in the Two-Dimensional Turbulent Boundary Layer of an Accelerated Compressible Flow," *Int. Journal Heat Mass Transfer*, Vol. 23, pp. 1635-1642.

Boldman, D. R., Neumann, H. E., and Schmidt, J. F., 1967, "Heat Transfer in 30° and 60° Half-Angle Convergence Nozzles With Various Diameter Uncooled Pipe Inlets," NASA TN D-4177.

Boldman, D. R., and Graham, R. W., 1972, "Heat Transfer and Boundary Layers in Conical Nozzles," NASA TN D-6594.

Chambers, A. J., Antonia, R. A., and Fulachier, L., 1985, "Turbulent Prandtl Number and Spectral Characteristics of a Turbulent Mixing Layer," *Int. Journal Heat Mass Transfer*, Vol. 28, No. 8, pp. 1461-1468.

Chien, K.-Y., 1982, "Predictions of Channel and Boundary-Layer Flows With a Low-Reynolds-Number Turbulence Model," *AIAA Journal*, Vol. 20, p. 33.

Crawford, M. E., and Kays, W. M., 1976, "STAN5—a Program for Numerical Computation of Two-Dimensional Internal and External Boundary Layer Flows," NASA Contractor Report CR-2742.

Table 4 Injection conditions for mainstream mass flow; $\square \dot{m} = 2.457$ kg/s, slot height $s = 12 \times 10^{-3}$ m

Symbol (figs.10,11)	X	Y	Z	
\dot{m}_c	0.157	0.113	0.090	kg/s
\dot{m}_c/\dot{m}	6.4	4.6	3.6	%
$\frac{(\rho u)_c}{\rho u}$	1.25	0.90	0.71	
$\frac{(\rho uu)_c}{\rho uu}$	1.00	0.51	0.33	
u_c/u	0.79	0.57	0.46	
u_c	46.8	33.9	27.2	m/s
T_c	299.2	301.2	302.6	kg/s
T_c/T	0.64	0.65	0.65	

Table 5 Injection conditions for mainstream mass flow; $\diamond \dot{m} = 2.695$ kg/s, slot height $s = 12 \times 10^{-3}$ m

Symbol (figs.12,13)	X	Y	Z	
\dot{m}_c	0.149	0.115	0.087	kg/s
\dot{m}_c/\dot{m}	5.5	4.3	3.2	%
$\frac{(\rho u)_c}{\rho u}$	1.08	0.84	0.63	
$\frac{(\rho uu)_c}{\rho uu}$	0.73	0.44	0.25	
u_c/u	0.67	0.53	0.40	
u_c	40.2	31.3	23.7	m/s
T_c	299.5	300.9	302.4	kg/s
T_c/T	0.63	0.63	0.64	

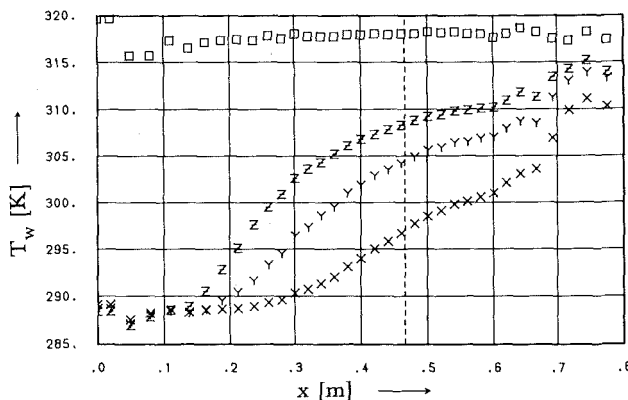


Fig. 10 Wall temperature $T_w(x)$ along plane nozzle wall

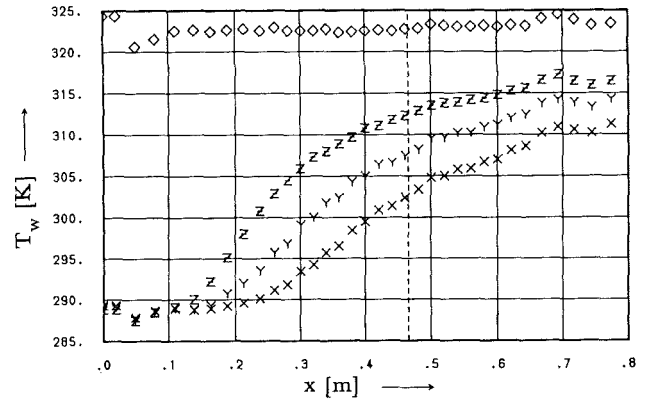


Fig. 12 Wall temperature $T_w(x)$ along plane nozzle wall

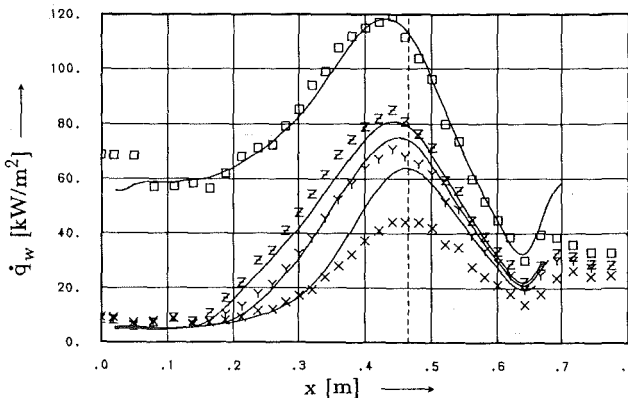


Fig. 11 Wall heat flux $q_w(x)$; $\square, \triangle, \times$ X,Y,Z measurements; — finite difference calculation

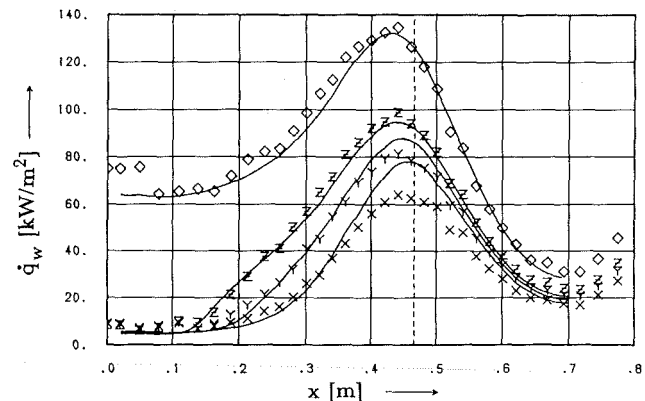


Fig. 13 Wall heat flux $q_w(x)$; $\diamond, \triangle, \times$ X,Y,Z measurements; — finite difference calculation

Crawford, M. E., 1986, "Lecture Series 1986-06: Convective Heat Transfer and Film Cooling in Turbomachinery," von Karman Institute for Fluid Dynamics, Brussels, Belgium.

Favre, A., 1965, "Equations des gaz Turbulent Compressible," Part I: *Journal de Mecanique*, Vol. 4, No. 3, pp. 361-390; Part II: *Journal de Mecanique*, Vol. 4, No. 4, pp. 391-421.

Favre, A., 1975, "Equations statistiques des fluides turbulents compressibles," *Proceedings Veme Congres canadien de Mecanique Appliquee*, New Brunswick, pp. G3-G34.

Fiedler, H. E., 1974, "Transport of Heat Across a Plane Turbulent Mixing Layer," *Adv. Geophys.*, Vol. 18, pp. 93-109.

Gibson, M. M., 1978, "An Algebraic Stress and Heat Flux Model for Turbulent Shear Flow With Streamline Curvature," *Int. Journal Heat Mass Transfer*, Vol. 21, pp. 1609-1617.

Hanjalic, K., and Launder, B. E., 1980, "Sensitizing the Dissipation Equation to Irrotational Strains," *ASME Journal of Fluids Engineering*, Vol. 102, pp. 34-40.

Hay, N., Lampard, D., and Saluja, C. L., 1985, "Effects of the Condition of the Approach Boundary Layer and of Mainstream Pressure Gradients on the

Heat Transfer Coefficient on Film-Cooled Surfaces," *ASME Journal of Engineering for Gas Turbines and Power*, Vol. 107, pp. 99-110.

Hien, H. M., Vandromme, D. D., and MacCormack, R. W., 1980, "Comparison of Computation With Experiment," *ASFOSS-IFP Conference Proceedings*, Stanford.

Jones, T. V., and Forth, C. J. P., 1986, "The Scaling of Film Cooling—Theoretical and Experimental Results," Lecture Series 1986-06: *Convective Heat Transfer and Film Cooling in Turbomachinery*, von Karman Institute for Fluid Dynamics, Brussels, Belgium.

Jones, W. P., and Launder, B. E., 1972, "The Prediction of Laminarization With a Two Equation Model of Turbulence," *Int. Journal Heat Mass Transfer*, Vol. 15, pp. 301-314.

Julien, H. L., Kays, W. M., and Moffat, R. J., 1969, "The Turbulent Boundary Layer on a Porous Plate: Experimental Study of the Effects of a Favorable Pressure Gradient," Thermosciences Division Department of Mechanical Engineering, Stanford University, Report No. HMT-4.

Kays, W. M., Moffat, R. J., and Thielbar, W. H., 1970, "Heat Transfer to the Highly Accelerated Turbulent Boundary Layer With and Without Mass Addition," *ASME Journal of Heat Transfer*, Vol. 92, pp. 499-505.

Kebede, W., Launder, B. E., and Younis, B. A., 1985, "Large-Amplitude

Periodic Pipe Flow: A Second-Moment Closure Study," *Proc. 5th Turbulent Shear Flow Symposium*, Cornell University, pp. 16.23-16.29.

Klingbeil, E., 1966, *Tensorrechnung für Ingenieure*, Bibliographisches Institut AG, Mannheim.

Lam, C. K. G., and Bremhorst, K., 1981, "A Modified Form of the $k-\epsilon$ Model for Predicting Wall Turbulence," *ASME Journal of Fluids Engineering*, Vol. 103, pp. 456-460.

Ligrani, P. M., and Camci, C., 1985, "Adiabatic Film Cooling Effectiveness From Heat Transfer, Measurements in Compressible Variable-Property Flow," *ASME Journal of Heat Transfer*, Vol. 107, pp. 313-320.

Ljuboja, M., and Rodi, W., 1980, "Calculation of Turbulent Wall Jets With an Algebraic Reynolds Stress Model," *ASME Journal of Fluids Engineering*, Vol. 102, pp. 351-356.

Ljuboja, M., and Rodi, W., 1981, "Prediction of Horizontal and Vertical Turbulent Buoyant Wall Jets," *ASME Journal of Heat Transfer*, Vol. 103, pp. 343-349.

Norris, L., 1975, "Turbulent Channel Flow With a Moving Wavy Boundary," Dissertation, Department of Mechanical Engineering, Stanford University, Stanford, CA.

Norris, L. H., and Reynolds, W. C., 1975, "Turbulent Channel Flow With a Moving Wavy Boundary," Rept. No. FM-10, Department Mechanical Engineering, Stanford University, Stanford, CA.

Patankar, S. V., and Spalding, D. B., 1970, *Heat and Mass Transfer in Boundary Layers—A General Calculation Procedure*, Intertext Books, London.

Patel, V. C., Rodi, W., and Scheurer, G., 1985, "Turbulence Models for Near-Wall and Low Reynolds Number Flows: a Review," *AIAA Journal*, Vol. 23, No. 9, pp. 1308-1319.

Rodi, W., and Scheurer, G., 1983, "Scrutinizing the $k-\epsilon$ Model Under Adverse Pressure Gradient Conditions," *Proc. 4th Turbulent Shear Flow Symposium*, Karlsruhe, Federal Republic of Germany.

Rodi, W., and Scheurer, G., 1985, "Calculation of Heat Transfer to Convection-Cooled Gas Turbine Blades," *ASME Journal of Engineering for Gas Turbines and Power*, Vol. 107, pp. 620-627.

Rotta, J. C., 1972, *Turbulente Strömungen—Eine Einführung in die Theorie und ihre Anwendungen*, B. G. Teubner, Stuttgart, Federal Republic of Germany.

Rued, K., and Wittig, G., 1985, "Free-Stream Turbulence and Pressure Gradient Effects on Heat Transfer and Boundary Layer Development on Highly Cooled Surfaces," *ASME Journal of Engineering for Gas Turbines and Power*, Vol. 107, pp. 54-59.

Thielbar, W. H., Kays, W. M., and Moffat, R. J., 1969, "The Turbulent Boundary Layer: Experimental Heat Transfer With Boiling, Suction, and Favourable Pressure Gradient," Thermosciences Division, Department of Mechanical Engineering, Stanford University, Report No. HMT-5.

Townsend, A. A., 1976, *The Structure of Turbulent Shear Flow*, Cambridge University Press, Great Britain.

Vandromme, D. D., and Minh, H. H., 1984, "Solution of the Compressible Navier-Stokes Equations: Applications to Complex Turbulent Flows," Lecture Series 1984-04: *Computational Fluid Dynamics*, von Karman Institute for Fluid Dynamics, Brussels, Belgium.

Wang, T., Simon, T. W., and Buddhavarapu, J., 1985, "Heat Transfer and Fluid Mechanics Measurements in Transitional Boundary Layer Flows," *ASME Journal of Engineering for Gas Turbines and Power*, Vol. 107, pp. 1007-1015.

Wilcox, D. C., and Rubesin, M. W., 1980, "Progress in Turbulence Modeling for Complex Flow Fields Including Effects of Compressibility," NASA TP 1517.

Winkler, W., and Griggull, U., 1977, "Wärmeübergang turbulenter kompressibler Grenzschichtströmungen mit starken negativen Druckgradienten (Wärmeübergang in einer Lavaldüse)," *Wärme- und Stoffübertragung*, Vol. 10, pp. 281-291.

Stagnation Film Cooling and Heat Transfer, Including Its Effect Within the Hole Pattern

W. J. Mick

R. E. Mayle

Department of Mechanical Engineering,
Rensselaer Polytechnic Institute,
Troy, NY 12180-3590

Detailed film effectiveness and surface heat transfer measurements were obtained for secondary air injection through rows of holes into the stagnation region of an incident mainstream flow. Tests were performed using a blunt body with a circular leading edge and a flat afterbody. Rows of holes were located at ± 15 deg and $+44$ deg from stagnation. The holes in each row were spaced four hole diameters apart and were angled 30 deg to the surface in the spanwise direction. Measurements were taken for three cooling-to-incident flow mass flux ratios both in the leading edge region within the hole pattern and downstream to a distance of about 85 hole diameters. The results indicate that large spanwise variations in both film effectiveness and heat transfer coefficient exist, and that the highest values of each do not in general correspond. Near the holes, film effectiveness values as high as 0.7–0.8 were found, while heat transfer coefficients with injection were as much as three times those without. Far downstream the film effectiveness decayed to values near 0.1, while the heat transfer coefficient remained about 10 percent above that without injection. Nevertheless, it is shown that for typical turbine temperatures, leading edge injection reduces the surface heat load everywhere for all but the highest mass flux ratio. The exception produces an increase in heat load within the injection region.

Introduction

The high inlet temperatures of modern gas turbines necessitate the use of sophisticated cooling schemes to protect the exposed components. Common techniques include rather elaborate internal convective schemes, film cooling, and a combination of both. In film cooling, relatively cool air is injected through the component's surface in such a way that it forms a protective layer between the surface and the hot mainstream gas. Film cooling has been extensively applied to gas turbine airfoils by injecting the coolant through rows of closely spaced discrete holes. Current designs of turbine airfoils incorporate film cooling holes near the leading edge as well as on both the suction and pressure surfaces. Film cooling near the leading edge not only protects this region but also affects the fluid mechanics and heat transfer over the entire airfoil surface.

In the past, there have been many investigations concerning film cooling of flat or mildly curved surfaces under a variety of mainstream conditions, e.g., [1–5]. Although most studies were concerned with obtaining film effectiveness data for various blowing rates and injection geometries, several made detailed measurements near injection and also obtained the necessary heat transfer information for a complete description of the film cooling effects.

Considerably less information, however, is available on film cooling with injection in the leading edge region of an airfoil. The leading edge problem contains the additional aspects of high acceleration, thin boundary layers, and coolant injection at angles nearly opposite to the main flow direction. Discharge coefficients for injection into a stagnation region were determined by Tillman and Jen [6] and Tillman et al. [7] for a large variety of injection geometries and blowing rates. Experiments by Hanus and L'Ecuyer [8] provided heat transfer information for a single row of holes on the leading edge of a turbine vane. Typical of engine conditions, the coolant-to-mainstream density ratio was 2.15. Spanwise-averaged values of the film cooled Stanton number are reported for different mass flux ratios, leading edge row locations, and coolant hole injection angles. The data, presented for a region 10 to 110 hole diameters downstream from injection, indicates that a mass flux ratio of about 1.0 provided a maximum reduction in the surface heat flux. Luckey et al. [9] used a circular cylinder to model the leading edge region and present local Stanton number data in the region between 6 and 15 hole diameters from injection for various mass flux ratios. Holes angled 20, 30, and 40 deg to the surface in the spanwise direction were used. Large spanwise variations in the surface heat flux were detected and were found to vary with both the injection geometry and mass flux ratio. A correlation is also presented for the optimum blowing rate in terms of the coolant-to-mainstream velocity ratio and the injection angle. Luckey and L'Ecuyer [10] later extended this work to include two, three,

Contributed by the Heat Transfer Division and presented at the ASME Winter Annual Meeting, Anaheim, California, December 7–12, 1986. Manuscript received by the Heat Transfer Division May 2, 1986. Paper No. 86-WA/HT-48.

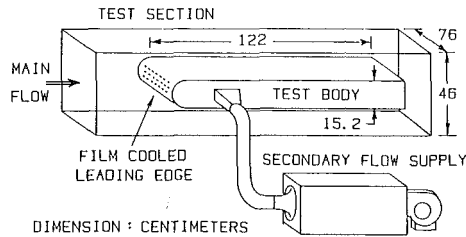


Fig. 1 Test facility

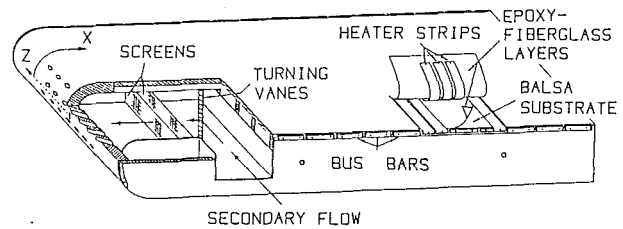


Fig. 2 Heat transfer model with leading edge injection

and five-row injection configurations. Of particular note is the increase, rather than decrease, in heat load that they detected directly behind the holes for the higher blowing rates. Sasaki et al. [11], using a flat plate model with a blunt leading edge (as in the present investigation), tested three different leading edge film-hole configurations, each with four rows of holes. While local film effectiveness data for various mass flux ratios were obtained both within and downstream of injection up to a distance of 78 hole diameters, no heat transfer information is presented. Nevertheless, the effectiveness near injection was found to decrease beyond a mass flux ratio of about 1.0 as the injection penetrated further into the mainstream. Further downstream, however, the effectiveness was found to increase continually with blowing rate. Recently, Camci and Arts [12] presented heat transfer data in and downstream of the leading edge region under typical engine conditions, where it was found that injection significantly disturbs the boundary layer development downstream of injection. A somewhat different approach to the problem was taken by Wadia and Nealy [13], whose measurements included the heat transferred on the coolant side and in the holes as well as on the film cooled side of the leading edge.

The present work was undertaken to provide a very detailed picture of a single, though typical, leading edge film cooling scheme. Film effectiveness and heat transfer measurements were obtained both within and downstream of the film hole pattern for a typical engine Reynolds number and range of mass flux ratios.

Experimental Apparatus

The facility consisted of two separate air supply systems: One supplied the primary or incident flow while the other provided the secondary or injection flow. The primary air system was a low-speed, open-circuit wind tunnel powered by a centrifugal fan. All of the tests were conducted with the test body placed in the tunnel's test section as shown in Fig. 1. The flow velocity incident on the model, nominally maintained at 9.8 m/s, was uniform to within $\frac{1}{2}$ of 1 percent except at the walls where a 2-cm-thick boundary layer existed. This velocity could be varied by adjusting the inlet guide vanes to the centrifugal fan and was continually monitored by a pitot-static tube in the

test section. Air leaving the tunnel entered the room, mixed with the surrounding air, and circulated back to the fan inlet. An air conditioner in the room with its sensor placed in the tunnel automatically controlled the primary air temperature to within 1°C .

The secondary system supplied air to the leading edge film holes. This air could be heated uniformly by a series of nichrome wire grids strung across the flow in the heater section. An insulated duct carried this heated air to a plenum inside the test body. Its temperature was measured by two thermocouples centrally located in two of the film holes on either side of the hole pattern. The secondary-air mass flow rate was measured using a calibrated nozzle at the end of the heater section.

The test model spanned the entire 76-cm width of the test section and was held in position by steel rods passing through the body and each side wall of the test section. The model was centered between the top and bottom walls of the test section and could be pivoted about its forward support rod so as to adjust its angle of attack. This adjustment was used to fine tune the flow around the top and bottom of the model and position the stagnation line at the body's midplane on the leading edge.

The model itself has a cylindrical, semicircular leading edge with a 7.6-cm radius that smoothly joined two parallel, flat, 1.22-m-long surfaces. As shown in Fig. 2, it was constructed mostly of wood and has a composite, constant-heat-flux test surface. Mahogany ribs running lengthwise provided the structural backbone of the model, while a 13-mm-thick layer of balsa wood covering the ribs formed the heated-surface substrate. A plenum in the forward portion of the model provided a uniform flow of the secondary air from an inlet in the model's side to the leading edge holes. Thin turning vanes, designed according to Salter [14], were used in the plenum to turn and evenly diffuse the flow before it passed through two 32-mesh screens. Measurements of the centerline velocity for each hole indicated that the flow through all holes in a row was the same to within ± 3 percent for the row at 44 deg and ± 8 percent for the rows closest to stagnation.

The heated surface consisted of 37 0.025-mm-thick, 38-mm-wide stainless steel heater strips bonded side by side on the balsa wood substrate between two layers of fiberglass fabric

Nomenclature

d = injection hole diameter	P = pitch of holes in row	T_m = measured surface temperature
D = leading edge diameter	q = convective heat flux	T_0 = actual surface temperature
h = convective heat transfer coefficient	q_0 = convective heat flux without injection	T_s = secondary or injected air temperature
h_0 = convective heat transfer coefficient without injection	q_{cond} = heat transferred by conduction	T_∞ = mainstream or incident air temperature
L = length of injection hole	q_{gen} = heat generated by metal strips	x = streamwise distance measured from stagnation
M = average secondary-to-incident mass flux ratio	q_{rad} = heat loss by radiation	z = spanwise distance
Nu_D = Nusselt number based on leading edge diameter	Re_D = Reynolds number based on the incident velocity and leading edge diameter	η = adiabatic film effectiveness
	T_{aw} = adiabatic wall temperature	ϕ = overall cooling effectiveness

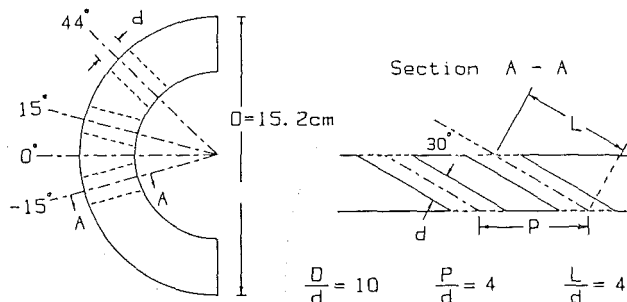


Fig. 3 Injection hole geometry

and epoxy resin. The metal strips were run spanwise across the model, separated from one another by a distance of about 0.25 mm. At each end, they were connected in series by copper bus bars buried in the model. The whole surface was heated by passing a measured electric current (d-c) through the circuit. This surface nominally produced a constant-heat-flux test surface when heated (except in those strips containing the holes) and an adiabatic surface when unheated, similar to that used by Ericksen and Goldstein [3].

The surface temperature distribution was measured using a total of 118 0.075-mm thermocouples, bonded between the strips and balsa substrate. Their leads ran in opposite directions along the surface for a short distance to minimize heat loss, and then through the balsa substrate. In addition, a number of thermocouples were attached at various locations along the back of the balsa in order to determine the heat conducted through the substrate. All of the thermocouples were located within the central spanwise portion of the body and hole pattern. Since large variations of the film effectiveness and heat transfer were expected around and immediately downstream of the film holes, most of the surface thermocouples were placed in this region. Placement was chosen to provide sufficient resolution for drawing the film effectiveness and heat transfer contour plots, and to obtain accurate spanwise-averaged values of both. Thermocouples were also placed to take advantage of the periodicity in the injection hole pattern. In order to check for spanwise periodicity with secondary flow injection, several thermocouple positions were duplicated across the span of the hole pattern at various streamwise locations.

The film hole configuration used in this study is shown in Fig. 3. Rows of circular holes were located at ± 15 deg and at $+44$ deg from the stagnation line. This configuration may be considered to model a four-row, symmetric injection scheme if the row which would exist at -44 deg is assumed to have negligible effect on the results above the stagnation line. Each hole had a diameter of $d = 1.52$ cm and was angled at 30 and 90 deg to the surface in the spanwise and streamwise directions, respectively. There were seven holes in each row which were spaced four hole diameters apart, $P/d = 4$. The hole-to-leading edge diameter ratio was $d/D = 0.1$ and the hole length-to-hole diameter ratio was $L/d = 4$. The hole construction was actually a three-step process dictated by a test procedure intended to evaluate the effects of the nonuniformity in surface heat flux as a result of cutting holes in the heater strip. This required that heat transfer tests be conducted with: (1) an uncut heated surface, (2) with the holes cut in the metal heater strips only, and finally (3) with holes cut completely through the surface and with injection. In order to accomplish this, the model was constructed such that the holes penetrated through the balsa wood substrate from its back to within 3 mm of the test surface. The heated surface was applied over the whole surface, including that covering the holes. Holes were then carefully cut first through only the metal strips and then finally through the 3 mm of remaining balsa after each heat transfer test in the evaluation sequence.

Surface pressure taps were installed on the model at the location of each row of holes in order to measure the representative hole exit pressure. Pressure taps were also provided on the top and bottom of the model and along its span to align the model so that stagnation occurred on the leading edge along the model's midplane. All of the pressure-tap tubing, thermocouple leads, and power leads were led out of the back of the model. The internal cavity was filled with commercial fiberglass to reduce conduction losses and the surface was painted with a high-emissivity black paint. A detailed account of the model's fabrication is presented by Mick [15], and the heater construction is described by DiElsi and Mayle [16].

Test Conditions and Procedures

All the tests were conducted at a nominal Reynolds number Re_D of 100,000 based on the incident velocity and leading edge diameter, and at a mainstream temperature of 18°C . The secondary air temperature for the film effectiveness tests was maintained approximately 28°C above the mainstream. This temperature difference resulted in a secondary-to-mainstream density ratio of 0.91. For the heat transfer tests, the secondary and mainstream air temperatures were the same. All tests were conducted under steady-state conditions and, although steady state was normally attained in about 3 h, measurements were not taken until 6–8 h after the experiment commenced.

Both the film effectiveness and heat transfer tests were conducted with secondary-to-incident mass flux ratios M of 0.38, 0.64, and 0.97. These values are based on the average mass flow injected through only the two upper rows of holes at $+15$ deg and $+44$ deg even though air was always injected through all of the rows. On this basis, the present results may be compared directly to other symmetric injection schemes having the same average mass flux ratio. The flow split between the three rows of holes was determined by measuring the centerline velocity in each hole and forming a ratio between the average centerline velocity in each row. The ratio of the flow in the row at $+44$ deg to that at $+15$ deg was found to be 2.97, 2.44, and 1.72 for $M = 0.38, 0.64,$ and 0.97 , respectively. The ratio between that for the rows at ± 15 deg was always within 10 percent of unity.

As mentioned before, the film effectiveness tests were conducted by injecting heated air through the film holes without supplying power to the surface heater strips. Since the test surface is not truly adiabatic and the thermocouples were not exactly on the surface, several corrections had to be applied to the measured temperatures in order to obtain the adiabatic film effectiveness. These corrections included the effect of heat transfer by conduction through the substrate and heat loss by radiation to the surroundings. Interestingly, since the secondary air heated the inside of the model, heat was actually transferred to the surface by conduction in the film effectiveness tests. A one-dimensional heat balance on an element of the surface yields

$$q + q_{\text{rad}} + q_{\text{cond}} = 0$$

where q is the convective heat flux from the surface to the film, and q_{rad} and q_{cond} are the radiated and conducted heat flux from the surface, respectively. With

$$q = h(T_0 - T_{aw})$$

where h is the heat transfer coefficient with injection. T_0 and T_{aw} are the actual surface and adiabatic wall temperatures, respectively, the film effectiveness η is obtained as

$$\eta = \frac{(T_{aw} - T_\infty)}{(T_s - T_\infty)} = \frac{(T_m - T_\infty - \Delta T)}{(T_s - T_\infty)} + \frac{q_{\text{rad}} + q_{\text{cond}}}{h(T_s - T_\infty)}$$

where T_m is the measured surface temperature, T_∞ is the mainstream temperature, ΔT is the surface temperature correction, and T_s is the secondary air temperature. The

temperature correction ΔT was typically less than 0.5 percent of the secondary and mainstream temperature difference. While the magnitudes of q_{rad} and q_{cond} varied somewhat over the surface, they tended to cancel each other. Near the leading edge, the last term in the above expression for η was almost negligible, while farther downstream, where the effect of heating from the secondary air in the plenum was less, the last term produced a 3–10 percent correction on the effectiveness. In addition to making these corrections, estimates were made of the heat conducted parallel to the surface through the strips as a result of surface temperature gradients. Typically, it was found that conduction along the surface affected the effectiveness by less than 1 percent everywhere but near the injection holes, where large spanwise temperature gradients at a few locations between and immediately downstream of the holes produced estimated errors as high as 10–15 percent. Since accurate corrections for this effect are difficult to make, and since the areas affected were quite localized, the correction was not included in reducing the data. As a result, the reported film effectiveness data around the holes will be somewhat smoother than actually exists and the contours of constant effectiveness will be broader. The effect on the spanwise-averaged results is, however, considered negligible since the larger spanwise temperature gradients were simply smoothed.

The heat transfer tests were conducted by injecting air through the film holes with power supplied to the surface heater strips. Typically, the generated heat flux was about 780 W/m^2 and surface temperatures ranged from 26 to 46°C . The steady-state boundary condition on the heated surface was nominally that of constant heat flux everywhere except on the heater strips which contained holes. On the strips without holes, however, a slight modification was caused by surface radiation and heat conduction through the substrate. These effects, along with the local variations in strip resistance resulting from metal temperature variations, were included in the calculation of the heat transfer coefficients using an energy balance on a heated surface element

$$q + q_{rad} + q_{cond} = q_{gen}$$

together with

$$h = q / (T_m - T_\infty - \Delta T)$$

where q is the convective heat flux from the surface, h is the heat transfer coefficient with injection, as before, and q_{gen} is the measured generated surface heat flux. The approximate magnitudes of the heat flux and temperature corrections were: radiation, 10 percent of the generated heat flux; heat loss through the substrate, 2 percent; and temperature correction ΔT about 0.2 percent of the local wall, freestream temperature difference. As with the effectiveness data, the effect of heat conduction within the heater strips was estimated, but not included. The estimates indicate that downstream of the leading edge, $x/d > 9$, the heat conduction within the heater strips was less than 1 percent of the generated heat flux, while it was as high as 6 percent at a few locations near the holes. Again, as with the effectiveness data, the reported heat transfer results near these locations will be somewhat smoother than that which actually exists, while the effect on the spanwise-averaged results is negligible.

The variation of the generated heat flux q_{gen} in the strips with the holes was determined by comparing the data with holes cut in the strips alone (not through the balsa substrate) to those obtained without the holes. In both cases the flow and heat transfer results between the stagnation line and the centerline of the first row of holes should be identical. By assuming that the heat transfer coefficients in this region were the same both with and without holes cut in the strips, the actual heat flux generated q_{gen} around the holes could be determined. These calculated values were then used in the above

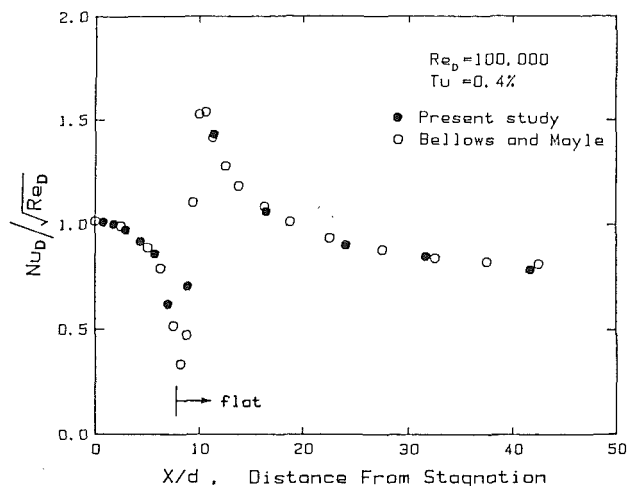


Fig. 4 Comparison of present two-dimensional heat transfer results with those of Bellows and Mayle [18]

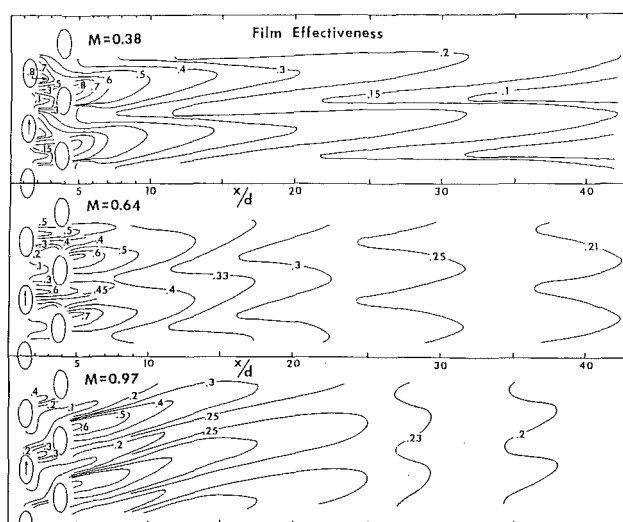


Fig. 5 Film effectiveness contours for three injection rates

equations for q_{gen} to determine the heat transfer coefficients on the strips with the holes. The same tests were used to evaluate the thermal history effect which resulted from the unequal heating of the surface. Once the variation of the generated surface heat flux around the holes was determined, the remaining difference in the results downstream of the holes was attributed to the effect of nonuniform surface heating on the development of the thermal boundary layer. Typically, the largest differences occurred immediately downstream of the holes where nearly a step change in heating took place as the flow passed from the balsa covered film hole onto the heating strip. The effect quickly disappeared and by $x/d = 6$ (within two hole diameters of the last row) the heat transfer coefficient for both cases differed by only 10 percent. Since the thermal history for the flow immediately behind the hole with injection was not modeled by this test, no correction was applied there. Slightly downstream, however, where the flow was perceived to be more in the streamwise direction, a correction which varied from about 10 percent near injection to zero further downstream was applied according to these results.

An uncertainty analysis was carried out for both the film effectiveness and heat transfer data according to the method of Kline and McClintock [17]. Downstream of the leading edge, based on 20-to-1 odds, the uncertainty is 3.5 percent for both. In the leading edge region, however, the uncertainty could be

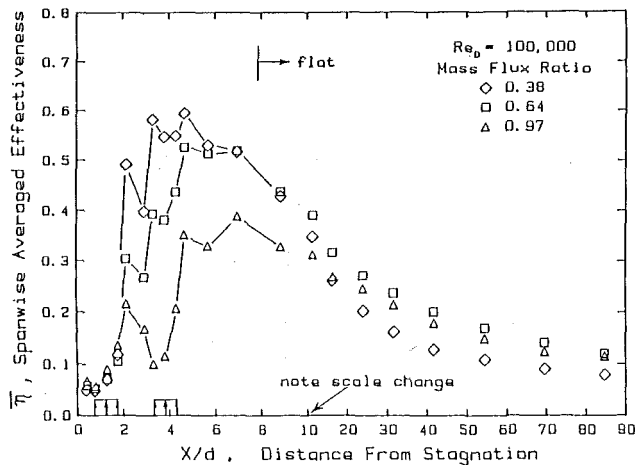


Fig. 6 Spanwise-averaged film effectiveness distributions

as high as 17 percent at those locations around and immediately downstream of the holes where the parallel conduction in the metal strips was neglected.

Results

As part of the test procedure outlined above, heat transfer tests were conducted on the model with the film holes covered and the heater strips uncut. For this case, the heat transfer coefficient depends only on the streamwise distance x along the surface. These results are presented in Fig. 4 as a Nusselt number Nu_D (based on the leading edge diameter) scaled by the square root of the Reynolds number. To reduce confusion in later comparisons, the abscissa has been scaled using the injection hole diameter d , even though the holes did not exist. The results of Bellows and Mayle [18] for an identically shaped model, test configuration, and identical flow conditions are also shown in the figure. As discussed in [18], the precipitous decrease and rapid rise of the Nusselt number around $x/d = 8$ is a result of a separating leading edge laminar boundary layer followed by a turbulent reattachment. Evidently, the flow over the previous model, including the separation bubble, has been accurately reproduced in the present experiment.

The film effectiveness results for each secondary-to-mainstream mass flux ratio are shown in Fig. 5. In this figure, isoeffectiveness contours are shown over a span of two hole pitches even though only enough data were taken to describe the distribution uniquely over a single pitch. These contours are shown only for x/d less than 40. Beyond these streamwise locations, the effectiveness only decayed slightly. The direction of secondary-air injection is toward the top of the figure.

Between the stagnation line and the first row of holes, the effectiveness was nearly uniform in both the spanwise and streamwise directions. For the lowest mass flux ratio $M = 0.38$, very little secondary-air flow is injected through the holes at ± 15 deg (about $\frac{1}{3}$ that through the second row). This is evident in the figure from the shape of the film effectiveness contours just downstream of the first row, which indicate little flow reaching the furthest spanwise extremity of the holes. In contrast, the flow appears to reach the furthest extremity of the holes in the second row which, without much flow from the first row, produces rather large spanwise variations in film effectiveness downstream of the hole pattern. For $M = 0.64$, the film effectiveness distribution is much more uniform in the spanwise direction. This is a result of the increased flow from the first row of holes covering the surface between the holes in the second row. Directly downstream of the holes in both rows, however, a noticeable decrease is seen in the film effectiveness

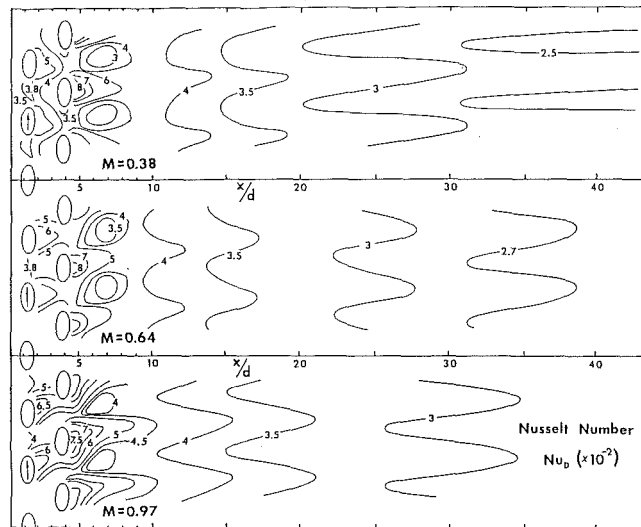


Fig. 7 Nusselt number contours with injection

compared to that for the lower mass flux. Evidently, this is a result of the air from the second row of holes being injected farther into the mainstream. The overall increase in the injected secondary flow dominates, however, and produces an increased film effectiveness over most of the downstream surface. Further increasing the mass flux ratio to $M = 0.97$ apparently increases the penetration of injected air into the mainstream and actually reduces the effectiveness around the holes below that for either $M = 0.38$ or $M = 0.64$. In addition, it can be seen that the flow from holes in the second row interferes with that from the first, perhaps raising it off the surface. More important, however, is that the flow from the first row does not cover the surface between the holes in the second row, thus permitting the mainstream to flow near the surface between the holes in both rows reducing the effectiveness. Interference between flows from spanwise-directed holes and its adverse effect on film effectiveness have been noted before by Mayle and Camarata [19].

The spanwise-averaged film effectiveness $\bar{\eta}$ is presented in Fig. 6 for all three mass flux ratios. These values were calculated using

$$\bar{\eta} = \frac{1}{P} \int_0^P \eta(x, z) dz$$

where z is the spanwise distance and P is the hole pitch. For spanwise averages between the holes, the average was taken over only the surface between the holes and not over the hole area.

The reasons for the general trends in the spanwise-averaged effectiveness are similar to those just described. The lowest mass flux ratio is seen to provide the highest average effectiveness in the leading edge region because even though the amount of secondary air injected is small, it remains near the surface. Although lower in the leading edge region, the effectiveness for injection with $M = 0.64$, is highest over the rest of the surface. Injection at the highest mass flux ratio, however, produces the lowest average effectiveness initially, and never rises above that for $M = 0.64$. Obviously, the effectiveness for the high injection rate suffers from excessive penetration, jet interference, and the subsequent mixing such that although the volume of injected air is large, it becomes highly diffused within the mainstream.

Contour plots giving the variation of the Nusselt number with injection are presented in Fig. 7. For the purpose of comparison, it is helpful to know that the Nusselt number over the leading edge region without injection is about 300 (from Fig. 4

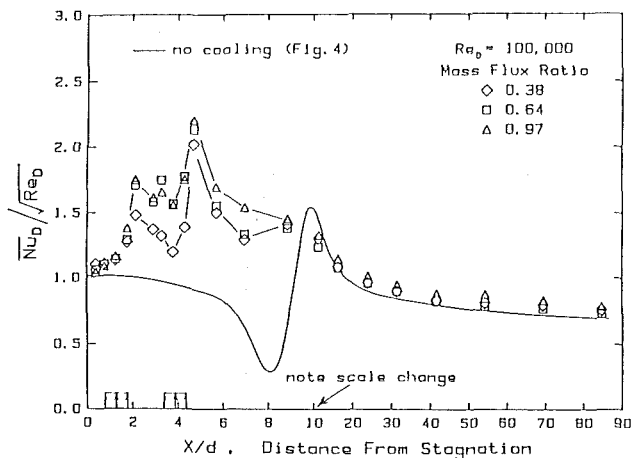


Fig. 8 Spanwise-averaged Nusselt number distributions

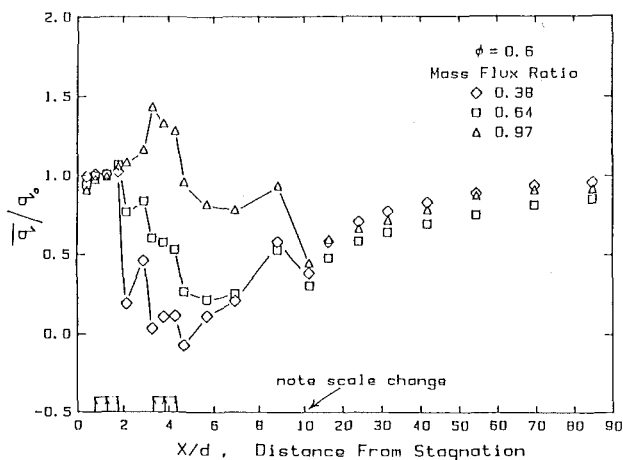


Fig. 9 Effect of film cooling on the surface heat load, $\phi = 0.6$

with $Re_D = 100,000$). In the region between the stagnation and the first row of holes, the heat transfer distribution for all the flow rates is uniform in both the streamwise and spanwise directions and only slightly above that without injection. Immediately downstream of injection, however, significant variations of the Nusselt number are found having values two to three times higher than those without injection. In general, the regions of high Nusselt number do not correspond to the locations where the film effectiveness is high. In fact, a careful comparison of Figs. 5 and 7 indicates that the high Nusselt number regions lie roughly between the regions of highest and lowest effectiveness and are further displaced toward the regions of low effectiveness as the mass flux ratio is increased. If one considers the region of high effectiveness as the location of the secondary air jet, then the high heat transfer coefficients are found along the edge of the jet on the side nearest the hole. High heat transfer coefficients along a cooling jet's edge were also found by Erickson and Goldstein [3] for injection through a streamwise-angled hole. As will be shown shortly, this has a far-reaching implication with regard to the actual benefit of a leading edge cooling scheme.

The distributions of the spanwise-averaged Nusselt number are presented in Fig. 8. These values were calculated using

$$\bar{Nu}_D = \frac{1}{P} \int_0^P Nu(x, z) dz$$

in accordance with the expression for determining the spanwise-averaged film effectiveness. Within the leading edge region, a substantial increase over the case without injection is

evident. In particular, the variation for all three blowing rates is quite similar, increasing only slightly with an increasing mass flux ratio. There are noticeable peaks immediately downstream of each row of holes, presumably caused by the flow of the mainstream around, and perhaps under, the injected air. For the low mass flux ratio, the peak following the first row is somewhat smaller and decays quicker than for the other two flow rates. This is most likely a result of the injected fluid from the first row remaining near the surface for this case. The spanwise-averaged Nusselt number downstream of the leading edge ($x/d > 10$) is only slightly greater than that without injection. This increase is about 8, 5, and 12 percent for the mass flux ratios of 0.38, 0.64, and 0.97, respectively.

Application of the present results to leading edge film cooling requires calculating the local heat load distribution over the film cooled surface. For a film-cooled surface, the local heat flux to the surface is given by

$$q = h(T_{aw} - T_0)$$

With the heat flux to an uncooled surface given by

$$q_0 = h_0(T_\infty - T_0)$$

where q_0 is the heat flux for a smooth surface without holes and h_0 is the corresponding heat transfer coefficient, the ratio of heat flux with film cooling to that without may be expressed as

$$q/q_0 = (h/h_0)(1 - \eta/\phi)$$

where η is the local film effectiveness, and ϕ is the overall cooling effectiveness, i.e.,

$$\phi = (T_\infty - T_0)/(T_\infty - T_s)$$

For modern gas turbine components, ϕ is typically about 0.6.

Distributions of the spanwise-averaged heat flux ratio \bar{q}/q_0 are presented in Fig. 9 for each of the mass flux ratios. The ordinate of this figure has been calculated using

$$\bar{q}/q_0 = \frac{1}{P} \int_0^P [h(x, z)/h_0][1 - \eta(x, z)/\phi] dz$$

with $\phi = 0.6$. Curves for different values of ϕ can be obtained by using the information presented in this figure as well as that in Fig. 8. Note that the above expression involves the average of the product between the heat transfer coefficient and the film effectiveness, and not the product of their averages. Using the latter can produce errors of ± 100 percent in the calculated heat flux near injection as may be determined simply from Figs. 6 and 8.

In general, leading edge injection is seen to reduce the heat flux over most of the surface for all three mass flux ratios. The striking exception is for injection at the high mass flux ratio where directly behind the second row of holes nearly a 50 percent increase in heat flux is found. Between stagnation and the first row of holes there is almost no effect on the heat flux, which simply implies that the small increase found there in both the film effectiveness and heat transfer coefficient offset one another. Over the remaining leading edge surface, however, the heat flux strongly depends on the mass flux ratio. In particular, the results for the low and middle mass flux ratio exhibit significant reductions in surface heat flux, with the $M = 0.38$ case actually yielding a negative value, i.e., heat flow from the surface to the film. As indicated earlier, the regions of high effectiveness corresponded more closely to the regions of high heat transfer coefficient (Nusselt number) for the lowest injection rate. In fact, at $M = 0.38$ for $\phi = 0.6$, there are significant regions behind and downstream of injection where $q(x, z)/q_0 < 0$ and heat is transferred to the coolant. In this case, the jets may be considered to be acting as heat exchanger tubes attached to the surface. As the blowing rate is increased, however, both the disparity between the regions of high effectiveness and Nusselt number increases

and the film effectiveness decreases. This in turn reduced the benefit of cooling in the leading edge region to a point where for $M = 0.97$ it is minimal and in some areas detrimental. As pointed out earlier, Luckey and L'Ecuyer [10] obtained a similar result. Downstream of the leading edge, however, injection always decreases the surface heat flux. For $\varphi = 0.6$, the reduction varies from roughly 60 percent near the leading edge to about 10 percent far downstream. Unlike the leading edge result, however, the reduction in heat flux is greatest for the intermediate mass flux ratio of 0.64. Presumably, this is a consequence of too little coolant being injected at the low mass flux ratio and too much being injected, such that it penetrates too far and mixes into the mainstream, at the high mass flux ratio. Using the simple criterion established by Luckey et al., for estimating the coolant blowing ratio for an optimum film cooling performance when $x/d > 6.5$, one obtains $M_{opt} = 0.76$ for the present series of tests. Although this is seen to agree with the present downstream results, it is apparent that the same criterion cannot be applied to the leading edge region itself.

Conclusions

Detailed measurements of film effectiveness and heat transfer indicate that large variations of these quantities exist both in the leading edge region within the hole pattern and downstream. Downstream of the holes, the variations are mainly in the spanwise direction corresponding more or less to a direction normal to the jets. In particular, the film effectiveness immediately behind the holes was found to be about 0.6–0.8 depending on the mass flux ratio, while further downstream it approached 0.1. Near the holes, heat transfer coefficients as high as three times that without injection were measured. Shortly downstream, however, they quickly approached values approximately 10 percent above that without injection.

In the leading edge region, the film effectiveness was actually found to decrease with an increase in the mass flux ratio. This behavior is quite different from that found downstream of the leading edge and is attributed to an increased penetration of the injected air into the mainstream. Farther downstream, where most of the previous investigations concentrated, however, a balance is found between the amount of air injected and its penetration such that an optimum effectiveness is attained at a higher mass flux ratio. The mass flux ratio for which this occurred in the present tests was 0.64, which closely corresponds to the values obtained by others. For the turbine designer, this implies that a decision must be made to film cool either the leading edge or the downstream surface efficiently.

Finally, it was found that the regions of high effectiveness do not necessarily correspond to the regions having a high heat transfer coefficient, and that the disparity between the two increases with increasing mass flux ratio. This is particularly important in the leading edge region between and immediately

behind the holes where large variations in both are observed. For high mass flux ratios, the disparity not only reduces the film cooling benefit to a point where it is nonexistent, but reverses it.

Acknowledgments

The work reported in this paper was sponsored by Pratt & Whitney Aircraft, United Technologies Corporation, East Hartford, CT.

References

- 1 Metzger, D. E., and Fletcher, D. D., "Surface Heat Transfer Immediately Downstream of Flush, Nontangential Injection Holes and Slots," AIAA Paper No. 69-523, 1969.
- 2 Goldstein, R. J., "Film Cooling," *Advances in Heat Transfer*, Vol. 7, Academic Press, New York, 1971, pp. 321-379.
- 3 Eriksen, V. L., and Goldstein, R. J., "Heat Transfer and Film Cooling Following Injection Through Inclined Circular Tubes," *ASME Journal of Heat Transfer*, Vol. 96, 1974, pp. 239-245.
- 4 Mayle, R. E., Kopper, F. C., Blair, M. F., and Bailey, D. A., "Effect of Streamline Curvature on Film Cooling," *ASME Journal of Engineering for Power*, Vol. 99, 1977, pp. 77-82.
- 5 Ito, S., Goldstein, R. J., and Eckert, E. R. G., "Film Cooling of a Gas Turbine Blade," 1977 Tokyo Joint Gas Turbine Congress, 1977, Paper No. 03.
- 6 Tillman, E. S., and Jen, H. F., "Cooling Airflow Studies at the Leading Edge of a Film-Cooled Airfoil," *ASME Journal of Engineering for Gas Turbines and Power*, Vol. 106, 1984, pp. 214-221.
- 7 Tillman, E. S., Hartel, E. O., and Jen, H. F., "The Prediction of Flow Through Leading Edge Holes in a Film Cooled Airfoil With and Without Inserts," *ASME Journal of Engineering for Gas Turbines and Power*, Vol. 107, 1985, pp. 92-98.
- 8 Hanus, G. J., and L'Ecuyer, M. R., "Leading Edge Injection for Film Cooling of Turbine Vanes," *Journal Energy*, Vol. 1, 1977, pp. 44-49.
- 9 Luckey, D., Winstanley, D., Hanus, G. J., and L'Ecuyer, M. R., "Stagnation Region Gas Film Cooling for Turbine Blade Leading-Edge Applications," *Journal of Aircraft*, Vol. 14, 1977, pp. 494-501.
- 10 Luckey, D. W., and L'Ecuyer, M. R., "Stagnation Region Gas Film Cooling—Spanwise Angled Injection From Multiple Rows of Holes," NASA CR 165333, 1981.
- 11 Sasaki, M., Takahoru, K., Sakata, K., and Kumagai, T., "Study on Film Cooling of Turbine Blades," *Bulletin Japan Soc. Mech. Engrs.*, Vol. 19, 1976, pp. 1344-1352.
- 12 Camci, C., and Arts, T., "Experimental Heat Transfer Investigation Around the Film-Cooled Leading Edge of a High Pressure Gas Turbine Rotor Blade," *ASME Journal of Engineering for Gas Turbines and Power*, Vol. 107, 1985, pp. 1016-1021.
- 13 Wadia, A. R., and Nealy, D. A., "Development of a Design Model for Airfoil Leading Edge Film Cooling," ASME Paper No. 85-GT-120, 1985.
- 14 Salter, C., "Experiments on Thin Turning Vanes," ARC RM 2469, 1946.
- 15 Mick, W. J., "An Experimental Study of Stagnation Region Film Cooling for Application to Gas Turbine Airfoils," Master's Thesis, Rensselaer Polytechnic Institute, Dec. 1983.
- 16 DiElsi, G., and Mayle, R. E., "A Composite Constant Heat Flux Test Surface," in: *Heat and Mass Transfer in Rotating Machinery*, D. E. Metzger and M. H. Afgan, eds., Hemisphere, Washington, DC, 1984, pp. 259-268.
- 17 Kline, S. J., and McClintock, F. A., "Describing Uncertainties in Single Sample Experiments," *Mechanical Engineering*, 1953, pp. 3-8.
- 18 Bellows, W. J., and Mayle, R. E., "Heat Transfer Downstream of a Leading Edge Separation Bubble," *ASME Journal of Turbomachinery*, Vol. 108, 1986, pp. 131-136.
- 19 Mayle, R. E., and Camarata, F. J., "Multihole Cooling Film Effectiveness and Heat Transfer," *ASME Journal of Heat Transfer*, Vol. 97, 1975, pp. 534-538; Air Force Aero Propulsion Laboratory Report AFAPL-TR-73-30, 1973.

Turbulence Measurements in Turbine Blade Passages and Implications for Heat Transfer

W. J. Priddy¹

Mechanical Engineer,
B. P. Research Center,
Sunbury-on-Thames

F. J. Bayley

Professor of Mechanical Engineering,
University of Sussex,
Brighton, BN1 9QT,
United Kingdom

This paper describes a program of research in which, by using laser-Doppler anemometry, the variations of artificially induced flow perturbations to represent turbulence in an engine have been measured through the passages of a cascade of modern turbine blades. Although based upon commercially available laser-Doppler equipment, the special problems of making reliable and reproducible measurements in the demanding flow conditions of highly loaded turbine blades required special facilities in the apparatus and these are briefly described in the paper. The results themselves provide some confirmation of the common—but hitherto unjustifiable—assumption that the absolute level of velocity fluctuation remains essentially constant as the time-mean velocities change significantly. The results also show significant departures from this assumption, especially on the forward suction surface and near the leading edge. These observations throw some light upon the observed variation in the distribution of convective heat transfer rates to blades in the highly unsteady conditions which characterize the flows in the real turbine, compared with the idealizations of many experimental and theoretical simulations.

Introduction

It is well known that the unsteadiness in the flow of working fluid through real turbines affects the associated rates of convective heat transfer. Equally well known are the difficulties of classifying this unsteadiness, whether it results from the essentially random fluctuations that are defined as “turbulence” in fluid dynamics or the more ordered fluctuations that result, for example, from the passage of an upstream row of rotor blades. Many parameters have been argued as of significance in defining an unsteady flow, and some of our own work has demonstrated the apparently separable role of the frequency of the fluctuations, more especially when these are of large amplitude [1]. Generally, however, the “intensity” of the fluctuations—defined as the root mean square of the fluctuations of the velocity components normalized with reference to the local time-mean velocity vector of the main flow—has emerged as the most significant quantifying parameter of an unsteady flow. Certainly, variations in heat transfer rates over general areas of a blade, like the leading edge or over the pressure surface, appear to be affected most critically by the intensity or amplitude of fluctuation, leaving the effects of all other definable variables as secondary by comparison.

The intensity of the turbulence—to use this term as generic for all unsteady flows—is measured most commonly by

¹Formerly, Research Fellow, Thermo-Fluid Mechanics Research Centre, University of Sussex, United Kingdom.

Contributed by the Gas Turbine Division of THE AMERICAN SOCIETY OF MECHANICAL ENGINEERS and presented at the 32nd International Gas Turbine Conference and Exhibit, Anaheim, California, May 31–June 4, 1987. Manuscript received at ASME Headquarters February 19, 1987. Paper No. 87-GT-195.

anemometers of the hot-wire type, in which the variation in heat loss from the wires can be calibrated to give an accurate measure of instantaneous velocity vector. Although such instruments can be made small and maneuverable, it is not possible to traverse these through the narrow confines of realistic turbine blade passages, certainly not without the finite bulk of the instrument disturbing the sensitive flows in them. Thus for turbine blades it has hitherto been the universal practice to measure the intensity of fluctuation upstream of the blade rows and to use such measurements as the only representation of the conditions within the passages. It has been necessary to assume either that the upstream intensity, unrealistically, is unchanged by the acceleration and decelerations of the flows over the blade surfaces; or more usually, although hitherto as unjustifiably other than on the grounds of convenient simplicity, that the absolute level of velocity fluctuation remains constant or changes in some arbitrary way.

The availability of sophisticated laser-Doppler anemometry has made possible the nonintrusive tracking of velocities, both time-mean and instantaneous values, in many of the complex and restricted geometries associated with engineering components. This is certainly the case for the blade passages that are the subject of the present paper, although the sharp curvature of the flows and the high levels of acceleration make for special problems, the solution of which are described in the following text.

Apparatus

Wind Tunnel and Cascade. This part of the equipment

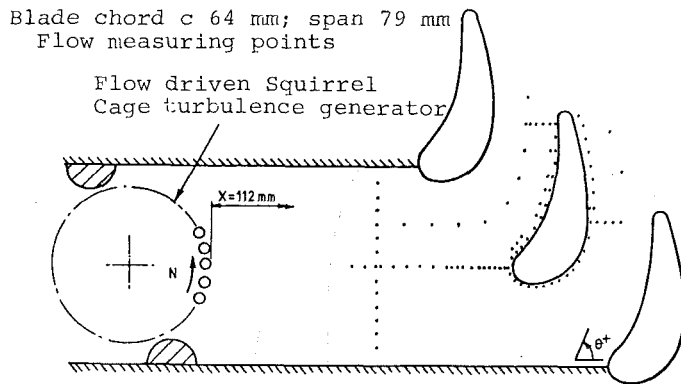


Fig. 1 Blade cascade and turbulence generator

used in the present investigation has been previously described in detail [1, 2] and is only briefly outlined here. A centrifugal blower supplies air at pressures equivalent to outlet Mach numbers up to a little over 0.8, through a contraction designed to give a uniform velocity and a turbulence intensity of about $\frac{1}{2}$ of one percent in the absence of deliberately induced perturbations. These can be provided by static grids of different meshes to alter the turbulence intensity or by a "squirrel cage," which can if required, and as fully described in [1], be driven electrically over a range of speeds to control separately the frequency of the perturbations and, either by changing the diameter of the bars of the squirrel cage or its distance from the blades, the intensity, or amplitude, of fluctuation at the cascade entrance. For the present work, the squirrel cage, fitted with 30 bars, 2.4 mm in diameter pitched 6 mm apart, was positioned upstream of the cascade so that it produced a mean turbulence intensity of about 10 percent at the leading edge plane, with no characteristic frequency but a spectrum ranging up to about 10 kHz when rotated freely by the mainstream air flow through it. This device had been found [3] to give a uniform two-dimensional flow through the cascade up to turbulence intensities in excess of 20 percent, unlike the coarse grids normally used for this purpose which were found to distort the flow.

The cascade comprises three blades which, for the present work, had the profile of the midsection of the first-stage rotor blades of a current aeroengine (blade A of [3]). The two outer blades were manufactured from an aluminum-plastic material, while the center blade was made of steel. Flow visualization using surface paints had previously established the two-dimensional nature of the flow over this blade at the midspan of the cascade with and without the squirrel cage turbulence generator. A similar blade, instrumented with pressure tappings staggered over its center $\frac{1}{3}$ span, had provided data on the velocity distribution through the cascade [3].

For the present program the side walls of the cascade, in the view shown as Fig. 1, were manufactured from rectangular slabs of float glass 1 cm thick. These formed a tight butt fit

with the surrounding aluminum frame and were held in place at the edges by clamps cushioned by thin PTFE strips. The center blade was supported from the glass sidewalls by dowels surrounded by an annulus of 0.4 mm of epoxy resin and this design minimized the thermal stresses on the glass while allowing maximum optical access to the flow channels on either side of the blade.

Laser-Doppler Anemometry. The choice of anemometry system was largely determined by the flow conditions in the cascade, in which time-mean velocities up to 400 m/s occur, more especially in a region of high surface curvature, with streamwise and cross-stream gradients up to 30 m/s per mm. Onto this were to be superimposed the turbulent fluctuations of 10 percent and more of the approach velocity with frequencies of up to 10 kHz. The required spatial resolution in a flow with such large velocity gradients dictated an optical probe volume of around 0.1 mm diameter, and the associated optics implied Doppler frequencies in the range 1 to 100 MHz.

Consequent signal processing requirements then led inevitably to the burst counter mode of operation in which the signals resulting from single particle transits through the probe volume can be analyzed. Unfortunately, the burst counter is highly susceptible to noise so that with the need to make measurements close to the blade surface under the demanding velocity conditions described above, which in their turn constrained seeding conditions (to be described later), a relatively powerful laser source became necessary, and a 2-W argon unit was selected. With the consequent optical requirements and the limited space in the test cell, a compact, double-deck arrangement of laser and optical train had to be designed and is shown in the photograph of Fig. 2. The cascade and the center blade may be seen in the top right of the figure with the argon laser below and running the full width of the rig. Its beam is deflected up and back by two mirrors in the cylindrical column to the right of the photograph, through the main transmission optics in which the laser beam is first split into two and then focused down to converge at the probe volume in the flow through the cascade. A traversing mechanism, located below the laser, utilizing stepper motors operating at 2000 steps per second with 400 steps per mm in the horizontal direction and 1000 vertically, allowed the probe volume to be located in the cascade with an accuracy estimated at 1.5 mm per meter horizontally, and better than this vertically.

The transmission optics, based like the complete anemometry system upon a commercially available package from TSI (Inc.), was chosen for single component velocity measurement and to give a 9-mm separation between the split beams which with the lens system gave better than the required 0.1 mm probe diameter at the intersection, with ten fringes of nominally $7.9 \mu\text{m}$ pitch. A collimator was found necessary to achieve uniform pitching of the fringes along the length of the probe volume, which was estimated from the transmission optics to be about 2 mm, comparable with hot-wire anemometer dimensions and acceptable.

Nomenclature

c = blade chord	number of time/velocity samples	U_i = instantaneous velocity measurement
h = local heat transfer coefficient in perturbed stream	Re = exit Reynolds number	v, w = cross-stream fluctuating velocity components
h_0 = local heat transfer coefficient in steady flow	Re_θ = boundary layer momentum thickness Reynolds number	V_2 = exit velocity
i = index of summation	Tu = turbulence intensity = $\langle u \rangle / U \times 100$	V_∞ = approach velocity far upstream
K = acceleration parameter = $(v/U^2) (dU/dx)$	u = fluctuating streamwise velocity component	x = surface distance measured from geometric leading edge
N = cage rotational speed;	U = mean streamline velocity	ν = kinematic viscosity



Fig. 2 The LDA rig

Beyond the cascade in Fig. 2 may just be seen the collection optics of the system, working as all the requirements of this investigation dictated, in the forward scatter mode. Here accurate alignment with appropriate manual adjustment was necessary to discriminate and optimize the light scattered from the probe volume to the photodetector surface, as indicated by the raw and conditioned signals on the monitor, examples of which are shown in Fig. 3. The conditioning was achieved by filtering and amplification before counting inside selected threshold levels in the standard TSI unit which may be seen in the racks on the left of Fig. 2. This equipment allowed the number of cycles counted to be selected and four was adopted corresponding to approximately half the number of fringes in the probe volume, a choice recommended to reduce biasing in regions of highly fluctuating velocities with significant transverse components. All the velocity measurements made used the so-called comparison option in which the selected number of cycles is counted and then the burst time compared with that of a separate count of half the number of cycles. If the two-to-one comparison was not satisfied within a predetermined tolerance the reading was rejected. The minimum available tolerance of 0.8 percent was selected in this program with entirely acceptable processing times. A sample of up to 4000 transit times could be processed, but 400 gave acceptable results even at the highest levels of velocity fluctuation.

In the example of typical signals from the investigation shown as Fig. 3, raw burst data can be compared with the corresponding signal after conditioning but before counting and transmission to the computer, also visible in the racks of Fig. 2. As well as controlling the traversing mechanism, this has been programmed to convert the time measurements and fringe spacing to velocities. A typical steady flow velocity histogram from the computer is shown as Fig. 4. Preliminary study of such histograms permitted the elimination of obviously spurious observations, in particular those resulting from the velocity lag caused in regions of especially high ac-

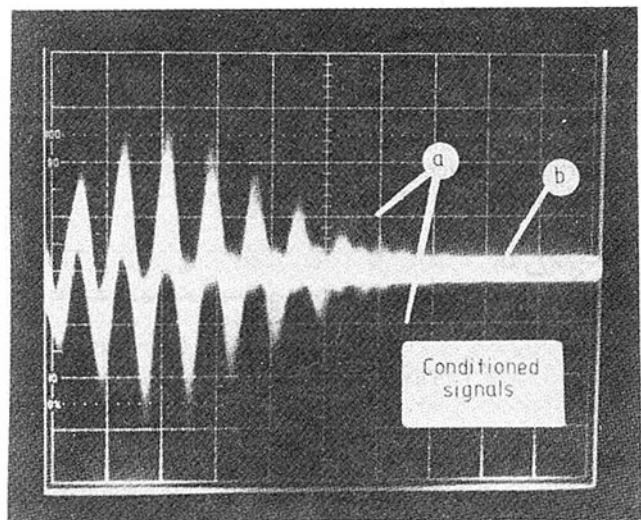
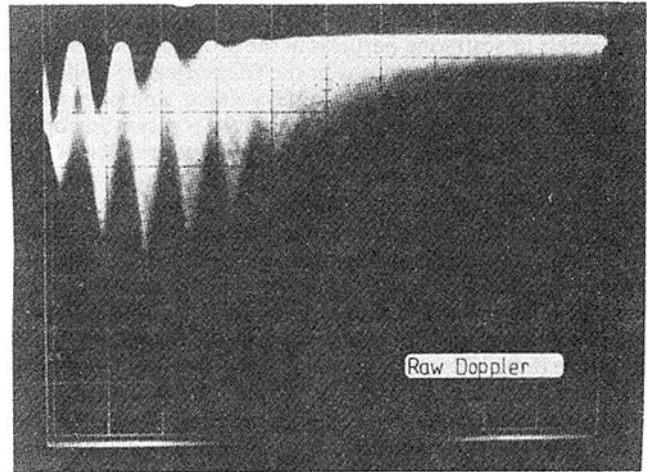


Fig. 3 Doppler signals on scope: (a) threshold level of burst counter; (b) high-frequency noise level

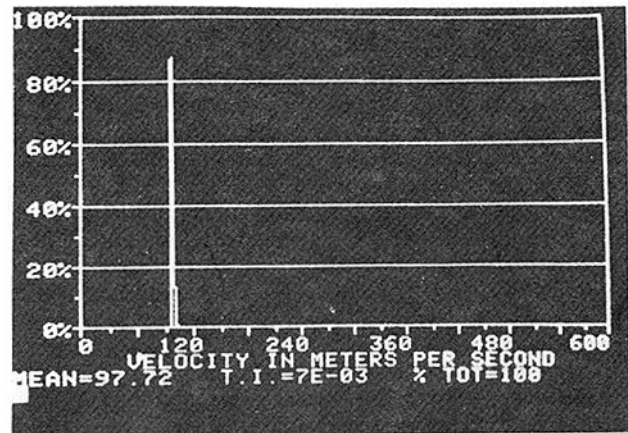


Fig. 4 Velocity histogram for low-turbulence flow

celeration by inappropriate seeding and which showed typically as a low-velocity tail to the histogram.

The criticality of the seeding level, both with respect to particle size and number, early became very clear in this investigation. Too high a seeding concentration could cause the threshold amplitude criteria of the signal processor to be violated. Also, although increases in laser power and gain in

the signal conditioner could be made to compensate for sparseness of scattering particles in the probe volume in terms of signal strength, distortions in the fringe spacing well away from the bright center of the probe volume, and only partly removed by the use of the collimator in the transmitting optics previously described, could give spurious results. Overdependence upon light scattered from large, possibly naturally occurring, particles which tend to lag rapidly accelerating flows and not to follow highly curved streamlines, also leads to erroneous steady and fluctuating velocity measurements. However, comparison with earlier results obtained near the cascade inlet with conventional hot-wire anemometry allowed the optimization of the seeding process. A commercially available theatrical smoke generator – the Concept Genie – using Shell Ondina 17 oil with a carbon dioxide driving pressure of 2.8 bar was found to give the appropriate density of particles and with only 1 percent greater than 0.6 μm diameter. Brief injections of such seeding at the blower intake for only a few seconds when test conditions were ready for readings to be taken also delayed fouling of the glass sidewalls of the cascade to a degree at which signal levels were vitiated.

With the apparatus as described above, it became possible to make measurements through the blade cascade entirely consistent with mean velocities derived from the pressure-tapped blade and, where comparison was valid, with the earlier hot-wire anemometry observations, of the time-mean velocity and the turbulence intensity of the flow. These were defined respectively for the laser-Doppler analysis by

$$U = \frac{1}{N} \sum_{i=1}^N U_i$$

$$Tu = \frac{\text{rms}}{U} = \frac{1}{U} \sqrt{\frac{\left[\sum_{i=1}^N U_i^2 - NU^2 \right]}{(N-1)}}$$

Fuller details than are necessary for the present paper of the laser-Doppler equipment and experimental technique are given in [4].

Experimental Measurements – Procedure

The mounting system of the transmission optics provided for rotation of the beam splitter module, thus permitting the direction of measurement in the plane of the intersecting beams and perpendicular to the optical axis to be set at any angle with an accuracy estimated at one degree. In this way the flow streamlines could be traced and the local turbulence intensity was defined in terms of the fluctuating velocity component in the mean direction of the flow.

To measure the flow conditions in the free stream immediately outside the boundary layer, the optical probe volume was located at a number of stations close to the center blade surface. At each of these points the beam plane was yawed to the local angle of the tangent to the blade profile. The geometric leading edge of the blade section was chosen as the origin of the traverses, and with the tunnel operating temperature of 90°C causing a movement from cold of about 2 mm, it was necessary to await thermal equilibrium before aligning the laser beam at the leading edge datum. After each set of measurements in the flow the anemometer was returned to the datum position to check for further movement and the datum itself verified. It is estimated that by these procedures positional accuracies of within ± 0.5 mm were achieved in the placement of the probe volume.

On the pressure side of the blade, where the effects of mainstream fluctuation on rates of heat transfer are known to be especially significant, traverses were made along the blade section at distances of 1 mm and 3 mm from the surface. For

the conditions of the present tests the boundary layer thicknesses were of the order of 0.5 mm and it was not possible to detect the edge of the boundary layer, but the excellent agreement between the laser-Doppler measurements of mean velocity at 1 mm from the blade and those derived from the surface pressure readings suggested that the former were representative of mainstream conditions in the flow just outside the boundary layer. Furthermore, there was little detectable difference between the measurements of turbulence levels at the 3 mm and the 1 mm positions.

On the suction or convex side of the blade, in the upstream regions of extreme acceleration in the flow, boundary layers are even thinner than on the pressure side and readings at 1 mm from the surface were taken also as representative of mainstream conditions close to the edge of the boundary layer. On the downstream half of the blade the boundary layer is thicker and measurements 1 mm from the surface revealed the velocity decrement. Thus in these regions, where, because of the earlier transition to turbulence even in unperturbed flow, superimposed fluctuations have little effect upon the transport properties of the boundary layer, laser-Doppler readings were taken only at the 3-mm level.

Traverses of the anemometry system were also made along the flow at the channel centerlines. At these positions the mean flow direction had to be estimated and a 2 percent variation in the mean velocity was observed as the probe direction was varied through ± 10 deg. The apparent fluctuating component was more sensitive to probe orientation and its magnitude could be varied by up to 10 percent by rotation. However, the direction of the time-mean vector could be more closely estimated, so that this potential source of error was not significant.

As may be seen in Fig. 1, where the measurement locations are indicated, traverses along the stream were made also toward the geometric leading edge of the center blade and across the flow at the cascade inlet and at the blade throats. Generally it is estimated that the time-mean velocity could be measured at all positions within a random error of 1 percent. Measurements of the fluctuating components are more sensitive, as has been seen with the effects of probe rotation above. In addition, the data collection and analysis procedure has a tendency to biasing toward the high-velocity end of the histogram, leading to errors which can be important in highly unsteady flows, and especially in the apparent turbulence intensity which is, after all, a relatively small fraction of the mean velocity. The rigor of the experimental procedure adopted here was designed to minimize the errors and certainly the turbulence intensity was repeatable generally to within 5 percent of its mean magnitude. The scatter is shown where significant in Figs. 5–8.

General Observations

Figure 5 shows a set of readings of turbulence intensity obtained by the procedures described above. The flow parameters are specified in the figure and represent conditions of turbulence intensity which are thought to be typical of those in a turbine. The highest frequency of the perturbations is less than might be found in an engine, but earlier work has shown that the turbulent energy, especially at the higher frequencies, downstream of the turbulence generator spreads rapidly across the full spectrum. The Reynolds number is rather less than would be found in modern engines, certainly at full power, but the present work over the range of variables studied indicates that the distribution of turbulence intensity indicated in Fig. 5 is very typical.

The mean intensity of turbulence measured in the approach plane is 13.1 percent, although the flow-driven rotating turbulence generator skews the distribution with lower values to

Exit Reynolds No. 7.4×10^5 ; $V_2 = 210$ m/s
Speed N 9,500 r.p.m.

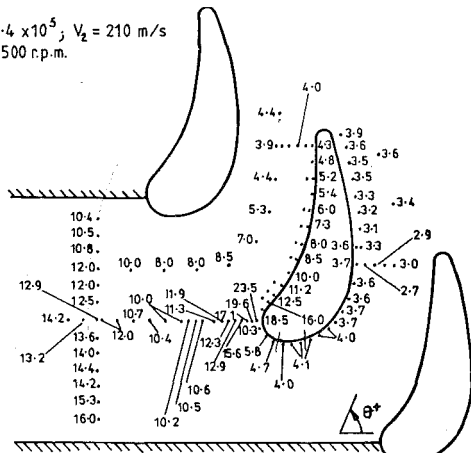


Fig. 5 Typical measurements of turbulence intensity

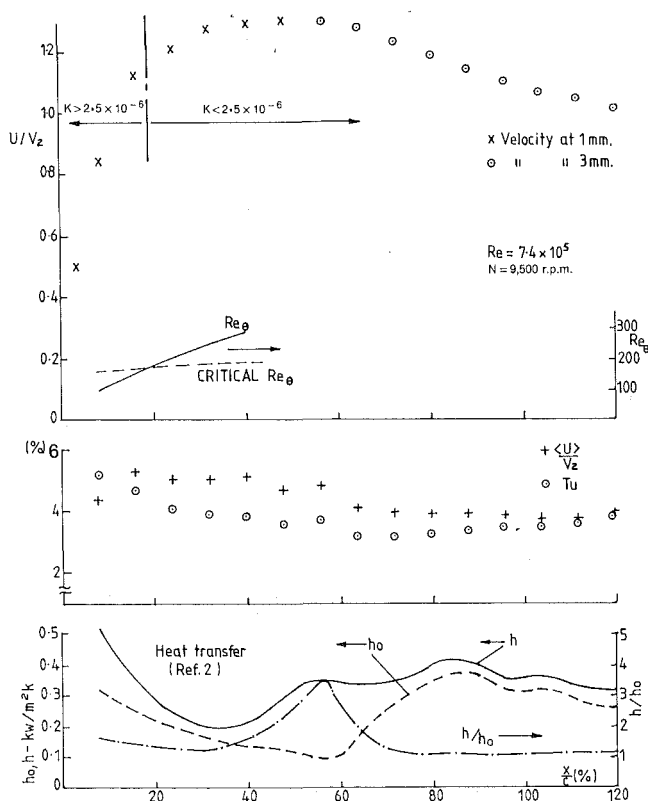


Fig. 6 Local turbulence and heat transfer—suction surface

the top of the tunnel. The traverse of the anemometer probe volume along the centerline of the passages between the blades gives a general representation of how the turbulence intensity varies through the passage. It is seen to fall almost monotonically from the high approach level to a value of 4.4 percent in the left-hand passage and to just under 4 percent in the right-hand passage where, because of the cascade stagger to simulate the rotation vector, the path length of the flow is longer. Also noteworthy are the almost constant turbulence intensities in the cross-stream traverses at the cascade throats and exit. Comparing these observed variations in turbulence intensity in the blade passages with the velocity distributions around the blade section, as in Figs. 6 and 7, indicates that the absolute amplitude of the turbulent fluctuations is little changed through the passages, certainly when compared with the observed changes in local turbulence intensity. This conclusion is confirmed in general by consideration of the fluctua-

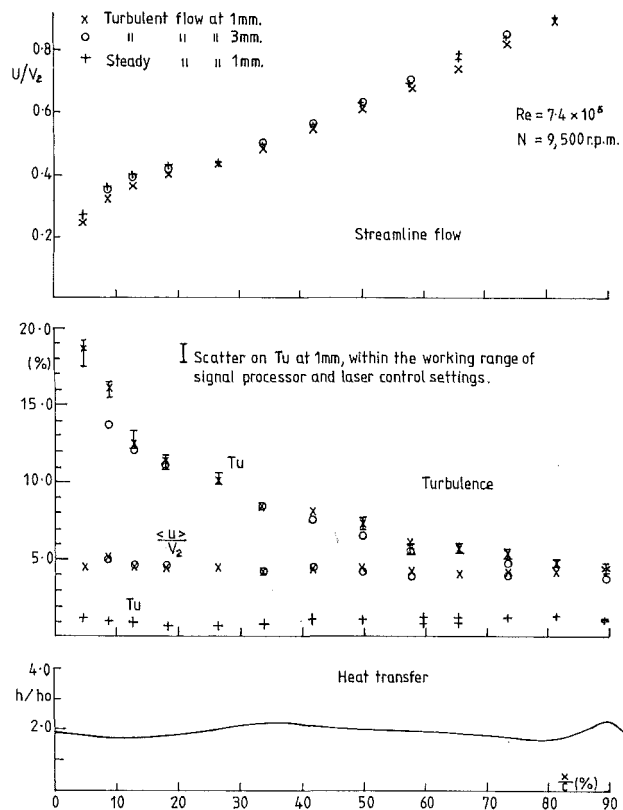


Fig. 7 Local turbulence and heat transfer—pressure surface

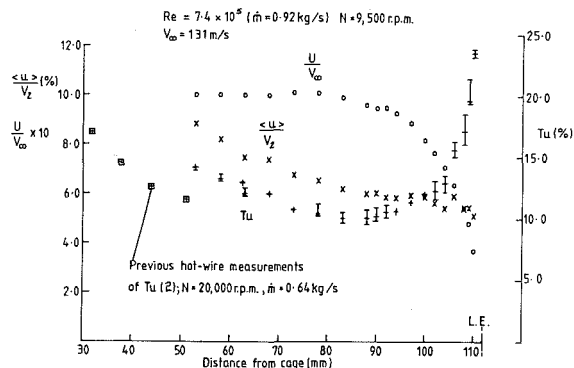


Fig. 8 Centerline traverse into leading edge

tion amplitudes measured in more detail at the perceived edges of the boundary layer, as shown also in Figs. 5, 6, and 7.

On the suction surface, where the acceleration is initially very high, the turbulence intensity falls rapidly from the high values near the stagnation point, but remains fairly constant in the still accelerating flow over the region of high curvature approaching the minimum pressure point on the convex surface. Indeed, in this region, as may be seen in Fig. 6, there is a slight tendency for the absolute level of the velocity fluctuations to increase. From just beyond the minimum pressure point the perturbations fall to about 4 percent of the exit velocity, remaining thereafter almost constant while the local turbulence intensity increases slightly from a minimum of about 3 percent as the mainstream velocity falls toward the trailing edge.

On the concave pressure surface of the blade, the distribution of turbulence intensities at the edge of the boundary layer again reflects the variation in mainstream velocity with the concept of the constant, or "frozen," absolute magnitude of fluctuation. This is graphically demonstrated in Fig. 7 in

which, as in Fig. 6, the variation in local velocity, normalized with respect to the exit velocity, is plotted in the upper figure and the local mainstreamwise velocity perturbation, similarly normalized, is shown below. This is seen to be almost constant along the full length of the pressure surface. The corresponding turbulence intensity in the perturbed flow represented here is plotted in the same figure, and may be compared with the measurements in the comparable unperturbed flow also shown.

A similarly detailed plot of the measurements made at the same flow conditions when the anemometer probe volume was traversed along the centerline toward the blade leading edge is shown in Fig. 8. The sharp falling away toward the stagnation point of the mean streamwise velocity, here normalized with respect to the approach velocity to the cascade, is clearly observed in the uppermost set of points. A corresponding reduction in the absolute magnitude of the fluctuation in velocity, normalized as for the other surfaces for this parameter with respect to the cascade exit velocity, is observed to begin earlier than the mainstream deceleration, from about 9 percent far upstream to an almost asymptotic value, even as near the blade leading edge as measurements could be made, of about 5 percent. The apparent persistence of these fluctuations very near to the leading edge leads to a sharp rise in turbulence intensity in these regions as shown in the figure, to values approaching twice those in the approaching mainstream.

Implications for Heat Transfer

The observations of the variation of velocity fluctuations and turbulence intensity reported above can be considered in the light of the information upon the distribution of convective heat transfer around this, and indeed the many other, blade profiles that is available. In [2], for example, measurements of heat transfer coefficients are reported from the present blade section for a range of turbulence intensities and noted in particular is the relatively small increase in the rate of heat transfer to the upstream part of the convex suction surface of this blade even with approach turbulence intensities ranging up to over 30 percent. The observations from the present program offer some explanation of this result if the importance of turbulence intensity in enhancing heat transfer is accepted. Figures 5 and 6 have demonstrated how even with an average approach value of over 13 percent the turbulence intensity falls rapidly to 4 percent in this region. On the convex surface of the blade it is shown in [3] how critical is the role of laminar-turbulent transition in the boundary layer in determining the effect of mainstream fluctuations upon heat transfer rates. Indeed, as is well established, after transition the perturbations have little effect. The position on a blade of transition is determined by several factors, and in a steady flow on many blade sections is associated with a separation bubble induced in the boundary layer either by inverse pressure gradients or shock wave interaction. Such a transition is indicated by the heat transfer observations in a steady flow over the suction surface of the present blade shown by the dashed line in the lower part of Fig. 6. The characteristic rapid rise in the convective heat transfer coefficient is evident.

An alternative type of transition from that triggered by a separation is the so-called natural transition, in which instabilities in a laminar boundary layer, characterized by the Reynolds number of the flow, develop more gradually over a significant length of the surface. A comprehensive study of such transitions has been made by Abu-Ghannam and Shaw [5] who demonstrated that the momentum thickness Reynolds number, Re_θ , is the parameter quantifying the likelihood of a natural transition. In a steady flow these workers show that the critical Reynolds number can be as high as 1000 in a highly favorable pressure gradient, but that it falls to a limiting value

independent of pressure gradient of about 160 reached with mainstream turbulence intensities of about 5 percent. In the upper part of Fig. 6, the currently measured local free-stream turbulence intensities have been used to derive the critical momentum thickness Reynolds numbers according to [5], which are compared with the values of Re_θ calculated for the flow conditions over this blade. The criterion of [5] suggests that transition will occur at about 20 percent chord, earlier than suggested by the turbulent flow heat transfer results available for this blade shown in Fig. 6. However, Abu-Ghannam and Shaw defined turbulence intensity in terms of the fluctuations in each of the orthogonal velocity components, u , v , w which could give (assuming cross-stream fluctuations are less than streamwise) a higher critical momentum thickness Reynolds number than shown in Fig. 6. In this figure, as in all the present work, turbulence intensity is based upon fluctuations in the mainstream direction only. Also, as indicated in the plot of velocity distribution over the blade suction surface shown in Fig. 6, the acceleration parameter K exceeds the usually accepted "laminarization" value of 2.5×10^{-6} over almost the upstream 20 percent of the convex surface. At these higher values the acceleration of the flow is known to suppress transition to turbulence, as all our heat transfer measurements on a range of blades have confirmed [3].

The present laser-Doppler anemometer measurements are thus consistent with the general observation of a relatively small effect of mainstream flow perturbations on heat transfer to convex suction surfaces. The intensity is observed to be heavily attenuated in the highly accelerating flows over the upstream regions of such surfaces and serves mainly to advance the onset of the laminar-turbulent transition, sometimes as in Fig. 6 to a limited extent, and with a correspondingly small effect upon the heat transfer rates, other than in the immediate neighborhood of the original transition region.

Conversely, compared with the relatively small increases in heat transfer over the convex blade surface, up to fourfold increases in heat transfer have been observed over the arc of the blade leading edge. Again the observations in the present program are consistent with this result, for Fig. 8 shows how the absolute amplitude of the fluctuations persists toward the stagnation point with a corresponding increase in turbulence intensity to twice the approaching mainstream value. The factors affecting heat transfer near the leading edge of a blade are known to be complex; for example, they might be determined in part at least by roll-cell type instabilities, as discussed in [3], which could in their turn be affected by the fluctuations which the present work show to persist into the stagnation region.

The pressure surface of a turbine blade poses an equally complex picture, for with the present blade and others studied in the heat transfer program, the flow is neither wholly laminar, nor turbulent beyond a clearly identifiable local transition zone, as on the suction surface. The present profile, in steady flow and at the higher Reynolds numbers of greatest interest, exhibited transitional characteristics with the heat transfer rates rising toward the trailing edge over the whole pressure surface. Detailed analysis of the boundary layer [3] shows that the inherent instability of this concave surface was possibly affected by Taylor-Goertler vortices, countered at lower Reynolds numbers by the stabilizing influence of the high acceleration rates all along this surface and quantified by the parameter K discussed above in connection with the suction surface. In steady unperturbed flows, the boundary layer on the pressure surface of a modern heavily loaded turbine blade is in a finely balanced state. It is thus reasonable to anticipate that, as indeed all the investigations of heat transfer rates to this blade and others have confirmed, the pressure surface is highly susceptible to the effect of superimposed mainstream fluctuations.

This is especially the case when, as in the present program, the acceleration rates tend to suppress the transitional behavior associated with higher velocities (for which K is less). Under these conditions, the measurements from the laser-Doppler anemometry suggest strongly that the increase in heat transfer correlates with the absolute amplitude of velocity fluctuations. Figure 7 demonstrates the close similarity between the enhanced levels of heat transfer and the absolute magnitude of the fluctuations along the whole pressure surface and the striking dissimilarity with the variation in the dimensionless turbulence intensity over the same region.

Conclusions

From the research reported in this paper the following principal conclusions may be drawn:

1 A commercially available laser-Doppler unit has been shown, with rigorous attention to operational detail, especially with respect to seeding and signal-conditioning, to be capable of yielding repeatable data on the variation of time-mean and instantaneous fluctuating velocities through the passages of modern heavily loaded turbine blades.

2 Mean velocities agreeing closely with measurements by traditional techniques of anemometry and pressure measurements from a pressure tapped blade gave confidence in the accuracy of the measuring technique. Although the fluctuating velocity components were more sensitive to possible sources of error, scatter of results and comparisons where possible with earlier work suggested that uncertainties could be reduced to within 5 percent in peak-to-peak amplitude.

3 Generally, the variations in fluctuating velocity through the cascade were observed to remain sensibly constant in absolute amplitude. This offers confirmation of the common assumption in the hitherto absence of the measurements such as reported here, of a "frozen" perturbation, with the consequent dimensionless intensity reflecting mainly the variations in local mean velocity by which it is normalized.

4 On the suction surface of the blade tested, there was some departure from the general observation in paragraph 3 above, for on the highly curved convex surface near the leading edge of the blade the local perturbations in velocity appeared to increase slightly to maintain the turbulence intensity

almost constant as the mainstream continued to accelerate to the minimum pressure point. On the suction surface the principal effect upon heat transfer of the perturbations is by advancing the transition to a turbulent boundary layer, after which, once most of the surface is subject to turbulence, there is little further consequential effect on increased amplitude of fluctuation.

5 Near the leading edge of the blade, where rates of heat transfer are greatly enhanced by unsteadiness in the flow, the laser-Doppler measurements correspondingly show that the amplitude of the velocity fluctuations persists into the region of reducing mean velocity toward the stagnation point.

6 On the pressure surface of the blade, complex and generally unstable flow results from the interaction between the effects of surface curvature and continuing mainstream acceleration. A clear congruence is here observed between earlier observations of an effectively constant enhanced convective heat transfer rate for a given inlet flow condition and an equally constant amplitude of absolute velocity fluctuation along the whole blade surface.

Acknowledgments

The authors would place on record their appreciation of support of the work reported here by Rolls-Royce, GEC-Ruston Gas Turbines, and the Science and Engineering Research Council, and to the Royal Commission for the Exhibition of 1851 for the award of a fellowship to Dr. Priddy.

References

- 1 Bayley, F. J., and Milligan, R. W., "The Effect of Free-Stream Turbulence Upon Heat Transfer to Turbine Blading," AGARD PEP Conference on High Temperature Problems in Gas Turbine Engines, CP 229, Paper No. 37, 1977.
- 2 Bayley, F. J., and Priddy, W. J., "Effects of Free-Stream Turbulence Intensity and Frequency on Heat Transfer in Turbine Blading," *ASME Journal of Engineering for Power*, Vol. 103, 1981, pp. 60-64.
- 3 Priddy, W. J., and Bayley, F. J., "Effects of Free-Stream Turbulence on the Distribution of Heat Transfer Around Turbine Blade Sections," *International Journal of Heat Fluid Flow*, Vol. 6, No. 3, 1985.
- 4 Priddy, W. J., "LDA Measurements of Mainstream Turbulence Between Turbine Blading," University of Sussex, Thermo-Fluid Mechanics Research Centre Report 85/TFMRC/74, 1985.
- 5 Abu-Ghannam, B. J., and Shaw, R., "Natural Transition of Boundary Layers," *I.Mech.E. Journal of Mechanical Engineering Science*, Vol. 22, 1980.

Measurements of the Turbulent Transport of Heat and Momentum in Convexly Curved Boundary Layers: Effects of Curvature, Recovery and Free-Stream Turbulence

J. Kim
T. W. Simon

University of Minnesota,
Minneapolis, MN 55455

The effects of streamwise convex curvature, recovery, and free-stream turbulence intensity on the turbulent transport of heat and momentum in a mature turbulent boundary layer are investigated. A special three-wire hot-wire probe developed for this purpose is described. Two cases with free-stream turbulence levels of 0.68 and 2.0 percent, taken in the same facility with moderate strength of curvature, $\delta/R = 0.03$, are compared. Profiles of $u'v'$, t' , $u't'$, and $v't'$ are dramatically reduced within the curve, with asymptotic profiles being achieved quickly for the low TI case. Recovery occurs rapidly, with the profiles often overshooting flat-wall upstream values. Increased free-stream turbulence has the effect of increasing the profiles throughout the boundary layer on the flat developing wall. Profiles agreeing with the asymptotic profiles of the low TI case are observed by the end of the curve, however, illustrating the dominance of curvature over free-stream turbulence intensity. For the higher TI case, a reversal in the sign of $u'v'$ in the outer half of the boundary layer is observed, leading to negative values of the turbulent Prandtl number in this region. This indicates a breakdown in Reynolds analogy.

Introduction

Measurement Techniques. The following describes the development of a three-element hot-wire probe to measure the fluctuating components of velocity and temperature in two-dimensional boundary layers, and its use in a turbulent boundary layer over a convex surface. The probe is based on a design by Blair and Bennett (1984). These measurements are important to the gas turbine industry for they support the development of turbulent transport models used to predict the convective heat transfer to the turbine blades. These measurements are difficult and the data base is small. In fact, the effects of moderate-to-strong curvature, recovery, and turbulence intensity on the turbulent transport of heat have been studied here for the first time.

Previous investigators have measured fluctuating velocity and temperature. Representative examples of their work are reviewed below. A description of the use of multiple overheats in hot-wire anemometry to separate the temperature and velocity components in a flow was given by Corrsin (1947). He

measured temperature fluctuations in the mixing of heated gas streams and concentration fluctuations in the mixing of different gases at constant temperature. His use of a single wire, however, precluded the possibility of simultaneous temperature/concentration and temperature/velocity measurements. Sakao (1973) used two parallel 5- μm wires 0.2 mm apart operating at constant but different temperatures to simultaneously measure instantaneous streamwise velocity and temperature. A good response to frequencies to 300 Hz was reported. Hishida and Nagano (1978) used the same configuration but operated the front wire at constant current and the rear wire at constant temperature. No contamination from the front wire was reported and the frequency response was reported to be 6 kHz.

Chen and Blackwelder (1978) used a triple-wire probe to measure two components of velocity, and temperature. The probe consisted of a conventional cross wire with a resistance thermometer placed directly in front of the center of the cross wires and in the plane perpendicular to them. The probe dimensions and frequency response were not presented. Smits and Perry (1981) used a technique similar to that used by Chen and Blackwelder (1978), but with the temperature sensing element placed in a plane next to and parallel with the cross wires. The methodology for separating the velocity and

Contributed by the Gas Turbine Division of THE AMERICAN SOCIETY OF MECHANICAL ENGINEERS and presented at the 32nd International Gas Turbine Conference and Exhibit, Anaheim, California, May 31-June 4, 1987. Manuscript received at ASME Headquarters February 19, 1987. Paper No. 87-GT-199.

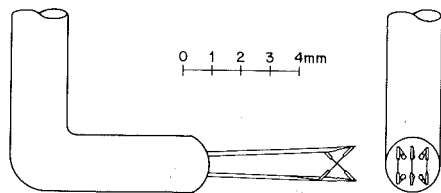


Fig. 1 Schematic of wire configuration

temperature components was presented, but no measurements were taken. A third configuration, used by Gibson and Verriopoulos (1984), consisted of a conventional cross wire with a third "cold" wire positioned between and in a plane parallel to the planes of the cross wires. A good response to frequencies to 6.5 kHz was reported.

A four-wire probe designed to measure three components of velocity and temperature was described by Fabris (1978). Three wires were operated in the constant-temperature mode, while the fourth was of constant current. All wires were 0.625 μm in diameter, minimizing contamination between the wires. The velocity components and temperature were found by simultaneously solving the four nonlinear response equations for the sensors on a computer. A good response to frequencies to 2000 Hz was reported.

Blair and Bennett (1984) described a three-wire probe for use in two-dimensional boundary layers. The probe consists of three wires located in three parallel planes. The two outer wires are orthogonal, forming an X array, while the third center wire is parallel to one of them. All three are operated at constant temperature with the center wire operated at a much lower temperature than the two outer wires. The instantaneous temperature is found from the two parallel wires, and the instantaneous velocity from the two orthogonal wires. A disadvantage to this design is that the measurement of temperature is not direct. The temperature must be determined by simultaneously solving two closely coupled nonlinear equations. The advantages are numerous, however, for only constant-temperature anemometers are used and frail submicron diameter constant-current wires are avoided. A good response to frequencies to 50 kHz was reported. For this reason, the scheme of Blair and Bennett (1984) was chosen for the present study. The wire configuration of the probe used in this study is shown on Fig. 1.

Measurements. The probe was used to measure profiles of turbulence quantities in a zero-pressure-gradient, turbulent boundary layer influenced by convex curvature. Streamwise

curvature is known to affect the structure of turbulent boundary layers markedly. The changes in boundary layer turbulence intensity, wall skin friction, and Stanton number from the corresponding flat-wall values are generally an order of magnitude greater than the magnitude of the strength of curvature, δ/R . A number of studies concerning the effects of curvature on the mean flow and surface heat flux are described by You et al. (1986a). Early work consists almost entirely of mean temperature profiles and surface heat flux measurements. Simon and Moffatt (1982a, 1982b) were the first to report heat transfer data in which the details of the velocity field were known—given by Gillis and Johnston (1980). They were also the first to document heat transfer during recovery from curvature. Their strength of curvature was $\delta/R = 0.1$, indicating strong curvature. You et al. (1986a) added heat transfer and fluid mechanics data on a mildly curved convex surface, with recovery, to the data base. Two strengths of curvature ($\delta/R = 0.013, 0.03$), obtained by bending the test wall, were investigated. This study by You et al. (1986a) is the basis for the present study. Some of their results were: (1) Profiles of the mean velocity and temperature showed shortened log-linear regions and enhanced wake regions in the curve. (2) Curvature increased the turbulent Prandtl number, deduced from the mean velocity and temperature profiles, by about 20–25 percent. (3) A rapid decrease in St and $C_f/2$ at the beginning of the curve was observed followed by a slow decrease within the curve. Decreases of about 20 and 10 percent from expected flat-wall values were observed for $\delta/R = 0.03$ and 0.13, respectively. Recovery was extremely slow, with St recovery leading $C_f/2$ recovery. (4) Normal stress profiles responded rapidly to the beginning of curvature. During recovery, an increase in turbulence intensity originated near the wall at $y/\delta \approx 0.15$ propagating slowly to the outer layers. (5) Shear stress profiles responded quickly to curvature, reducing to about 55 percent of the upstream flat-wall values for $\delta/R = 0.03$. Recovery occurred slowly, with the wake recovering faster than the near-wall flow. Asymptotic shear stress behavior (first observed by Gillis and Johnston, 1980) was found when $\delta/R > 0.04$.

There are very few studies in which the effect of free-stream turbulence intensity on boundary layer heat transfer has been investigated. The study by You et al. (1986b) was the first and only work to document free-stream turbulence effects ($TI = 0.68$ and 1.85 percent) on heated curved flows. No recovery data were taken due to the disappearance of the potential core in recovery for the higher turbulence case. This turbulence in-

Nomenclature

b = offset	u = instantaneous streamwise velocity	Subscripts
d = diameter of wire	U = time-averaged streamwise velocity	
H = shape factor	v = instantaneous cross-stream velocity	an = anemometer
k = conductivity of air or correction coefficient of Champagne	V = voltage	ef = effective
l = active length of wire	w = instantaneous cross-span velocity	pw = potential value at wall—reference value
m = slope	x = streamwise distance	sw = static value at the wall
Nu = Nusselt number	y = distance normal to wall	w = wire or wall value
OH = overheat ratio of wire based on free-stream temperature	α = angle between main flow direction and direction normal to wires	∞ = free-stream value
P = static pressure	δ = boundary layer thickness based on 99.5 percent of free-stream velocity	θ = momentum thickness
Pr_t = turbulent Prandtl number	μ = dynamic viscosity	Superscripts
R = radius of curvature	ρ = density	
Re = Reynolds number		' = fluctuating component or rms, depending on context
St = Stanton number		" = per unit area
t = instantaneous temperature		. = per unit time
T = time-averaged temperature		— = time average
TI = turbulence intensity		

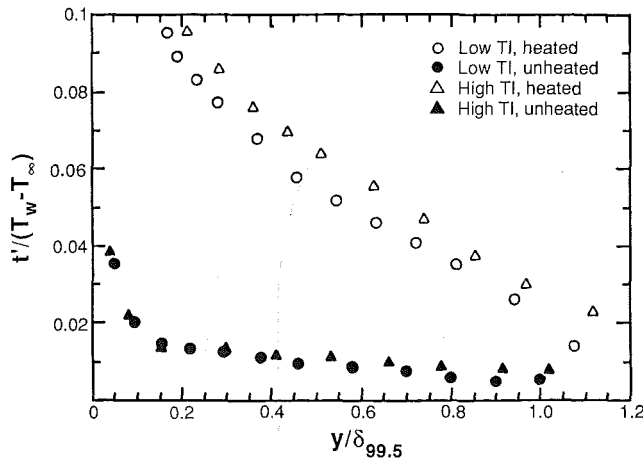


Fig. 2 Comparison of apparent t' with the t' in a heated boundary layer

tensity study by You et al. (1986b) also provides a base for the present measurements. Some results were: (1) The curvature effect dominated the turbulence intensity effect. (2) The skin friction coefficient, deduced by use of the Clauser technique, decreased more within the curve than did Stanton number. (3) Similar streamwise normal turbulence intensity profiles for the two cases of different TI were found near the end of the curve in spite of the different profiles upstream of the curve. (4) Profiles of shear stress showed the same trend for both cases: a dramatic response to the introduction of curvature and asymptotic turbulent shear stress profiles by the end of the curve. A reversal in the sign of the shear stress was seen in the high TI case at the entry to the curve.

Gibson and Verriopoulos (1984) were the first and, until the present study, the only workers to take turbulence measurements in a heated curved ($\delta/R = 0.01$) flow. Their measurements indicated that $\overline{v't'}$ was affected by curvature more than was $\overline{u'v'}$. An initial sharp fall, then a continuous decrease of $\overline{v't'}$ was observed. $\overline{u't'}$ was less strongly affected by curvature. It responded more slowly to the step change in curvature. Its profiles at the last two stations in the curve were very nearly similar. Pr_t values were scattered, but the authors felt that a rise in Pr_t was observable. This is consistent with the values deduced from mean velocity and temperature profiles, and with the results of Simon and Moffatt (1982a, 1982b) and You et al. (1986a). A final conclusion was that turbulence in the boundary layer is modified by wall curvature such that heat transfer was stabilized more effectively than momentum transfer.

Probe Design and Development

In designing special purpose hot-wire arrays, consideration must be given to a multitude of factors, some of which are spatial averaging, prong and shaft interference, end conduction, sensor cross-talk, and survivability. The probe for the present study was constructed using the guidelines presented by Blair and Bennett (1984). The wires are 2.5- μm -dia platinum-plated tungsten with an active length-to-diameter ratio of 200 and a separation distance of 0.35 mm (Fig. 1). The ends of the wires are plated to reduce prong interference and end conduction loss.

The response equation of each sensor is assumed to be of the form

$$Nu = A_1 + B_1 Re^{0.435}$$

which is a slight variation of King's law. Substituting in the definition of Nu and Re, modeling the property variations as

$$\mu \sim t_\infty^{0.75}, \quad k \sim t_\infty^{0.80}, \quad \rho \sim t_\infty^{-1}$$

and rearranging leads to the sensor response equation

$$u_\infty^{0.435} = A t_\infty^{0.76} + \frac{B}{(t_w - t_\infty)} V_{an}^2$$

where A and B are assumed constant. This is the equation used by Blair and Bennett (1984) in modeling sensor response. The authors have found, however, that A and B are slight functions of temperature. This variation is incorporated into the response equation using a least-squares fit to the calibration data. The final response equation is given by

$$u_\infty^{0.435} = (m_A t_\infty + b_A) t_\infty^{0.76} + \frac{(m_B t_\infty + b_B)}{(t_w - t_\infty)} V_{an}^2$$

The two assumptions made when reducing the data are (1) the boundary layer is two-dimensional, and (2) the instantaneous velocities seen by the two parallel wires are equal. The first assumption is needed since the third component of velocity (w) cannot be determined. If the probe is aligned with the flow, however, and if the boundary layer is two dimensional, the w component makes only second-order contributions to sensor response and may be safely neglected. If the second assumption holds, the velocity term (u_{ef}) may be eliminated from the response equations for the two parallel wires, resulting in an equation in which the sole variable is the ambient temperature t_∞ . The ambient temperature is found by iteratively solving for t_∞ using the Newton-Raphson method. The instantaneous velocities u and v may then be found from the signals of the two outer orthogonal wires using Champagne's (1967) form of the k^2 relations

$$u_{1,ef}^2 = (u \cos \alpha + v \sin \alpha)^2 + k^2(u \sin \alpha - v \cos \alpha)^2$$

$$u_{2,ef}^2 = (u \cos \alpha - v \sin \alpha)^2 + k^2(u \sin \alpha + v \cos \alpha)^2$$

Knowing the instantaneous values of u , v , and t , the rms fluctuation quantities (u' , v' , and t') and their cross correlations ($\overline{u'v'}$, $\overline{u't'}$, and $\overline{v't'}$) may be determined. The probe was calibrated as a function of both velocity and temperature.

Qualification of the probe was in a zero-pressure gradient flat-plate turbulent boundary layer with a momentum thickness Reynolds number of 2670 and a uniform wall heat flux of 160 W/m². The boundary layer thickness and free-stream velocity were 2.25 cm and 15.5 m/s, respectively. The probe was traversed across the boundary layer and measurements of $\overline{u'v'}$, t' , $\overline{u't'}$, and $\overline{v't'}$ were made. These quantities, normalized on the free-stream velocity (U_∞) and the wall to free-stream temperature difference ($T_w - T_\infty$), were compared with the boundary layer data of Blair and Bennett (1984) and Gibson and Verriopoulos (1984). The three data sets agreed well except in the vicinity of the wall ($y/\delta < 0.25$) where the present data increased beyond those of other researchers. Insight into this discrepancy may be found from measurements of apparent t' . Apparent t' is the t' measured by the probe in an unheated boundary layer, and is a result of the two parallel wires not experiencing the same velocity. If the probe were perfect, the apparent t' across the boundary layer would, of course, be zero. A large apparent t' would indicate serious problems with the probe. Results of the measurements for TI = 0.68 percent and TI = 2.0 percent, shown on Fig. 2, show that the apparent t' values are a small percentage of the actual values in the outer part of the boundary layer, but rise rapidly as the wall is approached. This is expected since the eddy size decreases with decreasing normal distance from the wall, increasing the likelihood of the two parallel wires not seeing the same velocity. It may also be seen that turbulence intensity has little effect on apparent t' , further suggesting that distance from the wall is the controlling parameter. The effect of apparent t' on the actual t' is smaller than the curves suggest since the apparent t' affects the actual data in a root-sum-square manner.

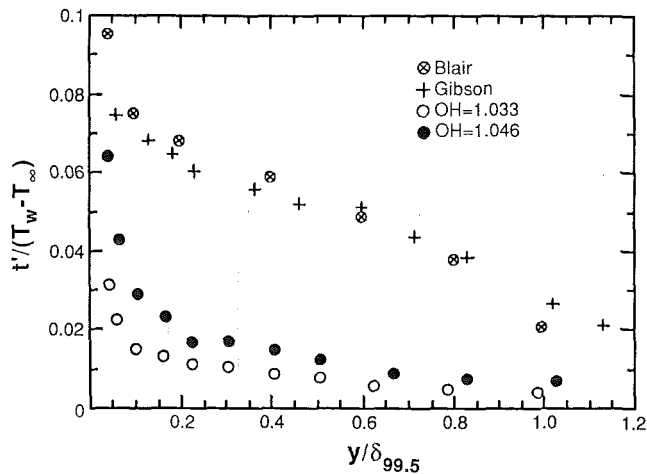


Fig. 3 Effect of overheat ratio (OH) on apparent t'

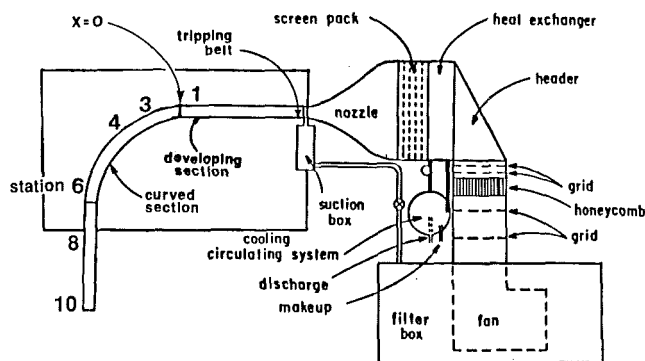


Fig. 4 Plan view of the curved boundary layer facility

The turbulent Prandtl numbers (Pr_t) deduced from the measurements of $\overline{u'v'}$ and $\overline{v't'}$ were compared with the data of Blair and Bennett (1984) and Gibson and Verriopoulos (1984). There was some unavoidable scatter, but the three data sets agreed within their uncertainties (≈ 20 percent).

The effect of overheat ratio (OH) on apparent t' , presented in Fig. 3, shows that increasing OH increases t' . Furthermore, very low OH are needed to achieve low apparent t' . Why this is the case is not presently known, but it is thought to be tied to the disappearance of the velocity dependence and the reduction of the solution matrix stiffness as the wire temperature is reduced. There was some worry that the low frequency response of the probe would affect the measurements, but, judging from the qualification data, the probe seems to follow fluctuations associated with important scales of the flow. A good response to frequencies as large as a few hundred hertz is expected.

As a last check on the probe, the measurements of shear stress were taken with the two outer orthogonal wires and again with the two inner orthogonal wires to check for prong interference and cross-talk. The difference in the two data sets was well within the uncertainty, and the curves agreed well with the data of Gibson and Verriopoulos (1984). No evidence of interference or other forms of contamination was evident.

In summary, the probe performs well except in the near vicinity of the wall. The uncertainty in the measurements is estimated at 15 percent for the correlations and 20 percent for Pr_t .

Description of the Test Facility

The present experiment was conducted in an open-circuit, blown-type wind tunnel constructed with an upstream

Table 1 Summary of boundary layer parameters

Low TI Case ($TI=0.68\%$)

Station	x(cm)	Re_θ	H
1	-29.87	2696	1.42
3	26.16	3940	1.44
4	52.83	4784	1.54
6	106.68	5919	1.65
8	150.62	5633	1.52
10	206.50	6400	1.47

High TI Case ($TI=2.0\%$)

Station	x(cm)	Re_θ	H
1	-29.87	2640	1.35
2	26.16	4053	1.41
3	52.83	4155	1.42

developing section, a curved section, and a downstream recovery section. A schematic of the test facility is shown on Fig. 4. Details of the tunnel are given in You et al. (1986a, 1986b). The test channel is rectangular, 68 cm in span and 11.4 cm deep. The heated test wall consists of a 1.4-m-long developing section and a 1.4-m-long curved section of 0.9 m radius of curvature followed by a 1.4-m-long straight recovery section.

The laminar boundary layer was tripped in the lower-turbulence case, with a 1.0-mm-high, 12.7-mm-wide strip beginning 10 cm downstream of a suction slot; a mature boundary layer was established in the measurement area. The free-stream turbulence intensity, normalized on U_{pw} , was 0.68 percent. Higher turbulence levels were obtained by inserting a coarse grid constructed of 2.5-cm aluminum strips in a square array on 10-cm centers at the entrance of the nozzle. The boundary layer trip was removed and the boundary layer was allowed to pass naturally through transition. A turbulence intensity of 2.0 percent was achieved in the test section with the grid in place. Stanton numbers were spanwise uniform to within 4 percent of the centerline value upstream of the curve in both cases.

The test wall was heated to nominally 6°C above the free-stream temperature with a uniform heat flux of 160 W/m^2 . Static pressure on the test wall was uniform. Static pressures were measured through 0.64-mm-dia taps in the opposite wall and end walls. In the curved region, these pressures were used to estimate the static pressure at the test wall assuming potential flow.

Results and Discussion

Measurements of $\overline{u'v'}$, t' , $\overline{u't'}$, and $\overline{v't'}$ were taken at the flat upstream developing station (station 1), three stations in the curve (stations 3, 4, and 6), and two stations in the recovery (stations 8 and 10). Data were not taken beyond station 6 in the high TI case due to merging of the test-wall and opposite-wall boundary layers. Descriptors for the two cases are presented in Table 1. The flexible outer walls were adjusted such that the pressure coefficient C_p defined as

$$C_p = \frac{P_{sw} - P_{sw,ref}}{\rho U_{pw}^2 / 2}$$

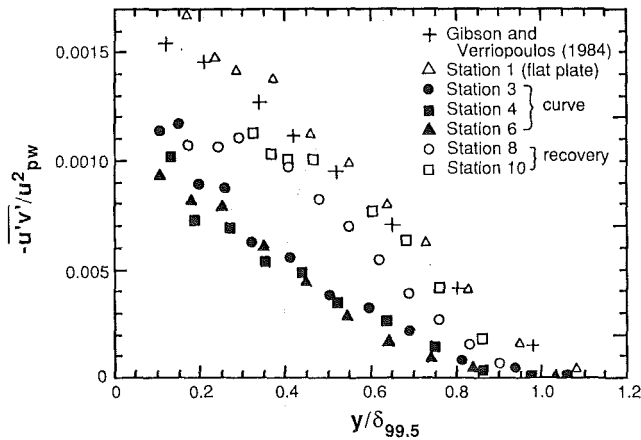


Fig. 5 Effect of curvature and recovery on $\overline{u'v'}$, $TI = 0.68$ percent

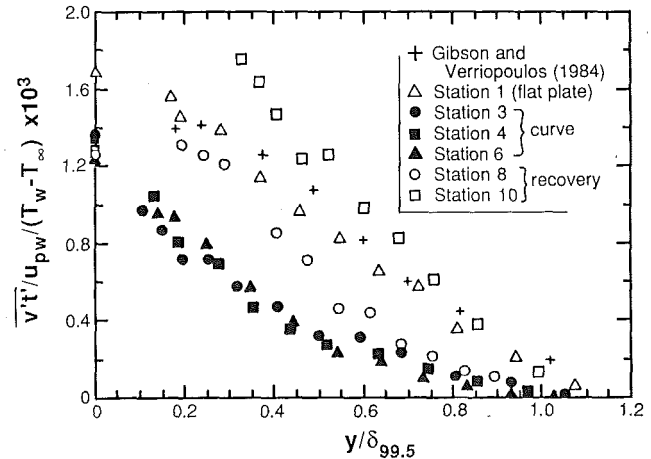


Fig. 8 Effect of curvature and recovery on $\overline{v't'}$, $TI = 0.68$ percent

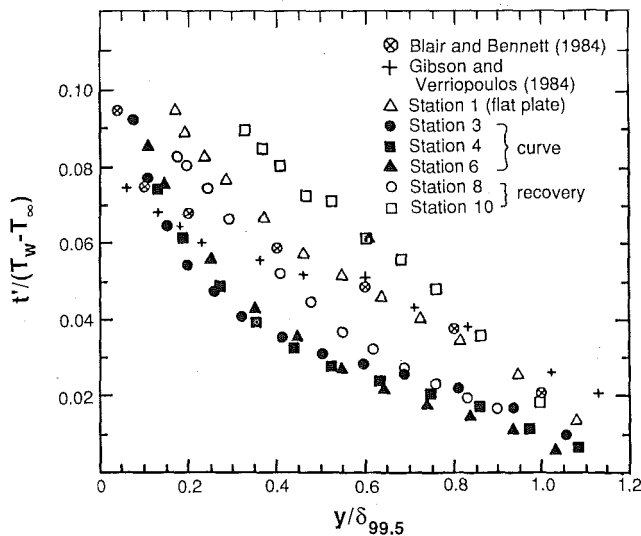


Fig. 6 Effect of curvature and recovery on t' , $TI = 0.68$ percent

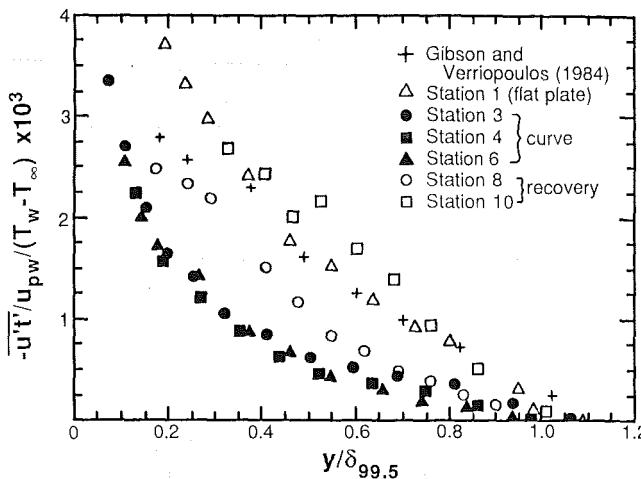


Fig. 7 Effect of curvature and recovery on $\overline{u't'}$, $TI = 0.68$ percent

the appearance of what appears to be an asymptotic state in the curve occur. Curvature is seen to reduce the shear stress by about 45 percent below the flat wall values throughout the curve. Recovery of shear stress is slow, with recovery seemingly complete in the wake by station 10 (see Fig. 4 for station locations). You et al. (1986a) have shown that the near-wall values of $\overline{u'v'}$ recover very slowly. All the trends are consistent with the observations of Gillis and Johnston (1983) and You et al. (1986a)

Profiles of t' are plotted on Fig. 6. The flat upstream values (station 1) agree with the measurements of Blair and Bennett (1984) and Gibson and Verriopoulos (1984) within the uncertainty of the measurement, except near the wall. The profiles within the curve assume an asymptotic shape for $y/\delta < 0.5$. A slight evolution of the profiles for $y/\delta > 0.5$ is evident. Recovery has a dramatic effect on t' . Values at station 10 are seen to overshoot the station 1 values. It is believed that the profile eventually returns to the station 1 shape. The recovery length was too short to observe this in the present experiment, however.

The effects of curvature and recovery on the streamwise turbulent heat flux $\overline{u't'}$ are shown on Fig. 7. Station 1 values agree well with the data of Gibson and Verriopoulos (1984). The effect of curvature on $\overline{u't'}$ is dramatic. The profiles in the curve "snap" into an asymptotic shape for $y/\delta < 0.5$ while slow evolution of the profiles for $y/\delta \geq 0.5$ may be observed. Recovery is seen as an overshoot of $\overline{u't'}$ beyond the station 1 values, although the profile is expected to eventually return to the station 1 values.

Profiles of cross-stream turbulent heat flux $\overline{v't'}$ are shown on Fig. 8. The effects of curvature and recovery on $\overline{v't'}$ are very similar to those observed for $\overline{u't'}$ —a dramatic reduction in the curve to an asymptotic shape, followed by an overshoot in the recovery. Values of an effective, extrapolated $\overline{v't'}$ at the wall as calculated from the wall heat flux measurements are located on the $y = 0$ axis in Fig. 8. The wall values and the profile measurements agree very well at station 1 and in the curve. The values of $\overline{v't'}$ in the recovery region, however, rise above the wall heat flux values, especially for station 10. This may be seen more clearly on Fig. 9 where $\overline{v't'}$ has been normalized on the wall heat flux. The profiles at station 1 and within the curve approach unity near the wall while the profiles in the recovery section rise above unity. It is believed that the profiles turn down and approach unity as the wall is approached. The measurements cannot be taken this close to the wall, however. A positive slope in $\overline{v't'}$ suggests mixing of increasing intensity with increasing distance away from the wall.

Profiles of turbulent Prandtl number Pr_t are shown in Fig. 10. The data show some unavoidable scatter which makes it

was adjusted to within 3 percent of the mean. The reference pressure was taken to be the static pressure at station 1.

Low TI Case ($TI = 0.68$ Percent). Shear stress profiles are shown on Fig. 5. The profiles are seen to respond quickly to curvature. A dramatic reduction at the onset of curvature and

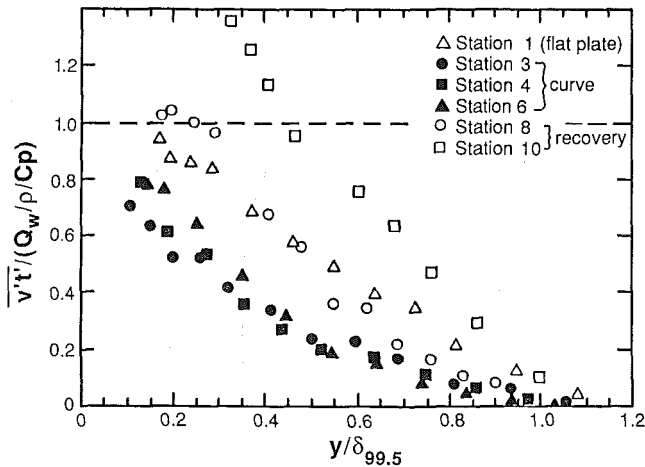


Fig. 9 $\overline{v't'}$ normalized on wall heat flux, TI = 0.68 percent

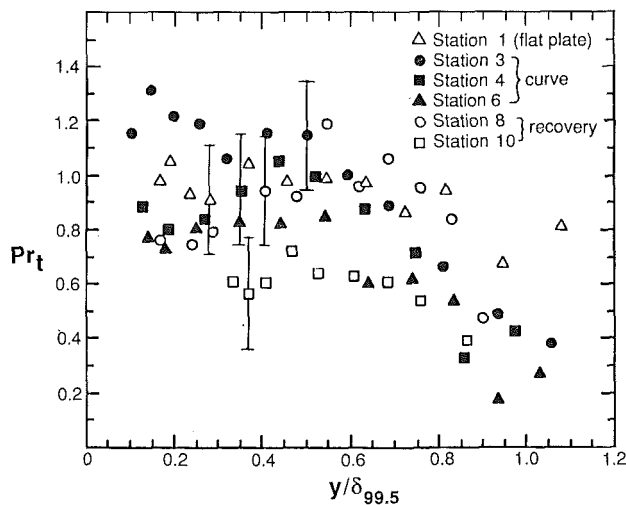


Fig. 10 Effect of curvature and recovery on Pr_t , TI = 0.68 percent

difficult to draw firm conclusions about the effect of curvature. Gibson and Verriopoulos (1984), You et al. (1986a), and Simon and Moffatt (1982a, 1982b) stated that Pr_t in the log-linear region rises due to convex curvature. The You et al. (1986) and Simon and Moffatt (1982a, 1982b) studies cite indirect Pr_t values deduced from mean temperature and velocity profiles which represent average values for the turbulent core. Because of scatter in Fig. 10 the only conclusion which can be drawn from these data is that the preplate and curved-flow Pr_t values are not vastly different (> 20 percent) from one another whereas the data at the end of the recovery section are lower.

A plot of the triple product $\overline{u'v'^2}$ representing the cross-stream flux of turbulent stress is presented on Fig. 11. The flat-wall data are compared to the data of Gibson and Verriopoulos (1984), and are seen to be higher throughout the boundary layer. Why this is the case is not presently known. The effect of curvature on $\overline{u'v'^2}$ is dramatic. Values of $\overline{u'v'^2}$ are reduced to 15 to 25 percent of the flat-wall values by station 6, indicating that the transport of stress from the near-wall production layer to the outer flow is virtually shut off. A sharp drop at the introduction of curvature followed by a slow continued decrease is evident. The profiles are seen to recover slowly. The near-wall values remain low (which is consistent with the downturn in the shear stress profiles near the wall) within the recovery section, as discussed earlier. The peak in the profiles increases and is seen to move away from

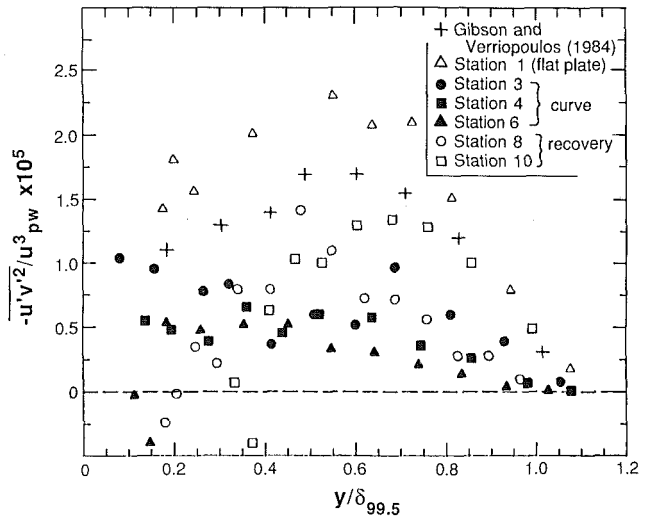


Fig. 11 Effect of curvature and recovery on $\overline{u'v'^2}$, TI = 0.68 percent

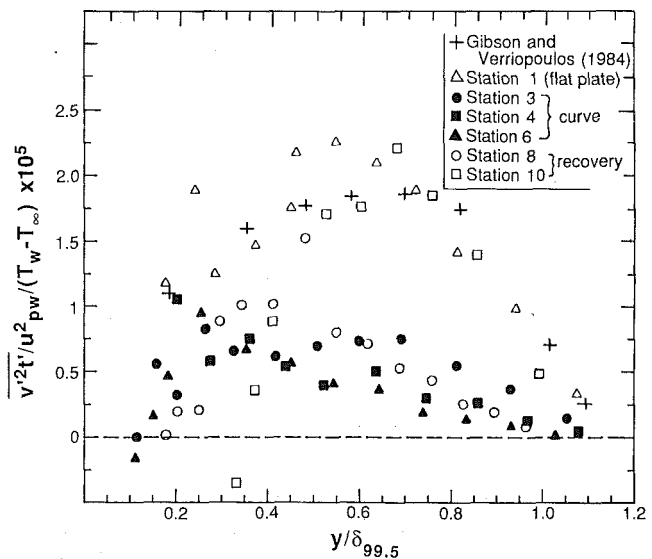


Fig. 12 Effect of curvature and recovery on $\overline{v'^2 t'}$, TI = 0.68 percent

the wall with increasing streamwise distance. The profile appears to become negative for $y/\delta < 0.35$, indicating diffusion of stress toward the wall.

Profiles of the triple product $\overline{v'^2 t'}$, the cross-stream flux of $\overline{v' t'}$, are presented on Fig. 12. The flat-wall values are seen to be somewhat higher than the data of Gibson and Verriopoulos (1984), as was the case for $\overline{u'v'^2}$. Curvature is seen to affect $\overline{v'^2 t'}$ in much the same way as with $\overline{u'v'^2}$. A sharp reduction in $\overline{v'^2 t'}$ followed by a slow evolution to values 15 to 25 percent of the magnitude of the upstream flat-wall values is evident. Recovery of the profiles with the peak moving away from the wall is again seen, and a reversal in sign of $\overline{v'^2 t'}$ is seen for $y/\delta < 0.35$, as was seen for $\overline{u'v'^2}$. The latter indicates that the turbulent heat flux decreases as the wall is approached. This is consistent with the observed downturn in $\overline{v' t'}$ upon recovery.

High TI Case (TI = 2.0 Percent). Shear stress profiles for the higher free-stream turbulence case are presented on Fig. 13. Higher turbulence intensity has the effect of increasing the shear stress throughout the boundary layer. This is expected. The profiles immediately assume an asymptotic shape within the curve for $y/\delta < 0.5$, as in the low TI case. The asymptotic

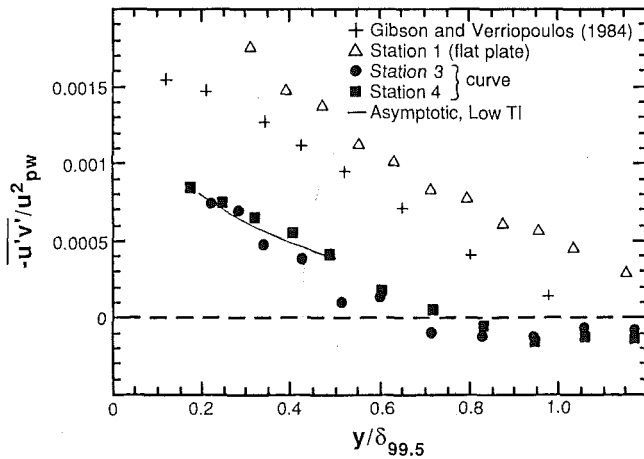


Fig. 13 Effect of curvature on $u'v'$, $TI = 2.0$ percent

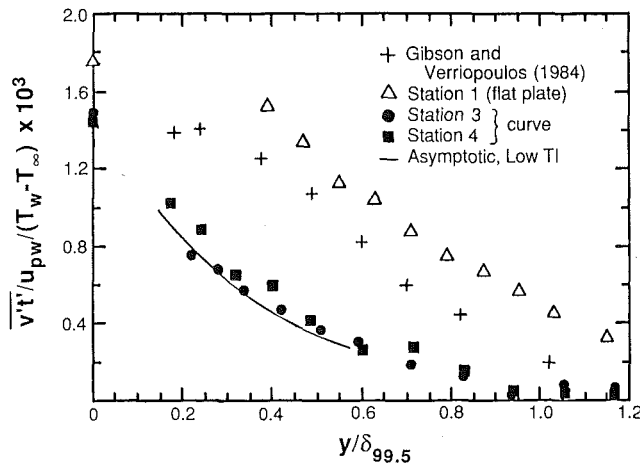


Fig. 14 Effect of curvature on $v't'$, $TI = 2.0$ percent

profile for the low TI case is also plotted on Fig. 13 where it is seen to agree well with the high TI curved flow data. A reversal in the sign of the shear stress is seen to occur in the outer part of the boundary layer. This reversal in sign has also been observed by Gillis and Johnston (1983) for more strongly curved flows. An explanation for the reversal in shear stress given by Honami (1980) was presented in Gillis and Johnston (1983). Within the curve, the dominant production terms in the budget equation for shear stress are given by

$$P = \overline{v'^2} \frac{\partial U}{\partial y} - (2\overline{u'v'^2} - \overline{v'^2}) \frac{U}{R}$$

For a flat wall, the second term on the right-hand side is zero. As the flow enters the curve, however, the second term appears. Since $\overline{u'^2}$ is usually greater than $\overline{v'^2}$, the production rate is decreased by this term, and even goes negative, as shown by calculations performed for the high TI case. It is interesting to note that a large decrease in the production level in the study by Gillis and Johnston (1983) occurred due to the relatively small radius of curvature ($\delta/R = 0.1$), while a large decrease in the production level in the present study is obtained by increasing the turbulence intensity while keeping the radius of curvature large ($\delta/R = 0.03$).

Profiles of $v't'$ are given in Fig. 14. Values of $v't'$ higher than the corresponding low TI values are seen at station 1, while an asymptotic profile agreeing with the asymptotic profile for the low TI case is achieved in the curve. This dramatically illustrates the dominance of curvature over turbulence intensity. The profiles are seen to agree well with the

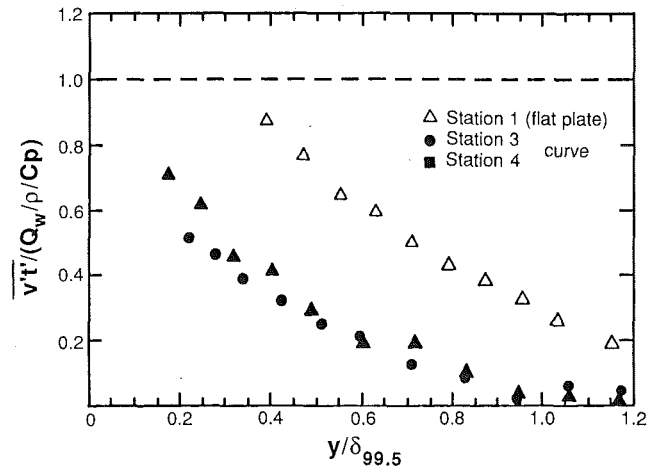


Fig. 15 $v't'$ normalized on wall heat flux, $TI = 2.0$ percent; effect of curvature

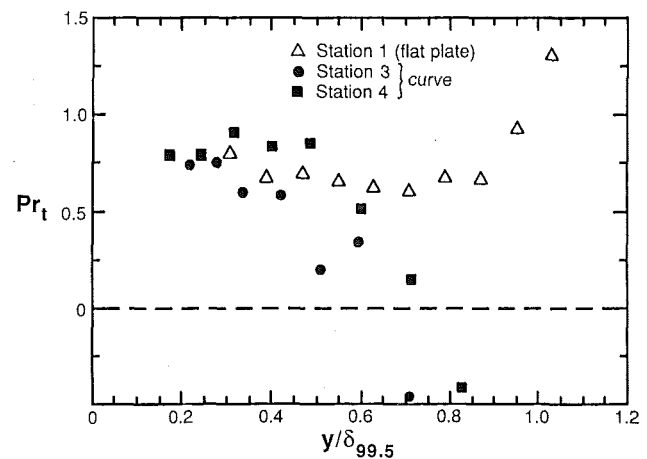


Fig. 16 Effect of curvature on Pr_t , $TI = 2.0$ percent

wall heat flux measurements. Profiles of $v't'$ normalized on the extrapolated, effective value computed from the wall heat flux are shown on Fig. 15. The values are expected to approach unity as the wall is approached.

The effect of turbulence intensity on t' and $\overline{u't'}$ is similar to its effect on $u'v'$ and $v't'$. The flat-plate values are greater than the corresponding low-turbulence values, but this increase is eliminated by the end of the curve where the values agree with the asymptotic profile of the low TI case.

Turbulent Prandtl number profiles are shown on Fig. 16. It is interesting that, with high TI , values of Pr_t become negative in the wake region of the boundary layer due to the sign reversal in shear stress with no equivalent reversal in the sign of the turbulent heat flux, as discussed earlier. This strong variation in Pr_t indicates that Reynolds analogy is not valid.

Increasing the turbulence intensity was seen greatly to increase the values of $u'v'^2$ and v'^2t' . Inside the curve, the diffusion was reduced, reaching the order of the corresponding low TI values by the end of the curve.

Conclusions

The effects of curvature, recovery and turbulence intensity on turbulent boundary layer heat transfer were studied. The main conclusions are:

- 1 Profiles of $\overline{u'v'}$, t' , $\overline{u't'}$, and $\overline{v't'}$, are reduced in the curve with an asymptotic profile being achieved by station 4.

Recovery in the wake region occurs quickly, with the profiles often overshooting the flat upstream (station 1) values.

2 A reversal of sign in shear stress is seen for the high TI case (TI = 2.0 percent) for $y/\delta > 0.5$. A reversal of sign was also observed by other researchers in strongly curved flows with lower turbulence intensity.

3 Because the measured turbulent Prandtl number profiles show considerable scatter, one can only conclude that the effect of curvature is no more than about 20 percent. But the data appear to show a decrease by the end of recovery from curvature. This does not refute Pr_t values deduced in earlier studies from mean velocity and temperature profiles, but does not provide support for the 20 percent increase noted by You et al. (1986a). Negative turbulent Prandtl numbers were seen in the wake for the high TI case, indicating a breakdown in Reynolds analogy.

4 Curvature effects dominate turbulence intensity effects for the cases studied.

Acknowledgments

This study was supported by the Air Force Office of Scientific Research grant number F49620-83-C0062. The grant monitor is Dr. James D. Wilson. Funding was also provided by the NASA-Lewis Research Center grant number NAG 3-286. The grant monitor is Dr. Raymond Gaugler. Additional support was provided by the Graduate School of the University of Minnesota and by the AMOCO Foundation.

References

Blair, M. F., and Bennett, J. C., 1984, "Hot Wire Measurements of Velocity and Temperature Fluctuations in a Heated Turbulent Boundary Layer," ASME Paper No. 84-GT-234.

Champagne, F. H., Sleicher, C. A., and Wehrmann, O. H., 1967, "Turbulence Measurements With Inclined Hot-Wires, Parts 1 and 2," *JFM*, Vol. 28, pp. 153-182.

Chen, C. P., and Blackwelder, R., 1978, "Large-Scale Motion in a Turbulent Boundary Layer: A Study Using Temperature Contamination," *JFM*, Vol. 89, Part 1, pp. 1-31.

Corrsin, S., 1947, "Extended Applications of the Hot-Wire Anemometer," *Review of Scientific Instruments*, Vol. 18, No. 7, pp. 469-471.

Fabris, G., 1978, "Probe and Method for Simultaneous Measurements of 'True' Instantaneous Temperature and Three Velocity Components in Turbulent Flow," *Review of Scientific Instruments*, Vol. 49, No. 5, pp. 654-664.

Gibson, M. M., and Verriopoulos, C. A., 1984, "Turbulent Boundary Layer on a Mildly Curved Convex Surface," *Expt. in Fluids*, Vol. 2, Springer-Verlag, New York, pp. 73-80.

Gillis, J. C., and Johnston, J. P., 1980, "Experiments on the Turbulent Boundary Layer Over Convex Walls and Its Recovery to Flat-Wall Conditions," *Turbulent Shear Flows*, Vol. 2, pp. 116-128.

Gillis, J. C., and Johnston, J. P., 1983, "Turbulent Boundary Layer Flow and Structure on a Convex Wall and Its Redevelopment on a Flat Wall," *JFM*, Vol. 135, pp. 123-153.

Hishida, M., and Nagano, Y., 1978, "Simultaneous Measurements of Velocity and Temperature in Nonisothermal Flows," *ASME Journal of Heat Transfer*, Vol. 100, pp. 340-345.

Honami, S., 1980, Private Communication.

Sakao, F., 1973, "Constant Temperature Hot Wires for Determining Velocity Fluctuations in an Airflow Accompanied by Temperature Fluctuations," *J. of Physics E, Scientific Instruments*, Vol. 6, pp. 913-916.

Simon, T. W., and Moffatt, R. J., 1982a, "Turbulent Boundary Layer Heat Transfer Experiments: A Separate Effects Study on a Convexly Curved Wall," *ASME Journal of Heat Transfer*, Vol. 105, No. 4, pp. 835-840.

Simon, T. W., and Moffatt, R. J., 1982b, "Convex Curvature Effects on the Heated Turbulent Boundary Layer," *Proc. 7th Int. Heat Transfer Conf.*, Vol. 3, pp. 295-301.

Smits, A. J., and Perry, A. E., 1981, "A Note on Hot-Wire Anemometer Measurements of Turbulence in the Presence of Temperature Fluctuations," *J. of Physics E, Scientific Instruments*, Vol. 14, pp. 311-312.

You, S. M., Simon, T. W., and Kim, J., 1986a, "Boundary Layer Heat Transfer and Fluid Mechanics Measurements on a Mildly-Curved Convex Wall," *Proc. 8th Int. Heat Transfer Conf.*, Vol. 3, pp. 1089-1094.

You, S. M., Simon, T. W., and Kim, J., 1986b, "Free-Stream Turbulence Effects on Convex-Curved Turbulent Boundary Layers," ASME Paper No. 86-WA/HT-46.

R. M. Watt

J. L. Allen

Department of Engineering Science,
University of Oxford,
Oxford, OX1 3PJ, United Kingdom

N. C. Baines

Department of Mechanical Engineering,
Imperial College,
London, SW7 2BX, United Kingdom

J. P. Simons

M. George

Rolls-Royce Ltd.,
Filton, Bristol, BS12 7QE,
United Kingdom

A Study of the Effects of Thermal Barrier Coating Surface Roughness on the Boundary Layer Characteristics of Gas Turbine Aerofoils

The effect of thermal barrier coating surface roughness on the aerodynamic performance of gas turbine aerofoils has been investigated for the case of a profile typical of current first-stage nozzle guide vane design. Cascade tests indicate a potential for significant extra loss, depending on Reynolds number, due to thermal barrier coating in its "as-sprayed" state. In this situation polishing coated vanes is shown to be largely effective in restoring their performance. The measurements also suggest a critical low Reynolds number below which the range of roughness tested has no effect on cascade efficiency. Transition detection involved a novel use of thin-film anemometers painted and fired onto the TBC surfaces.

Introduction

The importance of increased turbine entry temperature has led to rapid developments in blade cooling technology over the past few decades, and while this advance has mainly been based on film and internal cooling, the use of ceramic thermal barrier coatings (TBCs) has recently also attracted interest.

Zirconia-based, plasma-sprayed coatings have low thermal conductivity and are known to be effective in providing thermal protection for turbine aerofoils while retaining light weight [1]. A possible side effect, however, is a deterioration in aerodynamic performance due to an inferior, rougher, surface finish, which can cause earlier onset of laminar-turbulent transition and, for a fully turbulent boundary layer, increased skin friction. These effects are apparent in numerous cascade and turbine (and compressor) rig tests involving a range of roughness types [2-6].

The present paper describes a preliminary study of TBC surface finish effects as measured in "cold-air," two-dimensional cascade tests recently undertaken in the Oxford University Short-Duration Transonic Blowdown Tunnel [7]. In this facility the Mach and Reynolds numbers can be varied continuously, independently, and over realistic ranges for present-day turbines; these features are particularly relevant since roughness effects are largely Reynolds number dependent. The parameter of prime importance is the "roughness Reynolds number," where the characteristic length is the average height of the roughness elements. The transition

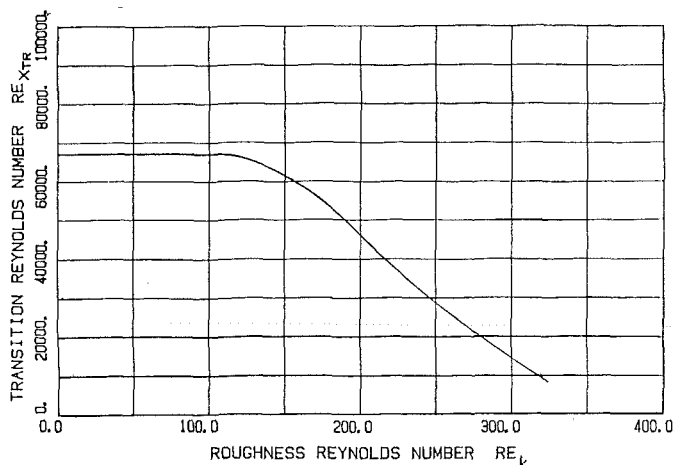


Fig. 1 Influence of surface roughness on transition (after Feindt [8])

studies of Feindt [8], for instance, show that, for the case of incompressible flow past a flat plate with sand-grain roughness, $Re_k = 120$ represents a critical value below which the onset of transition is unaffected (see Fig. 1). At higher Reynolds numbers the point of onset of transition moves progressively nearer to the plate leading edge with increasing Re_k .

The magnitude of Re_k also determines the degree of influence of roughness on fully developed turbulent boundary layers, as can be seen from Fig. 2. Generally speaking, at high Reynolds numbers ($Re_k > 1000$), the rougher the surface, the greater the skin-friction coefficient, or, alternatively, roughness imposes a lower limit on the value of skin-friction coefficient attainable. On the other hand, for Re_k lower than

Contributed by the Gas Turbine Division of THE AMERICAN SOCIETY OF MECHANICAL ENGINEERS and presented at the 32nd International Gas Turbine Conference and Exhibit, Anaheim, California, May 31-June 4, 1987. Manuscript received at ASME Headquarters February 19, 1987. Paper No. 87-GT-223.

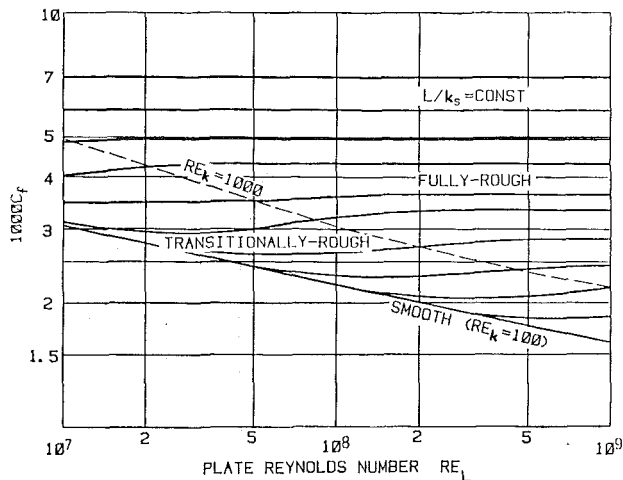


Fig. 2 Skin-friction coefficient for turbulent boundary layer on sand-roughened plate (Prandtl-Schlichting)

100 turbulent boundary layer skin friction is effectively independent of roughness and varies only with Reynolds number. The following three flow regimes are conventionally identified:

- $Re_k < 100$ ($C_f = f(Re)$) : Hydraulically smooth
- $100 < Re_k < 1000$ ($C_f = f(Re, k)$) : Transitionally rough
- $Re_k > 1000$ ($C_f = f(k)$) : Fully rough

The usual physical interpretation of the transition process from hydraulically smooth to fully rough is that the viscous sublayer thickness is decreasing relative to the average height of the roughness elements, to the point where the sublayer is relatively insignificant in fully rough flow. The proposed mechanism for increased skin friction during this process is form drag incurred by the roughness peaks, which pierce the sublayer and protrude into the fully turbulent region. In fully rough conditions all of the roughnesses are viewed as contributing to an enhancement of turbulent mixing and hence increased rate of loss of momentum, or shear.

The effects of roughness are therefore dependent on properties of the fluid, which is particularly relevant since operating pressures vary throughout the turbine. As a result, HP-stage aerofoils are most sensitive to the effects of surface roughness and require most stringent effort to avoid exceeding the "admissible" roughness level which, as a general rule, is given by $k_{adm} = 100 \nu/U$.

Definition of Surface Roughness

Surface roughness is usually defined simply in terms of an easy-to-measure average height normally obtained from a "Tallysurf" stylus trace. Two typical such amplitude parameters are: R_a , the "arithmetic mean deviation" of a surface from the mean line, commonly termed the "center line average" (CLA) value, and R_z , the "ten-point height," for irregularities, known as the "peak-to-valley height," which is

Table 1 Cascade details (nominal)

Profile scale	1:1
True chord length, mm	69.0
Axial chord length, mm	37.4
Pitch spacing, mm	54.7
Aspect ratio	2.2
Suction surface length, mm	83.6
Pressure surface length, mm	67.0
Stagger angle	55.5
Inlet Mach No.	0.168
Exit Mach No.	0.91
Design exit Reynolds No.	2.3×10^6
Exit flow angle	73.3
Inlet turbulence intensity, percent	4

equal to the difference in height between the five highest peaks and the five lowest valleys measured from an arbitrary base line.

In the case of machined finishes, R_z typically exceeds R_a in the ratio 5:1 [6].

In fluid dynamics applications different types of finish are often characterized by their retarding effects on the free stream, and for this a standard used for comparison is: k_s , the "equivalent sand roughness," which is defined as the height of sand-grain roughness which would give the same skin friction in fully rough flow.

The main reason for the use of sand-grain roughness is the existence of a comprehensive body of experimental data based on that roughness type [10].

Correlations between R_a or R_z and k_s tend to be specific to certain types of finish, and so, for other than these, equivalent sand roughness is best determined unequivocally from aerodynamic tests. R_z is generally $2.56 k_s$ for typical machined finishes where the flow direction is normal to the machining marks [9].

Associated characteristics such as spatial distribution, surface waviness, and the intrinsic shape of the roughness elements themselves may also produce effects which prevent description in terms of k_s alone [11]. In this regard an interesting alternative approach involves Fourier spectral analysis of Tallysurf signals. A surface texture parameter of the type derived by Mulvaney and Newland [12] may possibly provide a more complete description of roughness profiles which gives improved correlation with experimental observations.

Cascade Test Details

A series of standard aerodynamic measurements was made on a plane cascade of each of three surface finishes of a development NGV. This mid-height section is designed to operate at a nominal Reynolds number (based on vane true chord length) of 2.3×10^6 and at an exit Mach number of 0.91. Further operating details are given in Table 1.

The three variants were as follows:

- (i) uncoated, polished surface to act as a "hydraulically smooth" datum;
- (ii) "as-sprayed" TBC, of roughness 7-10 μm (300-400 $\mu\text{in.}$) CLA;
- (iii) polished TBC, of roughness $\sim 2 \mu\text{m}$ (60-80 $\mu\text{in.}$) CLA.

Nomenclature

C_f = coefficient of total skin friction	Re_k = roughness Reynolds number = $U_0 k_s / \nu$	ν = kinematic viscosity
k = roughness element height	S = surface length	
k_s = equivalent sand roughness	U = velocity	Subscripts
L = length	X_{tr} = length to transition	0 = stagnation, free-stream
p = pressure	η = cascade primary efficiency	1 = inlet
Q = dynamic pressure	θ = boundary layer momentum thickness	2 = exit
		s = isentropic

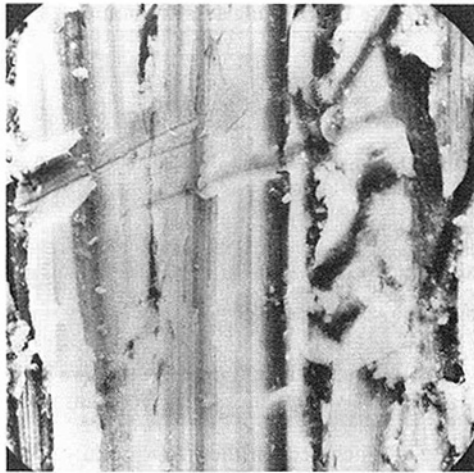


Fig. 3(a) Uncoated aluminum alloy

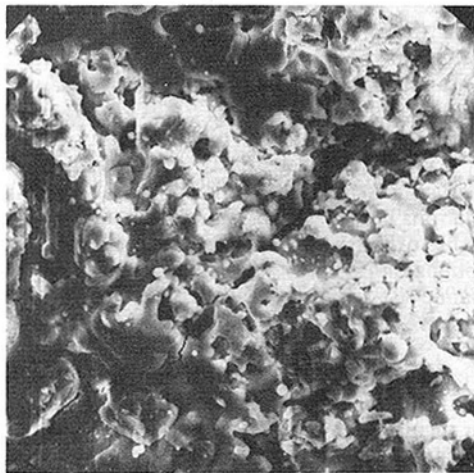


Fig. 3(b) "As-sprayed" TBC

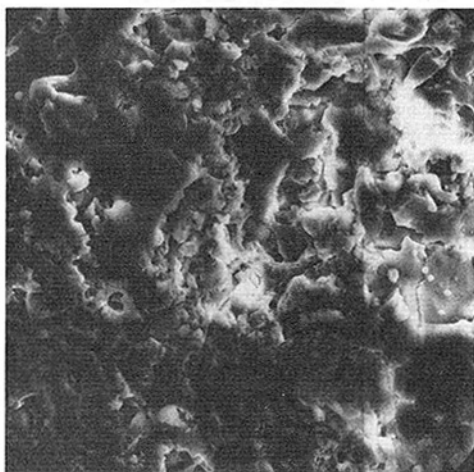


Fig. 3(c) Polished TBC

Fig. 3 Electron micrographs of test surfaces ($\times 860$)

(A normal production cast finish is around $100 \mu\text{in. CLA}$ and a polished cast finish is approximately $20\text{--}40 \mu\text{in. CLA}$.)

The thermal barrier coating was zirconia partially stabilized with yttria ($\text{ZrO}_2\text{-}12\text{Y}_2\text{O}_3$) plasma-sprayed onto an MCrAlY metallic bond coating. The total coating thickness was nominally 0.33 mm , which was allowed for in cutting the metal blades so as to minimize dimensional differences in the

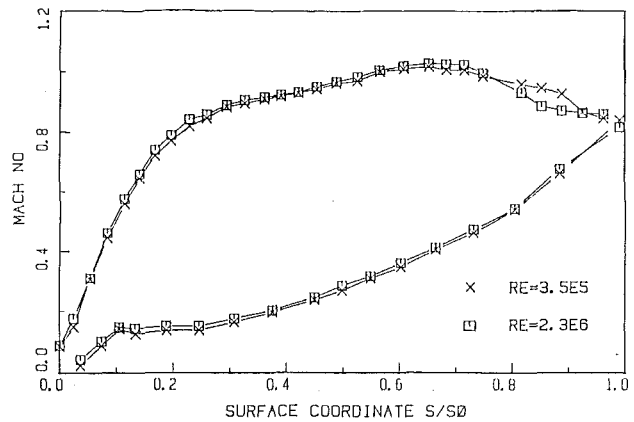


Fig. 4 Vane Mach No. distributions

three finished profiles. The profiles were compared on an expanded scale and found to correspond except for a slight thickening of the trailing edges of the TBC relative to the uncoated vanes.

The TBC polishing is a production process which involves "tumbling" the vanes for some hours in a drum containing abrasive pellets and which is effective in smoothing the surfaces evenly. The underlying structure of plasma-sprayed TBC is, however, still discernible after this process, as can be seen from Fig. 3.

Measurements

Vane Surface Pressures. There are significant practical difficulties involved in measuring surface static pressures with pneumatic tappings on the coated vanes, and so, because roughness was expected to influence these only slightly [4, 5] pressure distributions were measured for the untreated variant only.

As can be seen from Fig. 4, the wide range of Reynolds number involved has particular effect over the last 25 percent of the suction surface, after the point of minimum pressure.

Profile Loss. This is a collective term for aerofoil drag comprising skin friction, form or pressure drag, and wave drag due to the existence of shocks in supersonic flow. Of these the skin-friction component normally dominates, in the absence of strong shock waves or large flow separations.

The efficiency for energy conversion, or "primary efficiency," is given in terms of enthalpy by

$$\eta = \frac{h_{02} - h_2}{h_{01} - h_{2S}}$$

The above performance coefficient was monitored from pressure measurements upstream and downstream of the cascade, where the latter vary pitchwise due to the trailing-edge wakes. "Steady" downstream parameters were obtained by applying the method of Amecke [13] which uses the laws of conservation of mass, momentum, and energy to transfer the flow to an imaginary plane where it is considered homogeneous, or "mixed-out."

A trident (combined-exit-survey) probe, of the type described in [14], was used to measure the variation of total and static pressure and flow angle in the exit plane, approximately one axial chord length from the cascade. Measured pressure variations through a wake of each variant at the design condition are shown in Fig. 5. Once processed according to the Amecke procedure, these contribute to the plot of "primary loss coefficient" ($1 - \eta$) versus Reynolds number (Fig. 6). The majority of data points in Fig. 6 correspond to nominally 4 percent inlet turbulence intensity, generated in this facility by

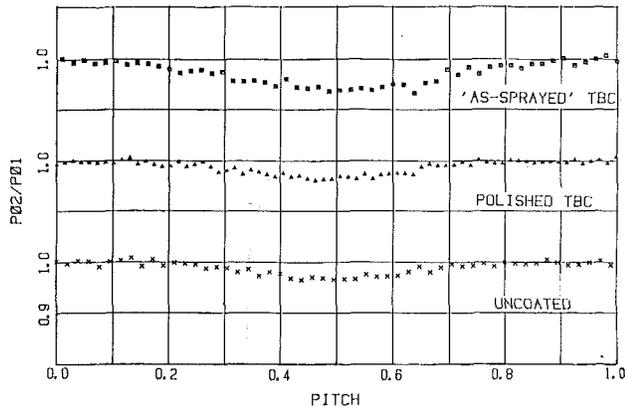


Fig. 5 Total pressures through wakes at design condition

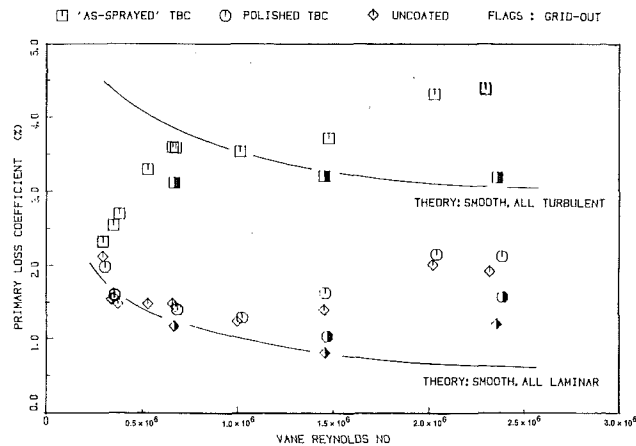


Fig. 6 Profile loss measurements

means of a single row of bars upstream of the cascade. The influence of free-stream turbulence on primary efficiency is simply tested at a few selected conditions by measurements with the turbulence grid removed.

Transition Detection. Laminar-turbulent transition was investigated using two distinct techniques.

For the uncoated vanes a flattened pitot probe was trailed along the surface at a constant height to detect the change in the boundary layer mean velocity profile which accompanies transition. The associated steepening of the velocity gradient results in a higher velocity at the height of the probe, and hence the dynamic pressure ratio

$$Q/Q_0 = \frac{P_{\text{probe}} - P_{\text{static}}}{P_{01} - P_{\text{static}}}$$

will also increase and this can be used as a transition indicator.

The variation of Q/Q_0 for the uncoated variant at three Reynolds numbers spanning the range of the loss measurements of Fig. 6 is illustrated in Fig. 7.

The principal method used for detecting transition on the TBC vanes was by a novel use of heated thin-film anemometers painted onto the TBC surfaces. The applied substance, designated "liquid bright platinum 05-X" (Englehard Industries), is a mixture of metallo-organic compounds dissolved in inorganic solvents containing platinum but also with small amounts of other metals. Fired in an oxidizing atmosphere to 640°C, the organic portion is burned away leaving a very thin, continuous metallic film. As many as six or seven coats are applied with firing after each until an acceptable film resistance is obtained. The maximum film thickness, according to [15], is 0.25 μm per application, which

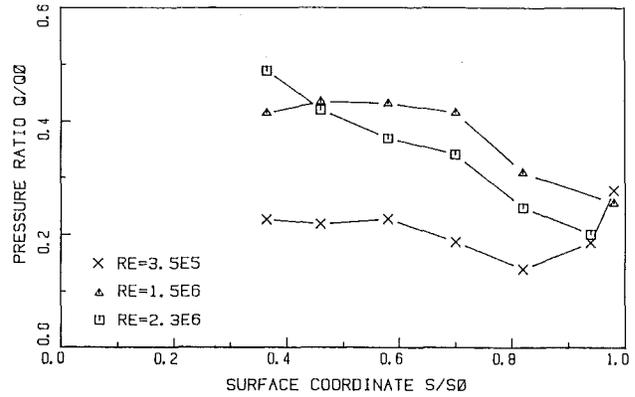


Fig. 7 Surface-pitot measurements on uncoated vane

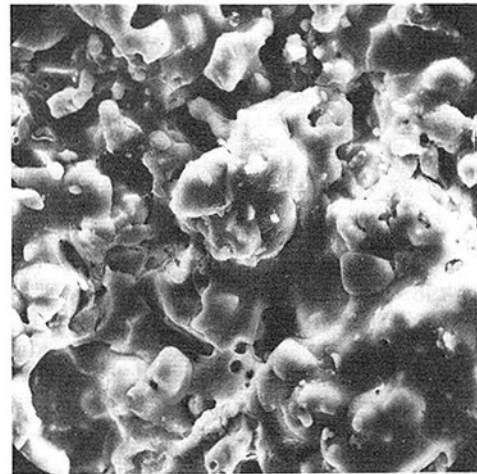


Fig. 8 Electron micrograph of sensing film on as-sprayed TBC surface (x 860)

in this case would result in a maximum total film thickness of less than 2 μm – the approximate measured (CLA) roughness of the polished TBC vanes. The actual total film thickness is likely to be less than this due to the porous nature of the plasma-sprayed TBC, which, according to [1], resembles "a solid material connected with a network of fine voids interspersed with larger voids." In fact, from magnified (1000×) Tallysurf traces, there is no discernible increase in height due to the films, which are only identifiable from a slight smoothing of the surface across their 0.5-mm width. This is because the liquid bright platinum is partially absorbed by the TBC, and tends to settle in the surface "troughs," as can be seen from Fig. 8, which shows an electron micrograph of a film on an as-sprayed TBC surface.

From the sensing films, silver-based conducting-paint tracks ran to castellations in the ends of the vanes as shown schematically in Fig. 9. Similar checks were made to ensure that roughness due to these was admissible. In the ends of the vanes the leads were bonded to wires for connection to a DISA 55M01 anemometer main unit.

The operating principles of "constant temperature" anemometry are well documented and are thus not discussed in depth. Suffice to say that the sensing films work on the principle that the rate of heat transfer is related to the wall shear stress [16], and hence that the state of the boundary layer is reflected in film power. The fluctuating (rms) output is a sensitive indicator of transition which peaks at approximately the mid-point of the process.

A high-pass filter was used to separate the high- and low-frequency components which were then digitized prior to being stored on a Digital Equipment Corporation PDP 11/24

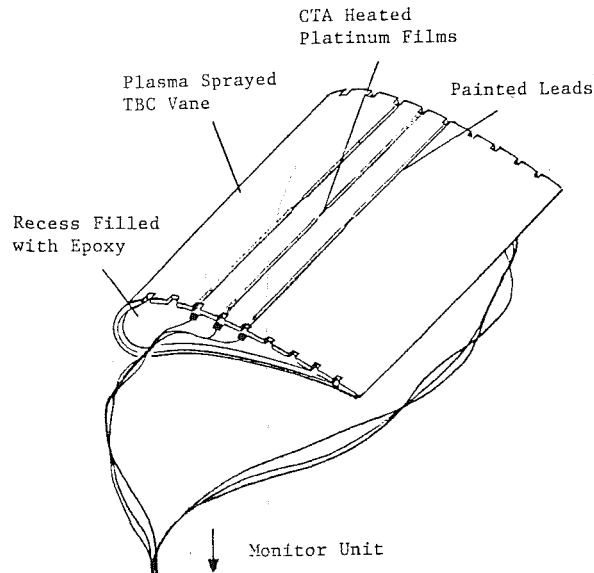


Fig. 9 Schematic of thin-film arrangement

computer. The high-frequency data were preserved by sampling at the rate of 200 kHz using a Datalab DL 2800 transient recorder. A low-pass 50 kHz filter was used prior to acquisition to avoid aliasing errors.

Variations of a-c rms with suction-surface distance at various Reynolds numbers are plotted for both TBC variants in Fig. 10. The data are normalized by the mean, or d-c, voltage to eliminate differences in film surface area and degree of "overheat."

The suction surfaces only are considered since roughness on these is expected to be most influential. For example, in cascade tests [6], emery-paper roughness over the whole of the convex surface was three times as detrimental to cascade performance compared with that over the whole of the concave surface. The critical area was found to be from the throat to the trailing edge along the convex surface.

Discussion of Results

The variation of primary loss coefficient is shown as a function of Reynolds number in Fig. 6, together with theoretical estimates for smooth vanes for the two cases of (a) all laminar, and (b) all turbulent boundary layers. These are specific to this particular profile and are obtained from a simplified theoretical analysis, detailed in [6], which assumes that the flow is two-dimensional, incompressible, and always attached.

The inference from this comparison is that the steep rise in loss for the as-sprayed TBC variant is attributable to a rapid advance of transition from around the trailing-edge region at $Re \sim 2 \times 10^5$ to near to the leading edge at $Re \sim 1 \times 10^6$. This appears to be confirmed by the thin-film measurements of Fig. 10(a), where the thin-film a-c signal peak shifts from around 75 to 35 percent of the suction-surface length over the Reynolds number range 3.5×10^5 to 5.5×10^5 . A possible explanation for the wayward variation at the lowest Reynolds number of 3.5×10^5 is an oscillating region of separated flow. According to Figs. 4, 7, and 10, this Reynolds number is the only test condition for which the boundary layer is predominantly laminar at the point of minimum pressure, where the pressure gradient turns "adverse." However, this also applies in the case of the "smooth" profiles which in this respect appear well behaved.

The as-sprayed TBC thin-film measurements stop at $Re = 5.5 \times 10^5$ since beyond this (1×10^6 and above) the signals

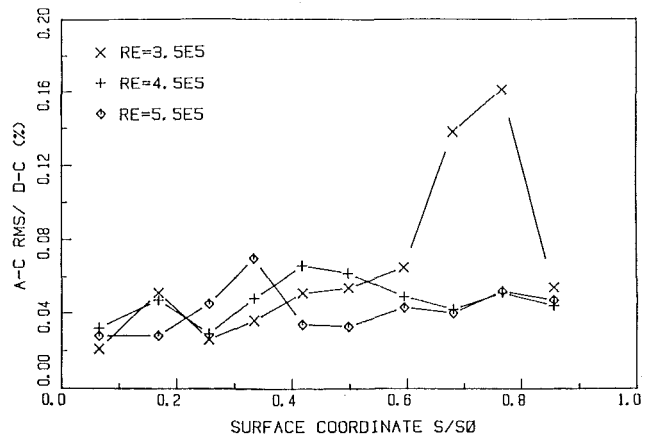


Fig. 10(a) Thin-film measurements on as-sprayed TBC vane

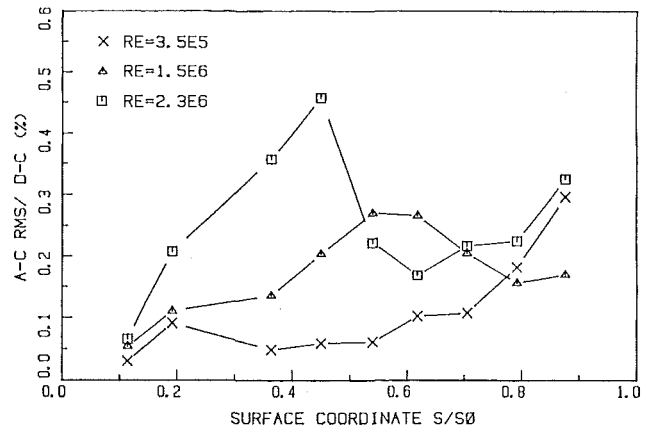


Fig. 10(b) Thin-film measurements on polished TBC vane

became noisy and unusable. This may have been due to the onset of rough flow where the peaks of the films themselves would be expected to shed wakes of their own as well as suffer direct buffeting from the turbulence. The apparently asymptotic rise in loss thereafter is therefore difficult to explain conclusively – particularly since this characteristic is shared by the smooth variants and Figs. 7 and 10(b) suggest that these may be experiencing further transition.

The key to understanding the variations at high Reynolds number may possibly be provided by the measurements with the turbulence grid removed. Based on these admittedly few points, the rapid advance of transition onset of the as-sprayed TBC vane appears to be simply delayed, and the loss appears to become independent of Reynolds number, as though fully rough, almost immediately afterward. In contrast, the "grid-out" curves of the uncoated and polished TBC variants appear to retain their shape, as though the same process of advancing transition occurs, though delayed, without the excitation of a turbulent free-stream.

The above interpretation implies that although all of the "grid-in" curves appear similar in form above $Re \sim 1 \times 10^6$, this is not necessarily due to the same cause. The question that remains is: What might be responsible for the rise in the as-sprayed TBC loss if advancing transition is discounted?

The effects of free-stream turbulence on turbulent boundary layer skin friction and heat transfer are known to be potentially significant [17–19]. More specifically, the strength of these influences is considered to depend on mainly three parameters: turbulence intensity, the momentum thickness Reynolds number, and the ratio of free-stream dissipation length scale to boundary layer thickness [20, 21]. Concentrating on the second of these, according to the analysis of

[20], turbulent boundary layers will be particularly susceptible to the influence of free-stream turbulence when the momentum thickness Reynolds number exceeds a nominal "threshold" level of about 5000 (reduced viscous damping of turbulence entrained from the free-stream being a possible physical explanation). This indeed appears to be evident in a number of experimental studies, e.g., [17, 22, 23], giving rise to anomalous heat transfer data in particular (free-stream turbulence appears to have a significant effect in some cases while a negligible effect in others).

Although this is not normally an issue since gas turbine aerofoil momentum thickness Reynolds numbers are usually well below the so-called threshold level, in this case, based on the measured trailing-edge boundary layers at the highest vane Reynolds number, Re_θ , for the uncoated, polished TBC, and as-sprayed TBC variants were approximately 4500, 6000, and 11,400, respectively (which relative values are consistent with other measurements [4]).

In addition, the ratio of free-stream dissipation length scale to boundary layer thickness, previously referred to, may also be relevant. Free-stream turbulence should be expected to have maximum impact when this ratio is equal to unity [21], and this may be more likely in the case of the as-sprayed TBC vanes due to their appreciably thicker boundary layers.

Hence, although the evidence is somewhat circumstantial, it is possible that at high Reynolds numbers the as-sprayed TBC variant suffers more from an exaggerated effect of free-stream turbulence on turbulent shear, as distinct from advancing transition detected on the smooth vanes.

Finally, it is useful to ask whether any quantitative comparisons can be drawn between the data and established relationships such as Feindt's critical roughness for transition, or the demarcation of the roughness regimes. A possible approach, given the uncertainty in defining k_s , is to accept and make use of the Feindt criterion, so that $Re \sim 2 \times 10^5$, around which point the as-sprayed TBC loss starts to take off, corresponds to the critical roughness Reynolds number, $Re_k = 120$. This gives $k_s \sim 40 \mu\text{m}$ for the as-sprayed surface ($10 \mu\text{m}$ CLA) which is reasonable considering that the quoted "critical" vane Reynolds number is neither precise nor local. The hypothesis of fully rough flow above $Re \sim 1 \times 10^6$ for the case of the as-sprayed TBC variant is also seen to be feasible given the choice of the above critical roughness datum.

Conclusions

The measurements confirm the general importance of surface finish in terms of its effect on cascade efficiency. In particular, there is the possibility of significant extra loss, depending on Reynolds number, due to the thermal barrier coating in its as-sprayed state. In this situation polishing coated vanes is shown to be largely effective in restoring their performance. In addition, there appears to be a critical low Reynolds number below which the range of roughness tested has no effect on cascade efficiency.

The profile loss measurements are substantiated by transition and other boundary layer measurements, where the former involves a novel use of thin-film anemometers painted and fired onto the TBC surfaces. Although the technique was

unsuccessful at high Reynolds numbers thought to coincide with fully rough conditions, it was otherwise effective.

Acknowledgments

The authors wish to thank the staff of Oxford University Engineering Department who have assisted in this project. The advice and guidance of Professor D. L. Schultz, Rolls-Royce Ltd., and the Ministry of Defence (Procurement Executive) are also gratefully acknowledged, as is the support of the Science and Engineering Research Council.

References

- 1 Stepka, F. S., et al., "Summary of NASA Research on Thermal-Barrier Coatings," NASA TM X-73584, 1977.
- 2 Stabe, R. G., and Liebert, C. H., "Aerodynamic Performance of a Ceramic-Coated Core Turbine Vane Tested With Cold Air in a Two-Dimensional Cascade," NASA TM X-3191, 1976.
- 3 Bammert, K., and Sandstede, H., "Measurements Concerning the Influence of Surface Roughness and Profile Changes on the Performance of Gas Turbines," ASME Paper No. 72-GT-34.
- 4 Bammert, K., and Sandstede, H., "Measurement of the Boundary Layer Development Along a Turbine Blade With Rough Surfaces," ASME JOURNAL OF ENGINEERING FOR POWER, Vol. 102, 1980, pp. 978-983.
- 5 Bammert, K., and Milsch, R., "Boundary Layers on Rough Compressor Blades," ASME Paper No. 72-GT-48.
- 6 Forster, V. T., "Performance Loss of Modern Steam-Turbine Plant Due to Surface Roughness," *Proc. Inst. Mech. Eng.*, Vol. 181, Pt. 1, No. 17, 1966.
- 7 Baines, N. C., et al., "A Short-Duration Blowdown Tunnel for Aerodynamic Studies on Gas-Turbine Blading," ASME Paper No. 82-GT-312.
- 8 Feindt, E. G., "Untersuchungen über die Abhängigkeit des Umschlages Laminar-Turbulent von der Oberflächenrauigkeit und der Druckverteilung," Diss., Braunschweig, 1956.
- 9 Schlichting, H., "Experimentelle Untersuchungen zum Rauigkeitsproblem," English trans. in *Proc. Soc. Mech. Eng. USA*, 1936.
- 10 Nikuradse, J., "Stromungsgesetze in rauhen Röhren," English trans. NACA TM 1292, 1950.
- 11 Han, Lit S., "Turbulent Flow Over Rough Turbine Airfoils," AFWAL TR-85-2056, 1985.
- 12 Mulvaney, D. J., and Newland, D. E., "Identification of Surface Roughness," *Proc. Inst. Mech. Eng.*, Vol. 199, 1985, pp. 281-286.
- 13 Arnecke, J., "Anwendung der Transsonischen Ähnlichkeitsregel auf die Strömung durch ebene Schaufelgitter," Göttingen, 1968.
- 14 Sieverding, C., "Pressure Probe Measurements in Cascades," AGARD-AG-207, Section 1, pp. 20-36.
- 15 Hopper, R. T., "How to Apply Noble Metals to Ceramics," *Ceramic Industry*, June 1963.
- 16 Bellhouse, B. J., and Schultz, D. L., "Determination of Mean and Dynamic Skin-Friction, Separation and Transition in a Low-Speed Flow With a Thin-Film Heated Element," *Journal of Fluid Mechanics*, Vol. 24, Pt. 2, 1966, pp. 379-400.
- 17 Charnay, G., Compte-Bellot, G., and Mathieu, J., "Development of a Turbulent Boundary Layer on a Flat Plate in an External Turbulent Flow," AGARD-CP-93, Paper 27, 1971.
- 18 Hancock, P. E., "Effect of Free-Stream Turbulence on Turbulent Boundary Layers," Ph.D. Thesis, Imperial College, University of London, 1980.
- 19 Simonich, J. C., and Bradshaw, P., "Effect of Free-Stream Turbulence on Heat Transfer Through a Turbulent Boundary Layer," *ASME Journal of Heat Transfer*, Vol. 100, 1978, pp. 671-677.
- 20 McDonald, H., and Kreskovsky, J. P., "Effect of Free-Stream Turbulence on the Turbulent Boundary Layer," *International Journal of Heat and Mass Transfer*, Vol. 17, 1974, pp. 705-716.
- 21 Bradshaw, P., "Effect of Free-Stream Turbulence on Turbulent Shear Layers," ARC Paper No. 35648, 1974.
- 22 Kline, S. J., Lisin, A. V., and Waitman, B. A., "Preliminary Investigation of Effect of Free-Stream Turbulence on Turbulent Boundary Layer Growth," NASA TN-368, 1960.
- 23 Blair, M. F., "Influence of Free-Stream Turbulence on Turbulent Boundary Layer Heat Transfer and Mean Profile Development," Pts. 1 and 2, *ASME Journal of Heat Transfer*, Vol. 105, 1983, pp. 33-47.

A Review of Staggered Array Pin Fin Heat Transfer for Turbine Cooling Applications

J. Armstrong

D. Winstanley

Mechanical Component Design,
Garrett Turbine Engine Company,
Phoenix, AZ 85010

A review of heat transfer and flow friction data for staggered arrays of pin fins in turbine cooling applications is presented. This review presents discussions on local- and array-averaged heat transfer, the effects of different geometric parameters such as pin height and pin spacing on heat transfer and flow friction, and the effect of the accelerating flow in converging pin fin channels. A review of current heat transfer correlations is also presented with recommendations for correlating parameter limits and correlation accuracy. The correlations currently available for friction factor are reviewed, with an attempt to account for the effects of the converging channels.

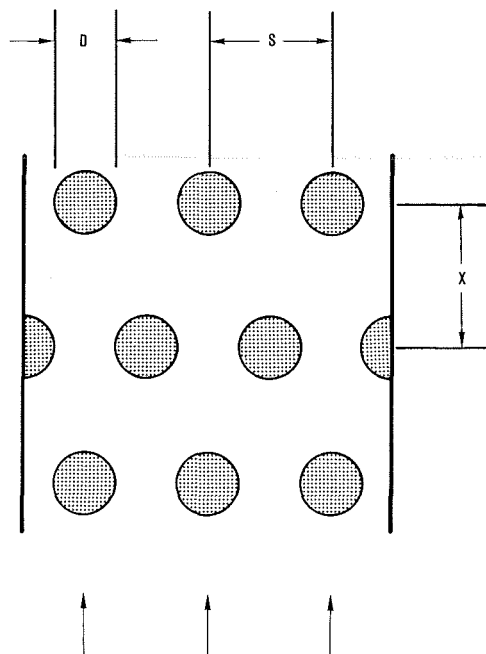
Introduction

Pin fin banks are one common geometry used to increase the internal heat transfer to a turbine blade or vane. A pin fin bank is an array of short cylinders which usually span the cooling flow passage. They increase the internal wetted (cooled) surface area and increase the passage flow turbulence. One common arrangement of pin fins is a staggered array (Fig. 1).

The pin fins commonly used in turbine cooling have pin height-to-diameter ratios H/D between $1/2$ and 4 due to blade size and manufacturing constraints (Lau et al., 1985). Arrays of long cylinders ($H/D > 8$) have been in use in the heat exchanger industry for some time. The heat transfer in long pin arrays is dominated by the cylinders while the endwall effects have been shown to be secondary (Zukauskas, 1972). Short pins ($H/D < 1/2$) are used in certain types of plate-fin heat exchangers where the cooling crossflow normal to the pins is closely constrained by the endwalls (Webb, 1980). The heat transfer in these arrays is dominated by the endwalls and the exposed surface area is actually reduced with the presence of the pins. Interpolation between these two cases will not solve the case of intermediate-sized pin fins used in turbine blades and vanes.

The heat transfer in turbine blade pin fin arrays combines the pin heat transfer with the endwall heat transfer. The endwall heat transfer is considerably greater than the smooth wall case as would be expected. The pins serve to break up the flow and increase the turbulence. The pin heat transfer is dominated by the edge effects. Sparrow et al. (1984) used a long cylinder attached to a wall in crossflow to demonstrate the cylinder-endwall interaction. Flows with $Re_D = 3500$ to $23,000$ (where $Re_D = \rho U_\infty D / \mu$ and D is the cylinder diameter) were tested. His boundary layer thickness ($U/U_\infty = 0.98$) varied from $y/D = 0.8$ for the highest Reynolds number to

$y/D = 1.3$ for the lowest Reynolds number. Using both flow visualization and a naphthalene mass transfer technique, Sparrow showed that the wall-cylinder interactions were all confined to within one diameter of the wall. The effect of the wall was shown to decrease the nearwall cylinder heat transfer relative to the heat transfer away from the wall where the cylinder is unaffected by the endwall. The conclusion to be drawn from this study is that the average pin heat transfer for relatively short pin fins in turbines should be lower than long cylinder heat transfer rates.



STAGGERED PIN FIN ARRAY

Fig. 1 Pin fin array notation

Contributed by the Gas Turbine Division of THE AMERICAN SOCIETY OF MECHANICAL ENGINEERS and presented at the 32nd International Gas Turbine Conference and Exhibit, Anaheim, California, May 31-June 4, 1987. Manuscript received at ASME Headquarters February 19, 1987. Paper No. 87-GT-201.

The cooling air flow is characterized by the pin fin bank Reynolds number. Zukauskus (1972) divides the flow into three categories for long tubes. Below $Re_D < 10^3$, the flow pattern is predominantly laminar. This case has been numerically investigated by Launder and Massey (1978) for long tubes. An intermediate flow regime occurs between $10^3 < Re_D < 2 \times 10^5$, where the boundary layer around the cylinder contains both laminar and turbulent regions. This is the operating regime associated with turbine blade cooling. Both cylinder vortex shedding and turbulence production occur within this range. Flow rates higher than $Re_D > 2 \times 10^5$ are classified as critical flows since the flow is highly turbulent.

Pin Fins Under Uniform Flow: Staggered Array Heat Transfer

Array Averaged Heat Transfer. Van Fossen (1982) published an early paper on pin fin cooling in a staggered array. He used two four-row banks with pins placed in an equilateral triangular spacing. The two geometries tested were $H/D = 1/2$, $x/D = 1.732$, $S/D = 2.0$, and $H/D = 2$, $x/D = 3.464$, $S/D = 4.0$. Although Van Fossen developed a correlation based on volume and area averaging (to be discussed later), his data and correlation can be recast to demonstrate a Reynolds number dependence of

$$Nu_D = 0.153 Re_D^{0.685} f(\text{geometry}) \quad (1)$$

for $300 < Re_D < 120,000$

Metzger and associates (Haley, 1983; Metzger et al., 1981, 1982a, 1982b, 1986) have done extensive studies of pin fin banks with $H/D = 1.0$ and $S/D = 2.5$. Most recently, Metzger et al. (1986) correlated the effect on heat transfer of streamwise pin spacing, for geometries varying from $x/D = 1.5$ to $x/D = 5$. The data were correlated using

$$Nu_D = 0.135 Re_D^{0.69} (x/D)^{-0.34} \quad (2)$$

for $1.5 < x/D \leq 5.0$
 $S/D = 2.5$
 $H/D = 1.0$
and $10^3 < Re_D < 10^5$

After applying a correction factor to Van Fossen's data to account for the difference in number's of rows averaged,

Metzger stated that the above equation predicted Van Fossen's data well and should be good for $0.5 < H/D < 3.0$.

Arora and Abdel Messeh (1983) studied pins for $H/D = 1$. They used a ten-row length pin fin rig similar to Metzger's. Copper pins were glued onto the copper sidewalls with a high conductivity epoxy to reduce the pin-endwall contact resistance. Four different pin fin array geometries were tested. Arora's data are well predicted by both the Metzger and Van Fossen correlations. Out of the 17 points compared by the authors, only one point differed from these correlations by more than 20 percent.

Zukauskus (1972) proposed a heat transfer correlation for long tubes of the form

$$Nu_D = 0.35 Re_D^{0.60} f(\text{geometry}) \quad (3)$$

This Reynolds number exponent was also confirmed by Sparrow et al. (1978, 1980). Simoneau and Van Fossen (1984) studied the heat transfer on the pins in a staggered array with relatively short pins ($H/D = 3.0$). They found the Reynolds number exponent varied between 0.59 and 0.65 when correlated row by row.

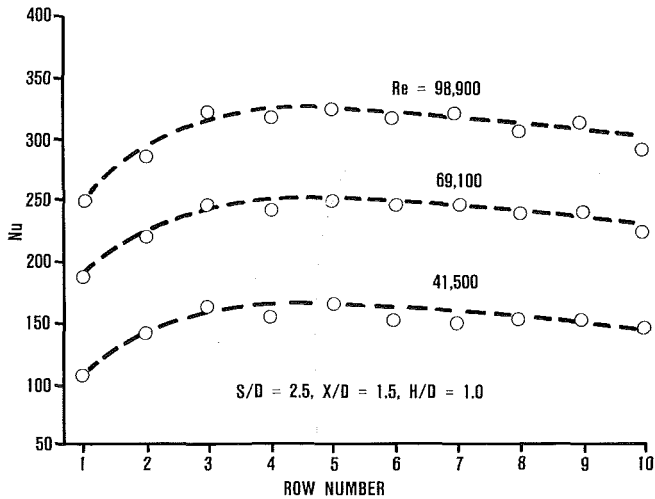
The classic research on long pin fins ($H/D = 7.72$) was documented by Kays and London (1955) (PF-4) for heat exchanger applications. The results show significantly higher heat transfer than the previously quoted short pin fin studies. These data showed a Reynolds number dependence that was approximately 0.5, suggesting a fundamental difference in flow phenomena between short and long pin fins. Kays and London's test section contained wire trips on the endwalls. This may alter the interpretation of comparisons with smooth wall pin fin results.

Brigham and Van Fossen (1984) studied taller pins of height $H/D = 4$. Both a four-row and an eight-row test section were studied. Higher heat transfer coefficients were measured than were reported in the shorter pin fin rigs, similar to the findings of Kays. Here again, a different Reynolds number dependence suggests a different mechanism for heat transfer.

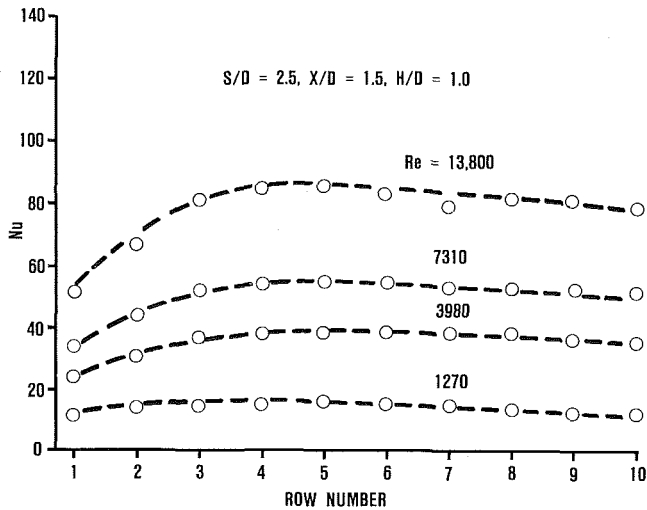
Peng (1984) studied longer pin fins with $H/D = 4$ and $H/D = 6$. He varied the pin spacing while keeping the ratio of transverse to longitudinal pin spacing equal to unity. Peng used 8, 11, and 16 row arrays, depending on pin spacing, to determine channel-averaging Nusselt numbers. Unfortunately

Nomenclature

A' = Van Fossen average flow area of pin fin bank (equation (9))	L = streamwise length of pin fin bank	Nu_D = pin fin array Nusselt number = hD/k
A_{\min} = minimum flow area of pin fin bank	m = fin effectiveness (equation (16))	NuD' = Van Fossen Nusselt number = hD'/k
A_t = total heat transfer surface area	\dot{m} = mass flow rate of air through pin fin bank	Nu_{Dh} = hydraulic diameter Nusselt number = hD_h/k
A_f = pin fin heat transfer surface area	M = flow Mach number	Nu_w = Nusselt number of wall
D = pin diameter	N = number of rows of pins in streamwise direction	Nu_p = Nusselt number or pins
D' = Van Fossen hydraulic diameter (equation (7))	S = transverse distance (center-to-center) between pins	Re_D = pin fin Reynolds number = $\dot{m}D/(\mu A_{\min})$
D_h = tube bank hydraulic diameter (equation (12))	U_∞ = free-stream fluid velocity	Re_{Dh} = hydraulic diameter Reynolds number = $\dot{m}D_h/(\mu A_{\min})$
f = flow friction factor = $\Delta P/2\rho V_{\max}^2 N$	V = open volume in pin fin bank	η_{fin} = fin efficiency of pin
h = heat transfer coefficient	V_{\max} = maximum flow velocity between pins at A_{\min}	η_t = pin fin bank efficiency
H = height of pin	W = width of entire channel transverse to flow	θ = channel convergence angle
k = thermal conductivity of air	x = streamwise distance between pins	μ = viscosity of air
k_{pin} = thermal conductivity of pin material	y = vertical distance from end-wall (Sparrow et al., 1984)	ρ = density of air
		ϕ = converging array heat transfer multiplier equation (5)



A) HIGH REYNOLDS NUMBER



B) LOW REYNOLDS NUMBER

Fig. 2 Local row resolved pin fin heat transfer (Metzger et al., 1981)

ly, his test rig had a very low aspect ratio ($W/H = 2$ and 3); heat transfer also took place from the side walls, which were parallel to the pins. Peng's results do show higher heat transfer than the short pin fins and a different Reynolds number dependence.

It is evident from the above studies that the heat transfer varies to the Reynolds exponent of about 0.60 for arrays with long pins and for the pins themselves. This is perhaps not surprising when viewed in light of the heat transfer for a single cylinder in crossflow; for example, Holman (1972) suggests

$$\text{Nu}_D = 0.193 \text{Re}_D^{0.618} \quad (4)$$

for the average heat transfer around a single cylinder in crossflow in the Reynolds number range $4000 < \text{Re}_D < 40,000$ (the approximate range of interest here). This equation, for a single cylinder, bears an amazing resemblance to equations (1) and (2), which were for arrays of short pin fins. A comparison of the Reynolds number exponent for the single cylinder with the value for pin fin arrays and the pins themselves indicates that the physical mechanism driving the heat transfer for long pin fins and the pins is flow around the pin (with the attendant vortex shedding, etc.).

The impact of the endwall on heat transfer for shorter pin fins can be expected to have a greater Reynolds number dependence; smooth wall heat transfer channel correlations for turbulent flow vary with the 0.8 power. The 0.69 Reynolds

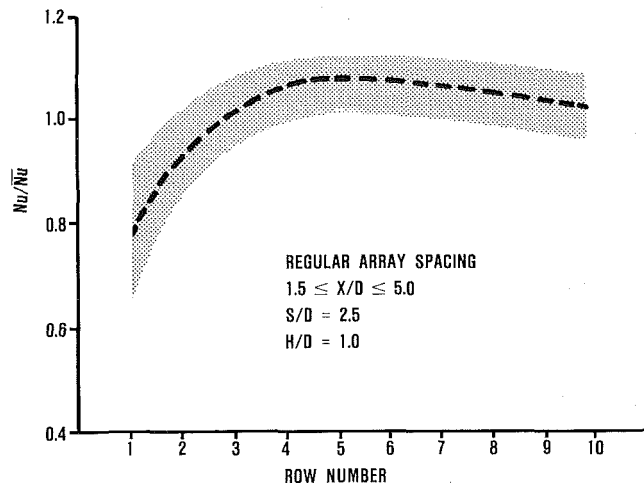


Fig. 3 Local row-resolved heat transfer correlation (Metzger et al., 1986)

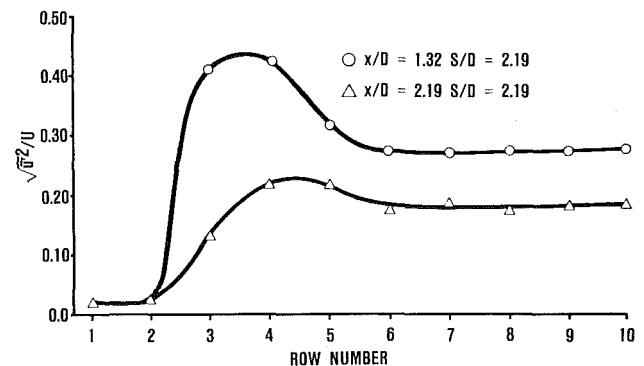


Fig. 4 Local turbulence intensity as measured by Metzger and Haley (1982a)

exponent of Metzger and Van Fossen for short pins clearly results from the combination of these two phenomena (i.e., the endwall impact on long pin or cylinder heat transfer).

Local Heat Transfer. Limited work has been done to study the local variation in heat transfer through a pin fin bank. Metzger et al. (1981) studied the row-by-row variation of heat transfer in a pin fin bank for a staggered array. Heat transfer was found to increase for the first few rows, reach a peak or maximum, and then slowly decrease toward an asymptotic, fully developed value. Typical results from this study are given in Fig. 2. Haley (1983) found the location of the row where the peak heat transfer occurred was observed to vary with streamwise pin spacing x/D . This peak moved from the fifth or sixth row for $x/D = 1.05$ up the second or third row for $x/D = 5.0$.

Metzger et al. (1986) characterized the row-by-row variation with a single curve given in Fig. 3. The shaded area in this curve represents the variance of the data tested. This curve was used to account for the differing number of rows used in the different studies. For example, when comparing the four-row data of Van Fossen (1982) with the ten-row data sets of Metzger et al. (1982b), the four-row data were multiplied by the factor $\bar{\text{Nu}}_{10}/\bar{\text{Nu}}_4$ calculated from Fig. 3. Both $\bar{\text{Nu}}_4$ and $\bar{\text{Nu}}_{10}$ are averages calculated from this figure. Although Fig. 3 was derived for pins of height $H/D = 1$, the curve's applicability was assumed to apply to all of the pin heights.

Metzger and Haley (1982a) found that the local maximum and subsequent decrease in heat transfer was related to the turbulence level. The hot-wire turbulence intensities measured showed a similar peak and decrease in turbulence level. Figure 4 is a reproduction of their hot-wire results. These results

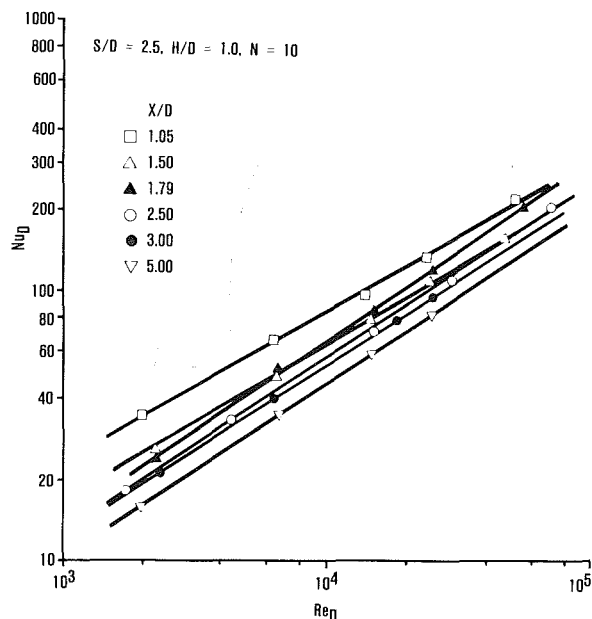


Fig. 5 Effect of streamwise spacing on array-averaged pin fin heat transfer (Metzger et al., 1982)

should be used with caution since the measurements were made at only one point in each row. The highly complex nature of the flow field makes these turbulence measurements highly dependent upon probe location. The relative fourth row maximum of turbulence displayed in Fig. 4 helps to explain the local row heat transfer trends. The higher turbulence levels would contribute to higher heat transfer rates measured at the third and fourth rows.

Simoneau and Van Fossen (1984) also measured the turbulence intensities in a six-row pin fin channel for a staggered array. The measurements showed that for a channel with pins $H/D = 3.01$, a peak turbulence intensity occurs at the third to fourth row with decreasing turbulence following through to the sixth row. This is consistent with Metzger's observations.

Brown et al. (1980) studied the row-by-row variation of heat transfer in a converging pin fin channel. The flow accelerated in the streamwise direction. However, as Metzger suggests, "Even though the heat transfer is resolved to individual rows, the large number of parameters involved, coupled with relatively high experimental uncertainties make the results difficult to generally interpret" (1981). The absence of guard heaters for the first and last row further complicate the results.

Effect of Streamwise Spacing of Pins. Metzger et al. (1982b) studied the relative effects of streamwise pin spacing (x/D) on array heat transfer. Test rigs using copper endwalls and wooden pins were constructed for this test. The use of wooden pins in measuring pin fin array heat transfer was demonstrated by Metzger and Haley (1982a). They used both thermally conducting copper pins and nonconducting wooden pins in similar arrays. Nusselt numbers in the latter study were based on the uncovered wall heat transfer area as opposed to the total exposed wall and pin surface area used in the former study. The nonconducting pin rig results predicted the conducting pin heat transfer coefficients within 10 percent. This conclusion afforded the possibility of testing many different pin fin geometries without having new rigs built.

The streamwise pin spacing variation experiments were run using the nonconducting wooden pins. The study found that the heat transfer does vary significantly with streamwise pin spacing as shown in Fig. 5. Clearly, increasing the streamwise spacing between pins results in decreasing the array heat transfer. The difference between the closely spaced pins

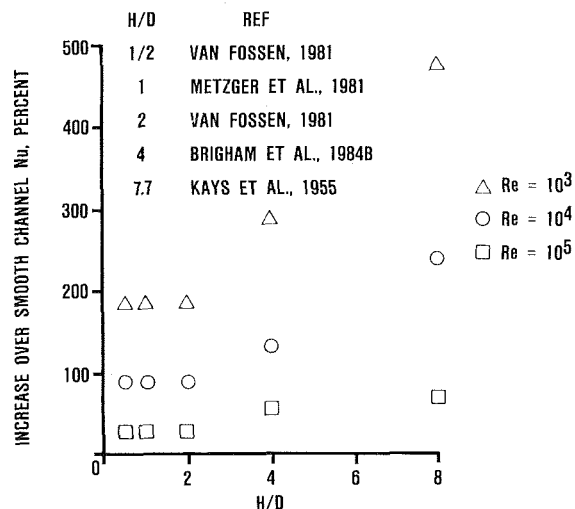


Fig. 6 Effect of pin fin height-to-diameter ratio on array-averaged pin fin heat transfer (Brigham and VanFossen, 1984)

($x/D = 1.05$) and the most widely spaced pin array ($x/D = 5$) was approximately 100 percent at $Re_D = 10^3$. This difference decreased to 50 percent at $Re_D = 10^5$. The inconsistency of the $x/D = 1.79$ case is possibly noise related (Metzger et al., 1982b). Similar noise effects were observed by Theoclitus (1966) for in-line pin arrangements. Equation (2) (Metzger et al., 1986) appears best to correlate this effect.

Effect of Pin Height on Array-Averaged Heat Transfer. Brigham and Van Fossen (1984a) investigated the effect of pin height on array-averaged heat transfer. Their results on the effect of H/D are presented in Fig. 6. Unfortunately, a single constant smooth channel Nusselt number was used to normalize all the pin fin data in this figure. Figure 6 does represent the relationship between pin height and overall heat transfer level, not the heat transfer increase over a smooth channel. Nevertheless, these results clearly show that for H/D less than three, there is no effect of H/D on array-averaged heat transfer. For H/D greater than three, the heat transfer increases rather significantly with increasing H/D . These results concur with the previous discussion of short versus long pin fin heat transfer.

A physical explanation for this observation can be made. For short pins, the endwalls compose a significant portion of the heat transfer surface; the pin heat transfer is dominated by the endwall interactions. The scale of the turbulent vortices can be expected to be of the order of the pin diameter, which is of the same order as the channel height for short pins. The flow will be well mixed with no separation of wall and pin effects. As the pins lengthen, a greater percentage of the surface area is comprised by the pin. Endwall-pin interactions no longer dominate the flow near the center of the channel. This is consistent with the previously mentioned observations of Sparrow et al. (1984), where a cylinder is affected by the endwall on the order of one diameter away from the wall. The pin heat transfer average, therefore, approaches cylinder-in-crossflow, which is higher than short pin fin heat transfer. The available data suggest that increases in pin heat transfer coefficient and area dominate the reduced fin efficiency as H/D increases, thereby leading to higher overall heat transfer.

Heat Transfer: Pin Versus Endwall. Simoneau and Van Fossen (1984) studied the heat transfer on the pins in a staggered pin fin array. The channel aspect ratio was quite small (2.05). The results showed a 7 to 15 percent difference in heat transfer between a single pin alone in the channel and a single pin in a row of pins. The ratio of the maximum velocities, however, was 1.55. Simoneau concluded that, at least for the pin heat transfer, maximum flow velocity based on the

Table 1 Row-resolved pin heat transfer (Simoneau and Van Fossen [1984])

$H/D=3.01, S/D=2.67, x/D=2.67$	
Row number	Percent increase in pin heat transfer over the first row
2	21
3	64
4	58
5	46
6	46

minimum free flow area was not the proper correlating parameter. Simoneau claimed that the average channel velocity should be used as the reference velocity for the Reynolds number. However, the correlation by Metzger et al. (1986), equation (2), uses the maximum channel velocity and gives good results thereby indicating that Simoneau's conclusion does not apply to the combined pin and endwall.

The heat transfer results measured by Simoneau agree well with the array heat transfer trend of Metzger. These data are presented in Table 1. A third row peak in the pin heat transfer level was measured with decreasing heat transfer from the fourth row on.

Metzger and Haley (1982a) also studied the individual pin heat transfer rates in a staggered array. They used a microfoil gage attached to a heated pin to measure heat transfer with respect to circumferential location on a pin. All measurements were made at the midspan of the pin and circumferential heat transfer was averaged. They observed the third to fifth row peak in Nusselt number that Simoneau had noted. Metzger also got good agreement between his first row Nusselt number and those predicted by Zukauskus for long pins. Heat flux measurements were not made at the ends of the pins, so that endwall effects could not be studied.

Van Fossen (1982) studied the average heat transfer effects of the first four rows of pins in a staggered pin fin array. Through the use of two different pin materials, copper and wood, the heat transfer coefficient of the pins relative to the endwalls was deduced. For the four-row rig used, Van Fossen claimed the pins have a 35 percent higher heat transfer coefficient than the endwalls; this claim has never been verified.

Metzger et al. (1982a) studied the endwall heat transfer as compared to the overall pin fin array heat transfer in a staggered pin fin array. They used thermally nonconducting wooden pins and calculated the heat transfer based on the exposed endwall surface area only. They found the endwall heat transfer coefficient to have almost the same level as the combined pin-endwall average. The endwall heat transfer did show a slightly lower Reynolds number dependence than the overall pin-endwall average for spacing of $x/D = 1.5$, $S/D = 2.5$, $H/D = 1.0$, and $x/D = S/D = 2.5$, $H/D = 1.0$. No attempts were made to confirm Van Fossen's conclusion that the pin heat transfer coefficient was 35 percent higher than the endwall heat transfer coefficient.

Effect of Channel Convergence on Heat Transfer. Brigham (1984b) studied the effect of channel convergence on pin fin heat transfer. Two rigs were constructed with four rows of pins of spacing $S/D = 4$ and $x/D = 3.464$. The first rig had a constant height of $H/D = 2.0$ with the side walls moving closer together, decreasing the rig width. This was designed to measure just the effect of flow acceleration. The second rig had a constant width with converging endwalls and the channel height varying from $H/D = 2.0$ to 1.0. The included angle was 3.8 deg. This rig was designed to measure the combined effect of accelerating flow and decreasing pin

height. Both test sections had the same inlet-to-outlet area ratios.

Brigham found that the constant height pin fin channel produced Nusselt numbers that were virtually equivalent to the nonaccelerating heat transfer numbers. The decreasing pin height rig however produced Nusselt numbers that were about 20 percent below those of the constant pin height case. Brigham therefore concluded that changing pin height was the dominant effect. However, based on the previous discussion, pin height does not have a significant impact on pin fin heat transfer for $H/D < 3$; so it seems that (local, between pin) acceleration is a more likely candidate for explaining the observed decrease in heat transfer with convergence.

Metzger et al. (1986) studied the local row heat transfer in a pin fin array converging at an angle of 2.54 deg. The six-row geometry tested had $S/D = 2.5$, $x/D = 1.5$, and the pin heights decreased from $H/D = 1.0$ to $H/D = 0.6$. Metzger verified the findings of Brigham that the converging array heat transfer fell below the constant height, nonconverging data. He attributed this phenomenon to the effect of the accelerating flow. Decreases in accelerating flow heat transfer have been measured over smooth flat plates and explained as the suppression of turbulence by the acceleration; whether this is also the case in converging pin fins remains to be seen. Metzger proposed a multiplying factor ϕ to account for this accelerating effect and correct the average heat transfer coefficient in converging channels

$$\phi = 2.28 \text{Re}_D^{-0.096} \quad (5)$$

Brown et al. (1980) also studied the effect of channel convergence. Unfortunately, the heat transfer data did not appear to follow a specific trend. More data are still required before the effects of channel convergence can be known with any confidence.

Effect of Entrance Condition on Heat Transfer. Limited work has been done on the problem of how the entrance flow condition affects the pin fin array heat transfer. Lau et al. (1985) recently used the naphthalene mass transfer technique to measure endwall heat transfer in a pin fin array. Two smooth duct entrances with lengths of 4 and 21 hydraulic diameters were used to determine how far into the array the entrance condition affects the endwall heat transfer. They found no dependence on entrance effect occurred after the second row.

The effect of a row of jets impinging on a pin fin array has not directly been studied. However, a related study on tube banks was carried out by Sparrow and Yanezmoreno (1983). They used long cylinders ($H/D = 12$) with different entrance conditions. They had a square duct and placed square area ratio contractions in front of the tube array. Using a flow visualization technique, they found that a 2:1 area ratio contraction affected the flow up to about the fifth row and a four-fold contraction had effects up to the eighth row. The effect of a row of jets impinging on a pin fin bank is expected to be less penetrating, owing to the more even distribution of jets and the damping effects of the endwalls.

Evaluation of Current Pin Fin Correlations for Array-Averaged Heat Transfer

Current heat transfer correlations for staggered pin fin arrays were examined to verify their accuracy with the published staggered array data. The Metzger equation (2) and the Van Fossen equation (1) appear to predict the short pin array heat transfer well. The Faulkner (1971) equation should be used to evaluate the array-averaged heat transfer in pin fin arrays with longer pins.

The literature data used in the following figures were collected from the references previously mentioned. Typical heat

A	83	:2.83	2.42	1.07	B	83	:2.83	2.22	1.07	C	83	:3.39	2.46	1.28	D	83	:1.41	2.42	1.07				
E	81	:2.5	2.5	1.0	F	81	:1.5	2.5	1.0	G	M	82B	:1.05	2.5	1.0	H	M	82B	:1.5	2.5	1.0		
I	M	82B	:1.79	2.5	1.0	J	M	82B	:2.5	2.5	1.0	K	M	82B	:3.00	2.5	1.0	L	M	82B	:5.00	2.5	1.0
M	V	82	:3.46	4.0	2.0	N	V	82	:1.73	2.0	0.5												

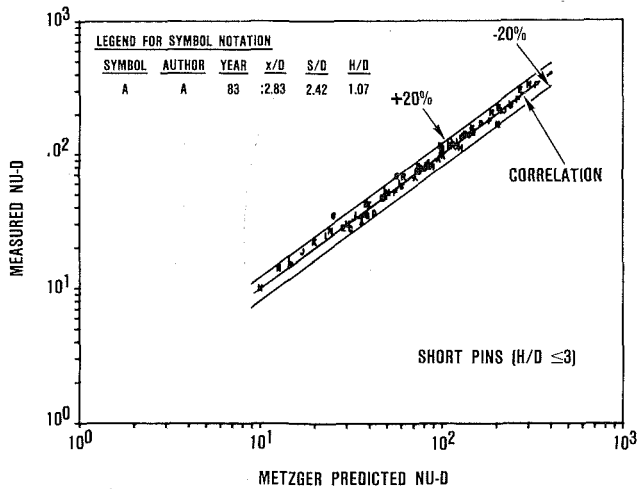


Fig. 7 Comparison of Metzger-predicted heat transfer to measured literature data—short pins

A	83	:2.83	2.42	1.07	B	83	:2.83	2.22	1.07	C	83	:3.39	2.46	1.28	D	83	:1.41	2.42	1.07				
E	81	:2.5	2.5	1.0	F	81	:1.5	2.5	1.0	G	M	82B	:1.05	2.5	1.0	H	M	82B	:1.5	2.5	1.0		
I	M	82B	:1.79	2.5	1.0	J	M	82B	:2.5	2.5	1.0	K	M	82B	:3.00	2.5	1.0	L	M	82B	:5.00	2.5	1.0
M	V	82	:3.46	4.0	2.0	N	V	82	:1.73	2.0	0.5												

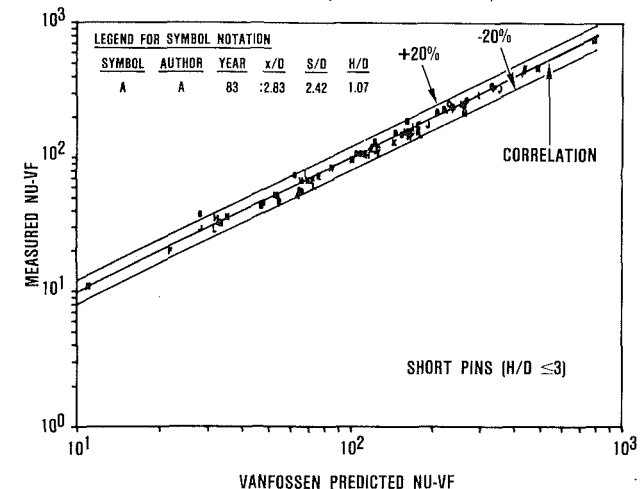


Fig. 9 Comparison of VanFossen-predicted heat transfer to measured literature data—short pins

O	B	84A	:3.46	4.0	4.0	P	P	84	:2.0	2.0	6.0	Q	P	84	:3.0	3.0	6.0	R	P	84	:4.0	4.0	6.0
S	P	84	:2.0	2.0	4.0	T	P	84	:3.0	3.0	4.0	U	P	84	:4.0	4.0	4.0	V	K	55	:1.92	3.06	7.72

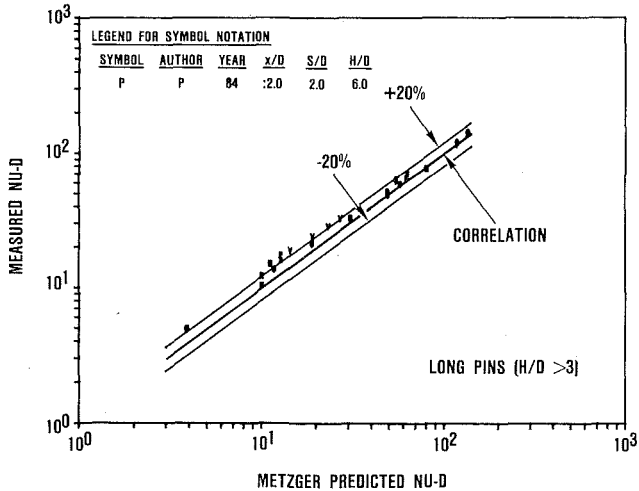


Fig. 8 Comparison of Metzger-predicted heat transfer to measured literature data—long pins

transfer coefficients were determined either from tabulated values or graphically. Only a few points were used from each study. These points spanned the range of Reynolds numbers tested. The data were then converted to the appropriate non-dimensional parameters where necessary.

A comparison of published data to the correlation of Metzger is given in Figs. 7 and 8. Figure 7 contains data points for $H/D \leq 3$; Fig. 8 covers the longer pins. These figures present the relationship between the measured pin fin Nusselt numbers and those predicted by Metzger. In order to derive those predicted values, equation (2) was modified to account for the number of pin rows tested. This multiplying technique was previously discussed in reference to Fig. 3. Therefore, the predicted Metzger Nusselt number was found using

$$Nu_D = \frac{\bar{Nu}_{x \text{ rows}}}{\bar{Nu}_{10 \text{ rows}}} Nu_D \quad (6)$$

Figures 7 and 8 present lines representing 20 percent over and 20 percent under the correlation. The legend at the top of each figure contains the initial of the lead author, the year of the publication as contained in the bibliography, and the x/D , S/D , and H/D of each study, respectively.

The Metzger correlation provides a reasonably accurate prediction of the short pin fin heat transfer. Only one point lies outside the ± 20 percent range; the data which fall outside of the correlation are for extremely close streamwise spacing of the pins ($x/D = 1.05$). The correlation is much less accurate for the longer pin heat transfer (Fig. 8). Based on the previous discussion of the effect of H/D on pin fin heat transfer, this result is not unexpected.

Figures 9 and 10 show Van Fossen's pin fin correlation in relation to the measured data. These graphs are similar to those of Figs. 7 and 8, except that the Nusselt numbers are based on the Van Fossen hydraulic diameter D' , instead of the pin diameter D , and the Reynolds numbers on the Van Fossen flow area, A' , instead of A_{\min} . The measured data were converted to the Van Fossen definitions using the following equations:

$$D' = \frac{4V}{A_t} \quad (7)$$

$$\frac{D'}{D} = \frac{(H/D)[4(x/D)(S/D) - \pi]}{2(x/D)(S/D) + \pi[H/D - 1/2]} \quad (8)$$

and

$$A' = \frac{V}{L} \quad (9)$$

$$\frac{A'}{A_{\min}} = \frac{(S/D) - (\pi/4)(x/D)^{-1}}{(S/D) - 1} \quad (10)$$

The final Van Fossen predictions were also adjusted for row effects using Fig. 3.

The Van Fossen correlation provides a reasonable prediction of the short pin results (Fig. 9). The very short streamwise x/D spacing data of Metzger were poorly predicted by Van Fossen as they were by Metzger. Figure 10 illustrates that the Van Fossen correlation is even less accurate than Metzger's for prediction of long pin data.

A correlation was proposed by Faulkner (1971) based on long pin fin data. He considered only equilateral triangular spaced pin fin geometries, where $x/D = (\sqrt{3}/2)(S/D)$. He used infinitely long cylinders and Kays data (1955) ($H/D \approx 8$) to correlate the endwall heat transfer. He correlated the data successfully with

S B 84A :3.46 4.0 4.0 | P P 84 :2.0 2.0 6.0 | Q U P 84 :3.0 3.0 4.0 | R V P 84 :4.0 4.0 6.0
 P 84 :2.0 2.0 4.0 | T P 84 :3.0 3.0 4.0 | U P 84 :4.0 4.0 4.0 | V K 55 :1.92 3.06 7.72

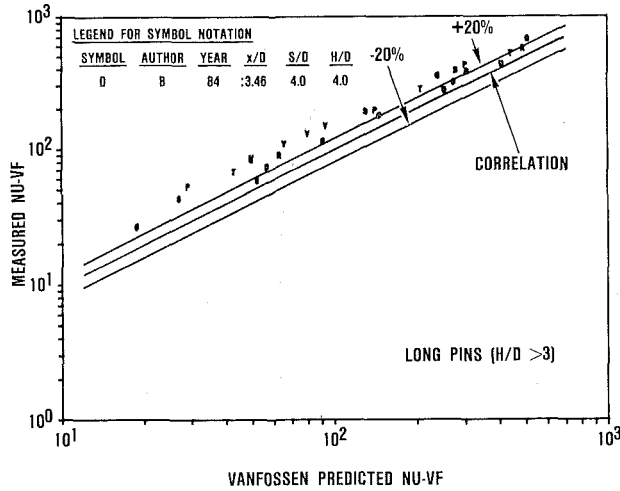


Fig. 10 Comparison of VanFossen-predicted heat transfer to measured literature data—long pins

S B 84A :3.46 4.0 4.0 | P P 84 :2.0 2.0 6.0 | Q U P 84 :3.0 3.0 4.0 | R V P 84 :4.0 4.0 6.0
 P 84 :2.0 2.0 4.0 | T P 84 :3.0 3.0 4.0 | U P 84 :4.0 4.0 4.0 | V K 55 :1.92 3.06 7.72

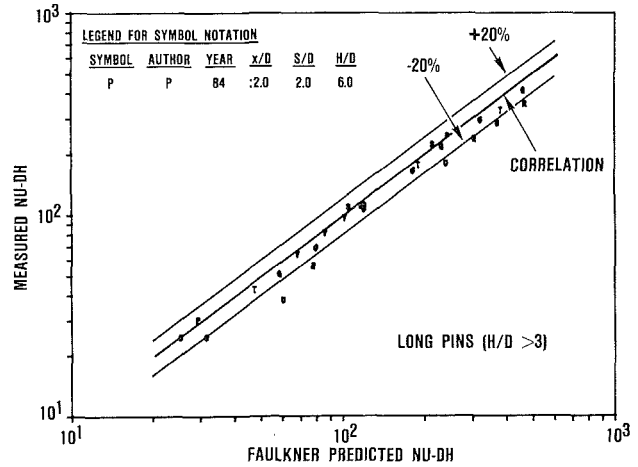


Fig. 12 Comparison of Faulkner-predicted heat transfer to measured literature data—long pins

A A 83 :2.83 2.42 1.07 | B A 83 :2.83 2.22 1.07 | C G A 83 :3.39 2.46 1.28 | D H A 83 :1.41 2.42 1.07
 E M 81 :2.5 2.5 1.0 | F M 81 :1.5 2.5 1.0 | G K M 82B :1.05 2.5 1.0 | H L M 82B :1.5 2.5 1.0
 I M 82B :1.79 2.5 1.0 | J M 82B :2.5 2.5 1.0 | K M 82B :3.00 2.5 1.0 | L M 82B :5.00 2.5 1.0
 N V 82 :3.46 4.0 2.0 | O V 82 :1.73 2.0 0.5

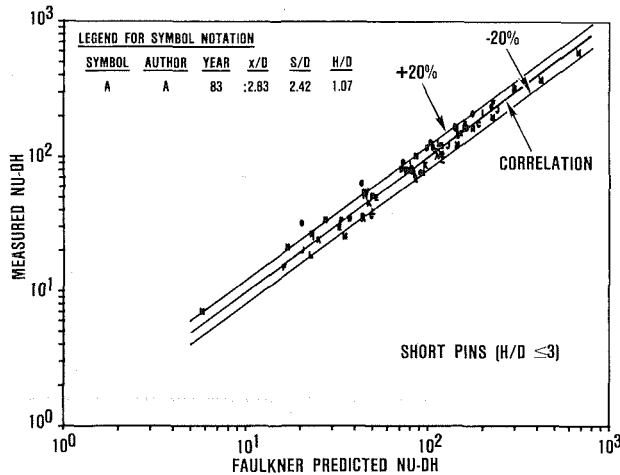


Fig. 11 Comparison of Faulkner-predicted heat transfer to measured literature data—short pins

Here again, Fig. 3 was used to modify equation (11). Since the Faulkner equation only considered triangularly spaced arrays, two different methods were used in determining the pin spacing parameter S . The first method was to use the transverse pitch as the characteristic pin spacing length. The second approach was to use the triangulated average of the transverse pitch and the distance between two pins of adjacent rows. The latter approach did not correlate the data as well as the transverse pin approach. Use of the transverse pitch in the Faulkner correlation will be implied from this point on.

For short pins (Fig. 11), the data fall within 20 percent of the correlation with a few notable exceptions. The correlation accuracy is apparently good for a limited range of x/D . For very close spacing, the Faulkner correlation underpredicts the heat transfer data of both Metzger et al. (1982b), and Arora and Abdel Messeh (1983). The lower limit on x/D appears to be 1.5. The very long streamwise spacing of Metzger ($x/D = 5$) is well below the predicted Faulkner Nusselt numbers. Arora's data for $x/D = 3.39$ correlate with the Faulkner curve. Therefore the streamwise pin spacing limits are $1.5 \leq x/D \leq 3.4$.

For long pins (Fig. 12), the Faulkner correlation is reasonably accurate except for widely spaced pins. The data of

$$Nu_{Dh} = \left[0.023 + \frac{4.143 \exp[-3.094D/S - 0.89(S/H)^{0.5075}]}{Re_{Dh}^{0.2946}} \right] Re_{Dh}^{0.8} Pr^{1/3} \quad (11)$$

where

$$Dh = \frac{4A_{\min} L}{A_t} \quad (12)$$

This correlation had the advantage of approaching the long tube correlations for large H/D . It also collapsed to the smooth duct correlation for small H/S and large S/D . The reason for choosing the correlating parameters H/S and D/S was strictly because they best fit the data.

The Faulkner correlation is compared with the existing data in Figs. 11 and 12. The measured data were converted to Nusselt and Reynolds numbers based on the hydraulic diameter D_h using

$$D_h = \frac{4A_{\min} L}{A_t} \quad (13)$$

$$\frac{D_h}{D} = \frac{4(x/D)(H/D)(S/D-1)}{2(x/D)(S/D) + \pi(H/D-1/2)}$$

Brigham and Van Fossen (1984a), Peng (1984), and Van Fossen (1982) all fall below the Faulkner correlation. The transverse pin spacing limits are therefore recommended to be $S/D < 4$.

The conclusion to be drawn from the data comparisons is that two correlations should be used to characterize pin fin heat transfer. Separate correlations should be used for the short and long pins. The short pin heat transfer ($H/D \leq 3$) should be predicted using either equation (1) or (2). Both do an equally good job of representing the data. Metzger's correlation appears more accurate than Van Fossen's (though not adequate) for long pins, and requires less mathematical calculation. Based on the data correlated, suggested limits for pin spacing are $1.5 \leq x/D \leq 5.0$ and $2.0 \leq S/D \leq 4.0$.

Long pin heat transfer ($H/D > 3$) should be predicted using the Faulkner correlation, equation (11). As stated before, the limits on the correlation's accuracy appear to be $1.5 \leq x/D \leq 3.4$ and $2.0 \leq S/D \leq 4.0$. For both short and long pins,

row effects should be accounted for using Fig. 3. If pin geometries conform to the above limits, a ± 20 percent accuracy can be expected.

In using the above correlations, it is important to understand the use of the resulting heat transfer coefficients. The heat transfer coefficients used are defined based on the total exposed area of both pin and endwall, and on an average surface temperature (again, pin and endwall). In thermal modeling of pin fins, the pins must be modeled, or the pin fin channel effectiveness must be accounted for.

This pin fin channel efficiency is found using:

$$\eta_t = 1 - \frac{A_f}{A_t} (1 - \eta_{fin}) \quad (14)$$

where

$$\eta_{fin} = \frac{\tanh(m H/2)}{(m H/2)} \quad (15)$$

and

$$m = \sqrt{\frac{4h}{k_{pin} D}} \quad (16)$$

The conductance for a wall with a pin fin array attached is then calculated as:

$$hA_{pin\ fin} = \eta_t h_{correlation} A_t \quad (17)$$

Pin-Fins Under Uniform Flow: Staggered Array Friction Factor

Average Friction Factor. Limited attention has been focused on the problem of the hydraulic resistance in a pin fin bank. This is because the relative pressure drop across the pin fin bank is often small when compared to the losses associated with impingement slots and other flow restrictions. However, accurate friction data are still desirable in turbine blade design.

Damerow et al. (1972) studied pin fin channels with ten rows of pins. His H/D varied from 2 to 4 with various pin spacing geometries. He found that H/D had no effect on the friction factor. Damerow did find that his data were well above the long tube correlation of Jacob (1938). Jacob's correlation was given as

$$f = \left[0.25 + \frac{0.1175}{(S/D - 1)^{1.08}} \right] Re_D^{-0.16} \quad (18)$$

Damerow used the Reynolds exponent from the above correlation to derive the correlation:

$$f = [2.06 (S/D)^{-1.1}] Re_D^{-0.16} \quad (19)$$

He found that for low pin fin bank inlet Mach numbers ($M < 0.36$), friction factor was not a function of row number.

Metzger et al. (1982b) measured the friction factors in arrays with short cylinders. Contrary to Damerow, they observed that their data were well represented by long tube correlations of Jacob. Metzger correlated his data with the curves

$$f = 0.317 Re_D^{-0.132} \quad (20)$$

$$\text{for } 10^3 < Re_D < 10^4$$

and

$$f = 1.76 Re_D^{-0.318} \quad (21)$$

$$\begin{aligned} &\text{for } 10^4 < Re_D < 10^5 \\ &\text{and } H/D = 1, S/D = 2.5, \\ &\text{and } 1.5 \leq x/D \leq 5.0 \end{aligned}$$

With the exception of $x/D = 1.79$, where unusually high friction measurements were recorded, the correlation fit the data to ± 15 percent.

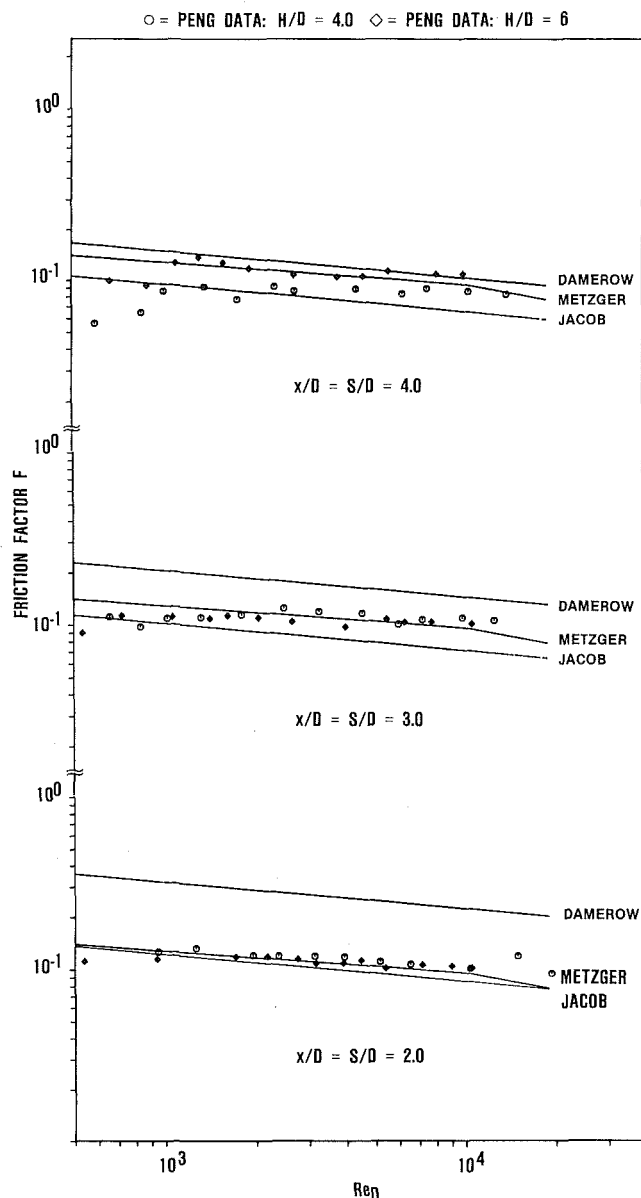


Fig. 13 Comparison of staggered array friction factor data

Comparisons between the correlation of Metzger et al. (1981) and the data of Peng (1984) are illustrated in Fig. 13. In Fig. 13, Peng's data agree quite well with the Metzger correlation. Note that H/D appears to have little effect on the friction level, except at the widest transverse spacing. The effect of S/D is more pronounced. As S/D becomes larger, the Damerow predicted friction factor decreases, approaching Metzger. Damerow's smallest transverse pin spacing was $S/D = 4.24$, which may account for this observation. Equations (20) and (21) appear to be quite accurate for a large range of H/D and S/D (specifically, $0.5 \leq H/D \leq 6.0$, and $2.0 \leq S/D \leq 4.0$).

Brown et al. (1980) reported friction measurements for a nonconverging pin fin array. A pin fin geometry of $x/D = 1.23$, $S/D = 3.0$, and $H/D = 1.5$ was investigated. Friction factor results were well above the correlations of Metzger, Damerow, and Jacob. One possible explanation for this deviation could be that the pins were quite close in the streamwise direction.

Effect of Channel Convergence on Friction Factor. Brown et al. (1980) measured the effects of channel con-

vergence on friction factor. Convergence angles of 0, 10, 15, and 20 deg. were used in this study. A reproduction of his results are presented in Fig. 14; clearly, the friction factor decreases as the convergence angle increases. Even though Brown's nonconverging data did not agree with other correlations, an attempt was made to correlate the relative effect of convergence using a single correlation factor (similar to the approach Metzger used with heat transfer). Each convergence angle data set was correlated with $Re_D^{-0.16}$ as suggested by Jacob. A multiplying factor was then correlated with

$$\frac{f_{\text{angle}}}{f_{0 \text{ deg}}} = \exp(-0.0612\theta) \quad (22)$$

for $0 < \theta < 20$
 $10^4 < Re_D < 10^5$
 $S/D = 3, X/D = 1.23, H/D = 1.5$

The resulting correlation is shown in Fig. 14. It is interesting to note that a 15 percent decrease in friction factor is predicted for the $\theta = 2.54$ case. The equivalent decrease in heat transfer as measured by Metzger is from 6 percent to 20 in heat transfer for $Re_D = 10,000$ – $50,000$. Further verification of equation (22) is necessary, since the effects of flow separation make a Reynolds analogy type of comparison inappropriate.

Conclusions

Pin fin heat transfer averaged over the array appears to vary with Reynolds number to a power between 0.6 and 0.7, depending on H/D . The local row-resolved heat transfer in staggered pin fin arrays increases to a peak in the first three to five rows followed by a slight decay in the succeeding downstream rows. The heat transfer split between the endwall and the pins remains unclear, although they appear to be of the same magnitude. There is no significant effect of pin height to diameter ratio below H/D of 3.0; for pin heights with H/D greater than 3.0, the array heat transfer increases with increasing H/D and approaches the long tube value. The effect of pin fin channel convergence appears to be separate from the pin-height effect; converging pin fin channels can reduce heat transfer and flow friction by as much as 20 percent.

The Faulkner correlation appears to be appropriate for array averaged heat transfer of long pins. Both Metzger and Van Fossen provide adequate heat transfer correlations of short pin fin data. Metzger provides an acceptable approach for staggered array flow friction.

Recommendations

There are a number of areas in pin fin heat transfer and flow friction that still require research. Some of these have been previously mentioned; there are others that require comment. One of the most glaring omissions in the area of short pin fins is the effect of the pin-endwall fillet; for most turbine cooling applications this fillet radius is approximately equal to the pin diameter. All of the research to date has been accomplished with little or no pin-endwall fillet. Since a significant amount of the turbulence associated with short pin fins can be expected to be generated in the corners at the pin-endwall junction, the impact of the corner fillet may be significant. It is recommended that research be performed to determine the impact of the pin-endwall fillet on pin fin heat transfer.

The impact of pin fin array inlet conditions also requires some attention. Many cooling designs use inlet impingement on the first row of pins. The inlet impingement is usually assumed to increase the heat transfer in the first rows and bring the heat transfer to a "fully developed" value at the second or third row. Additional research is recommended to confirm this assumption.

The row resolved heat transfer requires further research. An

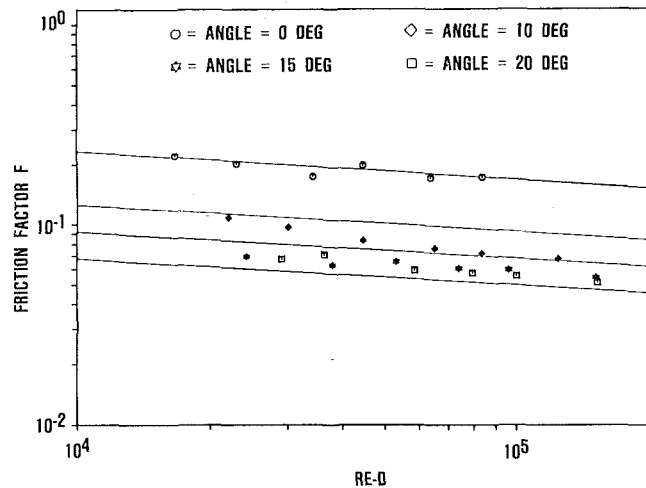


Fig. 14 Comparison of Brown's friction factor data to equation (22)

attempt, by the authors, to develop a generalized correlation for row resolved heat transfer had to be abandoned when it became obvious that there were insufficient data for a generalized correlation. The row-resolved curve suggested by Metzger (Fig. 3) is the best available; however, its general applicability is questionable.

A generalized correlation of the effect of pin channel convergence must await additional research in spite of the fact the vast majority of cooling designs using pin fins do so in a converging channel. Even though this effect is only on the order of 20 percent, when combined with the uncertainty of this and the other heat transfer correlations, it may lead to significant uncertainties in airfoil metal temperatures and turbine lives.

References

- Arora, S. C., and Abdel Messch, W., 1983, "Heat Transfer Experiments in High Aspect Ratio Rectangular Channel With Epoxied Short Pin Fins," ASME Paper No. 83-GT-123.
- Brigham, B. A., and VanFossen, G. J., 1984a, "Length-to-Diameter Ratio and Row Number Effects in Short Pin Fin Heat Transfer," ASME *Journal of Engineering for Gas Turbines and Power*, Vol. 106, pp. 241-245.
- Brigham, B. A., 1984b, "The Effect of Channel Convergence on Heat Transfer in a Passage With Short Pin Fins," NASA TM-83801.
- Brown, A., Mandjicas, B., and Mudyawa, J. M., 1980, "Blade Trailing Edge Heat Transfer," ASME Paper No. 80-GT-45.
- Damerow, W. P., Murtaugh, J. C., and Burgraf, F., 1972, "Experimental and Analytical Investigation of the Coolant Flow Characteristics in Cooled Turbine Airfoils," NASA CR-120883.
- Faulkner, F. E., 1971, "Analytical Investigation of Chord Size and Cooling Methods on Turbine Blade Requirements," NASA CR-120882, pp. 189-194.
- Haley, S. W., 1983, "Effects of Streamwise Spacing and Heated Entry on Heat Transfer in Pedestal Arrays," M.S. Thesis, Arizona State University, Phoenix, AZ.
- Holman, J. P., 1972, *Heat Transfer*, 3rd ed., McGraw-Hill, p. 186.
- Jacob, M., 1938, "Heat Transfer and Flow Resistance in Cross Flow of Gases Over Tube Banks," *Trans. ASME*, Vol. 59, pp. 384-386.
- Kays, W. M., and London, A. L., 1955, *Compact Heat Exchangers*, National Press, Palo Alto, CA, pp. 137-218.
- Lau, S. C., Kim, Y. S., and Han, J. C., 1985, "Effects of Fin Configuration and Entrance Length on Local Endwall Heat/Mass Transfer in a Pin Fin Channel," ASME Paper No. 85-WA/HT-62.
- Lauder, B. E. and Massey, T. H., 1978, "The Numerical Prediction of Viscous Flow and Heat Transfer in Tube Banks," ASME *Journal of Heat Transfer*, Vol. 100, pp. 565-571.
- Metzger, D. E., Berry, R. A., and Bronson, J. P., 1981, "Developing Heat Transfer in Rectangular Ducts with Arrays of Short Pin Fins," ASME Paper No. 81-WA/HT-6.
- Metzger, D. E., and Haley, S. W., 1982a, "Heat Transfer Experiments and Flow Visualization for Arrays of Short Pin Fins," ASME Paper No. 82-GT-138.

Metzger, D. E., Fan, Z. X., and Shepard, W. B., 1982b, "Pressure Loss and Heat Transfer Through Multiple Rows of Short Pin Fins," *Heat Transfer 1982*, Vol. 3, U. Grigull et al., eds., Hemisphere, Washington, pp. 137-142.

Metzger, D. E., Shepard, W. B., and Haley, S. W., 1986, "Row Resolved Heat Transfer Variations in Pin Fin Arrays Including Effects of Non-uniform Arrays and Flow Convergence," ASME Paper No. 86-GT-132.

Peng, Y., 1984, "Heat Transfer and Friction Loss Characteristics of Pin Fin Cooling Configurations," ASME *Journal of Engineering for Gas Turbines and Power*, Vol. 106, pp. 246-251.

Simoneau, R. J., and Van Fossen, G. J., 1984, "Effect of Location in an Array on Heat Transfer to a Short Cylinder in Crossflow," ASME *Journal of Heat Transfer*, Vol. 106, pp. 42-48.

Sparrow, E. M., and Ramsey, J. W., 1978, "Heat Transfer and Pressure Drop for a Staggered Wall-Attached Array of Cylinders with Tip Clearance," *Int. J. of Heat and Mass Transfer*, Vol. 21, pp. 1369-1377.

Sparrow, E. M., Ramsey, J. M., and Altemani, C.A.C., 1980, "Experiments on In-line Pin Fin Arrays and Performance Comparisons with Staggered Arrays," ASME *Journal of Heat Transfer*, Vol. 102, pp. 44-50.

Sparrow, E. M., Stahl, T. J., and Traub, P., 1984, "Heat Transfer Adjacent to the Attached End of a Cylinder in Crossflow," *Int. J. of Heat and Mass Transfer*, Vol. 27, pp. 233-242.

Sparrow, E. M., and Yanezmoreno, A. A., 1983, "Heat Transfer in a Tube Bank in the Presence of Upstream Cross-Sectional Enlargement," *Int. J. of Heat and Mass Transfer*, Vol. 26, pp. 1791-1803.

Sparrow, E. M., Stahl, T. J., and Traub, P., 1984, "Heat Transfer Adjacent to the Attached End of a Cylinder in Crossflow," *Int. J. of Heat and Mass Transfer*, Vol. 27, pp. 233-242.

Theoclitus, G., 1966, "Heat Transfer and Flow-Friction Characteristics of Nine Pin-Fin Surfaces," ASME *J. of Heat Transfer*, Vol. 88, pp. 385-390.

VanFossen, G. J., 1982, "Heat Transfer Coefficients for Staggered Arrays of Short Pin Fins," ASME *Journal of Engineering for Power*, Vol. 104, pp. 268-274.

Webb, R. L., 1980, "Air-Side Heat Transfer in Finned Tube Heat Exchangers," *Heat Transfer Engineering*, Vol. 1, pp. 33-49.

Zukauskas, A. A., 1972, "Heat Transfer From Tubes in Cross Flow," *Adv. in Heat Transfer*, Vol. 8, pp. 116-133.

Aerodynamic Design of a Power Turbine for an Aircraft Derivative Marine Gas Turbine

Ji Guiming
Senior Engineer.

Tan Zengxiang
Senior Engineer.

Zhang Mingchang
Engineer.

Marine Boiler & Turbine
Research Institute,
Harbin, People's Republic of China

Based on the aerodynamic design and development of a power turbine for an aircraft derivative marine gas turbine in our engineering practice and taking account of the specific features of a marinization effort, this paper describes the design approach and aerodynamic characteristics of the said power turbine, including parameter selection, design methodology, comparison of flow calculation results obtained by simple radial equilibrium and full radial equilibrium method, and a versatile design of the power turbine capable of rendering two power ratings. Also described is the use of variable geometry stator blades to accommodate a small amount of adjustment to the gas generator outlet parameters.

Introduction

In 1967 the British royal Navy made the momentous decision that all large and medium-sized naval surface ships would from then on be powered by gas turbines. Since then, more and more gas turbines have been used as propulsion plants in Soviet and U.S. naval surface vessels. Today, gas turbine engines have been favorably and widely accepted by the navies of nearly all major powers.

The fast-growing aircraft engine manufacturing industry has provided many high-quality gas turbines which can serve as prototype engines for marinization units. There are the following advantages to such aircraft derivative marine gas turbines: low cost, simplicity in installation, light weight, and modular construction. The above-cited features have greatly facilitated marinization efforts. The modification of aircraft engines for marine use has now been widely acknowledged as an important means of obtaining reliable main propulsion plants for naval surface vessels and has since demonstrated its superior potentialities.

In China a great deal of work has been done concerning the marinization of certain types of aircraft engines with some experience being accumulated in the process. In this paper the authors intend to sum up the experience gained in their work on the aerodynamic design and development of power turbines for marine gas turbines.

Power turbines of naval gas turbines operate, as a rule, under off-design conditions. Many gas turbines are designed to work at all loads with partial loads accounting for a predominant portion of the load profile. Power turbines of a versatile design are preferred, because such a design makes them fit for use on various gas generators and for many applications, thereby resulting in a low cost. Consequently, such

factors as long life, high efficiency, low loading, versatile design, and low production cost should be given special attention during the aerodynamic design of power turbines.

Selection of Parameters

After turbine initial data have been set, during the ensuing aerodynamic calculation some design parameters of the power turbine should be selected with due consideration of the design philosophy to be followed and past successful experience. Several of these parameters may sometimes be contradictory with one another, in which case one has to weigh the pros and cons and then decide on an optimum solution.

Determination of the Number of Turbine Stages. In designing a new turbine, the first problem encountered is to decide how many stages should be selected, i.e., how large a stage loading to be used. In recent years, with the advances in transonic stage design techniques and the application of control vortex design, etc., there emerged a marked increase in turbine stage loading. In spite of this, a restriction in loading magnitude still exists, above which a deterioration in efficiency will result.

In their design practice to change the two-stage power turbine of the MGT-2 marine gas turbine to a one-stage turbine, the authors discovered that after increasing the stage loading the modified stage experienced a marked increase in aerodynamic loading with the result that the said stage even at the design point would work under near-sonic or transonic conditions with a significant deterioration of stage outlet conditions (a significant increase in outlet Mach numbers, a conspicuous deviation of the outlet flow from the axial direction, an increase in nonuniformity of outlet temperature and pressure fields, etc.) and the modified single stage was subject to more unfavorable conditions in terms of component strength. With regard to engines for naval use, several aspects have to be considered. Such engines are often required to work

Contributed by the Gas Turbine Division of THE AMERICAN SOCIETY OF MECHANICAL ENGINEERS, and presented at the 32nd International Gas Turbine Conference and Exhibit, Anaheim, California, May 31-June 4, 1987. Manuscript received at ASME Headquarters January 30, 1987. Paper No. 87-GT-9.

under off-design conditions; a decision has to be made whether the engine is to work as a boost gas turbine (in this case, a smaller number of stages and higher stage loading are feasible) or as an engine operating at various loads; concerning the tapping of engine potential power there should be a design margin to serve as a reserve; and lastly, whether a cantilever support system for the engine should be used. Nowadays the average stage enthalpy drop of power turbines is set at approximately 20-25 kcal/kg. During the MGT-10 power turbine design, our calculations have shown that with the two-stage version being changed to a three-stage one, the increase in efficiency is only 0.5 percent. Therefore, taking account of the production cost and mechanical support requirements, the authors have settled for the two-stage version.

Distribution of Enthalpy Drop. Calculations of various versions have shown that in the case of multistage turbines, if a larger portion of enthalpy drop is allocated to the front stages, a somewhat higher turbine efficiency will result. However, such a stage is more sensitive to off-design working conditions. In the MGT-10 power turbine design, in consideration of the off-design conditions, the authors have selected a slightly higher enthalpy drop for the second stage, i.e., higher than the average by 7.1 percent.

Speed Selection. Under a definite load factor requirement, the power turbine speed selection shall be governed by the following factors: turbine dimensions, turbine component strength (blade stress, disk rim stress, limitation of shaft journal speed, etc.), its effect on rear transmission gears, tapping of potential power output, optimum speed ratio and leaving-velocity loss, etc. The authors hold that it is appropriate to set the power turbine speed at less than 6000 rpm.

Determination of Speed Ratio U/C_T . Speed ratio U/C_T , α average blade speed divided by $\sqrt{\Delta H_T}$ is a main parameter having an effect on the power turbine performance. In selecting speeds, allocating stage enthalpy drops and determining the stage average diameter, the speed ratio should be kept within an optimum range.

Selection of the Meridional Channel Form. The use of a constant inner diameter for the power turbine can lead to a relatively simple manufacturing technology being required, but the outer wall expansion angle will be rather great. For the selection of expansion angle, the following values are used: the upper expansion angle of the flow path < 25 deg, the lower expansion angle < 20 deg, the total expansion angle of the flow path < 35 deg, and the abrupt change in expansion angle not greater than 7 deg. Practice has shown that the meridional channel form has a marked effect on flows (flow angle and flow velocity) and the degree of reaction.

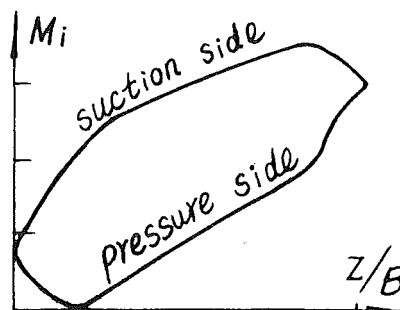


Fig. 1 Calculated speed distribution along blade profiles

Selection of Turbine Outlet Mach Number M_{C_2} . As far as marine gas turbines are concerned, the magnitude of outlet Mach number has a great effect on the engine static efficiency, weight, and dimensions as well as component strength. With M_{C_2} assuming a high value, the leaving velocity loss will be high, turbine static efficiency will decrease, and engine power output will be reduced. In contrast to this, a small value of M_{C_2} will lead to an increase in the last stage and exhaust piping dimensions. Calculations of the MGT-10 engine in various versions have shown that when M_{C_2} is increased from 0.3156 to 0.3558, the turbine static efficiency will be reduced from 87.56 to 84.25 percent. The authors hold that for power turbines of gas turbines with a medium power output or higher it is proper to set M_{C_2} at less than 0.30-0.32.

Methodology of Design and Calculations

In the aerodynamic design of power turbines, the authors have employed a one-dimensional aerodynamic design and characteristics calculation method, a simple radial equilibrium calculation method, and a meridional streamline curvature method based on a complete radial equilibrium. For blade profiles, an engineering analytical method has been used along with the method of calculating flows around blade profiles by solving direct problem of blade-to-blade flows.

Through their design practice the authors hold that the following design methodology can basically satisfy the engineering requirements of the present-day power turbine aerodynamic design: By use of the meridional streamline curvature method based on a complete radial equilibrium, an indirect problem design is conducted to determine the radial flow parameters of various sections, i.e., to determine the velocity triangles of various sections; following this, an engineering analytical profiling method (or graphic profiling

Nomenclature

A = thermal equivalent of work	S = entropy	ρ = density
C = gas absolute velocity	T = temperature	ω = rotational speed
C_T = theoretical velocity	U = blade speed	
corresponding to stage	w = gas relative velocity	Subscripts
enthalpy drop	Y = quasi-normal direction	i = local
G = mass flow	α = absolute gas flow angle	m = meridional
g = gravitational acceleration	β = relative gas flow angle	u = tangential
i = incidence angle	ΔH = stage enthalpy drop	0 = stator inlet
\tilde{i}_w^* = stagnation rothalpy	$\Delta\alpha$ = stator blade outlet angle	1 = stator exit or rotor inlet
K = streamline curvature	increment	2 = rotor exit
L_{TU} = turbine stage theoretical work	δ_T = turbine expansion ratio	I = first stage
M = Mach number	ϵ = included angle between the	II = second stage
m = meridional direction	normal and quasi-normal	
p = pressure	direction	Superscripts
R = radius	η_T = turbine efficiency	* = stagnation
R_e = degree of reaction	λ = nondimensional velocity	- = nondimensional

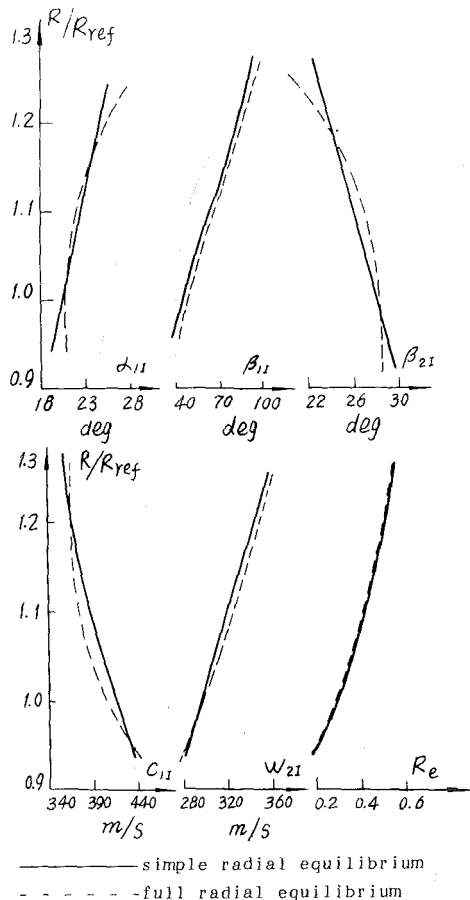


Fig. 2 Comparison of calculation results of full radial equilibrium and simple radial equilibrium methods

method) can be employed to design the blade profiles of various sections; then, with direct problem calculation of blade-to-blade flows, the flow distribution around blade profiles of various sections is calculated (Fig 1). In case the speed distribution falls short of expectations, corrections to the blade profiling should be carried out, until a satisfactory pressure distribution is obtained. At the same time, a direct problem calculation for the turbine design shall be performed to determine the turbine characteristics. During the calculation of direct and indirect problems for the turbine design, a certain margin should be reserved for the stage design. As regards efficiency, the turbine should be provided with a design "zone," instead of a point.

Selection of Design Vortex. When using the streamline curvature calculation method, the rotor blade outlet vortex C_{2u} serves as input data. In selecting vortex versions, one can use the traditional free vortex design or the controlled vortex design. The authors are of the opinion that the basis for making such a selection should be the magnitude of stage loading and the degree of reaction in the radial direction. Our design experience has shown that if the power turbine stage being designed pertains to the category of medium loading with relatively large hub/tip ratio and small expansion angle, it is proper to employ free vortex design or a design very similar to it. In case the use of free vortex design leads to a calculated degree of reaction having a deteriorating radial distribution with the degree of reaction at the root excessively low or rotor blade deflection angle excessively large, it is necessary to employ the controlled vortex design. In addition, when engaging in a controlled vortex design according to the optimum loading coefficient $\bar{L} = gL_{Tu}/U^2$ it is possible with an increase

in radius to accordingly increase the element stage enthalpy drop of various sections. Our design experience has shown that even for a stage of medium loading, the radial unequal amount of work done should not be made too great, otherwise there will emerge supercritical flows. The authors hold that it is proper to keep the change in enthalpy drop from hub to tip within the range of 5-7 percent.

Comparison of Complete Radial Equilibrium Calculation and Simple Radial Equilibrium Calculation. In the design of the MGT-10 engine power turbine, the calculation based on simple radial equilibrium $C_u^2/R = dP/\rho dR$ has been compared with that using the full radial equilibrium (in this case, the radial pressure gradient has not only been balanced by the centrifugal force produced by a circumferential velocity component, but balanced by the centrifugal force which is produced by the streamline curvature term and the slope term; in addition, the radial change in entropy has also been taken into account).

$$\frac{\partial W_m}{\partial Y} = \left[\frac{\sin \epsilon}{W_m} \cdot \frac{\partial W_m}{\partial m} - K_m \cos \epsilon \right] W_m + \left[\frac{g}{A} \left(\frac{\partial \bar{i}_w^*}{\partial Y} - T \frac{\partial S}{\partial Y} \right) - \frac{W_u}{R} \frac{\partial (RW_u + \omega R^2)}{\partial Y} \right] \frac{1}{W_m}$$

The results of comparison are shown in Fig. 2. From the comparison of these results it can be shown that in a turbine stage of medium loading with relatively large hub/tip ratio and small expansion angle, its three-dimensional effect is not very pronounced. In such circumstances there will not be a significant difference between the calculation results of the full radial equilibrium and simple radial equilibrium methods. Consequently, the use of the conventional simple radial equilibrium method can still result in a moderate reliability.

Versatile Design

In aircraft derivative engine marinization efforts a question may be raised of providing a versatile design capable of accommodating two power ratings. For example, by adding a stage or two to the original low-pressure compressor, an uprated engine can be obtained with a minimum modification of the power turbine. In the proposed versatile design, the two power ratings differ by 13.3 percent with the turbine of lower power rating having a relatively large decrease in nondimensional mass flow, i.e., $\Delta \bar{G}_1 = -14.72$ percent.

Key Parameters Exercising a Decisive Influence on a Versatile Design. Our experience of realizing a versatile design has shown that the key parameters of a versatile design are the turbine inlet nondimensional mass flow $\bar{G}_1 = G \sqrt{T_0^*}/P_0^*$ and the stage speed ratio U/C_T (or stage loading coefficient $\bar{L}_{Tu} = gL_{Tu}/U^2$). The decisive one of these two parameters, however, is the turbine inlet nondimensional mass flow, which has an effect on continuity equations, flow path area, and expansion ratio, and has a direct bearing on the success or failure of rendering the anticipated power output. The magnitude of the power turbine inlet nondimensional mass flow of the two-power-rating engine plays an important role in realizing a versatile power turbine (i.e., no need for turbine modification) or in deciding by what means to achieve such a versatility of design. The speed ratio U/C_T has a relation to velocity triangles, blade profiling, and the possibility of retaining the same working points for the two-power-rating power turbine, i.e., it has a direct bearing on the efficiency and performance achievable by the versatile turbine design.

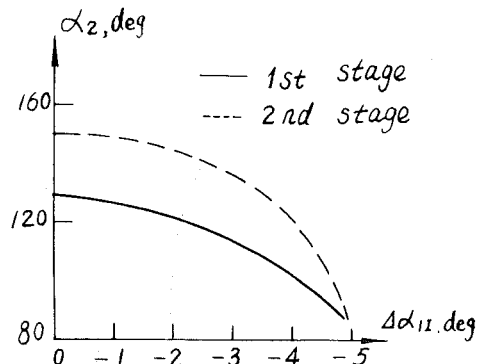


Fig. 3 Variation of α_2 with $\Delta\alpha_{11}$

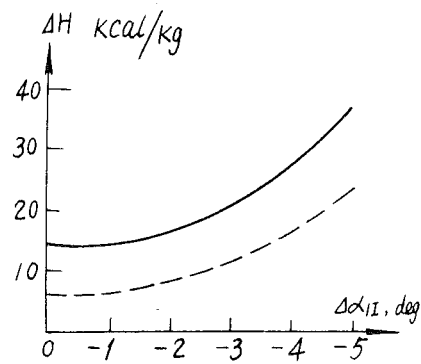


Fig. 5 Variation of ΔH with $\Delta\alpha_{11}$

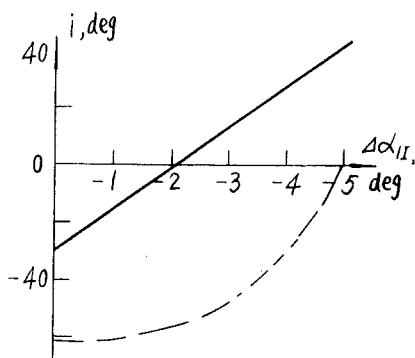


Fig. 4 Variation of i with $\Delta\alpha_{11}$

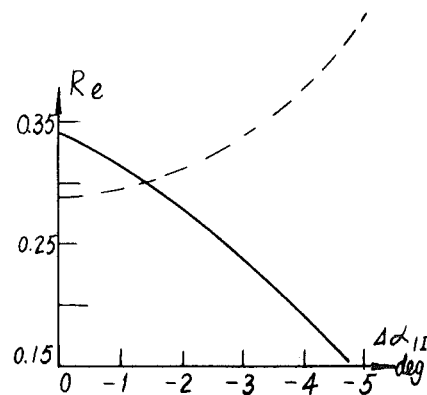


Fig. 6 Variation of R_e with $\Delta\alpha_{11}$

Methods Used to Effect a Versatile Design. The versatile design of the power turbine is closely related to that of the engine. The gas generator outlet parameters (through the intermediary of the transition section) are simply the power turbine inlet parameters. In fact, in the versatile design of a two-power-rating engine, the gas generator and the power turbine should always be considered as an integrated whole.

A Single Power Turbine Accommodating Two Power Ratings. When the inlet nondimensional mass flow of the two-power-rating power turbine remains nearly constant, it is possible to use one and the same power turbine. For example, IM2500 and IM2000 have, respectively, $\bar{G}_{12500} = 0.0528$ and $\bar{G}_{12000} = 0.05241$. Their nondimensional mass flow differs by $\frac{\Delta\bar{G}_1}{\bar{G}_1} = (\bar{G}_{12500} - \bar{G}_{12000})/\bar{G}_{12500} = 0.317$ percent. To cause the inlet nondimensional mass flow of the two-power-rating turbine to remain nearly unchanged, a versatile design for the gas generator was carried out by introducing adjustable guide vanes for the compressor and changing the design of high-pressure turbine stator and rotor blades. By maintaining a relatively good speed ratio (working point) one can modify the power turbine speed to make it match with the loading.

In case the inlet nondimensional mass flow of the two-power-rating turbine has different values, a versatile design can be realized through the following measures: changing the throat area of stator blades for the power turbine, changing the meridional channel (blade cropping), making the second stage of the higher-power-rating engine a versatile design.

Use of Adjustable Stator Blades. The use of a variable geometry turbine constitutes an effective way of improving engine off-design performance. Adjusting the turbine stator area enables the turbine within a certain range of nondimensional mass flow to work under a fixed pressure ratio. Due to the fact that in a versatility-oriented adjustable angle calculation,

with the exception of the change of stator blade outlet absolute flow angle α_1 , the turbine flow has already been set, one can employ the turbine characteristics calculation method to conduct the adjustable angle calculation aiming at a versatile design.

For a certain power turbine under the designed values of \bar{G}_{1L} and λ_{u1L} when decreasing the setting angle of the first stage stator blade outlet angle, the calculated characteristics curves of the following values, which are shown in Figs. 3-7, can be obtained: rotor blade outlet absolute flow angle α_2 , rotor blade incidence angle i , stage enthalpy drop, the degree of reaction of stage isentropic enthalpy drop R_e , power turbine stagnation expansion ratio δ_T^* .

To achieve the expansion ratio required by design purposes, the setting angle of the first stage stator blades should be made smaller by 4.81 deg. Compared with the higher-power-rating

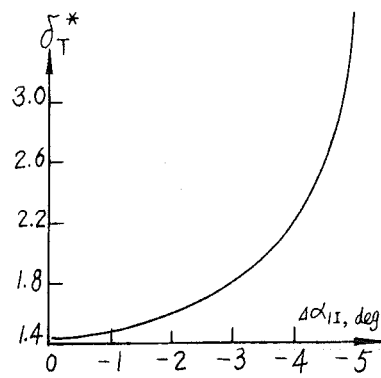


Fig. 7 Variation of δ_T^* with $\Delta\alpha_{11}$

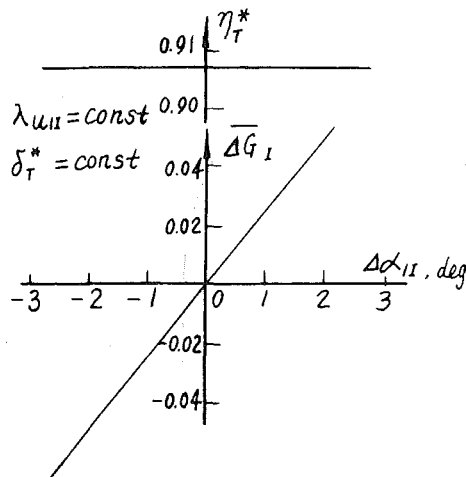


Fig. 8 Variable geometry characteristics of the MGT-10A engine power turbine

version, this is equivalent to a decrease in area of 21.33 percent. In this case the inlet incidence angle of the first stage rotor blades assumes a value as high as 26.5 deg and the degree of reaction at the average diameter decreases from 0.3552 to 0.1654. In this versatile design, the authors also made calculations of some versions by assigning simultaneously a smaller setting angle for these two stages of stator blades. The version with $\Delta\alpha_{II} = -4.1$ deg and $\Delta\alpha_{III} = -4.2$ deg has been found to be a better one under which the required expansion ratio is attained. Compared with the case when the setting angle of only one stator blade row is made smaller, the simultaneous decrease in setting angles of two rows of stator blades can lead to somehow improved incidence angles, degree of reaction, and distribution of enthalpy drop.

When the use of the power turbine versatile design is such that the lower-power-rating turbine is called on to work as a higher-power-rating one, taking account of the increase in turbine inlet nondimensional mass flow, one can use the method of increasing the setting angle of the stator blades. Our calculations have shown that for a multistage turbine, the greater setting angle of only the first-stage stator blades will not bring about a significant improvement, because such an approach is restrained by the blockage effect produced by the subsequent rows of stator blades (of course, including the rotor blades of respective stages).

Changing Meridional Channels (Blade Cropping). When the power turbine versatile design is used in such a way that the higher-power-rating turbine is called on to work as a lower-power-rating one, the blades of the higher-power-rating power turbine may be properly cropped as required, i.e., to change the form of the boundary streamlines. The input vortex value C_{2H} can be obtained from the meridional flow calculation results of the higher-power-rating power turbine by way of interpolation. The adjustment calculation should be conducted several times until the desired performance and appropriate parameters are obtained.

In our versatile design, the blade height relative to the higher-power-rating power turbine has been successively decreased by 14, 11.8, 12, and 10 percent in order to satisfy design requirements. The radial aerodynamic parameters of the lower-power-rating turbine (such as α_1 , β_1 , β_2 , α_2 , etc.) assume values nearly equal to the geometry parameters (to be determined by the higher power rating). The values of α_1 and β_2 which determine the cascade outlet area differ by less than 0.5 deg. The rotor positive incidence angle at the average diameter is about 4 deg and the maximum value at the tip can be as high as 5–6 deg.

A Versatile Design for the Second Stage of the Higher-Power-Rating Turbine. In the versatile design of a certain engine, the nondimensional mass flow of the two versions differs by $\Delta G_I = -2.3$ percent. The second-stage flow path dimension of the higher-power-rating engine has been retained with the rotor and stator blade profile unchanged and first stage redesigned.

Some Measures Taken to Improve the Versatile Design. In performing a versatile design, the overall engine design should be well coordinated with the power turbine design. It is necessary to select the gas generator outlet gas parameter very carefully in order to establish a sound basis for the versatile design. The important thing to remember is to keep the value of the nondimensional mass flows of the higher- and lower-power-rating power turbines as nearly equal as possible. This can be achieved by proper control and adjustment of the gas flow rate and temperature as well as the pressure ratio during the gas generator modification design.

To enable the higher- and lower-power-rating power turbine to have the working points arranged as closely as possible to one another, it is desirable to keep the speed ratio U/C_T constant as far as possible. If necessary, one can change the power turbine speed.

It is preferable to use a low loading for the power turbine along with a certain reserved margin of aerodynamic loading and component strength. The radial distribution of the degree of reaction should be rational. An excessively low degree of reaction, especially at the root, is to be avoided.

In conducting a versatile design, the difference in U/C_T values of the higher- and lower-power-rating engines will inevitably lead to an incidence loss. Consequently, during the blade profile design process, it is recommended, depending on specific circumstances, to select some negative incidences, the magnitude of which can be determined, using the data of Ji and Qiang (1979). If possible, it is recommended to increase rotor blade leading edge radius properly in order to improve off-design performance.

Use of Adjustable Stator Blades to Accommodate a Small Amount of Adjustment of the Gas Generator Outlet Parameters

In the modification design of aircraft derivative engines for marine use, the power turbine to be matched with the gas generator is sometimes required to accommodate a certain amount of adjustment of the gas generator outlet parameters, as is the case with the design of the MGT-10A engine.

To satisfy the abovementioned requirements, the authors have introduced adjustable stator blades for the first stage of the power turbine. The turbine characteristics under various setting angles have been calculated in order to determine its performance when adjustable stator blades are used.

From Fig. 8 it can be seen that at a definite value of $\lambda_{u_{II}}$ and δ_T^* with the adjustment value of $\Delta\alpha_{II}$ being not great, ΔG_I is basically linear with $\Delta\alpha_{II}$ and the variation in efficiency may be neglected.

Conclusions

1 The design of power turbines for marine use should be conducted with due emphasis on long life, high efficiency, low loading, and a versatile design. Parameters such as the number of stages, enthalpy drop distribution, rotating speed, outlet Mach number, etc., have been selected with the above-cited design philosophy in mind.

2 The power turbine aerodynamic design method described in this paper can satisfy relevant design objectives. By following the abovementioned design approach a high-

quality, reliable, and rugged power turbine can be obtained. The design vortex should be selected with due attention to the special features of marine use. In many applications, the free vortex design has been a frequently used design approach. With the increase in stage loading, decrease in hub/tip ratio and the enhancement of the expansion angle of meridional channel, etc., the use of controlled vortex design has become indispensable.

3 Among the key parameters in the power turbine versatile design we can list the power turbine inlet nondimensional mass flow and speed ratio. When the power turbine nondimensional mass flow undergoes a very small change, we can use one and the same power turbine. In case the change is relatively small with ΔG_1 not greater than 3–4 percent, it is possible to retain the second stage and design anew the first-stage versatile version (reference is made to the two-stage power turbine). When the ΔG_1 change does not exceed 10–15 percent, the versatile design can be realized by way of manipulating the adjustable stator blades (a decrease of the stator blade setting angle). With a still greater variation of the value of ΔG_1 , the implementation of versatile design by changing the meridional channel (blade cropping) is in order.

4 The authors have emphatically pointed out that in carrying out a versatile design, the design of the whole engine should be meticulously made to fit in with that of the power turbine and, with respect to the gas generator outlet gas parameter, minor changes are sometimes advisable in order to provide a good basis for the versatile design.

5 The use of adjustable stator blades for the power turbine first stage can accommodate a small amount of change in gas generator outlet parameters. This will facilitate the adjustment testing of the gas generator as well as the adjustment on the test rig of the engine as a whole.

Acknowledgments

The authors are grateful to Chief Engineer of our Institute Wen Xueyu for his review of the paper and his valuable comments.

References

- Ji, G. M., and Qiang, K. F., "Off-Design Performance Losses of Turbine Cascades and the Rational Selection of Design Incidence Angles" [in Chinese], *Shipbuilding Engineering*, Jan. 1979, pp. 26–33.

Performance Characteristics of Two- and Three-Dimensional Impellers in Centrifugal Compressors

H. Harada

EBARA Research Co., Ltd.,
Fujisawa, Japan

The overall performance of two- and three-dimensional impellers of a centrifugal compressor were tested and compared. A closed-loop test stand with Freon gas as the working fluid was employed for the experiments. The inlet and outlet velocity distributions of all impellers were measured using three-hole cobra probes. As a result, it has been revealed that three-dimensional impeller in terms of efficiency, head coefficient, and operating range. Further, it has also been clarified that the impeller slip factor is affected by blade angle distribution.

Introduction

Both two- and three-dimensional impellers are widely used in centrifugal compressors. Three-dimensional means twisted blade and two-dimensional means constant blade angle from hub to shroud. The high-pressure single stage impellers used for turbochargers and gas turbine compressors are three-dimensional inducer impellers, because of the high performance requirements. In multistage centrifugal compressors, on the other hand, two-dimensional welded or cast type impellers have so far been used, because of the need to reduce axial length and manufacturing costs. However, three-dimensional impellers have been increasingly used for industrial multistage compressors in order to meet energy saving requirements.

In the case of high specific speed two-dimensional impellers, the leading edge of the blade is almost parallel to the axis and the blade inlet angle distribution from hub to shroud is almost constant. The distribution of radial velocity component between the hub and shroud for such an impeller is nonuniform. Therefore, a large incidence loss at the inlet occurs as a result of mismatching between the inlet flow and blade angle. In order to achieve a smooth inlet flow into the impeller, and to improve impeller performance, it is necessary to incorporate leading edge twist and to vary blade angles from hub to shroud throughout the impeller. Mishina et al. [1] investigated the performance of high specific speed three-dimensional impellers, and showed that the three-dimensional impellers has superior characteristics to the two-dimensional one.

On the other hand, as low specific speed impellers have short inlet length, the flow nonuniformity between hub and shroud is so small that incidence loss at the inlet can be greatly

reduced. The overall performance of a two-dimensional impeller is thought to be better than that of a three-dimensional one due to the short flow path through the impeller channel. The difference in performance between two- and three-dimensional impellers in centrifugal compressors has, until now, undergone little investigation. Therefore, it is not yet clear to some designers whether to select a two- or a three-dimensional impeller for a given specific speed. To investigate the difference in performance between a three-dimensional impeller and a two-dimensional one, the author designed four types of impeller with the same diameter, blade exit width, blade exit angle, and number of blades. These consisted of a three-dimensional type with an inducer (3DI), a three-dimensional type (3D), a quasi-three-dimensional type (Q3D), and a two-dimensional type (2D). These were designed using a quasi-three-dimensional flow analysis method [2, 3]. In this study, the overall performance and exit flow pattern of each compressor were measured, and the performance differences among them were compared.

Design Method

Relative velocity distributions were calculated by use of a quasi-three-dimensional flow analysis. All the impellers were designed to have nearly the same mean relative velocity deceleration ratios, on the shroud streamline, at the design flow rate. The meridional and blade shape of each impeller are shown in Fig. 1. All impellers were made by aluminum alloy precision casting. The blade camberline of the 2D type was circular. The dimensions of the tested impellers are shown in Table 1.

Table 1

$D_2 = 0.57$ m
$b_2 = 0.018$ m
$\beta_{b2} = 45$ deg
$Z = 15$
$N_s = 0.321$

Contributed by the Gas Turbine Division of THE AMERICAN SOCIETY OF MECHANICAL ENGINEERS and presented at the 31st International Gas Turbine Conference and Exhibit, Düsseldorf, Federal Republic of Germany, June 8-12, 1986. Manuscript received at ASME Headquarters January 30, 1986. Paper No. 86-GT-154.

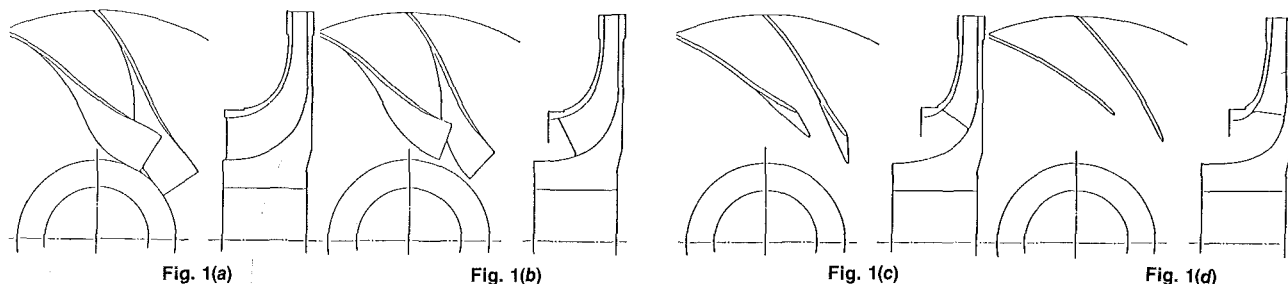


Fig. 1 Impeller types: (a) three dimensional with inducer (3DI); (b) three dimensional (3D); (c) quasi-three dimensional (Q3D); (d) two dimensional (2D)

The blade angle distribution on the mean streamline is illustrated in Fig. 2 as a function of the nondimensional meridional streamline length. This angle is measured from the tangential direction. It is clear from this figure that the angle distributions of the 2D impellers gradually increase from inlet to outlet; however those of the Q3D, 3D, and 3DI types initially increase up to the middle of the flow path, and then decrease toward the impeller outlet. Figures 3(a, b) indicate the ratio of relative velocity to the circumferential velocity of each impeller at the design flow rate through the flow path, as a function of nondimensional meridional streamline length. Relative velocity distributions on the shroud streamline are shown in Fig. 3(a), and those of the hub streamline are shown in Fig. 3(b). It is clear that the inlet relative velocities of the 2D and Q3D type are slightly higher than those of the 3DI and 3D as the result of large blade inlet diameter, but the relative velocity reduction ratio on the shroud streamline is thought to be nearly the same for each impeller. Relative velocity distributions through the hub streamline of the 3D and 3DI impellers decelerate greatly at the inlet section, whereas those of 2D and Q3D types have nearly the same pattern as at the shroud streamline.

Apparatus

In order to test with circumferential Mach numbers up to unity, Freon gas was used in a closed loop, thus enabling reduction in rotational speed and input power to the compressor. A direct current motor was used to drive the compressor through a step-up gearbox, and the compressor speed was changed from 1000 to 6000 rpm.

Loop layout and dimensions were per ASME PTC10-1965. Flow rate was measured by a D-1/2D tapped orifice. To check for system thermodynamic stability, the energy balance between the compressor input power and the heat rejection from the gas cooler was monitored. Input power was measured by a

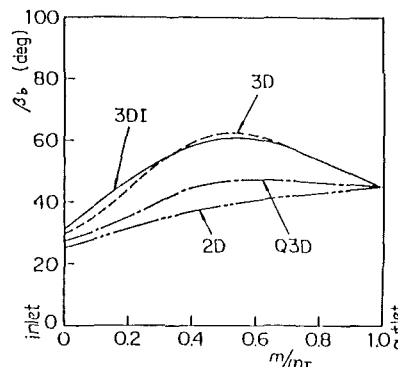


Fig. 2 Blade angle distribution

torque meter with a speed counter installed on the high-speed shaft, and the amount of rejected heat from the gas cooler was measured from the cooling water heat gain. When both energy values coincided within a predetermined range, the system was considered stable. Prior to the test, the loop gas was analyzed by gas chromatograph to determine the air content. Compressor performance was corrected according to the results of the analysis. System pressure was kept slightly higher than atmospheric pressure, to prevent air leakage into the loop. An automatic data processing device using a personal computer was used for real-time performance calculations.

Experimental Method

Pressure measurements were carried out using semiconductor pressure transducers having a ± 0.2 percent F.S. accuracy. The transducers were calibrated before testing, using a quartz pressure gage of ± 0.07 percent F.S. accuracy. C-C thermocouples were used for measuring fluid temperatures. These were calibrated using a quartz thermometer of $\pm 0.001^\circ\text{C}$ accuracy, dipped into a constant-temperature bath kept within a

Nomenclature

a = velocity of sound, m/s	x = length, m	
b = width, m	Z = number of blades	
C = absolute velocity, m/s	β = relative flow angle referenced tangential, rad	
D = diameter, m	β_b = blade exit angle referenced tangential, rad	
H = polytropic head, kgfm/kgf	η = efficiency, percent	
M_{u_2} = circumferential Mach number = U_2/a	σ = slip factor	
m = meridional length, m	ϕ = flow coefficient = $4Q/\pi D^2 U_2$	
N_s = specific speed = $\phi^{1/2}/\psi^{3/4}$	ψ = head coefficient = gH/U_2	
P = pressure, kgf/m ²	Ω = angular velocity, rad/s	
Q = volume flow, m ³ /s		
r = radius, m		
U = circumferential velocity m/s		
W = relative velocity, m/s; work coefficient		
	Subscripts	
	0 = stagnation condition at the impeller inlet	
		1 = impeller inlet
		2 = impeller outlet
		3 = diffuser inlet
		4 = diffuser outlet
		9 = return channel outlet
		imp = impeller
		m = radial
		p = pressure side
		s = suction side
		u = tangential
		* = reference point (maximum efficiency point of the 3DI impeller)

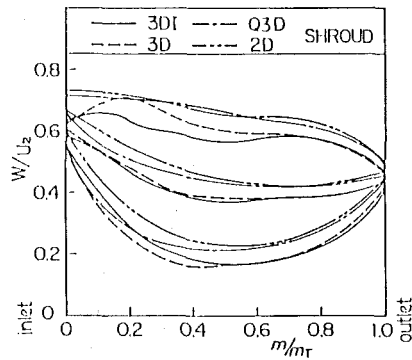


Fig. 3(a) Relative velocity distribution on the shroud

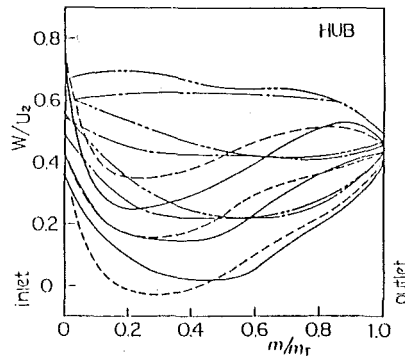


Fig. 3(b) Relative velocity distribution on the hub

range of $\pm 0.03^\circ\text{C}$. All calibration data were stored in a memory, and were used for real-time calculations of measured values.

A single-stage compressor with an overhanging shaft and parallel wall vaneless diffuser was used for this study. A return channel was installed after the diffuser, as shown in Fig. 4. Outlet flow from the return channel was collected by a volute casing through the L-turn section. For the purpose of evaluating stage performance, a stage was defined to be from the impeller inlet to the return channel outlet. Inlet total temperature was measured by using four total temperature probes, each mounted on the same cross section of the inlet pipe and symmetrically arranged. Inlet total pressure was measured by two Kiel probes each located 10 mm upstream of the 3DI impeller and symmetrically attached. The locations of the probes were fixed during the performance test of four impellers. Static pressures were measured at 12 points of the impeller inlet, at 6 points of the impeller outlet, and 12 points of the diffuser outlet, each point symmetrically arranged at the same cross section. Data for each location were averaged and used for calculation. Auto-traversers controlled by personal computer were used to drive the cobra probes. These probes were used for measuring the impeller inlet and outlet, and also distribution of diffuser outlet flow.

As the outlet flow from the return channel was expected to be complex, six Kiel probes and four total temperature probes were installed at the return channel exit to measure the flow accurately, as shown in Fig. 5. The measured values from each of these probes were averaged for calculation. Total pressure distribution at the return channel outlet was measured by using a three-hole cobra probe, and compared with the values measured by using Kiel probes. Figure 6 shows the result of the comparisons where the abscissa indicates the nondimensional return channel width, and the ordinate indicates the ratio of measured pressure to the mean value of the cobra probes. The solid line indicates the ratio of the measurement obtained at each traverse point with the cobra probe to the

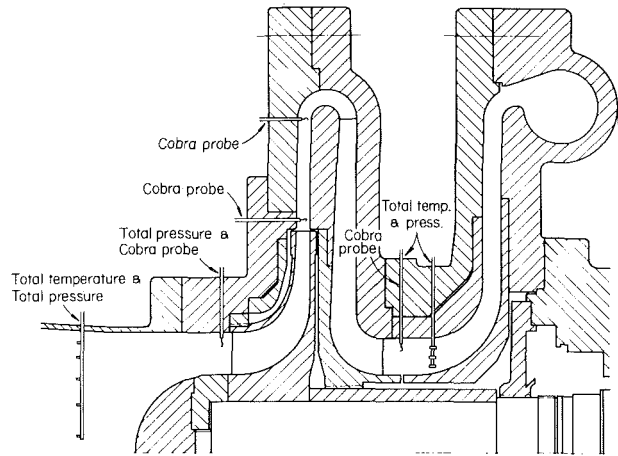


Fig. 4 Experimental apparatus cross section

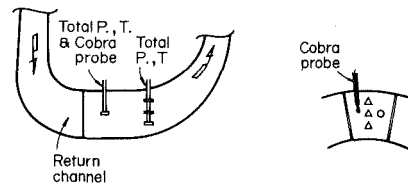


Fig. 5 Location of probes at the exit of return channel

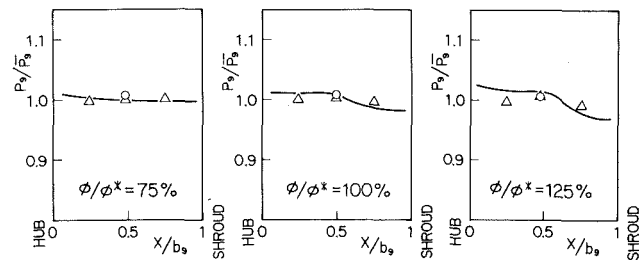


Fig. 6 Total pressure distribution at the exit of the return channel

arithmetic mean of the measurements taken over the entire passage. For the Kiel probe, the results are also represented by the ratio of each measurement to the arithmetic mean. As shown in this figure, the measured values from the Kiel probes coincided with the mean cobra probe value. Therefore the average of the Kiel probe data was taken representatively for calculations of compressor performance.

Experimental Results

Figures 7(a, b) show in dimensionless values the overall performances of impellers. Figure 7(a) indicates the results at $M_{u2} = 0.7$, and Fig. 7(b) at $M_{u2} = 1.0$. The maximum efficiency of the 3DI is determined as the 100 percent value. Ellipses in these figures represent the measurement uncertainty bounds at 95 percent probability of the 3DI impeller, i.e., the true value is believed to lie within this estimated uncertainty bounds at 95 percent probability, but other marks only represent the arithmetical average points. The test uncertainties of latter marks were nearly the same as the values of the 3DI impeller. It is clear from this figure that the 3DI impeller is superior to the others, in terms of head coefficient and operating range. Little difference in efficiency and operating range was observed between the 3DI and 3D impellers, except for the head coefficient. The Q3D and 2D impellers showed relatively inferior performance to 3D and 3DI impellers with respect to both head coefficient and operating range. When

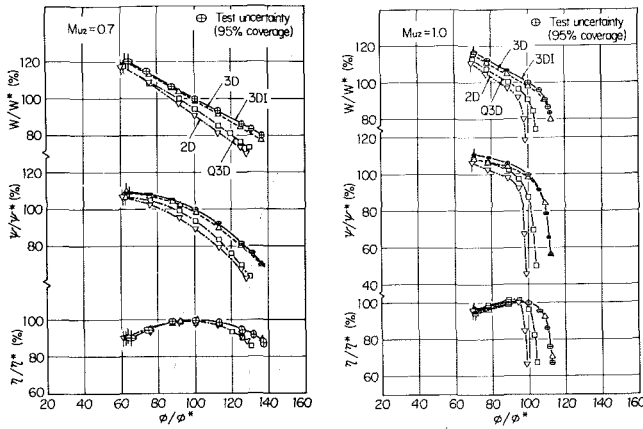


Fig. 7 Performance diagram: (a) $M_{u_2} = 0.7$; (b) $M_{u_2} = 1.0$

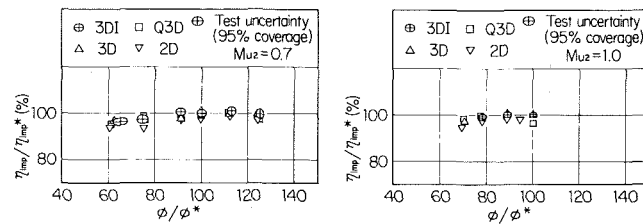


Fig. 8 Impeller efficiency: (a) $M_{u_2} = 0.7$; (b) $M_{u_2} = 1.0$

the compressor was operated at $M_{u_2} = 1.0$, the efficiency of the Q3D and 2D impellers at lower flow rates was better than that of the 3D and 3DI impellers. The choke flow is different for each impeller because of different throat areas. This is due to the design of each impeller, which has the same relative velocity distribution from inlet to outlet; this brought about the difference of throat area of each impeller. The work coefficients of each impeller were quite different, as shown in Figs. 7(a, b).

Figures 8(a, b) show the impeller efficiencies. To calculate the efficiency, mass-flow average total pressures were used, which were measured by traversing the cobra probes at eight points across the diffuser inlet ($r/r_2 = 1.05$) width. Figure 8(a) is at $M_{u_2} = 0.7$ and Fig. 8(b) is at $M_{u_2} = 1.0$. In both figures, the maximum efficiency of the 3DI impeller is determined as the 100 percent value. From these figures, it can be seen that the efficiencies of 3DI and 3D impellers were superior to those of Q3D and 2D impellers. If a gas other than Freon is used for a similar experiment, the differences in impeller performance characteristics will differ slightly from those obtained with Freon because of the difference in Reynolds number and specific heat ratio. However, this problem is out of the scope of this study.

Figure 9 shows the measured axial and circumferential velocity components at the impeller inlet obtained by traversing cobra probes across the cross section. The ordinate shows the nondimensional impeller inlet flow passage. The inlet flow distributions were almost the same for each impeller as shown.

Figure 10 shows the measured velocity distributions at the diffuser inlet obtained by traversing the cobra probes across the width. Immediately after the impeller exit, the gas presents a complex flow pattern. Yet, it is known that impeller wake mixing is nearly completed before the wake reaches a point equal to 1.05 times impeller diameter. Accordingly, a cobra probe was installed at this point to measure the well-mixed flow. The abscissa indicates nondimensional diffuser width. The ordinate shows the tangential and radial velocity components divided by the circumferential velocity of the im-

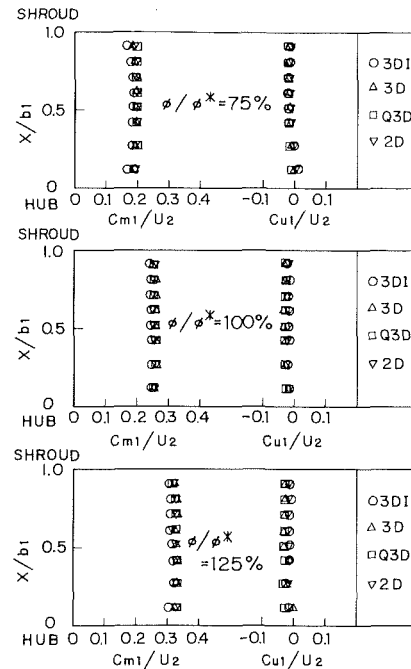


Fig. 9 Impeller inlet velocity distribution at $M_{u_2} = 0.7$

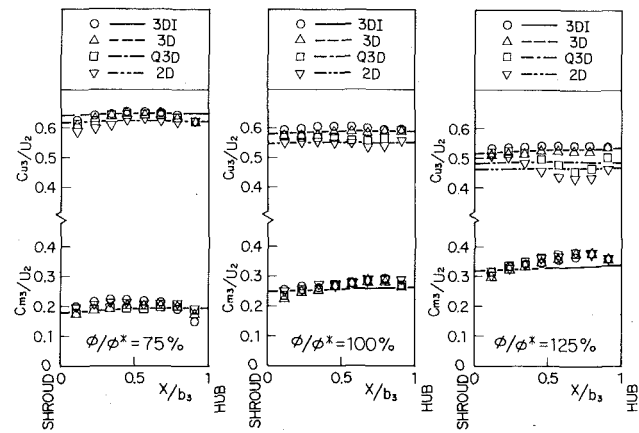


Fig. 10 Diffuser inlet velocity distribution at $M_{u_2} = 0.7$

PELLER. These figures show that the radial velocity components are nearly the same in each impeller, but tangential velocity components increase with dimensionality from 2D to 3D. The drawn lines in the figure indicate the calculations obtained by quasi-three-dimensional analysis, assuming perfect gas conditions. It was obvious that the calculated values are in agreement with the measured values. The impeller exit radial velocity was checked by iterative calculation from the total enthalpy, mass flow, and impeller exit static pressure. This value was compared with the measurement taken with a cobra probe. These two values are in agreement with each other within an accuracy of ± 5 percent.

According to the work coefficient curve shown in Fig. 7 and the velocity distribution shown in Fig. 10, it can be deduced that the slip factors of these impellers were different.

Figure 11 shows the slip factors versus flow coefficient for each impeller. For the calculation of slip factors the impeller outlet velocity was measured by a cobra probe whose measuring position was 1.05 times impeller diameter. Pressure loss between the measuring position and impeller outlet were neglected. To see the influence of rotational speed, circumferential Mach numbers were changed from 0.7 to 1.0 at 0.1 intervals. The \star marks in Fig. 11 indicate the calculated

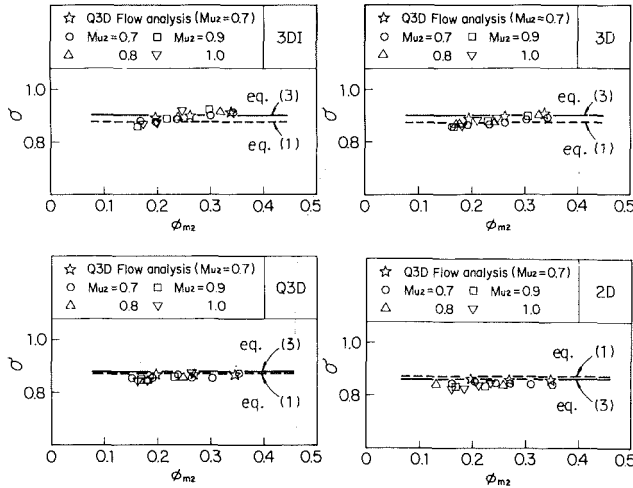


Fig. 11 Slip factor

slip factor obtained by quasi-three-dimensional flow analysis at $M_{u_2} = 0.7$.

The dotted line in Fig. 11 indicates the calculated value from the following equation, i.e., Wiesner's formula [4];

$$\sigma = 1 - \sqrt{\sin \beta_{b2} / Z^{0.7}} \quad (7)$$

However, as these lines do not coincide with experimental data the author examined this a little more closely as follows. Senoo [5] explained that the flow slip in the impeller is caused by blade loading which gradually decreases toward the blade trailing edge. The relative velocity differences at the suction and pressure surfaces (blade loading) of the actual impeller are expressed by equation (2) assuming that the streamline is along the blade surface [5]

$$(W_s - W_p) = \frac{2\pi}{Z} \left\{ (2r\Omega - W \cos \beta) \sin \beta \frac{dr}{dm} + \frac{rWd\beta}{dm} \right\} \quad (2)$$

The suction side relative velocity must coincide with that of the pressure side at the impeller exit, so equation (2) must equal 0 at the impeller exit. For the right-hand terms of equation (2) to equal 0, the value of $d\beta/dm$ needs to be negative. Therefore the relative flow angle β must become smaller than the blade angle β_b , therefore flow slip in the impeller channel occurs. Distributions of the blade angle β_b at the impeller exit are expected to affect the flow slip in the impeller channel.

From Fig. 2 the angle change along the meridional direction is different for each impeller. As $d\beta_b/dm$ is negative near the outlet of Q3D, 3D, and 3DI impellers according to Fig. 2, the blade loading becomes smaller from equation (2). On the other hand, with a 2D impeller the blade loading becomes larger because of the positive value of $d\beta_b/dm$. Wiesner's formula indicates that the greater the number of blades Z and the smaller the impeller exit angle β_{b2} , the smaller the slip of the fluid. This coincides with the assertion that the smaller the value on the right-hand side in equation (2), the smaller the slip of the fluid. It can be considered that for the impellers used to derive equation (1), $dr/dm = 1$ and $d\beta_b/dm = 0$. To apply equation (1) where these conditions are not satisfied, it is necessary to replace $\sin \beta_{b2}$ in equation (1) with

$$\sin \beta_b \frac{dr}{dm} + \frac{rW}{2r\Omega - W \cos \beta_b} \frac{d\beta_b}{dm}$$

Since $W \cos \beta_b$ is considerably smaller than $2r\Omega$ and the second term in the above expression is smaller than the first term, the following expression can be used in place of $\sin \beta_{b2}$ in equation (1):

$$\sin \beta_{b2} \frac{dr}{dm} + \frac{W}{2\Omega} \frac{d\beta_b}{dm}$$

As a result, the author modified Wiesner's equation to the following:

$$\sigma = 1 - \sqrt{\sin \beta_{b2} \frac{dr}{dm} + \frac{W}{2\Omega} \frac{d\beta_b}{dm} / Z^{0.7}} \quad (3)$$

The solid line drawn in Fig. 11 represents the values calculated from equation (3). As $d\beta_b/dm$ near the impeller exit is almost constant according to Fig. 2, the constant value between 90 and 100 percent of the impeller exit diameter is used. The slip factor estimation must be performed at the time the impeller is designed so that the author used impeller exit relative velocity W for ideal flow. For this reason, it was assumed that this value is the same for all four types of impeller. The solid line shows a little higher value than the experimental data. As to this, the author assumed that equation (3) was derived from equation (1) and Wiesner's slip factor has the possibility of arrangement from many data having the same angle distributions at the impeller exit. Further investigation on an empirical formula that gives the angle distribution along the radius will give better predictions of the slip factor of impellers.

Conclusion

The performances of four different types of impeller with the same exit diameter, blade exit width, blade exit angle, and number of blades, i.e., a three-dimensional impeller with an inducer (3DI), a three-dimensional (3D), a quasi-three-dimensional (Q3D), and two-dimensional impeller (2D), were tested and examined. It was found that the 3DI impeller indicated 12.0 percent greater head coefficient and 1.6 percent higher efficiency at the maximum efficiency point of $M_{u_2} = 0.7$ and 13.8 percent greater choke flow rate at $M_{u_2} = 1.0$ than the 2D impeller. The 3D impeller had nearly the same performance as the 3DI impeller, except for its head coefficient.

In this study the impeller design specific speed is 0.321, while in the literature [1] it is 0.619. Therefore, at least within this range, three-dimensional impellers should be adopted.

The slip of the impeller and, especially, the angle distribution near the impeller outlet, are affected by the blade loading. A modified Wiesner's slip formula (3) will give better slip factor for the three-dimensional impeller.

Acknowledgments

The author wishes to express his sincere thanks to Prof. Senoo for his helpful discussions and to Mr. T. Kashiwakura for his assistance in conducting experiments.

References

- 1 Mishina, M., and Gyobu, I., "Performance Investigation of Large Capacity Centrifugal Compressors," ASME Paper No. 78-GT-3.
- 2 Senoo, Y., and Nakase, Y., "A Blade Theory of an Impeller With an Arbitrary Surface of Revolution," ASME Journal of Engineering for Power, Vol. 93, No. 4, Oct. 1971.
- 3 Senoo, Y., and Nakase, Y., "An Analysis of Flow Through a Mixed Flow Impeller," ASME Journal of Engineering for Power, Vol. 94, No. 1, Jan. 1972.
- 4 Wiesner, F. J., "A Review of Slip Factor for Centrifugal Impellers," ASME Journal of Engineering for Power, Vol. 89, No. 4, Oct. 1967.
- 5 Senoo, Y., "Naibu Nagare Gaku To Ryutaikikai," Yokendo [in Japanese].

Analysis of Measurements in Vaned Diffusers of Centrifugal Compressors

W. Stein

Research Assistant.

M. Rautenberg

Professor.

Institute of Turbomachinery,
University of Hannover,
Hannover, Federal Republic of Germany

In vaned diffusers of centrifugal compressors many different flow phenomena interfere with one another, and different geometric parameters influence the flow field. Variations of these parameters allow the designer to optimize the diffuser for a certain application or to use a variable geometry for controlling the stage over a wide range. Two vaned diffusers that differ only in their passage widths are investigated using different types of measuring technique, in order to analyze the flow structure and to use it as a verification of a calculation method that allows detailed predictions of flow field parameters inside the diffuser, by taking into account geometric variations. Using this method predictions of the flow field of a variable geometry diffuser are made and are compared with the measured performance curves of the stage.

Introduction

There are different ways to describe the characteristics of the diffusion process inside diffusers. Published interpretations show at least two kinds of description depending on how the diffusion process is viewed. General correlations of diffuser performance such as pressure recovery with geometry or thermodynamic parameters as inlet Mach number exist in a large variety and are very helpful and handy for designers. To understand what is really happening inside the diffuser, a more detailed knowledge is necessary, which needs much more efforts in measurement or more complicated procedures in calculation.

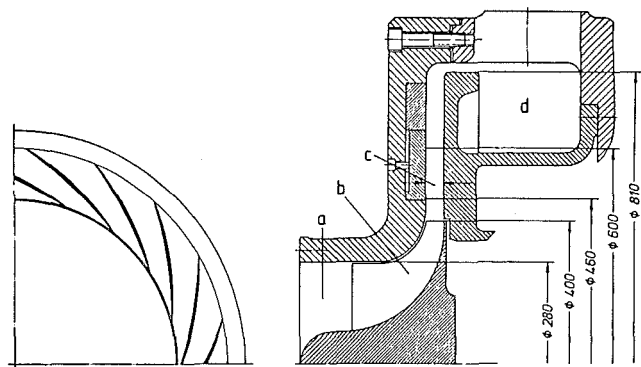
In this paper detailed measurements, steady and instantaneous, are shown. They are evaluated in steady flow field data as already shown in [1] or instantaneous data as shown in this paper, as well as in some general correlations.

Based on this detailed information, a time-marching method has been developed by Wiedermann [2] and verified using steady measurements.

One of the aims of this project was to find design criteria for variable geometry diffusers. Besides other data and criteria taken from published literature, both the correlations and the calculation method mentioned above are employed here to calculate the detailed flow field inside a variable geometry diffuser. In order to compare these computations with measurements, they are evaluated as averaged general performance data and are compared with measured values for the stage, because more detailed measurements are not available at the moment.

Experimental Facility

The test rig is already described in [1] and shown in Fig. 1. It consists of a centrifugal compressor having a radial ending impeller of 400 mm diameter with 28 blades, 14 of which are splitter blades, and two different cambered vane diffusers with 19 vanes each. The vane shape is the same in both cases with leading edges at a radius ratio relative to impeller exit of $\lambda_4 = r_4/r_2 = 1.15$ and an outer radius ratio of the vaned part of $\lambda_6 = 1.5$. The difference of these two diffusers originates from a change of the passage width from $b_2 = 24$ mm to $b_2^* = 21.6$ mm in the parallel walled part, leading to an alteration of the inlet shroud shape between impeller exit and vane leading edge. The general result of this variation can be seen in the map shown in Fig. 2 and is already discussed in [1]. This figure



a inlet
b impeller
c diffuser

d collecting chamber

Fig. 1 Simplified sectional view of the compressor

Contributed by the Gas Turbine Division of THE AMERICAN SOCIETY OF MECHANICAL ENGINEERS and presented at the 32nd International Gas Turbine Conference and Exhibit, Anaheim, California, May 31-June 4, 1987. Manuscript received at ASME Headquarters February 17, 1987. Paper No. 87-GT-170.

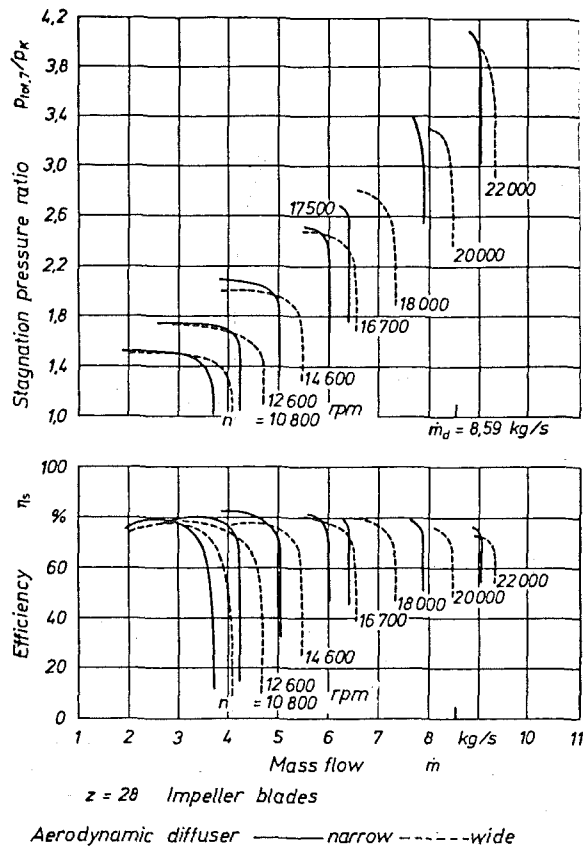


Fig. 2 Compressor maps with wide and narrow diffuser

shows the pressure ratio of the stage versus mass flow, reduced to standard conditions of $p = 1.013$ bar and $T = 288.15$ K, as well as the isentropic efficiency of the stage. Measurements are made with probes for total pressure and total temperature in the inlet and pressure pipe and a nozzle in the pressure pipe, respectively. The uncertainties of these measurements can be quoted at about ± 0.1 percent in pressure ratio, ± 0.8 percent in efficiency, and ± 0.2 percent in mass flow. These results are compared with the results of steady probe measurements in the radial space between impeller and vanes as well as downstream of the vanes combined with a measurement of pressure distribution throughout the whole diffuser. These measurements could help to explain the variation in overall performance that is characterized by a shift of the lines for constant shaft speed to the left and a rise in pressure ratio and efficiency mainly at high speeds. In the lower speed range the

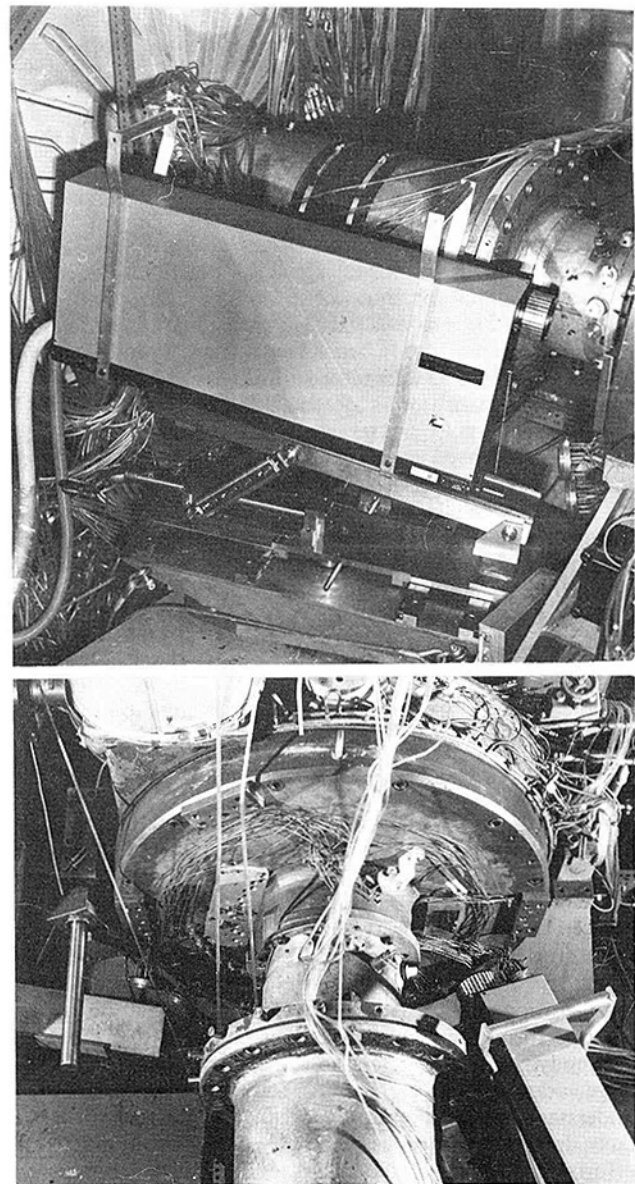


Fig. 3 L2F velocimeter in front of compressor

difference in mass flow between the two diffusers is proportional to the reduction of throat area. In the higher range it is less. In [1] it is shown that this is a result of a smoothed flow

Nomenclature

A = area, m^2
 a = velocity of sound, m/s
 B = blockage
 b = diffuser width, mm
 c = absolute flow velocity, m/s
 c_p = pressure recovery, kJ/kgK
 \dot{m} = mass flow, kg/s
 M = Mach number
 n = shaft speed, $1/min$
 p = pressure, bar
 R = gas constant, kJ/kgK
 r = radius, m
 T = diffuser pitch or temperature, (K)

t = impeller pitch, time, m (s)
 u = circumferential speed, m/s
 w = relative velocity, m/s
 Y = absolute circumferential coordinate, m
 y = relative circumferential coordinate, m
 Z = axial coordinate, m
 α = angle in absolute system
 Δ = difference
 λ = radius ratio
 π = pressure ratio
 φ = flow rate coefficient
 χ = isentropic exponent
 ψ = pressure rise coefficient

Subscripts

0 = inlet
 2 = impeller exit
 3 = diffuser inlet measurement plane
 4 = leading edge
 5 = throat
 6 = vaned diffuser exit
 eff = effective
 geom = geometric
 i = inlet
 o = outlet
 s = vane
 tot = stagnation

profile at diffuser inlet, which leads to equalized incidence angles between hub and shroud.

These measurements had been performed with different probes for total pressure, total temperature, and flow angle that had been traversed from hub to shroud at four positions across the diffuser pitch. By calibrating each type of probe up to Mach 0.6 the uncertainty of the measurements could be kept below 0.5 percent.

Knowing that the steady character of the flow that could be measured in this way is, at least in a zone immediately downstream of the impeller, strongly influenced by the fluctuating flow pattern leaving the impeller, these instantaneous effects could be investigated mainly using the L-2-Focus technique. Using different windows in the shroud of the compressor (one is shown in Fig. 3) the measuring position could be traversed from hub to shroud at least at two different radii, $\lambda = 1.017$ and $\lambda = 1.1$, and at four positions over the diffuser pitch in accordance with those investigated with the steady probes.

As the evaluation of L2F measurements can only be made by statistic calculations of the distribution of about 2000 to 10,000 measured data for each position, one gets an average value that has no applicable basis for the analysis of instantaneous processes. However by correlating phases of measurement with certain phases of the impeller movement, values of absolute velocity and flow angle could be obtained from this measurement technique in different time-dependent phases of rotor movement. When investigating the wide diffuser, only four phases of one type of impeller flow channel could be discerned due to this time-consuming technique. Later on in the narrow diffuser 16 phases including the splitter blade channel could be measured in even less time using improvements of the sampling system. The reliability of these results depends a lot on the particle size of scattering particles. Using oil droplets of less than $1 \mu\text{m}$ diameter, the flow directions of fluid and particles show important differences only in connection with strong accelerations as they appear in shocks.

The uncertainty of the measurement and evaluation method of the flow angle is difficult to define. The statistical data analysis of many measurements helps to eliminate some uncertainties in the results. On the other hand, it is not easy to define what the exact averaged flow angle within an interval with flow fluctuation should be.

In order to have an indication for the accuracy of the measurements the mass flow distribution inside the diffuser was calculated out of instantaneous pressure measurements and the L2F velocity and flow angle measurements. This distribution is mainly influenced by the flow angle. The integration of this mass flow compared to the measured overall mass flow never differed more than 10 percent. If this difference were due to flow angle the uncertainty is less than ± 2 deg. If the 4 percent tolerance of pressure and a 1 percent tolerance of absolute velocity is taken into account, ± 1 deg in flow angle explains the resulting mass flow difference.

General Correlations

In order to compare the results from the steady measurements with those already published, for instance by Kenny [4] or Conrad [5], and to use them as design criteria for vanned diffusers, averaged values are calculated out of the measurements in the different cross sections. The diffusion performance can be described by the pressure recovery

$$c_p = \frac{P_o - P_1}{P_{\text{tot},i} - P_i} \quad (1)$$

for the whole diffuser from the impeller exit to the measuring plane downstream of the diffuser or can be discerned in the diffuser inlet and mixing zone upstream of the throat and the diffuser channel downstream of the throat.

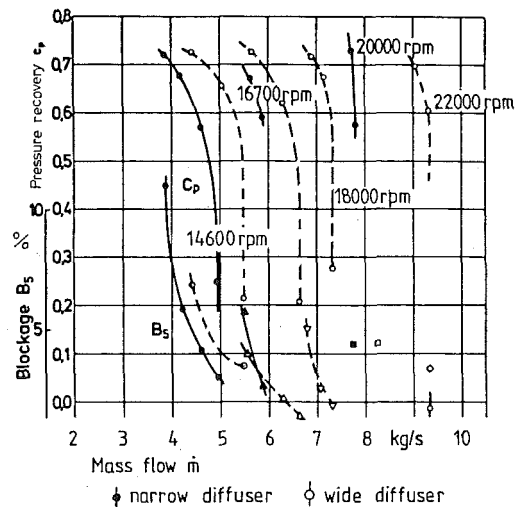


Fig. 4 Diffuser map

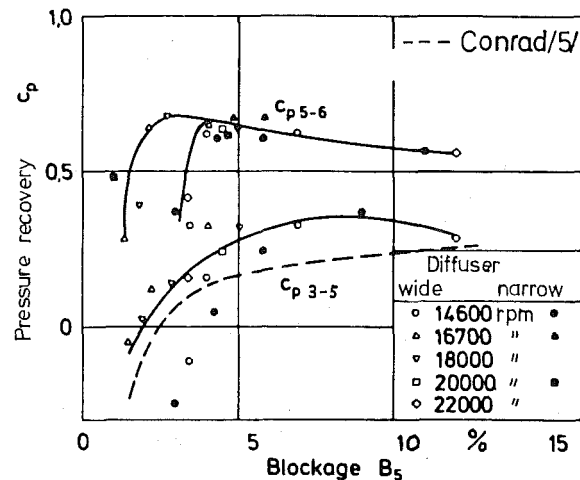


Fig. 5 Pressure recovery as a function of throat blockage

The overall performance of the diffuser plotted in Fig. 4 as pressure recovery versus mass flow looks similar to the compressor map. An uncertainty of about ± 3 percent results for c_p , which is calculated out of differences of measured pressures. The important difference is that the lines for constant speed do not reach the horizontal direction before surge appears. Overall pressure recovery in the diffuser still rises when surge is reached and shows no indication for instability, although it can be expected that surge is caused by the diffuser vanes, because in combination with the vaneless diffuser surge appears at lower mass flow.

Figure 5 looks into the diffuser more in detail and shows the pressure recovery for the inlet part and the channel as a function of throat blockage, defined as

$$B_5 = 1 - \frac{A_{\text{eff},5}}{A_{\text{geom},5}} \quad (2)$$

with A_{eff} calculated from the measurement

$$A_{\text{eff},5} = \frac{\dot{m} R \cdot T_{\text{tot},2}}{p_5 \cdot a_5 \cdot M_5} \left(\frac{\pi_5}{\pi_{\text{tot},5}} \right)^{\frac{x-1}{x}} \quad (3)$$

From this calculation, the uncertainty of blockage is about ± 3.5 percent. Corresponding to the increase in mass flow in Fig. 4, blockage decreases continuously. The decrease of the channel recovery $c_{p,5-6}$ with increasing blockage therefore is caused by the decline in mass flow combined with higher pressure recovery in the inlet portion leading to lower Mach numbers at the throat.

In discussing the relations between diffuser inlet pressure

recovery and throat blockage, the latter should be caused by the flow field of the inlet. The higher the pressure recovery is in the inlet, the thicker the boundary layer can grow at least at hub and shroud. Parameters other than blockage seem to have a dominating influence on inlet pressure recovery. One fact that can be verified with the measurements from Verdonk [6] and others is that when inlet recovery reaches $c_{p\ 3-5} \approx 0.4$, an approach to surge is indicated. As Fig. 5 shows, blockage varies in a wide range while $c_{p\ 3-5}$ is nearly constant, after it has risen quickly with increasing blockage. The dashed line indicates the results of Conrad [5]. The two diffusers do not differ significantly in this diagram.

Pressure recovery is caused by deceleration of the flow as a reaction of an enlargement of the flow area. This interrelation is displayed in Fig. 6 where a ratio of throat to inlet area is used. The inlet area is determined as

$$A_3 = 2\pi r_2 \lambda_3 b_3 \cdot \sin \alpha_3 \quad (4)$$

where α_3 is the measured mass-averaged flow angle at the radius ratio λ_3 of the measurement plane, and at the throat the smallest geometric cross section of the channel is employed. This is mainly a correlation useful for the inlet portion with the pressure recovery $c_{p\ 3-5}$, and the channel recovery $c_{p\ 5-6}$ again displays the influence of throat Mach numbers. Up to an area ratio of about 1.15 the measured values of the diffuser inlet pressure recovery form a straight line, starting at negative values as a result of a converging flow channel and pressure losses. With increasing area ratio $c_{p\ 3-5}$ rises more or less linearly until it reaches about 0.4, where it remains constant. The area ratio in this figure is bigger than that which could be taken into account from continuity considerations, because throat area has to be reduced by the blockage of boundary layer. As blockage rises very fast when c_p is above 0.3 in Fig. 6, the values of $A_5/A_3 > 1.2$ would be shifted by 10 percent and more to the left if one looks at the effective area ratio. This does not seem to become greater than about $A_{5\ eff}/A_3 \approx 1.15$ in both diffusers, because boundary layer blockage is growing faster than geometric area change. Compared with the line for an ideal pressure recovery as defined by Sprenger [7]

$$c_{p, id} = 1 - (A_3/A_5)^2 \quad (5)$$

the measured values for c_p are even somewhat higher.

As the possible pressure recovery is influenced by the area ratio of the flow channel as well as by the entropy rise or losses of this process, the stagnation pressure loss in the diffuser as shown in Fig. 7 for the different sections should be another indication for the quality of the flow mechanism. While in the diffuser channel and the collecting chamber the relative loss of total pressure is dominated by inlet Mach number, no concrete relation to the losses in the inlet portion can be seen. Therefore in Fig. 8 the losses are related to the real pressure rise. Ob-

viously compressor speed is a more dominant parameter, causing fairly big differences in the pressure losses. This may be due to the instantaneous fluctuations at impeller exit, which are a function of speed as well. Pressure losses of the narrow diffuser appear generally lower than those of the wide one. This would mean that besides the effect of the geometric change on the steady flow profile the changed shroud contour should have an influence on the effectiveness of the mixing process downstream of the impeller.

Laser-Two-Focus Measurements

As the pressure fluctuation at the impeller exit is small compared to the absolute value and disappears more or less before the flow reaches the diffuser vanes as shown in [3], there was no attempt to measure differences between the instantaneous pressure distributions. The fluctuation in flow velocity is more

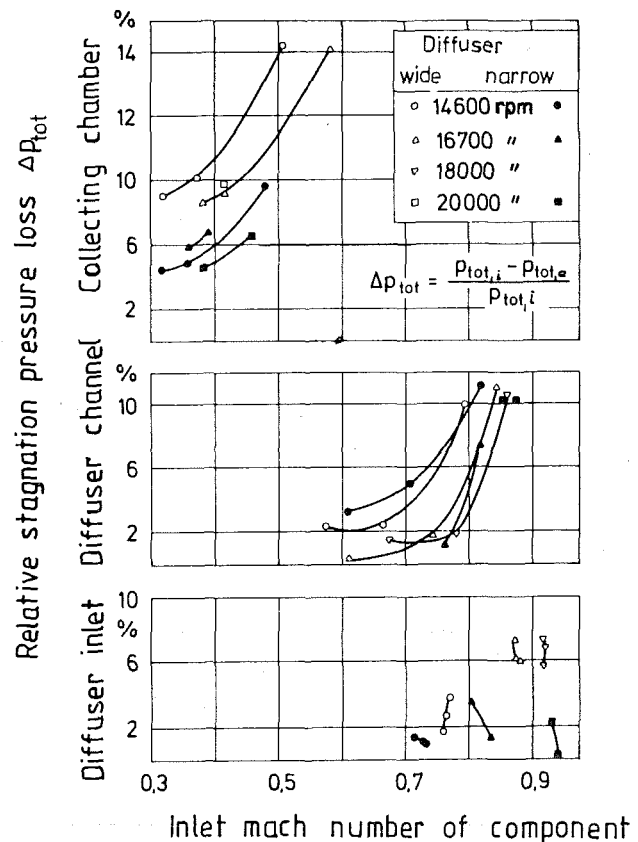


Fig. 7 Stagnation pressure loss of diffuser component as a function of inlet Mach number

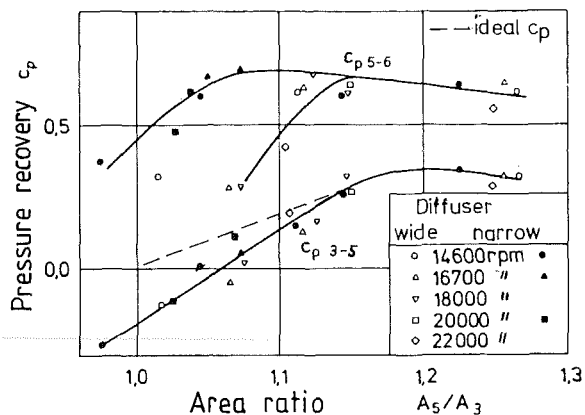


Fig. 6 Pressure recovery as a function of throat-to-inlet area ratio

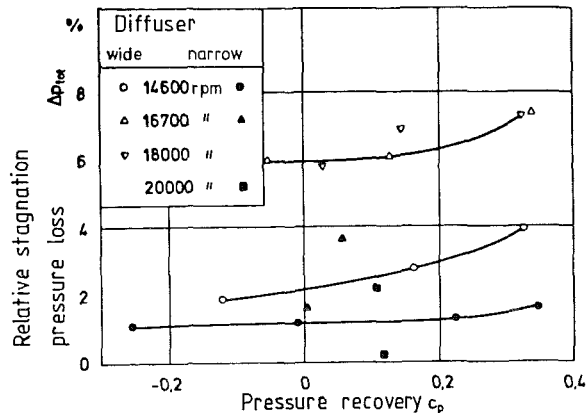


Fig. 8 Stagnation pressure loss at diffuser inlet as a function of pressure recovery

distinct and that of flow angle shows conspicuous differences between hub and shroud, as well as between jet and wake, as already shown by Eckardt [8]. The two-focus-velocimetry determines the flow vector in the plane perpendicular to the optical axis. Out of this, velocity and flow angle α , relative to the circumferential direction as shown in Fig. 9, are found. Figure 10 describes the position of the different phases of measurement as used in the following figures relative to the rotating system. The temporal cycle for the observer in the absolute system therefore goes from VIII to I.

Figures 11 and 12 reproduce the distribution of absolute flow angle referred to the relative system at different locations in the narrow and wide diffusers, respectively. At least near impeller exit the distributions are similar in both diffusers. In Fig. 11 the smoothing of fluctuation can be seen between $\lambda = 1.017$ and $\lambda = 1.1$ for the narrow diffuser. However, in Fig. 12 angular differences have not changed very much for the wide diffuser. The change of averaged flow angle as known from the steady measurements can also be found in these values. Although pressure fluctuation has been found to disappear upstream of $\lambda = 1.1$ the flow angle still shows strong oscillation at the diffuser leading edge. The reaction to the steady pressure distribution caused by the leading edges leads to differences in the flow angle distribution. This can be seen easily in the results for $\lambda = 1.1$, comparing those for different locations across diffuser pitch.

To show this influence more conspicuously, Fig. 13 displays the flow angle distributions in the absolute system for certain phases of flow leaving the impeller. Without the reaction from the diffuser leading edge, this should be more or less parallel lines showing the variation from hub to shroud. Gradients across the pitch are induced by pressure distributions due to the diffuser vanes. The zone where this effect can be observed moves a little at the measurement position at $\lambda = 1.1$ due to the change in mean flow direction between jet and wake. Only for phases I and III can this be seen clearly, while strong gradients in the other two phases result in more mixed distributions.

A picture of the flow vector field as obtained out of these measurements is displayed in Fig. 14. The dotted line shows the boundary from jet to wake, which leads to a change in direction and value of the vectors induced by the impeller. A slight influence of the diffuser vanes on the vectors can be seen near their leading edges.

Some more details of the instantaneous process inside a diffuser could be investigated but many different interactions made it impossible to find a quantitative dependency between

fluctuation and pressure losses. If we compare the results from both diffusers, the most obvious difference is that the zone of very low flow angles near the shroud, sometimes even backflow, has disappeared in the narrow one. The fluctuation between jet and wake has remained more or less the same. As the mixing loss seems to be an important loss factor in the diffuser inlet, this wake near the shroud could be the reason for the higher losses in the inlet of the wide diffuser.

Prediction of Diffuser Performance

In order to have a basis for predicting the performance of a diffuser design with a variable geometry by adjustable guide vanes, results out of these measurements, mainly the general correlations, are used as well as similar information out of the

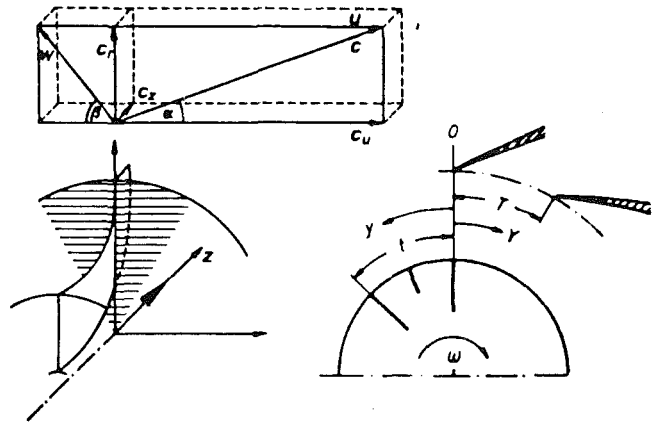


Fig. 9 Velocity vectors and coordinates

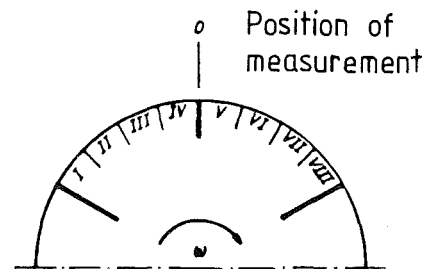


Fig. 10 Phases of measurement relative to the rotor

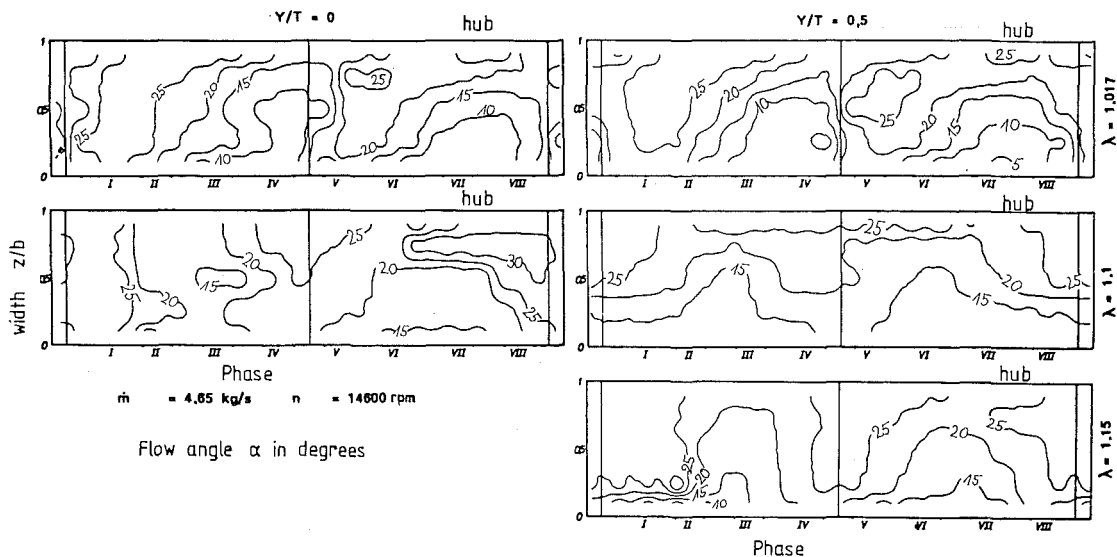


Fig. 11 Flow angle α in the narrow diffuser

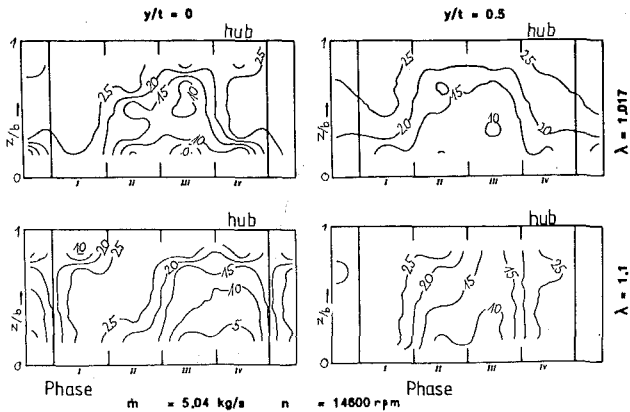


Fig. 12 Flow angle distribution in the wide diffuser

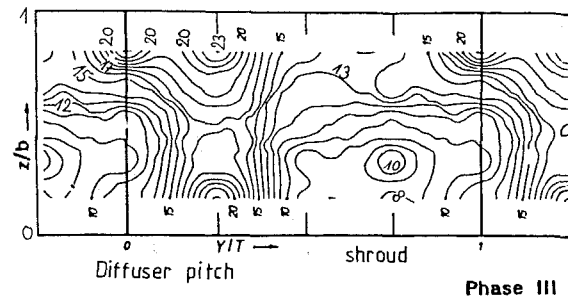
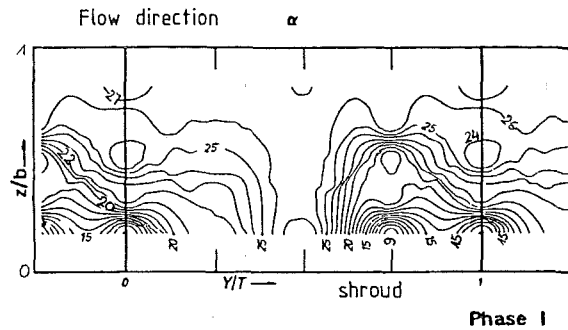


Fig. 13 Flow angle distribution in the diffuser at $\lambda = 1.1$

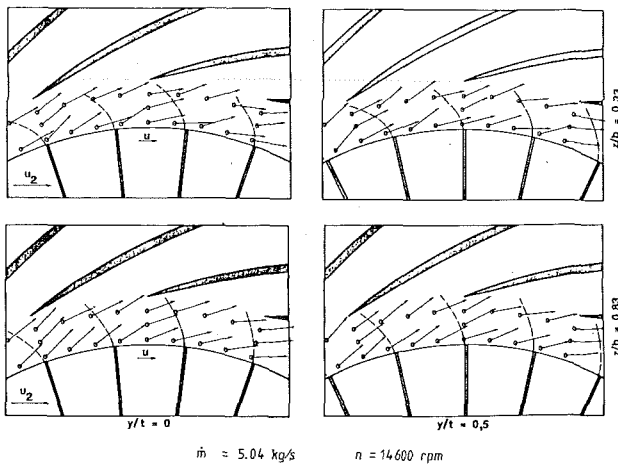


Fig. 14 Flow vector in diffuser inlet

literature. To calculate the flow field inside the diffuser and to have detailed information even at off-design conditions a calculation method developed by Wiedermann [2] was employed. This method had been verified in [9] with the results from the diffuser measurements shown above. This method allows calculation of pressure or Mach number distributions in plane diffusers even at transonic conditions.

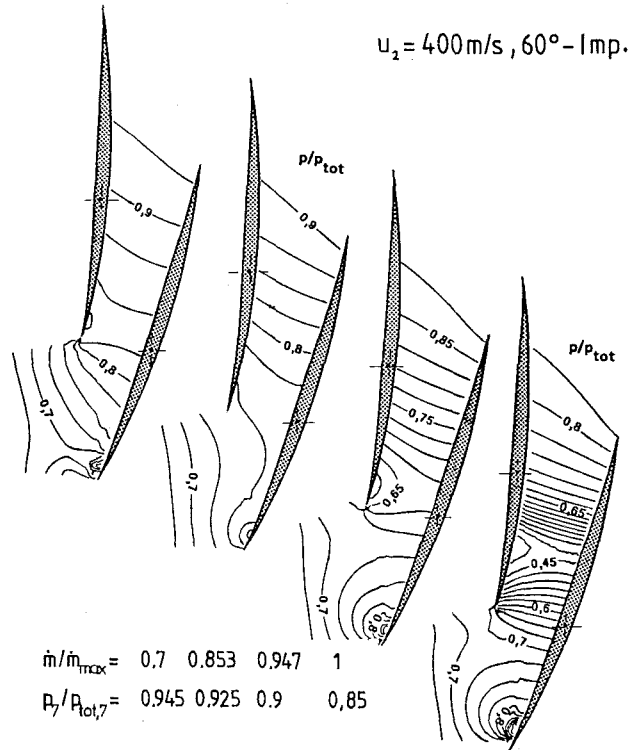


Fig. 15 Calculated isobars of variable diffuser with leading edge angle 25 deg

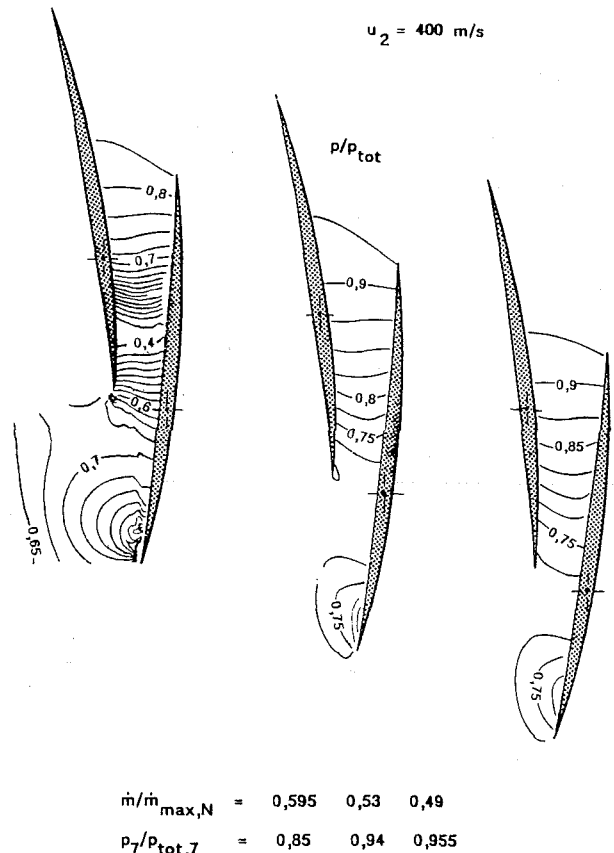


Fig. 16 Calculated isobars for different operating points with guide vane set at 15 deg

For a vaned diffuser with 25 vanes, designed for a backswep impeller at a circumferential speed of $u_2 = 400$ m/s, four pressure distributions at operating points between surge and choke are shown in Fig. 15. Near surge a continuous

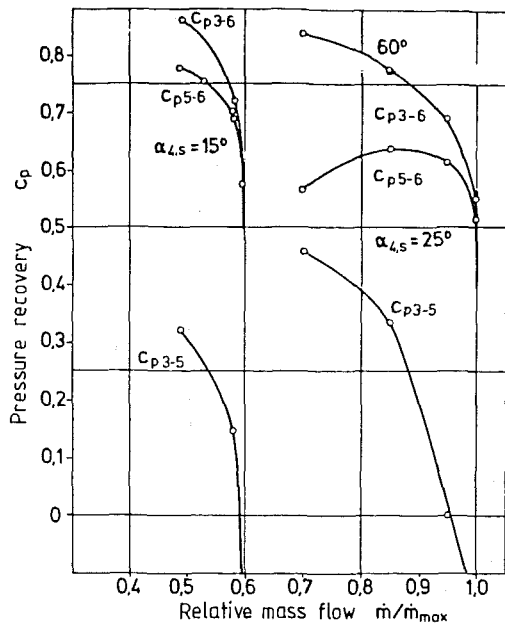


Fig. 17 Pressure recovery determined from the calculated pressure distribution

pressure rise can be observed while near choke accelerations and pressure drops appear at the entrance of the diffuser channel. After moving the vanes to an inlet angle of 15 deg these calculations have the results shown in Fig. 16. According to Fig. 4, out of these values lines for pressure recovery versus mass flow, related to choke flow of 25 deg stagger angle, are calculated and shown in Fig. 16. The recovery is split into those, inlet regions, and diffuser channels. Similar to the measured results mentioned above, the recovery of the inlet rises until surge is defined out of numerical instabilities. At 25 deg pressure recovery c_{p3-5} reaches about 0.45 and ends at about 0.35 with a 15 deg vane angle.

The overall pressure recovery rises until surge, due to the backswept impeller. The main difference between the lines for the two vane angles is shown in the channel recovery. While at 25 deg there is the known maximum before Mach number 1 is reached in the channel, within the narrow operating range at 15 deg this maximum does not appear. This would mean that a totally subsonic flow near the diffuser throat does not appear in this case. Deceleration in the inlet of the diffuser does not reach the range of continuous pressure rise throughout the whole diffuser that leads to the highest pressure recovery.

Because this calculation does not involve boundary layers and flow fluctuations, it shall be compared with results of measurements. Unfortunately detailed measurements in the variable geometry diffuser are not available at the moment. However the range between stall and surge can be compared in order to decide whether the indicated surge point is correct. Figure 18 displays a dimensionless map of the stage showing measured lines of pressure rise coefficient at different impeller speeds for different stagger angles of the vanes.

In general the measured lines have the same characteristics as the calculations. The dashed line for $u_2 = 1.16$ that corresponds to the calculated circumferential speed comprises more or less the same operating range. The shift of this range by adjusting the guide vanes is computed correct and the shape of the curves is rather similar. The instability indicated by the calculation at surge originates at the leading edge, where a zone of acceleration disappears. Although the criteria given by

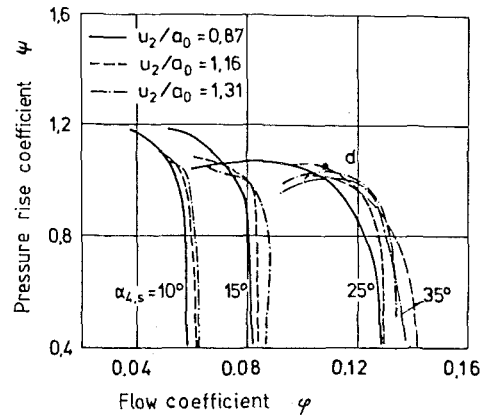


Fig. 18 Compressor map with variable diffuser

the general correlations do not explain surge in connection with low-pressure recovery of the diffuser inlet at low stagger angles the detailed calculation helps to get a sufficient prediction of the operating range.

Summary

Out of detailed measurements of the flow field inside a vaned diffuser, a calculation method is verified and afterward employed to calculate the flow field inside a variable-geometry vaned diffuser. Comparing these results to measured lines of the compressor stage, the computed performance characteristic of the diffuser fits the measurements. As no analytical loss model is incorporated in the calculation, the influence of pressure losses can only be estimated from relationships between losses and other data of the flow field. These are obtained out of measurements with steady probes in vaned diffusers. Using these instruments, performance predictions of variable geometry vane diffusers seem to be sufficient.

Acknowledgments

The authors want to thank Mr. A. Wiedermann for performing the calculations and Mr. P. Tanneberg and H. Quietmeyer for preparing and running the test facilities.

References

- Stein, W., and Rautenberg, M., "Flow Measurements in Two Cambered Vane Diffusers With Different Passage Widths," ASME Paper No. 85-GT-46, 1985.
- Wiedermann, A. R., "Die räumliche reibungsfreie Strömung in Diffusoren eines Radialverdichters bei transsonischer Anströmung," Dissertation, University of Hannover, Federal Republic of Germany, 1985.
- Stein, W., "Beitrag zur Analyse der gegenseitigen Beeinflussung von Laufrad und Diffusorbeschaukelung in Radialverdichtern," Dissertation, University of Hannover, Federal Republic of Germany, 1986.
- Kenny, D. P., "A Comparison of the Predicted and Measured Performance of High Pressure Ratio Centrifugal Compressor Diffusers," ASME Paper No. 72-GT-54, 1972.
- Conrad, O., Raif, K., and Wessels, M., "The Calculation of Performance Maps for Centrifugal Compressors With Vane-Island Diffusers," *Performance Prediction of Centrifugal Pumps and Compressors*, ASME, New York, 1980.
- Verdonk, G., "Vaned Diffuser Inlet Flow Conditions for a High Pressure Ratio Centrifugal Compressor," ASME Paper No. 78-GT-50, 1978.
- Sprenger, H., "Experimentelle Untersuchungen an geraden und gekrümmten Diffusoren," Dissertation, ETH, Zürich, 1959.
- Eckhardt, D., "Detailed Flow Investigations Within a High-Speed Centrifugal Compressor Impeller," *ASME Journal of Engineering for Power*, Vol. 98, 1976.
- Jansen, M., "Untersuchung über die Wechselwirkung zwischen Laufrad und Diffusor in Radialverdichtern," *Forschungsberichte Verbrennungskraftmaschinen*, Vol. 337, 1983.

Swirling Impeller Flow

H. Krain

Research Engineer,
DFVLR, Institut für Antriebstechnik,
Cologne, Federal Republic of Germany

The results of extensive laser measurements carried out in the blade passages of a newly designed backswept impeller are presented and discussed. Noticeable distortions of the throughflow patterns and a distinct swirling flow character were found inside the rotor. The measurement results and a simple theoretical approach suggest that the distorted throughflow patterns and the secondary flows are caused by a vortex flow. Although the relative flow has been significantly decelerated a comparatively smooth velocity profile has been identified at the rotor discharge that differed widely from the well-known jet/wake-type flow pattern.

Introduction

The actual discharge flow pattern of centrifugal compressor impellers is known to differ frequently from the ideal pattern predicted by potential theoretical calculation methods [1-3]. Usually, the actual flow pattern is assumed to be of the jet/wake type, generated by Coriolis, curvature, boundary layer, and tip clearance effects that separate the high and low-velocity fluid, resulting in an accumulation of low-kinetic-energy fluid in the shroud/suction side area and a collection of high-kinetic-energy fluid in the hub/pressure side area [1]. The philosophy indicated in the literature suggesting that the discharge flow pattern of centrifugal impellers can look quite different [3, 6]. Recently, Hamkins et al. [6] published their laser data taken in an unshrouded pump impeller showing a jet/wake development which is almost contrary to the flow character of the Eckardt impeller; i.e., in the pump impeller investigated the wake development was found close to the pressure side, whereas, in the Eckardt impeller, the wake was developing along the suction side. Obviously centrifugal impeller aerodynamics is rather complex and not yet completely understood.

However, the laser data to be presented in this paper will contribute to a further clarification of centrifugal impeller aerodynamics. Extensive laser measurements carried out within a newly designed impeller [7] and detailed studies of the vortex structure inside of the impeller gave evidence of basic flow phenomena that had not been detected in the past. The results obtained gave rise to a new view of the old jet/wake idea showing that the jet and the wake are part of a single flow phenomenon.

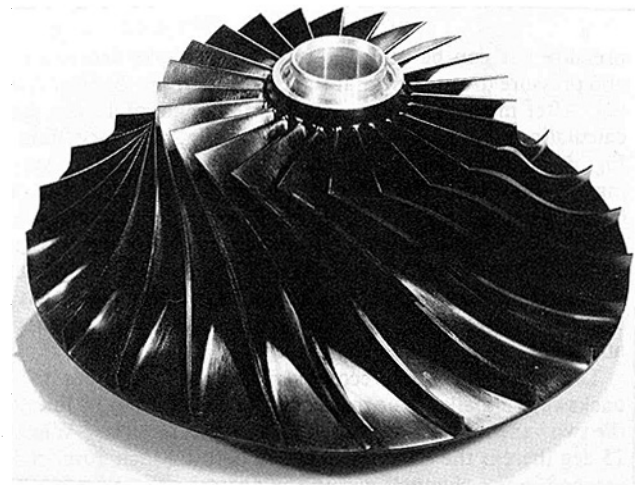


Fig. 1 30-deg backswept test impeller ($z_r = 24$)

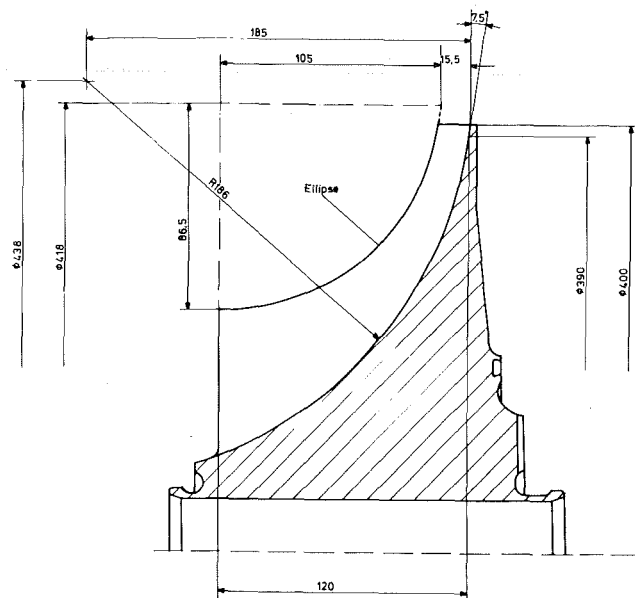


Fig. 2 Meridional cross section of the test impeller

Contributed by the Gas Turbine Division of THE AMERICAN SOCIETY OF MECHANICAL ENGINEERS and presented at the 32nd International Gas Turbine Conference and Exhibit, Anaheim, California, May 31-June 4, 1987. Manuscript received at ASME Headquarters February 3, 1987. Paper No. 87-GT-19.

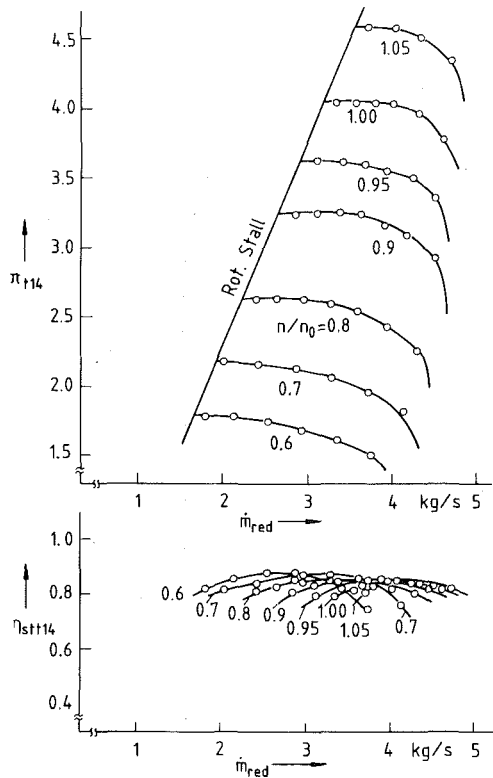


Fig. 3 Performance map of the centrifugal compressor stage composed of the test impeller and a vaneless constant area diffuser

Test Impeller

The impeller used for the flow analysis was a 30-deg backswept impeller which was designed by a CAD method described in detail in [7]. Figure 1 shows a photo of the impeller, and the meridional impeller cross section is submitted in Fig. 2. For the initial performance and laser measurements the impeller was coupled with a vaneless constant area diffuser that ensured a relatively wide flow range. For performance measurements total pressures and total temperatures have been measured at the inlet and exit of the compressor stage. Additionally, the static pressure development has been measured from rotor inlet to diffuser exit. The performance characteristics of the compressor stage are shown in Fig. 3. Maximum achieved total stage pressure ratio was about 4.5:1

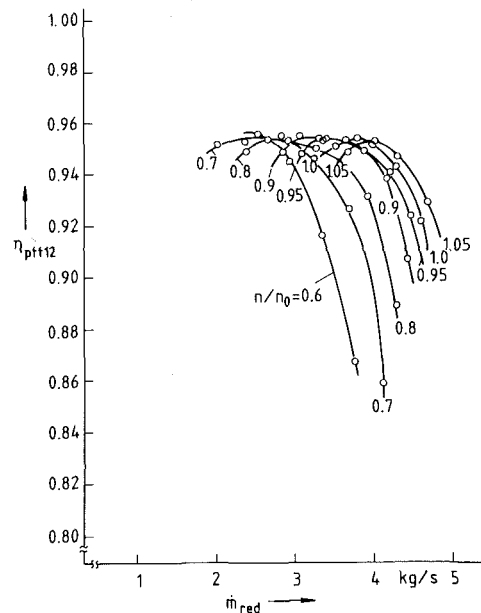


Fig. 4 Total/total polytropic impeller efficiency

and the maximum achieved total/total isentropic stage efficiency was 84 percent. The impeller efficiency has been deduced from total temperature, mass flow, and static pressure measurements taken by 24 tappings that were circumferentially distributed at the impeller discharge. The impeller efficiency has been derived by using the equations of energy and continuity and by assuming a zero blockage at the impeller exit.

Figure 4 shows the corresponding total/total polytropic impeller efficiency. For this first build ($N_s = 80$) that used the new design approach [7], a maximum impeller efficiency of 95 percent was achieved.

Velocity Measurements

The internal flow field of the new impeller was analyzed with the L2F technique available at DFVLR. The measurement system gives information about the magnitude and direction of the mean absolute flow vector and its turbulent components. The relative flow vector can be deduced from the velocity triangle. The error of mean absolute velocity

Nomenclature

c = absolute velocity
 c_m/u_2 = meridional velocity/tip speed
 c_ϕ = circumferential vortex velocity
 $c_{\phi L}$ = component of c_ϕ measured by L2F
 HU = hub
 \dot{m} = mass flow rate
 N_s = specific speed
 n/n_0 = shaft speed/design speed
 PS = pressure side
 p = static pressure
 r = radius
 r_{max} = maximum radius of vortex
 r_0 = radius of solid-body vortex
 SH = shroud
 SS = suction side
 u = circumferential velocity

w_b = velocity parallel to the blade
 w_L = velocity measured by L2F
 w_r = radial velocity component
 w_z = axial velocity component
 w_ϕ = circumferential vortex velocity (Fig. 20)
 x, y = Cartesian coordinates
 x/s_m = dimensionless shroud length
 y/t = dimensionless blade pitch
 z/b = dimensionless channel depth
 z_r = rotor blade number
 β_b = blade angle
 β_L = flow angle measured by L2F (Fig. 13)
 $\Delta\beta_R$ = flow angle difference (Fig. 22)

δ = swirl parameter (Fig. 22)
 η_{stt} = total/total isentropic efficiency
 η_{ptt} = total/total polytropic efficiency
 ν = kinematic viscosity
 π_t = total pressure ratio
 ϕ = circumferential coordinate
 ω = angular velocity of the solid-body vortex

Subscripts

0 = ambient condition
 1 = impeller inlet
 2 = impeller exit
 3 = vane diffuser inlet
 4 = diffuser exit
 red = corrected

Table 1 Positions of L2F measurement planes (Fig. 5)

Measurement plane	Locations x/s_m
I	0
II	0.2
III	0.4
IV	0.6
V	0.8
VI	1.004

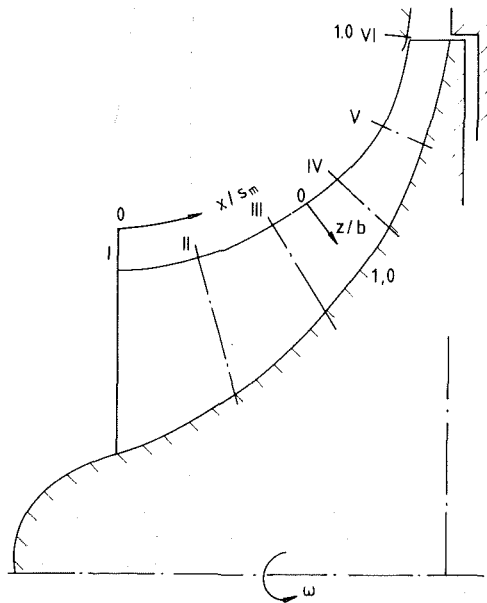


Fig. 5 Arrangement of the L2F measurement planes

measurements is usually less than ± 1 percent and the uncertainty of absolute flow angle measurements generally is less than ± 1 deg. Therefore, for the backswept impeller, the uncertainty of the relative flow angles is less than ± 0.5 deg, which can be derived from the velocity triangle. Further details about that measurement technique and its applicability to turbomachinery flows even under complex flow conditions are given in [8]. Measurements in the backswept impeller were performed at 70, 90, and 100 percent shaft speed. For each speed three mass flow rates were selected, located close to stall, at peak efficiency and close to surge (Fig. 3). The results presented in this paper were taken at the impeller design point ($n/n_0 = 1.0$, $\dot{m}_{red} = 4.0$ kg/s). Six measurement planes have been selected in the rotor area to analyze the internal flow field (Fig. 5). The measurement planes are perpendicular to the shroud casing throughout and their positions within the rotor are listed in Table 1.

The flow conditions at the impeller exit are generally believed to influence both flow range and efficiency of centrifugal compressor stages. Usually, the flow character present at the impeller exit already gives some insight into the quality of the overall impeller flow and into the diffuser inlet flow conditions. Therefore, laser measurements were started at plane VI, which coincides with the impeller exit (Table 1).

The result of these measurements is given in Fig. 6, which shows a comparison of three velocity profiles measured at the exits of three different impellers. The pattern at the top belongs to the radially ending Eckardt impeller [2], the pattern in the middle has been found close to the exit ($x/s_m = 0.89$) of a radially ending splitter blade impeller [3], and the flow pattern at the bottom has been analyzed at the exit of the new impeller. For each impeller the measured meridional velocity referred to the rotor tip speed c_m/u_2 is plotted versus flow area. It should be noted that the specific speeds of the radially ending impellers ($N_s = 115$) differed from that of the

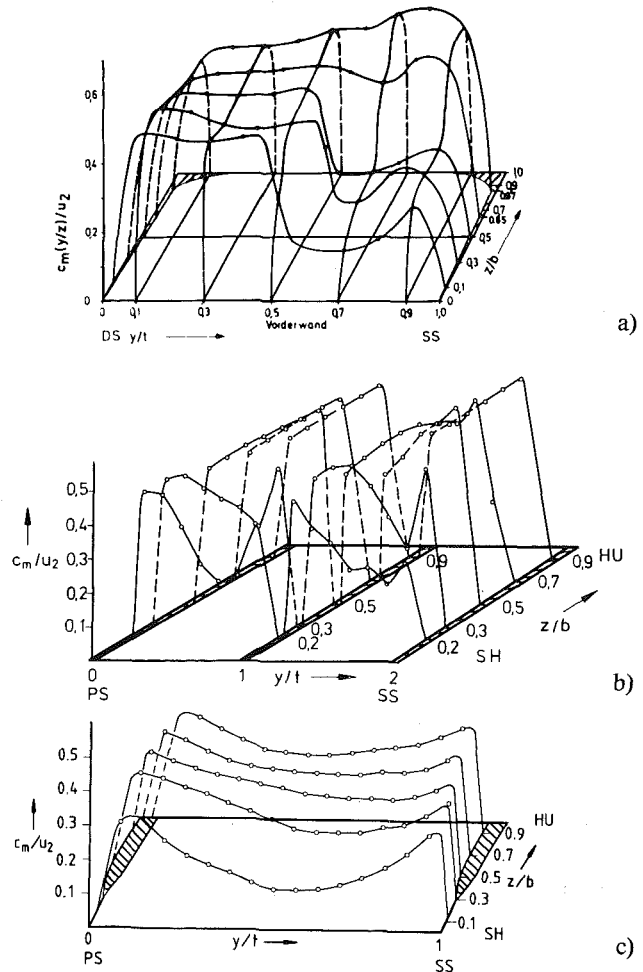


Fig. 6 Comparison of velocity profiles: (a) radially ending Eckardt impeller, 20 long blades [2]; (b) radially ending splitter-blade impeller, 14 + 14 blades [3]; (c) new backswept impeller (Figs. 1, 2)

backswept impeller ($N_s \approx 80$). Additionally, measurements at the exits of the radially ending impellers were carried out at pressure ratios of about 2:1 whereas the pressure ratio of the stage equipped with the new backswept impeller was 4:1 (Fig. 3).

Figure 6 clearly shows that a very smooth velocity profile, primarily in the pitchwise direction, is present at the discharge of the new impeller. A highly disturbed velocity profile resembling the classical jet/wake pattern is not seen at the exit of the new impeller. Above all, a smooth discharge flow was obtained, although the relative flow within the new impeller has been much more decelerated than the flow within the radially ending impellers, which agrees fairly well with the high impeller efficiencies shown in Fig. 4. An accumulation of flow with low kinetic energy is only observed very close to the shroud ($z/b = 0.1$) and outside of the impeller (Fig. 5). Tip clearance and mixing effects were at first believed to generate this flow character.

In summary, the design goals of this first build were met and we speculated whether it would make any sense to continue the laser measurements since it was believed that an impeller having such a smooth discharge flow pattern will also have a regular pattern throughout the rotor. However, measurements were continued proceeding from rotor inlet to rotor exit. The results obtained were rather surprising.

Figures 7 and 8 show the measured velocity profiles at planes I and II. As expected, the patterns are very regular and

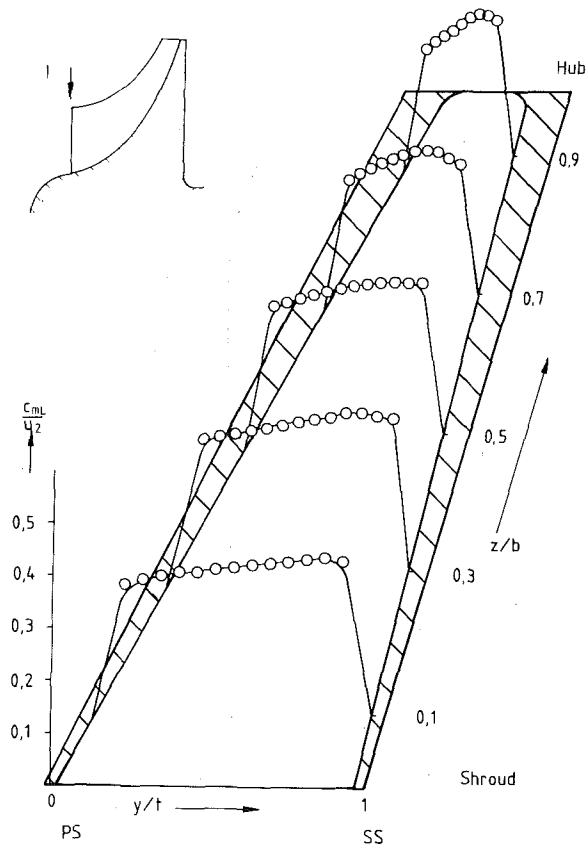


Fig. 7

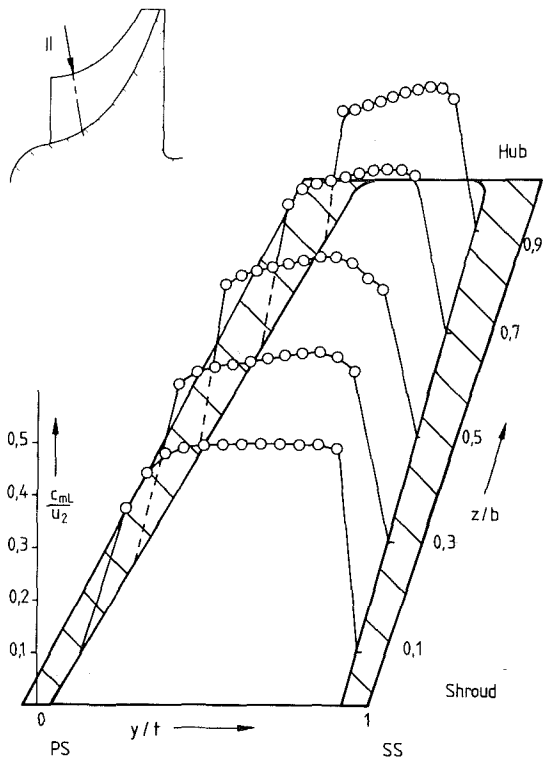


Fig. 8

the meridional velocity exhibits a positive gradient from the pressure to the suction side. Surprisingly, an unexpected irregular distribution of the meridional velocity profile was determined close to the shroud of plane III ($z/b=0.1$, Fig. 9) and the point of minimum velocity at this measurement position is located in the pressure side area rather than in the suc-

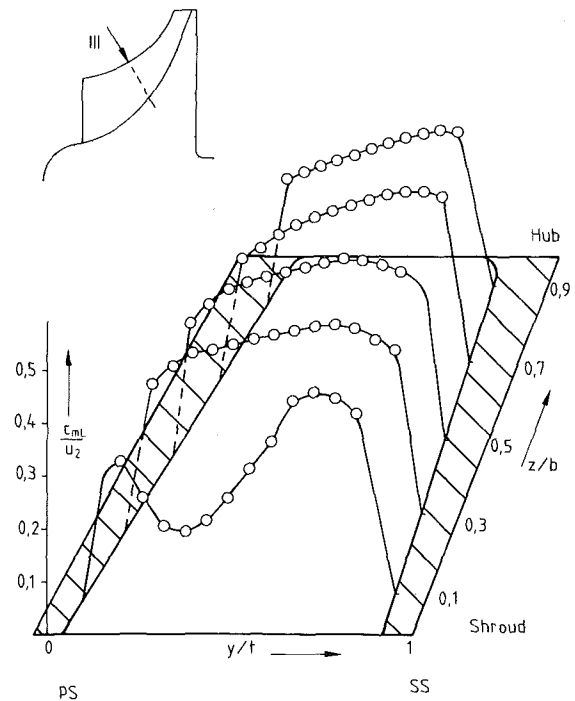


Fig. 9

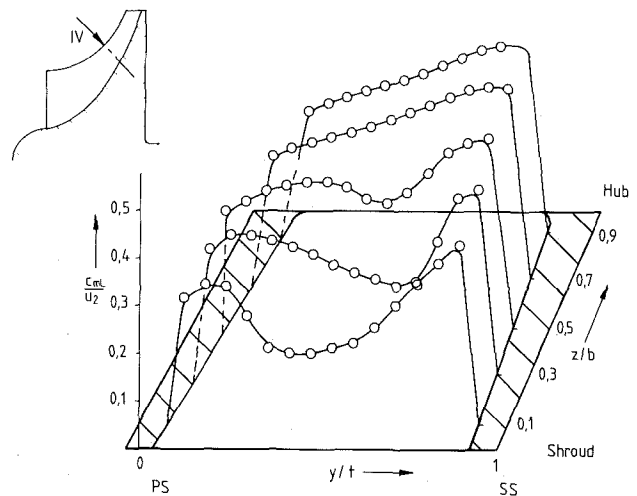


Fig. 10

tion side area ($y/t=0.3$). From plane III to plane IV the point of minimum velocity shifts toward the middle of the flow channel and the disturbed flow now has extended covering about 50 percent of the channel depth (Fig. 10). Close to the impeller exit, however, the meridional velocity profile is smoothing again (Fig. 11) and the exit flow (Fig. 12) is even more regular in the pitchwise direction.

In summary, the velocity patterns shown in Figs. 7–12 suggest that a wake flow is also present in this impeller. But in contrast to the original jet/wake philosophy previously pointed out and in contrast to the measurements available for radially ending impellers [2, 3], the wake now has a maximum inside the impeller and it decreases toward the impeller exit. Formerly, such a flow development has not been experienced. In order to get a better understanding of this type of impeller flow, a new data analysis procedure was applied that indeed gave more insight into the governing physical flow effects of that impeller.

Vortex Analysis by the L2F Technique

The most important information was extracted from the

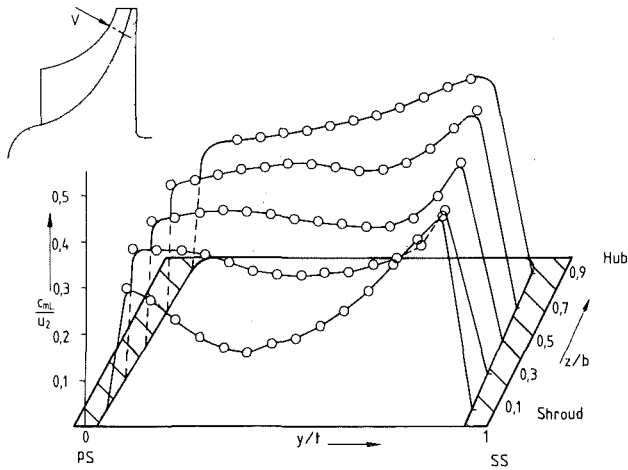


Fig. 11

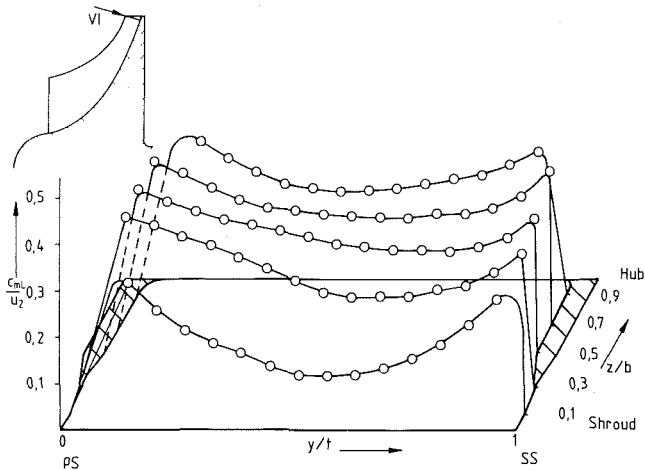


Fig. 12

Figs. 7-12 Meridional velocity profiles measured at planes I-VI ($n/n_0 = 1$, $\dot{m}_{red} = 4.0$ kg/s)

lines of constant flow angle (isoclines) plotted for the six measurement planes (Fig. 5). The shape of these isoclines gives information about the vortex flow within the impeller area. The basic equations for the isoclines of a real vortex, composed of a solid-body vortex and a potential vortex, are submitted in Fig. 13(a) and the result of the analysis for a throughflow inclined against the drawing plane ($\beta_b = 35$ deg) is shown in Fig. 13(b). Lines of constant flow angle are parallel in the solid-body vortex area ($0 \leq r \leq r_0$) whereas these lines are of elliptic type in the potential vortex area ($r > r_0$). The vortex center is always located in the middle of the parallel isoclines. The approach presented was originally applied by Binder [10] and has been used to identify a vortex flow within the impeller area. A real vortex, composed of a solid-body vortex and a potential vortex, was assumed to be present when isoclines similar to those shown in Fig. 13(b) were analyzed.

Flow Angle Analysis

Figures 14-19 show the results of the detailed flow angle analysis carried out for all measurement planes. At plane I (Fig. 14) the relative flow angle varies from 54 to 28 deg from hub to shroud, which is in agreement with the design specifications. At plane II (Fig. 15) the isoclines are primarily horizontal. Closed lines of constant flow angle, which may be interpreted as counterrotating corner vortices, are found in the shroud area. At plane III (Fig. 16), where the first distortion

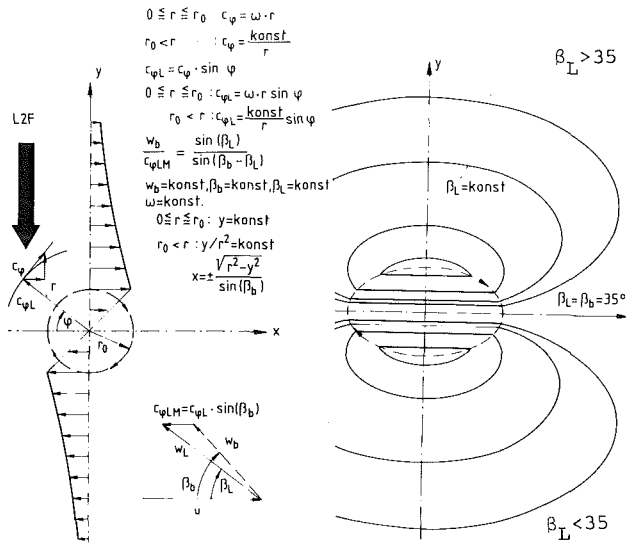


Fig. 13(a)

Fig. 13(b)

Fig. 13 Measurement of vortex flow with L2F-technique

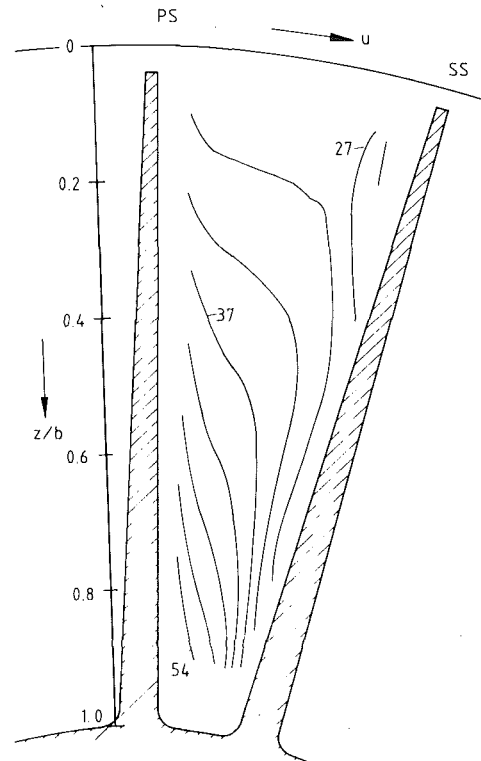


Fig. 14

of the throughflow was analyzed (Fig. 9), the isoclines for the first time exhibit a shape similar to that shown in Fig. 13. At plane IV (Fig. 17) the isocline pattern represents all features illustrated in Fig. 13. At this measurement position two counterrotating channel vortices are clearly identified. The centers of these vortices are roughly indicated. Additionally, parallel isoclines and a strong gradient in flow angle are present close to the shroud. However, a clearly developed vortex like that found in the middle of the flow channel is not resolved in this area. Obviously, a swirling flow covering the entire flow channel is present at this measurement plane. A similar flow character is seen at plane V (Fig. 18). The centers

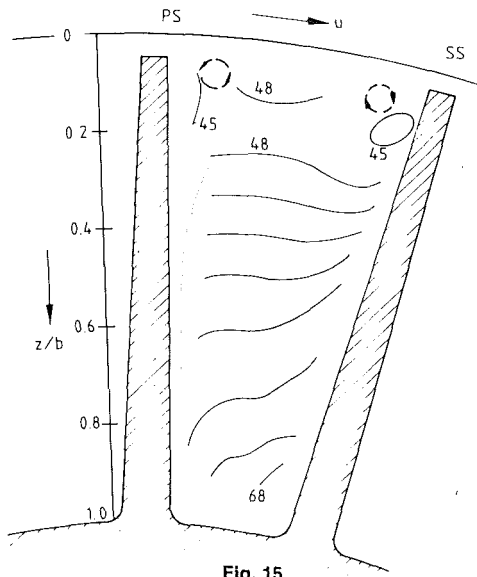


Fig. 15

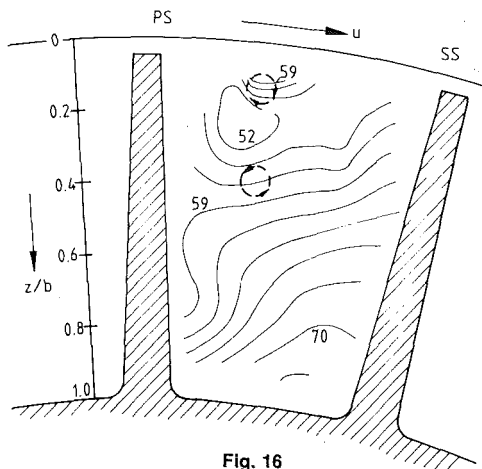


Fig. 16

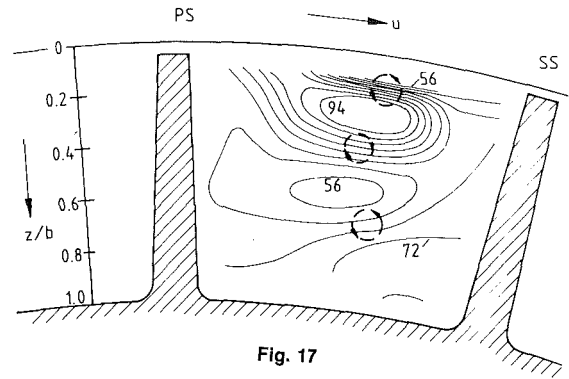


Fig. 17

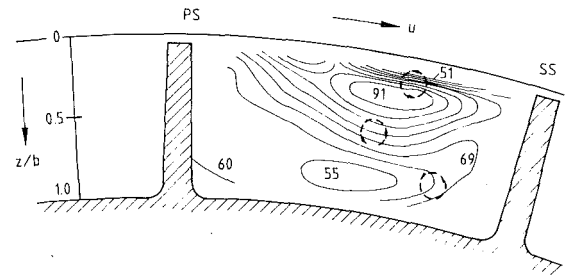


Fig. 18

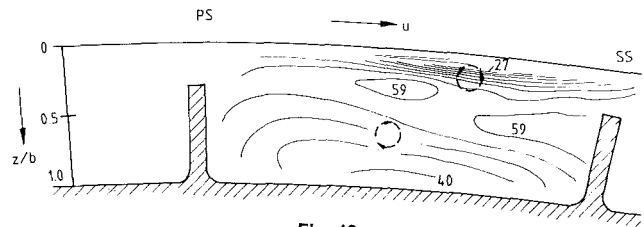


Fig. 19

Fig. 14-19 Isocline patterns ($\beta_L = \text{const}$) measured at planes I-VI ($n/n_0 = 1$, $m_{\text{red}} = 4.0 \text{ kg/s}$)

of the channel vortices have now shifted toward the middle of the flow channel and toward the hub/suction side. The vortex flow is again dominating the entire flow channel. A different pattern is present at the rotor exit (plane VI, Fig. 19). Here, only one channel vortex center is seen; the second has disappeared. But again the strong gradient in flow angle and the parallel isoclines are present close to the shroud. Obviously, the swirling flow present in any unshrouded impeller has a dominating influence on the overall flow development of the new backswept impeller. The isocline plots (Figs. 14-19) suggest that the swirling impeller flow, covering at least the entire flow channel, is initiated by the relative motion between the moving rotor and the stationary casing. Thus, this flow character seems to have its origin in the shroud area.

Vortex Flow and Throughflow

A comparison between Figs. 7-12 and Figs. 14-19 reveals that the distortions in the throughflow patterns have always been identified in those areas where the vortex flow is active. So, the question arises whether these flow phenomena belong together. A first answer of this question is obtained by a simple approach to the Navier-Stokes equations. A vortex flow with a zero radial velocity component ($w_r = 0$) and a throughflow component varying only in the radial direction ($w_z = w_z(r)$) was assumed. The remaining terms of the Navier-Stokes equations for these assumptions are submitted in Fig. 20. The throughflow velocity distribution $w_z = w_z(r)$ can be easily derived from the last equation. Figure 20 il-

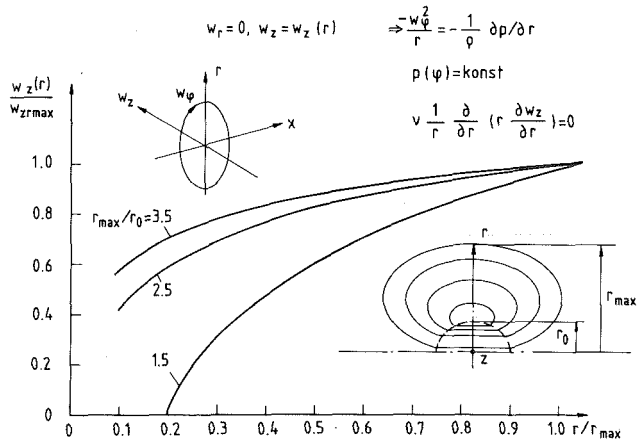


Fig. 20 Axial velocity distribution in a vortex

lustrates the result of this approach for three vortices. Obviously, the throughflow velocity is decreasing toward the vortex center and the declining rate is dependent on the vortex structure. This result qualitatively agrees with the measurement results found for the new backswept impeller and suggests that the distortions found in the throughflow patterns of the new impeller are due to the swirling impeller flow.

These effects are well known. A theoretical result for a turbulent compressible pipe flow with prescribed inlet swirl, calculated by Neuberger [9], is shown in Fig. 21. This figure il-

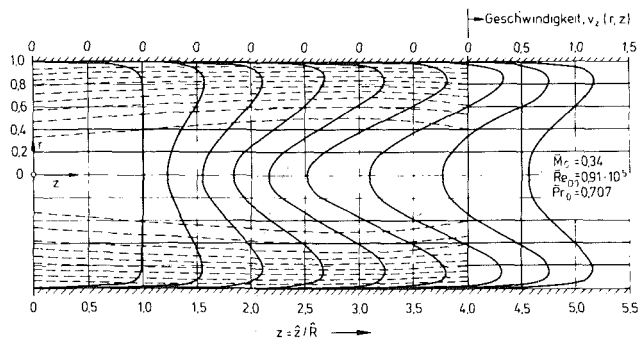


Fig. 21 Axial velocity profile development predicted for a pipe flow with prescribed inlet swirl [9]

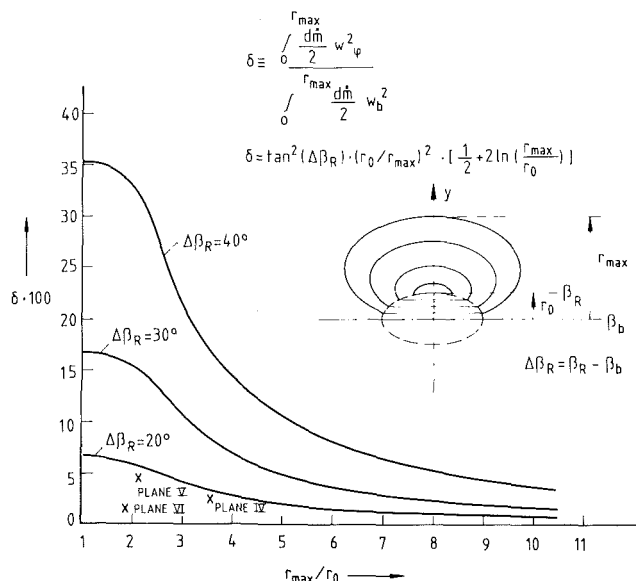


Fig. 22 Swirl parameter calculated for different vortex types; values calculated for the impeller flow are indicated by crosses

illustrates the axial velocity profile development for an inlet swirl chosen in such a way that backflow is avoided ($\hat{z}/\hat{R}=2.5$). Obviously, the smooth axial velocity profile present at the inlet at first is distorted and is smoothed again toward the exit. A comparison with the impeller flow reveals surprising similarities. Within the new impeller the distortions in the throughflow patterns are also smoothed toward the exit (Figs. 7-12). However, compared to the pipe flow the intensity of the swirling flow within the impeller seems to be low since the distortions of the throughflow patterns are moderate and the throughflow is obviously far from backflow. Very often the swirl parameter δ defined in Fig. 22 is used for a quantitative assessment of the swirling flow intensity. With the definition of Fig. 22 the swirl parameter has been calculated for different vortices. For each calculation a real vortex, composed of a solid-body vortex and a potential vortex, has been assumed. For that vortex type a simple relation has been derived by which the swirl parameter can be calculated. The relation of Fig. 22 indicates that the amount of the swirl parameter primarily depends on the vortex shape (r_{\max}/r_0) and

on the flow angle difference $\Delta\beta_R$. Obviously, the swirl parameter decreases when the potential vortex part is increasing and it also strongly decreases with decreasing flow angle difference $\Delta\beta_R$.

The relation of Fig. 22 has been used to calculate a swirl parameter for the main channel vortex of the backswept impeller. The values necessary for this assessment have been taken from Figs. 17, 18, and 19. The approach already indicates that the results obtained (Fig. 22) are only a rough estimate. The swirl parameters calculated by this procedure for measurement planes IV, V, and VI are indicated by crosses in Fig. 22. Although the swirling flow seems to have a significant influence on the overall flow character at these measurement planes the corresponding swirl parameters are all less than 5 percent, indicating a rather low swirl intensity.

Conclusions

The measurement results obtained for the new backswept impeller revealed a distinct vortex flow that considerably influenced the overall rotor flow character. Secondary flows and distorted throughflow patterns were caused by the swirling impeller flow inside the rotor. But toward the rotor exit the throughflow pattern was smoothed again resulting in a relatively regular discharge flow pattern that differed widely from the well-known jet/wake-type flow pattern. The swirling intensity of the main channel vortex estimated by the swirl parameter δ was found to be rather low. The swirl parameter δ derived for the backswept impeller was less than 5 percent. With regard to a general impeller design it should be noted that a vortex flow like that analyzed here will be present in any unshrouded impeller. Since the vortex flow seems to influence the throughflow pattern too, a slightly distorted impeller discharge flow seems to be inevitable unless the flow development is guided in such a way that the vortex flow fully disappears at the impeller discharge. How to reach this aim is not easy to derive from the results presented. Theoretical models capable of predicting the internal three-dimensional viscous flow of centrifugal compressor impellers could help to extract that information.

References

- 1 Dean, R. C., Jr., "The Fluid Dynamic Design of Advanced Centrifugal Compressors," Creare, TN-185, July 1974, p. 76.
- 2 Eckardt, D., "Detailed Flow Investigations Within a High-Speed Centrifugal Compressor Impeller," ASME *Journal of Fluids Engineering*, Vol. 98, 1976, pp. 390-402.
- 3 Krain, H., "A Study on Centrifugal Impeller and Diffuser Flow," ASME *JOURNAL OF ENGINEERING FOR POWER*, Vol. 103, No. 4, 1981, pp. 688-697.
- 4 Moore, J., and Moore, J. G., "Three-Dimensional Viscous Flow Calculation for Assessing the Thermodynamic Performance of Centrifugal Compressors: Study of the Eckardt Compressor," AGARD-CP-282, May 1980, pp. 9.1-9.19.
- 5 Bosman, C., "Computation of Three Dimensional Flow Through the Eckardt Compressor Impeller," AGARD-CP-282, May 1980, pp. 10.1-10.8.
- 6 Hamkins, C. P., and Flack, R. D., "Laser Velocimeter Measurements in Shrouded and Unshrouded Radial Flow Pump Impellers," ASME *JOURNAL OF TURBOMACHINERY*, Vol. 109, 1987, pp. 70-76.
- 7 Krain, H., "A CAD-Method for Centrifugal Compressor Impellers," ASME *JOURNAL OF ENGINEERING FOR GAS TURBINES AND POWER*, Vol. 106, 1984, pp. 482-488.
- 8 Krain, H., Schodl, R., Binder, A., and Dunker, R., "Successes in the Application of Laser Velocimetry to Turbomachinery Studies," Principal LS No. 1, Concepts ETI, Inc., 1986, pp. 5.1-5.22.
- 9 Neuberger, W., "Calculation of Compressible Swirling Flows in Pipes, Annuli and on Rotating Cylinders," DFVLR-FB 80-21, p. 107 (in German).
- 10 Binder, A., "Instationary Flow Effects in the Rotor of a Turbine," Thesis, University of Aachen, DFVLR-FB-85-66, p. 157 (in German).

Blade Excitation by Broad-Band Pressure Fluctuations in a Centrifugal Compressor

U. Haupt

Research Assistant.

M. Rautenberg

Professor.

Institute for Turbomachinery,
University of Hannover,
Hannover, Federal Republic of
Germany

A. N. Abdel-Hamid

Professor,
American University in Cairo,
Cairo, Egypt

The mechanism of blade excitation during the operation of a high-mass-flow, high-pressure-ratio centrifugal compressor has been investigated. This was carried out in the compressor operating range below 60 percent of design speed and in the zone of unsteady flow occurrence, where considerable blade vibration has been measured but no periodic unsteady pressure pattern such as rotating stall could be identified. Experiments conducted to study the mechanism of interactions between flow and blades were accomplished using several measuring methods simultaneously, such as measurements of blade vibration, flow angle at impeller inlet, unsteady pressure at different meridional and peripheral locations, as well as flow visualization by means of oil pattern. Analysis of the measurements showed typical broad-band characteristics of the unsteady pressure field and also for the blade vibration behavior. Results of flow angle investigations at the impeller inlet together with the analysis of oil pattern show that the broad-band pressure fluctuations and blade excitation can be attributed to a strong reverse flow near the suction side of the radial blade in the shroud zone. This reverse flow has its source downstream of the impeller and is extending back up to a location ahead of the impeller inlet. Similar results were obtained when the compressor was operated with vaneless and vaned diffuser configurations.

Introduction

In the design of modern high-mass-flow, high-pressure-ratio centrifugal compressors, stress and vibration characteristics have to be considered carefully in order to ensure high operational reliability. Dangerous dynamic stresses due to blade resonances can be avoided in many cases by means of the right choice of blade thickness values, if the compressor runs at constant rotational speed. Dynamic stress design becomes much more difficult if compressor operation is characterized by variable speed and part-load conditions.

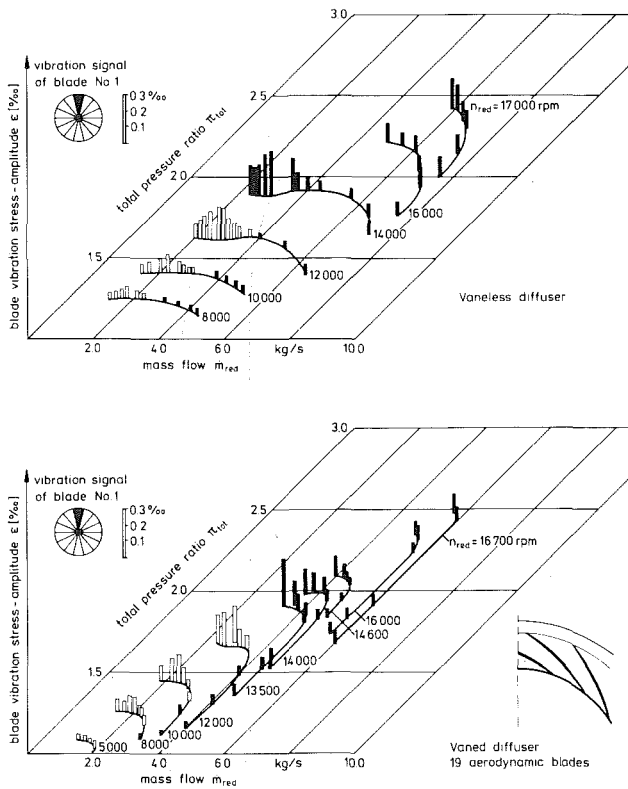
Because of the strong influence of the flow details on blade vibration, a better knowledge of the source of blade vibration can only be achieved by means of a detailed experimental investigation and analysis of the flow characteristics simultaneously with the blade vibration response. This approach has been adapted for axial flow turbomachines [1] for example, and is now being carried out for centrifugal machines [2-4].

Previous results of the present authors from measurements on a centrifugal compressor in [3] demonstrated the occurrence of significant and dangerous blade excitation during part-load compressor operation over a wide operating range before surge. At rotational speeds above 14,000 rpm detailed

measurements of unsteady flow in the compressor with a vaneless diffuser were carried out and results were published in [5], showing several superimposed rotating and nonrotating stall phenomena at a single operating point. It was demonstrated that the impeller blades are very sensitive to each of the different periodic excitations and interactions between flow and vibrating blade were clear. Understanding the sources of blade vibration at compressor speeds below 14,000 rpm was much more difficult because high levels of vibration existed at part-load operating conditions with no self-excited flow oscillations (Fig. 1).

Significant differences in the mechanism of blade excitation at compressor operation above and below 14,000 rpm as mentioned above are demonstrated by selected test results shown in Fig. 2. In addition to the first blade mode excitation the spectrum of the signal recorded at 16,000 rpm is dominated by different discrete frequencies representing an excitation due to rotating and nonrotating stall phenomena, while no discrete frequencies can be detected in the blade spectrum for 12,300 rpm. Similar results are shown in the pressure spectra for the two compressor speeds in Fig. 2. Because of the high level of blade mode excitation at low compressor speeds which cannot be related to deterministic pressure distributions, a systematic experimental investigation of the flow and vibration characteristics was carried out to identify its sources. The results presented in this paper clearly show the different flow regimes and operating conditions in which various vibration mechanisms dominate. Of particular interest is the existence

Contributed by the Gas Turbine Division of THE AMERICAN SOCIETY OF MECHANICAL ENGINEERS and presented at the 32nd International Gas Turbine Conference and Exhibit, Anaheim, California, May 31-June 4, 1987. Manuscript received at ASME Headquarters February 3, 1987. Paper No. 87-GT-17.



Blade excitation by known flow characteristics

Blade vibration due to unknown excitation source

Fig. 1 Results of blade vibration measurements at constant rotational speed on the compressor with vaneless and vanned diffuser; location of operating points with blade vibration of known and unknown excitation source

of a compressor operating range in which the pressure measurements show significant broad-band spectra in the frequency range containing a number of blade mode frequencies. The interaction between the blades and this random flow fluctuation resulted in high levels of excitation of the blade modes.

Compressor Test Facility

Blade vibration and flow measurements were carried out on a single-stage centrifugal compressor test rig operated with an open loop. The compressor is driven by a 1350 kW DC motor coupled to a gear box. The maximum values of compressor pressure ratio and mass flow were $\pi \approx 5$ and $\dot{m}_{red} \approx 10$ kg/s, respectively. Figure 3 shows a cross-sectional view of the compressor. The flow enters in the axial direction through a short suction pipe from a settling chamber and passes through the impeller and a long radial diffuser. Configurations of the diffuser may be changed to operate as a vaneless diffuser with

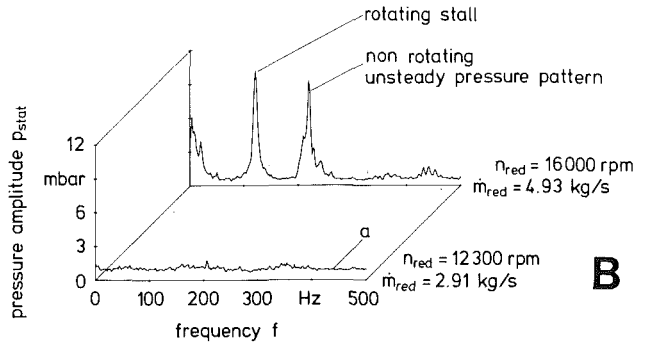
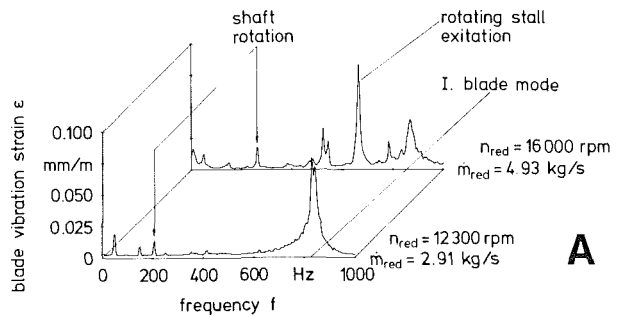


Fig. 2 Comparison of blade vibration and pressure spectra of signals recorded in the reduced mass flow regime of the test compressor operating with vaneless diffuser; actual speed values: 12,410 and 15,700 rpm. (A) Blade vibration characteristics during instability at different speeds; (B) corresponding flow characteristics at impeller inlet ($x/s = 0.2$)

constant radial flow area or as a vanned diffuser with 19 vanes. The flow downstream is collected in an annular collecting chamber and then leaves the compressor by the outlet tube which is tangential to the machine.

The unshrouded impeller of the test compressor used for this investigation is shown in Fig. 4. It has characteristic thin blades of about 1 mm thickness at the inlet tip and 4 mm at the outlet. The impeller has an outer diameter of 400 mm and 28 radial-ended blades with every second blade cut back at the inlet. The material is aluminum alloy.

Measurement and Analysis Systems

I Flow Measurements. Flow measurements were carried out by means of a number of high-frequency-response semiconductor pressure transducers to determine the time-dependent characteristics of unsteady flow. Twelve static wall pressure transducers were mounted in the compressor shroud and were simultaneously recorded with one selected blade vibration signal and the trigger on a 14-channel magnetic tape. A careful calibration of the transducers including the amplifier system had to be carried out before the test in order to enable a quantitative comparison of the different signals.

Nomenclature

D = diameter
 f = frequency
 h = radial distance from inducer inlet diameter
 \dot{m} = mass flow rate
 n = rotor speed
 p = pressure
 s = blade length at tip
 T = time period

w = relative flow velocity
 x = distance from inducer inlet at blade tip
 α = flow angle at impeller inlet versus axial direction
 ϵ = blade vibration strain
 φ = circumferential angle
 λ = diameter ratio = D/D_2
 π = pressure ratio

Subscripts

c = inlet plenum conditions
 red = reduced to reference conditions $T_c = 288.15$ K, $p_c = 1.01325$ bar
 rev = reverse direction
 $stat$ = static condition
 tot = stagnation condition
 1 = impeller inlet
 2 = impeller outlet

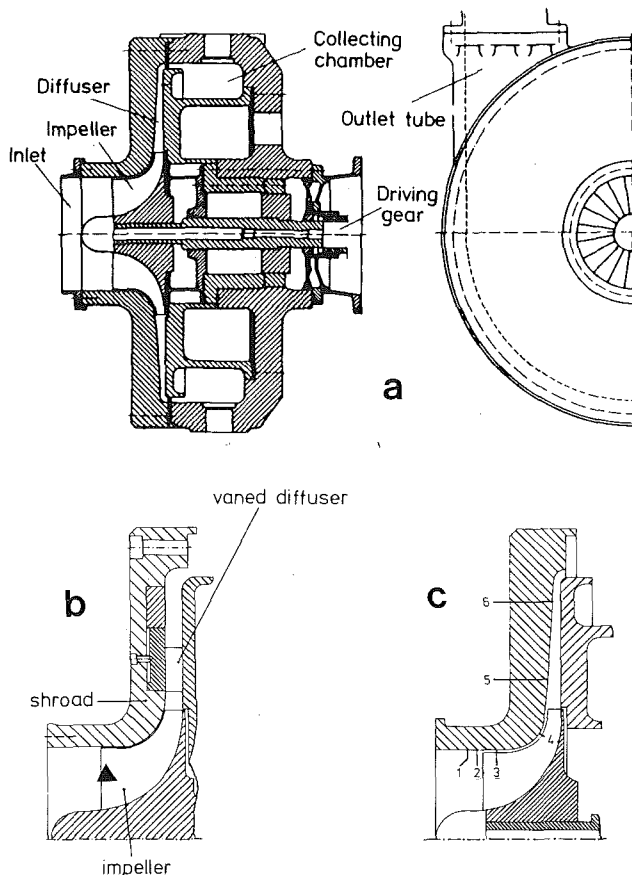


Fig. 3 Cross-sectional view of the test compressor with vaneless (a) and vaned diffuser (b); (c)=location of high-frequency-response pressure transducers; ▲ =location of strain gages on the blades; ① $x = -25$ mm; ② $x = -10$ mm; ③ $x/s = 0.2$; ④ $x/s = 0.8$; ⑤ $\lambda_D = 1.225$; ⑥ $\lambda_D = 1.825$

The locations of these high-frequency-response pressure transducers in the shroud wall were selected 10 and 25 mm upstream of the impeller inlet, in the impeller range at $x/s = 0.2$ and 0.8 with both positions on a line along the shape of the blade tip, and at $\lambda_D = D/D_2 = 1.23$ and 1.83 in the diffuser. These locations are shown in Fig. 3. x/s represents the distance from inducer inlet relative to the blade length measured at blade tip. Supplementary transducers were mounted in additional peripheral positions at $x = -10$ mm, $x/s = 0.8$, and $\lambda_D = 1.23$ in order to determine possible rotating stall characteristics. A schematic showing the positions of the various transducers is shown in Fig. 3.

Conventional pressure and temperature probes were used to determine the overall compressor performance. The circumferential uniformity of flow conditions in the compressor was measured by means of a large number of static pressure taps located on peripheral lines at 10 mm before impeller inlet, at $x/s = 0.8$, and in the diffuser at $\lambda_D = 1.83$. Measurements of the flow angle distribution at impeller inlet in order to determine the intensity and the radial extent of possible reverse flow were carried out using an adjustable cobra probe. An oil injection method to visualize flow reversal on the compressor shroud wall produced satisfactory results.

Conventional procedures were used in the analysis of stationary static pressure signals and results of flow angle measurements. Dynamic pressure signals recorded on the multichannel tape were analyzed using a Hewlett Packard 3582 A dual channel spectrum analyzer where data in the time and frequency domain were collected on a mass storage medium and then transmitted to a plotter. Typically 32 spectra

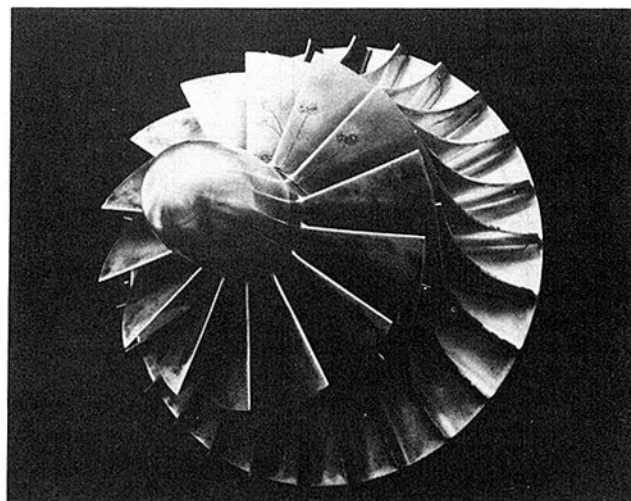


Fig. 4 Impeller used in the blade vibration and flow measurements with mounted 8-channel FM telemetry transmitter covered in the hollow impeller shaft

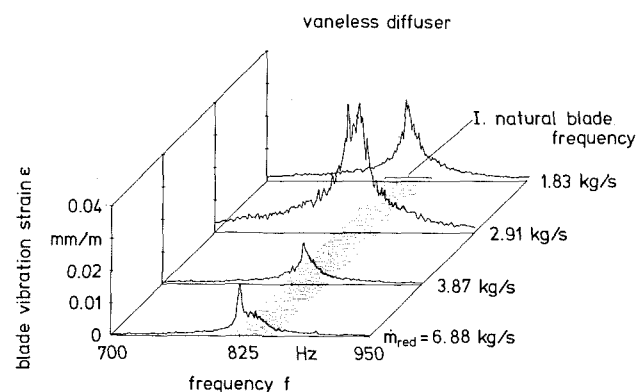


Fig. 5 Blade vibration spectra in the range of the first blade mode from signals recorded at different operating points at 12,300 rpm

were averaged and 250 spectral lines were used in the frequency range of interest.

II Blade Vibration Measurements. According to results in [5], blade vibration measurements are not only useful to determine the dynamic stress behavior of the blades; they also enable a very detailed distinction of unsteady flow characteristics where blades can be considered as a rotating probe. Blade vibrations were measured by means of semiconductor strain gages located in the zone of blade inlet. In fundamental calculations and tests [2, 3] these positions turned out to be the zones of maximum stresses for a vibration in modes I and II. These modes indeed were the main modes excited during unsteady flow compressor operation.

Strain gages from different blades with locations as shown in Fig. 3 were connected by thin wires to an 8-channel FM-telemetry transmitter mounted in the bore of the hollow shaft at impeller inlet. This transmitter is the rotating part of the telemetry system described in detail in [2]. The system, in addition, consists of an inductive power supply and the stationary receiver which accomplishes the reconversion process of high-frequency signals such as separation of channels, demodulation, filtering, and amplifying. Eight blade vibration signals transmitted by this system were recorded on a separate magnetic tape. One of these blade signals was selected for simultaneous recording with the different unsteady pressure signals on the 14-channel tape recorder used for collecting the pressure data. The same analysis procedure was used for blade and pressure data as described above.

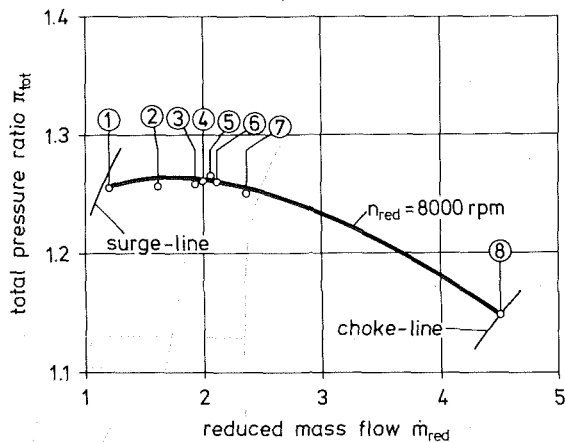


Fig. 6 Compressor operating points in the chart at constant rotational speed used for the investigation of broad-band blade excitation

Results and Discussions

I Fundamental Characteristics of Blade Excitation in the Zone of Unsteady Flow Below 1400 rpm. Significant differences in the characteristics of blade excitation at rotational speed of the compressor above and below 1400 rpm are shown in Fig. 2. A closer look at the blade vibration spectrum in the frequency range of the first blade mode at 12,300 rpm is shown in Fig. 5 for different mass flow rates. The zoomed spectra clearly show that the excitation is not of the discrete frequency type but rather broad in nature. For some reason the level of blade vibration increased significantly when the mass flow rate was decreased from 3.87 to 2.91 kg/s. Further reduction in the mass flow to 1.83 kg/s resulted in a reduction of the vibration level. The lower level of vibration at 3.87 kg/s indicates a blade reaction to normal pressure fluctuations commonly found in the flow.

The clear distinction between the character of the spectra shown in Fig. 5 and those resulting from blade interactions with deterministic pressure distributions whether stationary or rotating is the cornerstone for the interpretation of the results obtained in this investigation.

II Investigation of the Mechanism of Broad-Band Blade Excitation on the Compressor With Vaneless Diffuser. From the results in Figs. 1, 2, and 5 the question arises as to why broad-band excitation increases in a certain flow regime for each speed line and how to interpret this mechanism of blade excitation. To answer these questions fundamental measurements were carried out at a rotational speed of 8000 rpm at compressor operating points as shown in the chart in Fig. 6.

II.1 Extent of Static Pressure Nonuniformity. Results of an investigation concerning the peripheral static pressure distribution in some characteristic operating points at this speed are presented in Fig. 7 for conditions 10 mm before impeller inlet, at $x/s=0.8$ in the impeller range, and in the diffuser at $\lambda_D=1.83$. The strong influence of the tangentially positioned outlet tube is the reason for the pressure drop near 300 deg circumferential angle and only can be observed during compressor operation at high mass flow. Its influence decreases significantly in the upstream flow direction toward the impeller inlet zone. For operating points corresponding to lower mass flow rates this nonuniformity generally decreases and is mainly observed in the diffuser. Uniform peripheral characteristics were obtained before and in the impeller range.

II.2 Progression of Blade Vibration Spectra With Mass Flow Rate Reduction. Results of blade vibration

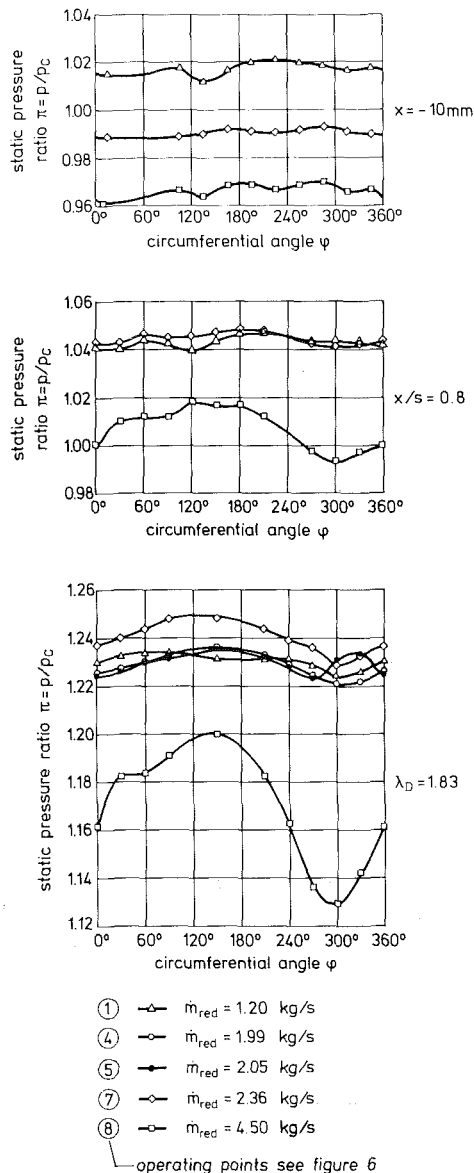


Fig. 7 Peripheral static pressure distributions at three different locations in the compression system at various mass flow rates; $n_{red} = 8000$ rpm

measurements are presented in Fig. 8 in spectra from signals recorded at different mass flow rates. Significant excitation of blade modes I and II can be observed in each spectrum of this diagram. At high mass flow rate ($\dot{m}_{red} = 4.5$ kg/s) the blade responds to the nonuniform static pressure distribution and significant discrete vibration components were found at shaft rotation frequency. At lower mass flow rates this amplitude decreases due to the more uniform pressure distribution resulting in a lower intensity of blade excitation. Throttling the valve from $\dot{m}_{red} = 2.36$ to 1.93 kg/s significantly increases the magnitude of the resonance amplitudes of blade modes I and II. The zoomed spectrum in Fig. 8 shows that this increase is not due to excitation by a multiple of shaft rotation frequency, which can be recognized usually as a sharp and discrete peak in the spectrum. Further reduction of the mass flow rate ($\dot{m} = 1.62$ kg/s) resulted in a substantial reduction in the vibration levels.

II.3 Progression of Unsteady Pressure Spectra With Mass Flow Rate Reduction. Unsteady pressure measurements

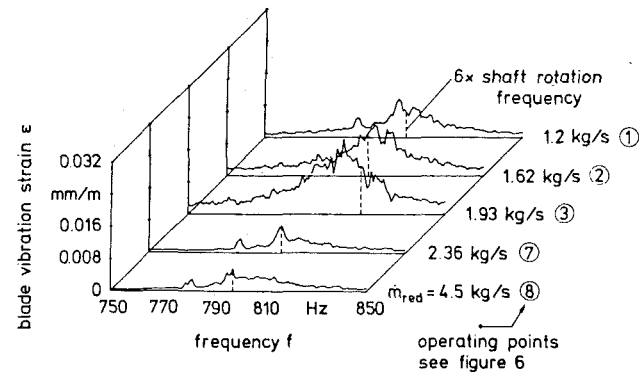
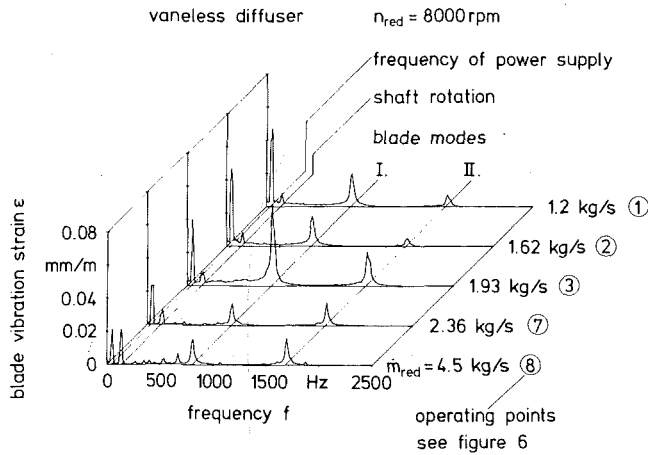


Fig. 8 Analysis of blade vibration measurements during compressor operation as indicated in Fig. 6

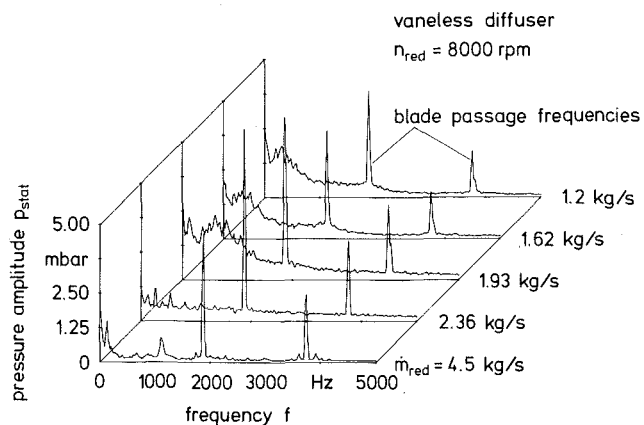


Fig. 9 Analysis of unsteady pressure data recorded by transducers near impeller inlet at $x/s = 0.2$ for various mass flow rates; operating points correspond to data in Fig. 8

were used to study the mechanism of blade excitation. Pressure spectra of signals recorded from transducers at $x/s = 0.2$ and at operating points to corresponding conditions in Fig. 8 are shown in Fig. 9. The change of the flow characteristics while throttling the compressor at 8000 rpm can be summarized as follows:

- No discrete frequencies can be observed in the spectra with the exception of the blade passage frequencies. There are no indications to the occurrence of periodic unsteady flow pattern such as rotating stall.

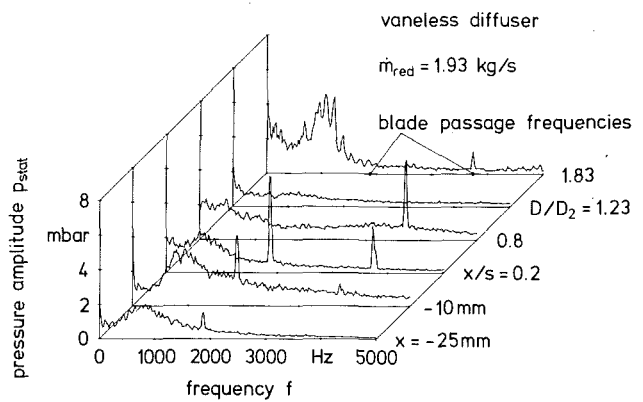


Fig. 10 Flow characteristics in different meridional locations along the flow path at 8000 rpm

- At mass flow rates less than 2.36 kg/s, the spectra show significant broad-band pressure fluctuations of considerable intensity in the frequency range below 2000 Hz.

- At compressor operating points near the surge line the maxima of these broad-band pressure frequency spectra shift to lower values of fluctuation frequencies. The corresponding value for the maximum in the spectrum of about 800 Hz for $\dot{m}_{red} = 1.93$ kg/s is $f_{max} \approx 200$ Hz for $\dot{m}_{red} = 1.2$ kg/s.

Pressure spectra from transducers of different meridional locations in the compressor from 25 mm before impeller inlet to a position $\lambda_D = 1.83$ in the diffuser are shown in Fig. 10, representing the analysis from signals recorded at 8000 rpm and $\dot{m}_{red} = 1.93$ kg/s. These data show increasing significance of broad-band pressure fluctuations from a location at 25 mm to 10 mm before impeller inlet. At further downstream locations in the impeller range the level of pressure fluctuations decreases with a shift in the peak of the broad-band component toward lower frequencies. In the diffuser significant pressure fluctuations exist at $\lambda_D = 1.83$ but not at $\lambda_D = 1.23$ and are not believed to be relevant to blade vibration.

II.4 Correlation Between the Pressure and Vibration Data. The pressure spectra shown in Fig. 9 and 10, representing the flow characteristics, together with the blade vibration behavior shown in Fig. 8, can be used to answer the question concerning the mechanism of blade excitation in this range of operating conditions. The shape of the pressure fluctuation spectrum at the operating point of $\dot{m}_{red} = 1.93$ kg/s in Fig. 9, with its maximum near 800 Hz, represents a strong excitation in the frequency range of blade mode I as observed in Fig. 8, and the blade response is correspondingly high. Pressure oscillations of lower intensity in the frequency band near 1700 Hz are the reason for a less significant mode II blade response ($f_{II} = 1.710$ Hz) in this figure. For compressor operation at still lower mass flow rates the shifting of the frequency maximum in Fig. 9 toward lower frequencies results in decreasing fluctuation amplitudes in blade mode I frequency range leading to lower values of blade vibration strain as shown in Fig. 8.

It should be mentioned that pressure fluctuations from transducers mounted in the shroud wall are signals in the fixed frame while blade vibration signals represent data measured in the relative rotating frame. The excitation frequencies in the rotating frame have to be shifted by $\pm f_s$. This change however is small compared to the bandwidth of the random fluctuations and it does not affect the basic conclusions described above.

II.5 Sources of Random Pressure Fluctuations. In view of the importance of the effects of broad-band pressure fluctuations on blade vibration, additional measurements were

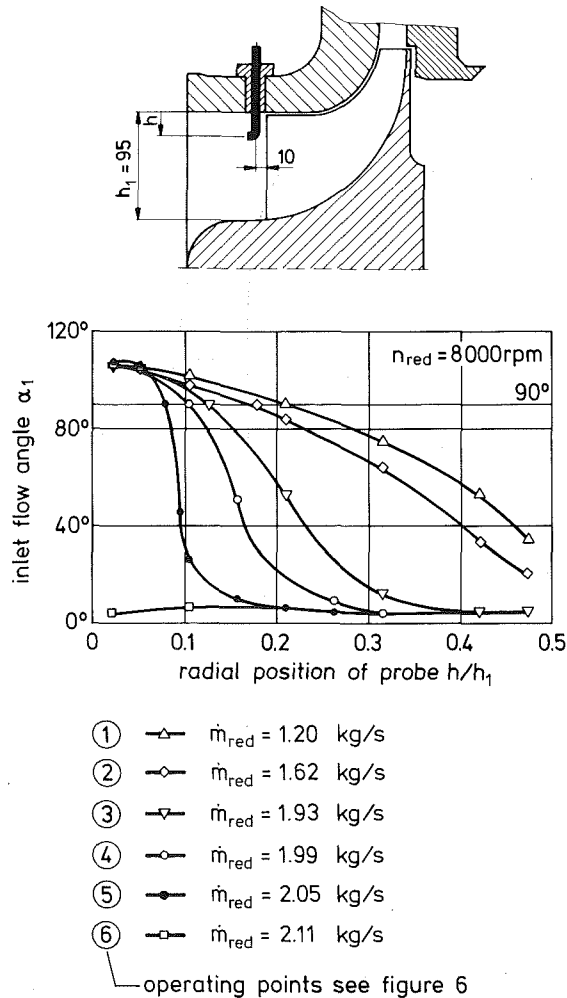


Fig. 11 Results of inlet flow angle measurements in the unsteady flow regime

carried out to investigate its sources. Flow angle measurements at impeller inlet were accomplished simultaneously with the flow and blade vibration measurements and the results are shown in Fig. 11. While axial directions of the flow can be obtained for operating points at 8000 rpm and $\dot{m}_{red} \geq 2.11 \text{ kg/s}$, a further reduction of mass flow results obviously in the occurrence of reverse flow near the outer diameter of the impeller inlet zone. The extent of this back flow range increases toward the hub for decreasing values of mass flow. These results also explain the slightly higher level of static pressure ratio, which could be obtained in the peripheral pressure measurements at a location 10 mm before inlet and $\dot{m}_{red} = 1.20 \text{ kg/s}$ in Fig. 7. Local reverse flow in the impeller inlet zone of a centrifugal compressor has been reported in [7, 8], while indications of local back flow phenomena at the impeller outlet were given in [10] with results obtained by means of LDA measurements.

According to results in Fig. 11, and since dynamic pressure transducers used in this investigations were mounted in the shroud wall immediately next to the location of the observed reverse flow zone, it can be concluded that dynamic pressure data shown in Fig. 9 and 10 are due to the occurrence of this reverse flow which in turn causes high levels of blade excitation.

Previous measurements concerning the same problem led to the supposition that material entering the impeller near the hub changed its flow direction in the inducer part and left the impeller in the reversed direction near the blade tip region.

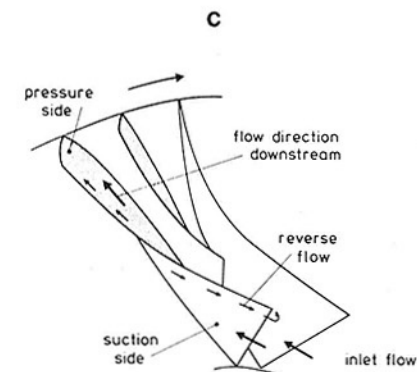
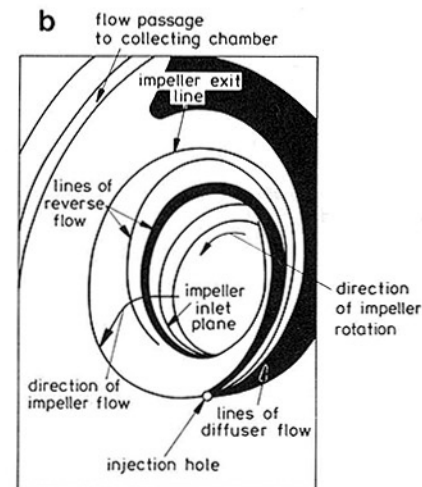
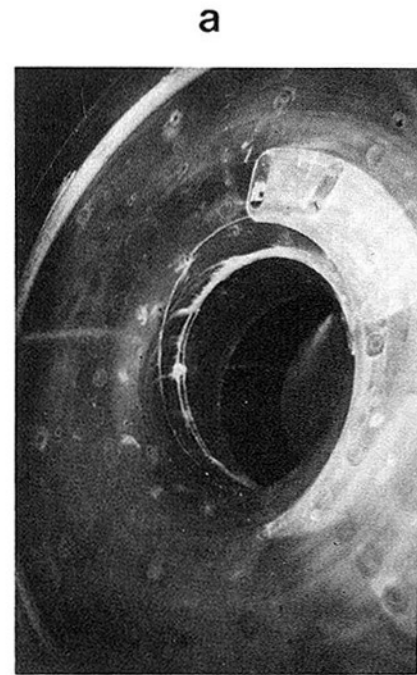


Fig. 12 Results of an oil injection test at an operating point at 14,000 rpm close to the surge line and of significant broad-band pressure fluctuation characteristics: (a) photo showing the compressor shroud wall from inside after disassembly; (b) schematic of flow characteristics according to (a); (c) schematic of impeller flow characteristics

Results of measurements on the same compressor [7] showed relatively high values of reverse flow temperatures in the impeller inlet zone, which could also be observed in the investigations described here. This was considered as an indication that

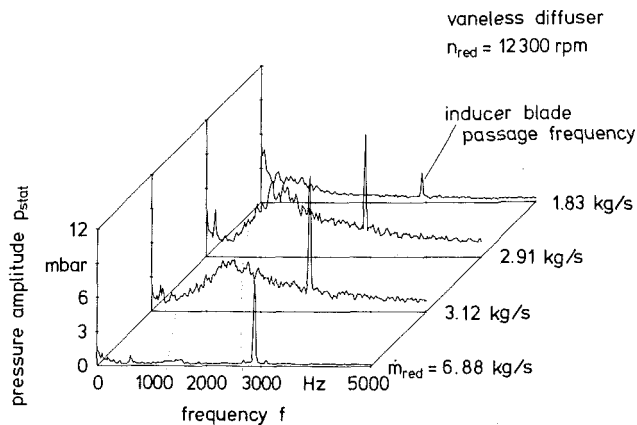


Fig. 13 Analysis of unsteady pressure data recorded by transducers located 10 mm before the impeller inlet for various mass flow rates

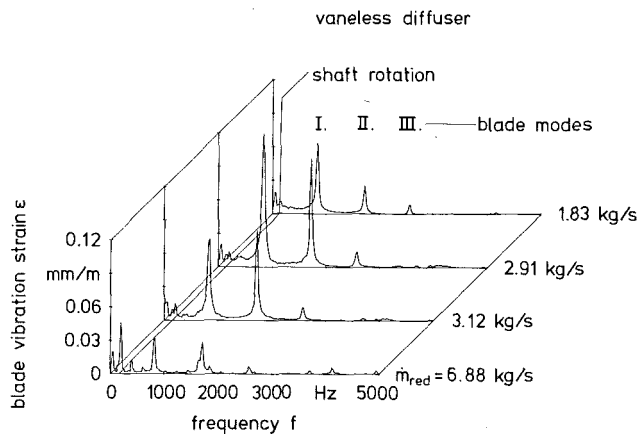


Fig. 14 Blade response to broad-band pressure fluctuations shown in Fig. 13

the origin of the reverse flow would be further downstream in the compression system.

II.6 Flow Visualization of the Reverse Flow. An additional test procedure was performed on the compressor to get further insight into the mechanism of the described reverse flow phenomenon as the cause for blade excitation in this operating range. Oil has been injected through a hole in the shroud wall entering the flow from a position near the impeller outlet. The compressor was operated for this fundamental test immediately before surge at the same corrected aerodynamic conditions as shown in Figs. 8–11 but at a higher rotational speed. After injection the compressor was stopped and upon disassembly the oil traces on the shroud wall were inspected carefully. A similar oil injection method has already been used in [9] to show basically the phenomenon of reverse flow in the impeller range.

The results of the tests are shown in Fig. 12. They can be described as follows:

- The main part of the flow particles which pass the injection hole during impeller rotation is moving on its way downstream on an outward-directed spiral curve to the collecting chamber, as can be recognized from the oil traces.
- One part of the flow particles passing the injection hole is moving in the reverse compressor flow direction also on a spiral curve upstream and reaches a zone before the impeller inlet where it probably mixes with the inlet flow and moves again in the downstream flow direction.
- The reverse flow line is sharp and strongly defined. This indicates a very stable reverse flow section at the impeller outlet, which is expected to be located at the blade suction side. Moreover, the clear line of reverse flow indicates the occurrence of the same characteristics of back flow in each channel of the impeller concerning its location and velocity. In addition the velocity of this reverse flow was analyzed considering the angle of the spiral trace from impeller outlet to inlet, the length s of the blade at the tip, and the time T_s of impeller rotation. This velocity turned out to be $w_{rev} \approx 54$ m/s.
- An additional test demonstrated that the oil injected farther upstream of the impeller range was mainly directed toward the upstream direction. It can be recognized that in this location the reverse flow extends nearly over the whole channel from suction to pressure side near the shroud wall while the reverse flow zone is much smaller at impeller outlet according to results in Fig. 12.

It is believed therefore that the broad-band pressure fluctuations shown in the frequency spectra in Figs. 9 and 10 are the result of a reversed flow near the shroud wall from the impeller outlet to the inlet. This seems to be the reason that the

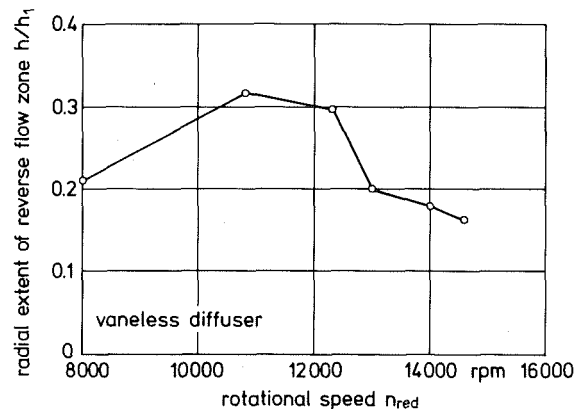


Fig. 15 Results of analysis of inlet flow angle measurements at operating points immediately before surge showing the extent of the reverse flow zone near the inlet tube wall for various rotational compressor speeds

spectra of pressure signals in Fig. 10 recorded from transducers of different meridional locations show decreasing significance of the broad-band nature of the signals toward the impeller outlet location due to increasing influence on the downstream-directed flow in each channel.

The shift of the broad-band pressure spectra toward lower frequencies with reduction in mass flow can be explained through the use of the results shown in Fig. 11. The increase in the radial extent of the reverse flow zone near the wall at lower values of mass flow means an increase in the characteristic length of the flow fluctuations and hence a reduction in the peak frequency of the spectrum.

Since reverse flow could be determined as the cause for the blade excitation mentioned above identifying it as a forced response problem, other possible excitation reasons, such as flutter, can be excluded. It should be mentioned that an occurrence of blade flutter has never been reported on centrifugal impeller blades due to their specific geometry of higher stiffness compared to axial compressor blades.

III Investigation of Broad Band Blade Excitation on the Compressor With Vaneless Diffuser at Higher Rotational Speed

III.1 Flow and Blade Vibration Measurements. Measurements similar to those described above were carried out at higher rotational speed. Frequency spectra of signals from fast-response pressure transducers located 10 mm upstream of the impeller inlet are shown in Fig. 13 for various mass flow rates at 12,300 rpm compressor speed. Similar to results in Fig. 9 broad-band pressure fluctuations—recognized

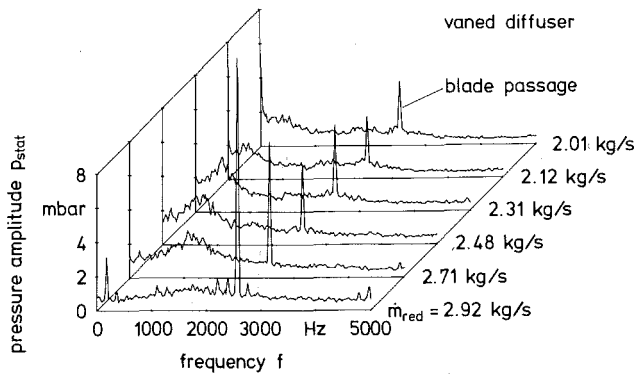


Fig. 16 Analysis of unsteady pressure data recorded on the compressor with vaned diffuser at 10,800 rpm near the inlet at $x/s = 0.1$ for various mass flow rates

as the characteristics of a reverse flow—are obtained at lower flow rates and a distinction between steady and unsteady flow is possible due to this significant characteristic. The shifting of the range of maximum pressure oscillation amplitude to lower frequencies—as could be observed in Fig. 9—also can be recognized for decreasing mass flow rates in this diagram.

Interesting results were obtained for the blade response data for the corresponding compressor operating points in Fig. 14. Significant blade excitation due to the nonuniform peripheral pressure distribution can be seen again in the spectrum of the high mass flow signal. This amplitude decreases similar to conditions in Fig. 8 when the mass flow is reduced and a more uniform peripheral flow distribution is achieved. In the spectrum of the blade vibration signal for $\dot{m}_{red} = 3.12$ kg/s broad-band blade response of considerable amplitude is obtained. In this result the amplitude for blade mode II is higher than mode I. This is due to the location of the frequency covered by the broad-band component of the spectrum. Blade excitation near $f_{II} = 1710$ Hz is stronger than near $f_I = 800$ Hz for this mass flow rate. Again the difference between the absolute and relative frame frequencies has to be taken into account. For compressor operation at still lower values of mass flow the oscillation maximum is shifting in a blade response where the mode I excitation becomes more and more dominant compared to the mode II vibration.

III.2 Flow Angle Measurements. Measurements of inlet flow angle distribution before the impeller inlet have been carried out during compressor operation immediately before surge. From these results the extent of the reverse flow zone near the wall could be determined and was plotted in Fig. 15. According to these data the area of this zone is increasing up to compressor operation at 10,800 rpm and then decreases to lower values at higher speed. These results give an indication that at rotational compressor speeds below 12,000 rpm the stable operating range seems to be slightly larger than that for conditions at higher speed values.

IV. Investigation of the Mechanism of Broad-Band Blade Excitation on the Compressor With Vaned Diffuser. Measurements similar to those described above were carried out on the same compressor after the installation of a vaned radial diffuser to investigate the changes in the characteristics of broad-band excitation or reverse flow with different geometric conditions in the diffuser flow.

Flow characteristics of high-performance centrifugal compressors with vaned diffusers have been previously investigated [11]. Unsteady flow behavior on the same compressor with the diffuser type used in this investigation has been published in [12]. Results show the occurrence of a two-lobe pattern rotating stall for compressor speed above 14,000

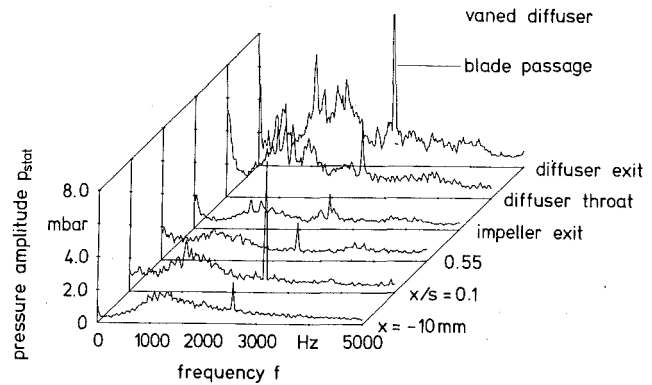


Fig. 17 Analysis of unsteady pressure data recorded at compressor operation at 10,800 rpm and $\dot{m}_{red} = 2.71$ kg/s; flow characteristics at different meridional locations along the flow path

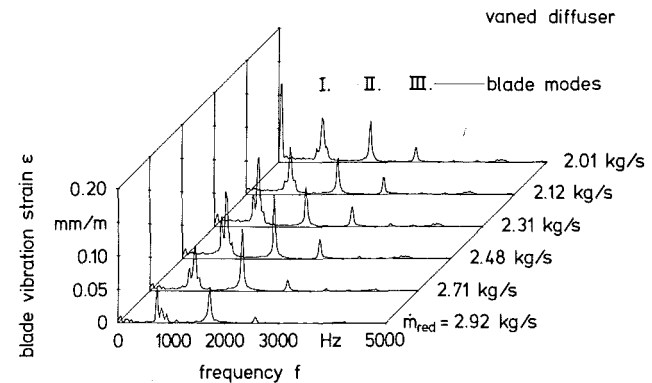


Fig. 18 Blade vibration response to broad-band pressure excitation shown in Fig. 16 at corresponding operating points; $n_{red} = 10,800$ rpm

rpm, while a three-cell rotating stall could be determined at compressor operation in the range of 12,300–13,000 rpm. Both patterns were rotating in the direction against the impeller. At a still lower compressor speed of 10,800 rpm no periodic unsteady flow phenomena could be obtained from the analysis of unsteady pressure signals. According to Fig. 16 broad-band characteristics can be recognized in the spectra for compressor operation at different mass flows in the unsteady flow regime. Shifting of the maximum of the pressure fluctuation frequency distribution to lower frequencies as an indication to a growing reverse flow area versus lower mass flow rates can clearly be recognized in this diagram. Results obtained here are very similar to those obtained with the vaneless diffuser in Fig. 9 and 13. Even results from transducers along the flow path as shown in Fig. 17 and according to this diagram even in the diffuser throat and exit show very good similarity to conditions with the vaneless diffuser. Blade response to reverse flow characteristics as shown in Figs. 16 and 17 is presented in Fig. 18 for corresponding operating points as shown in the diagram in Fig. 16. Very little difference in blade response characteristics to broad-band flow fluctuations was obtained for vaneless and vaned diffusers. The spectra in Fig. 18 demonstrate again a dominant excitation of blade mode II at 2.71 kg/s. Vibration characteristics change for compressor operation at 2.31 kg/s, where the spectra show more significant excitation of the first blade mode. This is due to the displacement of the flow fluctuation maximum versus lower frequencies shown in Fig. 16. The same reason has to be mentioned for the decreasing blade vibration amplitudes at still lower mass flow rates.

Conclusions

- Broad-band pressure fluctuations were determined as the

cause for strong blade vibration in unsteady flow regimes below 14,000 rpm.

- Compressor operation in unsteady flow regimes was characterized by the existence of a reverse flow zone near the wall at the impeller inlet. The radial extent of this zone increases toward lower mass flow rates.
- Broad-band pressure fluctuations were correlated with the occurrence of a reverse flow close to the shroud wall from impeller outlet to inlet.
- Maxima of broad-band pressure fluctuation amplitudes in the spectra shift to lower frequencies if mass flow is reduced due to the increasing reverse flow area in the impeller channel.
- A clear relationship between the cause of blade excitation and response could be demonstrated. Dominant blade mode II excitation was obtained at higher mass flow operation due to broad-band pressure fluctuations in this frequency range. If mass flow is reduced the pressure oscillation frequency decreases and consequently blade vibration in a lower mode (I) can be observed. Further reduction of mass flow leads to a decrease of total vibration amplitude due to the increasing difference between blade and pressure fluctuation frequency.
- For compressor speed above 10,800 rpm flow characteristics immediately before surge show a decreasing extent of the impeller inlet reverse flow zone. This means a slightly larger compressor operating range below 10,800 rpm.
- Similarity of the results for operating conditions with vaneless and vaned diffuser show that reverse flow, which is a significant source of blade excitation, can be considered as a typical phenomenon of the impeller.

Acknowledgments

The research described in this paper was funded by the German Research Association (DFG). The authors are thankful for this support.

The advice of Dr. Y. Chen of Fa. Gebr. Sulzer AG, Winter-

thur, in discussions concerning the mechanism of reverse flow is gratefully acknowledged. The authors thank Dipl.-Ing. U. Seidel for his contribution when running the tests, accomplishing data analysis, and assisting in finishing the paper, as well as Mr. Tanneberg for his assistance in the experiments.

References

- 1 Ishihara, K., and Funakawa, M., "Experimental Investigations on the Vibration of Blades Due to a Rotating Stall," *Bulletin of the JSME*, Vol. 23, No. 177, 1980.
- 2 Bammert, K., Mobarak, A., and Rautenberg, M., "Unsteady Flow Measurements in Centrifugal Compressors," *Atomkernenergie (ATKE)*, Vol. 27, 1976, pp. 217-228.
- 3 Haupt, U., Bammert, K., and Rautenberg, M., "Blade Vibration on Centrifugal Compressors—Fundamental Considerations and Initial Measurements," ASME Paper No. 85-GT-92, 1985.
- 4 Haupt, U., Bammert, K., and Rautenberg, M., "Blade Vibration on Centrifugal Compressors—Blade Response to Different Excitation Conditions," ASME Paper No. 85-GT-93, 1985.
- 5 Haupt, U., Abdel-Hamid, A. N., Kaemmer, N., and Rautenberg, M., "Excitation of Blade Vibration by Flow Instability in Centrifugal Compressors," ASME Paper No. 86-GT-283, 1986.
- 6 Mizuki, S., Kawashima, Y., and Ariga, I., "Investigation Concerning Rotating Stall and Surge Phenomena Within Centrifugal Compressor Channels," ASME Paper No. 78-GT-9, 1978.
- 7 Kaemmer, N., and Rautenberg, M., "A Distinction Between Different Types of Stall in a Centrifugal Compressor Stage," *ASME Journal of Engineering for Gas Turbines and Power*, Vol. 108, 1986, pp. 83-92.
- 8 Mizuki, S., et al., "Reversed Flow Phenomena Within Centrifugal Compressor Channels at Lower Flow Rate," ASME Paper No. 76-GT-86, 1976.
- 9 Benser, W. A., and Moses, J. J., "An Investigation of Back Flow Phenomenon in Centrifugal Compressors," NACA Annual Report No. 806, 1945.
- 10 Sideris, M. Th., and Van den Braembussche, R. A., "Influence of a Circumferential Exit Pressure Distortion on the Flow in an Impeller and Diffuser," *ASME JOURNAL OF TURBOMACHINERY*, Vol. 109, 1987, pp. 48-54.
- 11 Sovrano, R., and Avram, P., "Experimental Investigation of the Near-Surge Flow in a High Performance Centrifugal Compressor," *Publication de l'ONERA*, T. P. No. 1976-2, 1976.
- 12 Abdel-Hamid, A. N., Haupt, U., and Rautenberg, M., "Unsteady Flow Characteristics in a Centrifugal Compressor With Vaned Diffuser," ASME Paper No. 87-GT-142, 1987.

The Measurement of Boundary Layers on a Compressor Blade in Cascade: Part 2—Suction Surface Boundary Layers

S. Deutsch

W. C. Zierke

The Applied Research Laboratory,
The Pennsylvania State University,
State College, PA 16804

Using the facility described in Part 1 [29], eleven detailed velocity and turbulence intensity profiles are obtained on the suction surface of a double circular arc blade in cascade. At the measured incidence angle of 5 deg, transition through a leading edge separation bubble occurs before 2.6 percent chord. A continuing recovery from this leading edge separation is apparent in the measured boundary layer profiles at 2.6 and 7.6 percent chord. Recovery appears to be complete by 12.7 percent chord. The data then illustrate the evolution of the nonequilibrium turbulent boundary layers as they approach a second region of separation. Following the criteria established by Simpson et al. [1], we find that intermittent separation occurs near 60 percent chord while detachment occurs at 84.2 percent chord. Comparison between the measured profiles and the sublimation visualization studies indicates that the flow visualization is signaling the location of incipient detachment (1 percent instantaneous backflow). Measured profiles are also considered in light of similarity techniques for boundary layers approaching separation. Outer region similarity is shown to vanish for profiles downstream of detachment.

Introduction

Over the past two decades, techniques for computing complex flows have become increasingly more sophisticated. It is desirable that these techniques find their way into the turbomachinery design process. These numerical techniques are capable of very detailed predictions, but to be used with confidence, they should be tested against very detailed experimental data under typical flow conditions. As turbomachinery testing has generally been concerned with overall turbomachinery performance rather than with the details of the flow field, such data are lacking.

In order to provide some of the needed data, we used a one-component laser-Doppler velocimeter (LDV) to measure the two-dimensional, periodic flow field about a double circular arc, compressor blade in cascade. Eleven boundary layer profiles were taken on both the pressure and suction surfaces of the blade; two profiles were taken in the near wake. All measurements were made at a chord Reynolds number (Re_c) of 500,000 (± 1 percent) and an incidence angle of 5 deg (that is, the stagnation point is on the pressure surface). The turbulence intensity in the incident flow was 0.18 percent. With an incidence angle of 5 deg, the pressure surface exhibits a large region of laminar flow (up to roughly 60 percent chord);

transition on the pressure surface appears to be incomplete. The suction surface profiles appear to separate both at the leading edge and again somewhat beyond midchord; the leading edge separation apparently reattaches by 2.6 percent chord. Using the terminology of Simpson et al. [1], we found incipient detachment to occur at 60 percent chord on the suction surface and transitory detachment to occur at 83 percent chord. Inlet and outlet five-hole probe measurements and blade static-pressure measurements supplement the blade boundary layer profiles. Surface flow visualization, through sublimation, complements the transition and separation region data.

In Part 1 of this study [29] we described the cascade facility and the two-dimensional, periodic flow field established in the facility. The requirement of laser access to the blade pack made the cascade facility somewhat unique. In this, Part 2 of the study, we describe the LDV system and document the suction surface flow field. Particular attention is paid to the large separated region past midchord. Part 3 of the study will present the pressure surface flow field and the near wake.

Laser-Doppler Velocimeter

All blade boundary layer and near-wake measurements were made using a single-component LDV. For all the LDV measurements, a specially designed traversing mechanism was used that matched the arc of motion of an optics cradle to that of the blade curvature (two arcs were employed, one for

Contributed by the Gas Turbine Division of THE AMERICAN SOCIETY OF MECHANICAL ENGINEERS and presented at the 32nd International Gas Turbine Conference and Exhibit, Anaheim, California, May 31–June 4, 1987. Manuscript received at ASME Headquarters February 24, 1987. Paper No. 87-GT-249.

each of the pressure and suction surfaces). All measurements were made in the plane of the local blade normal. Translation of the optics cradle normal to the blade could be accomplished in step intervals as small as 0.0254 mm. Prior to the LDV measurements, a reference distance was established by focusing the LDV control volume on an insert that fit securely over the center measuring blade. Narrow lines had been etched on the insert (on arcs matching the blade curvature) to be known distances from the blade surface. Repeatability in establishing a measurement reference was estimated to be ± 0.05 mm, and this uncertainty is probably the major source of scatter in the velocity data.

A two-watt, Spectra-Physics, argon-ion laser was used for the measurements. Power on the blue line (488 nm wavelength) ranged between 0.5 W and 0.7 W on a day-to-day basis. Standard TSI backscatter optical components were used; the 371.3 mm focusing lens was chosen to allow the measurements to be made at the blade midspan. The ellipsoidal measurement volume was reduced through the use of a (2.71:1) beam expander; the predicted measurement length in the direction normal to the blade was $37 \mu\text{m}$. While this length was small when compared to the length scales of the turbulent boundary layers on the suction surface, we shall show in Part 3 that it is roughly half the size of the displacement thickness of the initial laminar profile on the pressure surface. Where appropriate, optical shifting at 5 MHz was employed. Note that to measure close to the blade surface the optical cradle was tilted at an angle of roughly 1 deg. Silicon carbide particles having a mean diameter of $1.5 \mu\text{m}$ were used for laser seeding. In an attempt to maintain a uniform distribution, we injected the silicon carbide particles well upstream of the measurement station. The particles were suspended in a "cloud chamber," which was constructed for this study, and were injected into the tunnel by a small overpressure. Gain, on the counter-processor, was kept low, and particle counts averaged only 20 or so particles per second (as we will discuss,

however, the velocity probability distributions were remarkably clean).

LDV data acquisition and reduction was accomplished by using a direct link to a VAX 11/782 computer. Software allowed selection of the focusing lens half angle, the laser wavelength, the frequency shift, the minimum number of cycles employed in the calculation (eight here), and the number of particle counts per run. Initial output was in the form of a velocity histogram. Minimum and maximum velocity limits could be set by two cursors to eliminate obvious noise from the distribution. Final output was mean velocity, local turbulence intensity, and the percent of particle counts employed in the calculations. For some of the profiles measured, the skewness and kurtosis of the distribution were also calculated. The percentage of particle counts employed in the calculation may be used as an indicator of signal-to-noise ratio. At least 98 percent of the total particle counts were used for measurement stations in the boundary layer; at least 95 percent were employed for points in the free stream (the difference in percentages reflects the fact that fewer overall points were used at the free-stream locations).

For a counter-processor, employed in a highly turbulent flow, the calculation of mean velocity and turbulence intensity may not be straightforward. McLaughlin and Tiederman [2], Hoessel and Rodi [3], Giel and Barnett [4], Edwards [5], Edwards and Jensen [6], Johnson et al. [7], and Stevenson et al. [8] have all discussed the question of velocity bias in a highly turbulent flow. As pointed out first in [2], the problem arises because more high-speed particles than low-speed particles arrive in the measurement volume during a given measurement interval. A related problem, termed incomplete signal bias in [8], can be eliminated by employing a sufficiently high frequency shift.

McLaughlin and Tiederman [2] describe a correction for the phenomenon (with uniform seeding), but it requires complete velocity vector information. A more practical one-

Nomenclature

B = integral layer thickness in the Perry-Schofield theory	u = streamwise velocity	
c = blade chord length	u' = root-mean-square value of the turbulent velocity fluctuation	
C = law of the wall constant = 5.0	u^+ = dimensionless velocity in the inner boundary layer = u/u_τ	δ = boundary layer thickness (where $u = 0.99 U_e$)
C_f = skin friction coefficient = $\tau_w/(\rho U_e^2/2)$	u_τ = shear or friction velocity = $\sqrt{\tau_w/\rho}$	δ^* = displacement thickness = $\int_0^\infty (1 - u/U_e) dy$
C_p = static pressure coefficient = $(p - p_1)/(\rho V_1^2/2)$	U_{BF} = maximum backflow velocity	δ_{BF} = depth of backflow
H_{12} = first shape factor = δ^*/θ	U_e = velocity at the boundary layer or wake edge	θ = momentum thickness = $\int_0^\infty (u/U_e) (1 - u/U_e) dy$
ID = incipient detachment	U_m = velocity scale based on the maximum shear stress = $\sqrt{\tau_{\max}/\rho}$	κ = von Karman's mixing length parameter = 0.41
ITD = intermittent transitory detachment	U_s = velocity scale for the Perry-Schofield defect law	ν = kinematic viscosity (0.150 cm^2/s for air)
L = distance from the surface to the location of τ_{\max}	V = velocity	Π = Coles' wake parameter
LE = leading edge	$W(\cdot)$ = Coles' universal wake function = $2 \sin^2(\cdot) = 1 - \cos(\cdot)$	ρ = fluid density (1.205 kg/m^3 for air)
LDV = laser-Doppler velocimeter	x = streamwise coordinate	τ_{\max} = maximum shear stress
n = data point index	y = coordinate normal to the blade surface or across the wake	τ_w = wall or surface shear stress
N = number of data points	y^+ = dimensionless coordinate normal to the blade surface in the inner boundary layer = yu_τ/ν	
p = static pressure		
R_c = radius of curvature		
Re_c = blade chord Reynolds number = cV_1/ν		
Re_θ = momentum thickness Reynolds number = $\theta U_e/\nu$		
S_{FV} = location of separation from flow visualization tests		
TD = transitory detachment		
TE = trailing edge		

Subscripts

inv = inviscid
meas = measured
n = data point index
1 = inlet (upstream five-hole probe measurement station)
2 = outlet (downstream five-hole probe measurement station)

dimensional correction is also given, but this correction tends to overestimate the error for local turbulence intensities >20 percent. Edwards [5] shows that the biasing error can be made negligibly small for the case of a saturated data handling system (taking data at a fixed rate set by the slowest component of the system) by taking the particle density equal to the seeding rate (this assumes a validation circuit for the system). Stevenson et al. [8] used equal time interval sampling in a very highly seeded mixing layer as a bias-free test case. As pointed out by Edwards and Jensen [6], very high seeding rates may open the door to other types of errors, for example, by reducing the actual number of statistically independent samples used to form the velocity statistics. Moreover, a very high seed rate may be difficult to achieve in precisely those regions in which the bias is expected to be high. Often, in fact, a counterprocessor is chosen over a tracker processor because of its ability to act at very low seeding rates.

The bias question is obviously quite complex, and a consensus opinion on how to correct data is still lacking. Some issues, such as nonuniform particle seeding, of interest particularly in air flows, have not yet been the subject of detailed studies (see [3], for instance). Giel and Barnett [4] conducted an experiment favorable to obtaining statistical bias, but no consistent bias was evident, thus further obscuring the bias question. In the current study, we employed simple arithmetic averaging. For many of the boundary layers measured, we monitored the skewness with the idea that a change of shape from the classical distribution in the boundary layer might signal significant velocity bias. No such deviations were observed. We note that both McLaughlin and Tiederman [2] and Johnson et al. [7] show that the overestimate of the mean velocity goes roughly quadratically with turbulence intensity, being 5 percent for a local turbulence intensity near 20 percent, and being 12 percent for a local turbulence intensity near 35 percent.¹ These numbers should be borne in mind not only when evaluating the data presented here, but also when evaluating any measurements made in highly turbulent flows. The mean velocity here was taken as

$$u = \frac{1}{N} \sum_{n=1}^N u_n$$

the local turbulence intensity was taken as

$$\frac{u'}{u} = \frac{1}{u} \left[\frac{1}{N} \sum_{n=1}^N (u_n - u)^2 \right]^{1/2}$$

and the turbulence intensity was taken as u'/U_e .

Experience has shown that quite satisfactory repeatability of the mean velocity and turbulence intensity can be guaranteed in boundary layer flows by using 1000 particle counts in regions in which the local turbulence intensity exceeds 5 percent. In regions of local turbulence intensity of less than 5 percent but more than 2 percent, 500 points are used, while 200 points are used in regions of less than 2 percent. At each chord position, profiles were defined by statistically treating the data for six individual experiments. Six experiments were chosen as the statistics found from six experiments showed less than 1 percent scatter in the free-stream data. Error bands, presented on the LDV data plots, represent 95 percent confidence levels as determined by a Student's t test.

The preliminary data analysis is automated on the VAX 11/782 computer. The effect of the normal pressure gradient

¹It is not obvious that turbulence intensity is the only relevant variable. For example, the values of the higher moments of the velocity probability distribution are no doubt also of importance.

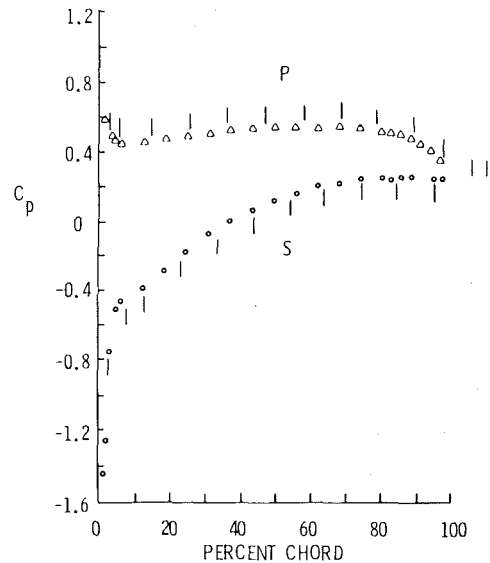


Fig. 1 Blade static-pressure distribution (the vertical line segments represent the locations of LDV measurements: P is the pressure surface; S is the suction surface)

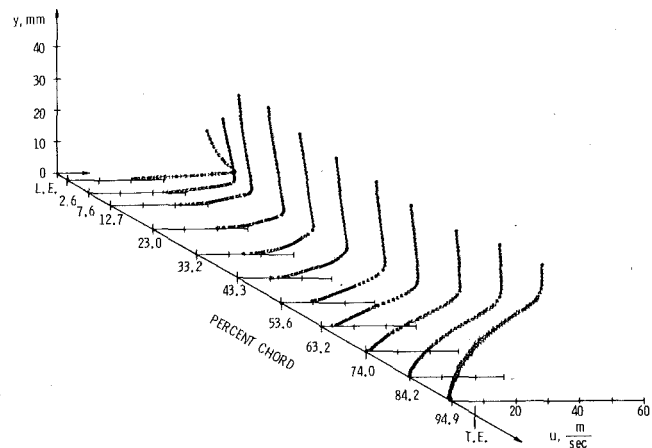


Fig. 2 Measured suction surface boundary layers

on the boundary layer profiles is accounted for first. Details of the technique are given by Zierke and Deutsch [9] and basically follow the approach suggested by Mellor and Wood [10] and Ball et al. [11]. Briefly the technique assumes that the profile may be represented as

$$u = u_{\text{meas}} - u_{\text{inv}} + U_e$$

so that the edge velocity U_e can be determined by extrapolating the outer inviscid flow u_{inv} to the wall (where $u = u_{\text{meas}} = 0$) in some reasonable manner. The method is not rigorous in its definition of the inviscid region, and hence in the manner of extrapolation. Our own experience with the 22 boundary layers measured here, however, is that the edge velocity is quite insensitive to any reasonable choice of the inviscid region.

Suction Surface Boundary Layers

Suction surface boundary layers were taken at 11 chordwise locations on the center blade. Figure 1 shows these chordwise locations as well as the static-pressure distribution. A very large adverse pressure gradient exists near the leading edge.

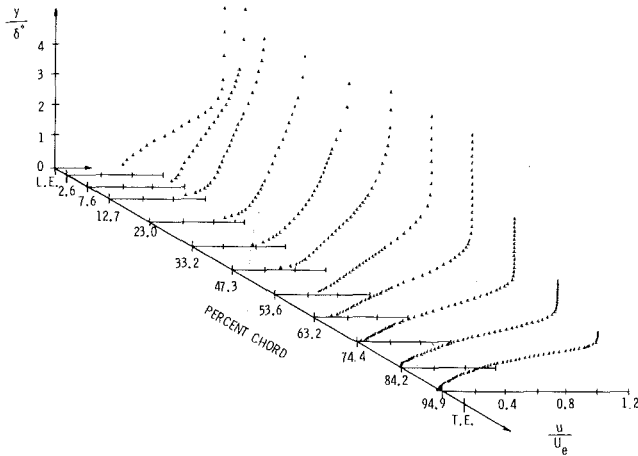


Fig. 3 Reconstructed suction surface boundary layers in outer variables

This gradient gradually becomes less severe with downstream distance and vanishes entirely near 80 percent chord. No pressure gradient is evident the last 20 percent of the chord, which indicates a possible separation region, that is, a region that cannot sustain a streamwise pressure gradient.

The measured suction surface boundary layers are presented in Fig. 2.² The inviscid regions show the effects of the normal pressure gradient. As noted earlier the influence of the normal pressure gradient was first removed by the method described by Zierke and Deutsch [9]. Note how the large curvature in the streamlines near the leading edge results in a highly curved inviscid region. The 95 percent confidence bands are quite small for all the boundary layers except in two regions. First, the thin boundary layer at 2.6 percent chord has a large velocity gradient near the surface; because of this large gradient, the sensitivity to probe placement is heightened, and the measurements are less repeatable. Second, as suspected, the boundary layer at 94.9 percent chord was separated, and the unsteadiness in the separation process resulted in larger error bands.

All of the measured suction surface boundary layers are turbulent. This implies that transition took place before the measurement station at 2.6 percent chord, which is not surprising considering the very large adverse pressure gradient near the leading edge. The separation of a laminar boundary layer under an adverse pressure gradient results in a free shear layer, which is unstable. The transition to turbulence takes place very rapidly. Once turbulent entrainment increases, the shear layer is enlarged which results in a pressure recovery and a rapid reattachment. Thus, the separation "bubble" can be quite short and close to the leading edge.

Although the transition takes place very close to the leading edge, the recovery process extends some distance downstream. This process can be seen from the mean-velocity profiles plotted in dimensionless outer variables. These plots are shown in Fig. 3 where the normal pressure gradients have been taken into account as described previously (see [9]). The recovery process can be seen to extend through the 2.6 and 7.6 percent chord locations by observing the shape of the profiles. As we will show later, the shape of the velocity profiles results in higher values of H_{12} during the recovery process. The local turbulence intensity profile at 2.6 percent chord also indicates recovery. This turbulent boundary layer was the only one measured in which there was a maximum value of local turbulence intensity away from the surface.

²Tabulated data will be supplied on request.

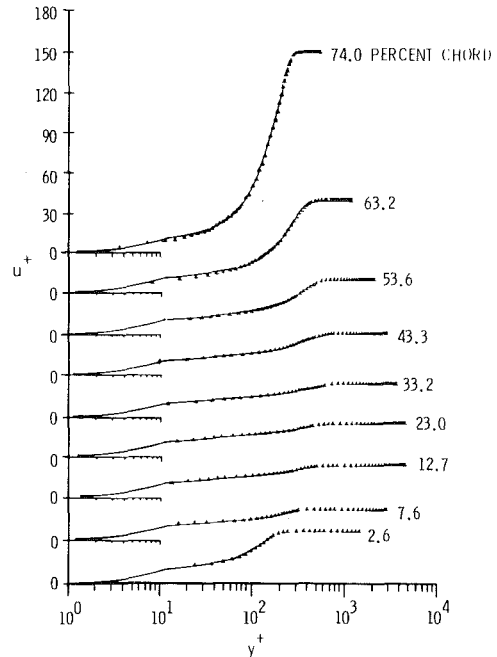


Fig. 4 Reconstructed suction surface boundary layers in inner variables

The mean velocity data were fit to the wall-wake equation of Coles [12]

$$\frac{u}{u_\tau} = \frac{1}{\kappa} \ln\left(\frac{y u_\tau}{\nu}\right) + C + \frac{\Pi}{\kappa} W\left(\frac{y}{\delta}\right)$$

through a least-squares technique described by Zierke and Deutsch [9]. For a given boundary layer thickness, the technique simultaneously calculates the values of u_τ and Π that yield the best fit to the data. Figure 4 shows the velocity profiles in inner variables. The logarithmic region reaches a maximum and the wake region reaches a minimum at 12.7 percent chord. This seems to be a second indication of complete recovery from the leading edge separation "bubble." As we move farther downstream, Coles' wake parameter Π (which controls the size of the wake region) increases, and this results in a reduction in the extent of the logarithmic region. As separation is reached, the logarithmic region disappears and the wall-wake equation cannot be fit to the data. This conclusion was reached earlier by Simpson et al. [13], who found the law of the wall valid until intermittent separation (flows containing instantaneous flow reversals) was reached.

Although the influence of surface curvature cannot be extracted from the data, one must suspect that this influence is indeed present. The convex curvature on the suction surface ($0.01 < |\delta/R_c| < 0.2$) and the concave curvature on the pressure surface ($0.002 < |\delta/R_c| < 0.02$) have opposite effects on turbulent boundary layers. Ramaprian and Shivaprasad [14] show that convex curvature reduces the logarithmic region and increases the relative strength of the wake component. Except for the initial region of curvature, convex curvature increases the rate of growth of Re_θ and decreases C_f . Shivaprasad and Ramaprian [15] claim that the effects of convex curvature on the behavior of the turbulent boundary layer are even stronger than the effects of concave curvature at the same value of $|\delta/R_c|$. Their measurements showed that convex curvature reduces turbulence intensity and Reynolds shear stress. Measurements by So and Mellor [16], Gillis and Johnston [17], and Gibson et al. [18] agreed. These results indicate that for very strong convex curvature effects, regions can be found where turbulence cannot exist. Bradshaw

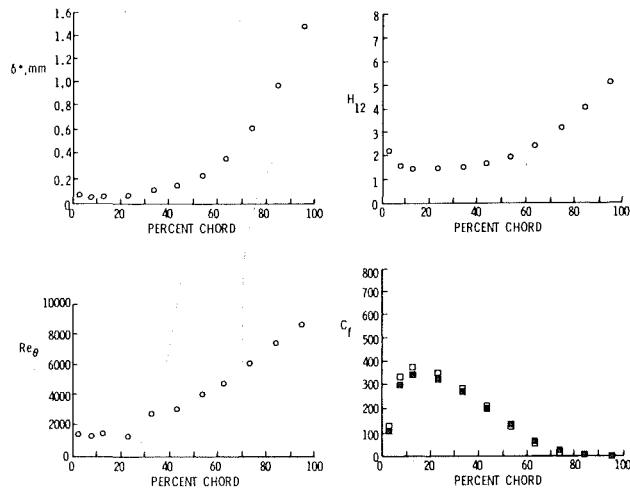


Fig. 5 Variation of displacement thickness, first shape factor, momentum thickness Reynolds number, and skin friction coefficient on the suction surface (○—obtained from a smoothed cubic spline fit; □—obtained from a least-squares fit of the wall-wake equation; ■—obtained from a smoothed cubic spline fit and the Ludwig-Tillman equation)

[19] showed that the behavior of the turbulent boundary layer is very sensitive to streamline curvature as mild as $|\delta/R_c| = 0.003$. He used an analogy between the effects of streamline curvature and buoyancy to estimate quantitatively the effect of curvature on mixing length distribution in the boundary layer. So [20] verified this buoyancy analogy mathematically. Shivaprasad and Ramaprian [15] made measurements which support the buoyancy analogy of Bradshaw [19] for mild convex curvature. For concave curvature, they found the buoyancy analogy useful only for values of $|\delta/R_c|$ near 0.01.

Figure 5 includes plots of δ^* , H_{12} , Re_θ , and C_f . These parameters were calculated from a smoothed cubic spline fit of the data, except for C_f , which was calculated from the least-squares fit of the data to the wall-wake equation. Values of H_{12} and Re_θ were also used to calculate C_f from the empirical equation of Ludwig and Tillman [21]. The displacement thickness increases gradually at first and then increases rapidly through separation. The plot of H_{12} indicates a turbulent boundary layer beginning near the leading edge. Recovery from the leading edge separation “bubble” results in an initial decrease of H_{12} . Separation of turbulent boundary layers is usually approximated using values of H_{12} near 2.2, which corresponds here to a suction surface location near 60 percent chord. Sandborn and Kline [22] proposed a relation for intermittent separation

$$H_{12} = 1 + \frac{1}{1 - \frac{\delta^*}{\delta}}$$

which yields 66.9 percent chord (corresponding to $H_{12} = 2.70$) as the location of intermittent separation for the data presented here. Values of C_f appear to be near zero at the leading edge which corresponds to the vanishing skin friction at the beginning of the leading edge separation “bubble.” C_f reaches a maximum after the boundary layer has totally recovered from the leading edge separation and then decreases as the trailing edge separation of the turbulent boundary layer is reached. C_f vanishes near 80 percent chord.

Defining separation as the entire process of the breakdown of boundary layer flow, Simpson et al. [1] quantified the various stages of separation with the instantaneous backflow near the wall. Incipient detachment (ID) occurs with 1 percent

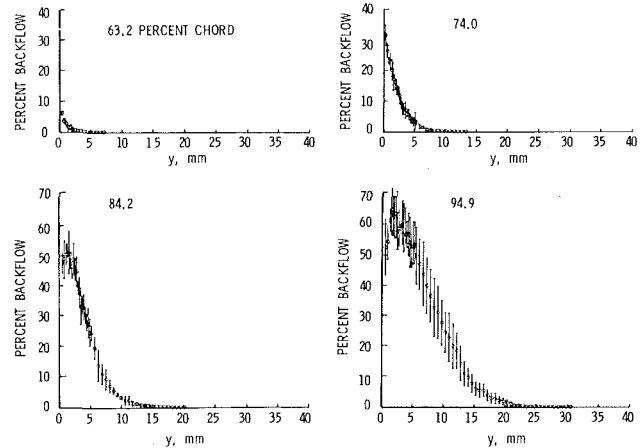


Fig. 6 Instantaneous backflow measurements of the 63.2, 74.0, 84.2, and 94.9 percent chord locations on the suction surface

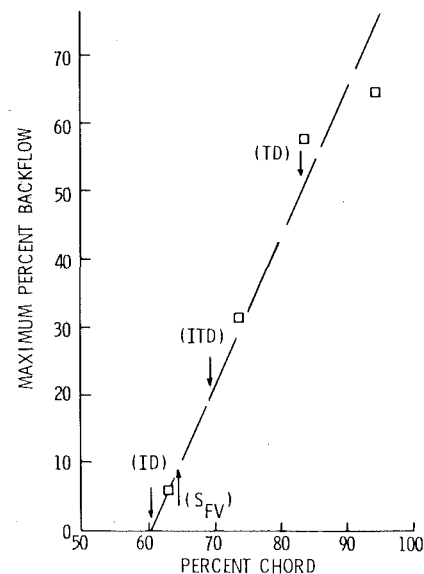


Fig. 7 Maximum percent backflow on the suction surface (ID = incipient detachment; ITD = intermittent transitory detachment; TD = transitory detachment; S_{FV} = separation point from flow visualization)

instantaneous backflow; intermittent transitory detachment (ITD) occurs with 20 percent instantaneous backflow; transitory detachment (TD) occurs with 50 percent instantaneous backflow; and detachment occurs when the wall shear stress becomes zero. The percent backflow is easily calculated as the portion of the measured velocity distribution that includes negative velocities. Figure 6 shows the instantaneous backflow measurements at the 63.2, 74.0, 84.2, and 94.9 percent chord locations. Figure 7 shows the maximum percent backflow as a function of percent chord. The sublimation flow visualization tests showed separation to occur at 65.6 ± 3.5 percent chord, and a comparison with the maximum instantaneous backflow data of Fig. 7 shows that flow visualization yields a value for separation which is only slightly downstream of incipient detachment. Locating turbulent separation by observing when H_{12} nears 2.2 also seems to indicate incipient detachment. We might note that although Simpson et al. [1] state that detachment and transitory detachment need not be at the same location, our skin friction calculations show that the chordwise locations of detachment and transitory detachment are quite close to one another.

Restrictions in applying the wall-wake equation in the

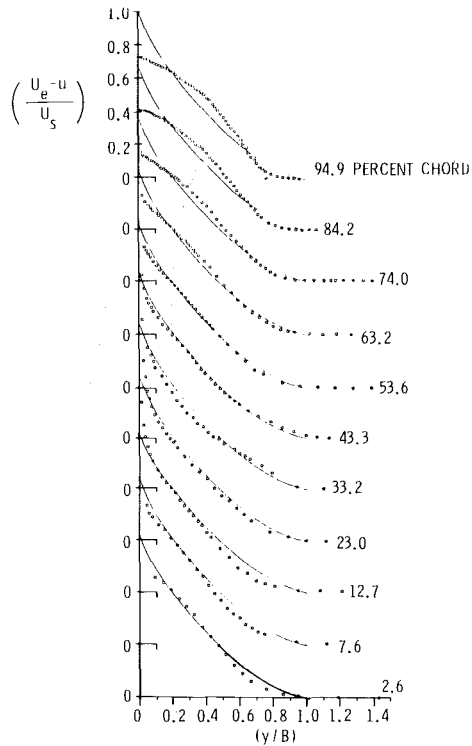


Fig. 8 Reconstructed suction surface boundary layers in defect form with Perry-Schofield similarity

vicinity of separation result from the velocity scale, u_τ , approaching zero. A vanishing u_τ leads to a vanishing logarithmic region, which would not cause concern if the separated flow profiles followed the law of the wake. Unfortunately, experimental data prove otherwise (see [1], for example). Perry and Schofield [23] developed a similarity defect law based on the maximum shear stress rather than the wall shear stress. The defect law was originally developed for attached boundary layers under moderate to strong adverse pressure gradients where $\tau_{\max}/\tau_w > 1.5$. The defect law is

$$\frac{U_e - u}{U_s} = 1.0 - 0.4 \left(\frac{y}{B} \right)^{1/2} - 0.06 \sin \left(\frac{\pi y}{2B} \right)$$

where

$$U_s = 8.0 \left(\frac{B}{L} \right)^{1/2} U_m$$

and

$$B = 2.86 \delta^* \left(\frac{U_e}{U_s} \right)$$

U_m is a velocity scale based on the maximum shear stress ($U_m = \tau_{\max}/\rho$) and L is the distance from the wall to τ_{\max} . The velocity scale U_s is found using the methodology that Clauser [24] used to determine u_τ . A half-power equation is used near the wall

$$\frac{u}{U_e} = 0.47 \left(\frac{U_s}{U_e} \right)^{3/2} \left(\frac{y}{\delta^*} \right)^{1/2} + 1.0 - \frac{U_s}{U_e}$$

Perry and Schofield [23] suggested using the defect law for the outer 90 percent of the boundary layer with the half-power equation forming the innermost portion of that defect law. They recommended the law of the wall as an inner wall matching condition. Schofield [25] extended the model to detached flows by suggesting that the similarity would hold provided that the origin of the normal coordinate has been moved from the wall to the location at which $u = 0$.

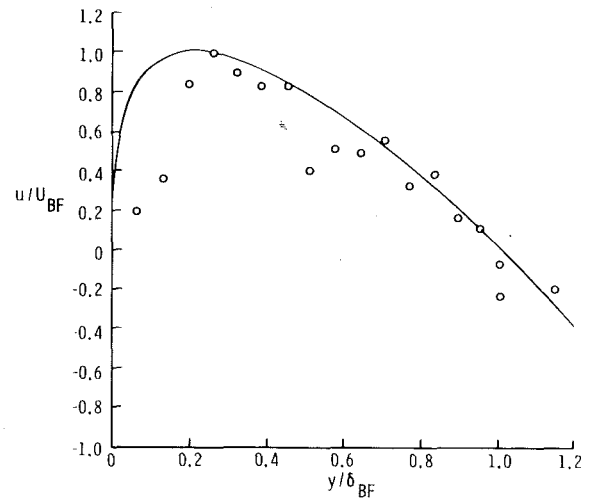


Fig. 9 Backflow similarity of the reconstructed boundary layer at 94.9 percent chord on the suction surface (the solid line represents the backflow similarity of data measured by Simpson et al. [1, 13])

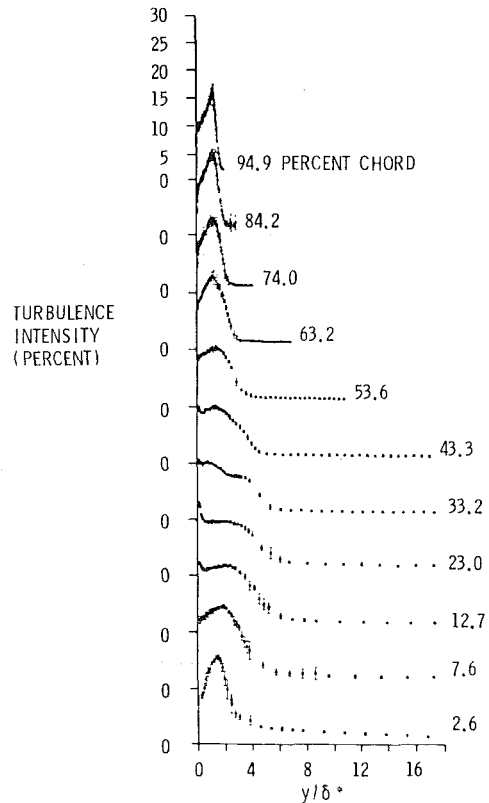


Fig. 10 Turbulence intensity data for the suction surface boundary layers

The suction surface boundary layers are plotted using the similarity relation of Perry and Schofield [23] in Fig. 8. In the outer 90 percent of the boundary layer, the similarity relation collapses the data quite well for chord locations upstream of the separated region. As the amount of instantaneous backflow increases, however, the data deviate more and more from the similarity relation. This deviation is in seeming contrast to the conclusions made by Schofield [25]. A close examination of his defect plots, however, shows similar trends in his analyzed data and the data shown in Fig. 8. The wall-wake equation appears to be the best of the similarity techniques for profiles approaching detachment.

No outer region similarity seems to exist downstream of detachment. Many researchers have attempted a law of the wake correlation without success (see [1], for example). For a turbulent boundary layer subjected to a streamwise pressure gradient, Mellor and Gibson [26] suggested replacing the shear velocity with a pressure velocity, $(\delta^*/\rho)(dp/dx)$, as the velocity scale. However, Schofield [27] has shown this scaling to be inadequate. Using the velocity scale corresponding to the maximum shear stress as suggested by Schofield [25] has been shown to give poor similarity in Fig. 8. Mehta and Goradia [28] had some success by assuming the outer region velocity profiles behave like a two-dimensional mixing layer. Their similarity variables were not found to give outer region similarity with the data measured here.

Similarity in the backflow region seems to show more promise. Simpson et al. [1] found good backflow similarity by normalizing the velocity by the maximum backflow velocity, and the distance from the wall by the distance to the maximum backflow velocity. Schofield [25] found that this backflow similarity could be improved by using the total backflow thickness as the length scale. Figure 9 shows this backflow similarity for the data at 94.9 percent chord. Despite the scatter, the backflow data seem to collapse quite well with the data measured by Simpson et al. [1, 13]. The only exceptions are the two data points closest to the wall: data for which the 95 percent confidence bands are larger than the magnitude of the mean velocity.

The turbulence intensity on the suction surface is shown for all 11 chord positions in Fig. 10. Recovery from the leading edge separation is apparent from the peaks in turbulence intensity that occur away from the surface for the 2.6 and 7.6 percent chord locations. These peaks also occur in the separation region from 63.2 through 94.9 percent chord. This shape reflects the movement in the location of the maximum mean-shear rate outward from the near-wall region.

Conclusions

Viscous calculations for turbomachinery applications have been handicapped by a lack of sufficiently detailed and precise data against which these calculation schemes can be compared. In order to help overcome this problem, we have presented measurements of the boundary layers and wakes (see Part 3) about a double circular arc, compressor blade in cascade. A two-dimensional, periodic cascade flow has been developed without the use of continuous side wall suction. This facility has allowed these measurements to be made with a nonintrusive LDV system. Despite the facts that the measured flow field was very complex and that only a one-component LDV system was used, the measurements presented here have led to an initial physical understanding of the cascade flow field. In this Part 2 of the study, we have presented detailed measurements of the suction surface flow field. Particular attention has been paid to the recovery from the leading edge separation bubble and to the separated region beginning near 60 percent chord.

The leading edge separation "bubble" on the suction surface was too small to be measured. Boundary layers measured downstream of this "bubble" are fully turbulent and the recovery process after reattachment extends downstream a distance of nearly 10 percent chord. The recovery process can be identified by the velocity profile shapes (including shape factors).

The nonequilibrium turbulent boundary layers downstream of the separation "bubble" follow the wall-wake equation of Coles [12] until detachment of the boundary layer is reached. These boundary layers also show good similarity using the defect law of Perry and Schofield [23] up to the location where instantaneous backflow is present. Similarity becomes worse

as the amount of instantaneous backflow is increased. No outer region similarity seems to exist downstream of detachment. In the backflow region, however, the data measured here seem to follow the backflow similarity shown by other researchers. Backflow similarity is found by using the maximum backflow velocity as the velocity scale and the total backflow thickness as the length scale.

Acknowledgments

We would like to extend our appreciation to NASA Lewis for supporting this work (NASA Grant No. NSG-3264) and to the NASA Lewis personnel for their advice and patience. A special thanks goes to Mr. Nelson Sanger who acted as the grant manager. Professor Robert E. Henderson and Professor Blaine R. Parkin gave valuable support throughout the research project. Other engineering and technical personnel at the Garfield Thomas Water Tunnel were instrumental in the success of the project. Finally, we give a special thanks to the many students who assisted us with the data acquisition and analysis.

References

- 1 Simpson, R. L., Chew, Y.-T., and Shivaprasad, B. G., "The Structure of a Separating Turbulent Boundary Layer. Part I. Mean Flow and Reynolds Stresses," *Journal of Fluid Mechanics*, Vol. 113, 1981, pp. 23-51.
- 2 McLaughlin, D. K., and Tiederman, W. G., "Biasing Correction for Individual Realization of Laser Anemometer Measurements in Turbulent Flows," *Physics of Fluids*, Vol. 16, No. 12, 1973, pp. 2082-2088.
- 3 Hoessel, W., and Rodi, W., "New Biasing Elimination Method for Laser-Doppler Velocimeter Counter Processing," *Review of Scientific Instrumentation*, Vol. 48, No. 2, 1977.
- 4 Giel, T. V., and Barnett, D. O., "Analytical and Experimental Study of Statistical Bias in Laser Velocimetry," *Laser Velocimetry and Particle Sizing*, H. D. Thompson and W. H. Stevenson, eds., Hemisphere, Washington, DC, 1979, pp. 86-99.
- 5 Edwards, R. V., "A New Look at Particle Statistics in Laser-Anemometer Measurements," *Journal of Fluid Mechanics*, Vol. 105, 1981, pp. 317-325.
- 6 Edwards, R. V., and Jensen, A. S., "Particle-Sampling Statistics in Laser Anemometers: Sample-and-Hold Systems and Saturable Systems," *Journal of Fluid Mechanics*, Vol. 133, 1983, pp. 397-411.
- 7 Johnson, D. A., Modarress, D., and Owen, F. K., "An Experimental Verification of Laser-Velocimeter Sampling Bias and Its Correction," *ASME Journal of Fluids Engineering*, Vol. 106, 1984, pp. 5-12.
- 8 Stevenson, W. H., Thompson, H. D., and Craig, R. R., "Laser Velocimeter Measurements in Highly Turbulent Recirculating Flows," *ASME Journal of Fluids Engineering*, Vol. 106, 1984, pp. 173-180.
- 9 Zierke, W. C., and Deutsch, S., "An Analysis to Facilitate the Interpretation of Boundary Layer Measurements," ARL/PSU TM 85-85, The Applied Research Laboratory, The Pennsylvania State University, May 25, 1985.
- 10 Mellor, G. L., and Wood, G. M., "An Axial Compressor End-Wall Boundary Layer Theory," *ASME Journal of Basic Engineering*, Vol. 93, No. 1, 1971, pp. 300-316.
- 11 Ball, C. G., Reid, L., and Schmidt, J. F., "End-Wall Boundary Layer Measurements in a Two Stage Fan," NASA TM 83409, June 1983.
- 12 Coles, D. E., "The Law of the Wake in the Turbulent Boundary Layer," *Advances in Applied Mechanics*, Vol. 1, 1956, pp. 191-226.
- 13 Simpson, R. L., Strickland, J. H., and Barr, P. W., "Features of a Separating Turbulent Boundary Layer in the Vicinity of Separation," *Journal of Fluid Mechanics*, Vol. 79, Part 3, 1977, pp. 553-594.
- 14 Ramaprian, B. R., and Shivaprasad, B. G., "Mean Flow Measurements in Turbulent Boundary Layers Along Mildly Curved Surfaces," *AIAA Journal*, Vol. 15, No. 2, 1977, pp. 189-196.
- 15 Shivaprasad, B. G., and Ramaprian, B. R., "Turbulence Measurements in Boundary Layers Along Mildly Curved Surfaces," *ASME Journal of Fluids Engineering*, Vol. 100, 1978, pp. 37-46.
- 16 So, R. M. C., and Mellor, G. L., "Experiment on Convex Curvature Effects in Turbulent Boundary Layers," *Journal of Fluid Mechanics*, Vol. 60, 1973, pp. 43-62.
- 17 Gillis, J. C., and Johnston, J. P., "Turbulent Boundary-Layer Flow and Structure on a Convex Wall and Its Redevelopment on a Flat Wall," *Journal of Fluid Mechanics*, Vol. 135, 1983, pp. 123-153.
- 18 Gibson, M. M., Verriopoulos, C. A., and Vlachos, N. S., "Turbulent Boundary Layer on a Mildly Curved Convex Surface - Part I: Mean Flow and Turbulence Measurements," *Experiments in Fluids*, Vol. 2, 1984, pp. 17-24.
- 19 Bradshaw, P., "The Analogy Between Streamline Curvature and Buoyancy in Turbulent Shear Flow," *Journal of Fluid Mechanics*, Vol. 26, 1969, pp. 177-191.

- 20 So, R. M. C., "A Turbulence Velocity Scale for Curved Shear Flows," *Journal of Fluid Mechanics*, Vol. 70, Part 1, 1975, pp. 37-57.
- 21 Ludweig, H., and Tillman, W., "Untersuchungen über die Wand-schubspannung in Turbulenten Reibungsschenkten," *Ing.-Arch.*, Vol. 17, 1949, pp. 288-299.
- 22 Sandborn, V. A., and Kline, S. J., "Flow Models in Boundary Layer Stall Inception," *ASME Journal of Basic Engineering*, Vol. 83, 1961, pp. 317-327.
- 23 Perry, A. E., and Schofield, W. H., "Mean Velocity and Shear Stress Distributions in Turbulent Boundary Layers," *Physics of Fluids*, Vol. 16, No. 12, 1973, pp. 2068-2074.
- 24 Clauser, F. H., "Turbulent Boundary Layers in Adverse Pressure Gradients," *Journal of Aeronautical Sciences*, Vol. 21, 1954, pp. 91-108.
- 25 Schofield, W. H., "On Separating Turbulent Boundary Layers," Mechanical Engineering Report 162, Department of Defense, Defense Science and Technology Organization, Aeronautical Research Laboratories, Sept. 1983.
- 26 Mellor, G. L., and Gibson, D. M., "Equilibrium Turbulent Boundary Layers," *Journal of Fluid Mechanics*, Vol. 24, Part 2, 1966, pp. 225-253.
- 27 Schofield, W. H., "Equilibrium Boundary Layers in Moderate to Strong Adverse Pressure Gradients," *Journal of Fluid Mechanics*, Vol. 113, 1981, pp. 91-122.
- 28 Mehta, J. M., and Goradia, S., "Experimental Studies of the Separated Flow Over a NASA GA(W)-1 Airfoil," *AIAA Journal*, Vol. 22, No. 4, 1984, pp. 552-554.
- 29 Deutsch, S., and Zierke, W. C., "The Measurement of Boundary Layers on a Compressor Blade in Cascade: Part I - A Unique Experimental Facility," *ASME JOURNAL OF TURBOMACHINERY*, Vol. 109, 1987, pp. 520-526.

The Measurement of Boundary Layers on a Compressor Blade in Cascade: Part 3—Pressure Surface Boundary Layers and the Near Wake

S. Deutsch

W. C. Zierke

The Applied Research Laboratory,
The Pennsylvania State University,
State College, PA 16804

Using the facility described in Part 1 [23], 11 detailed velocity and turbulence intensity profiles are obtained on the pressure surface of a double circular arc compressor blade in cascade. Two profiles are obtained in the near wake. Laminar boundary layer profiles, which agree well with profiles calculated from Falkner-Skan theory at the local pressure gradient, persist through 57.2 percent chord. The measurements indicate that the onset of transition occurs near 60 percent chord—a value in good agreement with the sublimation flow visualization studies (see Part 1). The lack of a logarithmic region in the data measured at the last chord position (97.9 percent chord) indicates that transition is not complete. The thin laminar boundary layers near the leading edge lead to some measurement problems, which are characterized by large turbulence intensities, in using the laser-Doppler velocimeter (LDV). Close examination of this problem shows that a combination of velocity-gradient broadening and a vibration of the LDV measurement volume causes an elevation of the measured turbulence levels. Fortunately only small errors in mean velocity are introduced. Because of the detached boundary layer on the suction surface, both of the near-wake velocity profiles exhibit regions of backflow. As expected, these near-wake velocity profiles do not exhibit similarity when tested against criteria derived for the far wake.

Introduction

Over the past two decades, techniques for computing complex flows have become increasingly more sophisticated. It is desirable that these techniques find their way into the turbomachinery design process. These numerical techniques are capable of very detailed predictions, but to be used with confidence, they should be tested against very detailed experimental data under typical flow conditions. As turbomachinery testing has generally been concerned with overall turbomachinery performance rather than with the details of the flow field, such data are lacking.

In order to provide some of the needed data, we used a one-component laser-Doppler velocimeter (LDV) to measure the two-dimensional periodic flow field about a double circular arc, compressor blade in cascade. Eleven boundary layer profiles were taken on both the pressure and suction surfaces of the blade; two profiles were taken in the near wake. All measurements were made at a chord Reynolds number Re_c of

500,000 (± 1 percent) and an incidence angle of 5 deg (that is, the stagnation point is on the pressure surface). The turbulence intensity in the incident flow was 0.18 percent. With an incidence angle of 5 deg, the pressure surface exhibits a large region of laminar flow (up to roughly 60 percent chord); transition on the pressure surface appears to be incomplete. The suction surface profiles appear to separate both at the leading edge and again somewhat beyond midchord; the leading edge separation apparently reattaches by 2.6 percent chord. Using the terminology of Simpson et al. [1], we found incipient detachment to occur at 60 percent chord on the suction surface and transitory detachment to occur at 83 percent chord. Inlet and outlet five-hole probe measurements and blade static-pressure measurements supplement the blade boundary layer profiles. Surface flow visualization, through sublimation, complements the transition and separation region data.

In Part 1 [23] of this three-part study, we described the cascade facility and the two-dimensional, periodic flow field established in it. In Part 2 [24], we described the LDV measurement system and presented and discussed the suction surface flow field data. In this, Part 3 of the study, we

Contributed by the Gas Turbine Division of THE AMERICAN SOCIETY OF MECHANICAL ENGINEERS and presented at the 32nd International Gas Turbine Conference and Exhibit, Anaheim, California, May 31–June 4, 1987. Manuscript received at ASME Headquarters February 24, 1987. Paper No. 87-GT-250.

describe the detailed LDV studies made on the pressure surface of the double circular arc blade and in the near wake.

Laser-Doppler Velocimeter

All blade boundary layer and near-wake measurements were made using a single-component LDV. The LDV system was described in detail in Part 2 of this study. For completeness, a brief description is also included here.

For all the LDV measurements, a specially designed traversing mechanism was used that matched the arc of motion of an optics cradle to that of the blade curvature. All measurements were made in the plane of the local blade normal. Prior to the LDV measurements, a reference distance was established by focusing the LDV control volume on an insert which securely fit over the center measuring blade. Repeatability in establishing a measurement reference was estimated to be ± 0.05 mm, and this uncertainty is probably the major source of scatter in the velocity data.

A two-watt, Spectra-Physics, argon-ion laser and standard TSI backscatter optical components were used for the measurements. The ellipsoidal measurement volume was reduced through the use of a (2.71:1) beam expander; the predicted measurement length in the normal to the blade direction was $37 \mu\text{m}$. While this length was small when compared to the length scales of the turbulent boundary layers on the suction surface, we shall show that it is roughly half the size of the displacement thickness of the initial laminar profile on the pressure surface. Where appropriate, optical shifting at 5 MHz was employed. Note that to measure close to the blade surface the optical cradle was tilted at an angle of roughly 1 deg. Silicon carbide particles having a mean diameter of $1.5 \mu\text{m}$ were used for laser seeding.

LDV data acquisition and reduction was accomplished by using a direct link to a Vax 11/782 computer. The mean velocity was taken as

$$u = \frac{1}{N} \sum_{n=1}^N u_n$$

the local turbulence intensity was taken as

$$\frac{u'}{u} = \frac{1}{u} \left[\frac{1}{N} \sum_{n=1}^N (u_n - u)^2 \right]^{1/2}$$

and the turbulence intensity was taken as u'/U_e . At each

chord position, profiles were defined by statistically treating the data for six individual experiments. Error bands, presented on LDV data plots, represent 95 percent confidence levels as determined by a Student's t test.

The preliminary data analysis is automated on the Vax 11/782 computer. The effect of the normal pressure gradient on the boundary layer profiles is accounted for first. Details of the technique are given by Zierke and Deutsch [2] and basically follow the approach suggested by Mellor and Wood [3] and Ball et al. [4]. Briefly the technique assumes that the profile may be represented as

$$u = u_{\text{meas}} - u_{\text{inv}} + U_e$$

so that the edge velocity U_e can be determined by extrapolating the outer inviscid flow u_{inv} to the wall (where $u = u_{\text{meas}} = 0$) in some reasonable manner.

Pressure Surface Boundary Layers

Boundary layer measurements were made at 11 chord locations on the pressure surface of the center cascade blade. To help interpret these velocity profiles, Fig. 1 shows the measurement locations along with the pressure distribution. The combination of continuously changing pressure and moderate surface curvature ($0.002 < |\delta/R_c| < 0.02$) signals a complicated nonequilibrium flow field. At the leading edge, for example, the large incidence angle (5 deg) results in a strong acceleration which promises a region of laminar flow. In the region from 8 percent chord to 62 percent chord, the flow is subjected to a mildly adverse gradient so that the onset of transition might be expected in this region. The subsequent favorable gradient, however, makes the eventual complete transition to turbulence problematic.

The measured pressure surface boundary layers are shown in Fig. 2.¹ The blade-to-blade pressure gradient affects the inviscid region of each profile. This pressure gradient varies from a strong, nonlinear gradient near the leading edge, where the streamlines have a large curvature, to a nominally zero gradient near the trailing edge. As previously noted, each profile was measured six times and the symbols in Fig. 2 represent velocity data averaged over the six tests. The error bands give 95 percent confidence levels as determined by the Student's t

¹Tabulated data will be supplied upon request.

Nomenclature

c = blade chord length
 C_f = skin friction coefficient = $\tau_w / (\rho U_e^2 / 2)$
 C_p = static pressure coefficient = $(p - p_1) / (\rho V_1^2 / 2)$
 H_{12} = first shape factor = δ^* / θ
 LE = leading edge
 L_p, L_s = pressure and suction surface length scales from the point of minimum velocity to a point where the velocity defect is $(U_e - u_{CL})/2$
 LDV = laser Doppler velocimetry
 n = data point index
 N = number of data points
 p = static pressure
 R_c = radius of curvature
 Re_c = blade chord Reynolds number = cV_1/ν
 Re_θ = momentum thickness Reynolds number = $\theta U_e/\nu$

TE = trailing edge
 u = streamwise velocity
 u' = root mean square of the turbulent velocity fluctuation
 U_e = velocity at the boundary layer or wake edge
 V = velocity
 y = coordinate normal to the blade surface or across the wake
 δ = boundary layer thickness (where $u = 0.99 U_e$)
 δ^* = displacement thickness = $\int_0^\infty (1 - u/U_e) dy$
 η = normalized distance across the wake

θ = momentum thickness = $\int_0^\infty (u/U_e)(1 - u/U_e) dy$
 ν = kinematic viscosity = $0.150 \text{ cm}^2/\text{s}$ for air
 ρ = fluid density = $1.205 \text{ kg}/\text{m}^3$ for air
 τ_w = wall or surface shear stress

Subscripts

CL = at the wake centerline
 inv = inviscid
 meas = measured
 n = data point index
 p = pressure surface
 s = suction surface
 1 = inlet (upstream five-hole probe measurement station)
 2 = outlet (downstream five-hole probe measurement station)

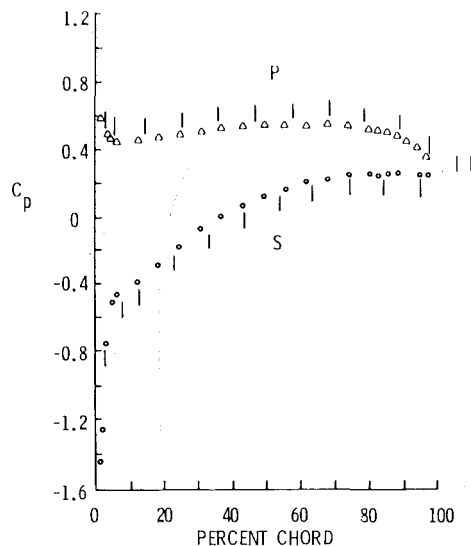


Fig. 1 Blade static-pressure distribution (the vertical line segments represent the locations of LDV measurements: P is the pressure surface; S is the suction surface)

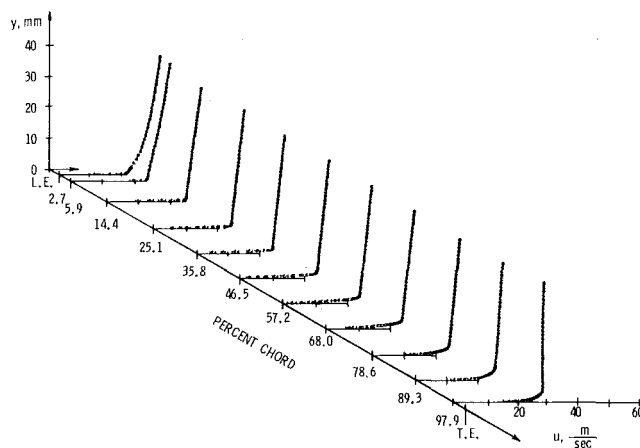


Fig. 2 Measured pressure surface boundary layers

test. These error bands are quite small, particularly in the inviscid regions. The exception appears at 2.7 percent chord where the boundary layer is so small that the LDV could only nominally penetrate the layer, and correspondingly, the resolution is poor.

The boundary layers were analyzed using the methods described by Zierke and Deutsch [2]. The influence of the normal pressure gradient was first removed. The reconstructed boundary layer data were then compared with a Falkner-Skan velocity profile (see [5]) at the local streamwise pressure gradient. For the velocity profiles measured near the trailing edge, an attempt to fit the results to the wall-wake equation of Coles [6] was also made. Finally, integral parameters were obtained both from a smoothed cubic spline fit of the data and from the Falkner-Skan solutions. The velocity profiles are replotted nondimensionally in Fig. 3. In spite of the influence of both curvature and changing pressure gradient on the flow field, the Falkner-Skan approximation appears to reasonably represent the mean velocity profiles through about 57.2 percent chord. At 68.0 percent chord and beyond, there is an increased thickening of the measured profiles relative to the Falkner-Skan correlation, which indicates transitional boundary layers.

Empirical relationships have been developed for the predic-

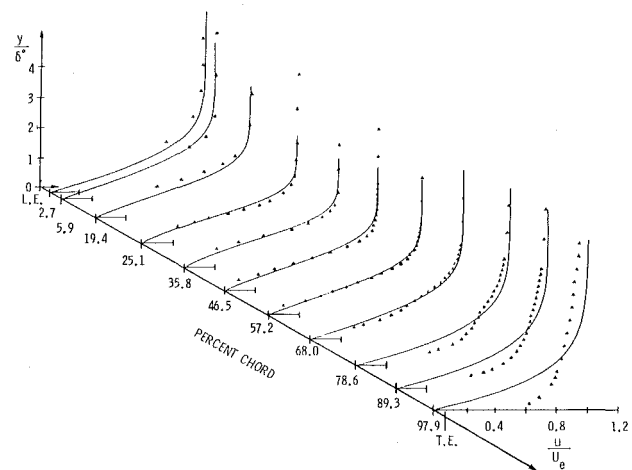


Fig. 3 Reconstructed pressure surface boundary layers in outer variables with Falkner-Skan approximations (solid lines)

tion of the beginning and end of transition; these relationships include the effects of free-stream turbulence and streamwise pressure gradient. Using the relationships of Abu-Ghannam and Shaw [7], for example, we predicted the onset of transition for the pressure surface data using the measured pressure distribution and a free-stream turbulence intensity (in the blade pack) of 1.5 percent. This turbulence intensity value was determined from hot-wire measurements at the edge of the boundary layer, close to the blade leading edge. Onset of transition was predicted to be at a momentum thickness Reynolds numbers (Re_θ) of 342, and comparison with the Re_θ found from the profiles put this onset at 47.8 percent chord. By onset here, we mean the first location at which the intermittency, as measured with a flush-mounted film probe for example, would be greater than zero. Because of the strong favorable gradient near the trailing edge, the scheme also predicted that a fully turbulent boundary layer would not develop on the pressure surface. There do not seem to be any empirical prediction schemes which include the effect of surface curvature. While convex curvature apparently has no effect on transition, the concave curvature of the pressure surface can promote the generation of Gortler vortices (see [8]), which can cause transition to occur earlier.

Sublimation flow visualization studies helped determine the transition point on the pressure surface. The average of five flow visualization tests placed the transition point at 64.2 ± 3.9 percent chord with 95 percent confidence. Figure 4 shows a plot of mean velocity, normalized by the edge velocity, for a fixed distance ($y=0.508$ mm) above the plate and a varying chord location. At this distance above the surface, the measurement volume is above the boundary layer for the first two chord locations. The decrease in mean velocity with chord location over the first half of the blade reflects the growth of the boundary layer relative to the fixed distance. The rapid rise in mean velocity near 60 percent chord indicates the onset of transition (see for example, [9]). Agreement with the flow visualization studies appears to be quite good. However, the simple empirically based calculations of Abu-Ghannam and Shaw [7] pick too small a chord value for the onset of transition. The fact that the mean velocity does not reach a constant (or decreasing) value with increasing chord location indicates that the transition process is not complete.

Integral parameters can also characterize transitional boundary layers. Plots of displacement thickness (δ^*), first shape factor (H_{12}), and momentum thickness Reynolds number (Re_θ) are shown in Fig. 5. Also shown are values for the skin friction coefficient C_f . Most of the integral

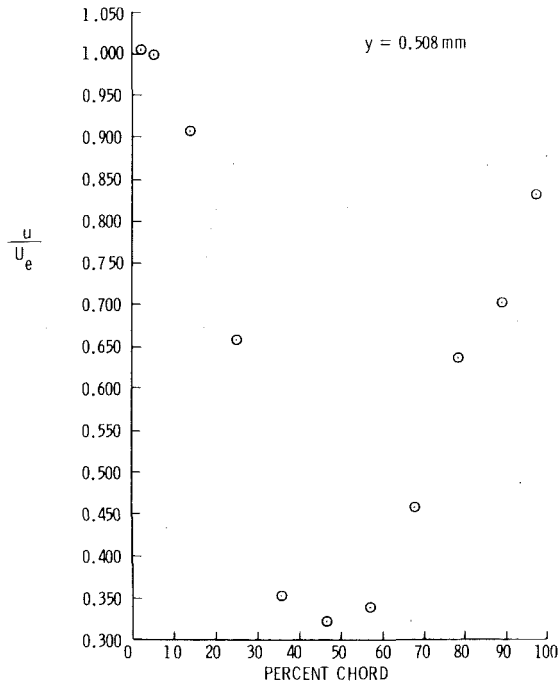


Fig. 4 Variation of velocity, 0.508 mm from the blade, on the pressure surface

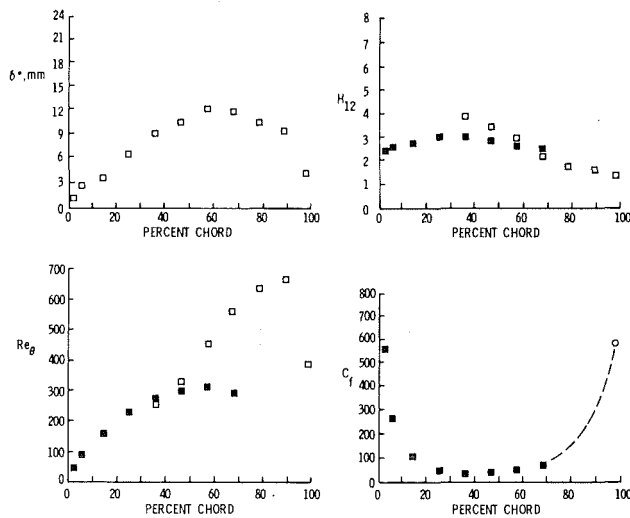


Fig. 5 Variation of displacement thickness, first shape factor, momentum thickness Reynolds number, and skin friction coefficient on the pressure surface (□—obtained from a smoothed cubic spline fit; ■—obtained from a Falkner-Skan approximation, ○—obtained from a smoothed cubic spline fit and Ludweig-Tillman equation)

parameters shown in Fig. 5 were obtained from a smoothed cubic spline approximation. Because of the lack of near-wall measurements for some of the extremely thin layers, we felt that the values of momentum thickness obtained from the spline fit were not accurate, so that some values of H_{12} and Re_θ (as shown in Fig. 5) were calculated from the appropriate Falkner-Skan approximations. Note the large decrease in δ^* as the flow encounters the favorable pressure gradient near the trailing edge. H_{12} shows laminarlike values until just before the 68.0 percent chord location, at which point the values drop into the turbulent regime. The values of C_f are determined from the Falkner-Skan approximations. At the leading edge, the skin friction goes to infinity. In the transition regime, the C_f values, although known to increase, cannot be easily estimated. To indicate how large C_f might become near the trailing edge, a value based on the Ludweig-Tillman empirical

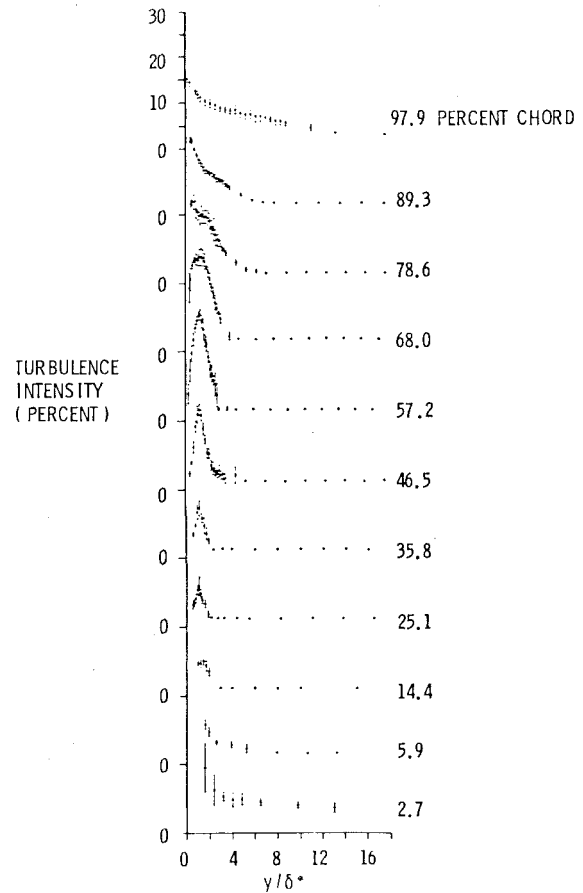


Fig. 6 Turbulence intensity data for the pressure surface boundary layers

expression (see [10]) is given for the 97.9 percent chord location. Use of the Ludweig-Tillman expression here is not strictly valid, as the boundary layer profile is probably not fully turbulent at 97.9 percent chord.

An attempt was made to fit the boundary layer profile at 97.9 percent chord to the wall-wake equation, but no logarithmic region was obtained. Purtell et al. [11] concluded that the logarithmic region seems to be an inherent characteristic of the turbulent boundary layer. That is, for fully developed turbulent boundary layers, they found the extent of the logarithmic region to be roughly a constant fraction of the boundary layer thickness as Re_θ was decreased. Murlis et al. [12] found strong evidence for the validity of the logarithmic law of the wall, at zero pressure gradient, for Re_θ values as low as 700, while Smits et al. [13] found a logarithmic region, for favorable pressure gradients, at Re_θ as low as 261. Since no logarithmic region was found for the boundary layer at 97.9 percent chord, it must be concluded that either the boundary layer was not fully turbulent at a Re_θ of 388, or (less likely) that the logarithmic region was so small that it could not be detected.

Turbulence intensity data for the pressure surface boundary layers are shown in Fig. 6. As the Falkner-Skan approximation has been shown to be reasonable for the profiles to 57.2 percent chord, the large turbulence intensities near the wall are disturbing. A typical profile of the skewness versus y/δ^* , which is shown for the 5.9 percent chord location in Fig. 7, adds considerably to the problem in that this profile might reasonably resemble the shape of a skewness profile one might expect to find from measurements of a turbulent boundary layer.

This problem was examined in some detail. Using both calibrated hot-wire probes in the boundary layer and un-

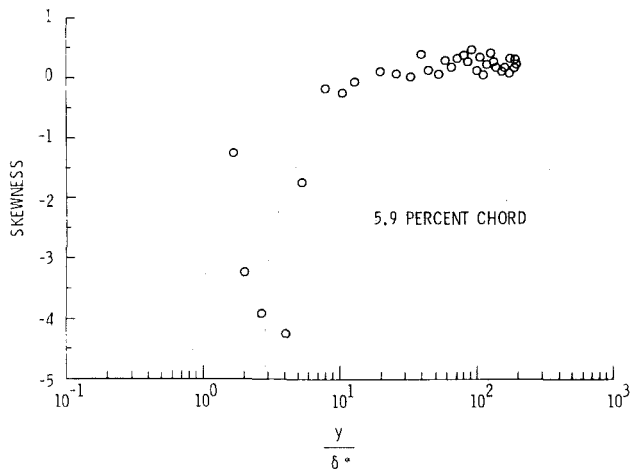


Fig. 7 Skewness distribution for the pressure surface boundary layer at 5.9 percent chord

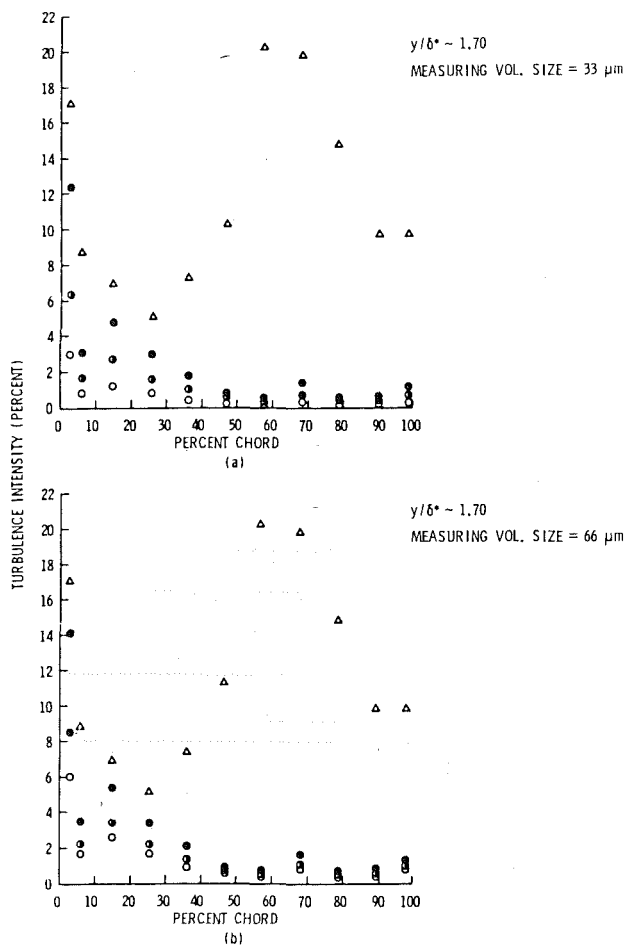


Fig. 8 Pressure surface turbulence intensities at $y/\delta^* \sim 1.70$, both measured data and data estimated by mean-velocity-gradient broadening and measurement volume vibration (Δ —measured data; \circ —vibration amplitude of $0 \mu\text{m}$; \circ —vibration amplitude of $25.4 \mu\text{m}$; \bullet —vibration amplitude of $50.8 \mu\text{m}$)

calibrated hot films flush-mounted on the surface, we determined that the profiles near the leading edge were indeed laminar. Typically, at the edge of these leading edge boundary layers, the intensity was found to be near 1.5 percent. The difference between this value and the 0.18 percent found in the approach flow is probably due to the interaction of the flow with the blade pack. Having shown the boundary layers to be laminar, we next suspected that the intensity measurements

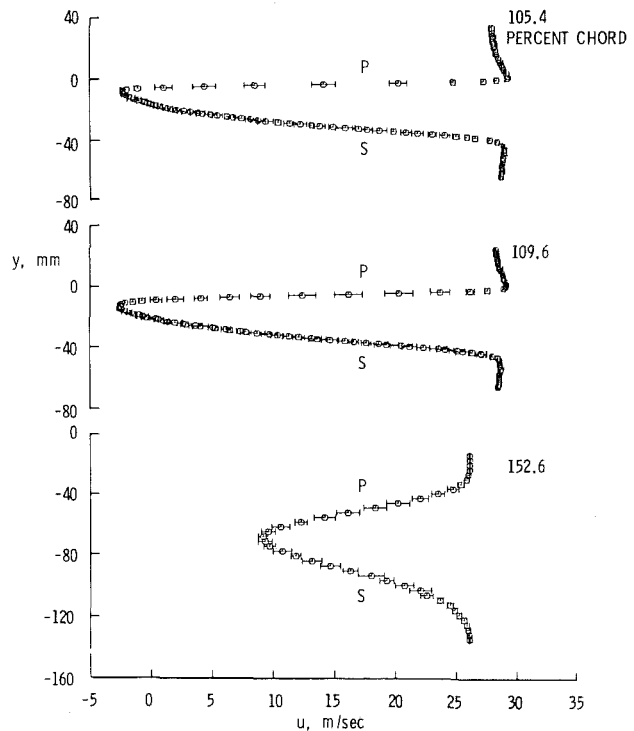


Fig. 9 Measured wakes (the wakes at 105.4 and 109.6 percent chord were measured with the LDV, while the wake at 152.6 percent chord was measured with a five-hole probe: P is the pressure surface; S is the suction surface)

might be contaminated by mean-velocity-gradient broadening. This problem has been considered previously by Edwards et al. [14], Goldstein and Adrian [15], and Kried [16]. For simplicity in the current study, the laser intensity was taken to be constant for the entire measurement volume. In the present case then, error estimates could be easily made by assuming the Falkner-Skan approximate profiles or by using the smoothed cubic spline fit. Similar results are obtained for either estimate. In Fig. 8(a), an estimate of the turbulence intensity caused by mean-velocity-gradient broadening is shown against percent chord for a measurement volume roughly as large as the volume estimated in the LDV section ($37 \mu\text{m}$). As it seemed plausible that the actual measurement volume might be larger than the volume estimated theoretically, we repeated the calculations for a measurement volume roughly twice that of the estimated volume. These results are shown in Fig. 8(b). Figures 8(a) and 8(b) show estimates for a constant y/δ^* of roughly 1.70; the measurement points are also given. It is clear from a comparison of the turbulence intensity calculated from the velocity-gradient broadening against the measured data, that the gradient broadening alone cannot account for the entire intensity. In addition, the skewness when calculated from an assumption of velocity-gradient broadening is much smaller than that observed experimentally.

As a second approach to the problem, we assumed that in addition to the gradient broadening problem, a small vibration may have contaminated the velocity signal. Calculations are again straightforward using either the spline fit or the Falkner-Skan approximations. Results for vibration amplitudes of $25.4 \mu\text{m}$ and $50.8 \mu\text{m}$ are again given in Fig. 8. With the exception of the points at 5.9 percent chord, which appear to have been biased by an inaccurate calculation of δ^* (see Fig. 5), the calculations agree reasonably well with the measurements for a measurement volume of $66 \mu\text{m}$ and a vibration amplitude of $50.8 \mu\text{m}$. Comparison between the measured and calculated skewness is also much closer. Some simple measurements with an accelerometer indicated that vibration amplitudes of this magnitude were not unreasonable

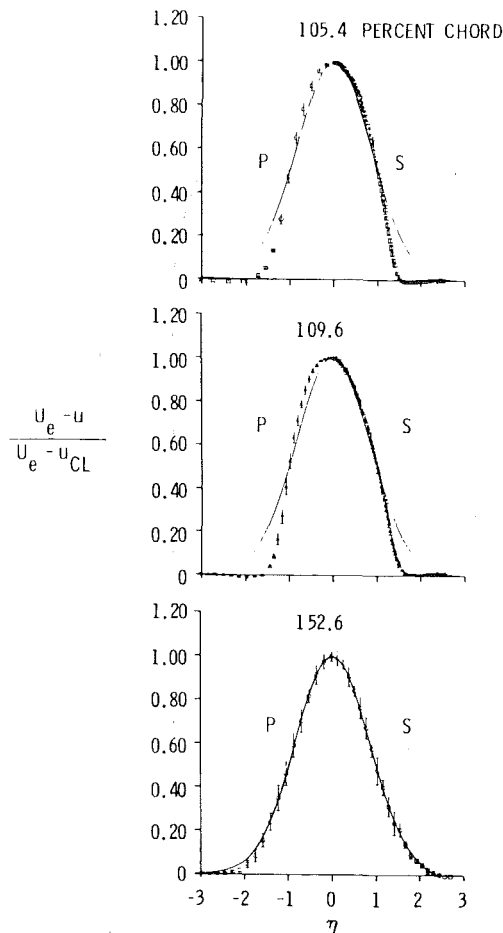


Fig. 10 Wakes in defect form with Gaussian similarity (solid lines) (P is the pressure surface; S is the suction surface)

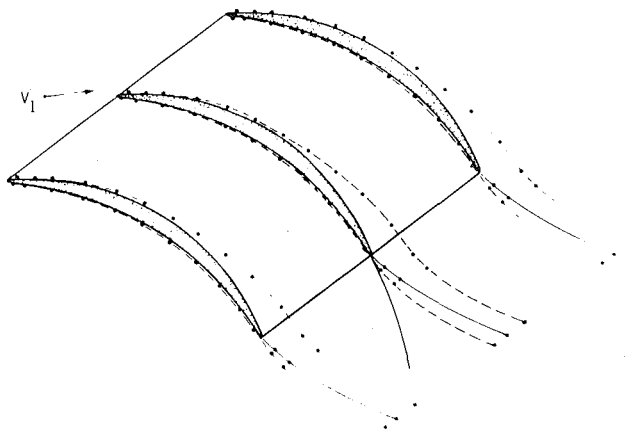


Fig. 11 Cascade blades with wake centerline and displacement thickness (the two near wakes were measured with respect to the extended pressure surface arc, which is shown)

to expect, so that a combination of velocity-gradient broadening with a vibration of the measurement volume seems a likely cause for the elevated turbulence levels. As shown in Figs. 8(a) and 8(b) (and as can be shown for the suction surface turbulent profiles), the effect becomes quite small as the boundary layer grows. In the present situation, the bias can probably be considered negligibly small for chord positions larger than about 25 percent.

Turbulence intensity profiles are shown for the transitioning boundary layers on the pressure surface in Fig. 6. The data show classical shape (see [9]) and agree reasonably well with the measurements of Wang et al. [17].

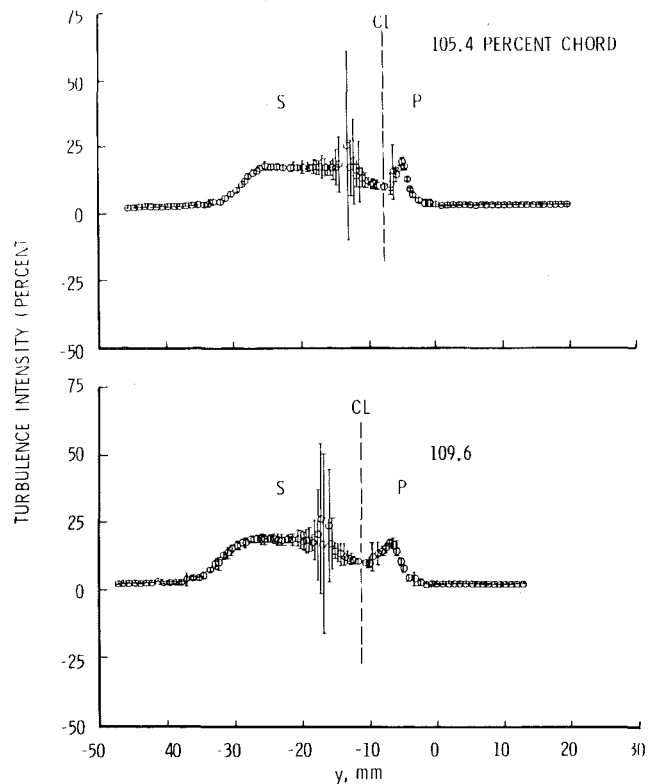


Fig. 12 Turbulence intensity data for the near wakes (P = pressure surface; S = suction surface; CL = wake centerline)

Wakes

Near-wake measurements were made at 105.4 percent chord and 109.6 percent chord using the LDV technique. Five-hole probes were used to measure the far wake at 152.6 percent chord. Figure 9 shows the data points and their 95 percent confidence bands for all three wake positions. The two near-wake profiles, which are quite similar, are very asymmetric because of the large difference in trailing edge boundary layer thicknesses on the two surfaces of the blade. The separation of the suction surface boundary layer (see Part 2) leads to negative mean velocities at the center of the near wake. Other researchers have also measured negative mean velocities in near wakes. Wadcock [18], using a flying hot wire, measured negative mean velocities in the near wake of an airfoil. Braden et al., [19] used an LDV to measure negative mean velocities in the near wake of an airfoil with confluent boundary layers.²

Wakes become similar only at distances far downstream of their source. A Gaussian distribution can be used to correlate these far-wake data. Lakshminarayana and Davino [20] suggested the correlation

$$\frac{U_e - u}{U_e - u_{CL}} = e^{-0.693\eta^2}$$

where η is the normalized distance across the wake. The suction and pressure sides of the wake use different length scales, L_s and L_p , L_s and L_p are the distances on the suction and pressure sides of the wake centerline from the point of minimum velocity to a point where the velocity defect is $(U_e - u_{CL})/2$. The far-wake data of Lakshminarayana and Davino [20] showed similarity away from the wake edge for both inlet guide vane wakes and stator blade wakes. This similarity was corroborated by Hobbs et al. [21] for distances greater than 30 percent axial chord downstream of the trailing edge of their compressor cascade blades. Figure 10 shows that

²Confluent boundary layers develop on an airfoil with leading edge slats or trailing edge flaps, which causes the boundary layers from the various surfaces to interact.

our wake data have Gaussian similarity in the far wake. However, the two near-wake profiles exhibit no similarity.

Integral parameters can be calculated from the wake velocity profiles. Using the location of the wake centerline and displacement thicknesses on either side of the centerline, the displacement surface can be drawn as seen in Fig. 11. The curvature of the displacement surface in the near-wake region can be explained by the pressure difference of the two blade surfaces. The location of the displacement surface in the far-wake region can be partly explained by the large amount of separation on the suction surface of the neighboring blades. However, another explanation for this curvature of the displacement surface in the far-wake region is the confinement of the far wakes between the two tailboards (see Part 1). The effects of the tailboards must be taken into account when considering this displacement surface for wake modeling.

Turbulence intensity profiles are presented for the two near wakes in Fig. 12. As with the turbulence intensity profiles in the separating boundary layers, the turbulence intensity peaks are displaced outward, essentially tracking the regions of large mean-velocity gradients. These data, although more detailed, are quite similar to the data of Hah and Lakshminaraya [22] for the near wake of an isolated airfoil.

Conclusions

Viscous calculations for turbomachinery applications have been handicapped by a lack of sufficiently detailed and precise data against which these calculation schemes can be compared. In order to help overcome this problem, we have presented measurements of the boundary layers and wakes about a double circular arc, compressor blade in cascade. A two-dimensional, periodic cascade flow has been developed without the use of continuous side wall suction. This facility has allowed these measurements to be made with a nonintrusive LDV system.

Despite the facts that the measured flow field was very complex and that only a one-component LDV system was used, the measurements presented here have led to an initial physical understanding of the cascade flow field. Regions of laminar flow, transition, recovery from a leading edge separation "bubble," nonequilibrium turbulent flow, separated flow, and near-wake flow have all been investigated. Prediction of a flow field that includes all these flow regions will be a severe test for any viscous computational technique.

Despite the varying streamwise pressure gradient, the laminar velocity profiles near the leading edge on the pressure surface show reasonable agreement with Falkner-Skan velocity profiles (computed at the same streamwise pressure gradient). Transition was identified through a departure of the measured profile shape from the Falkner-Skan profile shape, or through the boundary layer shape factors. Sublimation flow visualization tests agree well with the position of the transition region, but empirical relationships predict onset of transition somewhat early. Transition on the pressure surface was incomplete.

A problem was encountered with the LDV measurements in the extremely thin laminar boundary layers on the pressure surface. Large turbulence intensities were indicated. This problem was traced to a combination of mean-velocity-gradient broadening and measurement volume vibration. Turbulence intensity profiles in the transitional and turbulent boundary layers were not affected.

The near-wake velocity profiles are asymmetric and include negative mean velocities at the wake center. These profiles do not show the Gaussian similarity shown in the far-wake profile measured with a five-hole probe.

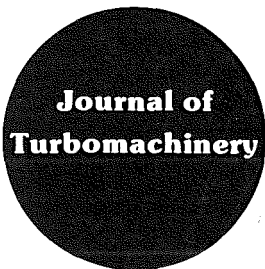
Acknowledgments

We would like to extend our appreciation to NASA Lewis

for supporting this work (NASA Grant NSG-3624) and to the NASA Lewis personnel for their advice and patience. A special thanks goes to Mr. Nelson Sanger who acted as the grant manager. Professor Robert E. Henderson and Professor Blaine R. Parkin gave valuable support throughout the research project. Other engineering and technical personnel at the Garfield Thomas Water Tunnel were instrumental in the success of the project. Finally, we give a special thanks to the many students who assisted us with the data acquisition and analysis.

References

- 1 Simpson, R. L., Chew, Y.-T., and Shivaprasad, B. G., "The Structure of a Separating Turbulent Boundary Layer. Part I. Mean Flow and Reynolds Stresses," *Journal of Fluid Mechanics*, Vol. 113, 1981, pp. 23-51.
- 2 Zierke, W. C., and Deutsch, S., "An Analysis to Facilitate the Interpretation of Boundary Layer Measurements," ARL/PSU TM 85-85, The Applied Research Laboratory, The Pennsylvania State University, May 25, 1985.
- 3 Mellor, G. L., and Wood, G. M., "An Axial Compressor End-Wall Boundary Layer Theory," *ASME Journal of Basic Engineering*, Vol. 93, No. 1, 1971, pp. 330-316.
- 4 Ball, C. L., Reid, L., and Schmidt, J. F., "End-Wall Boundary Layer Measurements in a Two Stage Fan," NASA TM 83409, June 1983.
- 5 Falkner, V. M., and Skan, S. W., "Some Approximate Solutions of the Boundary Layer Equations," *Phil. Mag.*, Vol. 12, No. 7, 1931, pp. 865-896.
- 6 Coles, D. E., "The Law of the Wake in the Turbulent Boundary Layer," *Advances in Applied Mechanics*, Vol. 1, 1956, pp. 191-226.
- 7 Abu-Ghannam, B. J., and Shaw, R., "Natural Transition of Boundary Layers—the Effects of Turbulence, Pressure Gradient, and Flow History," *Journal of Mechanical Engineering Science*, Vol. 22, No. 5, 1980, pp. 213-228.
- 8 Gortler, H., "Über eine dreidimensionale Instabilität laminarer Grenzschichten an konkaven Wänden," *Nachr. Ges. Wiss. Göttingen, Math. Phys. Klasse*, New series 2, No. 1, 1940.
- 9 Klebanoff, P. S., Tidstrom, K. D., and Sargent, L. M., "The Three-Dimensional Nature of Boundary-Layer Instability," *Journal of Fluid Mechanics*, Vol. 12, No. 1, 1962, pp. 1-34.
- 10 Ludweig, H., and Tillman, W., "Untersuchungen über die Wand-schubspannung in Turbulenten Reibungsschichten," *Int.-Arch.*, Vol. 17, 1949, pp. 288-299.
- 11 Purtell, L. R., Klebanoff, P. S., and Buckley, F. T., "Turbulent Boundary Layers at Low Reynolds Numbers," *Physics of Fluids*, Vol. 24, 1982, pp. 802-811.
- 12 Murlis, J., Tsai, H. M., and Bradshaw, P., "The Structure of Turbulent Boundary Layers at Low Reynolds Numbers," *Journal of Fluid Mechanics*, Vol. 122, 1982, pp. 13-56.
- 13 Smits, A. J., Matheson, N., and Joubert, P. N., "Low Reynolds-Number Turbulent Boundary Layers in Zero and Favorable Pressure Gradients," *Journal of Ship Research*, Vol. 27, No. 3, 1983, pp. 147-157.
- 14 Edwards, R. V., Angus, J. C., French, M. J., and Dunning, J. W., Jr., "Spectral Analysis of the Signal From the Laser Doppler Flowmeter: Time-Dependent Systems," *Journal of Applied Physics*, Vol. 42, No. 3, 1971, pp. 837-850.
- 15 Goldstein, R. J., and Adrian, R. J., "Measurement of Fluid Velocity Gradients Using Laser-Doppler Techniques," *The Review of Scientific Instruments*, Vol. 42, No. 9, 1971, pp. 1312-1320.
- 16 Kreid, D. K., "Laser-Doppler Velocimeter Measurements in Nonuniform Flow: Error Estimates," *Applied Optics*, Vol. 13, No. 8, 1974, pp. 1872-1881.
- 17 Wang, T., Simon, T. W., and Buddhavarapu, J., "Heat Transfer and Fluid Mechanics Measurements in Transitional Boundary Layer Flows," *ASME Journal of Engineering for Gas Turbines and Power*, Vol. 107, 1985, pp. 1007-1016.
- 18 Wadcock, A. J., "Simple Turbulence Models and Their Application to Boundary Layer Separation," NASA Contractor Report 3283, May 1980.
- 19 Braden, J. A., Whipkey, R. R., Jones, G. S., and Lilley, D. E., "Experimental Study of the Separating Confluent Boundary-Layer," NASA Contractor Report 3655, June 1983.
- 20 Lakshminarayana, B., and Davino, R., "Mean Velocity and Decay Characteristics of the Guide Vane and Stator Blade Wake of an Axial Flow Compressor," *ASME Journal of Engineering for Power*, Vol. 102, 1980, pp. 50-60.
- 21 Hobbs, D. E., Wagner, J. H., Dannenhoffer, J. F., and Dring, R. P., "Experimental Investigation of Compressor Cascade Wakes," ASME Paper No. 82-GT-299, 1982.
- 22 Hah, C., and Lakshminarayana, B., "Measurement and Prediction of Mean Velocity and Turbulence Structure in the Near Wake of an Airfoil," *Journal of Fluid Mechanics*, Vol. 115, 1982, pp. 251-282.
- 23 Deutsch, S., and Zierke, W. C., "The Measurement of Boundary Layers on a Compressor Blade in Cascade: Part 1—A Unique Experimental Facility," *ASME JOURNAL OF TURBOMACHINERY*, Vol. 109, 1987, pp. 520-526.
- 24 Deutsch, S., and Zierke, W. C., "The Measurement of Boundary Layers on a Compressor Blade in Cascade: Part 2—Suction Surface Boundary Layers," *ASME JOURNAL OF TURBOMACHINERY*, this issue.



A Note on Spanwise Mixing

P. W. James¹

1 Introduction

Adkins and Smith [1] consider five flow processes that result in streamsurfaces in turbomachinery blading departing from an axisymmetric shape. These authors derived a diffusion equation for the transport of any fluid property normal to the axisymmetric surfaces and also presented a method for the evaluation of the diffusion coefficient, which leads to good agreement between theory and experiment. The purpose of this note is less ambitious. It is to show that a diffusion equation for rothalpy can be derived in a semi-rigorous way through the process of passage-averaging.

2 Mathematical Formulation

The starting point for the analysis is an approximate form of the energy equation

$$\mathbf{W} \cdot \nabla I = 0. \quad (2.1)$$

Here I is the rothalpy, defined by

$$I = h + \frac{1}{2} W^2 - \frac{1}{2} \Omega^2 R^2, \quad (2.2)$$

h is the static enthalpy, \mathbf{W} the total relative velocity in a frame of reference rotating about the machine axis with constant angular velocity Ω (see Fig. 1), and R is the radial coordinate. Equation (2.1) is a good approximation if the effects of viscosity and thermal conductivity in the gas are negligible. We are primarily concerned with the effect of spanwise mixing on the transport of rothalpy and since neither viscous nor thermal diffusion are major contributors to this process, the above equation is a good approximation.

The continuity equation

$$\nabla \cdot (\rho \mathbf{W}) = 0, \quad (2.3)$$

where ρ is the gas density, can be combined with equation (2.1) to give

$$\nabla \cdot (\rho \mathbf{W} I) = 0. \quad (2.4)$$

This equation is now passage-averaged – a process by which any flow variable Q , which depends on all three independent polar coordinates X , R , and θ , is rendered two-dimensional according to the equation²

$$\bar{Q}(X, R) = \frac{1}{\Delta\theta} \int_{\theta_a(X, R)}^{\theta_b(X, R)} Q(X, R, \theta) d\theta. \quad (2.5)$$

Here the overbar denotes passage-averaged value, $\theta = \theta_a$ and $\theta = \theta_b$ define the blade surfaces, and $\Delta\theta = \theta_b - \theta_a$. If there are N blades in the blade row then the blockage B can be defined by

$$B = N(\theta_b - \theta_a)/2\pi. \quad (2.6)$$

The passage-average of equation (2.4) is then

$$\frac{\partial}{\partial x} (BR \overline{\rho w I}) + \frac{\partial}{\partial r} (Br \overline{\rho u I}) = 0, \quad (2.7)$$

where x and r are “leaned” coordinates (to allow for blades with non-radial leading and trailing edges) and w and u are the components of \mathbf{W} in these directions (see Fig. 1). Making use of the passage-average of the continuity equation, equation (2.7) may be written

$$\bar{W}_m \frac{\partial}{\partial m} \hat{I} = \frac{1}{BR\bar{\rho}} \frac{\partial}{\partial r} \left\{ BR \left[\frac{\overline{\rho u}}{\rho w} \overline{\rho w I} - \overline{\rho u I} \right] \right\}, \quad (2.8)$$

where W_m is the meridional velocity ($= (u^2 + w^2)^{1/2}$), $\partial/\partial m$ is the rate of change along a meridional streamline, defined as

$$\bar{W}_m \frac{\partial}{\partial m} \equiv \bar{w} \frac{\partial}{\partial x} + \bar{u} \frac{\partial}{\partial r}, \quad (2.9)$$

a tilde denotes density-weighted average, and a circumflex a flux-averaged, i.e.,

$$\bar{W}_m = \overline{\rho W_m} / \bar{\rho}, \quad \hat{I} = \overline{\rho w I} / \overline{\rho w} = \tilde{w} I / \tilde{w}. \quad (2.10)$$

If we now introduce the density-weighted hade angle $\tilde{\lambda}$, defined by

$$\tan \tilde{\lambda} = \bar{u} / \bar{w}, \quad (2.11)$$

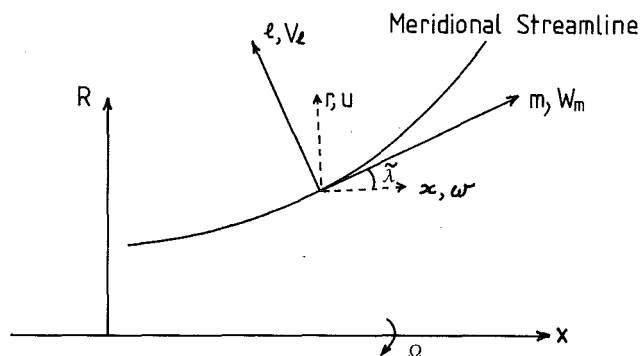


Fig. 1 The coordinate system

¹Senior Lecturer, Department of Mathematics and Statistics, Plymouth Polytechnic, Drake Circus, Plymouth, United Kingdom.

²For a more detailed discussion of the consequences of passage-averaging see the appendix to the paper by Jennions and Stow [2].

Contributed by the Gas Turbine Division for publication in the JOURNAL OF TURBOMACHINERY. Manuscript received by the Gas Turbine Division October 29, 1986.

then

$$\begin{aligned} \frac{\rho u}{\rho w} \overline{\rho w I} - \overline{\rho u I} &= \tan \tilde{\lambda} \overline{\rho w I} - \overline{\rho u I}, \\ &= \overline{\rho I (w \tan \tilde{\lambda} - u)}, \\ &= -\frac{1}{\cos \tilde{\lambda}} \overline{\rho V_\ell I}, \end{aligned} \quad (2.12)$$

where V_ℓ is the velocity normal to the axisymmetric blade-to-blade surfaces, i.e.,

$$V_\ell = -w \sin \tilde{\lambda} + u \cos \tilde{\lambda} = W_m \sin (\lambda - \tilde{\lambda}). \quad (2.13)$$

Equation (2.8) now becomes

$$\tilde{W}_m \frac{\partial}{\partial m} \hat{I} = -\frac{1}{BR\bar{\rho}} \frac{\partial}{\partial r} \left(\frac{BR}{\cos \tilde{\lambda}} \overline{\rho V_\ell I} \right). \quad (2.14)$$

This equation shows clearly that the transport of (flux-averaged) rothalpy depends on the spanwise velocity V_ℓ . It is an exact equation but to recast it in a more usable form we make some assumptions. First we assume that $\tilde{\lambda}$ does not vary significantly with r so that $\partial \tilde{\lambda} / \partial r$ may be taken to be zero. Secondly we assume that

$$\cos \tilde{\lambda} \frac{\partial}{\partial r} > \sin \tilde{\lambda} \frac{\partial}{\partial m},$$

from which it follows that

$$\frac{\partial}{\partial r} \approx \cos \tilde{\lambda} \frac{\partial}{\partial \ell},$$

where ℓ is in the direction normal to the meridional streamlines. Equation (2.14) then reduces to

$$\tilde{W}_m \frac{\partial}{\partial m} \hat{I} = -\frac{1}{BR\bar{\rho}} \frac{\partial}{\partial \ell} (BR\bar{\rho} \tilde{V}_\ell I) \quad (2.15)$$

Further, more speculative assumptions are discussed in the next section.

3 Mixing Length Hypothesis

Further progress with equation (2.15) can be made if V_ℓ , and hence the average $\tilde{V}_\ell I$, can be modeled. Adkins and Smith [1] consider various mechanisms which contribute to a nonzero V_ℓ . Their approach has been criticized recently by Gallimore and Cumpsty [3] who claim that turbulent diffusion is the most important mechanism rather than the "deterministic" mechanisms, for example secondary flow, considered in [1]. Very recently Wisler et al. [4] carried out experiments that show that both mechanisms can contribute significantly to the spanwise mixing process. Here, we assume that spanwise mixing is a process analogous to that of the mixing length theories of turbulence, in which the flux of the quantity being mixed is expressed as the local gradient of the mean,³ the precise mechanism that generates a nonzero V_ℓ being unspecified. We may then write

³Stow [5] gives an alternative method for deriving equation (3.5) from equation (2.15).

$$\tilde{V}_\ell I = \tilde{V}_\ell (\hat{I} + I') = \tilde{V}_\ell \hat{I} + \tilde{V}_\ell I' = \tilde{V}_\ell I', \quad (3.1)$$

where we have used the fact that, by definition, $\tilde{V}_\ell = 0$, and we have written

$$I = \hat{I} + I'. \quad (3.2)$$

The mixing length assumption gives

$$V_\ell I' = V_\ell L_I \frac{\partial \hat{I}}{\partial \ell}, \quad (3.3)$$

where L_I is a length scale in the ℓ direction over which \hat{I} is transported by V_ℓ . Pursuing the analogy with mixing length theory, we further assume that

$$V_\ell \propto -\frac{\partial \tilde{W}_m}{\partial \ell} L_I, \quad (3.4)$$

giving

$$\tilde{W}_m \frac{\partial \hat{I}}{\partial m} = \frac{1}{BR\bar{\rho}} \frac{\partial}{\partial \ell} \left(\epsilon_I BR\bar{\rho} \frac{\partial \hat{I}}{\partial \ell} \right), \quad (3.5)$$

where

$$\epsilon_I = -V_\ell L_I = \ell_I^2 \left| \frac{\partial \tilde{W}_m}{\partial \ell} \right|, \quad (3.6)$$

and ℓ_I is a mixing length to be prescribed. The assumptions that lead to equation (3.5) are speculative but it is worth noting that equation (3.4) relates the spanwise velocity to a velocity gradient, i.e., a vorticity component, as does classical secondary flow theory. It is also noted that the diffusion equation derived by Adkins and Smith [1] is a simplified version of equation (3.5).

Acknowledgments

The author wishes to thank Rolls-Royce Plc. for permission to publish this paper and Dr. P. Stow for his comments.

References

- 1 Adkins, G. C., and Smith, L. H., Jr., "Spanwise Mixing in Axial-Flow Turbomachines," *ASME Journal of Engineering for Power*, Vol. 104, 1982, pp. 97-110.
- 2 Jennions, I. K., and Stow, P., "A Quasi-Three-Dimensional Turbomachinery Blade Design System: Part 1—Throughflow Analysis," *ASME Journal of Engineering for Gas Turbines and Power*, Vol. 107, 1985, pp. 301-307.
- 3 Gallimore, S. J., and Cumpsty, N. A., "Spanwise Mixing in Multistage Axial Flow Compressors: Part 1—Experimental Investigation," *ASME JOURNAL OF TURBOMACHINERY*, Vol. 108, 1986, pp. 2-9.
- 4 Wisler, D. C., Bauer, R. C., and Okiishi, T. H., "Secondary Flow, Turbulent Diffusion, and Mixing in Axial-Flow Compressors," *ASME JOURNAL OF TURBOMACHINERY*, Vol. 109, 1987, pp. 455-482.
- 5 Stow, P., "Modelling Viscous Flows in Turbomachinery," NATO Advanced Study Institute on Thermodynamics and Fluid Mechanics of Turbomachinery, Turkey, 1984.